

DEVELOPMENT, MODELING, SIMULATION, AND TESTING OF A NOVEL PROPANE-
FUELED BRAYTON-GLUHAREFF CYCLE ACOUSTICALLY-PRESSURIZED RAMJET
ENGINE

By

Richard B. Bramlette

Submitted to the graduate degree program in Mechanical Engineering and the Graduate Faculty
of the University of Kansas in partial fulfillment of the requirements for the degree of Doctor of
Philosophy.

Chairperson Prof. Christopher Depcik

Prof. Peter TenPas

Prof. Xianglin Li

Prof. Ray Taghavi

Prof. Saeed Farokhi

Date defended: 29 April 2016

The Dissertation Committee for Richard B. Bramlette

certifies that this is the approved version of the following dissertation:

DEVELOPMENT, MODELING, SIMULATION, AND TESTING OF A NOVEL PROPANE-
FUELED BRAYTON-GLUHAREFF CYCLE ACOUSTICALLY-PRESSURIZED RAMJET
ENGINE

Chairperson Prof. Christopher Depcik

Date approved: 10 May 2016

Abstract

Sometime in the 1950s, Eugene Gluhareff built the first working pressure jet engine, a variation on the classical ramjet engine with a pressurized inlet system relying on sonic tuning that allowed operation at subsonic speeds. The propane-fueled engine was originally intended to provide tip-propulsion for helicopter rotors; thereby, eliminating the majority of engine torque transmission that necessitates the conventional helicopter's tail rotor system that adds weight, complexity, and is infamously prone to damage. In this application (and others), it was an unqualified success earning Gluhareff several government contracts to pursue this new engine design. Unfortunately, after decades of sales and research, Gluhareff passed away leaving behind no significant published studies of the engine or detailed analysis of its operation. The design was at serious risk of being lost to history.

This dissertation is intended to address that risk by studying a novel subscale modification of Gluhareff's original design that operates on the same principles. Included is a background of related engine types like the classical ramjet and variations of the pulsejet as well as how Gluhareff's pressure jet is distinct. The preliminary sizing of a pressure jet using closed-form expressions is discussed, as well as their limited utility.

To completely model the engine including the effects of combustion on the flow, computational fluid dynamics (CFD) including chemical kinetic modeling was necessary. To that end, a review of chemical kinetic theory is included. To aid selection of a model for propane oxidation (referred to as "chemical kinetic mechanisms"), a thorough review of the available experimental data and mechanisms is included, as well as an accounting of how these mechanisms

have been used with prior CFD models. Lastly, the method of selecting the most accurate of these mechanisms is discussed.

Following that is a review of the CFD package (Convergent Science's CONVERGE CFD) and the selection of parameters necessary to model the engine. To build experience with the software and verify capability, a series of graduated simulations were performed. First, a non-reactive mixing flow was modeled to approximate the characteristics of an air/exhaust gas mixing box feeding a single-cylinder engine test cell. This served to verify the capability of the software to track species concentrations, as well as their mixing in a fluid flow similar to that encountered in the pressure jet engine. Second, a series of simulations modeling quiescent propane/air mixtures in spherical chambers were performed to test the accuracy of the chosen chemical kinetic mechanisms against published experimental data for flame temperatures and propagation speeds for a range of equivalence ratios. These simulations showed good agreement with experimental data from the single-cylinder engine test cell, as well as the available experimental data on propane-air oxidation.

At that point, all that remained was to test the engine on a purpose-built test stand with the necessary instrumentation to gather experimental data and compare it to CFD simulations under the same conditions. The test stand recorded chamber pressure, exhaust speed (via a pitot/static system), exhaust gas temperature, core temperature, two surface temperatures and finally thrust force via a load cell. The manufacturing process of building the engines from stainless steel sheet is detailed, as well as the procedures for starting, operating, and shutting down the engine.

The engine CFD simulation showed significantly higher pressures and temperatures than those seen on the engine test stand, as well as higher overall engine performance. Despite these quantitative differences, however, the simulation did produce a wide range of qualitative results

that matched the experimental data well. The simulation further exhibited strong recirculation flows both confirming notions of the importance of the engine head geometry in stabilizing the engine, as well as presenting for the first time, the role of three-dimensional flow on the engine cycle. The most important of these results was the matching of engine operating frequency with the simulations predicting a frequency of 300 – 350 Hz and the experimental data showing 250 Hz. The frequency appeared to be largely driven by the Kadenacy Effect, which is typically observed in valveless pulsejets and, due to the similar tuned intake system, was expected in this pressurized ramjet engine. The inclusion of radiative heat transfer effects in the CFD simulations showed a reduction in error on the engine temperatures, pressures, and operating frequency.

The research effort lastly opens the door for further study of the engine cycle, the use of pressurized intakes to produce static thrust in a ramjet engine, the Gluhareff pressure jet's original geometry, and a wide array of potential applications. A roadmap of further study and applications is lastly detailed in the final chapter followed by a series of appendices containing the information necessary to recreate the CFD simulations and improve upon them. It is important to note that this dissertation represents the first steps toward reviving Eugene Gluhareff's vision of an efficient, low cost pressurized ramjet engine and openly invites further study of its principles. All those goals are not yet achieved, but through continued study, they can be.



For Eugene Michael Gluhareff

Acknowledgments

This dissertation is the tip of a long research effort that predates my own work by decades. It goes back to the 1940s and 1950s when Eugene Gluhareff had the spark of inspiration surrounding the concept of using the fuel as a working fluid – that this nontrivial source of energy was being largely ignored and wasted, could provide a significant boost in performance if it could just be released in the right way. Like the Nikola Tesla of acoustics and flame, his innovation and experimentation probed concepts that were decades ahead of his time and were in danger of being lost to history, slowly disintegrating in a thousand basement projects and file folders. His work made the concept of rotorcraft tipjet propulsion feasible and small enough to fit on your back. The research contained in this dissertation is as much about Gluhareff's work as it is to honor his legacy. For that reason, this research effort is dedicated to his memory and represents the first steps toward reviving the philosophy of the fuel as a working fluid in jet propulsion.

None of this could have been possible without the efforts of Irina Gluhareff (Eugene's daughter) and the rest of his family in protecting what remains of Eugene Gluhareff's notes, prototypes, and other archival materials. Irina, specifically, has been instrumental in providing us with information that was never widely published and may now finally be presented in an effort to preserve Eugene's innovative legacy. If it was not for her efforts to save all the information, hardware, and prestigious awards Eugene left behind, it may have all been lost to landfills and junkyards. The world would have been a darker, quieter place.

Dr. Ron Barrett of the KU Aerospace Engineering Department originally started the initial foundation of this effort in 1988 as an undergraduate student advised by Dr. Saeed Farokhi in investigating the tip-jet propulsion concept with theory and experimental data (included in the

Appendices). It was not until recently that computing power was able to feasibly integrate combustion modeling and computational fluid dynamics (CFD) to allow full three-dimensional, transient simulation of the pressure jet engine. Nevertheless, he kept all the information he could, and was also able to consult on the engine's theoretical operation based on private conversations he had with Eugene during a visit to his California workshop in 1990. His inspiration, passion for the engine, helicopters, and history helped shape this dissertation and often times steered it back on track with a rare understanding of the engine's processes we hope to bring to the larger academic and industrial communities.

Experimentally, this research effort would never have progressed beyond a fleeting idea without a semester's worth of summer funding provided by Dr. Bob Honea and KU's former Transportation Research Institute (TRI). The TRI provided a grant to start experimenting with subscale pressure jets which resulted in an early working prototype by the summer's end. That proved the concept was feasible and helped lay the foundation for this research effort.

Dr. Christopher Depcik took me on as a transplant from the Aerospace Engineering department, taught me everything I now understand about chemical kinetics and kinetics modeling, and made modeling of combustion in CFD a possibility. He put in a tremendous amount of work helping me analyze chemical kinetic mechanisms and navigating the sea of available propane oxidation models to find the most applicable and why. Prior to his involvement, this research effort was purely experimental as I considered the inclusion of combustion in CFD to be completely infeasible.

Daniel Lee and Saurav Mitra of Convergent Science, Inc, the company behind the CONVERGE CFD solver used to model the engine, provided a license for me to learn how to use the solver and analyze the data. They did more than just supply me with access. They were always

available and worked extensively to help me navigate the wealth of options, how best to employ their adaptive meshing scheme, and troubleshooting simulations. Saurav Mitra, specifically helped me extensively to finish the final engine simulation, speeding up my engine runtimes from five to six weeks to less than one. Coming from a minor background in Fluent, the CONVERGE solver was much easier to learn and use, faster to modify, and never crashed unexpectedly.

Paul Calnon of KU's Information and Telecommunication Technology Center (ITTC) which operate's KU's Advanced Computing Facility (ACF) was instrumental in further speeding up my CFD simulations. The ITTC houses shared computing assets for university research and graciously allowed me to access the cluster which sped up my simulation runtimes by at least a factor of three. Paul Calnon personally sat down with me and walked me through the remote access interface, scripting, and terminal commands which got me started.

Wes Ellison of KU's Aerospace Engineering Department was always available to help with instrumentation and generally troubleshooting the engine test stand. Without his help, it is likely I would not have had any high frequency experimental data to present. His experience with electronics has helped tremendously on many of my projects, so it is no surprise that he would have contributed to this one as well.

Dr. Elder Mendoza, a chemical kinetics researcher at the Pontifícia Universidade Católica do Rio de Janeiro in Brazil provided an invaluable service in regard to actually testing chemical kinetic mechanisms. The mechanisms themselves are large data files, many of which were no longer published online. Without his help, many of these data files of hundreds to thousands of individual reactions would have to have been retyped and formatted by hand. I have to thank him for preserving my sanity.

Lastly, I must acknowledge the tireless effort of many of my fellow undergraduate and graduate students that helped me over the years in tinkering in KU's "Hawkworks" Adaptive Aerostructures Laboratory. These students often helped by doing much of the mundane work in building extra parts and machining or holding cameras or writing down measurements. Operating the engine on the thrust stand was eventually simplified to the point that I could do it alone, but it was always easier and better in the company of faculty members and my fellow students who were, after all, so easily excited with the promise of hot dogs, popcorn, and marshmallows scorched in the exhaust of a subsonic ramjet.

Table of Contents

Chapter	Page
I. Introduction	1
A. Continuous and Pulsed Jet Propulsion.....	1
1. The Classical Ramjet.....	1
2. The Valved Pulse Jet Engine.....	3
3. The Reynst Jet	5
4. The Valveless Pulse Jet Engine.....	7
5. The Pressure Jet Engine	9
6. The Pressure Jet Engine in Relation to Other Jet Engines	15
B. Computational Fluid Dynamics (CFD).....	16
1. General Theory.....	16
2. Working with CONVERGE CFD	19
3. Modeling of Pulse Jet Engines with CFD	23
C. Scope of Work	27
II. Estimating the Initial Engine Parameters	28
A. Important Geometric Parameters	28
B. Geometric Sizing Relations	31
1. Empirical Assumptions for Geometric Approximations.....	31
2. Injector Approximations	32
3. Three-Stage Inlet Approximations	33
C. The Limited Utility of Closed Form Approximations	35
III. Selection of Chemical Kinetics.....	37
A. Theory of Chemical Kinetics.....	37
B. Propane Oxidation Experimental Data	39
1. Common Experimental Setups.....	39
2. Minimum Ignition Energy.....	41
3. Constant Volume Shock Tube Experiments	42
4. Constant Volume Spherical Bomb Reactors	55

5.	Coflow and Counterflow Reactors	59
6.	Jet-Stirred Reactors	72
C.	Propane Oxidation Chemical Kinetic Mechanisms	79
1.	Review of Available Chemical Kinetic Mechanisms	79
2.	CFD Parameters in Use with Chemical Kinetic Models.....	105
3.	Application of Chemical Kinetic Models.....	107
D.	Mechanism Analysis with Zero-Dimensional Simulation.....	110
1.	Zero-Dimensional Simulation of Chemical Kinetics	110
2.	Mechanisms in Comparison via Zero-Dimensional Simulations.....	117
IV.	CFD Modeling With CONVERGE	121
A.	Typical Model Parameters	121
1.	Boundary and Initial Conditions	121
2.	Turbulence Model CFD Parameters.....	123
3.	Combustion Model CFD Parameters	125
4.	Adaptive Mesh Refinement (AMR).....	125
B.	Modeling of Nonreactive Mixing Flow	129
1.	Exhaust Gas Recirculation (EGR).....	129
2.	Single-Cylinder Engine Stand and EGR Mixing Box.....	132
3.	CFD Model Parameters of EGR Mixing Flow.....	136
4.	Comparison of CFD Model Results to Experimental Data.....	138
C.	Modeling of Quiescent Premixed Propane/Air Combustion	147
1.	Chemical Kinetic Mechanisms.....	147
2.	Spherical Chamber Model Geometry and Simulation Parameters.....	148
3.	Simulation Results and Comparison to Experimental Data.....	150
D.	Pressure Jet Engine CFD Model Parameters	160
1.	Pressure Jet Model Geometry	160
2.	Pressure Jet Model CFD Parameters	165
3.	The Validity of a Symmetry Boundary Assumption.....	168
V.	Experimental Setup	174
A.	Engine Manufacturing Process	174
B.	Engine Test Stand	177

C.	Instrumentation and Data Logging	181
1.	Pressure Sensors and Voltage Relation.....	181
2.	Temperature Sensors and Camera Equipment	185
3.	Load Cell and Calibration	188
D.	Pressure Jet Engine Procedures	191
1.	Pressure Jet Engine Startup Procedure.....	191
2.	Pressure Jet Engine Operating Procedure	192
3.	Pressure Jet Engine Shutdown Procedure	193
E.	MATLAB Image Processing Analysis	194
VI.	Computational and Experimental Results	198
A.	Computational Data Results	198
1.	Simulation Parameters.....	198
2.	Pressure Distributions	201
3.	Velocity Magnitudes	211
4.	Temperature Distributions.....	223
5.	Equivalence Ratio and Species Distributions.....	237
B.	Experimental Data Results and Comparison to CFD	249
1.	Chamber Pressure.....	250
2.	Nozzle Exhaust Speed.....	253
3.	Temperature Measurements and Apparent Temperature Distributions	257
4.	Load Cell Thrust, Estimated Fuel Consumption, and TSFC.....	264
5.	The Effects of Radiative Heat Losses	269
6.	Mass Flow Rate through the Engine	275
VII.	Conclusions and Future Research	280
A.	Validity and Utility of Computational Models	280
1.	Relative Error of the Engine Simulation and Possible Sources of Error	280
2.	Sources of Error on the Engine Test Stand	284
3.	Effects of Engine Scaling on Pressure Jet Engines	285
B.	The Brayton-Gluhareff Cycle	291
1.	Sonic Lock and Acoustic Tuning.....	294
2.	Engine Shape and Internal Flow	295

C.	Future Research	300
1.	Further CFD Modeling.....	300
2.	Modifications to Increase Performance.....	302
3.	Minimum Sizing for Ignition Delay and Supersonic Operation	306
4.	Preheat Coil Coking	307
VIII.	Appendices.....	309
A.	Propane Chemical Kinetic Mechanism CHEMKIN Files	309
1.	Detailed Kinetic Mechanisms for Propane Oxidation.....	310
2.	Reduced Kinetic Mechanisms for Propane Oxidation	318
3.	Global Westbrook and Dryer One-Step Mechanism Code for Propane Oxidation	331
B.	Complete CFD Model Input Parameters.....	333
1.	Nonreactive Mixing Flow Simulations	333
2.	Reactive Constant Volume Bomb Simulations.....	384
3.	Brayton-Gluhareff Cycle Pressure Jet Simulations.....	403
C.	MATLAB Source Codes.....	431
1.	Brayton-Gluhareff Cycle Approximate Sizing	432
2.	Temperature Contour Image Processing and Analysis (IMG2IR.m).....	437
D.	Selected Original Production Gluhareff Engine Drawings.....	439
E.	G8-2 Pressure Jet Technical Handbook.....	454
F.	Example Calculation Workbook for GTS-15 Teaching Stand	514
IX.	References.....	554

I. Introduction

A. Continuous and Pulsed Jet Propulsion

Since its inception, the ramjet engine has reigned as the simplest form of the jet engine. Although it is cheap to produce, it has always suffered from one major drawback – it cannot produce efficient thrust at speeds below Mach 1 (the speed of sound). This has greatly limited their use to systems that can find other ways of accelerating while engineers and academics largely accepted the impossibility of a subsonic ram jet [1]. That assumption would be true if not for the existence of a largely forgotten ramjet cycle – the “Brayton-Glukhareff” cycle pressure jet. This design is, however, only one of many in the field of jet propulsion. Those most similar to the pressure jet are described in the following sections.

1. The Classical Ramjet

The classical ramjet engine is the simplest application of jet propulsion and relies solely on compressible fluid mechanics and thermodynamics to generate positive thrust via combustion. This engine design operates via the conventional Brayton Cycle that involves four typical stages – (0-1) Inlet compression, (1-2) Combustion, (2-3) Exhaust Expansion, and (3-0) Return to Initial Conditions (shown graphically in Figure 1). In this case, supersonic airflow is slowed to subsonic speed that increases the total pressure of the flow. It then enters the combustion chamber, mixes with a fuel, and combusts converting the chemical energy into added heat and pressure. This high-pressure flow is then supersonically expanded, which ideally lowers the pressure to ambient conditions at high speed resulting in a thrust force [1-3]. As long as there is sufficient ram air being compressed into the engine inlet, flow will continue toward the exhaust. As the ram compression drops with decreasing Mach number, the airflow no longer resists the flame front pushing forward

and a “flame-out” will occur. This mechanism disallows the use of a conventional ramjet at lower subsonic inlet Mach numbers.

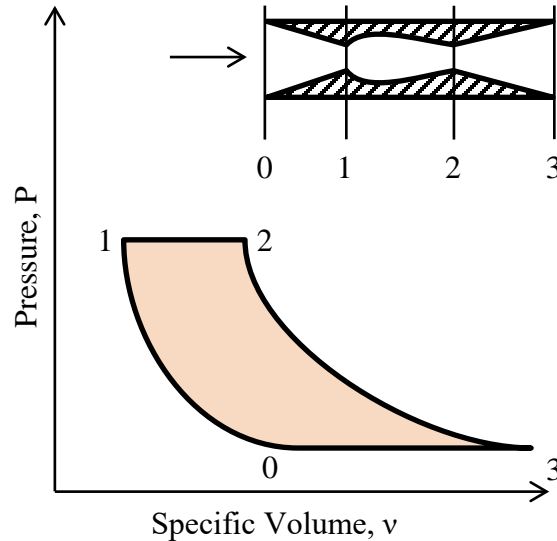


Figure 1: Conventional Brayton Engine Cycle for an Ideal Ramjet Engine

Despite this limitation, ramjet engines serve a significant niche in aerospace propulsion. Although they cannot produce positive subsonic thrust, they do provide a significant increase in fuel efficiency as compared to solid- and liquid-fueled rockets that may perform the same roles in similar altitude and Mach number regimes [1]. This typically results in vehicles with ramjets having an incrementally longer endurance and higher range than those relying on conventional rockets. Ramjet engines are, therefore, ideal candidates for high speed, low cost vehicles like supersonic cruise missiles, long-range interceptors, and reconnaissance aircraft.

Notable applications of the ramjet engine include the Lockheed X-7, D-21 “Tagboard” Drone, and Boeing CIM-10 BOMARC that all used the Marquardt Corporation’s large production ramjet engine designs. Also of note is the use of ramjet principles in the development of the Pratt and Whitney J58 used in the Lockheed SR-71 “Blackbird” aircraft. As the SR-71 accelerated to higher Mach numbers, ram compression from the inlet cone was used to provide extra bypass air that significantly augmented the engine’s thrust. [3, 4]

2. The Valved Pulse Jet Engine

Despite the ramjet engine's simplicity, the requirement of supersonic inlet Mach numbers significantly limits their application. An alternative design, the pulse jet, fills the potential role of a subsonic ramjet offering low cost, simple jet propulsion at low speeds. The first pulse jet engines were designed with a physical valve that quickly opened and closed during the engine cycle similar to the way a piston engine's intake valves open and close. The typical engine cycle involved (1) the inlet valves opening allowing intake of air, then (2) spray-mixing of fuel with the air. This is followed by (3) fuel combustion via a spark plug causing the inlet valves to close and (4) high pressure combustion gases escaping through a subsonic converging nozzle resulting in momentum thrust. Eventually the chamber pressure drops below the inlet pressure, the valves reopen, and the cycle repeats with fresh air [5]. This is illustrated in Figure 2.

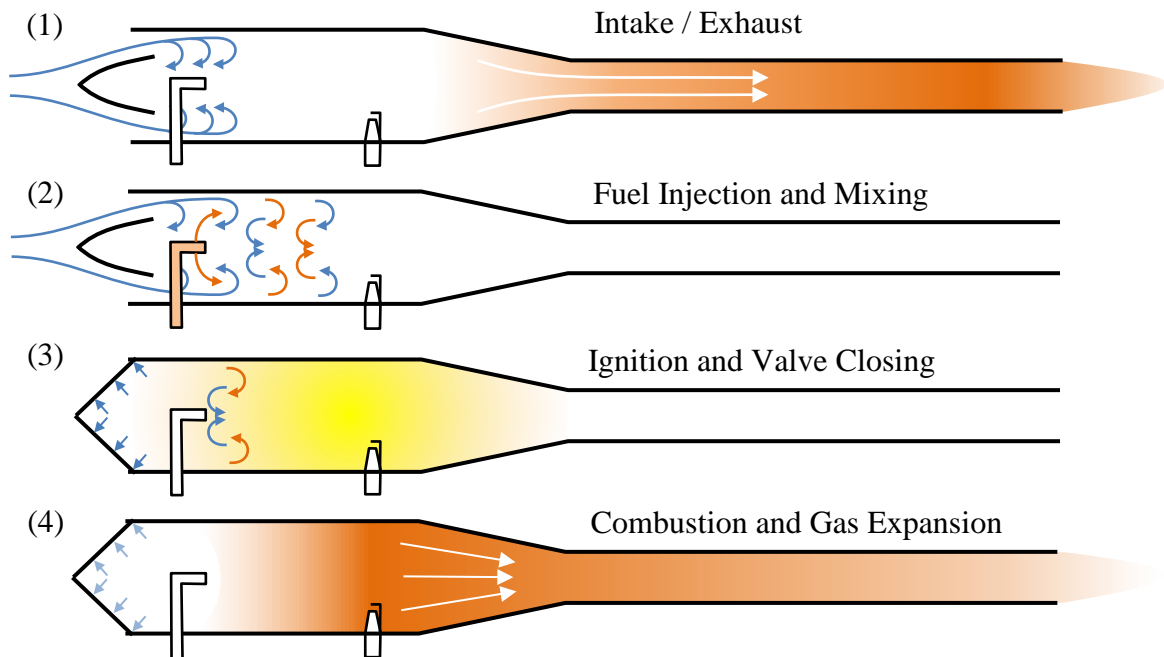


Figure 2: The Typical Valved Pulse-Jet Engine Cycle

The valved pulse jet was most notoriously used in the Second World War as the main propulsion system for the V-1 cruise missiles fielded by Germany. These aircraft were designed to be cheap and easy to manufacture while maintaining a high enough range to autonomously strike at Allied cities. Although the V-1 was designated in German as a “Vengeance Weapon” the Allies nick-named them “Buzz Bombs” due to the high-frequency, reverberating buzz caused by the pulse jet cycle as it flew past. In the decades following World War II, pulse jets were sold as hobbyist projects capitalizing on the “Jet Age.” Hobbyists eventually applied the pulse jet design to a wide range of projects including remote-control aircraft, bikes, and go-carts.



Figure 3: V-1 Cruise Missile (Top) and its Powerplant, the Argus As 014 Valved Pulse Jet Engine (Bottom), Images Taken by the Author at the National Museum of the US Air Force

Despite this wider applicability compared to ramjets, they suffer from a significant flaw – inlet valve fatigue. Because the inlet valve opens and closes often (approximately 200 Hz) and must endure brief high temperatures (over 2000 K), these thin, flat pieces of metal fatigue quickly and must be replaced often [6]. Multiple designs existed that attempted to simplify these physical valve mechanisms as summarized in detail by Diedrich [5] in the post-war period. The mechanism

used in the V-1 “flying bombs” for instance was the Schmidt valve (shown in Figure 4). This valve design used a sheet metal flap which closed against rib supports and automatically opened as the chamber pressure dropped. A similar mechanism is used in modern hobby engines but this series of flat sheets were replaced by a single radially-organized sheet commonly referred to as a “reed valve” (also shown in Figure 4). This single-piece valve uses flapping “petals” that open for a series of smaller, radially-arranged inlets.

Nevertheless, these modifications could not eliminate the problem of physical fatigue and this shortcoming remains today in valved pulse jet engines. The only means of eliminating this problem is to remove the mechanical valve assembly entirely but that requires alternative methods of preventing chamber pressure loss through the inlet structure.

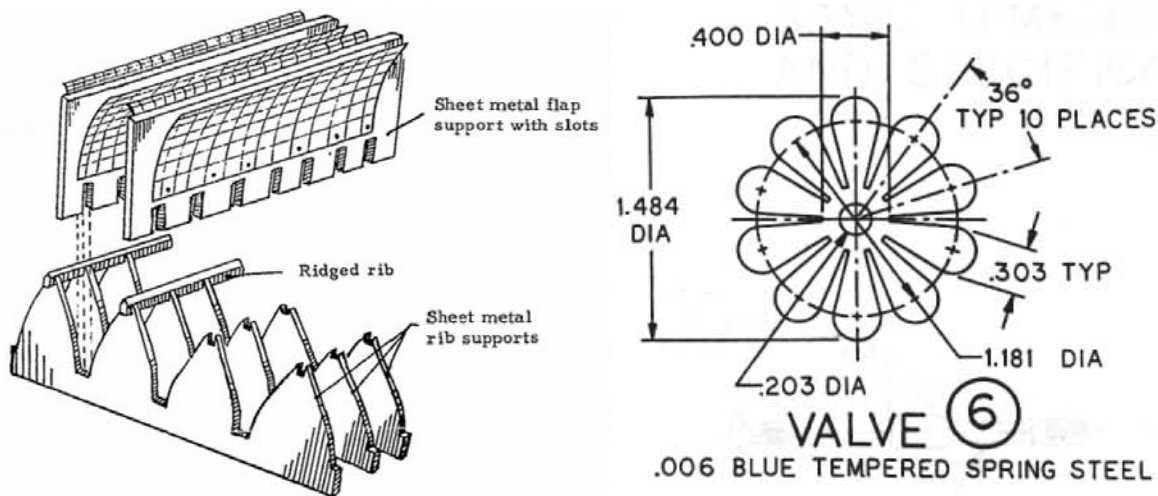


Figure 4: Schmidt Valve (Left) [5] and One Piece Reed Valve (Right) [7]

3. The Reynst Jet

The key to removing the mechanical valve from the pulse jet came from a simple jet engine developed by Francois Reynst. Instead of separate inlet and exhaust paths, it uses a single path for both. This “Reynst Jet” engine can be thought of as the common Helmholtz resonator (used to damp or otherwise control fluid acoustics) with an additional active combustion mechanism. This

engine is an enclosed chamber with an open combined inlet/outlet at one end sized such that the incoming air flow sets up an acoustic resonance with the internal flame front [5, 8].

Reynst was originally developing a pulsating heating device, and while the jet had “an impressive combustion intensity” [8], the design generally had a low combustion efficiency that made it an unlikely candidate for aerospace propulsion applications. [9] It also never found wide adoptance as a heating device due to the noise level during operation – a nontrivial factor for all jet engines, particularly those operating on tuned acoustic pressurization. For instance, the chamber Reynst originally tested stood one meter tall and apparently could be heard up to six miles away [8].

J.W. Porter continued Reynst’s work and developed closed-form models for the jet design. He found the frequency of a jet to be proportional to the chamber’s Helmholtz frequency:

$$\omega_H \propto \left[\frac{3\pi^2 \delta}{32 \mathbb{V}} \right] \quad (1)$$

where δ is the orifice diameter and \mathbb{V} is the chamber volume. [8] Porter verified his findings with high-speed Schlieren imaging that helped visualize the fluid structures involved in this heavily transient phenomenon.

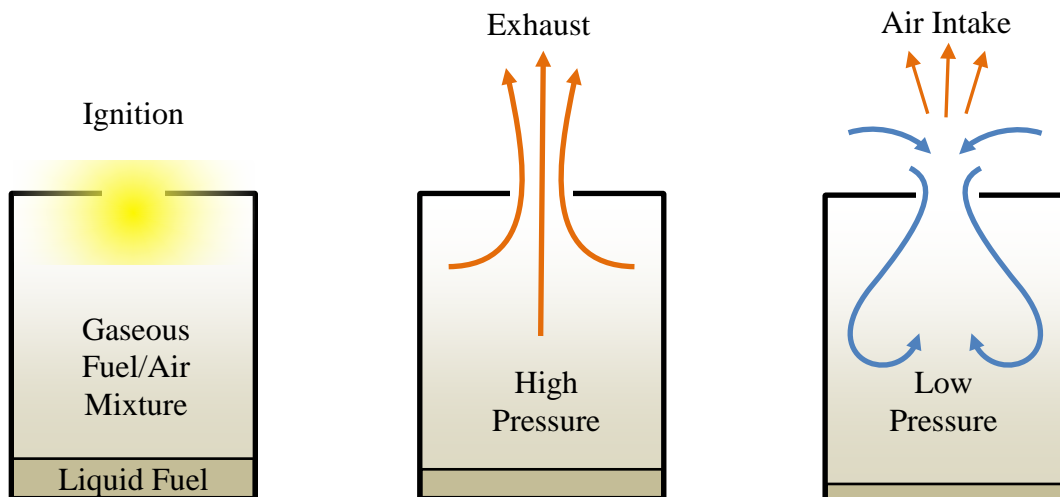


Figure 5: The Reynst “Jam Jar” Jet Engine Cycle [5]

The Reynst jet also survives as the simplest jet engine the average person can make – the “Jam Jar Jet.” Countless people have used discarded glass jars with a small hole cut in the lid to recreate Reynst’s design. The right mixture of fuel and air, when ignited, will incite the same resonance and can even build enough heat to catastrophically fail the jar.

4. The Valveless Pulse Jet Engine

A natural progression from the valved pulse jet design was to employ aerodynamic flow control into the inlet (similar to that of the Reynst resonator) to eliminate the need for a mechanical valve. Although the first valveless pulse jet dates back to Georges Marconnet in 1909 [5, 10], many other designs were developed in the century since (Schubert, Tesla, Escopette, CS, and Roe for instance). A detailed review of these different designs was compiled by Ogorolec [10]. The most well-known implementation of this idea was developed by Lockwood for the Hiller Aviation Company in the 1960s and boasted thrust-specific fuel consumptions as low as 2 lb/hr/lb ($I_{SP} = 1800$ s). [11-13] This redesign of the pulse jet concept returned to the greatest advantage of the classical ramjet – the lack of any moving parts – while retaining subsonic operation. Another significant advantage is the ability to operate without an external ignition source. Once started (typically with a spark plug or open flame), a properly designed combustion chamber does not expel the entire flame during a single cycle. Instead, there is remaining energy in the chamber to ignite the next charge of air and fuel.

It is important to note that pulse jets do not operate on a continuous flow cycle. Instead, they are unsteady flow combustors and are heavily affected by the propagation of pressure waves backward and forward through the engine’s geometry. This pressure wave propagation is the mechanism for engine resonance and it is this resonance that drives the engine’s cycle. It is also the reason no simple closed-form cycle analysis is possible [11].

Because of this pressure wave interaction, the engine cycle is a bit more complicated than that for a valved pulse jet. As the fuel-air mixture ignites, a compression pressure wave propagates outward from the combustion chamber at the speed of sound – out the inlet and exhaust simultaneously. This occurs much faster than either the fluid movement or flame front propagation. When the compression wave reaches the inlet, a low-pressure wave reflects back toward the combustion chamber. Another way to consider this effect is of the fluid inertia leaving the chamber and causing a local decrease in chamber pressure below the ambient inlet pressure. This is referred to as the “Kadenacy Effect” and acts to draw in the next charge of inlet air [10, 14]. Reynst referred to it as a thermodynamic effect he called “thermal breathing.” That is, the hot, expanding gases leave the chamber which cools, specific volume decreases, and the chamber “inhales” the next charge of fresh air [10].

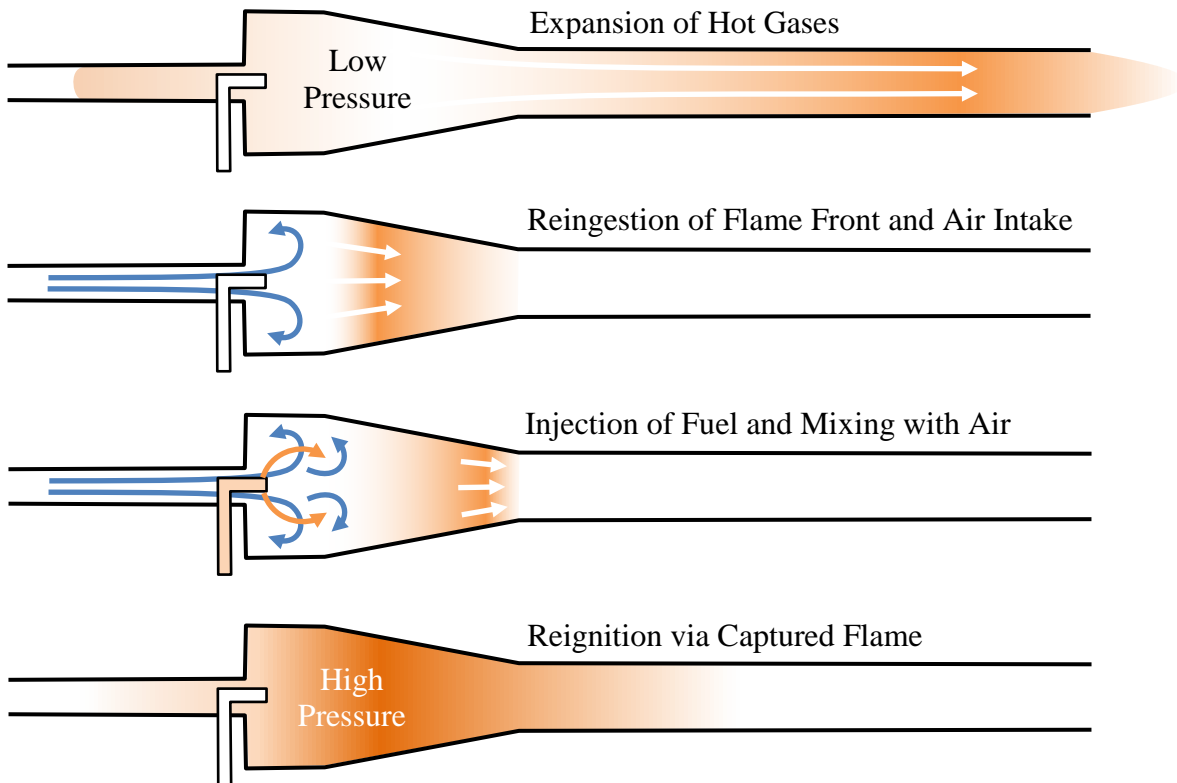


Figure 6: Schubert's Valveless Pulse-Jet Engine Cycle [10]

An alternative view of the design of a valveless pulsejet can be drawn through acoustics driven by the resonance of a standing pressure wave. Like the pipes of an organ, the resonant frequency is driven by the duct's length. Locations of low pressure will facilitate higher speed pipe flows for the inlet and exhaust. In other words, valveless pulse jets will have a high pressure 'antinode' ideally in the center of the chamber, and a low pressure node at the inlet lip and exhaust. Hence, these pipes act as connected quarter-wave oscillators and their lengths must, therefore, be tuned to produce an acoustic natural frequency conducive to forming this standing pressure wave. Too much or too little exhaust length compared to the inlet length, for instance, will result in a mismatch in resonant frequencies and thus non-optimal performance [10, 15].

5. The Pressure Jet Engine

The pressure jet engine was originally invented at some point in the early 1950s by Eugene Michael Gluhareff, a Russian-American who immigrated to the United States with his father and others (including Igor Sikorsky) to escape the Russian Revolution [16]. Working around the birth of the helicopter, he sought a method of eliminating the problem of torque-transmission that necessitates the conventional helicopter's tail rotor. Without a tail rotor, the torque from a fuselage-mounted engine would spin the fuselage out of control. A minority of his contemporaries found a solution – rotor tip propulsion [17]. By applying thrust forces to the blades at the tip rather than via a central drive shaft, there was minimal torque transmission to the fuselage and yaw control was possible without a tail rotor. Many ideas were tested, but the most successful vehicle at the time was one powered by ramjets built by Hiller – the YH-32 Hornet. Hiller's ramjet, however, was inefficient especially at low speeds [16]. Gluhareff, instead, developed a new kind of ramjet engine fundamentally distinct from the pulse jet engine to serve this purpose.



Figure 7: Gluhareff with G8-2-130 (Left) and the MEG-2X Helicopter (Right) [18]

Gluhareff used the resonant acoustics of combustion and fuel injection via ram intake to pressurize the inlets in stages as it entered the combustion chamber. [15, 19] He also investigated several propellants ultimately settling on liquid propane for its common availability, efficient high-pressure storage, and the ability to exploit the phase change from a cold liquid to a hot combustible gas. The result was an L-shaped ramjet engine with acoustically-tuned intake pipes unlike any other engine available in the 1950s [15, 19]. And yet, like the less-efficient ramjets, Gluhareff's pressure jet possessed no moving parts retaining their low cost of manufacture and maintenance. He mounted his new engine to helicopter blades and successfully demonstrated that he could eliminate the torque transmission problem by fitting flight hardware capable of lifting a person into the volume of a large backpack – the helicopter equivalent of a jet pack [16].

Gluhareff was also able to push his design to impressive levels of fuel efficiency through rigorous experimentation. His G8-2-130R engine minimized inlet losses with a round inlet and was able to achieve a TSFC of $0.78 \text{ lb}_m/\text{hr}/\text{lb}_f$ ($\text{ISP} \approx 4615 \text{ sec}$) [15] which is better than twice the efficiency of the Lockwood-Hiller valveless pulsejet with thrust augmenters [11] and even competitive with the TSFC of turbojets of the day. Today, however, the pressure jet would not be

competitive with the more efficient turbofans. Pressure jets are unable to produce a competitive pressure ratio or mass flow rate for the same amount of fuel. Moreover, the noise and surface temperatures of the pressure jet engine are also prohibitive. Its primary advantage is in its low cost of manufacture and operation as well as in studying acoustic tuning of combustion chambers. Further study could reduce the noise and control the surface temperature problems making it an attractive option for unmanned aircraft and experimental “kitplanes.”

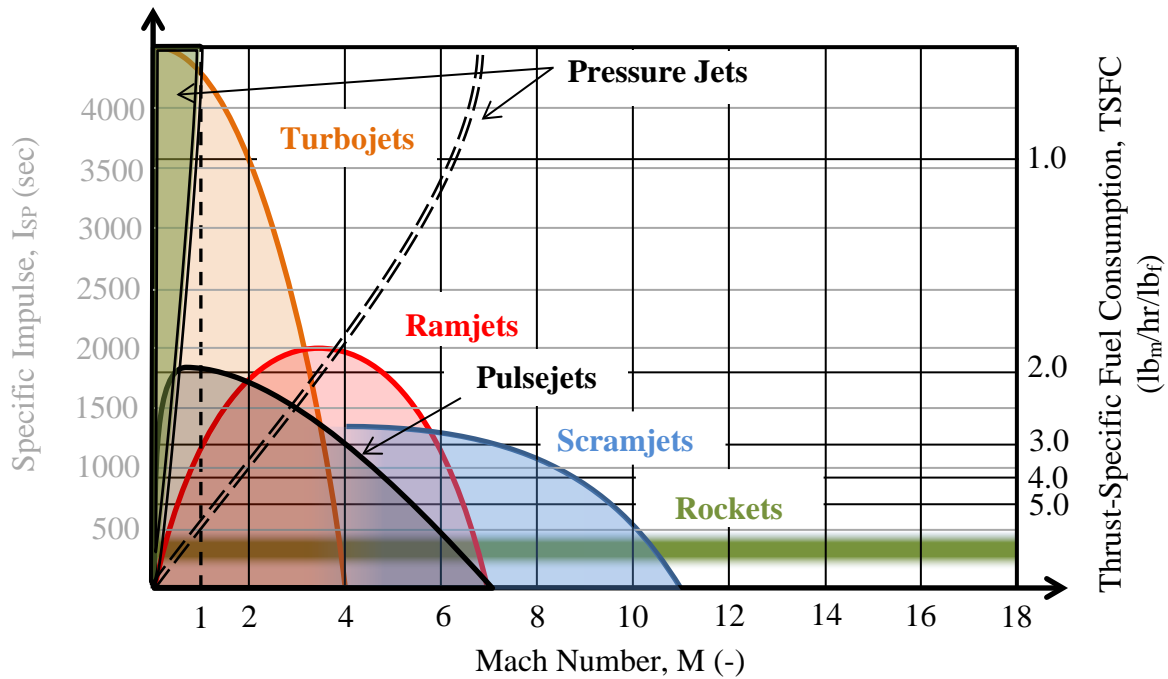


Figure 8: Jet and Rocket Comparative Fuel Efficiency (using Hydrocarbon Fuel) Showing Known Pressure Jet Performance and Potential for Supersonic Performance [1]

Nevertheless, the engine and its application to rotary-wing aircraft earned Gluhareff many government contracts, a research grant to test in NACA Langley’s wind tunnel [20, 21], and a private company (EMG Engineering) to build production engines. For decades, he sold plans, kits, and complete engines through his company and advertisements in magazines. The kits were referred to as “An amazing jet engine you can build in your own shop!” [22]. He noticed the static thrust could be scaled allowing smaller and larger engines than his original 15 lb_f thrust design. By the 1980s, Gluhareff eventually released a large catalog of engines listed in Table 1.

The G8-2-20 engine was used as a baseline for a wide variety of projects from jet-powered bikes and go-carts, to hovering platforms, and modified fixed-wing aircraft. Gluhareff even produced a fixed engine stand that provided a low-cost method of teaching jet propulsion and thermodynamic principles using his G8-2-15 engine [15]. His ultimate goal, however, was to build an aircraft that could be substantially cheaper than the lightest helicopters. Just a few years before his death, he built and flew the EMG-300, a mature ultralight-style kit-helicopter design using his pressure jet engine creating what he called a “flying motorcycle.” [16]

Table 1: Known EMG Engineering’s Production Engine Specifications [16]

Name	T _{MAX} lb _f	Length in.	OD _{COMB} in.	OD _{EXIT} in.	W lb _f	T/W -	Static SFC lb _m /hr/lb _f	I _{SP} sec
G8-2-5	5.2	22.0	3	2	1.5	3.5	No data	
G8-2-15	15	36.0	5	3.5	5.5	2.7	No data	
G8-2-20	23.5	36.0	5	3.5	5.5	4.3	4.8	750
G8-2-40	43	38.5	6.5	5.0	11.0	3.9	4.6	783
G8-2-80	82	45.0	8.5	6.5	21.0	3.9	4.2	857
G8-2-130	137	48.0	9.0	7.0	24.5	5.6	1.33	2707
G8-2-130R	137	48.0	9.0	7.0	24.5	5.6	0.78	4615
G8-2-350	350	No data						
G8-2-700	700	No data						

Following Eugene Gluhareff’s death, his company dissolved. The engine’s operating principles and design were all but lost. With the exception of some basic material sold with his engines and the teaching stand, almost no insight into the engine’s function exists [15]. From the late 1980s to today the only developments in the pressure jet design were from numerous private companies attempting to build new engines based solely on the old engines’ geometry or to patent knock-off concepts only legally distinct from Gluhareff’s original 1963 patent [23, 24].

Where the typical ramjet engine (described in Section 1) operates on the Brayton Cycle, a modified form was implemented in Eugene Gluhareff’s pressure jet and was referred to as the Brayton-Gluhareff Cycle [16]. In this case, the intake pressure is increased from the ambient by

producing a resonance called “sonic lock” whereby the incoming fuel-air mixture sets up an acoustic standing wave with the expanding combustion. The intake air at elevated pressure then encounters a region of continuous combustion thus feeding it. The resulting combustion products then blow over a heating coil that preheats and evaporates the cold liquid propane and exhausts through a subsonic nozzle producing momentum thrust.

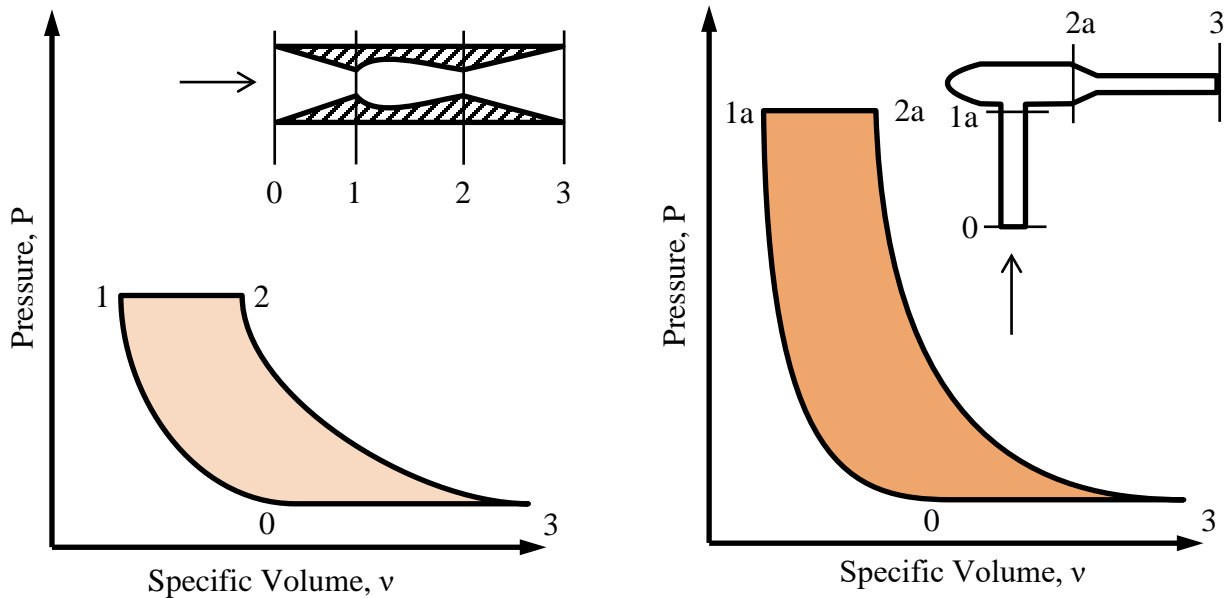


Figure 9: Brayton Cycle and Brayton-Gluhareff Cycle P-v Diagrams

In short, the primary difference between the cycles is that the Brayton-Gluhareff cycle simply extracts additional energy from preheating the fuel to a significantly higher pressure. That injection pressure is then used to produce an acoustic resonance throughout the three-stage inlet. The tuning of the inlet structure is designed such that low-pressure nodes exist at the inlets and entrain extra air that increases the chamber pressure beyond that of a conventional pulsejet or ramjet. This fundamental improvement is what led to the pressure jet’s improved fuel efficiency over Hiller’s ramjet and eventually even other valveless pulse jets. [15]

Throughout his testing, Eugene Gluhareff noted two important methods of augmenting this cycle. The first was to increase the injection pressure. Although the nozzle is choked and the fuel

flow rate is limited by the injector area, the increased pressure appeared to directly increase the engine thrust. [15] This was potentially due to an increase in the amount of air entrained by the fuel-injection. To maximize this, Gluhareff also recommended heating the propane tank or otherwise increasing the reservoir pressure of the fuel prior to being fed to the engine.

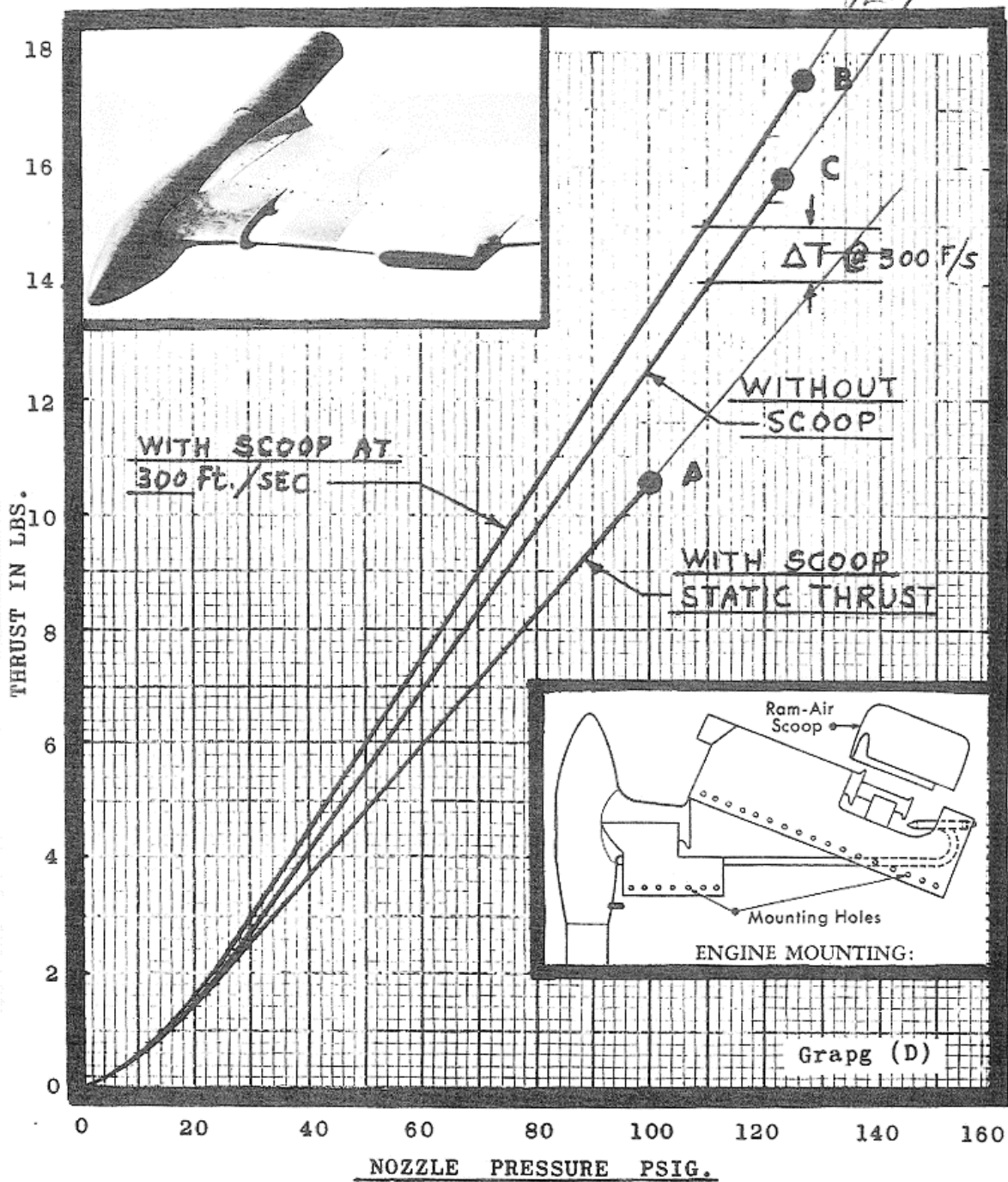


Figure 10: G8-2-15 Engine Data With and Without Ram Scoop [15]

The second method was to further increase the air into his engines by exploiting the ram effect for his engine inlets. This is a capability often lost by pulse jets like the famous Lockwood U-shaped pulse jet that orients both the inlet and exhaust aftward and must recover some of these losses with large thrust-augmenter ducts. Some of Gluhareff's original manufacturer's data with and without this inlet scoop are included in Figure 10. When Gluhareff's pressure jet engines were installed on his helicopters, he added a small duct to the first stage inlet which improved thrust by 6% during typical operation at 300 ft/sec [15]. Both of these augmentations did not alter the cycle but simply increased the maximum pressure of the cycle (P_{1a} in Figure 9) and, thus, the opportunity for power extraction.

6. The Pressure Jet Engine in Relation to Other Jet Engines

It is important at this point to note that the Gluhareff pressure jet engine is not simply an evolution of the pulse jet engine, but an improvement on the ramjet engine which allows subsonic and even static thrust generation. The primary mechanism of operation of the ramjet is high speed ram air which increases the intake pressure for combustion. This same mechanism is achieved in the pressure jet by means of supersonic injection of fuel and acoustically-tuned inlets. It is these factors that allow static thrust from a ramjet engine. It is also these factors that make it fundamentally distinct from the pulse jet family of engine designs developed by Gluhareff's contemporaries like Hiller and Lockwood. Although the valveless pulse jet also makes use of acoustic tuning, their primary mechanism of operation does not rely on ram air intake like ramjets and the pressure jet. This distinction between the pulse jet and pressure jet is critically important and is the source of the pressure jet's added performance by comparison.

B. Computational Fluid Dynamics (CFD)

As mentioned earlier, there are simply no closed-form methods to analyze the complex processes occurring within a pressure jet engine – the flow fields are unsteady, the pressure gradients, their propagation and interactions are nontrivial, turbulent structures have significant effect, and the chemical kinetics of combustion are the source of all of these. The only reasonable approach to capture all of these effects simultaneously is with a 3-dimensional (3-D), transient, reacting simulation using computational fluid dynamics (CFD).

1. General Theory

The foundations of CFD were laid as long ago as the 17th and 18th centuries in Europe with the development of the classical forms of the continuity, momentum, and energy equations. [25]

The compressible form of the continuity equation in Cartesian coordinates is:

$$\frac{\partial \rho}{\partial t} + \frac{\partial}{\partial x}(\rho u) + \frac{\partial}{\partial y}(\rho v) + \frac{\partial}{\partial z}(\rho w) = 0 \quad (2)$$

with velocity components, u , v , and w , and fluid density, ρ . [25-27] Likewise, the compressible

form of the momentum equation in Cartesian coordinates is:

$$\rho \frac{Du}{Dt} = -\frac{\partial P}{\partial x} + \left(\frac{\partial \sigma_{xx}}{\partial x} + \frac{\partial \sigma_{xy}}{\partial y} + \frac{\partial \sigma_{xz}}{\partial z} \right) + \rho F_x \quad (3)$$

$$\rho \frac{Dv}{Dt} = -\frac{\partial P}{\partial y} + \left(\frac{\partial \sigma_{yx}}{\partial x} + \frac{\partial \sigma_{yy}}{\partial y} + \frac{\partial \sigma_{yz}}{\partial z} \right) + \rho F_y \quad (4)$$

$$\rho \frac{Dw}{Dt} = -\frac{\partial P}{\partial z} + \left(\frac{\partial \sigma_{zx}}{\partial x} + \frac{\partial \sigma_{zy}}{\partial y} + \frac{\partial \sigma_{zz}}{\partial z} \right) + \rho F_z \quad (5)$$

where D/Dt is the substantial derivative, F are body forces like gravity, and σ_{ij} represents the components of the viscous stress tensor given by:

$$\sigma_{ij} = \mu \left[\left(\frac{\partial u_i}{\partial x_j} + \frac{\partial u_j}{\partial x_i} \right) - \frac{2}{3} \delta_{ij} \frac{\partial u_k}{\partial x_k} \right] \quad (i, j, k = 1, 2, 3) \quad (6)$$

where δ_{ij} is the Kronecker delta function [25-27]. Lastly, the compressible form of the energy equation in Cartesian coordinates (when expanded like the others) is:

$$\begin{aligned}
\rho \frac{DE}{Dt} = & \rho \dot{q} + \frac{\partial}{\partial x} \left(k \frac{\partial T}{\partial x} \right) + \frac{\partial}{\partial y} \left(k \frac{\partial T}{\partial y} \right) + \frac{\partial}{\partial z} \left(k \frac{\partial T}{\partial z} \right) \\
& - \left(\frac{\partial(uP)}{\partial x} + \frac{\partial(vP)}{\partial y} + \frac{\partial(wP)}{\partial z} \right) + \left\{ \left[\frac{\partial(u\sigma_{xx})}{\partial x} + \frac{\partial(u\sigma_{yx})}{\partial y} + \frac{\partial(u\sigma_{zx})}{\partial z} \right] \right. \\
& \left. + \left[\frac{\partial(v\sigma_{xy})}{\partial x} + \frac{\partial(v\sigma_{yy})}{\partial y} + \frac{\partial(v\sigma_{zy})}{\partial z} \right] + \left[\frac{\partial(w\sigma_{xz})}{\partial x} + \frac{\partial(w\sigma_{yz})}{\partial y} + \frac{\partial(w\sigma_{zz})}{\partial z} \right] \right\} \\
& + \rho(uF_x + vF_y + wF_z)
\end{aligned} \tag{7}$$

which include terms for the total energy, E , the heat flux, \dot{q} , and the thermal conductivity of the fluid, k . [25-27] The three grouped terms in brackets are often combined into a single term for fluid energy dissipation, typically denoted as Φ .

These equations mathematically maintain that (1) mass is conserved, (2) Newton's second law ($F = ma$) is enforced, and (3) energy is conserved. However, with the exception of some specific cases with favorable boundary conditions, solving these equations simultaneously must usually be done numerically as opposed to deriving an exact solution function. Moreover, while these equations may capture unsteady flows, direct numerical simulations (DNS) including turbulence are often impractical. Doing so requires the fluid properties and their dependent variables to be included instantaneously. Instead, somewhat simplified models of turbulence are typically used in CFD studies [26].

These turbulence models are typically separated into two categories: Reynolds-Averaged Navier Stokes (RANS) and Large Eddy Simulations (LES). A RANS simulation generally models turbulent characteristics as a "sub-grid" or averaged phenomena for each cell. This follows from

expressing the velocity and temperature distributions as the sum of their mean and perturbations (denoted with bars and apostrophes, respectively):

$$u = \bar{u} + u', \quad v = \bar{v} + v', \quad w = \bar{w} + w', \quad \text{and} \quad T = \bar{T} + T' \quad (8)$$

This leads to a two-equation turbulence model commonly referred to as the “Standard k- ϵ Model” [26, 27] where k in this case is the local turbulent kinetic energy and ϵ is the rate at which turbulent energy dissipates in the fluid. As a result of this fluid averaging, turbulent structures do not usually present at a scale larger than the local grid size – they are a property of the local cell. In other words, a RANS model of a fluid flow does not inherently produce turbulent structures that span multiple cells.

Although the RANS model is “well established, widely validated, and gives rather sensible solutions to most industrially relevant flows” [27] it is also limited to flows that do not involve flow separation, reattachment, and recovery as well as some unconfined flows, and complex geometries. The “Large Eddy Simulation” (an umbrella term for many different models of turbulent eddies in fluid flows) in general works to model the large eddies exactly and approximate the effects of small eddies [27]. In other words, the flow is separated into a “resolved field” that is spatially averaged as opposed to ensemble averaged and a sub-grid field for smaller eddies [28]. Simulation of eddies is particularly important for the mixing and transport or diffusion of species in a flow. Therefore, while averaged flow parameters (as in a RANS simulation) are often sufficient to model turbulent characteristics, those flows where turbulence drives a larger mechanism must model these larger eddies. This was found to be the case for a study of reacting flows (specifically propane oxidation reactions) that are heavily affected by the local mixture’s fuel-air ratio which is often dependent on turbulent mixing. The study is discussed in more detail later in Chapter III, Section C-2. Several different LES models are included in the software package and are discussed in the next section.

2. Working with CONVERGE CFD

To perform the Computational Fluid Dynamics (CFD) simulations, the CONVERGE CFD software package from Convergent Science was used. This software package consists of a pre-processing program “CONVERGE Studio” and the solver program that performs the actual simulation calculations. The solver saves time-histories of mass-averaged parameters (pressure, temperature, etc...), as well as summed parameters (mass flow rate through boundaries for instance) and complete 3-D output data files. While the averaged and summed parameters may be plotted as simple time-histories, the output data files must be loaded into visualization software so relevant slices of the 3-D space can be viewed at single instances in time or as animations. The software used to make these visualizations is CEI’s Enight (version 10). This general process is shown graphically in Figure 11.

CONVERGE CFD simulates turbulent transport with a series of different models. The solver includes three RANS Models – the Standard k - ϵ , Random Number Generated (RNG) k - ϵ , and a Rapid Distortion RNG k - ϵ . In this research effort, when a RANS turbulence model was used, the default Standard k - ϵ model was used. However, the majority of simulations used a LES turbulence model to better capture the formation of turbulent structures and the diffusion and mixing of chemical species. This leads to the question of what LES model to choose. The solver supports six different LES models split between two fundamental philosophies: “0-Equation” and “1-Equation.” The 1-Equation models add a transport equation to model a sub-grid turbulent kinetic energy (TKE). The 0-Equation models simply do not and, therefore, are expected to be lower-fidelity while offering slight improvements in runtime [28].

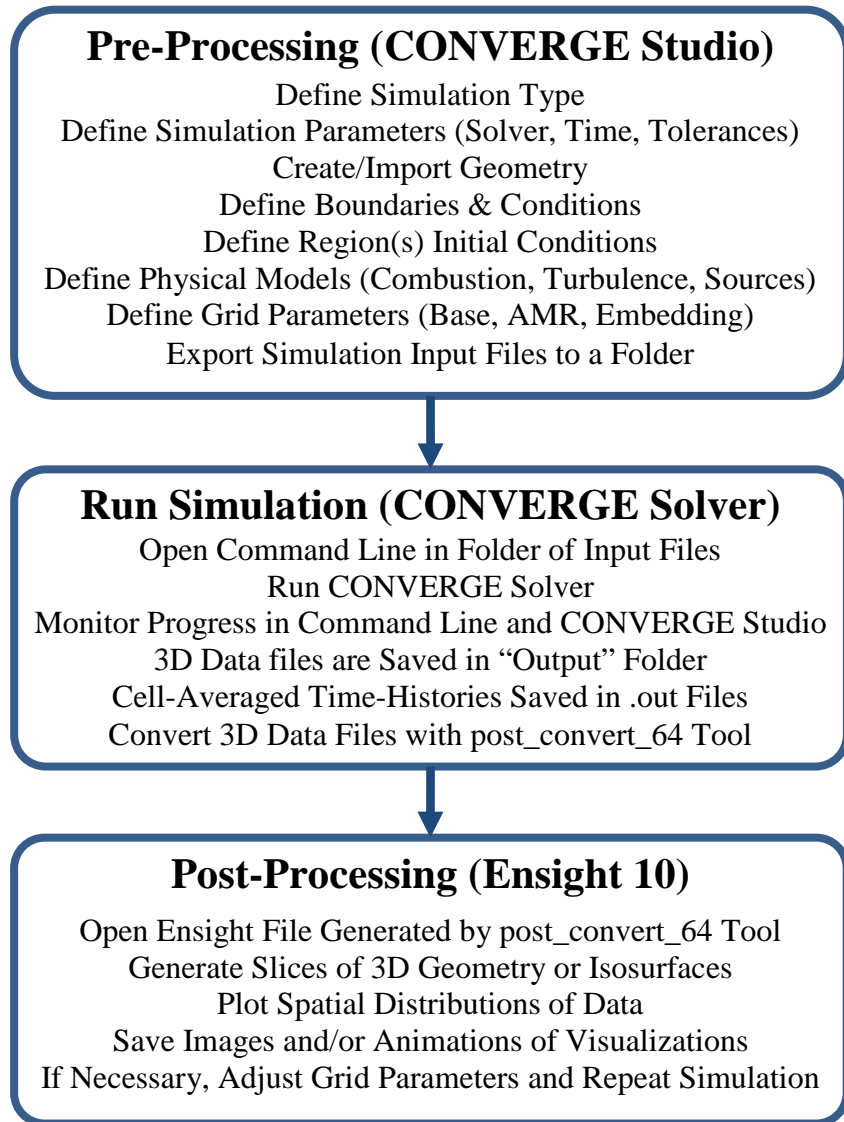


Figure 11: Procedure for Defining, Running, and Post-Processing CFD Simulations in CONVERGE CFD and Ensight 10

The available 0-Equation models are (1) the Upwind LES Model, (2) the Smagorinsky Model, and (3) the Dynamic Smagorinsky Model. The Upwind LES Model approximates a local sub-grid kinetic energy, k , and a sub-grid dissipation, ε :

$$k \cong \frac{1}{2} u'_i u'_i \quad \text{and} \quad \varepsilon \cong \frac{k^{1.5}}{\Delta} \quad (9)$$

where Δ is the cube-root of the local cell's volume and u'_i is an unresolved sub-grid velocity approximated as the first term of a Taylor series expansion. [28] The Smagorinsky Model instead relates a turbulent viscosity, ν_t , to the strain rate tensor, S_{ij} , and the size of the local cell:

$$\tau_{ij} = -2\nu_t \overline{S_{ij}} \quad \text{and} \quad \nu_t = C_s^2 \Delta^2 \sqrt{S_{ij} S_{ij}} \quad (10)$$

where C_s is a model constant which can be used to tune the model. The Dynamic Smagorinsky Model dynamically determines the constant, C_s , as it may vary in different flow regimes [28].

The available 1-Equation models are (4) the 1-Equation Viscosity Model, (5) the Dynamic Structure Model, and lastly (6) the Consistent Dynamic Structure Model. The 1-Equation Viscosity Model uses the additional transport equation for a sub-grid TKE to model the local turbulent viscosity and thus the local stress tensor:

$$\tau_{ij} = -2\nu_t \overline{S_{ij}} + \frac{2}{3} k \delta_{ij} \quad \text{and} \quad \nu_t = C_k k^{0.5} \Delta$$

$$\text{where} \quad k = \frac{1}{2} (\overline{u_i u_i} - \overline{u_i} \overline{u_i}) \quad (11)$$

with a tuning constant, C_k . In this model, the sub-grid dissipation is similarly tunable [28]:

$$\varepsilon = C_\varepsilon \frac{k^{1.5}}{\Delta} \quad (12)$$

The Dynamic Structure Model conversely does not operate through a turbulent viscosity it instead “enforce[s] a budget on the energy flow between the resolved and the sub-grid scales.” [28] In this case, the local stress tensor is calculated as a function of the sub-grid TKE. For simulations with a rotating frame of reference, the Consistent Dynamic Structure Model is recommended as being “more appropriate” where the stress tensor is calculated based on local averaged velocity gradients [28]. The software's default LES model is the 1-Equation Viscosity Model and in the absence of a clear reason to choose another option, the default was used with model values recommended by the pre-processing software ($C_k = 0.05$ and $C_\varepsilon = 1.0$).

The CONVERGE solver is capable of both finite difference and finite volume methods, however, the finite volume method was recommended for most simulations. This method numerically solves the integral forms of the conservation equations. The finite volume method was used because it conserves transport quantities for irregularly shaped cells that are likely to occur when ideally cubic cells are sliced by boundary curves. This is not necessarily the case for the finite difference approach [28].

Convergence of the simulation is handled on an individual time-step basis via the Courant-Friedrichs-Lewy (*CFL*) Numbers:

$$CFL_u = u \frac{\Delta t}{\Delta x}, \quad CFL_{Mach} = a \frac{\Delta t}{\Delta x}, \quad CFL_v = \nu \frac{\Delta t}{\Delta x^2} \quad (13)$$

That is, the current time step, Δt , is selected based on the grid spacing, Δx , and the cell velocity, u , sound speed, a , and viscosity, ν [28]. A maximum allowable CFL for each is chosen and during the simulation whichever breaches the limit will define the next time step size such that the simulation will converge. Alternatively, if none exceeds the CFL limit, the time step will be increased to speed up the simulation as much as possible while maintaining convergence.

To build confidence and test the accuracy of the CONVERGE CFD package, a series of incremental simulations were performed with the ultimate goal of modeling the full transient mixing and reacting flow involved in the operation of the Brayton-Gluhareff pressure jet cycle. The first simulation was to model the mixing flow of gas species in a simple rectangular geometry. This simulation was validated with experimental data from an identical mixing box used to supply an Exhaust Gas Recirculation (EGR) mixture to the KU Single-Cylinder Engine Test Cell. This effort was published in ASME Conference Proceedings [29] and is detailed in Chapter IV, Section 0. Following that, quiescent reacting flows were modeled using a slice of a spherical chamber to test chemical kinetic mechanisms with CONVERGE CFD. These simulations were used to select

a mechanism that represented a balance of speed and accuracy. This effort is detailed in Chapter IV Section 0. All that remained at that point was to model the pressure jet engine geometry with both a moving fluid flow and propane oxidation chemical mechanism and validate it with experimental data.

3. Modeling of Pulse Jet Engines with CFD

This is not the first research effort to simulate the operation of a pulse jet engine with CFD and validate it with experimental data. These studies, however, limited themselves to studying either commonly available hobby engines or attempts to miniaturize them. As such these efforts are limited to the valved and valveless pulse jets. Of particular note is the work of Tao Geng toward his dissertation at North Carolina State University in 2007 [30]. A series of papers were published investigating both valved [6] and valve-less [31, 32] pulse jets at different scales comparable to the scales in this effort. The dissertation focused on the computational modeling of pulse jets including fluid mechanics, acoustics, and chemical kinetics that drive the operation of pulse jets. It specifically highlighted significant differences in the air-breathing mechanisms of valved and valveless pulse jet engines. He noted that with proper geometric design of the inlets, chamber, and tail pipe, a functioning valveless pulse jet as small as 8 cm in length could be made. This was enabled by increasing the chamber volume and preheating the fuel of which the latter is a fundamental part of Gluhareff's pressure jet design. This served to control heat loss and the comparatively shorter residence time of the fuel/air mixture to burn completely [30, 32]. This engine, its major geometric features, and the domain used for simulating it in CFD are shown in Figure 12.

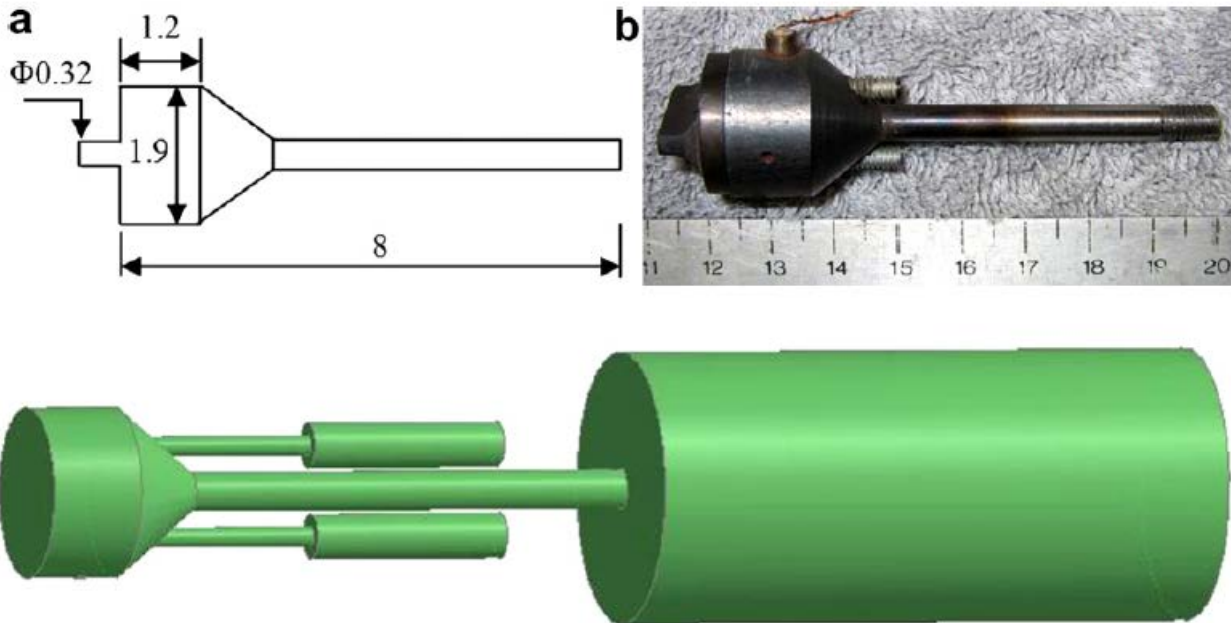


Figure 12: Small Scale Valveless Pulse Jet Engine (Dimensions in cm) and the CFD Simulation Domain [30, 32]

The CFD simulations in Geng's studies were performed using ANSYS's CFX 5.7 software package. Turbulence was modeled using a RANS standard $k-\epsilon$ model as it was shown to produce an operating frequency (232 Hz) within $\pm 5\%$ error [30]. The 1981 Westbrook-Dryer one-step propane oxidation mechanism was selected to model combustion during the simulation. This same mechanism was selected and calibrated to model combustion in the pressure jet and is discussed in more detail in Chapter III. Heat transfer to the ambient surroundings was modeled using an average heat transfer coefficient that was determined via a steady-state heat transfer analysis. The wall thickness effect on this transfer was neglected in the interest of reducing simulation time. Engine performance was measured in terms of the cycle's peak combustion chamber pressure. Thrust was estimated using exhaust velocity measurements and thrust-specific fuel consumption (TSFC) was estimated further based on the measured fuel flow rate. Lastly, as seen by Gluhareff [15] both the engine operating frequency and peak pressure (and thus engine performance) are driven by the fuel mass flow rate, \dot{m}_f [30].

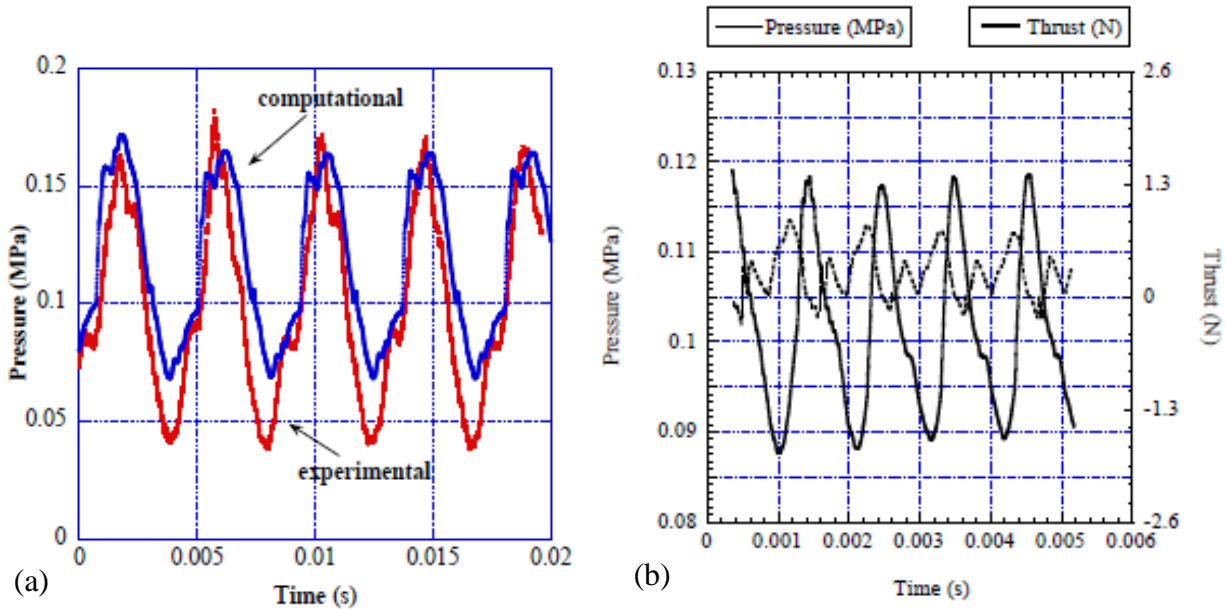


Figure 13: (a) Comparison of Simulation and Experimental Data for 50-cm Valved Pulsejet [6, 30] and (b) Simulation Data for 8-cm Valveless Pulsejet [30, 32]

Pulse jet research at North Carolina State University was continued by one of Geng’s contemporaries, Fei Zheng, in a 2009 dissertation on computationally simulating high-speed pulse jets. [33] The RANS standard $k-\epsilon$ turbulence model was again used to predict the effect of turbulence on the combustion process. This study used a five-step propane reaction mechanism provided by ANSYS’s CFX software but limited the simulation to a thin slice of the full circular domain to reduce simulation time. This resulted in a simulation that operated “reasonably well” predicting a chamber temperature and operating frequency between 5 and 10% higher than those found experimentally [33]. Zheng also suggested a new analytical model for the acoustics of a pulse-jet where the inlet is treated as a Helmholtz resonator and the exit duct as a wave tube. This model accurately predicted the pulse jet’s operating frequency and moreover found that when the inlet and exit frequencies matched, net thrust was maximized. [33] This phenomenon is similar to the phenomenon of “sonic lock” cited by Gluhareff in carefully tuning the lengths of his multi-stage inlet configuration. [15]

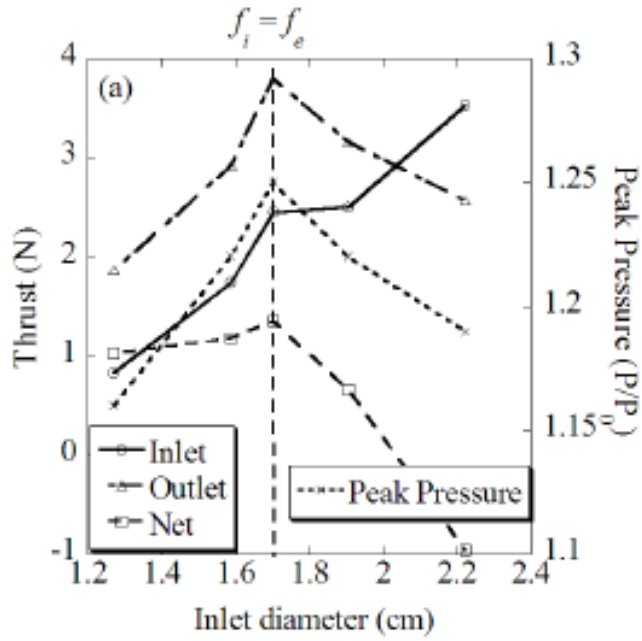


Figure 14: Thrust Force vs. Inlet Diameter Showing Maximum Net Thrust and Peak Pressure when Inlet and Exhaust Frequencies are Matched (CFD Simulations) [33]

C. Scope of Work

The purpose of this research effort was two-fold: (1) to successfully reverse engineer the Brayton-Gluhareff cycle pressure jet engine at a smaller scale than Eugene Gluhareff's smallest engine (the G8-2-5); and (2) to successfully model the operation of this engine. The first goal serves to both revive the technology and capabilities of a lost ramjet engine design and to study further miniaturization techniques with a novel architecture. The second goal represents the first comprehensive modeling effort in regard to the pressure jet engine despite several similar modeling efforts for conventional valved and valveless pulse jets. The goal of this research is *not* to optimize the performance of the Gluhareff engine, only to bring it to operation. At this point, matching a CFD simulation to the operation of a physical engine is the goal to prove the concept of reproducing the engine's operation at a smaller scale. Any improvements in fuel efficiency or performance are left for future research.

The next chapter details the first efforts used to determine initial estimates of the subscale engine specifications based on geometric scaling parameters. The third chapter details the available propane chemical kinetic mechanisms and the mechanism selected for modeling. The fourth chapter describes the use of computational fluid dynamics (CFD) and the efforts to validate incremental simulations toward a comprehensive engine simulation. The fifth chapter shows the construction of the physical engines and test stand hardware. Following that is the presentation of experimental and CFD data in comparison. The seventh chapter details the relevant conclusions and potential future research and applications that are lastly followed by a series of appendices including critical input files necessary to recreate the simulation data, MATLAB source codes, and a reprinting of historical information from the original EMG Engineering company through a partnership with Irina Gluhareff, the daughter of the pressure jet engine's inventor.

II. Estimating the Initial Engine Parameters

A. Important Geometric Parameters

Eugene Gluhareff's pressure jet engine design has many geometric parameters that all must be estimated to scale the engine up or down from a reference design. Because the operation of the engine is heavily dependent on the geometry, these dimensions need to be approximated to produce a scaled engine that will then need only minor adjustment to reach operation. There are two major lines of symmetry that lie perpendicular to one another – the inlet centerline and the exhaust centerline. A table of these dimensions as shown in Figure 15, as well as their descriptions and typical values for the G8-2-20, engine are included in Table 2. The dimensions for the G8-2-20 were measured from published plans.

Table 2: Gluhareff Pressure Jet Engine Geometric Parameter Definitions

Parameter	Parameter Description	G8-2-20 (in.)
δ	Spacing Between Fuel Injector and Inlet 1	0.125
L_1	Acoustic Length of Inlet 1	4.344
L_2	Acoustic Length of Inlet 2	10.469
L_{3i}	Length of Inlet 3 Structure	8.125
L_3	Acoustic Length of Inlet 3	10.625
L_H	Length of Chamber Head	6.125
L_C	Length of Combustion Chamber Core	7.625
L_T	Length of Transition Section	2.9375
L_N	Length of Tail/Nozzle	20.1875
D_i	Injector Inner Diameter	0.125
D_1	Inlet 1 Inner Diameter	0.835
D_2	Inlet 2 Inner Diameter	1.608
D_{3a}	Inlet 3 Minimum Inner Diameter	1.951
D_{3b}	Inlet 3 Maximum Inner Diameter	3.982
D_C	Combustion Chamber Maximum Inner Diameter	5.000
D_N	Tail/Nozzle Inner Diameter	3.436

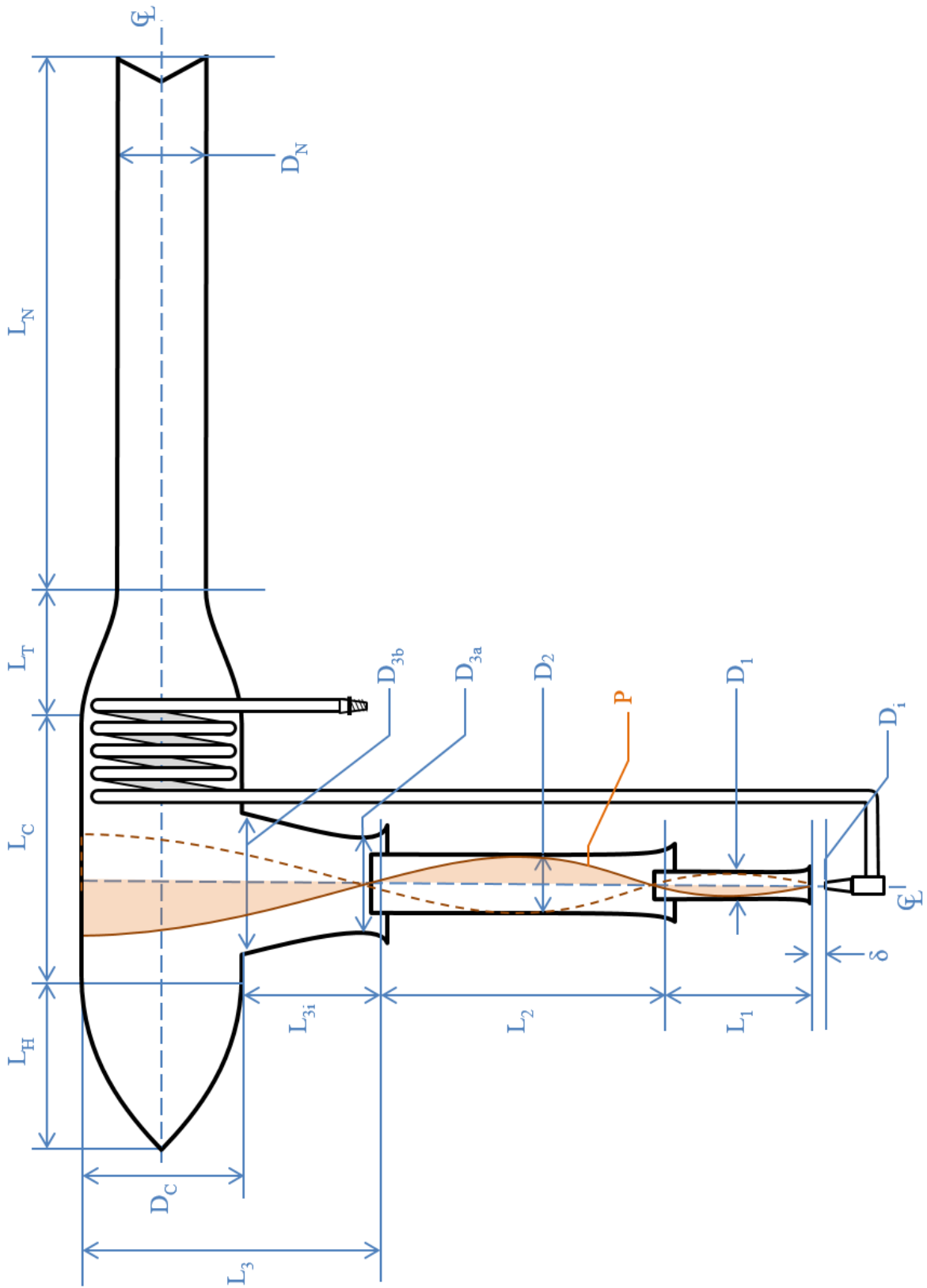


Figure 15: Gluhareff Pressure Jet Engine Geometric Parameter Definitions (Drawing Not to Scale)

There are some notable features critical to the design of the engine that are directly related to these parameters. Upon inspection of a pressure jet (of any scale) that has been run before, it is clear where the high temperatures of combustion stop in the third inlet due to high temperature discoloration. This occurs at approximately half the third-state inlet's length ($L_{3i}/2$). It is clear that part of the purpose of this final inlet stage is to slow the airspeed prior to combustion and capture the back-propagating flame-front.

The greater purpose of the inlet stages is to progressively entrain ambient air with the turbulent, rich mixtured, fuel/air core stream. These inlets' lengths are carefully tuned such that there is a low-pressure node at the inlets which acoustically drive extra air into the engine and increase engine performance. This pressure profile due to acoustics is represented in orange in Figure 15. This adjustment of tuned inlets is the only change between the G8-2-15 and G8-2-20 engines and resulted in a 33% increase in engine thrust. Further increases in engine performance were realized by flaring the inlet ducts and changing the inlet shapes to a circular cross-section, as opposed the lower-profile oval cross-section used to decrease drag when installed in a helicopter blade tip. Both decrease the inlet pressure losses, thereby increasing the inlet efficiency [15].

The length of the engine head, L_H , is also critical to the engine design and may be responsible for mainting stable operation. As the incoming flow enters the combustion chamber, some fraction of it gets caught in a burning recirculation zone while the rest expands outward toward the nozzle and inlet. It is thought (because no detailed analysis on the engine cycle exists in the literature) that this recirculation zone is meant to feed the chamber with a steadier flame should it start to blow out or otherwise become unstable.

B. Geometric Sizing Relations

The most detailed numerical analysis of the pressure jet engine is in the documentation meant to accompany the GTS-15 teaching stand. The GTS-15 was intended to provide a low cost jet propulsion teaching stand based around the G8-2-15 engine and includes a brief, closed-form walkthrough of some steady-state approximations and led to some insight in how to properly scale a pressure jet engine. This reference [15] (also included in Appendix E) was used to write a MATLAB code (see Appendix C-0) which could approximate the engine's geometry based on a series of empirical assumptions. This set of geometric parameters then represents an initial guess which may be physically built and experimented with until stable operation is possible.

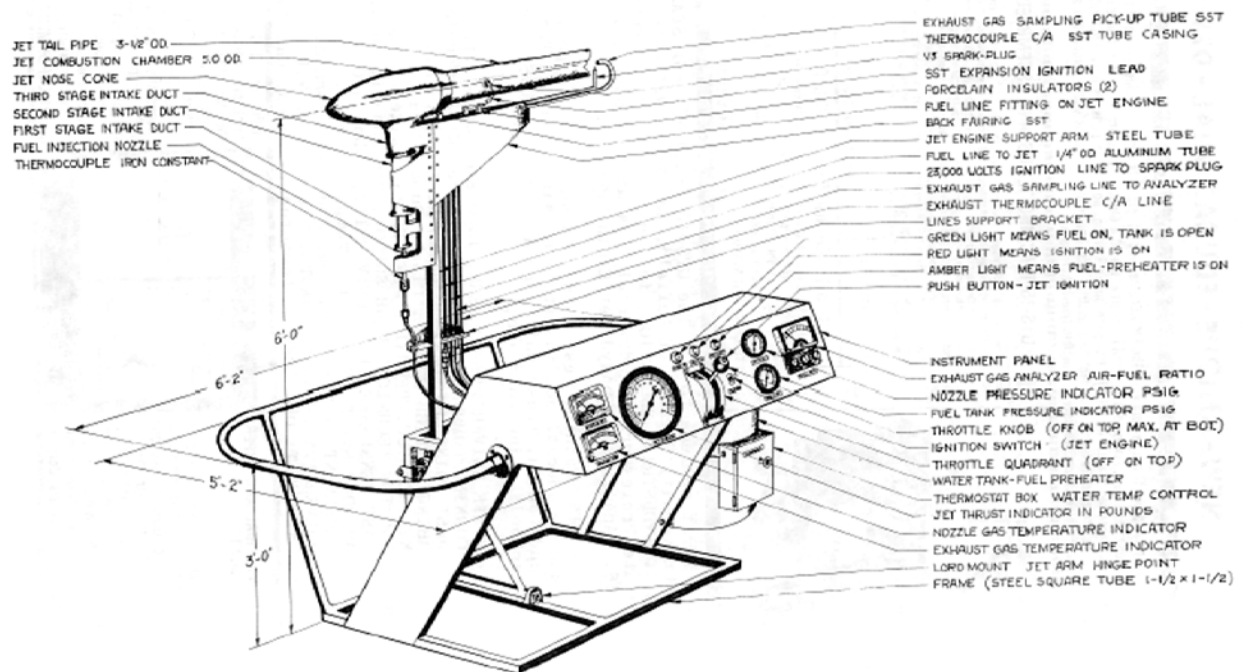


Figure 16: Diagram of the GTS-15 Teaching Test Stand Using an Instrumented Form of the G8-2-15 Pressure Jet Engine [15]

1. Empirical Assumptions for Geometric Approximations

A series of assumptions (listed in Table 3) based on Eugene Gluhareff's specifications and measurements were necessary to approximate the engine's dimensions. These values are based on

Gluhareff's own experimental measurements with the G8-2-15 engine as it was intended for use as a teaching tool. The efficiencies and equivalence ratios are particularly important as they size the inlet areas to result in a proper fuel-air mixture into the engine. The engine's operating frequency is scaled based on the G8-2-15 and sizes the inlet lengths.

Table 3: Gluhareff Pressure Jet Design Empirical Assumptions [15]

Parameter	Value	Units	Description
T_3	1670	°F	Temperature at 3 rd Stage Inlet
η_i	90.97	%	Injector Efficiency
η_1	67.47	%	Inlet Efficiency
ϕ_3	0.9429	-	3 rd Stage Inlet Equivalence Ratio
ϕ_2	0.8068	-	2 nd Stage Inlet Equivalence Ratio
ϕ_1	0.3807	-	1 st Stage Inlet Equivalence Ratio
$f_{G8-2-15}$	639	Hz	G8-2-15 Engine Operating Frequency
$D_{i_G8-2-15}$	0.125	in.	G8-2-15 Injector Inner Diameter

2. Injector Approximations

The engine is effectively sized around the injector size for several reasons. Because the necessary fuel-air mixture so heavily affects the inlet geometry, the amount of fuel being injected toward the engine is critical. In addition, because the injector is choked (having a pressure ratio approximately equal to ten), the fuel flow rate is limited by the injector diameter, D_i . The fuel mass flow rate was modeled based on the ideal choked flow subject to the assumed injector efficiency,

η_i :

$$\dot{m}_i = \eta_i P_f A_i \sqrt{\frac{\gamma_f}{R_f T_f} \left(\frac{2}{\gamma_f + 1} \right)^{\frac{\gamma_f + 1}{2(\gamma_f - 1)}}} \quad (14)$$

where the subscript 'f' indicates properties of fuel (heated gaseous propane), γ is the ratio of specific heats, R is the gas constant, A is the injector orifice area, T is the fluid temperature, and P

is the fluid pressure. [1] The engine operating frequency was assumed to scale with the size of the injector inner diameter to that of the G8-2-15:

$$f \cong f_{G8-2-15} \left(\frac{D_{i,G8-2-15}}{D_i} \right) \quad (15)$$

3. Three-Stage Inlet Approximations

At this point the flow characteristics out of the injector were known to satisfactorily proceed through the inlets step-by-step toward the combustion chamber. The total mass flow of fuel and air required for the first inlet was calculated from the equivalence ratio, ϕ , the stoichiometric fuel-air mixture ($f_{stoich} = 15.5$), and the injected fuel flow, \dot{m}_i :

$$\dot{m}_1 = f_1 \dot{m}_i = \phi_1 f_{stoich} \dot{m}_i \quad (16)$$

The inlet velocity (V_1) was calculated from the inlet efficiency and the injection kinetic energy:

$$V_1 = \sqrt{\frac{2 KE_1}{\dot{m}_1}} = \sqrt{\frac{2 \eta_1 KE_i}{\dot{m}_1}} = \sqrt{\frac{2 \eta_1 (1/2 \dot{m}_i V_i^2)}{\dot{m}_1}} = \sqrt{\frac{\eta_1 (\dot{m}_i V_i^2)}{\dot{m}_1}} \quad (17)$$

This velocity was then used to determine the inlet area, A_1 , necessary to capture a total (fuel and air) mass flow rate of \dot{m}_1 based on the definition of mass flow rate. The length of the first inlet stage is determined based on the sound speed into the first-stage inlet, a_1 , and the operating frequency of the engine :

$$L_1 = \frac{a_1}{2f} = \frac{\sqrt{\gamma_1 R_1 T_1}}{2f} \quad (18)$$

This relies on the fundamental physical theory behind a resonant column of air through a pipe with both ends open (described in Figure 17). Here the properties into the first inlet were approximated using a rule of mixtures based on the fuel-to-air ratio, f_1 . For instance, the ratio of specific heats was estimated as the sum of air and propane components:

$$\gamma_1 = \gamma_{air} \left(1 - \frac{1}{f_1}\right) + \gamma_f \left(\frac{1}{f_1}\right) \quad (19)$$

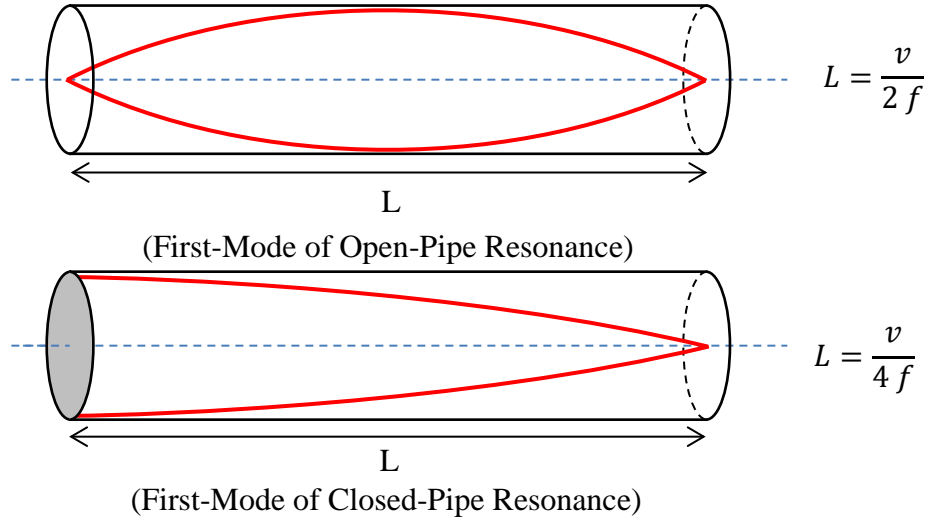


Figure 17: General Theory for First-Mode of Resonance for Open- and Closed-End Pipes

The second stage inlet was similarly analyzed starting with the necessary total mass flow rate based on the required fuel-air ratio:

$$\dot{m}_2 = f_2 \dot{m}_i = \phi_2 f_{stoich} \dot{m}_i \quad (20)$$

The velocity was again calculated from the inlet efficiency and injection kinetic energy:

$$V_2 = \sqrt{\frac{2 KE_2}{\dot{m}_2}} = \sqrt{\frac{2 (\eta_1)^2 KE_i}{\dot{m}_2}} = \sqrt{\frac{2 \eta_1^2 \left(\frac{1}{2} \dot{m}_i V_i^2\right)}{\dot{m}_2}} = \sqrt{\frac{\eta_1^2 (\dot{m}_i V_i^2)}{\dot{m}_2}} \quad (21)$$

This velocity and the total mass flow rate were used to determine the inlet area, A_2 while the length was estimated from the rule of mixtures-based sound speed and operating frequency:

$$L_2 = \frac{a_2}{2f} = \frac{\sqrt{\gamma_2 R_2 T_2}}{2f} \quad (22)$$

It should be noted here that the engine frequency is the same throughout the engine inlets, but because the fluid speed of sound changes, the wavelengths and the inlet lengths are different from inlet to inlet.

Lastly, the third stage inlet was approximated in similar fashion, determining the mass flow rate to reach the necessary equivalence ratio:

$$\dot{m}_3 = f_3 \dot{m}_i = \phi_3 f_{stoich} \dot{m}_i \quad (23)$$

followed by the third stage inlet velocity:

$$V_3 = \sqrt{\frac{2 KE_3}{\dot{m}_3}} = \sqrt{\frac{2 (\eta_1)^3 KE_i}{\dot{m}_3}} = \sqrt{\frac{2 \eta_1^3 \left(\frac{1}{2} \dot{m}_i V_i^2\right)}{\dot{m}_3}} = \sqrt{\frac{\eta_1^3 (\dot{m}_i V_i^2)}{\dot{m}_3}} \quad (24)$$

and finally the inlet length based on a rule of mixtures sound speed and the engine frequency:

$$L_3 = \frac{a_3}{4 f} = \frac{\sqrt{\gamma_3 R_3 T_3}}{4 f} \quad (25)$$

There are several differences at work here. First, the third stage temperature is assumed based on measurements from Gluhareff's experimentation [15]. At this point during the research effort, the temperature was assumed to be unaffected by engine scale. The other difference for the third inlet is based on the geometry of a closed-end pipe as opposed to a pipe with both ends open. This is fundamental to the engine's operation as the incoming fuel and air mixture reflects off the back wall of the combustion chamber ideally resulting in a peak pressure there as the mixture burns to extract energy from the fuel. Hence, because the standing wave is ideally a quarter wave (as opposed to a half wave as before) the denominator factor changes from two to four. It should also be noted that the length here is the *acoustic* length, L_3 , as shown in Figure 15

C. The Limited Utility of Closed Form Approximations

While at this point the tuned-inlet geometry is approximated, there was no simple analytical method through which to estimate the necessary combustion chamber volume and tail-pipe length. Instead these were based on geometric scaling based on the G8-2-5, G8-2-15, and larger engines.

Some simple geometric ‘rules of thumb’ were uncovered in studying the geometry of these engines. Regardless of scale, the length of the tail or nozzle was close to twice the length of the second stage inlet, i.e. $L_N \approx 2 L_2$. Similarly, the combustion chamber diameter was always close to half the acoustic length of the third-stage inlet, i.e. $D_C \approx L_3/2$. The nozzle diameter was typically 2/3 the diameter of the combustion chamber, i.e. $D_N \approx 2 D_C/3$. Lastly, the length of the combustion chamber was eventually estimated based on a curve-fit trendline including a 15% factor for the head length, L_H :

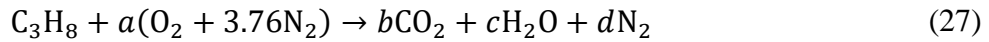
$$L_C + L_H = 1.15 [3.6988 D_i + 0.8307] L_2 \quad (26)$$

This analysis resulted in a complete geometric picture of a scaled Gluhareff pressure jet engine, but the reader is reminded these are at best a rough, first approximation and are likely to need adjustment after experimentation reveals a need for more or less fuel, tail pipe length to capture the exhaust flame, etc... Moreover, while the inlet areas and lengths are approximated, their locations along the inlet axis are also critical and may need minor adjustment to ‘tune’ them toward “sonic lock” and optimal performance. This can only be satisfactorily accomplished through lengthy, iterative computer simulations or quick physical experimentation.

III. Selection of Chemical Kinetics

A. Theory of Chemical Kinetics

Chemical reactions are typically modeled using “Chemical Kinetics” that involve quantifying the rates of prescribed chemical processes during the CFD solution process. A single global process, like the combustion of propane and air into carbon dioxide and water vapor, tends to be modeled instead as a series of reactions or reaction steps each with its own reactants, products, and an experimentally-determined rate. This reaction is shown in general form per mole of fuel in Eq. (27) below:



Manipulation of the amount of air, a , with respect to a single mole of fuel allows adjustment of the reaction to varying fuel-air ratios. For a stoichiometric reaction of propane and air, these coefficients balance to $a = 5$, $b = 3$, $c = 4$, and $d = 18.8$. [34]

The equation that is typically used to model a single reaction is either the two-parameter Kooij Equation [Eq. (28)] or the simplified version – the Arrhenius Expression [Eq. (29)] if $\ln(k)$ is linear with the inverse of temperature.

$$k = A \cdot T^m \cdot e^{-E_0/R_u \cdot T} \quad (28)$$

$$k = A \cdot e^{-E_a/R_u \cdot T} \quad (29)$$

Here A is an experimentally determined constant, T is temperature, R_u is the universal gas constant, and E is the activation energy of the reaction (an empiricism). The resulting reaction rate, k , may be defined for both the forward and reverse reaction. The forward reaction in this case would be fuel oxidation into carbon dioxide, water vapor, and potentially other nitrogen-based products (e.g. nitrogen oxides or NO_x). A reverse reaction rate models the tendency of some reactions’ products to reform into reactant species to reach equilibrium.

This reaction rate determines how quickly each species is consumed and changes the local species levels in the CFD model. It also affects how much energy is absorbed or released, and drives the reaction(s) to equilibrium. Mathematically this means the reaction rate, k , helps define the time-rate of change of species concentrations, R :

$$R_{C_3H_8} \equiv \frac{d}{dt} [C_{C_3H_8}] = k \cdot [C_{C_3H_8}]^{\nu_1} \cdot [C_{O_2}]^{\nu_2} \quad (30)$$

where ν_1 and ν_2 are curve fitting constants commonly around 1.0 or 0.5 and C is species concentration. So each reaction is modeled as being dependent on the presence of the chemical species involved and the Arrhenius constant, k . [34] All that remains is to experimentally determine a set of constants for each modeled reaction. Fortunately, completed models (with varying degrees of accuracy and applicability) are the goal of well-published research efforts presented in more detail in Section C of this chapter.

These combustion models typically conform to one of three types – detailed, reduced, or global kinetics models. Detailed kinetic mechanisms pursue maximum accuracy by attempting to capture as many independent reaction steps as possible. As a result, these are the most complete and accurate mechanisms but often include hundreds of reactions that must be curve-fit experimentally. By merit of the number of reactions involved, detailed mechanisms also generally require the most computational time. To reduce the computational time, reactions with little effect on desired conditions (temperature, ignition delay, etc...) are often removed. These mechanisms are referred to as “reduced.” Global mechanisms continue this philosophy by reducing the mechanism often to a single curve-fit reaction. This is intended to capture the overall thermodynamics of the reaction as opposed to the detail of intermediate processes. Because it typically occurs in a single step, this “black-box” method results in the fastest possible model of chemical kinetics.

B. Propane Oxidation Experimental Data

The chemical kinetic mechanisms discussed in Section A and the computational simulations that use them must be validated using experimental data prior to drawing any conclusions. This data is used specifically to determine the relative error of different kinetic mechanisms and aid in ultimately selecting the mechanism for modeling propane combustion in the pressure jet engine. A literature review showed a variety of experiments performed to accurately measure the properties of combustion (i.e. laminar flame speed, adiabatic flame temperature, etc.) and constants necessary for combustion modeling (e.g. pre-exponential factor, activation energies, etc...) at different equivalence ratios. The data used in this effort is generally reduced to the information necessary to match results from a model of premixed combustion in a closed spherical vessel.

1. Common Experimental Setups

There are many types of experimental configurations for determining combustion data some of the most common being continuous flow reactors (CFR), constant volume reactors (CVR), and jet-stirred reactors (JSR) The constant volume reactor is fundamentally a closed chamber in which fuel and an oxidizing medium (usually air) mix and burn under precisely controlled conditions. A co-flow reactor, however, involves continuous flow of both the fuel and oxidizer. This necessarily includes continuous mixing and combustion; whereas the closed chamber may be allowed to settle to quiescent initial conditions. Werle showed this turbulence effect caused a 150-200 K increase in the peak temperature for the co-flow reactor compared to a constant volume reactor [35].

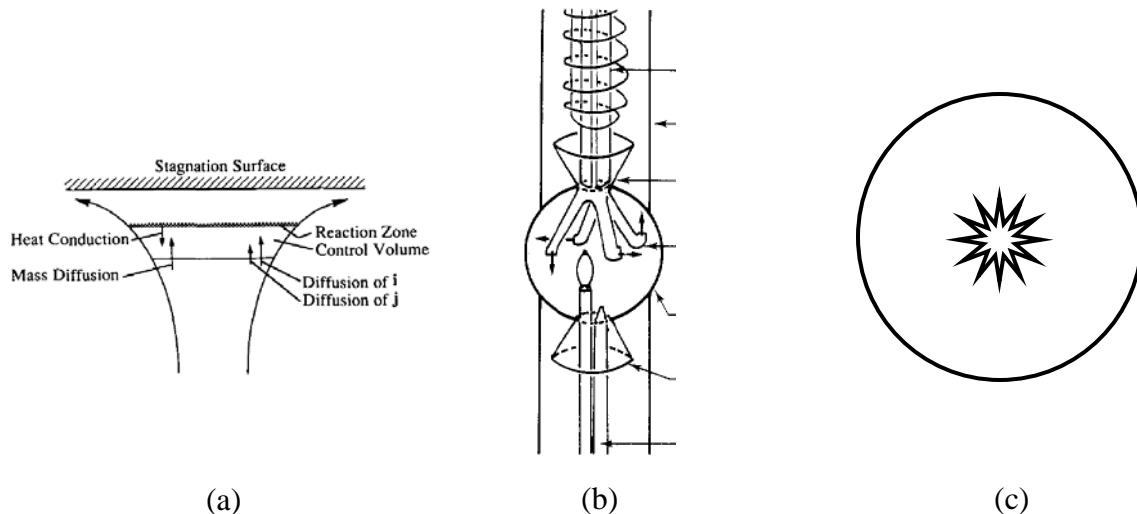


Figure 18: Common Hydrocarbon Oxidation Reactor Experimental Setups Showing (a) Counter Flow [36], (b) Jet Stirred [37], and (c) Constant Volume Reactors

An alternative form of continuous reactor is the jet-stirred reactor in which injecting jets enter a combustion chamber at some glancing orientation. This promotes turbulent mixing of the fuel and air similar to the conditions in many engines and increases residence time in the combustion chamber. A reactor design developed by Dagaut, *et al.* [37] was intended to study the oxidation of “light hydrocarbons” like propane at high pressures. In 2004 El Bakali, *et al.* used this form of jet-stirred reactor to study natural gas oxidation that also used shock tube data (a form of constant-volume reactor) to model ignition delay and laminar premixed flames to model laminar flame speed and showed good agreement with experimental data [38]. A similar design was used during a National Aeronautics and Space Administration (NASA) study on nitrogen oxide (NO) formation during propane combustion [39].

Constant volume reactors have also been extensively used to study propane oxidation and offer simple, symmetric geometry ideal for modeling as well as the ability to mix fuel and air and later induce ignition. The latter capability allows the mixture to reach quiescence; thus, minimizing the effect of turbulence and allowing the study of more ideally pre-mixed combustion. Norman, *et al.* used a spherical combustion chamber to study both auto-ignition temperatures and rich limits

of combustion [40]. Similarly Razus, *et al.* comprehensively studied propane oxidation and the effects of initial conditions using constant volume reactors [41-47].

While both the co-flow and jet-stirred reactors are useful methods of studying hydrocarbon oxidation, they necessarily introduce some level of mixing and turbulence that adds uncertainty and complicates modeling and simulation. This incremental complexity results in greater time necessary to compare different kinetic mechanisms. Alternatively, symmetrical constant volume reactors lend themselves easily to modeling of premixed combustion using zero-dimensional (0-D) analysis and prevent the data being tainted with mixing effects. As a result, the experimental data from spherical constant volume reactors (described in detail in the following sections) were chosen to compare the propane kinetic mechanisms described in Section III.0. The modeling theory and results of the comparison are then presented in Section III.0.

2. Minimum Ignition Energy

Prior to the initiation of combustion, a minimum amount of local energy must be provided. This is referred to as the “minimum ignition energy” and should be known to help set the energy level of a spark source in the CFD model. Recent experiments [48] suggested the classical value of 0.25 mJ [49] may be too conservative compared to a value of 0.48 mJ that was consistent with more recent experiments. Eckhoff and Olsen suggested that under the classical value’s definition of ignition (a 1% probability), the energy was between 0.40 and 0.45 ± 0.08 mJ [48]. As a result, an ignition energy of at least 0.5 – 1.0 mJ for near stoichiometric mixtures will be assumed for the CFD model using an energy point source. Once the mixture is ignited, it is then necessary to check the speed of the flame as it propagates. This is referred to as the flame speed or burning velocity and is dependent on the fuel type and the mixture properties (e.g., equivalence ratio, temperature, pressure, etc.).

3. Constant Volume Shock Tube Experiments

The first published shock tube study of propane/oxygen ignition was by Steinberg and Kaskan in 1955 and started an extensive catalog of shock tube studies [50]. The study tested stoichiometric mixtures of propane and oxygen for a small range of pressures and found the ignition delays to be largely independent of pressure effects. In 1966, Hawthorn and Nixon further studied qualitative trends of propane/oxygen oxidation in shock tubes using argon as a nonreactive, diluent gas [51].

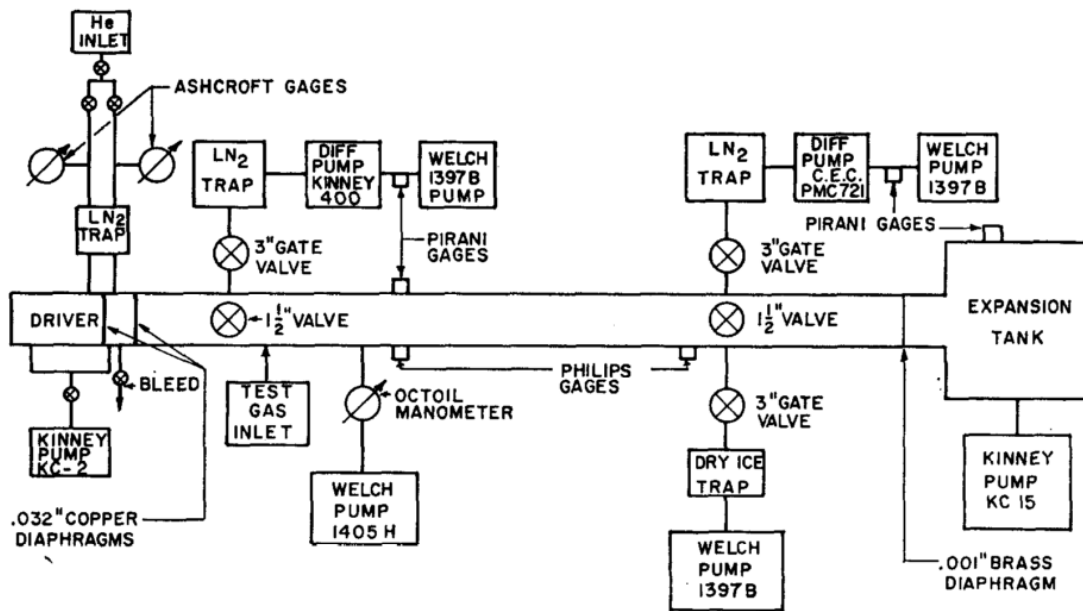


Figure 19: Shock Tube Apparatus as Published by Sulzmann [52] and Later Repeated by Myers and Bartle's Propane Study [53]

Myers and Bartle published a more extensive study a few years later intending to explore propane/oxygen oxidation for use in scramjet (Supersonic Compression Ramjet) engines [53]. They included measurements and correlations for reaction durations and ignition delay times and like Hawthorn and Nixon, used argon as a diluent gas. The apparatus was the same as that described by Sulzmann [52] and shown in Figure 19. It relied on a stainless steel tube activated by breaching a series of thin diaphragms and studying the propagating species' refractive indexes using a laser-Schlieren system. The ignition delay was determined using the initial rise of

hydroxide (OH) emissions, a second rise of OH emissions, and the initial rise in carbon dioxide (CO₂) emissions. It should be noted that this definition for ignition delay is significantly different from those used in other studies making direct comparisons of some findings difficult. The end of the reaction was determined based on the end of CO₂ formation, OH emission, and the final refractive index gradient (via the Schlieren system). Correlations using a least-squares fit were matched to major species reaction durations and ignition delays that revealed two distinct regions matching the authors' correlations well. Temperature and pressure dependencies were also found to match expectations from a prior study on kerosene and isooctane fuels [54].

In 1971, Burcat, *et al.* published two oft-cited studies on shock tube ignition delays for nine propane/oxygen/argon mixtures [55] and five different hydrocarbons between C₁ and C₅ [56]. Both studies used a single-pulse stainless steel shock tube with helium as the driver gas and studied the reflected shock waves using a gas chromatograph to identify species. The ignition delay data in the first study was curve fit with Arrhenius constants including species concentration power dependencies for argon, propane, and oxygen. These dependencies were determined graphically using the datasets' relative offsets. In the propane study, the authors found the ignition delays to be unaffected by the diluent gas meaning its power dependency was negligible despite argon composing a large fraction of the total mixture. Around stoichiometric mixtures they found that propane increased ignition delays but expected the power dependency on propane to diminish as the mixture was leaned. They also noted that significant decomposition of propane into other hydrocarbons occurred prior to ignition that could affect the ignition delay times. That same year Lifshitz, *et al.* published a similar study for methane mixtures [57] noting that only Glass [58] had found a dependence on argon but at concentrations as much as 10 times greater and thought to be dependent on oxygen dissociation.

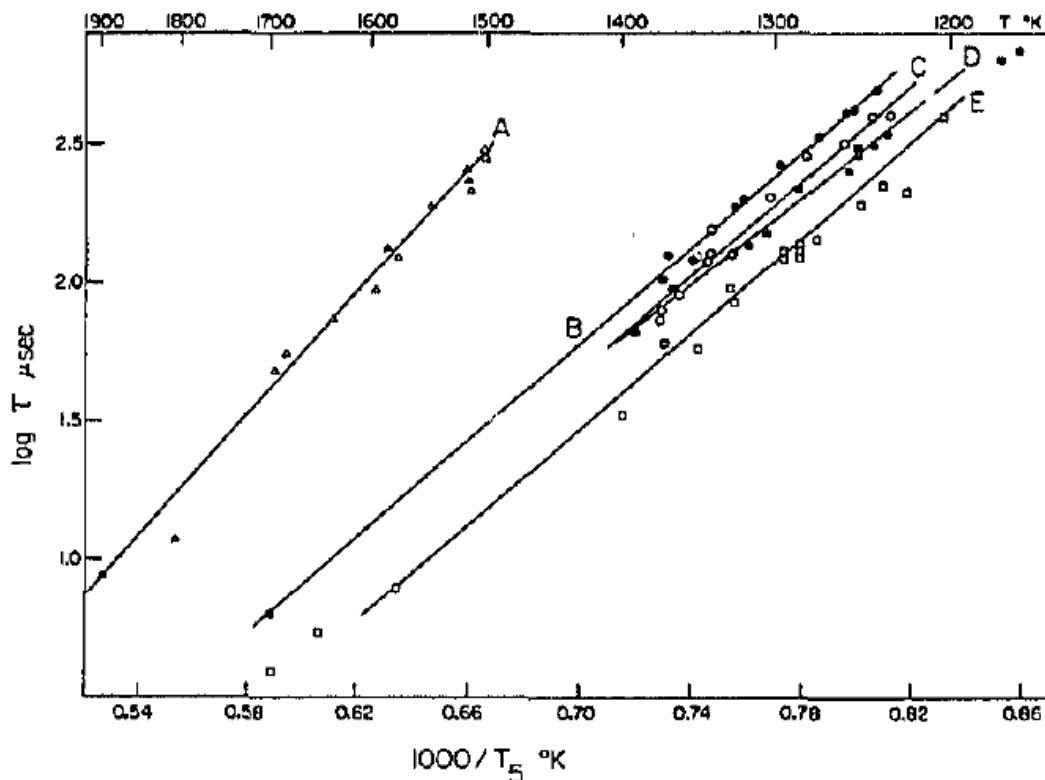


Figure 20: A Logarithmic Plot of Ignition Delay, τ , For a Range of Temperatures, T_5 , Using Five Different Fuels (A = Methane, CH_4 , B = Propane, C_3H_8 , C = Butane, C_4H_{10} , D = Pentane, C_5H_{12} , and E = Ethane, C_2H_6) as Published by Burcat, *et al* [56]

Burcat's second 1971 study used the same experimental apparatus to draw similar conclusions about $\text{C}_1 - \text{C}_5$ alkanes. For instance, methane showed a significantly higher activation energy than the rest of the hydrocarbons tested (presented graphically in Figure 20). All species but ethane fit the qualitative expectation that ignition delay should vary inversely with the number of carbon atoms. Ethane showed the lowest ignition delays of all the hydrocarbons tested. They supposed it likely that breaking the C-C bond in ethane was similar to breaking these bonds in heavier hydrocarbons and when combined with methane-like chain breaking of reaction products could decrease the ignition delay below those of the other hydrocarbons tested. No other suitable experimental data was available to comparatively test these ideas. The following year Burcat supported a study by Crossley, *et al.* investigating mixtures of methane and oxygen with higher alkanes including ethane, propane, butane, and pentane [59]. These mixtures all produced a

significant reduction in ignition delay time and showed that the additive influence was chemical as opposed to driven purely by thermal effects.

Shortly thereafter, in 1981, Eubank *et al.* published a study on the ignition of methane and simulated natural gas/air mixtures in reflected shock waves [60]. They used the same setup described by Olson's ethane study that involved the use of a rectangular shock tube and a helium-neon laser for laser-Schlieren analysis. The driver gas was a mixture of hydrogen (H_2) and nitrogen (N_2). The authors qualitatively matched prior findings [57, 59] showing that adding ethane (C_2H_6) and butane (C_4H_{10}) to stoichiometric mixtures of methane (CH_4) and air subsequently decreased ignition delays. Adding propane (C_3H_8) to these mixtures further reduced ignition delays. Two more methane studies were published shortly thereafter – Krishnan *et al* studying mixtures with acetylene [61] and Cheng studying mixtures with hydrogen [62].

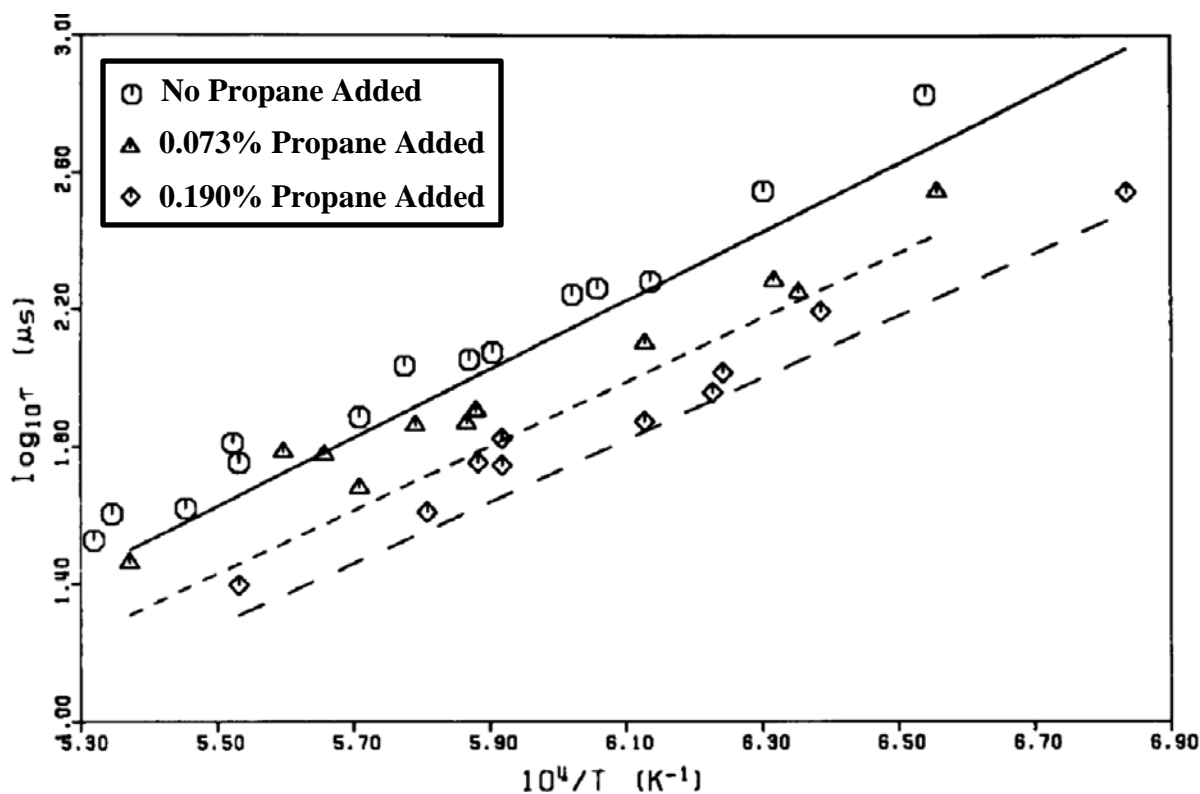


Figure 21: Frenklach and Bornside's Comparison of Experimental Methane Ignition Delays, τ , to Computer Predictions Using a Chemical Kinetic Mechanism. Experimental Data in Points and Corresponding Models Shown by Lines [63]

In 1984, Frenklach and Bornside published another oft-cited study into matching experimental shock tube data of methane/propane mixtures to a chemical kinetic mechanism-based computer model [63]. The mechanism used 140 reactions with 34 species. The experiments maintained a nearly constant density in the shock tube for temperatures between 1300 and 1600 K using a conventional stainless steel shock tube. Helium was used as the driver gas while argon was used as a diluent. An important distinction was made in regards to the measurement of ignition delays – different measurement locations produced dissimilar results. In other words, ignition delays measured at the end of the shock tube differed significantly from ignition delays measured at the contact surface between the driver and driven sections. The model agreed well with the experimental data, as well as the data published by Lifshitz [57] and Crossley [59] and was further subjected to a sensitivity analysis to improve the mechanism. The results of the sensitivity analysis using a saturated design method showed qualitatively similar results with a brute force method.

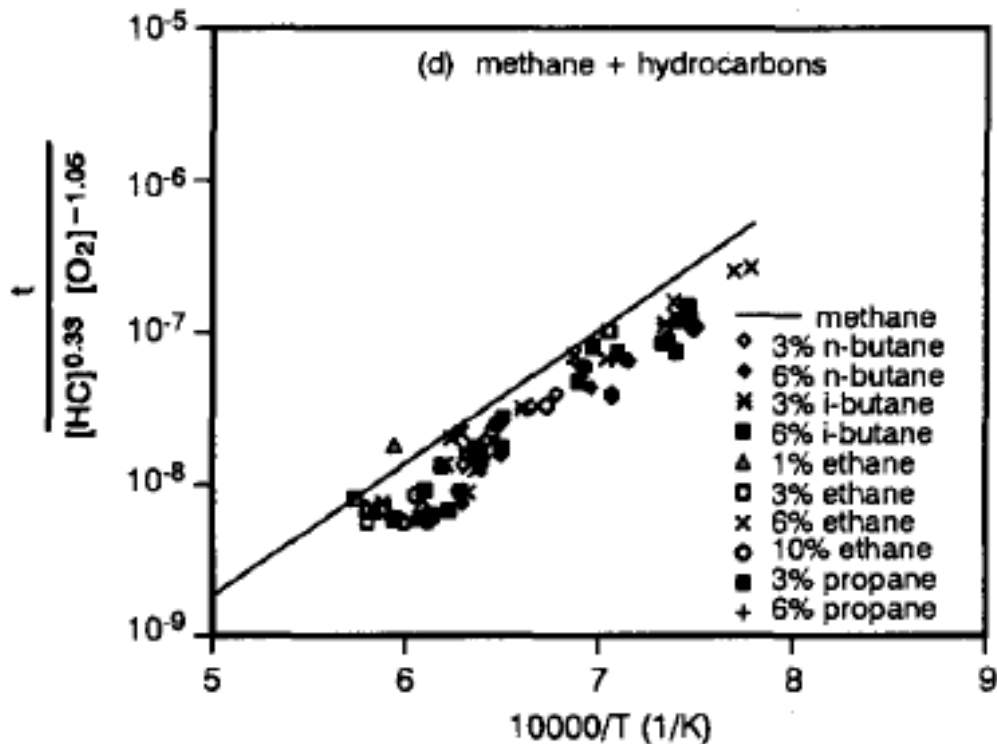


Figure 22: Effect of Hydrocarbon Contaminants on Methane Autoignition [64]

A decade later Spadaccini and Colket published a comprehensive literature review of methane and methane/hydrocarbon mixture oxidation and combined them to produce a series of general correlations for predicting mixture ignition delays. [64] The study also included new experiments using a conventional stainless steel shock tube with pressure transducers at multiple locations. Mixtures of methane including varying levels of ethane, propane, and butane reasonably matched the same Arrhenius-type curve fit for ignition delay. Of particular note is the inclusion of experimental data for multicomponent methane/hydrocarbon mixtures and the resulting fitting equations for mixture ignition delays. The findings further confirmed that small amounts of hydrocarbons added to methane resulted in reduced ignition delays. The data was also compared with the methane mechanism proposed by Frenklach [65] that matched published data and curve fits well, except under very lean conditions. The mechanism predicted longer ignition delays under these conditions that disagreed with the curve fits, but matched sparsely available data at such low equivalence ratios.

In 1998, Qin published a dissertation on comparing a propane oxidation mechanism with experimental data for propane/oxygen/argon ignition delays observed behind reflected shock waves [66]. In this case, ignition delay times were defined based on the time between the arrival of the reflected shock and the peak of OH absorption rise. Qin's mechanism was limited to C₃ chemistry and below and is discussed in more detail in Section C of this chapter. By adjusting some reaction rates to target the ignition delay data, good agreement was found between the mechanism predictions and the experimental data.

Afterward, in 1999, Brown and Thomas published a study on ignition delay and transition to detonation in ethylene/oxygen and propane/oxygen including a Schlieren analysis of the propagating shock waves [67]. A series of six mixtures were tested studying the influences of

argon and nitrogen as the diluent gas on ethylene and propane ignition. The use of diluent nitrogen tended to increase incident shock velocity as compared to tests with diluent argon. The ethylene and propane ignition delays matched well with other published works but noted that Jachimowski's data [68] was "not in good agreement" at low temperatures although it was extrapolated beyond its original scope.

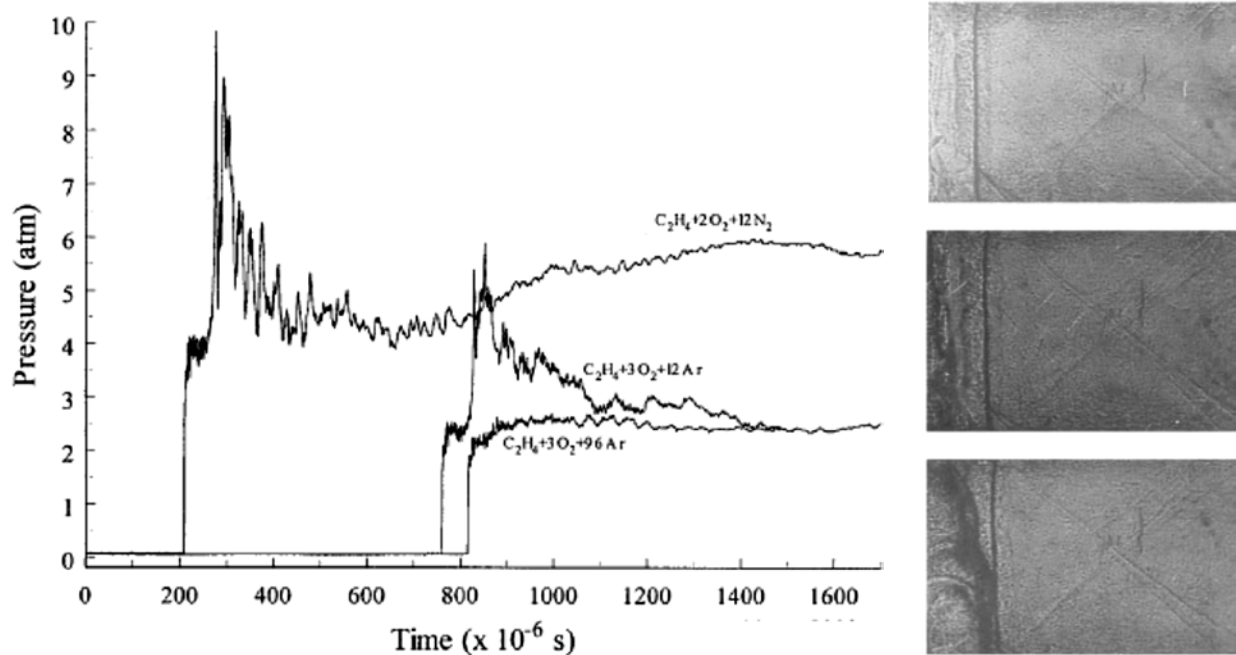


Figure 23: Pressure Traces for Ethylene/Oxygen Ignition Transition to Detonation at Low Nitrogen Dilution (Left) and Corresponding Schlieren Shadowgraph Images Taken 10 μ s Apart Showing Transition to Detonation (Right) as Published by Brown and Thomas [67]

The data comparison suggested that earlier ignition delay works using highly diluted mixtures may not necessarily produce an accurate model of ignition in less-dilute applications. For these cases of high dilution, little evidence of a strong reaction could be found in the data or Schlieren images. However, for less diluted mixtures the data showed a pressure increase following the wave reflection that the authors interpreted as the transition to mixture detonation. This transition was also visible in the Schlieren images.

A year later, Cadman *et al.* published a study on high pressure propane oxidation (up to 39.5 atm) at an equivalence ratio of $\phi = 0.5$ [69]. His experiments managed to lower the possible

temperatures of study to 800 K by adjusting the shock tube driving gas. At these “intermediate” temperatures, the activation energy (and thus slope of the ignition delay – $1/T$ plots) decreased significantly. Burcat noted a decrease from 192 kJ/mol to 156 kJ/mol while Cadman’s study suggested a significantly lower energy of 38 kJ/mol. The difference was thought to be due to the analysis method used. Cadman’s study used two separate curve fits as opposed to a single polynomial curve. In general, the measurements showed that ignition delays were shorter than expected if extrapolating from higher temperatures (above 1200 K).

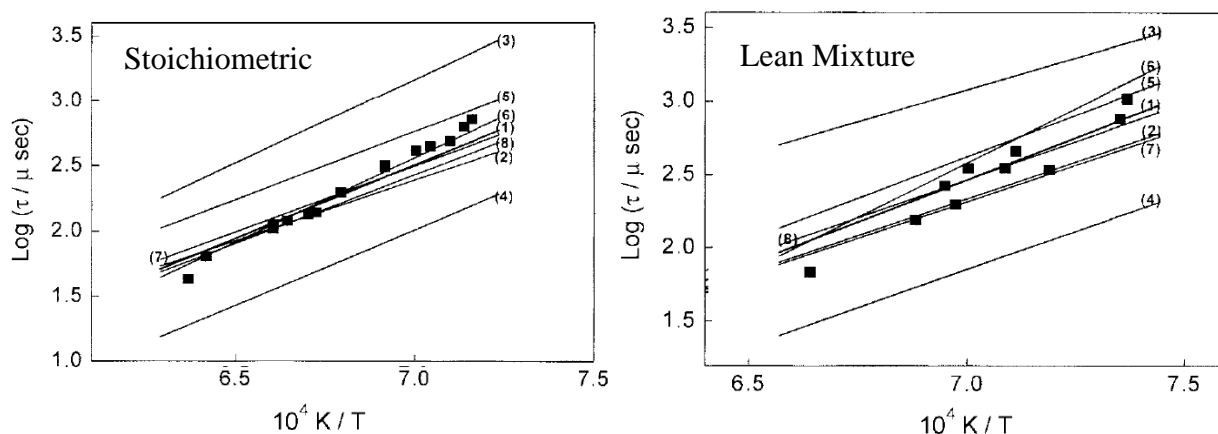


Figure 24: Experimental Ignition Delay Times for Stoichiometric (Left) and Lean (Right) Mixtures of Propane and Air Compared to Kinetic Mechanisms from (1) Sung [70], (2) Qin [66], (3) Westbrook [71], (4) Jachimowski [68], (5) Dagaut [72], (6) Glassman [73], (7) Konnov [74], and (8) UC Berkeley’s Gas Research Institute (GRI) Mechanism Version 3.0 [75] as Published by Kim [76]

In 2000, Kim and Shin published a study on propane ignition behind reflected shock waves and matched the data to a mechanism for propane ignition delay. [76] The ignition delay was determined based on the pressure rise and the formation of OH emissions. They collected data from other experiments and produced an empiricism for ignition delay in the Arrhenius form adding dependency on propane and oxygen concentrations. The experimental ignition delay data were found to match the predictions from several prior mechanisms (discussed in more detail in Section C) within the experimental data scatter.

The following year Qin studied the ignition of propene (C_3H_6), a common intermediate hydrocarbon in propane oxidation [77]. The study tested reflected shock waves at pressures as high as 4.7 atm, temperatures up to 1820 K, and equivalence ratios between 0.5 and 2.0. The data resulted in a pressure-based correlation for the ignition delay that also relied on the concentrations of propene and oxygen. The data and this correlation suggested that prior propene ignition delays from Burcat [78] were too long, but could not speculate as to why.

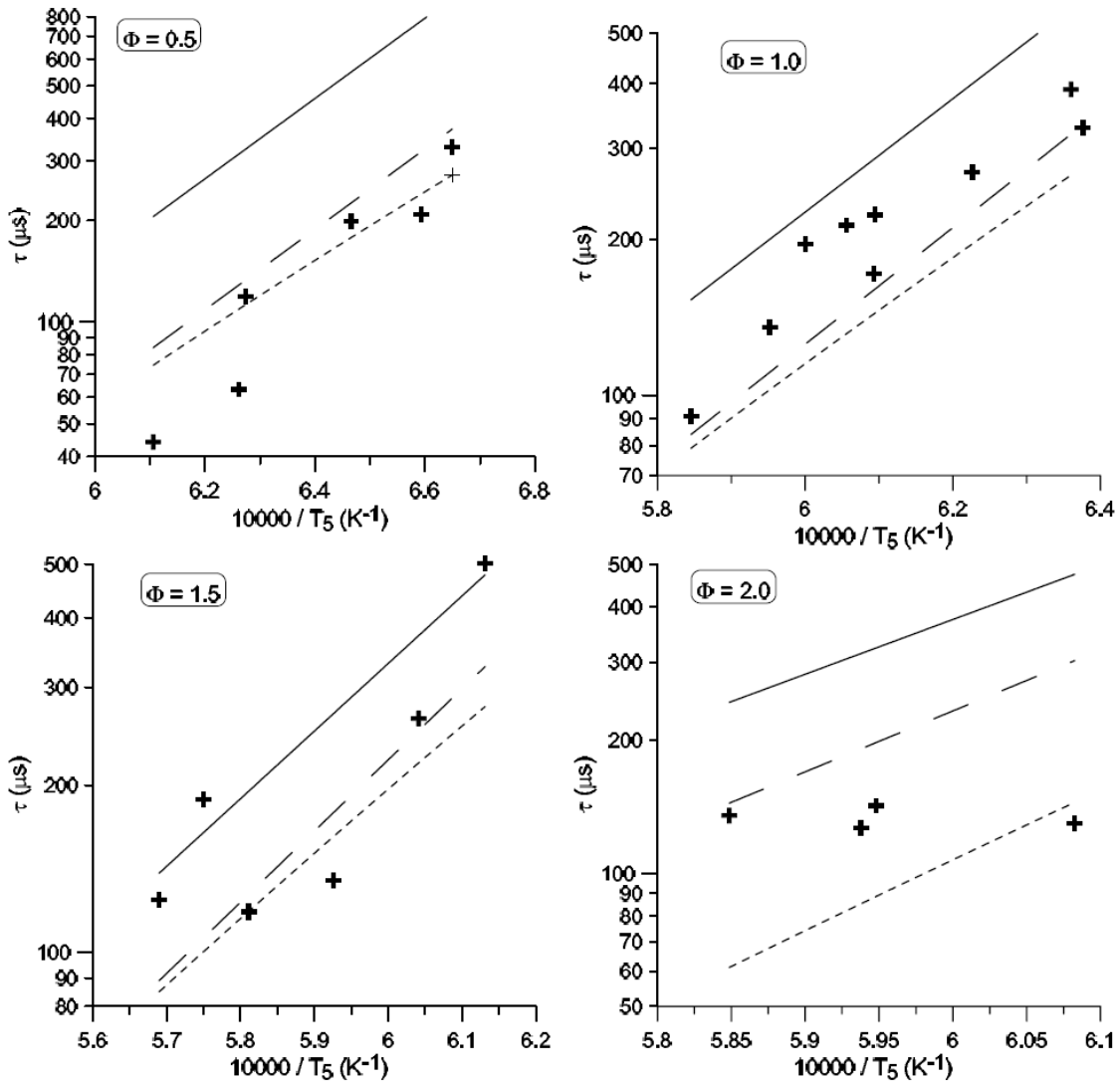


Figure 25: A Comparison of Kinetic Mechanism Predictions and Experimentally Measured Ignition Delays of Natural Gas/Oxygen Mixtures (Diluted 97% with Argon at 600 kPa) for a Range of Equivalence Ratios. Dashed Line Shows Tan's Mechanism [79, 80], Dotted Line Shows GRI Mech 3.0 [75], and Solid Line Shows a Curve Fit Equation as Published in Lamoureux [81]

In 2003, Lamoureux published a shock tube ignition delay study for natural gas behind reflected shock waves [81]. The study also compared ignition delays for different blends of natural gas from several different regions: Abu Dhabi, Indonesia, Russia, North Sea, Algeria, and Matheson (the same source as Spadaccini and Colket [64]) and checked them with two chemical kinetic mechanisms published by Tan [79, 80] and Smith (GRI Mech 3.0) [75]. The latter comparison of data with mechanism predictions is included in Figure 25 and shows the accuracy of a relatively simple curve fit based on the product sum of individual ignition delay times. Butane and higher hydrocarbons in the tested natural gas mixtures were found to not affect ignition delay times; hence correlations using the ignition delays of lower hydrocarbons (methane, ethane, and propane) were considered to have “generally good” agreement with the experimental data.

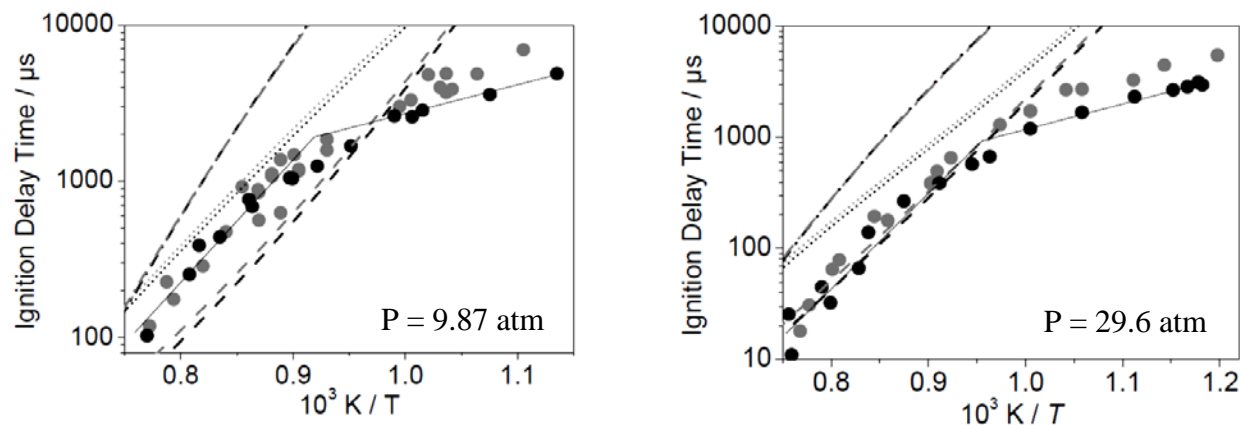


Figure 26: Measured Ignition Delays Compared to Predictions by Argon Data Trend (Solid Lines), Konnov’s Mechanism [82] (Dashed Lines), Curran’s Mechanism [83] (Dotted Lines), and GRI Mech 3.0 [75] (Dashed-Dotted Lines). Black Data Points Show Propane/Oxygen/Argon (at $\phi = 0.5$) while Grey Points Repeat the Conditions for Propane/Air Mixtures. As Published by Herzler [84]

The following year, Herzler, *et al.* published an ignition delay study on propane/oxygen mixtures with argon at intermediate temperatures (750 – 1300 K) and high pressures (up to 29.6 atm). [84] These conditions were studied because they recreate the regime where internal combustion engine “knock” that can cause serious engine damage. Propane was studied because it best matched the ignition properties of higher hydrocarbons. The ignition delay was determined

using the pressure trace and CH* radical emission. They found that low temperature data (below 1050 K) was “not well represented” by the computer simulations. The simulated ignition delays in oxygen were about 10% shorter than the comparable simulations in air. The authors also noted a decrease in activation energy at 1050 K that was stronger in oxygen mixtures than air. Despite good agreement at higher temperatures, the kinetic mechanism-driven simulations did not predict this change in the activation energy. The fact that this phenomenon appeared in both oxygen and air mixtures meant that it could not be explained by the thermal relaxation effect of nitrogen in air. They noted a need to improve the current kinetic mechanisms to capture this change in activation energy at low temperatures.

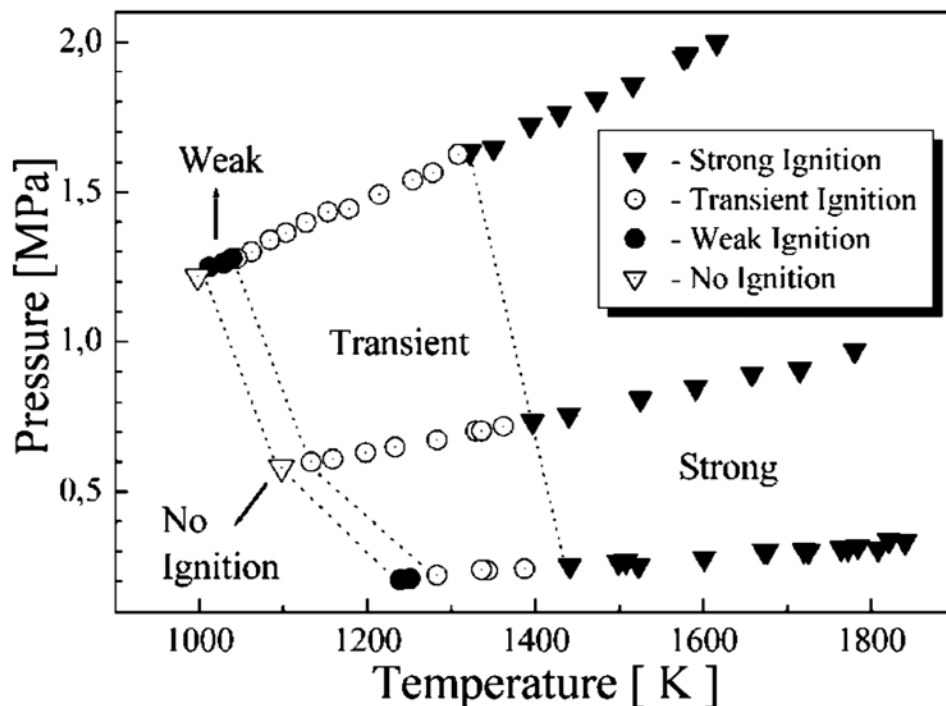


Figure 27: Measured Propane-Air Autoignition Domain for Stoichiometric ($\phi = 1.0$) Showing Pressures and Temperatures for Strong, Transient, and Weak Ignitions as well as Low Temperature Flammability Limits Published by Penyzkov [85]

Penyzkov, *et al.* also published a shock tube study that same year limited to propane-air mixtures but across three equivalence ratios ($\phi = 0.5, 1.0, \text{ and } 2.0$) [85]. The ignition delays were determined based on the pressure trace, C₂ emissions, and luminosity. These criteria were

independently compared with previously published correlations and showed good matching at high temperatures. The data gathered in the study also allowed a domain of autoignition to be generated for the range of equivalence ratios tested (shown for stoichiometric conditions in Figure 27). The steady-state detonation velocities at high temperatures were “very close” to those predicted by equilibrium codes. The increase in post-shock fuel and oxygen concentrations (via increasing local density) tended to increase the reaction rate and, therefore, reduce the low temperature threshold for weak ignition. In rich mixtures, this resulted in the measurement of cool flames.

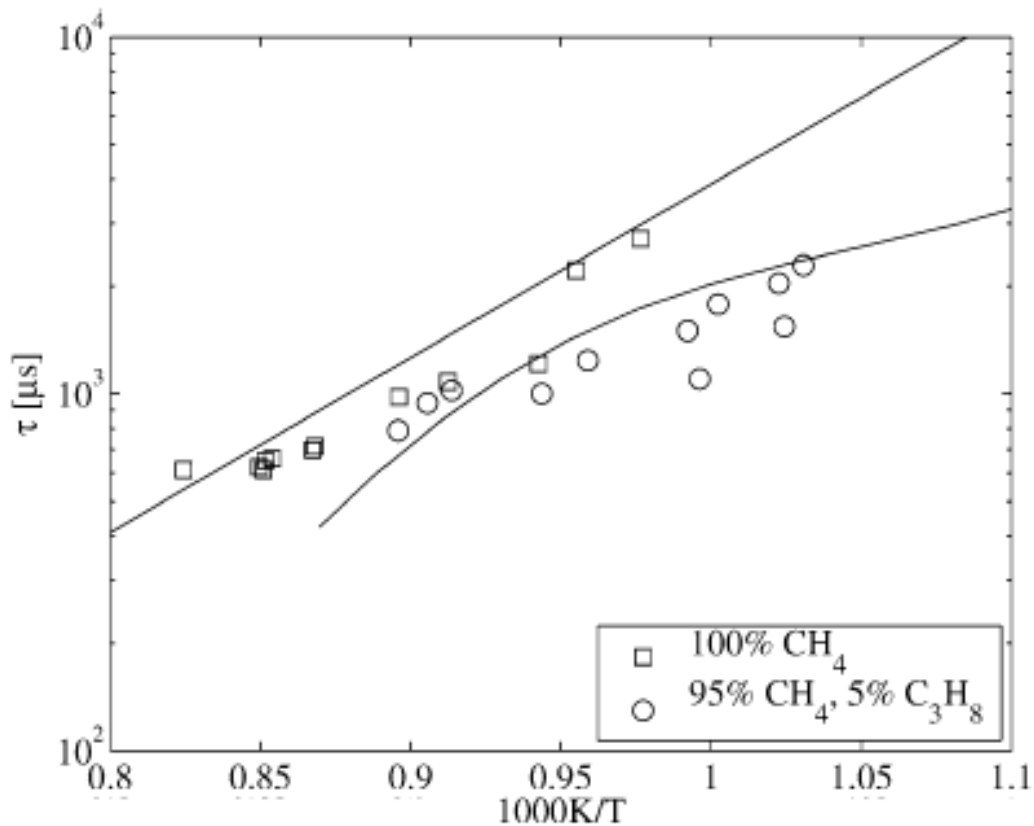


Figure 28: Ignition Delays of Methane With and Without a 5% Propane Additive Showing Decrease in Ignition Delay at 39.5 atm Pressure [86]

In 2006, Huang and Bushe published a shock tube study matching experimental data to results predicted by the GRI Mech 1.2 (an earlier version of GRI Mech 3.0 [75]) for autoignition of methane/ethane/air and methane/propane/air mixtures. [86] The data was measured from reflected shocks intended to simulate the conditions relevant to Homogeneous Charge

Compression Ignition (HCCI) engines and gas turbines (i.e. temperatures between 900 and 1400 K and pressures between 15.8 and 39.5 atm). Of major interest was the effect of different additives (in this case ethane or propane) that could result from using natural gas blends from different sources. While it was known that adding ethane or propane tends to reduce ignition delay, there was an observed minimum ignition delay with ethane added at 1100 K. With propane this effect was more prominent at lower temperatures. At high pressures (39.5 atm) with 1.25 - 5% propane added at 1100 K the ignition delay was reduced by 10 – 15% but at 1000 K the ignition delay was reduced by 50%. The detailed kinetic mechanism was used to study this ignition-promoting phenomenon as a function of the chemistry varying with temperature, specifically methylperoxy (CH_3O_2) and methylhydroperoxide (CH_4O_2). Natural gas mixtures have since been a topic of study and often include propane with other hydrocarbons added to methane to study their applicability to compression-ignition engines [87] and gas turbines [88].

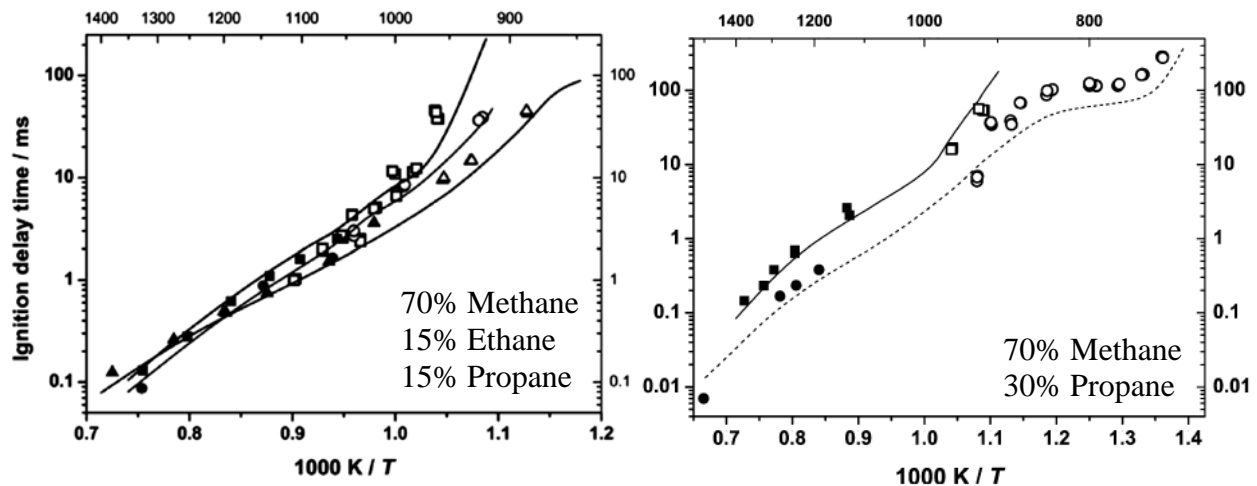


Figure 29: Ignition Delays of 70% Methane / 15% Ethane / 15% Propane at Varying Equivalence Ratios [89] (Left) and 70% Methane / 30% Propane at Varying Pressures [90] (Right) Solid Data Points Indicate Shock Tube Experiments and Empty Data Points Indicate Rapid Compression Machine Experiments. Lines Show Kinetic Mechanism Predictions via the HCT (Hydrodynamics, Chemistry, and Transport) Program

Two years later, Healy, Curran, *et al.* published a study on methane/ethane/propane mixtures at high pressures (1 – 50 atm) but for a wider range of temperatures (770 – 1580 K). [89]

The study employed both a high-pressure shock tube apparatus as well as a rapid compression machine to simulate the conditions of a compression ignition engine. That same year they also published a related study limited to methane/propane mixtures in the same temperature range but limited to pressures of 10, 20, and 30 atm [90]. These studies together represent an extensive analysis of methane/ethane/propane mixture ignition delays under the effects of varying temperature, pressure, and equivalence ratio with a fraction of the results included in Figure 29. The use of a rapid compression machine allowed the expansion of the temperature profile to lower temperatures that showed shorter ignition delays by as much as a factor of two (between 700 and 900 K). The computer predictions were able to capture the relative reactivities of different fuel mixtures qualitatively and showed “excellent” quantitative agreement with experimental data.

4. Constant Volume Spherical Bomb Reactors

Razus, *et al.* has performed extensive experiments in closed vessels at the various initial conditions that affect flame speed [41, 44, 45, 47]. The authors compared their experimental findings with several closed form solutions and a 1-D simulation using detailed kinetics and determined that for a stoichiometric mixture, a flame speed (S_U) at standard temperature and pressure of 38.9 cm/sec showed the least error using the following relationship:

$$S_U = R \cdot \left(\frac{k}{\Delta P_{max}} \right)^{1/3} \cdot \left(\frac{P_0}{P_{max}} \right) \quad (31)$$

where R is the radius of the chamber, k is a cubic law coefficient, ΔP_{max} is the maximum pressure rise during, P_0 is the initial pressure, and P_{max} is the sum of P_0 and ΔP_{max} .

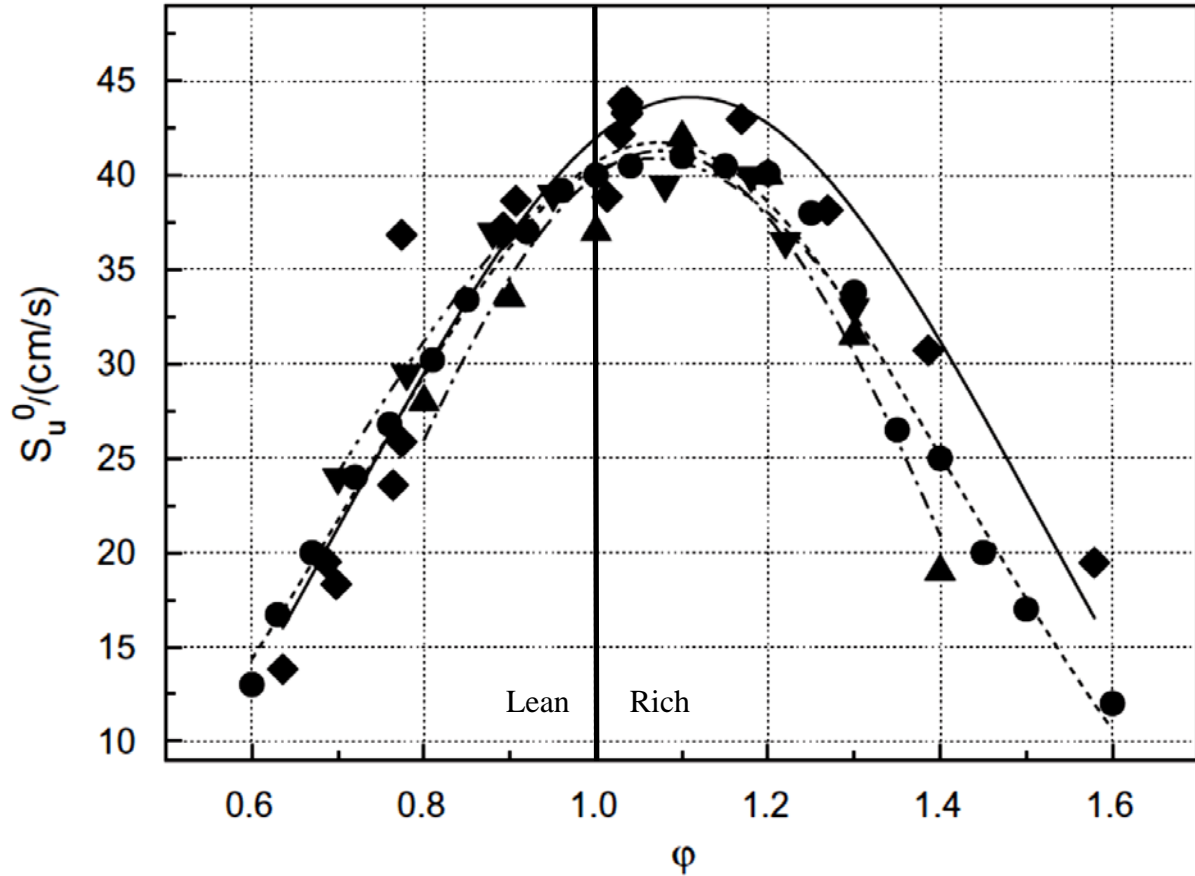


Figure 30: Flame Speed vs. Equivalence Ratio Comparing Several Closed-Form Solutions (Lines) with Measured and Referenced Experimental Data Points at Standard Temperature and Pressure [44]

The authors of that study also compared the flame speed trends at various initial temperatures and pressures noting that higher initial temperatures and lower initial pressures tended to increase the flame speed. They further compared their flame speed calculations at varying equivalence ratios to the solutions of other authors and found good agreement. This comparison is included in Figure 30 for its utility in eventually verifying the flame propagation seen in the reacting flow CFD model. It is clear that while there is some variation between different experimental sources and even between different estimation methods, the variation is generally low, especially for lean, near-stoichiometric mixtures. The reader should recall the premixed CFD model will remain in this region.

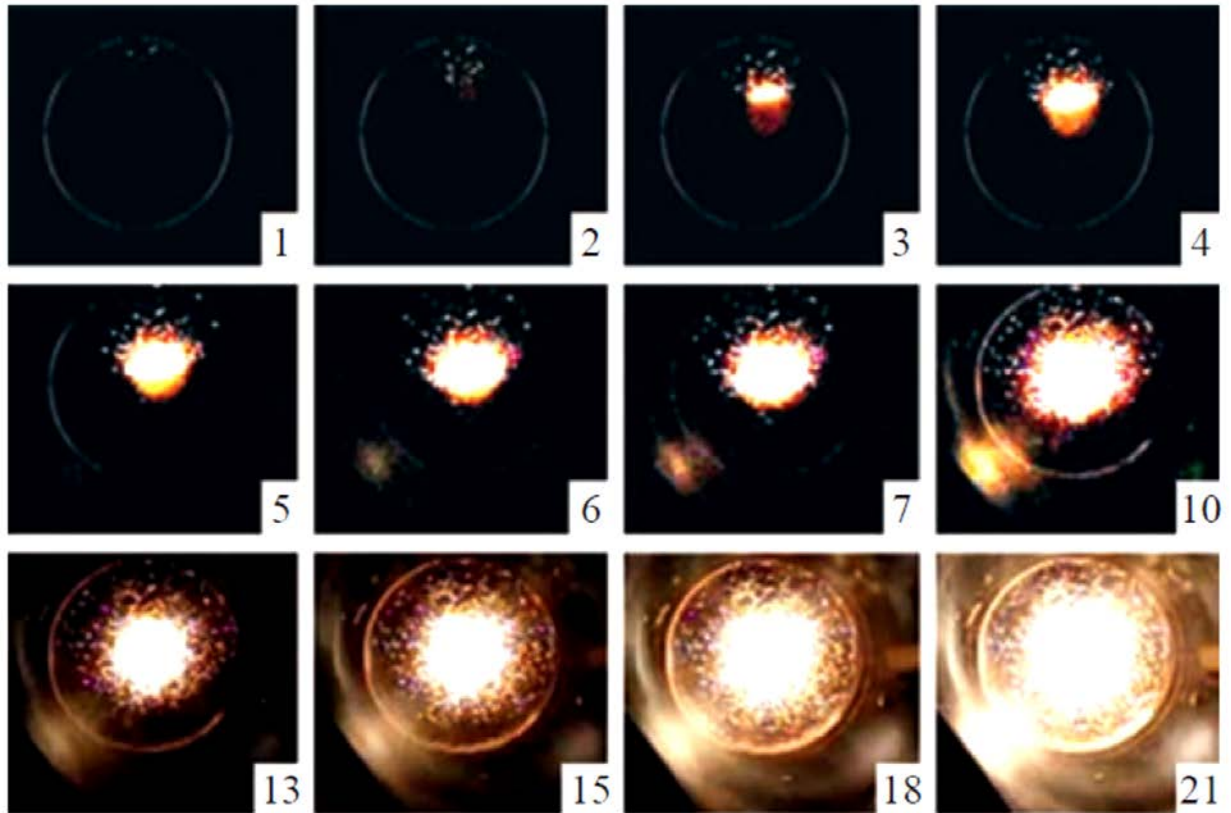


Figure 31: Image Sequence from Primary Ignition in a Rich 12.3% Propane-Air Mixture at 12.6 sec Recorded at 600 Hz [91]

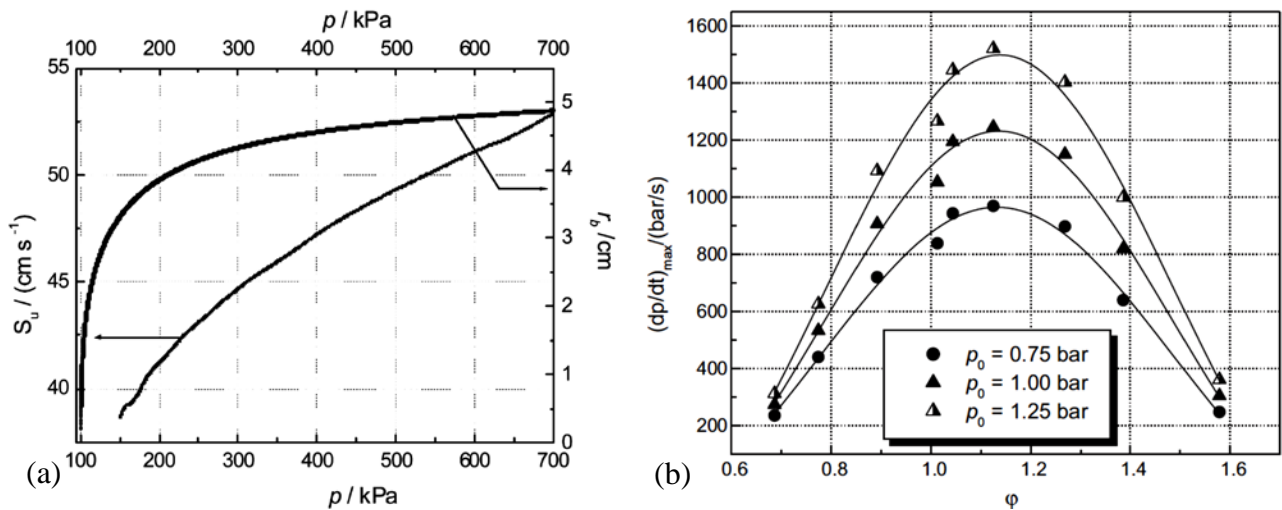


Figure 32: (a) Experimental Flame Radius and Burning Velocity of a Stoichiometric Propane-Air Mixture at Standard Temperature and Pressure [41] and (b) Maximum Rate of Pressure Rise in a Spherical Vessel at Various Equivalence Ratios and Initial Pressures at Standard Initial Temperature [42]

Subsequent research by Razus, *et al.* tested Eq. (31) based on the pressure-time response of propane-air explosions in the same spherical chamber architecture. They again showed a peak of flame speed at an equivalence ratio of about 1.1 and the same trends observed before with regard to initial temperature and pressure [41]. These temperature and pressure trends are further verified by Huzayyin, *et al.* in comparing pure propane-air and liquefied petroleum gas (LPG)-air mixtures [92], as well as by Razus for LPG-air mixtures [44]. Razus, *et al.* also included a useful plot of experimentally determined flame speed, S_U , and flame radius (the radius of burned mixture), r_b , which is included in Figure 32. To complement this data, high speed video showing the experimental ignition of propane-air mixtures was also published by Rubtsov, *et al.* that allowed direct verification of the linearity of flame radius with time [91]. Stills from this recorded data are included in Figure 31.

Further experimental data is available regarding the effects of temperature and pressure on both the explosion pressures [43] and maximum rates of pressure rise [46] of propane-air mixtures in a spherical closed vessel. These efforts were also performed by Razus, *et al.* to check the validity of closed-form solutions. They noted significant differences between explosion pressures measured in symmetrical and asymmetrical vessels and found that maximum pressures peaked at slightly rich equivalence ratios (i.e. 1.1 to 1.3). In addition, when comparing a cylindrical vessel to a spherical vessel, the latter was found to reach peak pressure sooner and is potentially advantageous for a transient CFD model – if the vessel reaches peak pressure sooner, it should burn faster, and require less time to simulate than an equivalent cylindrical vessel.

They also noted that minimum explosion times (and similarly maximum rate of pressure rise) occurred at equivalence ratios between 1.2 and 1.4, which suggest simulation of a richer mixture may slightly reduce computation time [42, 43]. Maximum rates of pressure rise were also

found to relate linearly to the initial pressure for a constant initial temperature and fuel-air ratio. The relation of pressure rate with equivalence ratio at several initial pressures is included in Figure 32. A similar study comparing cylindrical and spherical vessels using propylene-air explosions, showed the same trends, which suggests the effects of initial conditions on the speed of combustion are not limited to propane-air and may also occur for other reactions included in a more detailed kinetic mechanism [46].

5. Coflow and Counterflow Reactors

One of the earliest flow reactor studies involving propane oxidation was published by Wu and Law in 1984 [93]. They built a device using a constant flow nozzle impinging on a flat plate in close proximity to allow study of flames in stagnation flow during which flames have a varying amount of “stretch.” Flame stretch is governed by the negative velocity gradient (du/dx , defined as Γ or in some works, K) and can have a nontrivial effect on the local flame speed. Flow velocities were measured using Laser Doppler Velocimetry (LDV) allowing measurement of velocity distributions as a function of radius with a 0.1 mm resolution. Replacing the flat plate (made of brass and cooled) with a counterflow formed by either cold air, nitrogen, or an opposing flame was shown to not affect flow velocities and temperatures while having the added benefit of eliminating any contamination of the results from catalysis due to the plate material.

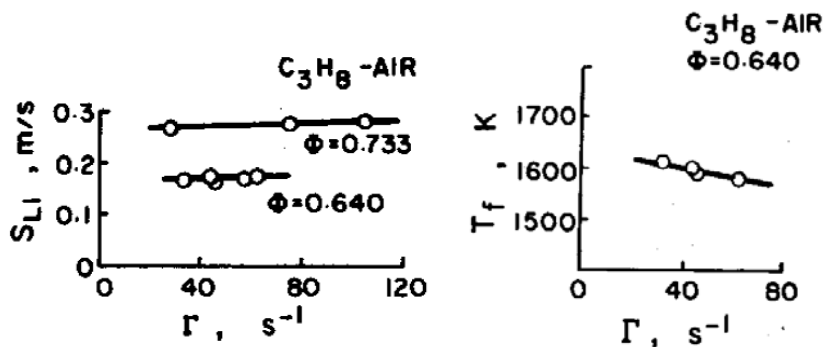


Figure 33: Experimental Data Showing the Effect of Flame Stretch, Γ , on the 1-D Laminar Flame Speed, S_{L1} , and Flame Temperature, T_f , for Lean Propane-Air Mixtures [93]

Wu and Law experimented with the combustion of hydrogen and air as well as several hydrocarbons including methane (CH_4) and propane (C_3H_8). Propane-air flame speeds showed a weak increase with growing flame stretch while flame temperatures showed a significant decrease. This was consistent with a Lewis number, Le , greater than 1 indicating the thermal diffusivity, α , (and thus thermal transport) was greater than the mass diffusivity, D , (and thus mass flow).

Two years later, Liu published a further study [94] investigating the effects of radiative heat loss (which can become significant at greater separation distances) using a well-studied double counterflow flame apparatus [95-98]. The study was limited to nonluminous blue methane-air flames that did not produce soot particles. Axial temperature profiles of the methane-air jets showed a minimum at the stagnation plane, and was considered to be due to particles taking longer paths the closer they were to the stagnation plane and, thus, having more time for cooling effects. Because combustion process occurred at a steady state with low fluid velocity, convective effects were considered negligible. Radial heat conduction was also ruled out as radial temperature profiles also showed a minimum at the center of the jet instead of at the periphery. Estimates for the heat loss due to radiation from nonluminous flames resulted in temperature drops that were in “favorable agreement” with those seen experimentally.

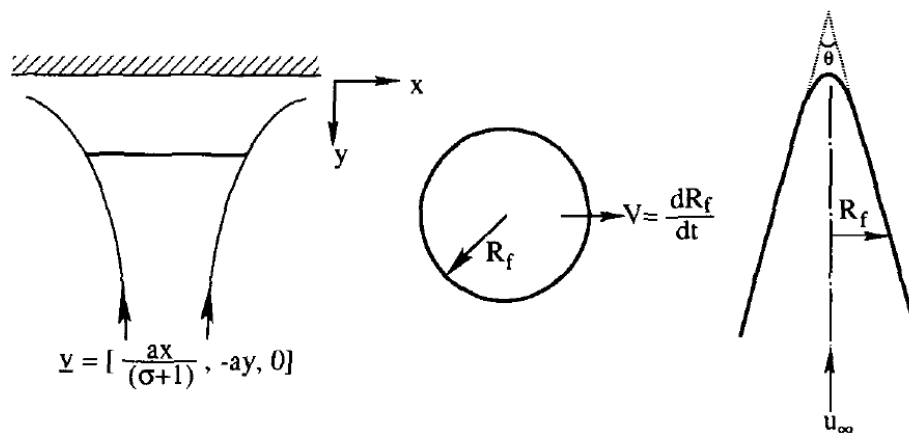


Figure 34: Three Examples of Stretched Flames – The Stagnation Flame, Impinged on a Symmetrical Boundary or Wall (Left), The Propagating Spherical Flame (Center), and The Axisymmetric Bunsen Flame (Right) [36]

In 1989, Law published a comprehensive study on the analytical and qualitative theory, as well as the experimental implications of stretched/strained premixed flames [36]. He noted three common examples of stretched flames (shown in Figure 34) and noted that hydrodynamic stretch and flame stretch can be “strongly coupled” as stretch in the fluid may impose stretch on the propagating flame. Furthermore, the study confirmed with experimental data that the flame temperature was unaffected by stretch but the burned mass of a stretched flame was lower than the ideal unstretched flame and pointed to flow divergence as the cause. Once the stretch rate is high enough, the burned mass will drop to zero and flame extinction can occur. This was found to occur in an ethane-air flame, for instance, at a stretch rate of 320 sec^{-1} .

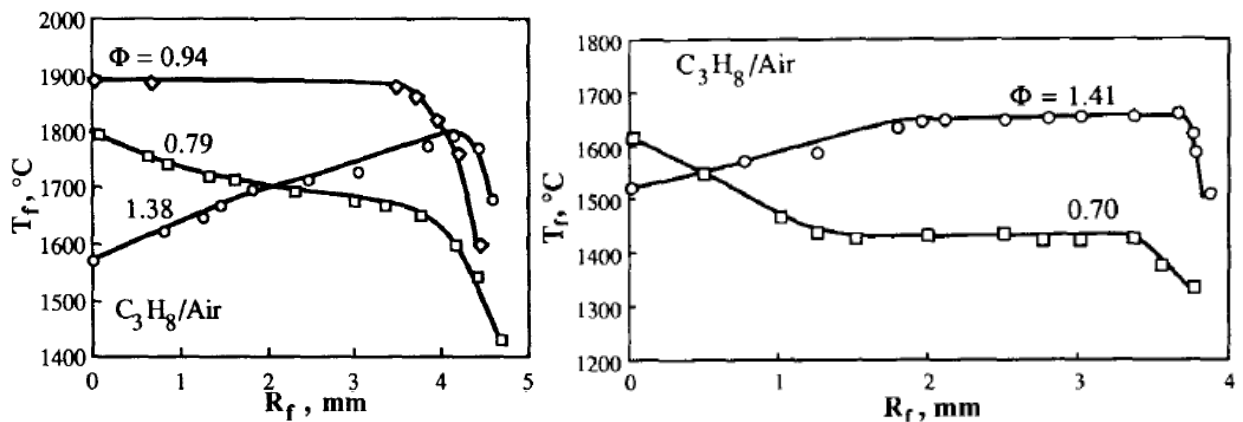


Figure 35: Propane/Air Bunsen Flame Temperatures as a Function of Flame Radius, R_f , for Several Equivalence Ratios. The Negatively-Stretched, Axisymmetric Bunsen Flames (Left) Show Preferential Diffusion Effects while the Two-Dimensional Bunsen Flames (Right) Do Not. As Published by Law [36] with Data from Mizomoto [99]

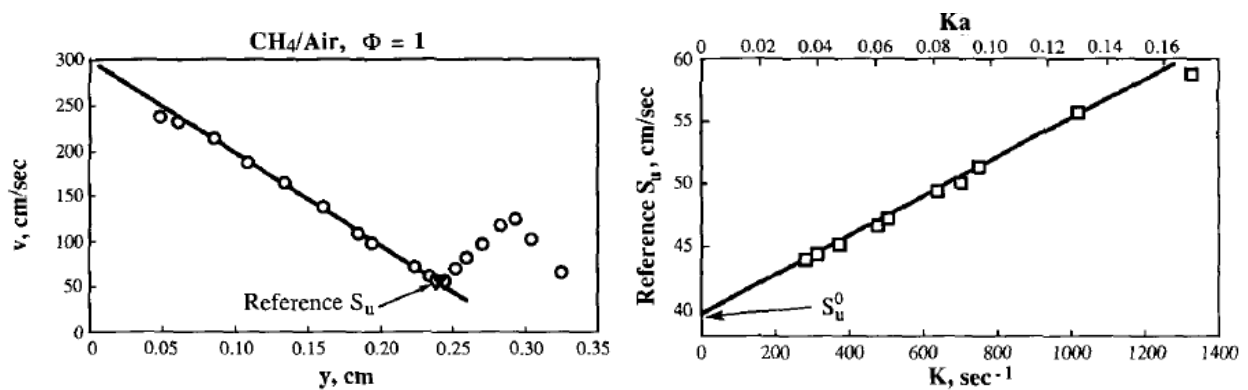


Figure 36: Determination of Zero-Strain Laminar Flame Speed, S_u^0 , for a Stoichiometric Mixture of Methane/Air via Linear Extrapolation to Zero Strain Rate, K [36]

In the case of a flame impinged on (and therefore restrained by) a stagnation surface, as the stretch rate increases toward the extinction limit the flame will move closer to the stagnation plane. Depending on the Lewis number, Le , the burning temperature may be increased ($Le < 1$) or decreased ($Le > 1$) by the resulting flame stretch. Experimental data [99] for propane/air combustion in a stagnation flame configuration for both lean, near-stoichiometric, and rich combustion showed this effect (see Figure 35). Experimental strain rates for extinction were also included showing a maximum capacity for flame stretch around an equivalence ratio of 1.2 for propane/air mixtures. Of particular importance to spherical chamber calculations, Law showed that the strain rate plays a nontrivial role and was shown to produce much higher flame speeds than the true laminar flame speed. The solution to removing the effect of flame stretch was to determine the strain rate for these flame speeds and to extrapolate the data linearly to a strain rate of zero. This method is referred to by many later studies regarding the proper method (with some variations) of determining the zero-strain laminar flame speed under controlled conditions.

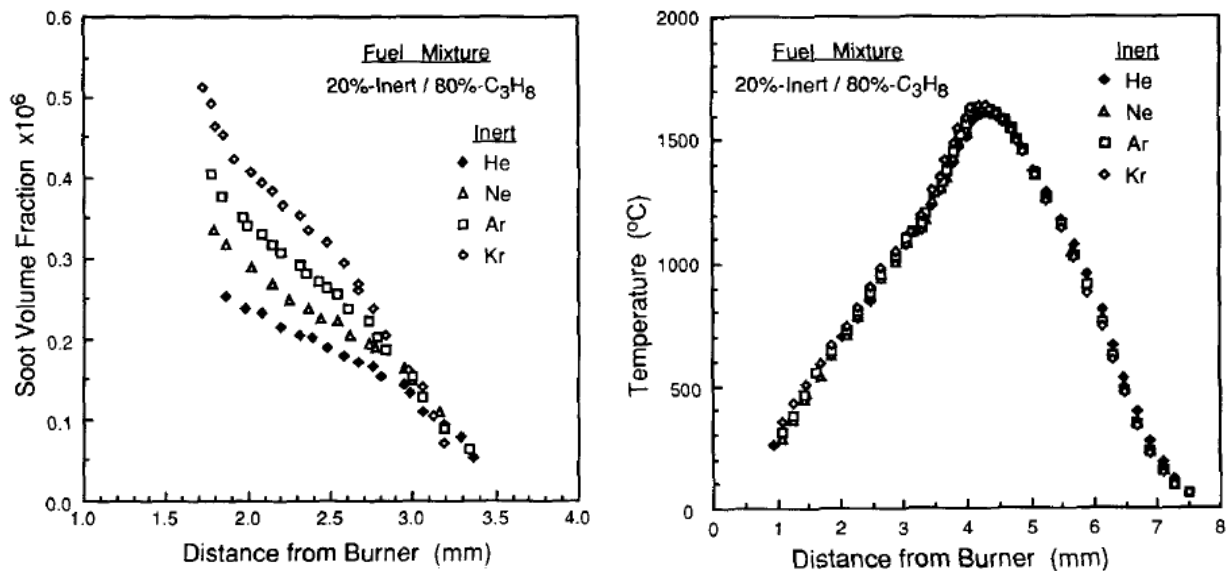


Figure 37: Propane Oxidation Soot Volume Fraction and Temperature Distributions with Different Inert Gases (Diluted by 20%) Showing Significant Effect on Soot Formation but Minimal Effect on Temperatures [100]

A year later, Axelbaum and Law published a study on the effect of inert additive gases (helium, argon, etc...) and their diffusion on the formation of soot in propane and ethylene counterflow flames [100]. They specifically studied differences between using the additive mixed with the fuel and oxidizer separately. They used the same burner assembly as Vandsburger [101] in which two flames in a chamber are oriented toward each other and the resulting steady-state distributions of temperature and species were measured. Soot volume fractions were found to be affected significantly by the selection of inert additive, but temperature distributions showed only slight changes with the heaviest additives resulting in a slight increase in flame temperature (see Figure 37). The effect on sooting could not be explained completely by the change in maximum flame temperature and was considered to be due to the diffusion of the inert gas additives.

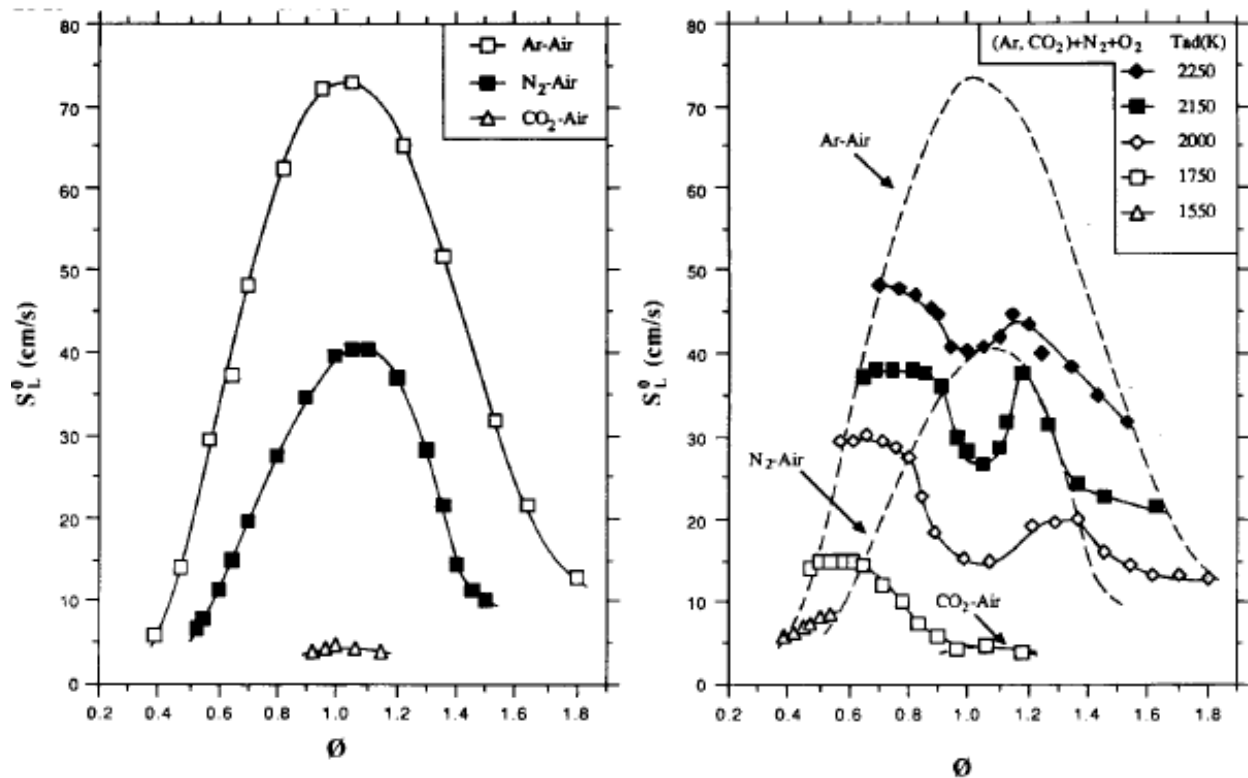


Figure 38: A Comparison of Zero-Stretch, Methane/Air Laminar Flame Speeds for a Range of Equivalence Ratios and Different Diluent Gases. The Right Plot Shows Lines of Constant Adiabatic Flame Temperature Between These Curves [102]

The same year Zhu, *et al.* published a flow reactor study of methane/air laminar flame speeds including mixtures of argon, nitrogen, and carbon dioxide using counterflow flames for a range of temperatures (1550 – 2250 K), pressures (0.25 – 2 atm), and equivalence ratios (0.5 – 1.5) [102]. The study compared experimental data to models using several different kinetic mechanisms. Laminar flame speeds were determined using the method for diffusion flames described by Law [36] to remove the effect of flame stretch on flame speed measurements. The use of diluting inert gases allowed the flame temperature to be controlled across a range of equivalence ratios such that constant temperature flame speed distributions could be studied and showed a significant effect on flame speed. The authors identified two primary sources affecting flame speeds under these conditions – transport effects due to substitution of the inert gases, and kinetic changes due to the changing stoichiometry. As pressures increased, the flame speeds generally decreased with increasing equivalence ratio (as the mixture became richer). The mass burning rate (the eigenvalue for estimating laminar flame propagation), however, increased with growing pressure as the density of the mixtures naturally increased. The C_1 and C_2 mechanisms tested agreed well with the data they presented.

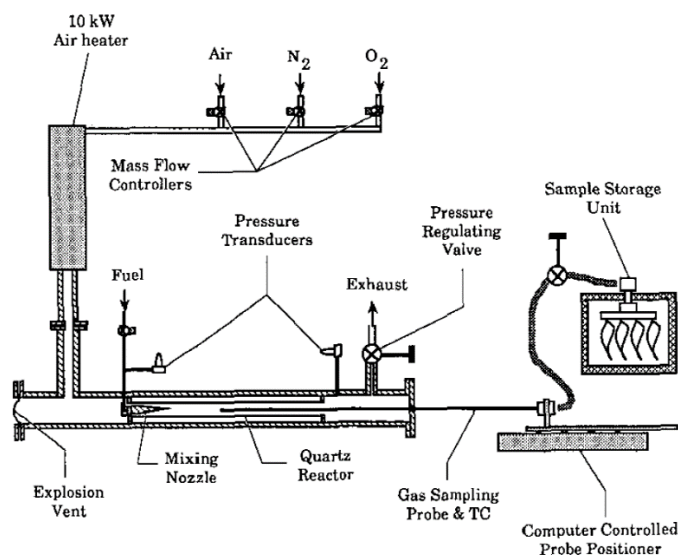


Figure 39: Koert's Pressurized Flow Reactor (PFR) Design for Studying Low Temperature, High Pressure Hydrocarbon Oxidation [103]

In 1992, Koert published pair of studies – the first detailed a new coflow reactor design intended for homogeneous gas phase oxidation [103], and the second explored the reactivity of propane in the “negative temperature coefficient” (NTC) region [104]. The reactor (shown in Figure 39) is referred to as a “Pressurized Flow Reactor” (PFR) and allows study of low to intermediate temperature hydrocarbon oxidation (up to 1000 K) at high pressures (up to 20 atm). In the reactor, pre-vaporized fuel, oxidizer, and diluents (like nitrogen) are electrically preheated and injected into a quartz chamber via a mixing nozzle where it reacts as it proceeds down the chamber tube. This means measurements taken at distances downstream of the nozzle correspond to kinetics with longer reaction times. Species samples were taken via a glass-lined, water-cooled probe intended to freeze the chemical kinetics preventing further reactions before the samples could be measured.

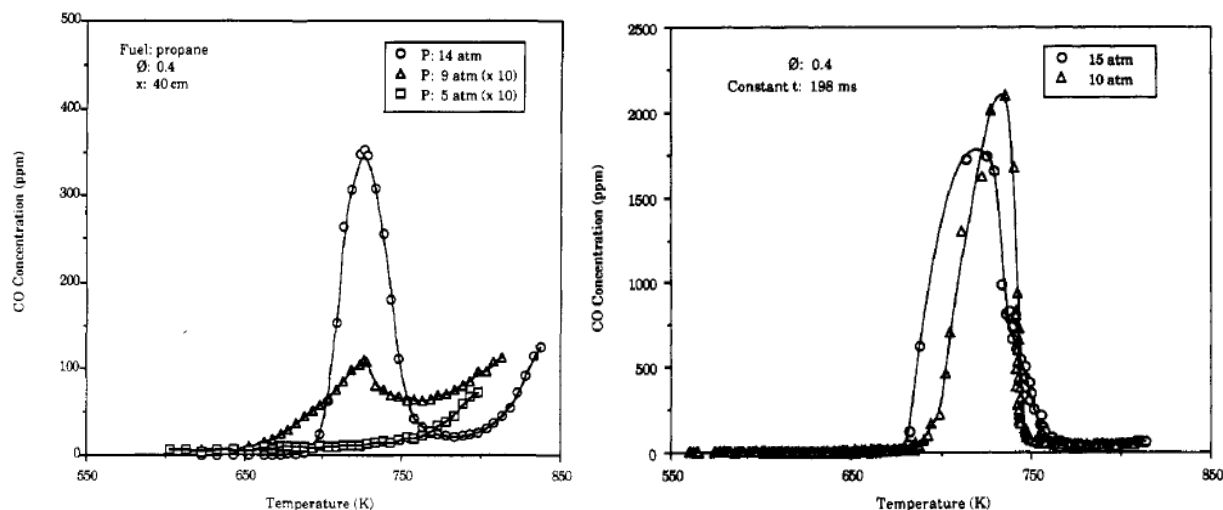


Figure 40: Propane Oxidation Carbon Monoxide Concentrations for a Range of Low Temperatures and High Pressures at an Equivalence Ratio of $\phi = 0.4$. Data on the Left was Gathered Using a Constant Probe Position. Data on the Right was Gathered Using a Constant Residence Time of 198 ms [104]

The design was considered advantageous because it allowed study of the full temperature regime of hydrocarbon oxidation in a single experiment via a controlled cool-down method. It specifically allowed study of the low temperature region (640 – 770 K) in which the reaction rate

decreases with increasing temperature hence its definition as the negative temperature coefficient region. The second study exploited this capability and presented the results of two types of experiments (the data from which are included in Figure 40). The first experiment held the probe in a fixed position allowing temperature to vary at a constant pressure which produced reactivity maps showing carbon monoxide (CO) concentration as a function of temperature and pressure. Under these conditions the residence time was not controlled. The second experiment was performed under a constant residence time of 198 ms that produced slightly different CO concentration distributions with temperature. The NTC region was experimentally mapped at high pressures between 9 and 15 atm and between temperatures of 640 and 770 K. Two years later, Koert expanded on his this study with an emphasis on preventing engine knock [105].

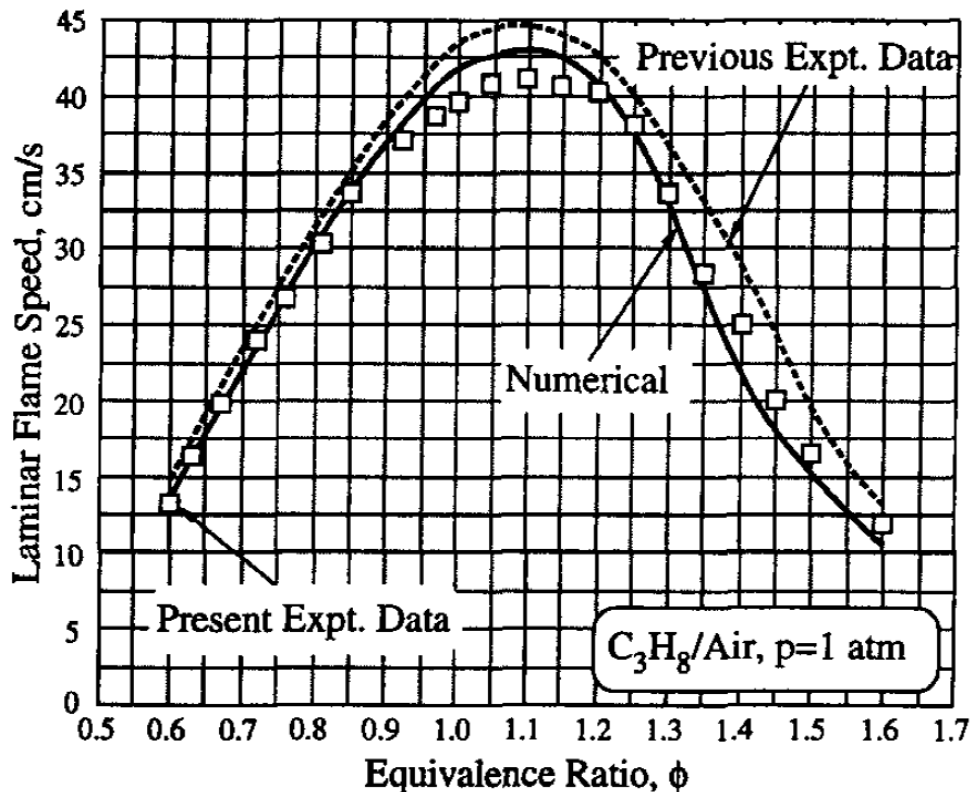


Figure 41: A Comparison of Experimental Propane/Air Laminar Flame Speeds to Numerical Predictions for a Range of Equivalence Ratios. Previous Experimental Data Included from Egolfopoulos [106]. Published by Vagelopoulos [107].

In 1994, Vagelopoulos, *et al.* published the first [107] of two often-cited studies of experimental data for propane/air (as well as methane/air, and hydrogen/air) laminar flame speeds using counterflow twin-flames technique described by Wu [93] and Zhu [102]. For propane/air mixtures, the study explored a range of lean ($\phi = 0.6$) to rich ($\phi = 1.6$) equivalence ratios at atmospheric pressure. Flame speeds were determined using the same linear extrapolation method described by Law [36] to remove the effects of flame stretch, K . The authors noted the change of flame speed with stretch was not actually linear as the stretch approached zero but that the error was small (approximately 8%). This correction helped better match experimental data to numerical simulations. They also noted the importance of a nondimensionalized factor related to flame stretch – the Karlovitz number:

$$K_a \equiv \frac{K\delta}{S_u^0} \quad (32)$$

where K is the flame stretch, δ is the characteristic flame thickness, and S_u^0 is the zero-stretch laminar flame speed. In practical terms, a lower K_a relates to a thinner flame and thus a lesser influence of the separation distance between the flames.

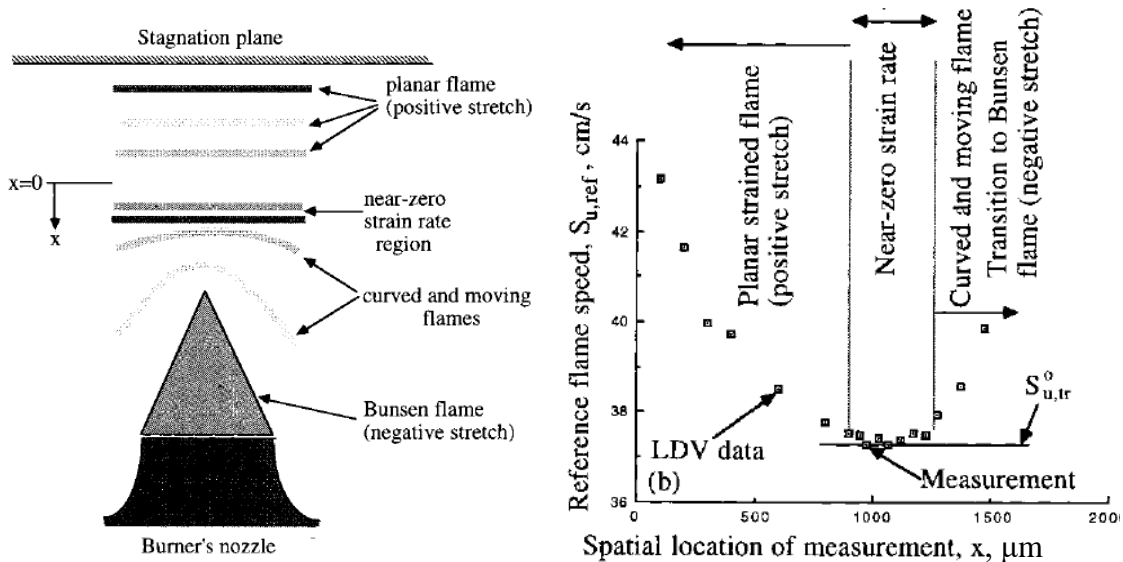


Figure 42: Single Jet-Plate Flame Configuration Showing Regions of Flame Stretch and Corresponding Flame Speed Measurements via Laser Doppler Velocimetry (LDV) [108]

In 1998, Vagelopoulos *et al* expanded on the earlier study by testing a single jet-plate configuration as opposed to using twin-jets to form a stagnation region. [108] This simpler configuration was shown to match identically with the twin-jet configuration published by Egolfopoulos [109] for low strain rates in methane/air mixtures. The study explored a slightly narrower equivalence ratio range (ϕ between 0.7 and 1.35) and employed Laser Doppler Velocimetry (LDV) to measure the laminar flame speeds of weakly strained laminar premixed flames directly. This setup exploited the smooth transition between planar flames (having positive stretch) and Bunsen flames (having negative stretch) to more directly measure flame speeds at the limit of near-zero stretch as opposed to extrapolating a limited dataset to zero stretch. This concept and representative data are illustrated in Figure 42.

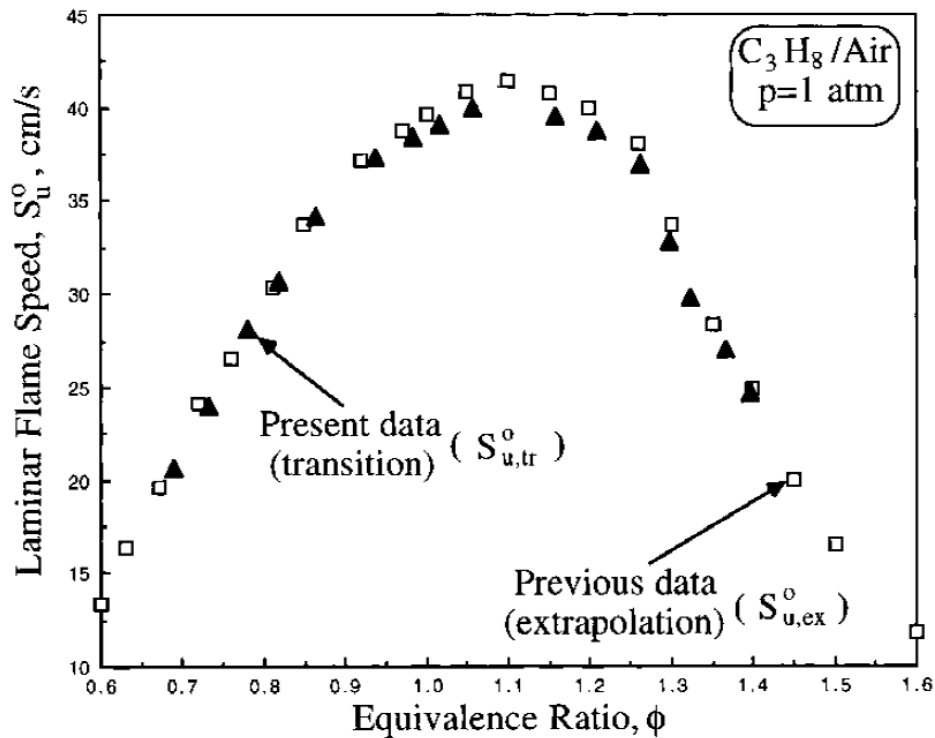


Figure 43: Comparison of Zero-Strain Laminar Flame Speeds Determined using the Extrapolation Method Described by Law [36] with Data from the 1994 Study [107] with Data Determined via Direct Measurement of Flame Speeds in Transition through Zero Strain Rate as Published by Vagelopoulos [108]

Of particular note in the study was the comparison of zero-strain flame speeds as determined by either extrapolation to zero strain rate (referred to as $S_{u,ex}^0$) and by direct measurement as the flame transitioned to zero strain (referred to as $S_{u,tr}^0$). These two methods (the extrapolated data taken from the earlier study [107]) are compared in Figure 43 and showed the greatest difference around stoichiometric mixtures. The authors noted that for propane/air mixtures (which have a Lewis number, $Le > 1$) instabilities in the flame “disk” were not seen as they were in lean methane/air mixtures ($Le < 1$). Although the data is sound for propane, the use of inert, diluent gases (to increase the Lewis number beyond 1) would be required to determine lean methane/air laminar flame speeds reliably at strain rates approaching zero.

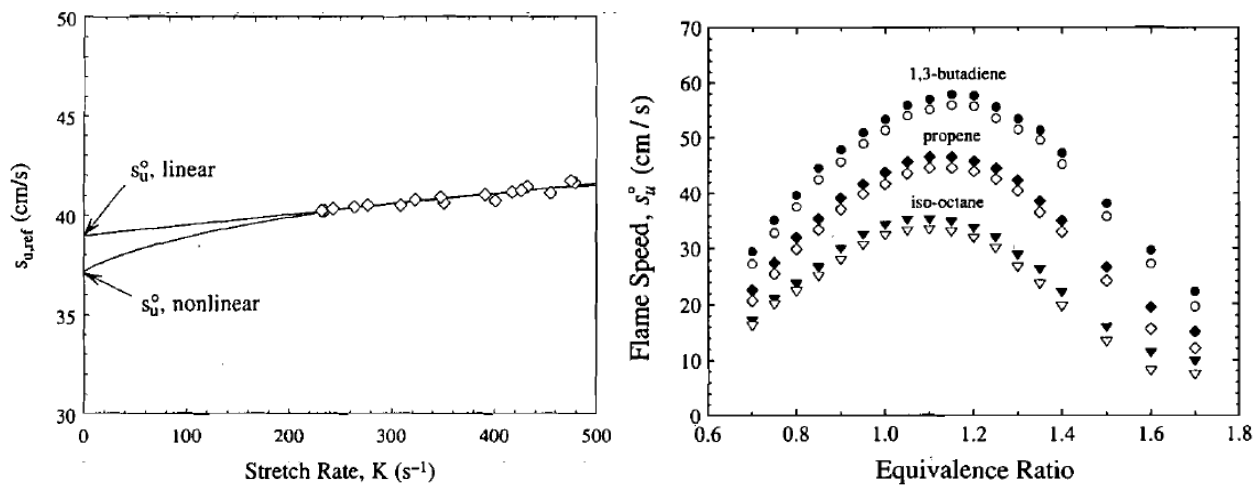


Figure 44: A Comparison of Linear and Nonlinear Extrapolation Methods for Determining Zero-Strain (Stretch) Flame Speeds for Several Fuels. On the Right, the Filled Symbols Correspond to Linear Extrapolation while Empty Symbols Correspond to Nonlinear Extrapolation as Published by Davis and Law [110].

That same year, Davis and Law published a broad study on laminar flame speeds using the counterflow twin-flame configuration for a range of hydrocarbons from C_1 as high as C_8 , though not explicitly including propane except as a slight propyne (C_3H_4) impurity [110]. Of particular note was their comparison between linear and nonlinear extrapolation methods to determine zero-

strain flame speed. The nonlinear extrapolations displayed a consistently lower flame speed than linear extrapolations, which was closer to numerical estimations.

In 2008, Holton published his Master's Thesis on using a coflow reactor to measure autoignition delay times of natural gas fuels independently and in a range of mixtures to better quantify the effects of individual species concentrations in natural gas mixtures [111]. His experiments were performed for a range of equivalence ratios (ϕ between 0.5 and 1.25) and temperatures (931 K to 1137 K) at atmospheric pressure. The apparatus used was the same described by Gokulakrishnan's studies on aviation fuels [112, 113] (similar to those described by Koert [103-105, 114]) and was validated with ethylene experimental data tested with computer predictions using several kinetic mechanisms including the GRI Mech 3.0 [75] and Konnov's mechanism [82] discussed in Section C.

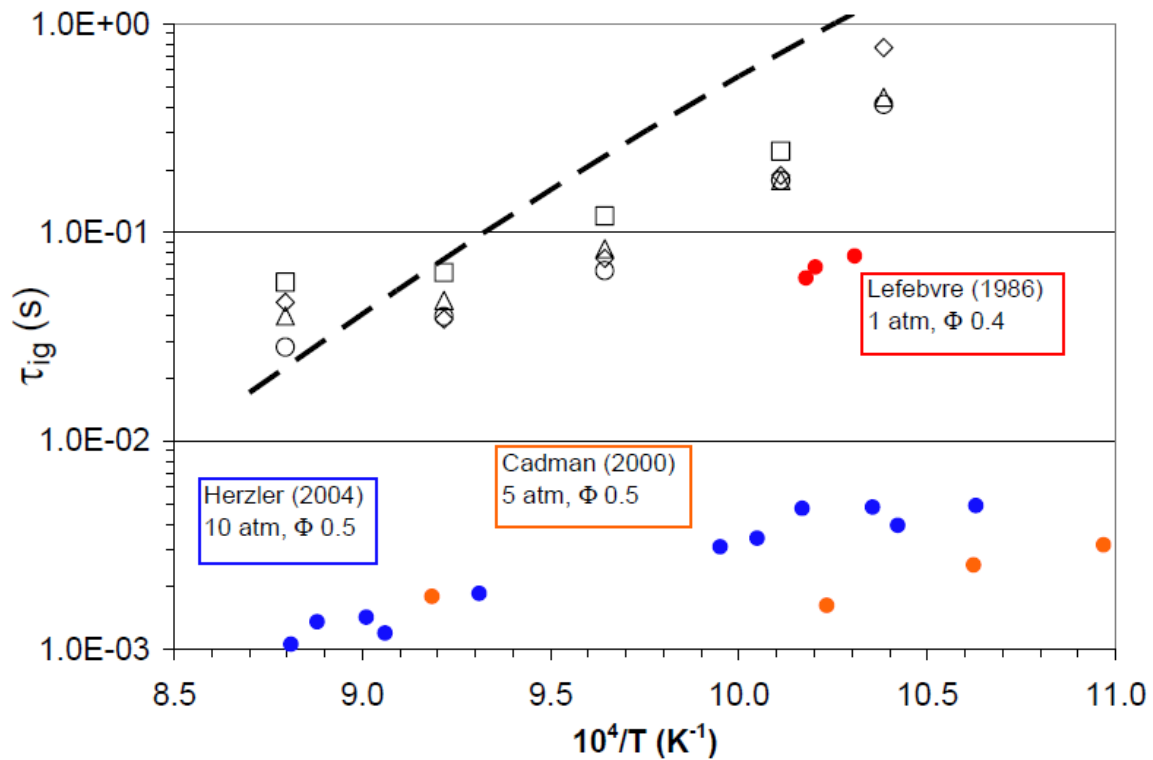


Figure 45: Measurements of Propane Autoignition Delay Time Compared to Experimental Data from Lefebvre [115], Herzler [84], and Cadman [69] as Published by Holton [111]

In regard to propane, Holton noted that although the GRI Mechanism predictions were closest to his data, it underpredicted ignition delays at high temperatures, overpredicted at low temperatures and failed to capture the asymptotic phenomena of ignition delay to approximately $\tau_{ig} = 0.05$ sec as temperature increased. Data from Lefebvre, *et al.* [115] (also at 1 atm) was an order of magnitude lower than Holton's data which he attributed to differences in accounting for mixing and chemical components. Herzler [84] and Cadman's [69] data were also compared but were at much higher pressures (10 atm and 5 atm respectively) and so showed much lower ignition delays. Holton published a further study [116] two years later expanding on this natural gas data which produced Arrhenius curve fits for predicting ignition delay as a function of temperature.

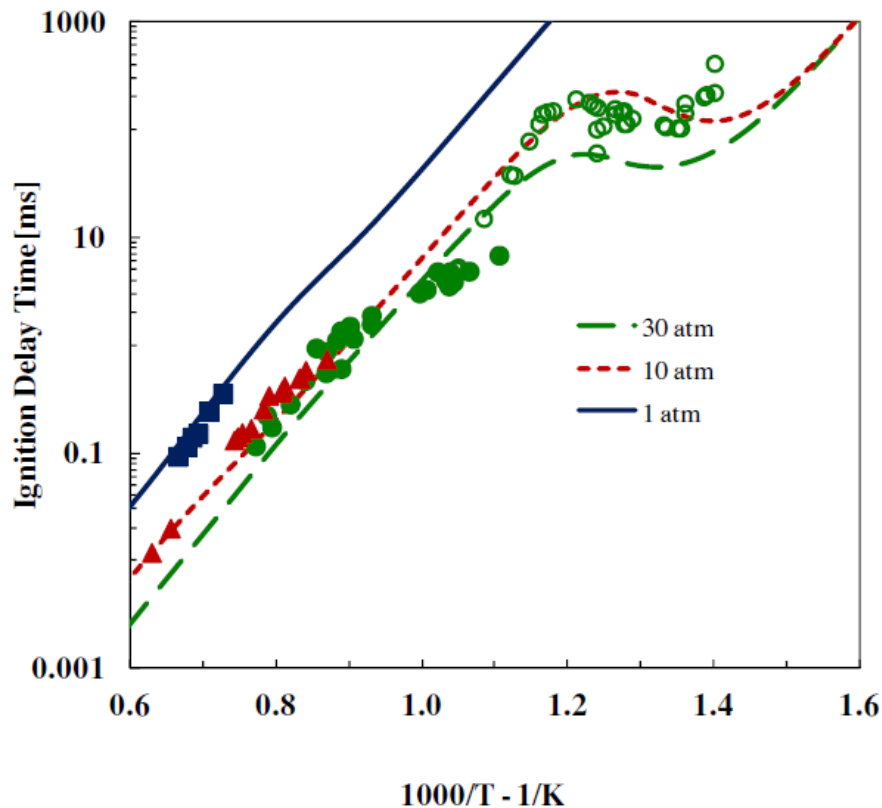


Figure 46: Experimental Propane/Air Ignition Delay Data (Points) at Three Pressures and Kinetic Mechanism Predictions (Lines). Square Points Show Data from Horning [117], Triangle Points from Burcat [55] (8-14 atm), Filled Circles from Herzler [84], and Empty Circles from Gallagher [118] as Published by Gokulakrishnan [119].

In 2014, Gokulakrishnan, *et al.* published a coflow reactor study on propane air combustion to determine the effect of NO_x on ignition delay times in vitiated air (air with a reduced oxygen concentration) [119]. A series of equivalence ratios (ϕ between 0.5 and 1.5) were tested at temperatures of 875 K and 917 K and pressures up to 30 atm. The data and kinetic models showed a significant reduction in ignition delay when “small amounts” of NO were added in this temperature regime. A set of data and model predictions without added NO is included in Figure 46 which shows good agreement between the data and mechanism predictions for ignition delays below approximately 1 ms. The authors noted that models run at longer ignition delays (beyond 1 ms) would need to account for “system non-idealities” to produce accurate predictions at lower temperatures. They showed good qualitative agreement (the model predicts a change in the activation energy consistent with prior experiments in the NTC region), but the model underpredicted lower-temperature ignition delays from Gallagher’s Rapid Compression Machine (RCM) study [118]. The study further investigated the effect of CO₂ dilution on laminar flame speeds denoting a significant reduction in flame speeds at all equivalence ratios when the mixture included 10% CO₂. The kinetic mechanism matched the experimental data well over the entire range of equivalence ratios, as well as with and without the inclusion of active or inert CO₂.

6. Jet-Stirred Reactors

One of the earliest jet-stirred reactors was published by Gray and Felton in 1974 while studying low temperature propane oxidation [120]. In studying reactors, he noted several disadvantages to those relying on closed, static chambers. The temperature distribution inside the closed vessel makes interpretation of the data difficult and at high pressures can induce convective currents [121, 122]. Furthermore, the data can be heavily affected by the chamber’s initial conditions and despite assumptions, there is a lack of truly steady conditions [123]. Lastly, closed,

static chambers are difficult to model theoretically without numerical computations that were prohibitive at the time. Alternatively, stirring the chamber has the effect of homogenizing it though this also adds turbulence. Their reactor does this mechanically with a stainless steel stirrer while later designs rely on fluid jets. This stirrer was coated with a ceramic layer to prevent surface reactions. Operation of the reactor was limited to 770 K due to glass components and the oven used to supply external heat. Their study resulted in the first experimental propane oxidation heat release rate data for a range of temperatures. They also noted nontrivial hysteresis and particularly different response if temperature was increasing or decreasing and led to study of the conditions that would result in damped or undamped oscillations.

In 1981, Cathonnet, *et al.* published a further study on propane and n-butane matching a numerical model based on a chemical kinetic mechanism for high temperature oxidation to experimental data gathered with a tubular reactor made of quartz [124]. The experiments were performed for an extensive range of equivalence ratios (ϕ between 0.05 and 25), at initial temperatures near 1000 K, and pressures from 0.99 atm to 5.9 atm. The fuels were highly diluted (less than 2% fuel by volume). Comparison of the data to mechanism predictions showed that except in very lean or very rich mixtures, good agreement was seen.

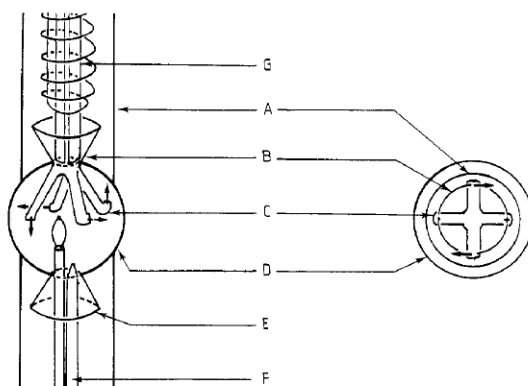


Figure 47: The Jet-Stirred Reactor Core Showing (A) the External Tube, (B) the Convergent Cone, (C) Fluid Injectors, (D) the Spherical Quartz Reactor, (E) the Divergent Cone, (F) the Sampling Sonic and Thermocouple Probes, and (G) a Capillary Surrounded by a Preheating Resistor as Published by Dagaut, *et al.* [37].

In 1986, Dagaut, *et al.* published what became a ubiquitous jet-stirred reactor (JSR) design which was suitable for high pressures (up to 10 atm) and temperatures up to 1200 K [37]. Moreover, as long as the temperature gradients are “moderate,” the design can be approximated as a plug-flow reactor allowing relatively simple theoretical modeling. The majority of the reactor is made from fused silica to prevent catalytic reactions at the walls. Stirring occurs as a result of the four angled injectors and results in mixture homogeneity under steady state operation. Operation at a steady state is particularly desirable because the lack of flow transport effects significantly simplifies kinetic modeling. Constant pressure is maintained via an exhaust pressure regulator.

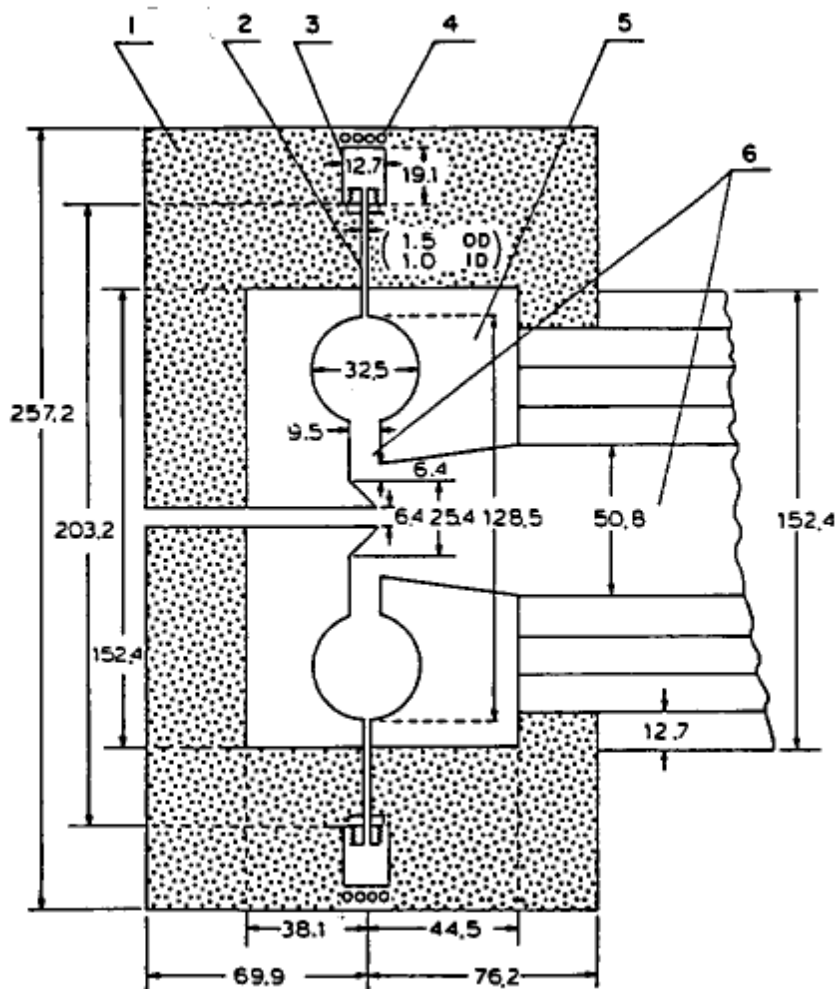


Figure 48: Toroidal Jet-Stirred Reactor Schematic Showing (1) Porous Insulation, (2) Feeding Tubes, (3) Fuel-Air Supply Ring, (4) Cooling Coils, (5) Alumina Reactor Body, and (6) Outlet. Note: All Dimensions are in Millimeters.

Two years later, Dagaut, *et al.* published a study using this reactor to investigate propene (C_3H_6) oxidation noted as important to propane oxidation as an intermediate species [125]. Experiments were performed for a range of temperatures (900 – 1200 K), pressures (1 atm to 8 atm), and equivalence ratios (ϕ from 0.15 to 4.0). This data was compared to predictions from a mechanism published by Warnatz [126] to model ethylene (C_2H_4), propene (C_3H_6), and propane (C_3H_8) oxidation. The data showed good species profile matching except acetylene (C_2H_2) that showed lower concentrations than those seen in the reactor experiments.

In 1991, Vaughn published a study for ethylene combustion in an alternative design – a toroidal jet-stirred reactor developed by Nenniger in 1983 [127, 128]. The reactor uses a series of 32 sonic jets arranged around a toroidal reaction zone that produces a “very highly turbulent, nearly uniform” mixture. The chamber’s design allowed study of oxidation at atmospheric pressure and temperatures as high as 1750 K. Moreover, the use of more injectors brings the design closer to the plug flow model and their orientation for crossflow results in the jets entraining 6 to 12 times as much gas than a jet in a hemispherical design. A model of the oxidation was run assuming a perfect mixture of fuel and air in the reactor and using a chemical mechanism with 135 combustion reactions and 75 nitrogen fixation reactions. Generally, the resulting model predictions matched well with the experimental data but methane concentrations at high equivalence ratios were underpredicted.

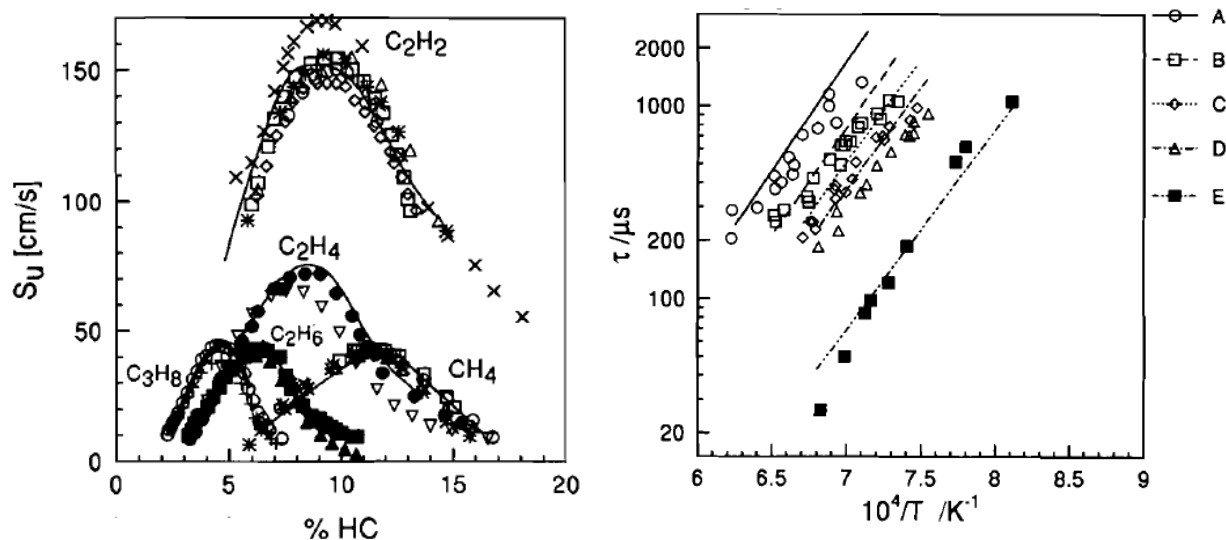


Figure 49: Comparison of Experimental Data for Multiple Hydrocarbons in Air to Kinetic Mechanism Predictions at 1 atm. Laminar Flame Speeds for Hydrocarbons Taken from a Variety of Sources Including Egolfopoulos [129] and Law [130] (Left). Ignition Delays for Hydrocarbon Mixtures with Data from Frenklach and Bornside [63] and Eubank [60] (Right). The Mixtures were (A) 9.5% Methane, 19% Oxygen in Argon, (B) 0.19% Propane Added to A, (C) 0.475% Propane Added to A, (D) 0.95% Propane Added to A, and (E) 1% Methane, 0.2% Ethane, 0.1% Propane in Air. [80]

In 1994, Tan, Dagaut, *et al.* published a study on oxidation of methane blends using propane and ethane as additives using Dagaut's JSR design [79, 80]. Species concentrations were measured for a range of pressures (1 – 10 atm), temperatures (900 – 1230 K), and equivalence ratios ($\phi = 0.1 - 1.5$) and used to validate a built-up mechanism drawing on prior single-fuel mechanisms published by Dagaut, *et al.* [131-135]. The study expanded on autoignition data published by Zamansky and Borisov for a wide range of blended hydrocarbons (some including propane) [136] and alternative fuels [137]. The authors found methane-ethane-propane to produce the best model of natural gas for a wide range of temperatures and pressures. They additionally found that adding propane and/or ethane to methane increased the reactivity (and decreased ignition delays) of the methane at 1 atm. Methane reactions occurred at temperatures 100 K lower than normal with added propane and 120 K lower by adding both propane and ethane to the blend. This effect was less evident at 10 atm.

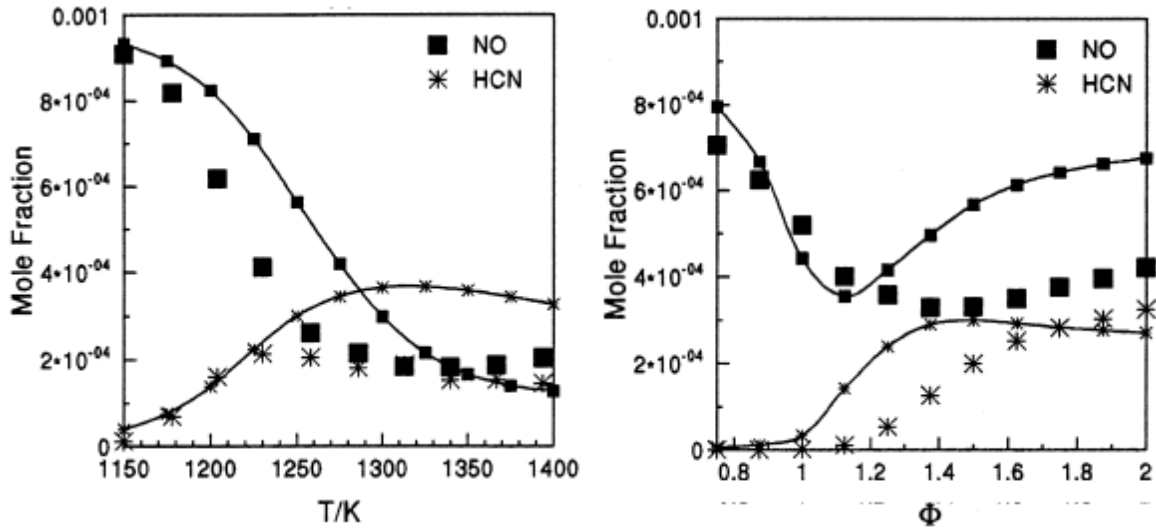


Figure 50: The Effect of Temperature on NO Reduction Using 2930 ppm of Propane at 1 atm and $\phi = 1$ (Left) and The Effect of Equivalence Ratio on NO Reduction Using 2930 ppm of Propane at 1 atm and 1250 K (Right). Note: Large Symbols Show Experimental Data, Lines Show Model Predictions [138].

In 2001, Dagaut, *et al.* published work on reducing NO concentrations in a JSR in the interest of reducing undesirable engine emissions [138]. The intent was to inject propane during a secondary stage of combustion (following the initial stage of lean combustion) to burn NO before it leaves the engine. To simulate these conditions experimentally, the authors used the same reactor Dagaut published previously in a similar study [37, 139] using natural gas as opposed to just propane. Experiments were performed for a range of equivalence ratios from $\phi = 0.5$ to $\phi = 1.5$ at 1 atm and temperatures between 1050 K and 1300 K. The data was matched with an NO-related kinetic mechanism described in the earlier natural gas study and showed the best matching of NO and hydrogen cyanide (HCN, a poisonous, acidic exhaust gas) species occurred at high temperature. Reduction of NO was “favored” by these rich, high temperature conditions and showed reasonable agreement with the mechanism data.

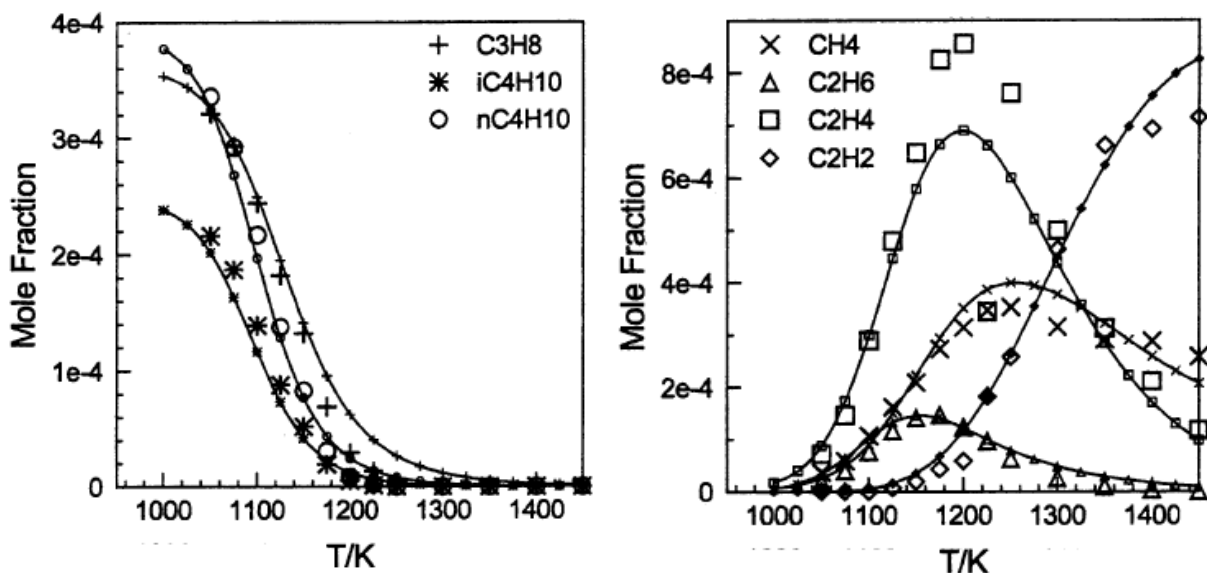


Figure 51: Species Mole Fractions of Liquid Petroleum Gas Oxidation in a JSR at Atmospheric Pressure, $\phi = 4.0$, and 0.1% Fuel [140]

Two years later, Dagaut and Hadj Ali published a kinetics study on the oxidation of a liquid petroleum gas (LPG) blend with new data gathered using Dagaut's reactor [140]. The blend was a mixture of propane, n-butane (nC_4H_{10}), and iso-butane (iC_4H_{10}) used in spark-ignition engines. The reactor was used to experimentally measure species fractions using sonic quartz probe sampling and gas chromatography during oxidation at 1 atm, at temperatures between 950 K and 1450 K and for a range of equivalence ratios from lean ($\phi = 0.25$) to rich ($\phi = 4.0$). The data was compared to a mechanism for LPG oxidation and was found to be in "very good agreement." An analysis of the individual reaction paths showed the blend to follow the same general oxidation paths studied for simple alkanes (methane, ethane, etc...).

C. Propane Oxidation Chemical Kinetic Mechanisms

Although kinetic mechanisms for propane exist, there is no single mechanism unanimously selected as *the* propane oxidation mechanism. Instead, researchers worldwide contribute to an experiments and analysis leading to different models of propane oxidation that are tailored to specific conditions like rich/lean mixtures or elevated temperatures and pressures. The following is a review of available propane models and their use in computational fluid dynamics (CFD).

1. Review of Available Chemical Kinetic Mechanisms

A review of the currently published chemical kinetic mechanisms for propane-air produced more than 30 options for modeling propane combustion in air across a wide range of equivalence ratios and spanning the full spectrum of approaches between detailed, reduced, and global. These are listed generally in Table 4 and some are reproduced in full detail necessary for use in the typical CHEMKIN format in Appendix A. The following is a brief discussion these propane oxidation mechanisms in the context of their development goals.

The earliest complete study into propane mechanisms was published by Westbrook and Dryer and introduces several kinetics models frequently used for their simplicity [141]. The authors list reaction mechanisms for a series of hydrocarbon fuels and several levels of fidelity including single-step, two-step, and multi-step reaction mechanisms. Although these mechanisms may be considered dated, they are still accurate and in use for modern CFD models [142-144]. Furthermore, their use of the fewest reactions possible represents the fastest mechanisms available. The reaction and corresponding single-step mechanism from Westbrook and Dryer [141] is:



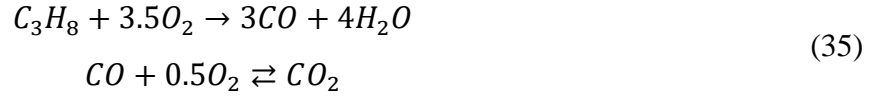
$$k_1 = 8.6 \times 10^{11} e^{(-30/R_u \cdot T)} \cdot [C_3H_8]^{0.1} \cdot [O_2]^{1.65} \quad (34)$$

where R_u is the universal gas constant (8.314 kJ/kmol) and T is the local temperature.

Table 4: Propane Chemical Kinetic Mechanisms

Ref	Mechanism	Reactions	Species	Validation Data	Press (atm)	ϕ Range
[141]	Westbrook 1981	1	4	One-Step Global Mechanism	1	1
[141]	Westbrook 1981	2	5	Two-Step Global Mechanism	1	1
[71]	Westbrook 1984	168	36	Oxidation and Pyrolysis	1 – 15	0.07 – 1.59
[68]	Jachimowski 1984	83	27	Shock Tube	0.2 – 50	0.125 – 2.0
[131]	Dagaut 1992	391	57	JSR, ST, Flow Reactor, Flame	No data	No data
[130]	Kennel 1993	9	13	Premixed Flame	1 – 10	No data
[130]	Kennel 1993	6	10	Premixed Flame	1 – 10	No data
[130]	Kennel 1993	4	7	Premixed Flame	1 – 10	No data
[130]	Leung 1993	9	12	Counterflow Diffusion Flame	No data	No data
[130]	Leung 1993	7	10	Counterflow Diffusion Flame	No data	No data
[145]	Leung 1995	451	87	Co & Counterflow Diffusion Flames	No data	No data
[146]	Koert 1996	?	?	High Pressure Flow Reactor	10 – 15	0.40
[147]	Marinov 1997	680	156	Counterflow Reactor	1	No data
[83]	Curran 1998	2450	550	Shock Tubes, Flow Reactors, Engine	1 – 42	0.3- 1.5
[70]	Sung 1998	619	92	Counterflow Diffusion Flame	1 – 5	< 16 pbv
[148]	Davis 1999	469	71	Counterflow Twin Flame Reactor	1	0.7 – 1.7
[75]	GRI 3.0 1999	325	53	Shock Tube, Lam. Flame Speed	0.1 – 10	0.1 – 5.0
[149]	Haworth 2000	73	29	Simulated IC Engine	4	0.5 – 3
[82]	Konnov 2000	1207	127	Shock Tube, Flow Reactor, Flames	No data	0.6 – 1.6
[150]	Qin 2000	463	70	Counterflow Reactor, Shock Tube	1	0.5 – 1.6
[151]	Curran 2004	?	?	Shock Tube, Flow Reactors, Engine	0.75 - 40	0.4 – 2.0
[152]	San Diego 2005	173	39	Shock Tube	1 – 2	0.5 – 2.0
[153]	Petrova 2006	177	37	Lam. Flame and Shock Tube	0.6 – 40	0.6 – 1.7
[154]	Koutmos 2007	9	9	Coflow Diffusion Flame	4	0.6 – 1.6
[155]	Peterson 2007	663	118	Shock Tube	5.3 – 31	0.5 – 3.0
[156]	USC 2.0 2007	784	111	Shock Tube, Flow Reactors, Flame	0.6 – 15	No data
[157]	Bourque 2008	1580	289	Shock tube, Rapid Compression	0.7 – 34	0.3 – 2.0
[158]	Le Cong 2008	1043	131	Jet Stirred Reactor	1 – 10	0.1 – 1.5
[159]	Healy 2010	1588	293	Rapid Compression, Shock Tube	7.9 – 29.6	0.5 – 2.0
[160]	Agafonov 2011	2500	260	Shock Tube	3.0 – 6.9	No data
[161]	Titova 2011	599	92	Shock Tube and CFRs	0.17 – 30	0.13 – 2.0
[162]	Andreis 2012	14	33	Co & Counterflow Diffusion Flames	No data	No data
[163]	Metcalf 2013	766	122	Shock Tube, JSR, Flow, Flames	0.65 - 260	0.05 – 6.0
[119]	Gokulakrishnan 2014	966	136	Shock Tube, JSR, Flow Reactors	1	0.5 – 1.5

The two-step reaction mechanism is similar but substitutes carbon dioxide (CO₂), for carbon monoxide (CO) and instead models the formation of CO₂ from CO separately:



$$\begin{aligned} k_1 &= 1 \times 10^{12} e^{(-30/R_u \cdot T)} \cdot [C_3H_8]^{0.1} \cdot [O_2]^{1.65} \\ k_2 &= 10^{14.6} e^{(-40/R_u \cdot T)} \cdot [CO]^1 \cdot [H_2O]^{0.5} \cdot [O_2]^{0.25} \\ k_{-2} &= 5 \times 10^8 e^{(-40/R_u \cdot T)} \cdot [CO_2]^1 \end{aligned} \quad (36)$$

Westbrook and Dryer's mechanisms predicted substantially-larger concentrations of free hydrogen (H) and oxygen (O) because it did not include reactions with CO or H₂ until the main fuel and other hydrocarbons were largely consumed [141]. The one-step and two-step models do not suffer from this problem and as a result, CO oxidation was able to occur early in the combustion process. Nevertheless, the reaction rate of the one-step mechanism was found to correctly reproduce experimental flame speeds for a wide range of equivalence ratios and pressures including $\phi = 1$ at standard temperature and pressure. The addition of intermediate species (such as CO) to form a two-step mechanism resulted in greater flame temperature and composition accuracy while requiring more computational time [141]. Westbrook and Dryer also developed a detailed propane mechanism [71] validated with oxidation and pyrolysis data over a range of equivalence ratios and at elevated pressures.

The same year Jachimowski (working for NASA's Langley Research Center) published a detailed mechanism for propane combustion intended for scramjet engines [68]. The mechanism covered 83 chemical reactions involving 27 independent species and was validated with data on ignition and combustion of propane in shock tube studies from Burcat [55] and McLain [164] for temperatures between 1150 K and 2600 K. He specifically investigated the effects of temperature and pressure on ignition delay and on methods of predicting ignition delay like the use of a

correlation function. The mechanism predicted experimental shock tube data “reasonably” well without modifying reaction rate coefficients. Testing of the mechanism without HO₂ and H₂O₂ reactions showed these reactions to be nontrivial and were considered to be “important chain propagating species.”

In 1988, Dagaut used his JSR [37] and resulting propane data to validate a detailed mechanism involving 277 reactions and 48 species [165]. This mechanism was designed to model oxidation of ethylene (C₂H₄), propene (C₃H₆), and propane by building on prior mechanisms. Four years later, Dagaut published an updated version of this mechanism (listed in Table 4) validated with a wider range of JSR data as well as ignition delay data from shock tubes, flow reactor data, and premixed flames modeled with the Premix code. This 1992 mechanism [131] built on the 1988 mechanism [165] by adding models for C₃-C₄ chemistry to a prior mechanism modeling C₁-C₂ chemistry [133, 134].

In 1993, a collection of hydrocarbon mechanisms and methods for building reduced and global mechanisms was published by Peters and Rogg [130]. This text included five propane mechanisms (among many others) – three developed by Kennel and two by Leung. Kennel started from a 9-step global mechanism for which each step used a reaction rate determined from a sum of intermediate reaction rates. This mechanism was reduced from a detailed C₃ mechanism by assuming all the hydrocarbons except propane, propene (C₃H₆), ethylene (C₂H₄), and acetylene (C₂H₂) were at a steady state. This assumption was considered valid as long as the reactions forming the species are slower than the reactions that consume the species. That is, there cannot be a build-up of these species if they are consumed faster than they are produced. Because each modeled species requires analysis, this significantly reduces runtime and complexity [130].

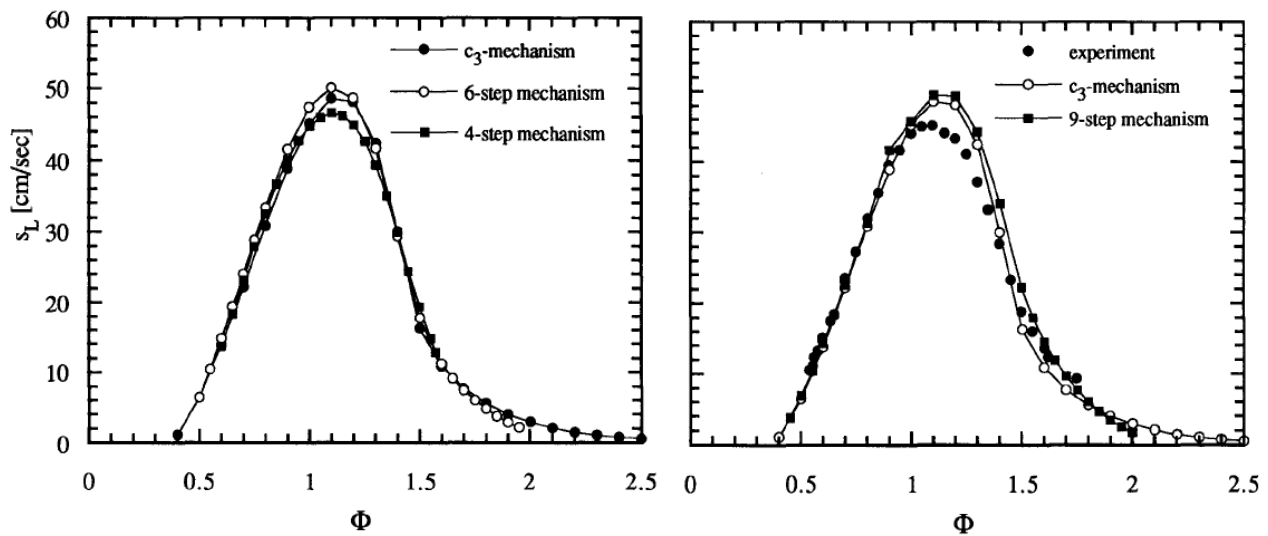


Figure 52: Comparisons of Burning Velocities for a Range of Equivalence Ratios as Determined from Law's Experiments, a Detailed C₃ Mechanism, and Kennel's 9-, 6-, and 4-step Propane-Air Mechanisms [130]

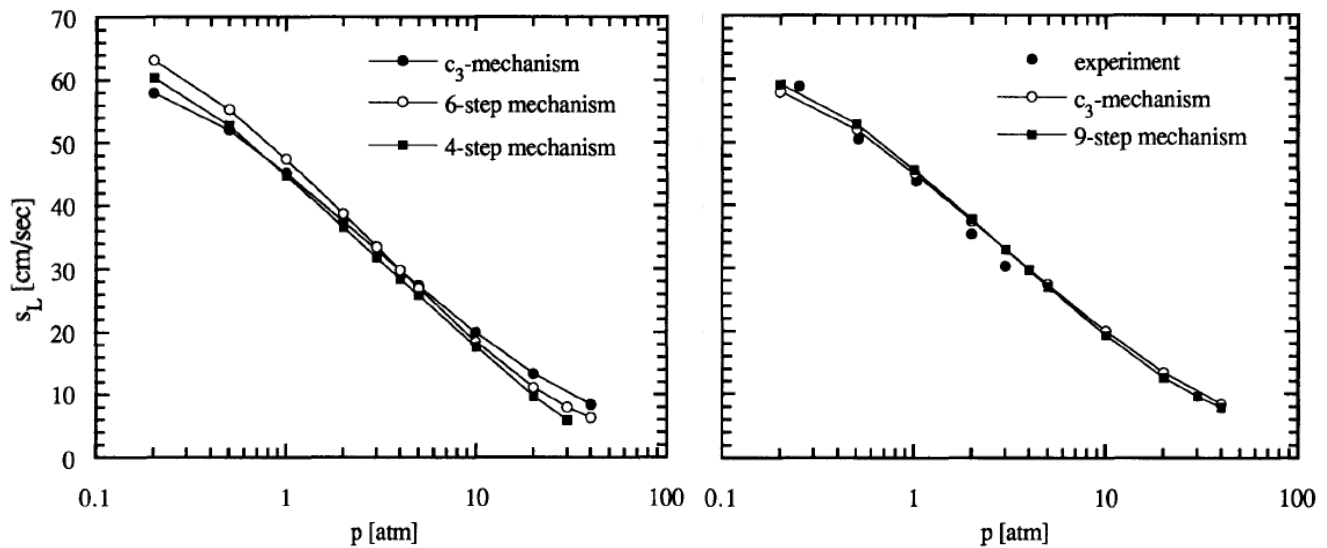


Figure 53: Comparisons of Burning Velocities for a Range of Pressures as Determined from Law's Experiments, a Detailed C₃ Mechanism, and Kennel's 9-, 6-, and 4-step Propane-Air Mechanisms [130]

Kennel further reduced this mechanism into 6- and 4-step mechanisms by applying the steady state assumption first to propene (C₃H₆), oxygen (O), and hydroxide (OH) and then additionally to ethylene (C₂H₄) and acetylene (C₂H₂) species. These three mechanisms were checked against flame speed data from Law (included in [130]) for a range of pressures and

equivalence ratios. While Kennel's 4-step mechanism produced good accuracy in terms of flame speed, he considered the 6-step mechanism as 'optimal' for propane flames because it did not require the 9-step mechanism's iterative scheme but was more accurate than the 4-step mechanism. [130]. These comparisons are included above in Figure 52 and Figure 53.

Similarly, Leung presented the development of 9-step and 7-step mechanisms in Peters and Rogg's text [130]. Leung's mechanisms follow a similar procedure to Kennel's though based on a reduced "skeleton" mechanism which used 56 reactions from the full C_3 mechanism. It is also worth noting that while Kennel's mechanisms were built for unstretched premixed flames (meaning the flames are not strained and of uniform equivalence ratio), Leung's mechanisms were intended for counterflow diffusion flames. Like Kennel's mechanisms, each reaction step's rate was determined as the sum of intermediate reactions from the original detailed mechanism. Due to coupling between the steady-state assumptions between multiple species concentrations, Leung's mechanisms must be solved iteratively [130].

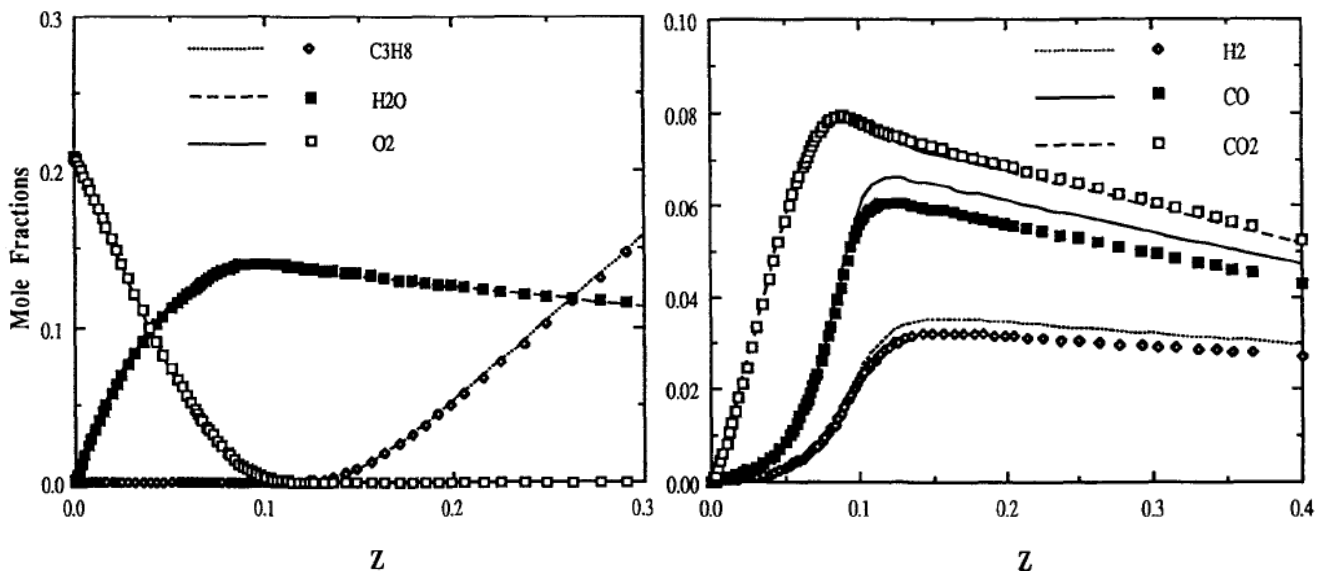


Figure 54: Comparisons of Major Species Mole Fractions for Different Mixture Fractions, Z , as Determined by a Detailed C_3 Mechanism (Points) and a 9-Step Mechanism (Lines) for a Propane-Air Diffusion Flame with Strain Rate of 150 1/s and at 1 bar Pressure [130]

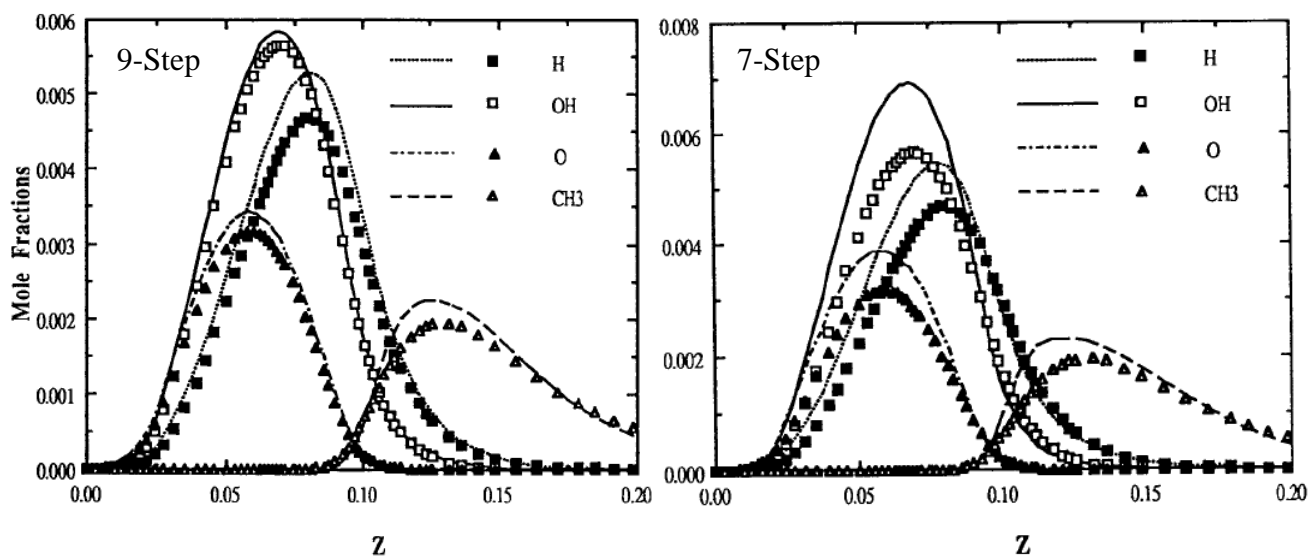


Figure 55: Comparisons of Major Radical Species Mole Fractions for Different Mixture Fractions, Z , as Determined by a Detailed C_3 Mechanism (Points) and Both 9-Step and 7-Step Reduced Mechanisms (Lines) for a Propane-Air Diffusion Flame with Strain Rate of 150 1/s and at 1 bar Pressure [130]

The 7-step mechanism was reduced from the 9-step by applying the steady-state assumption to oxygen (O) and hydroxide (OH) species. Reactions involving hydroperoxyl (HO_2) and hydrogen peroxide (H_2O_2) were also removed to prevent potential errors during the iterative solution. Most reactant and product mole fractions predicted by these mechanisms matched the detailed C_3 mechanism very well. The largest errors were in rich propane flames and due to the steady-state approximations. The authors noted that the rich side of the flame caused increased numerical stiffness that then caused changes in the flame structure [130]. They found methane (CH_4), acetylene (C_2H_2), and ethylene (C_2H_4) to be the most important intermediate species allowing most others to be neglected via steady-state approximations. Nevertheless, as shown in Figure 54 and Figure 55 these mechanisms are remarkably accurate at various mixture fractions, Z , of a nonideal (strained, non-premixed) diffusion flame. If nothing else, these mechanisms reinforce the notion that small, properly formulated chemical kinetic mechanisms (having a fraction of the computational overhead demanded by detailed mechanisms) can still produce accurate results.

Leung and Lindstedt published a detailed mechanism [145] validated with coflow [166-170] and counterflow flame data [171, 172], as well as laminar burning velocities from a variety of sources [65, 126, 173-176]. The study included a sensitivity analysis to highlight the most important reactions for modeling methane and propane diffusion flames. Computational results using the mechanism showed good agreement with experimental data of species profiles of methane-air and propane-air flames and laminar burning velocities of stoichiometric $C_1 - C_3$ diffusion flames. Despite a thorough analysis, the authors noted significant room for development including uncertainties about isomerization of heavier hydrocarbons, thermodynamic properties for some “minor C_3 species,” and the relative importance of different intermediate reactions.

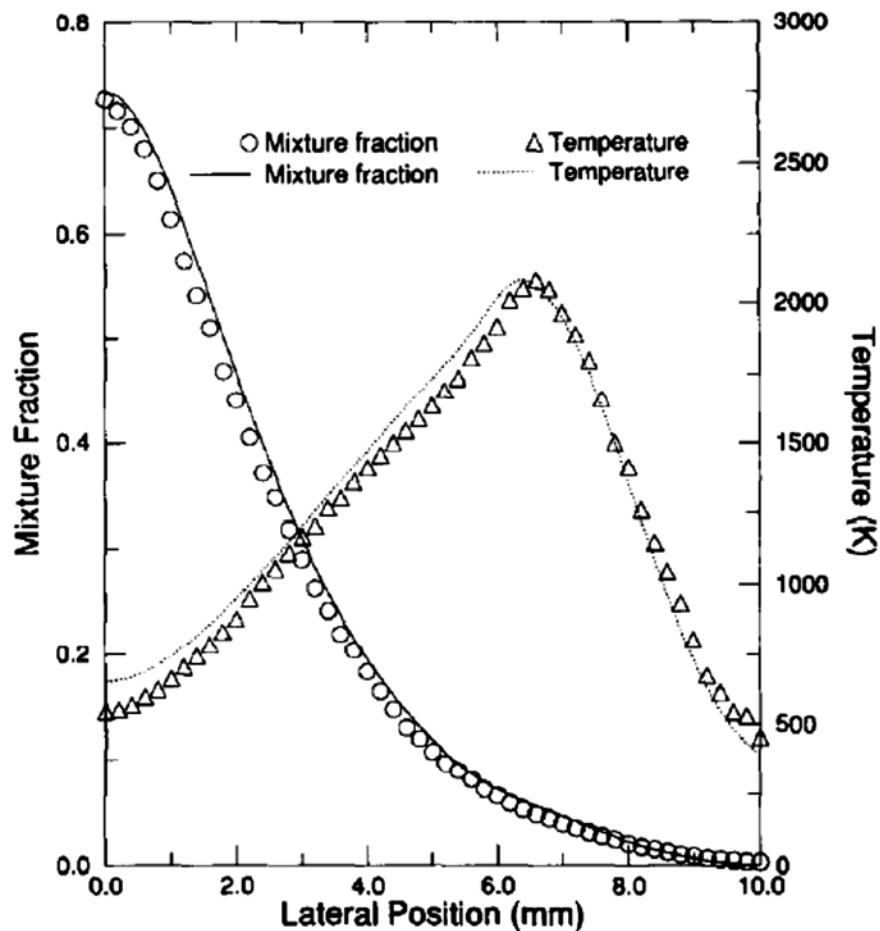


Figure 56: Comparison of Leung and Lindstedt's Mechanism Predictions and Experimental Data for both Methane-Air Mixture Fraction and Temperature at 9 mm Above the Exit of a Burner [145]

Koert, *et al.* developed a pressure-dependent kinetic mechanism intending to better model high-pressure oxidation of propane [146]. A high-pressure flow reactor was used to reach pressures of 10 to 15 atm. The study also specifically probed the kinetic effects of negative temperature coefficient (NTC) behavior, which was regarded as “critical” to engine knock in internal combustion engines and cool flame oscillations. In elevated pressures, maximum species concentrations and reaction rates appeared around 720 K. However, as temperatures increased, the species profiles changed indicating a zone of “intermediate temperature chemistry” wherein the reactivity decreased with rising temperature. At the time, studies related to high pressure propane oxidation had been performed [72, 124, 177], but none specifically studied this phenomena experimentally. Instead, they were concerned with oxidation at higher temperatures outside the NTC region. To confront this deficiency, Koert, *et al* presented an experimental study on oxidation under these conditions [105]. Their propane oxidation mechanism was then used to simulate the experiments of this study. The authors considered the study to be produce “reasonable” results while noting a need for further research into aldehyde levels [146].

Hori, Marinov, *et al* published a paper building on this mechanism by adding modeling of NO and NO₂ and matching it to data from a counterflow reactor where NO was added to the fuel [178]. They found, among other things, that if the ‘parent fuel’ (in this case propane) can oxidize to C₂H₄ or C₂H₃, then NO will form into NO₂. This occurred during oxidation of C₂H₃ when HO₂ and radicals like free oxygen and OH formed.

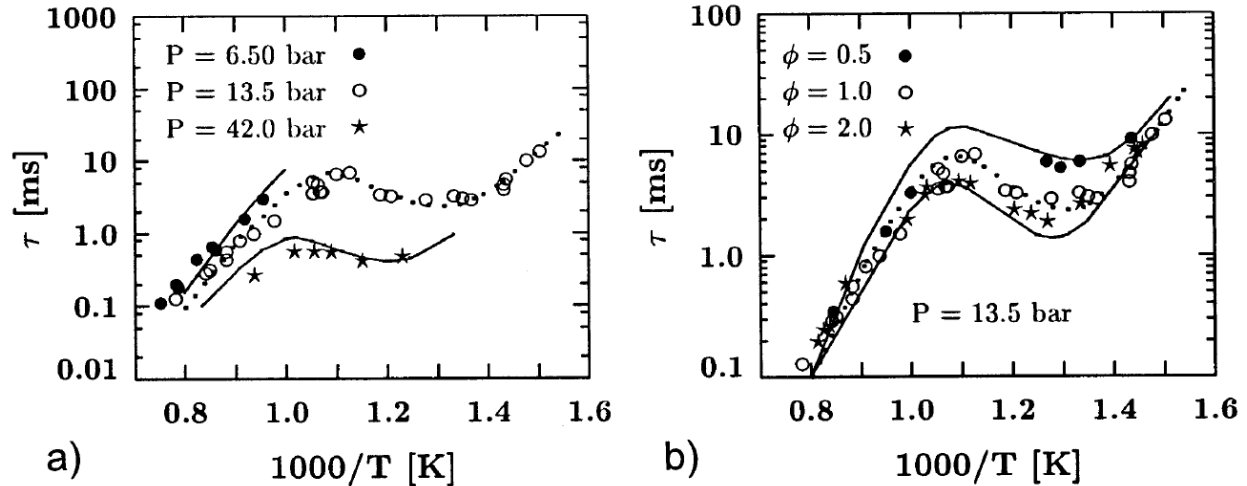


Figure 57: Comparison of Curran's Mechanism Predictions and Ciezki's Experimental Data on Shock Tube Ignition Delays for the Oxidation of n-Heptane (C_7H_{16}) at Various Initial Pressures and Equivalence Ratios [83]

Shortly after, Curran, *et al.* published an n-Heptane (C_7H_{16}) mechanism for application over a wide range of temperatures as high as 1700 K [83]. Although this mechanism was not strictly intended for propane oxidation, its modeling of heavier hydrocarbons up to C_7 chemistry necessarily includes some modeling of C_3 chemistry and propane oxidation. This may make the mechanism nonideal for modeling propane oxidation, but it is exceptionally detailed (with 2450 reactions) and was compared with a wide array of data sources. These sources on n-Heptane (C_7H_{16}) data include shock tubes [179-183], jet-stirred reactors [184-186], plug-flow reactors [187, 188], engines [189-195], and rapid compression machines [196-199] (intended to simulation compression ignition engines). This breadth of data also covers a wide range of pressures as high as 42 atm! This is potentially unnecessary for this study as both pulsejets and the pressurized ramjet being studied operate at much lower pressures on the order of 1 atm.

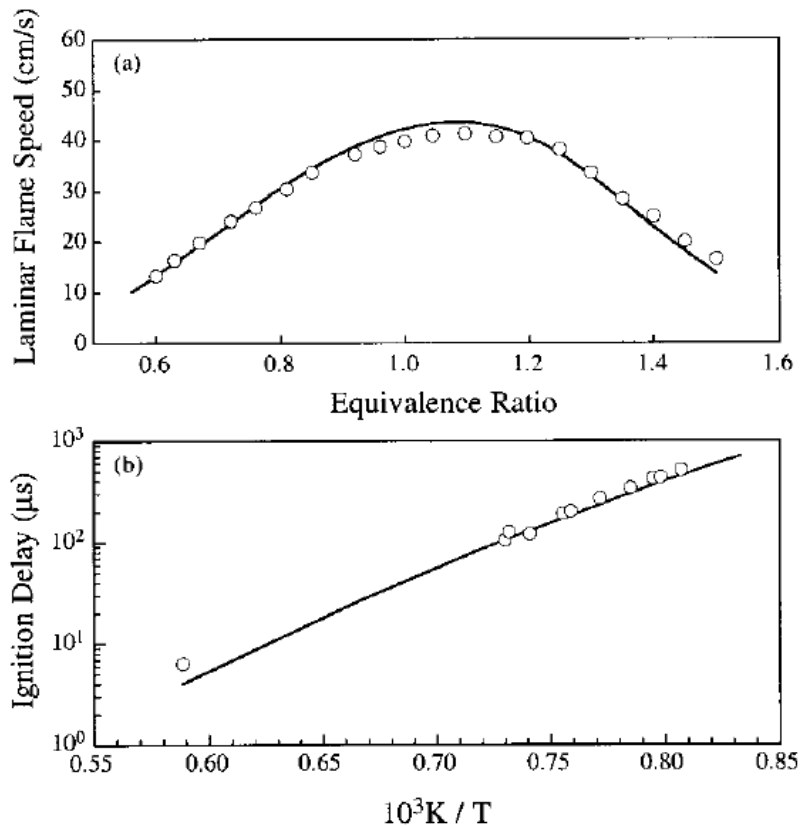


Figure 58: Comparison of Sung's Mechanism Computed Laminar Flame Speeds with Varying Equivalence Ratio at Initial Pressure of 1 atm, Data from Vagelopoulos [107] (Top) and Ignition Delays with Varying Temperature at Initial Pressure of 9.6 atm, Data from Burcat [56] (Bottom) for Propane/Air Mixtures

That same year, Sung published a mechanism [70] investigating the tendency of soot to form in methane and propane counterflow diffusion flames, which was validated with data nearly to temperatures of 1800 K. The effort followed the mathematical model and governing equations as laid out by Kee [174] and assumed the flow to be axisymmetrical. Oxidation of C₁ and C₂ species was based on GRI-Mech 1.2 (an older version of GRI-Mech 3.0 [75]) but included improvements for acetylene and ethylene [200, 201]. Modeling for the formation of aromatics was also added. Modeling of propane and propene, as well as rate parameters for reactions involving butane, isobutane, and butanes were used from Tsang's published reference data [202-204]. The mechanism was validated against laminar flame speed data for acetylene (C₂H₂) [176], ethylene (C₂H₄) [176], and propane (C₃H₈) [107], as well as shock tube ignition delays for propane [56].

The temperature and species concentrations from the resulting detailed kinetic model were considered to be in “good agreement” with the validation data.

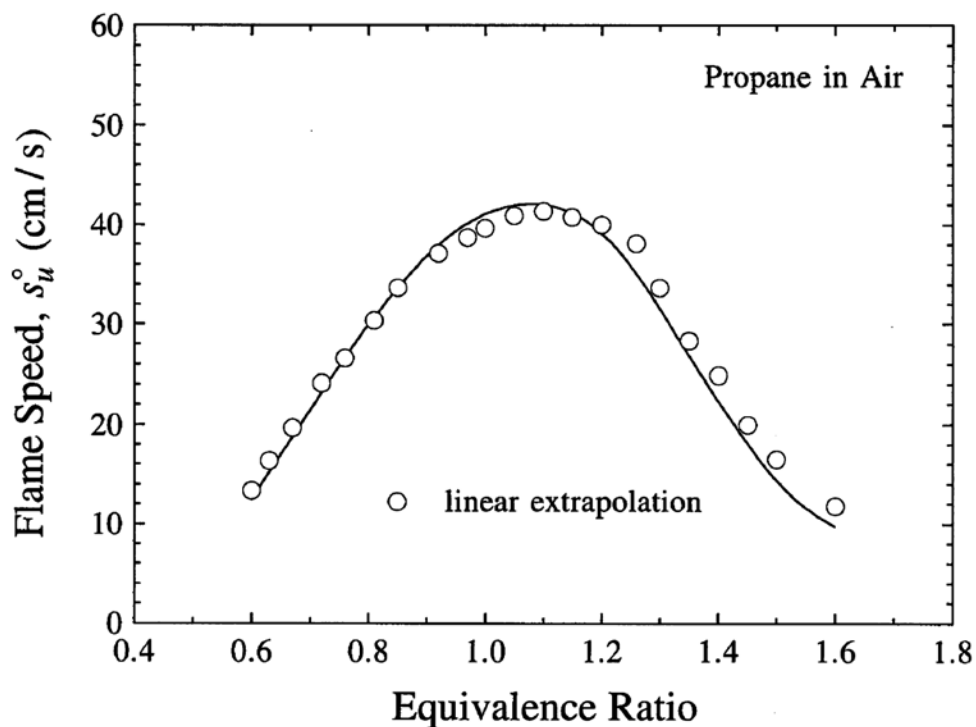


Figure 59: Comparison of Propane/Air Laminar Flame Speeds as Predicted by Davis's Mechanism (Line) and Experimental Data from Vagelopoulos [107] (Points) [148]

Davis, *et al.* also published a high temperature propene (C_3H_6) oxidation mechanism (around 1200 K) [148]. The mechanism was validated using laminar flame speed data from counterflow twin flames (using the methods for stretched flames presented by Law [36]). The C_1 and C_2 kinetics were based on an older version of the GRI Mechanism [75]. Building on this foundation, Davis's mechanism added 287 further reactions to cover C_3 chemistry (including propane) up to hydrocarbons as large as C_6 . The mechanism was then matched to methane (CH_4) [75, 205], ethylene (C_2H_4), and acetylene (C_2H_2) [200] laminar flame speeds. It was also adjusted using species profiles from laminar premixed flat flames [201] as well as acetylene and ethylene counterflow diffusion flames [200]. Davis's mechanism matched this data along with the oxidation of propane in shock tubes and flames as shown in Figure 59.

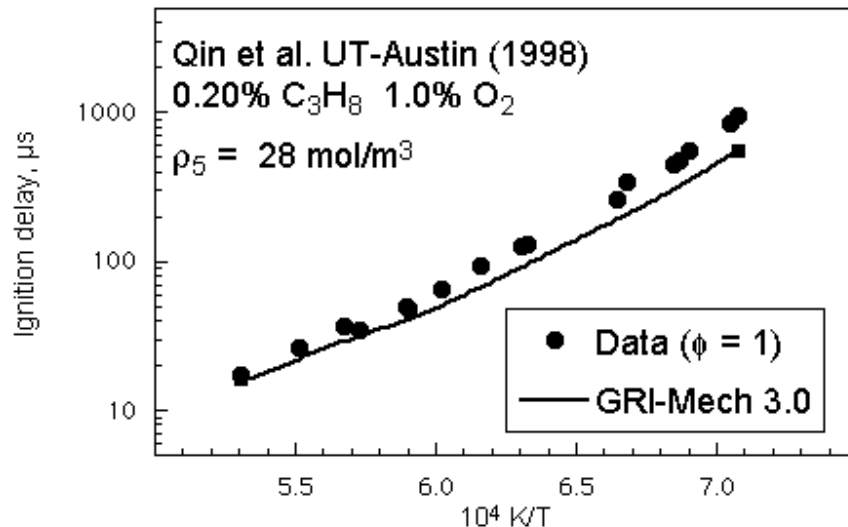


Figure 60: Propane-Air Shock Tube Ignition Delay as Predicted by GRI Mech 3.0 Compared to Experimental Data Published by Qin [66] for Varying Temperatures at an Equivalence Ratio of 1.0 [75]

Around the same time, UC Berkeley’s Gas Research Institute published what became the final version of its oft-cited mechanism, GRI-Mech 3.0 [75]. Although it is still available online, the GRI has “discontinued” its support of the mechanism as of February 2000. Nevertheless, the mechanism last updated in 1999 represents an optimized, comparatively lightweight effort. It was validated with an extensive collection of experimental data from shock tube ignition delays and species profiles to laminar flame speeds using a weighted sensitivity analysis to drive a systematic optimization striving for maximum accuracy and minimal computational time. This allows some datasets to be considered over others when adjusting parameters. Methane ignition delay was well-predicted, but propane ignition delays tended to be overpredicted. Flame speeds also tended to be slightly overpredicted [75]. Though accurate for smaller hydrocarbons, it is important to note that propane was only intended to be a small part of the mechanism as opposed to the main fuel. Moreover, the lower number of reactions means disregarding modeling of some intermediate species like propene. Though well-optimized for smaller hydrocarbons, it may not be the best candidate for propane oxidation.

In the year 2000, several more mechanisms were published. Haworth presented a remarkably lightweight, high-pressure (~4 atm) propane oxidation mechanism with just 76 reactions that was intended to model the conditions of a half liter-per-cylinder engine [149]. The mechanism was matched to data from such an engine with an 11-to-1 compression ratio operating at 2000 rpm and 330 kPa net mean effective pressure (NMEP) engine load.

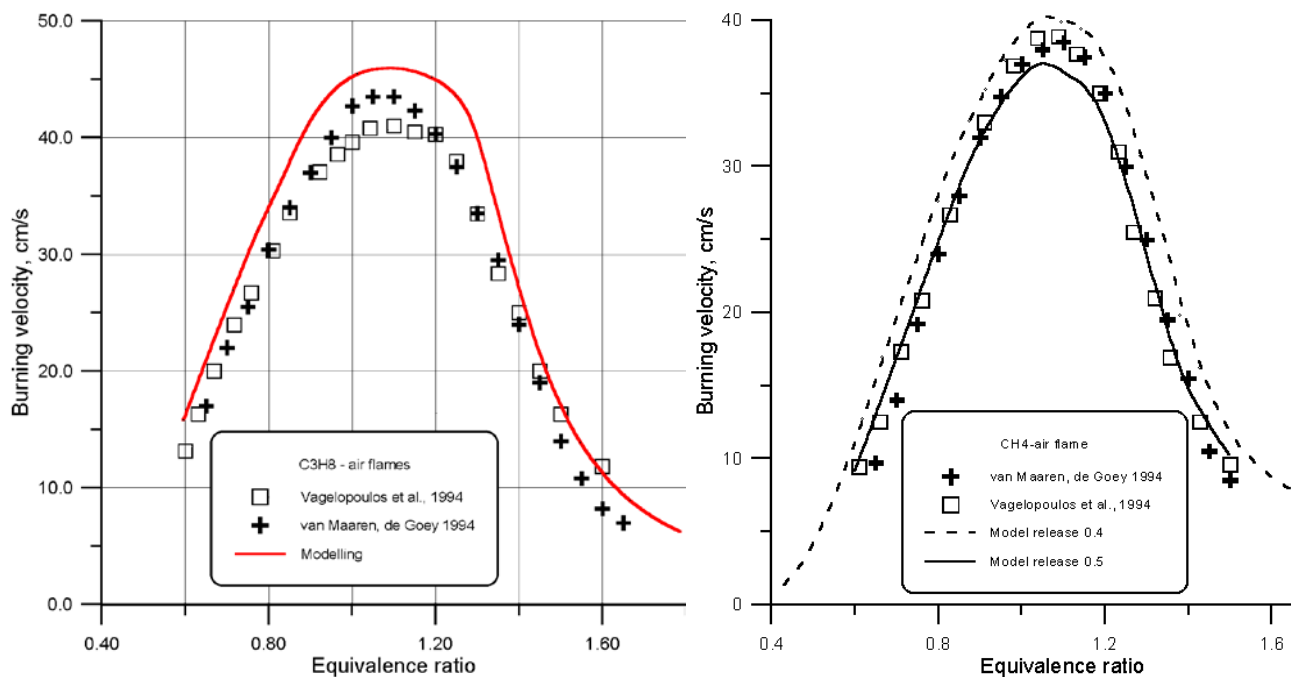


Figure 61: Comparison of Konnov's Mechanism to Experimental Data for Laminar Flame Speeds of Propane (left) and Methane (right) Oxidation at 1 atm Pressure Across a Range of Equivalence Ratios [74, 82, 107]

That same year, Konnov self-published a more niche methane/natural gas mechanism [74] that was validated with data primarily focused on H₂, CO, N₂O, NO₂, and NH₃ species as opposed to the major hydrocarbons (CH₄, C₂H₆, and C₃H₈ for instance) [155]. As a result, the mechanism offers more detailed N-H-O chemistry than other similar mechanisms. The data included shock tube ignition delays, laminar flame speeds and species profiles, and flow reactors. The mechanism slightly overpredicted experimental propane-air laminar flame speeds (as indicated by Vagelopoulos [107]) but matched methane flame speeds more closely. This data is shown in Figure

61. Note: The reader is cautioned that Konnov’s webpage (the typical citation found in most references) appears to no longer be directly available. A cached version (currently available at [82]) from as late as 2011 can be found which contains the final update from 2003, as well as data comparisons and the mechanism itself.

Qin also published a case-study for a detailed, high temperature propane-air mechanism [150] matched to laminar flame speed data published by Vagelopoulos [107, 108], as well as shock tube ignition delay data published as part of Qin’s own 1998 dissertation [66]. The mechanism relied heavily on the C₃ chemistry of UC Berkeley’s GRI 3.0 Mechanism [75]. Qin argued for this as the foundation of his mechanism because it was rigorously derived, thoroughly examined the reaction rate coefficients and was validated against all the available literature of high temperature combustion. The study also involved an attempt at optimizing mechanism parameters based on a sensitivity study of each reaction and found that experimental data for C₃ reactions could not be matched by only adjusting rate parameters optimized for reactions of smaller hydrocarbons.

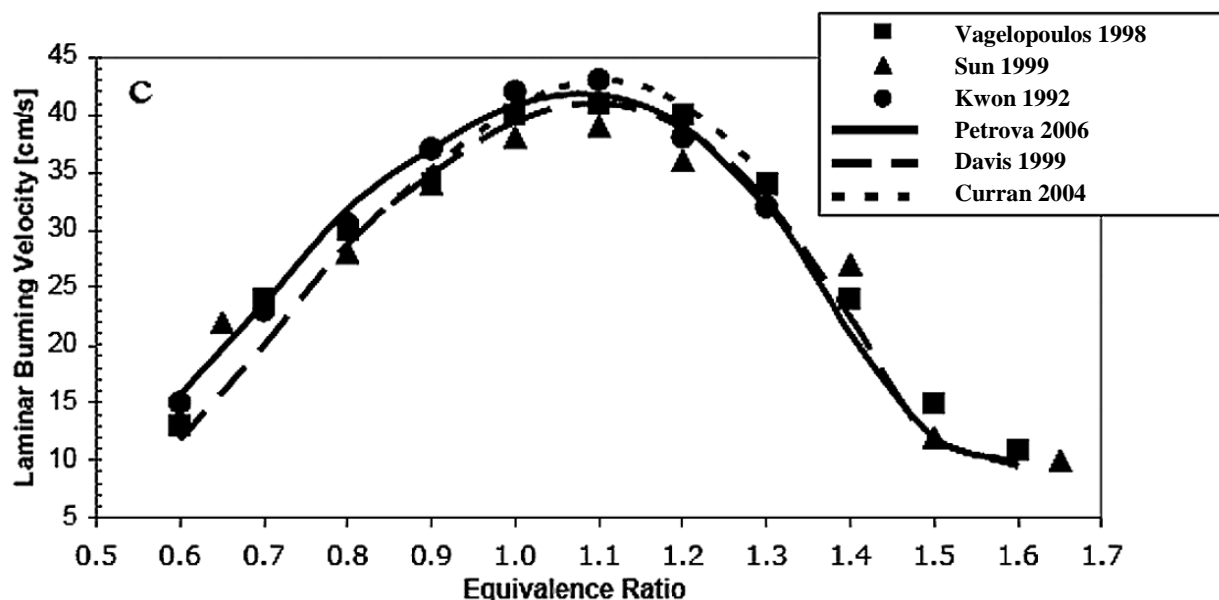


Figure 62: Comparison for Propane-Air Laminar Burning Velocities for Varying Equivalence Ratios Showing Petrova [153], Davis [148], and Curran [151] Mechanism Predictions with Experimental Data from Vagelopoulos [108], Sun [206], and Kwon [207]. Initial Pressure of 1 atm and “Room Temperature.” [153]

In 2006, Petrova, *et al.* published a relatively lightweight mechanism by limiting the kinetics modeling to C₃ chemistry and below. It combined multiple previously-tested mechanisms with another for propane, propene, allene, and propyne the result of which was tested against mechanisms from Davis [208] and Curran [209]. This also involved experimental data sources from both shock tube ignition delay published by Kim [76], and laminar flame speeds published from several sources [108, 206, 207]. The authors noted a deficiency (common in most propane mechanisms [84]) in predicting the autoignition of propane below 1100 K that could not be solved without adding “a substantial number of additional steps.”

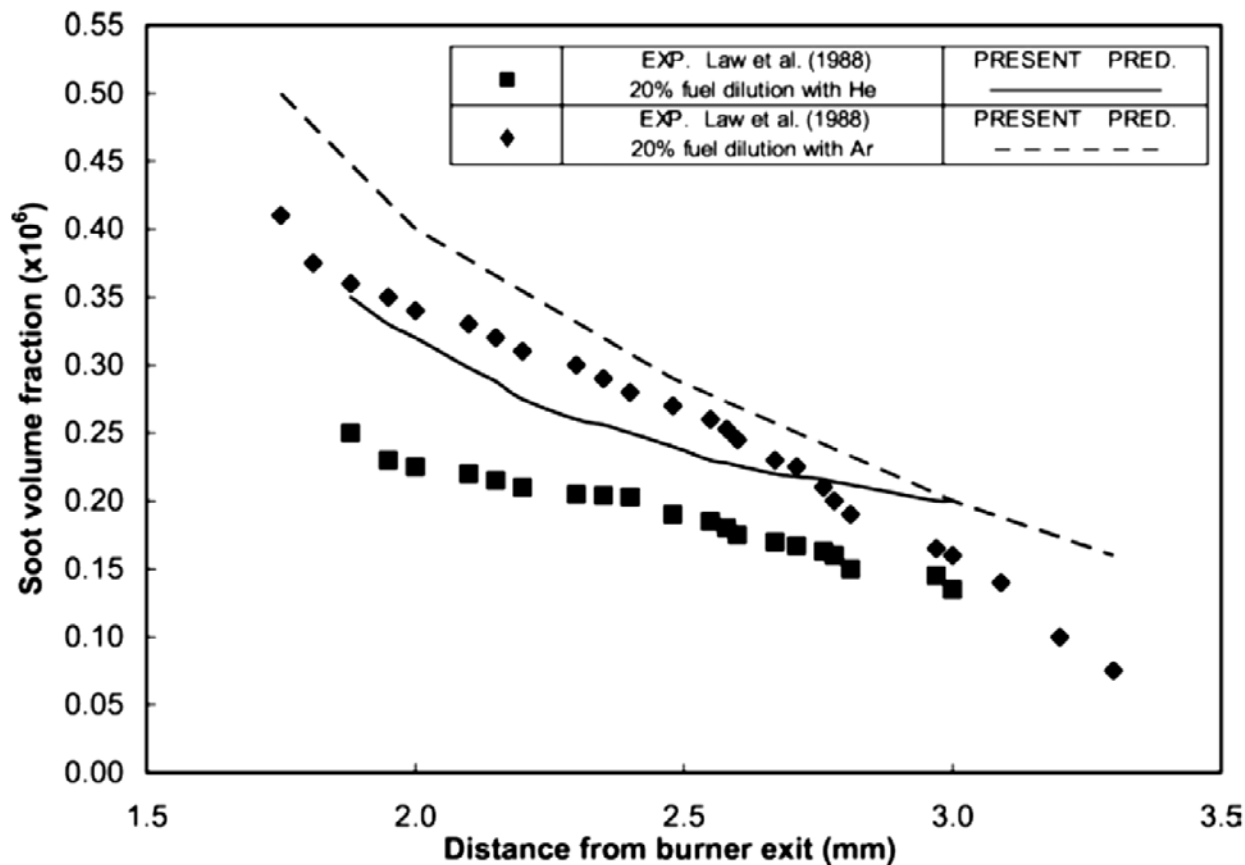


Figure 63: Comparison of Soot Volume Fraction for a Propane-Air Diffusion Flame as Measured by Law [100] and Predicted by Koutmos’s Mechanism [154]

In 2007, Koutmos published a small 9-step global kinetic mechanism for propane combustion intended specifically for modeling complex reacting flows with an emphasis on nitrogen chemistry and the generation of soot. [154] The mechanism started with a 3-step mechanism published by Kennel [210] (reduced from an 88-step mechanism). A 2-step NO_x production mechanism was added to account for NO_x effects (for instance prompt NO_x, thermal NO_x, N₂O, and species reburn in rich conditions). Lastly, a 4-step model for soot production developed by Leung [211] and Lindstedt [212] was added. The mechanism was then calibrated to match a broad collection of coflow diffusion flame data including those published by Haworth [149], Leung [211], and Kennel [210].

That same year, Peterson published a detailed mechanism intending to cover the data range of practical industrial gas turbines [155, 213]. The full mechanism was based on a hydrogen submechanism from Ó Conaire [214] adding part of Curran's dimethyl ether mechanism [215] to model methane/ethane oxidation. It also relied on a combination of Curran's iso-octane mechanisms [83, 216] to capture C₃ oxidation. The mechanism was compared to experimental data from reflected wave shock tube data. The data did not use a pure form of propane and instead investigated mixtures of methane/propane between 90/10% and 60/40% along with mixtures of methane/hydrogen, and methane/ethane. The mechanism tended to overpredict ignition time for the 30% propane case and underpredict the 10% case. The authors noted that the stability of combustion and ignition delay were "strongly dependent" on flame dynamics directly affected by the fuel's thermochemical parameters.

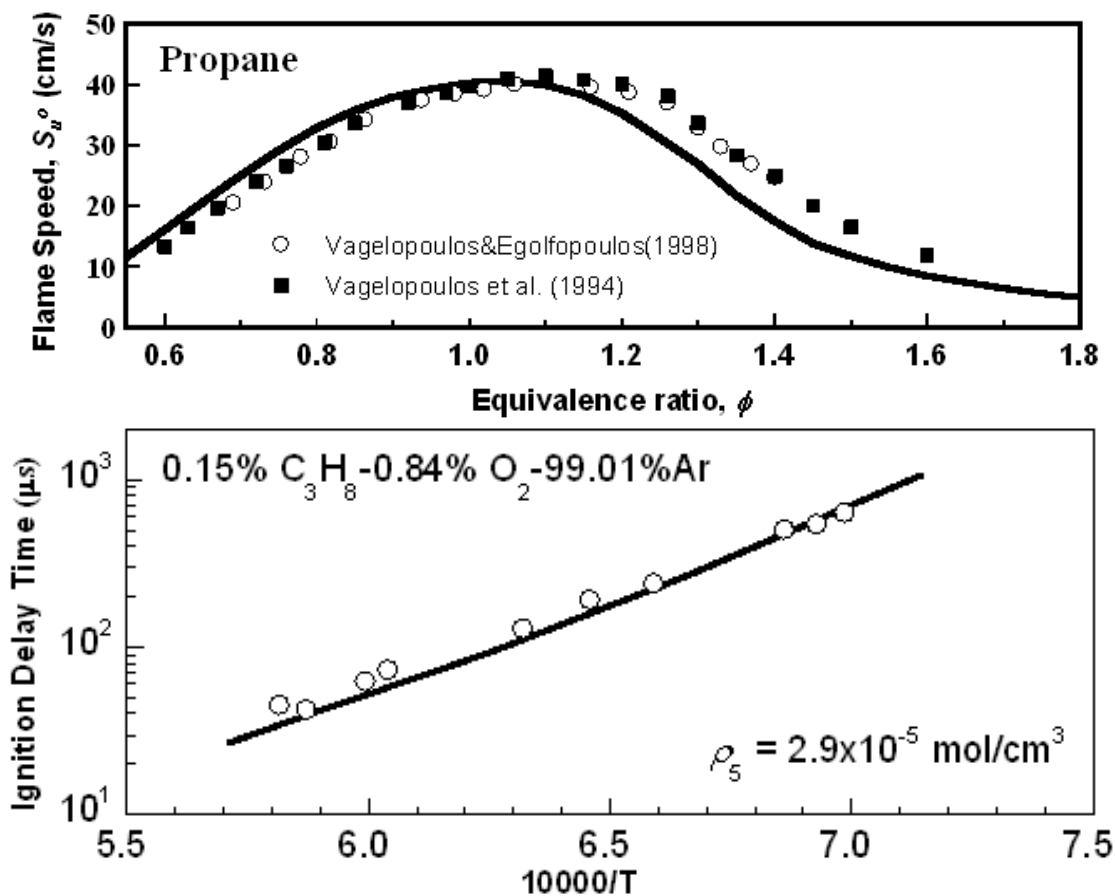


Figure 64: Matching Between Experimental Data and the USC Mech II for Propane-Air Flame Speeds (Top) and Ignition Delays (Bottom). Flame Speed Data from Vagelopoulos [107, 108] and Ignition Delay Data from Qin's Dissertation [66]. Plots from USC Combustion Kinetics Laboratory [156].

The latest version of another broadly tested detailed mechanism (referred to as USC Mech II) was also published in 2007 [156]. This mechanism is useful for a wide variety of applications involving high temperature oxidation of hydrogen, carbon monoxide, and C₁ – C₄ hydrocarbons. It does this by mixing parameters of several prior successful mechanisms. It drew on Davis's optimized mechanism [217] for H₂ and CO oxidation, as well as versions 1.2 and 3.0 of the GRI Mechanism [75]. Ethylene and acetylene were modeled using a mechanism published by Sun [200] and Wang [201]. It also made use of Davis's C₃ mechanism [148]. Lastly, the USC mechanism relied on a 1,3 butadiene (C₄H₆) mechanism for high temperature oxidation (1035 – 1185 K) as published by Laskin [218]. The USC mechanism was tested against a wide array of experimental

data for H_2 , CO, and C_1 - C_4 oxidation. Results were tested for propane/air oxidation using shock tube ignition delay data published by Burcat [56], as well as data from Qin's dissertation [66]. Propane/air laminar flame speed data published by Vagelopoulos [107, 108] was also used along with species concentration data from shock tubes (for H_2), flow reactors (H_2 and CO data), and ethylene (C_2H_4) burner stabilized flames.

The following year, Bourque published a much larger mechanism (1580 reactions) to study blends of natural gas with heavier (C_2 and larger) hydrocarbons. [90, 157] The mechanism was combined from several sources including the GRI Mech 3.0 [75] and Curran's 1998 [83] and 2002 [216] mechanisms. The study showed that mixtures with more heavy hydrocarbons exhibited faster ignition and tended to be affected more by pressure than stoichiometry. Laminar flame speeds at atmospheric pressure matched well, but were underpredicted by up to 25% at a greater pressure of 4 atm.

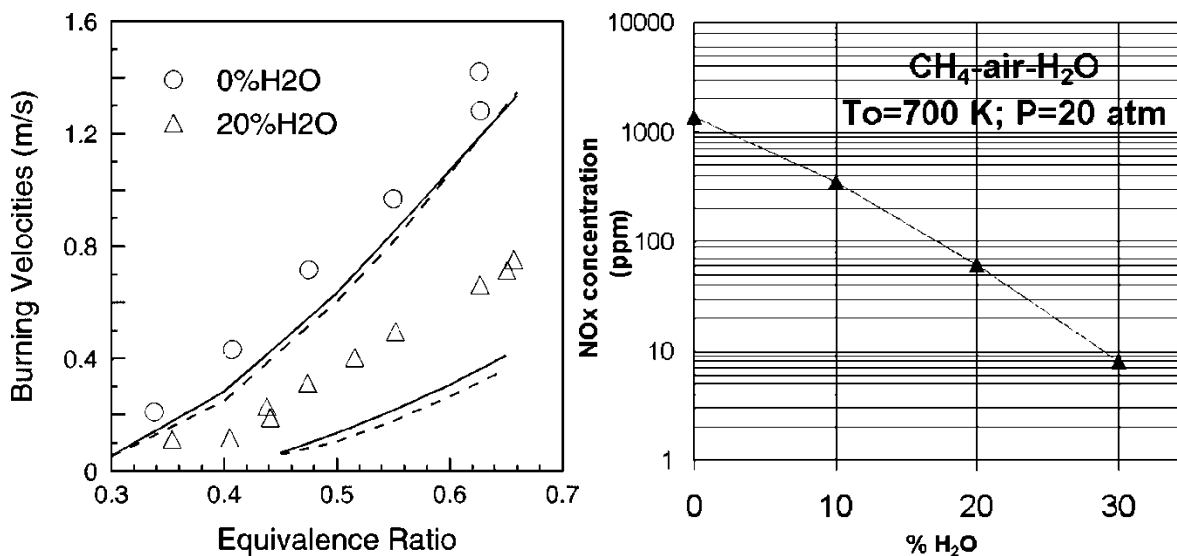


Figure 65: Flame Speeds of Hydrogen-Air Flames Affected by Water Vapor Dilution. Note: Solid Line Shows Le Cong Mechanism [158] and Dashed Shows GRI Mech 3.0 [75] (Left) and NO_x Reduction Potential of Water Vapor in Methane-Air Combustion (Right) [158].

The next year, Le Cong and Dagaut published another large mechanism matched to a new set of data from a JSR investigating the effect of water vapor dilution on hydrogen and natural gas

combustion. [158] The introduction of water vapor in the combustion process was considered as a means of reducing NO_x formation, particularly for gas turbine engines. The study used the same JSR setup previously published by Dagaut [37, 219] and had a residence time of 120 ms at a wide range of pressures. They simulated the conditions inside the reactor as well as those found in shock tubes and premixed flames and noted that in premixed flames that increased water vapor tended to lower flame speeds, adiabatic temperatures, and produce less NO_x .

In 2010, Healy published a 1588-reaction mechanism validated with both shock tube experiments and rapid compression machines [159]. The use of rapid compression machines allowed study of combustion at high pressures (up to 29.6 atm) necessary for recreating the environment in compression ignition engines. The inclusion of shock tube data was exhaustive covering 40 years of ignition delay data for various hydrocarbon blends largely involving methane but including some propane blends [38, 59-64, 81, 86-90, 157, 213, 220-225]. The mechanism was checked with blends of CH_4 , C_2H_6 , C_3H_8 , $n\text{-C}_4\text{H}_{10}$, and $n\text{-C}_5\text{H}_{12}$ using nitrogen and argon as diluent gases. To do this, the mechanism modeled reactions from C_1 to C_5 to adequately cover natural gas mixtures with these heavier hydrocarbon blends. The study produced greater accuracy in ignition delay calculations over simpler adiabatic simulations by accounting for significant heat losses.

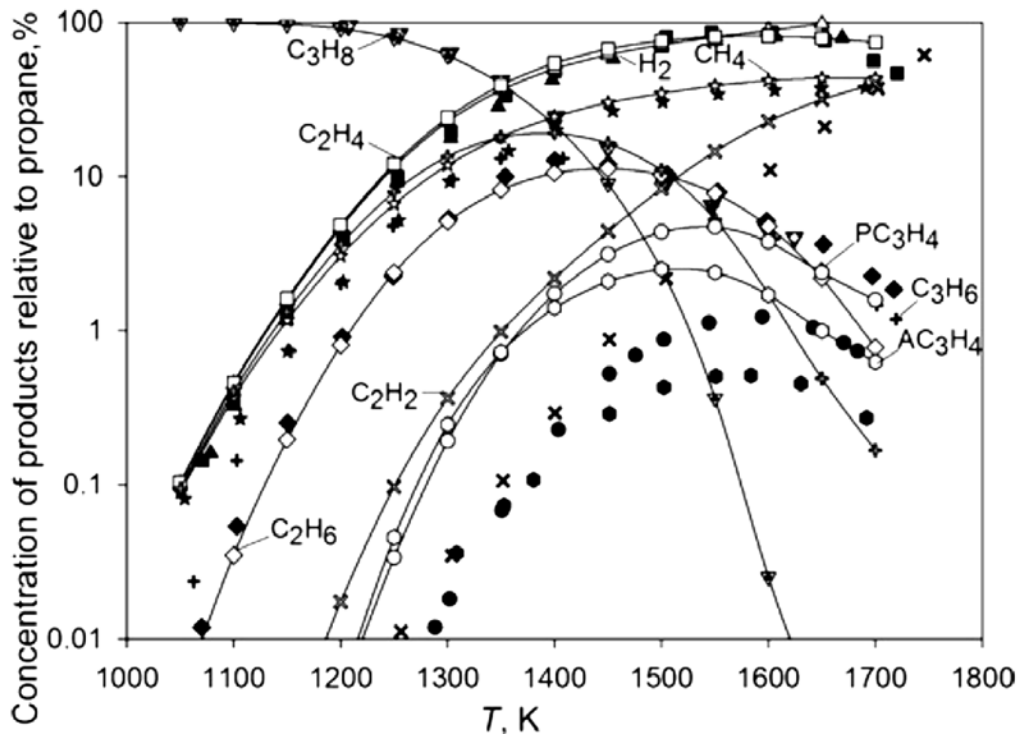


Figure 66: Comparison of Agafonov Mechanism and Experimental Data [226] for Propane Pyrolysis Product Yields at Various Temperatures at an Initial Pressure of 0.26 atm. (Mixture of 0.016 C₃H₈/Ar) [160]

The following year, Agafonov published a larger mechanism including propane pyrolysis and oxidation validated with shock tube experiments at elevated pressures (between 2.96 and 6.91 atm) [160]. The mechanism was intended to study high temperature combustion (up to 1700 K) and emphasized modeling the production of soot. It built on the USC Mech II for small hydrocarbons (CH₄ and C₂ to C₄ species) and extended it to model reactions of C₅ and C₇ species using mechanisms published by Richter [227] and Skjøth-Rasmussen [228]. The mechanism further included models for oxidation of aromatic species – benzene (C₆H₆) and toluene (C₇H₈) – as published by Richter [227] and Frenklach [229, 230], as well as a model for n-heptane (C₇H₁₆) from Correa [231]. Pyrolysis of a propane-argon mixture showed good agreement with published data from Lifshitz [232] and Naydenova [226]. Soot yields from methane and heavier hydrocarbons also showed good agreement.

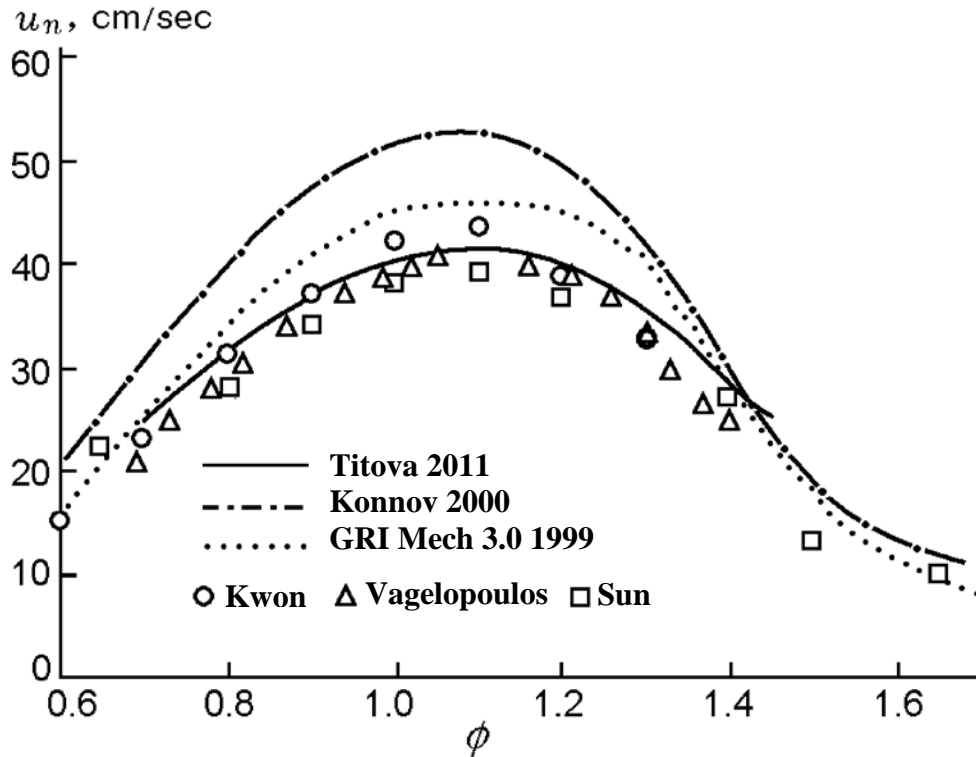


Figure 67: Laminar Flame Speeds from Titova [161] of Propane-Air Combustion at Varying Equivalence Ratios, ϕ , Under Initial Temperature, $T_0 = 300$ K and Pressure, $P_0 = 1$ atm. Mechanisms (lines) are Titova [161], Konnov [74, 82], GRI Mech 3.0 [75] and data (points) from Kwon [207], Vagelopoulos [108], and Sun [206].

Titova, Kuleshov, and Starik published a smaller propane kinetic mechanism (599 reactions using 92 species) validated with a broad array of experimental data sources [161]. This set of data drew from shock tube ignition delay times [55, 56, 85, 233-235], laminar flame speeds [108, 206, 207], and flow reactor species concentrations [108, 206, 207, 232]. This propane mechanism was compiled from Starik's previous mechanisms for methane (CH_4) [236, 237], propane (C_3H_8) and butane (C_4H_{10}) blend products [238], ozone interactions with methane (CH_4) and acetylene (C_2H_2) combustion [239], and syngas [240]. The mechanism also included reactions for oxidation of n-alkanes referenced from Kojima [241], and Curran [216]. The resulting mechanism was considered appropriate for a wide range of temperatures (680 – 1900 K) and pressures (0.17 – 30 atm). Titova's mechanism also more accurately matched laminar flame speeds than both the GRI Mech 3.0 [75] and Konnov's mechanism [74, 82].

In 2012, Andreis published a small reduced mechanism [162] in ten steps validated using diffusion flame data from Leung [145] and simulated with a 2nd order finite difference method including a large eddy simulation. This necessitated assuming steady state and partial equilibrium. The mechanism built on detailed and reduced propane mechanism work published by Kennel [130], Leung [130, 145], Qin [150], Marazioti, Curran [151], Anetor [144] (which used Westbrook's 2-step mechanism [141]), and the San Diego mechanism [152]. The mechanism also drew on an earlier mechanism modeling components of gasoline mixtures published by Mehl [242]. Good agreement was found for water vapor and carbon dioxide species formation.

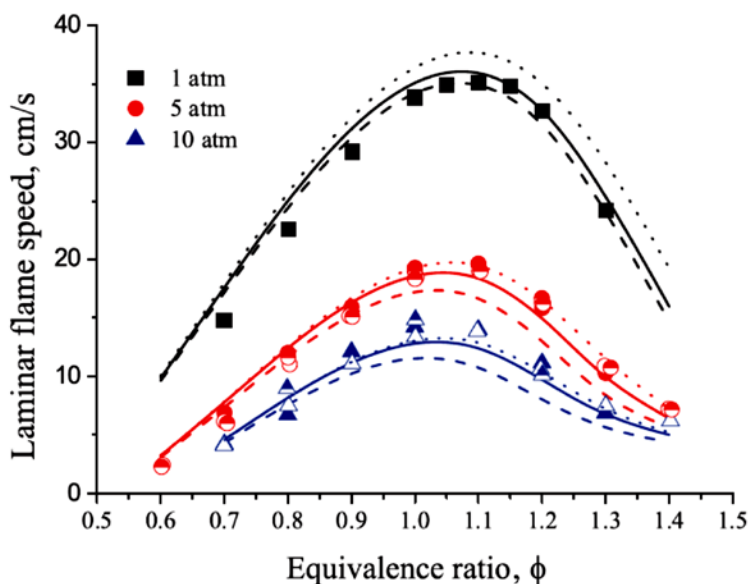


Figure 68: Comparison of Methane Flame Speed Data at Varying Equivalence Ratios and Pressures (at an Initial Temperature of 298 K) Between the AramcoMech 1.3 [163] (Solid Lines) and GRI-Mech 3.0 [75] (Dashed and Dotted Lines). [163]

The following year Metcalfe and coauthors published AramcoMech 1.3 that models species up to C₄ involving 1140 reactions and 171 species [163]. The mechanism was validated with a diverse set of experimental data including shock tubes, jet-stirred reactors, flow reactors, flame speeds, and flame species distributions. The authors performed a series of sensitivity analyses to find which reactions had the greatest effect on ignition delay and flame speeds. They then performed comparisons on the reactions with the highest sensitivities between experimental

data and other mechanisms like the GRI-Mech 3.0 [75] and Marinov's mechanism [178]. Those reactions studied in more depth included reactions associated with methane (CH_4), acetylene (C_2H_2), ethylene (C_2H_4), ethane (C_2H_6), and oxygenated hydrocarbons. One such comparison for methane (CH_4) flame speeds is included in Figure 68. The authors noted that the formation of propane and n-butane (nC_4H_{10}) from methyl (CH_3) and ethyl (C_2H_5) radicals is important in accurately simulating methane and ethane kinetics. Hence, the inclusion of C_3 and C_4 chemistry was considered necessary.

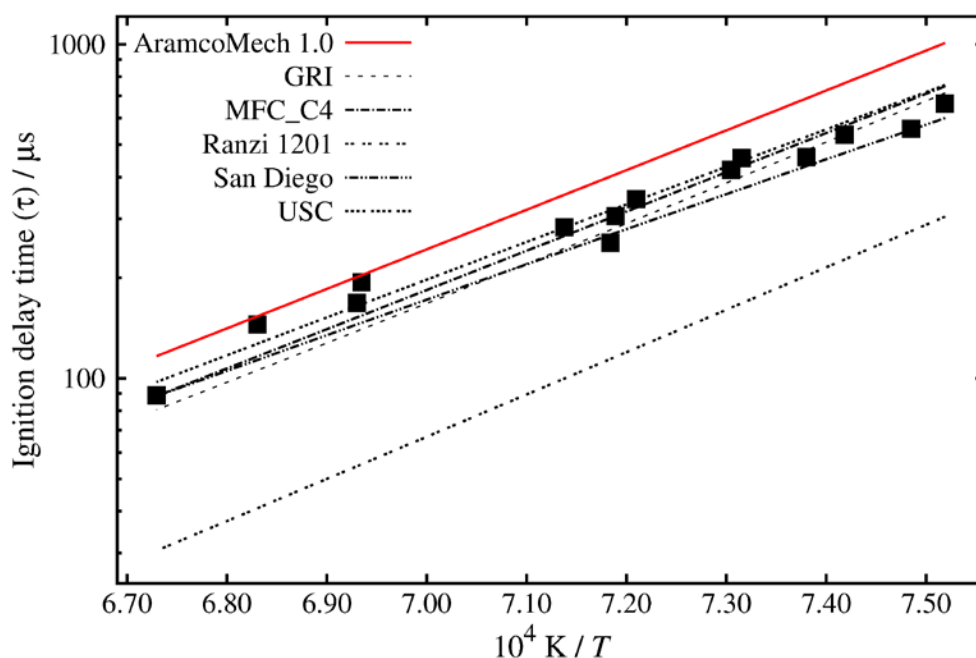


Figure 69: Propane-Air Ignition Delay Comparison Between Several Mechanisms and Shock Tube Data Published by Burcat [55] at an Equivalence Ratio of 1.0 and Initial Pressure of 2.36 atm. [243]

A complete presentation of the supplementary data (beyond investigation of C_1 and C_2 chemistry) is available from the NUI Galway Combustion Chemistry Center and includes the propane ignition delay validation included in Figure 69 [243]. At a stoichiometric equivalence ratio ($\phi = 1.0$) it is clear that most mechanisms (including those for propane discussed earlier) are within the scatter of the experimental ignition delay data. And despite the extensive study of

individually-sensitive reactions, the AramcoMech 1.3 does not appear to match Burcat's data as well as the USC, GRI-Mech 3.0 and San Diego mechanisms.

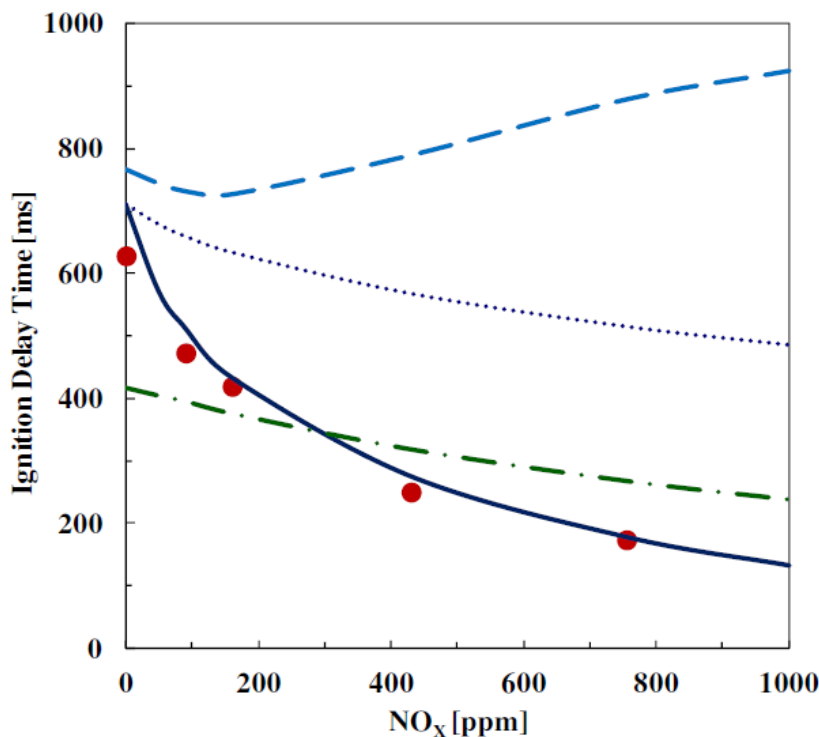


Figure 70: Vitiated Propane/Air Oxidation Ignition Delay Variation with NO_x Concentration at 875 K and $\phi = 1$ as Published by Gokulakrishnan [119]. Data Points Show Experimental Data and Solid Line Shows the Mechanism Predictions. The Dotted Line Shows the Mechanism without NO₂, the Dashed Line Shows Hori's Mechanism [178] Predictions and the Dashed-Dotted Line Shows Faravelli's Mechanism [244] Predictions.

In 2014, Gokulakrishnan, *et al.* published a propane combustion mechanism [119] involving vitiated air (air with a reduced oxygen concentration) as it applies to many things including turbine engines and improved combustors [245-252]. The mechanism used 966 reactions involving 136 species and was validated against a wide array of hydrocarbon experiments in the literature (shock tubes, jet stirred reactors, and flow reactors) as well as new data gathered for the study. It was intended to cover low-temperatures and low-oxygen content in propane/air combustion in order to capture NO_x effects. In particular, the study intended to capture the NTC behavior of propane oxidation at low temperatures. This region is noted by a reduction in reaction

rate with temperature as opposed to the more typical increase. The authors' mechanism predictions matched ignition delay data very well where Hori's mechanism [178] predicted an opposite trend and Faravelli's mechanism [244] showed a correct trend but with more significant error. This comparison is shown in Figure 70. The mechanism also matched the effect of CO₂ on propane laminar flame speeds for a wide range of equivalence ratios. In addition, the study found that CO₂ was more effective at reducing flame speeds than dilution with N₂ and that chemical kinetics played a more significant role in this than with N₂ which was typically treated as inert.

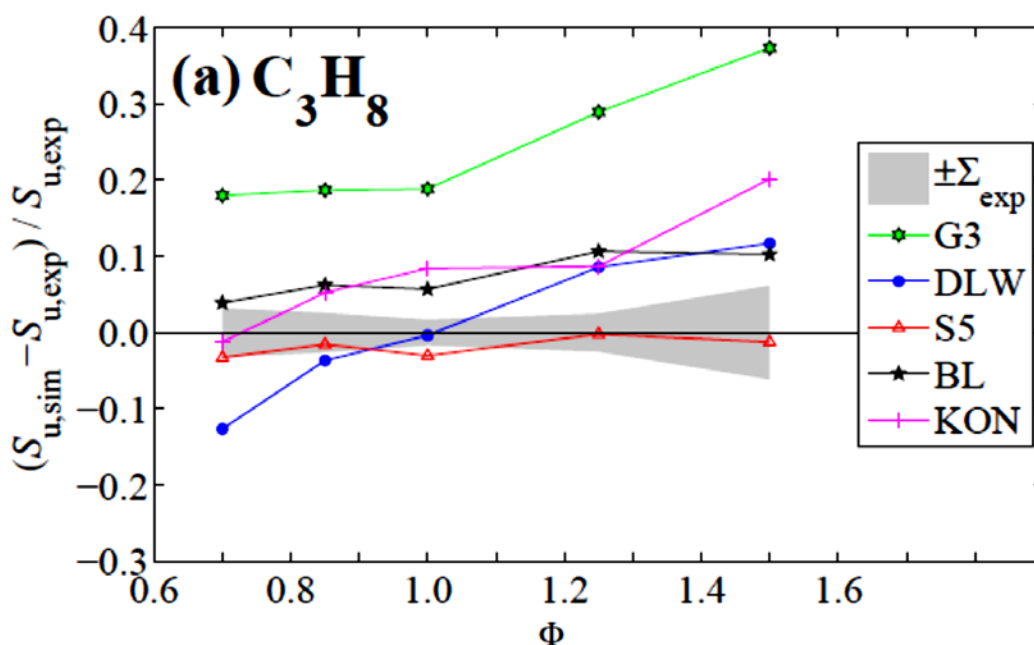


Figure 71: Difference Between Simulated and Experimentally-Measured Propane Stagnation-Flame Speeds Between Five Kinetic Mechanisms Showing the San Diego Mechanism (Referred to as “S5”) Exhibiting the Lowest Difference. [253]

Lastly, the only currently maintained mechanism developed by a research group is the San Diego mechanism [152]. This model has been regularly updated by the UC San Diego Combustion Research Group since 2001 with the latest version (at the time of this work) being published in late 2014. The mechanism focused on those conditions necessary for flames, high temperature ignition and detonation, and eliminated species and reactions which were not directly important. In doing so, they found that rate parameters for a fraction of the total steps were “of crucial

importance.” Meanwhile, there were numerous steps with smaller contributions that could be neglected. Following this approach resulted in a minimal number of species and reactions that require modeling. This suppressed the number of reactions down to 173 with just 39 individual species. Moreover, a 2008 thesis on premixed stagnation flames comparing 16 kinetic mechanisms (including the GRI-Mech 3.0 [75], and those published by Davis [148], Marinov [178], and Konnov [74], shown in Figure 71) found the San Diego mechanism best matched propane (and several smaller hydrocarbon) flame speeds [253]. As a result, the San Diego mechanism represents a lightweight, accurate propane oxidation mechanism (as shown in earlier independent comparisons) still in active development.

2. CFD Parameters in Use with Chemical Kinetic Models

Of primary concern for any transient simulation is the option of either a Reynolds Averaged Navier Stokes (RANS) or a Large Eddy Simulation (LES) for modeling turbulence (previously discussed in Chapter I, Section B). Concerning turbulent combustion systems, an Unsteady RANS formulation can only be expected to resolve mean flow structures and not independent turbulent structures. Although a RANS model is generally expected to be computationally faster, an overview of turbulent combustion models found LES predictions of combustion to be more reliable [254]. However, the authors of that review cautioned that if attached boundary layers are important, a LES model will require fine grids at the walls [254]. Although the wall interaction in a quiescent spherical explosion chamber is expected to be minimal, this limitation is mitigated by the use of Adaptive Mesh Refinement (AMR) that adjusts the grid fineness during the simulation based on local flow parameters. Another study presented in Figure 72 comparing temperature profiles of a flame using both LES and RANS methods also showed a tendency of greater accuracy using LES [255].

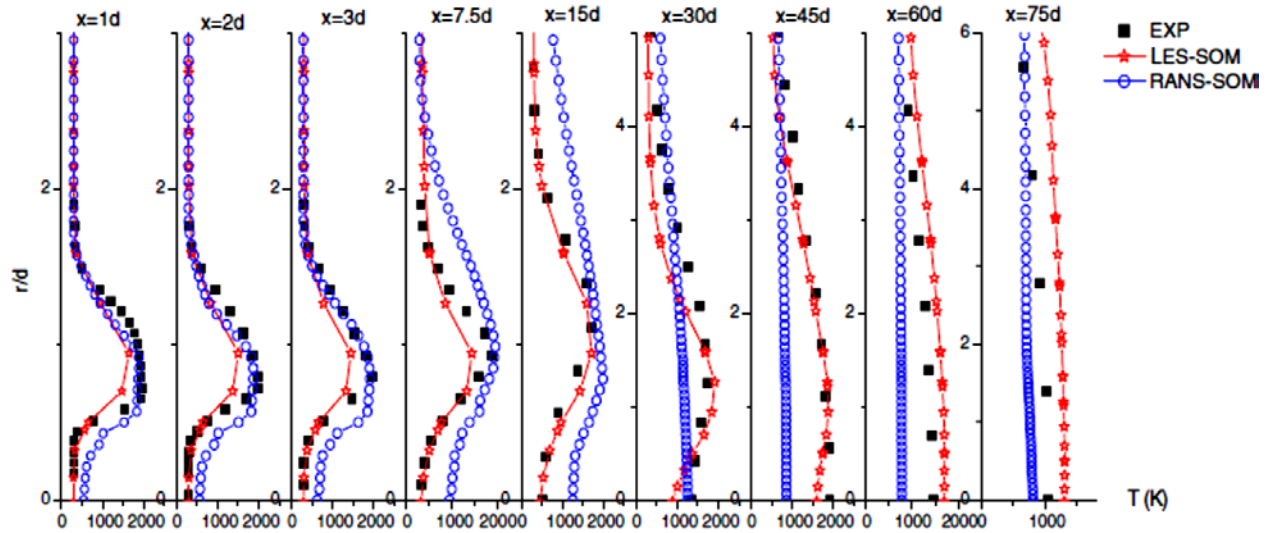


Figure 72: Time Averaged Temperature Profiles of a Cylindrical Methane-Air Combustion Chamber [255]

Other studies have also shown the effects of mesh sizing on LES models for reacting flows. One such study analyzed a turbine combustion chamber using three different mesh sizes separated into coarse (1.2 million cells), intermediate (10.6 million cells) and fine (43.9 million cells) [256]. While the coarse mesh is much finer than the expected 500,000 cell total limit imposed by the visualization software (Enight Free), it is clear the models involved did not use an adaptive meshing scheme that would offer a more optimized number of cells for similar fidelity. Nevertheless, the authors of that study determined the “flame position, its unsteady behavior, and the mean flow fields (velocity, temperature, and reaction rate) are ... reasonably insensitive to mesh resolution.” They did note, however, that finer grids showed higher root-mean-squared (RMS) temperatures over the whole domain reiterating the fact that combustion is still a subgrid phenomenon [256]. This means that although the flame propagation in general may be reliant on turbulent structures, the kinetics involved are still evaluated as averaged phenomena for an individual cell. This underscores the importance of an optimally sized mesh (and thus AMR) in

regards to the resulting flame temperature as opposed to merely analyzing the finest mesh that computational time will allow.

An alternative method of modeling flame propagation is to assume the flame is a geometric surface moving through space. This methodology is referred to as a level-set G-equation and is ideal for modeling the propagation of a flame surface of a premixed fuel-air mixture. As described by Wang, *et al.* [257], the surface is defined as the flame surface of unburnt mixture which can be represented mathematically as $G(x,y,z,t) = 0$. Specifically, assuming combustion occurs in a thin zone, the propagation of the flame front may be tracked in three-dimensions by solving for the “mean and variance of a non-reacting scalar.” [258] A less-rigorous method of producing a similar result may be found by plotting the propagation of a constant-concentration surface for a reaction product species like water vapor. An application of this method found that turbulent eddies had a large effect on the wrinkling of this flame surface in a rectangular channel. This wrinkling effectively increases the flame’s surface area and, thus, the speed of combustion [257]. However, this method is still comparatively new and does not appear to offer a significant improvement over the conventional sub-grid kinetic modeling. Moreover, the flame surface may still be indirectly resolved geometrically by plotting a surface of constant species concentration or temperature. Therefore, although the G-equation method is a novel method, it does not appear to be necessary and will not be used in this effort.

3. Application of Chemical Kinetic Models

With the chemical reaction mechanisms reviewed, it is worthwhile to investigate the applications of some mechanisms and what problems, if any, were encountered. Two studies modeling propane-air microflame stability [142] and a heat recirculation reactor [143] used the one-step reaction mechanism from Westbrook and Dryer [141]. The authors noted that this

approximation understandably failed to describe the formation of partial oxidation products like CO and O₂ and the kinetically controlled ignition temperature. The former issue (from the standpoint of CO production) can be mitigated using the two-step reaction mechanism. The authors recommended that because the flame location may be somewhat inaccurate, their results should represent trends rather than accurate predictions [142]. The latter study added the modeling of heat loss on flame stability that led to a correlation between lower heat loss and greater flame stability. This finding is intuitive considering that the heat lost cannot be used to maintain a stable flame [143] and reiterates the fact that an adiabatic simulation without heat transfer represents an idealization.

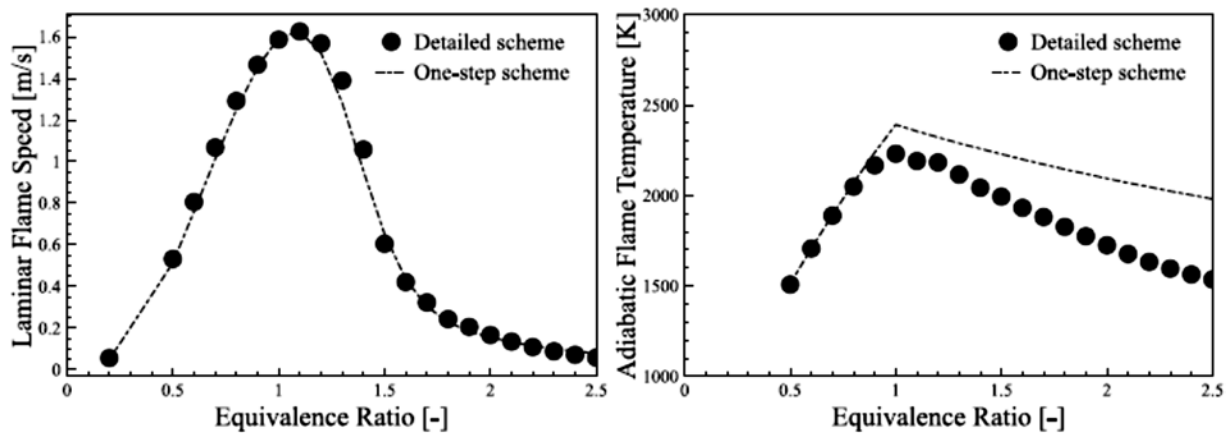


Figure 73: Comparison of Laminar Flame Speed and Adiabatic Flame Temperature Using a One-Step Reaction Mechanism and a Detailed Reaction Mechanism (from [130]) in a Ramjet Combustor [259]

Some computational simulations have also been performed to analyze combustion in an engine configuration similar to the pressure jet architecture. One such study compared numerical methods and LES combustion models for a ramjet engine [259] and a followup work applied the method to multiple flight conditions [260]. This study used a different model referred to as AVBP described only as an academic LES tool that includes a “dynamically thickened flame” to handle subgrid scale interactions of both turbulence and chemistry. The reaction mechanism was a global, one-step, irreversible scheme for the typical path of propane oxidizing to form CO₂ and H₂O.

Among the useful results was a set of comparisons showing the relative accuracy of the one-step AVBP mechanism against a more intensive detailed mechanism. Laminar flame speed matched relatively well at all equivalence ratios while flame temperature showed low error for lean-to-stoichiometric combustion with increasing error in richer combustion. [259, 260]

D. Mechanism Analysis with Zero-Dimensional Simulation

Kinetic mechanisms were compared under carefully controlled conditions using a zero-dimensional simulation program. This program simulates the progression of the chemical kinetics at a single point as opposed to a collection of points or “nodes” in one-, two- or three-dimensional space. This greatly reduces the computational time necessary to evaluate kinetic mechanisms and prevents contamination of data from unintended fluid motion effects like turbulence.

1. Zero-Dimensional Simulation of Chemical Kinetics

The modeling of a chemical reaction starts fundamentally with a change in mass of a reaction species as outlined by Norman [40] and Ye [261]. Depending on whether the species is a reactant (being consumed) or a product (being produced), this time rate of change of mass will be negative or positive respectively. This rate is balanced by the molar production rate, $\dot{\omega}$, of the species by elementary reactions converted by the molecular weight, \mathbf{W} , of each species. The reaction rate of the species is provided by CHEMKIN (a chemical thermodynamics library) that interprets the chemical kinetic mechanism. Because the mass is equal to the product of mixture density, ρ , and volume, \mathbb{V} , the mass rate of change may be rewritten in these terms. Note: Terms in bold indicate arrays, in this case potentially containing a list of many species subject to the kinetic mechanism.

$$\frac{d\mathbf{m}}{dt} = \frac{d(\rho\mathbb{V})}{dt} = \frac{\dot{\omega}\mathbf{W}}{\rho} = \mathbb{V}\dot{\omega}\mathbf{W} \quad (37)$$

Written in terms of species mass fractions, \mathbf{Y} :

$$\frac{d(\rho\mathbf{Y}\mathbb{V})}{dt} = \mathbb{V}\dot{\omega}\mathbf{W} \quad (38)$$

Expanding the time derivative of the mass product on the left, recovers:

$$\rho V \frac{dY}{dt} + VY \frac{d\rho}{dt} + \rho Y \frac{dV}{dt} = V\dot{\omega}W \quad (39)$$

At this point, no simplifications are made – the mass fraction, density, and volume may be time dependent as the chemical reaction proceeds.

This fundamental differential equation can be applied to many different processes. For example, in a closed, constant volume system, the conservation of mass demands the mass rate of change is zero. In terms of density and volume:

$$\frac{dm}{dt} = \frac{d(\rho V)}{dt} = 0 \quad (40)$$

Expanding the mass product on the left side:

$$\rho \frac{dV}{dt} + V \frac{d\rho}{dt} = 0 \quad (41)$$

Since the volume is constant, this reduces to simply:

$$\frac{d\rho}{dt} = 0 \quad (42)$$

This makes sense considering the assumptions made about the system. For a closed system with a constant volume, there can be no change in mass or volume, and thus no change in the mixture density. Meanwhile, conservation of species demands the following relation:

$$\rho V \frac{dY}{dt} = V\dot{\omega}W \quad (43)$$

Solving for the time rate of change of the species mass fraction array, Y :

$$\frac{dY}{dt} = \frac{\dot{\omega}W}{\rho} \quad (44)$$

Conservation of momentum follows a similar definition while including the fluid velocity vector, V , as an array of up to three velocity components, $[u \ v \ w]$:

$$\frac{d(\rho V V)}{dt} = 0 \quad (45)$$

Expanding the time derivative of the momentum product:

$$\frac{d(\rho V V)}{dt} = \rho V \frac{dV}{dt} + V V \frac{d\rho}{dt} + \rho V \frac{dV}{dt} = 0 \quad (46)$$

For a zero-dimensional simulation, the velocity components must all be constant – there is no direction for it to change, so:

$$\frac{dV}{dt} = 0 \quad (47)$$

The first law of thermodynamics in time rate form is:

$$\frac{d(\rho E V)}{dt} = 0 \quad (48)$$

which simplifies to:

$$\frac{d(\rho e V)}{dt} = 0 \quad (49)$$

because velocity is constant per Eq. (47). As a result, kinetic energy must be constant and so its time rate of change may be neglected simplifying the system energy term E to e . Expanding the time derivative:

$$\rho V \frac{de}{dt} + V e \frac{d\rho}{dt} + \rho e \frac{dV}{dt} = 0 \quad (50)$$

Applying the conservation of mass and constant volume assumptions means the internal energy must be constant. That is, the time rate of change must be zero:

$$\frac{de}{dt} = 0 \quad (51)$$

For an ideal mixture of gases, the internal energy of the mixture is:

$$e = \sum_{j=1}^N Y_j e_j \quad (52)$$

where Y_j is the mass fraction and e_j is the internal energy of species j . Applying the time derivative of this sum for application to the first law:

$$\frac{de}{dt} = \sum_{j=1}^N Y_j \frac{de_j}{dt} + \sum_{j=1}^N \frac{dY_j}{dt} e_j = 0 \quad (53)$$

Assuming the mixture gases are calorically perfect, then the internal energy is a function of the constant volume specific heat of each species, $c_{v,j}$, and the temperature, T , and so Eq. (53) expands to:

$$\sum_{j=1}^N Y_j c_{v,j} \frac{dT}{dt} + \sum_{j=1}^N \frac{dY_j}{dt} e_j = 0 \quad (54)$$

which can be rewritten in the following form:

$$c_v \frac{dT}{dt} = - \sum_{j=1}^N \frac{dY_j}{dt} e_j \quad (55)$$

Applying the conservation of species derived in Eq. (44), this becomes:

$$c_v \frac{dT}{dt} = - \sum_{j=1}^N \frac{e_j \omega_j W_j}{\rho} \quad (56)$$

The familiar ideal gas law, $p = \rho RT$, can be written in a rate form useful in this scenario:

$$\frac{dp}{dt} = \rho R \frac{dT}{dt} + \rho T \frac{dR}{dt} + RT \frac{d\rho}{dt} \quad (57)$$

which simplifies for the constant density condition resulting from the law of conservation of mass, Eq. (42):

$$\frac{dp}{dt} = \rho R \frac{dT}{dt} + \rho T \frac{dR}{dt} \quad (58)$$

Next, the change in the gas constant, R , must be determined using the universal gas constant, \bar{R} , and the molecular weight of the mixture, W_{mix} :

$$\frac{dR}{dt} = \frac{d}{dt} \left(\frac{\bar{R}}{W_{mix}} \right) = - \frac{\bar{R}}{W_{mix}^2} \frac{dW_{mix}}{dt} \quad (59)$$

The change in the mixture's molecular weight is similarly derived based on the mixture sum of the species' molecular weights W_j , and mole fractions, X_j :

$$\frac{dW_{mix}}{dt} = \frac{d}{dt} \left(\sum_{j=1}^N X_j W_j \right) = \sum_{j=1}^N \frac{dX_j}{dt} W_j \quad (60)$$

The mole fraction of each species can be related to the mass fraction of each species with the following equation using a second summation through the species, denoted by the counter, i :

$$X_j = \frac{\frac{Y_j}{W_j}}{\sum_{i=1}^N \frac{Y_i}{W_i}} \quad (61)$$

Differentiating this relation produces an expression for the rate of change of an individual species' mole fraction, X_j , as a function of the rates of the species' mass fractions Y_i and Y_j :

$$\frac{dX_j}{dt} = \frac{\frac{1}{W_j} \frac{dY_j}{dt} \sum_{i=1}^N \frac{Y_i}{W_i} - \frac{Y_j}{W_j} \sum_{i=1}^N \frac{1}{W_i} \frac{dY_i}{dt}}{\left(\sum_{i=1}^N \frac{Y_i}{W_i} \right)^2} \quad (62)$$

With regard to heat release, application of the principle of conservation of energy produces the following:

$$c_v \frac{dT}{dt} = - \sum_{j=1}^N \frac{e_j \omega_j W_j}{\rho} - \frac{h A_s}{\rho V} (T - T_{wall}) - \frac{\varepsilon \sigma A_s}{\rho V} (T^4 - T_{wall}^4) \quad (63)$$

where e is the species internal energy, h is a calibrated convective heat transfer coefficient, and ε is a calibrated emissivity (assuming the reaction products have a significant emissivity). T_{wall} is the temperature of the initial air mixture (assumed to also be the temperature of the reactor wall), and A_s is the surface area of the constant volume reactor. This heat release approximation including convective heat transfer coefficients in 0-D has been used prior for kinetic studies by Norman [40] and Ye [261].

To use this simulation to compare mechanisms under the same conditions, it must first be calibrated with experimental data like that published by Werle in 2010 [35]. Werle's data was chosen for this effort in part because of its consistency in tests between his model calibration effort

for methane oxidation and predictions. In that study's reactor, fuels beginning at room temperature were injected into a chamber already containing an oxidizer. Hence, the initial temperature of the mixture must account for this mixing process:

$$(m_a + m_f)e_2 - m_a e_1 = m_f h_e \quad (64)$$

where m_a and m_f are the air and fuel masses, respectively, h_e is the enthalpy of the incoming fuel (at room temperature, 300 K), e_1 is the internal energy of the air at the reaction chamber indicated temperature. An iterative routine was used to calculate the temperature of the mixture at state 2 which resulted in the internal energy, e_2 , balancing the equation.

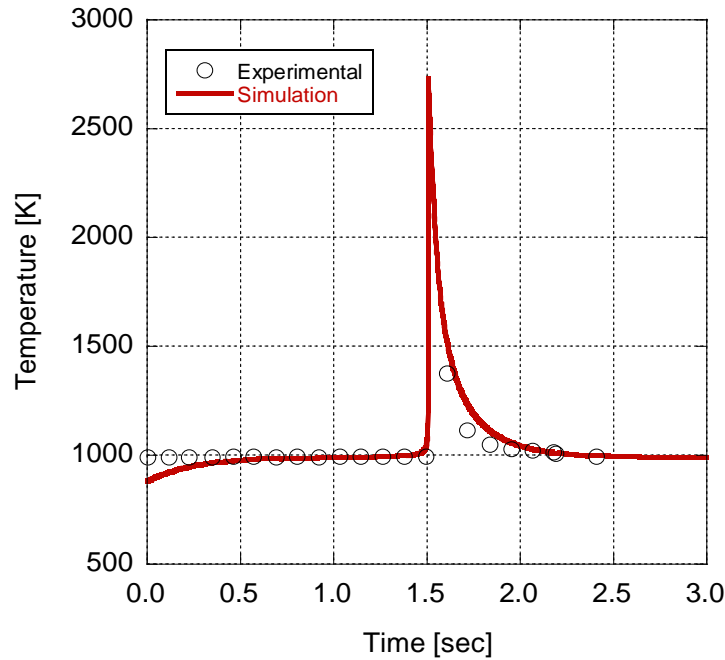


Figure 74: Calibration of Convective and Radiative Heat Transfer Coefficients to Methane (CH₄) Ignition Delay Data (from Werle [35]) at an Equivalence Ratio, $\phi = 0.91$, Oxidizer Temperature of 989 K

At this point the model is complete but the heat transfer parameters need to be calibrated. The GRI Mech 3.0 was used with this zero-dimensional numerical model to perform the calibration for methane (CH₄) oxidation since this mechanism is, effectively, an industry standard. Assuming the same experimental setup is used for gathering both methane and propane (C₃H₈) data (as was

the case for Werle's data [35, 262] in a constant volume bomb reactor), then these parameters may be calibrated with the methane data and used to test many different mechanisms for propane oxidation. Adjustment of the convective heat transfer and emissivity coefficients eventually produced a time-history of temperature that matched the data published by Werle and shown in Figure 74. It should be noted that the simulated temperature peak (a result of initial transient heating occurring on a 1 ms timescale) may not have been captured in the experimental data due to the low frequency of temperature data collection.

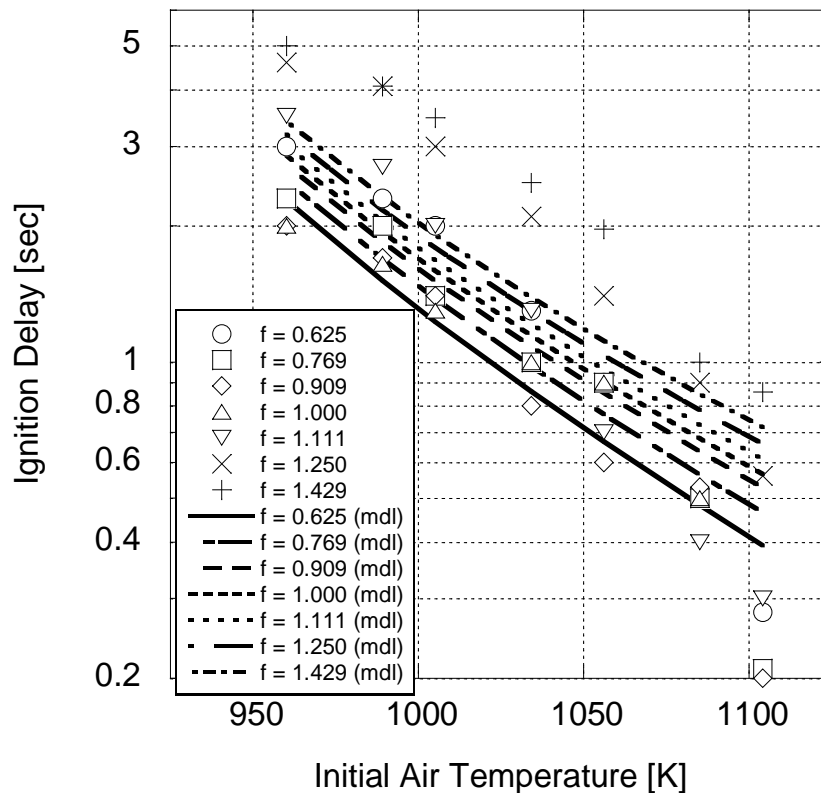


Figure 75: Validation of the Zero-Dimensional Model for CH₄ Ignition Delay using Estimated Heat Transfer Coefficients at a Range of Initial Air Temperatures and Equivalence Ratios, f. Experimental Data from Werle [35] Shown as Points, Model Results Shown as Lines.

Radiative transfer was included assuming at the high temperatures following combustion, the gas would radiate some energy, particularly during the cooldown phase after ignition. Doing so resulted in a better match to the available experimental data. This method was repeated for the

remaining methane equivalence ratios. This set of calibrated coefficients were then effectively averaged using a MATLAB optimization scheme tasked with minimizing the least-squares difference between the experimental ignition delay and that predicted by the corresponding simulation. The resulting averaged coefficients were $h = 2.510 \text{ W/m}^2 \text{ K}$ and $\varepsilon = 0.0644$ and application to the range of temperatures and mixtures published by Werle showed good matching (see Figure 75)

2. Mechanisms in Comparison via Zero-Dimensional Simulations

So far, three levels of chemical kinetic mechanisms were discussed: detailed mechanisms (the most complete list of reactions and rate constants), reduced mechanisms (removing the least significant reactions from detailed mechanisms), and global mechanisms (modeling an overall chemical process). The majority of the available mechanisms are detailed, requiring in depth research of intermediate reaction effects. Because the final goal of all these mechanisms is to estimate reaction rates (essentially, how quickly fuel and air are consumed and products are formed), they may all be compared on equal terms and their relative errors compared to the same set of experimental data.

The most readily-available mechanisms (a total of 17 including calibrated and reduced versions) were simulated using the zero-dimensional model and compared in the context of the same dataset used for calibration (published by Werle [35]). Three equivalence ratios were used to check ignition delays of lean, stoichiometric, and rich propane oxidation for a range of temperatures. These mechanisms include the full San Diego 2005 Mechanism (denoted SD) [152], the 1984 Westbrook and Dryer mechanism (W84) [71], the 1981 one- and two-step Westbrook mechanisms (W81(1) and W81(2), respectively) [141], the 2000 Qin mechanism (Q00) [150], the 1999 Davis mechanism (D99) [148], the 1998 Sung mechanism (S98) [70], the 2007 Peterson

mechanism (P07) [155], a 2008 version of the Healy mechanism (H08) [159], the Aramco mechanism, published by Metcalfe (A13), the 2007 USC mechanism (USC07) [156], the Le Cong mechanism (Le08) [158], the Marinov mechanism (Ma97) [147], and the Andreis reduced mechanism (An12) [162].

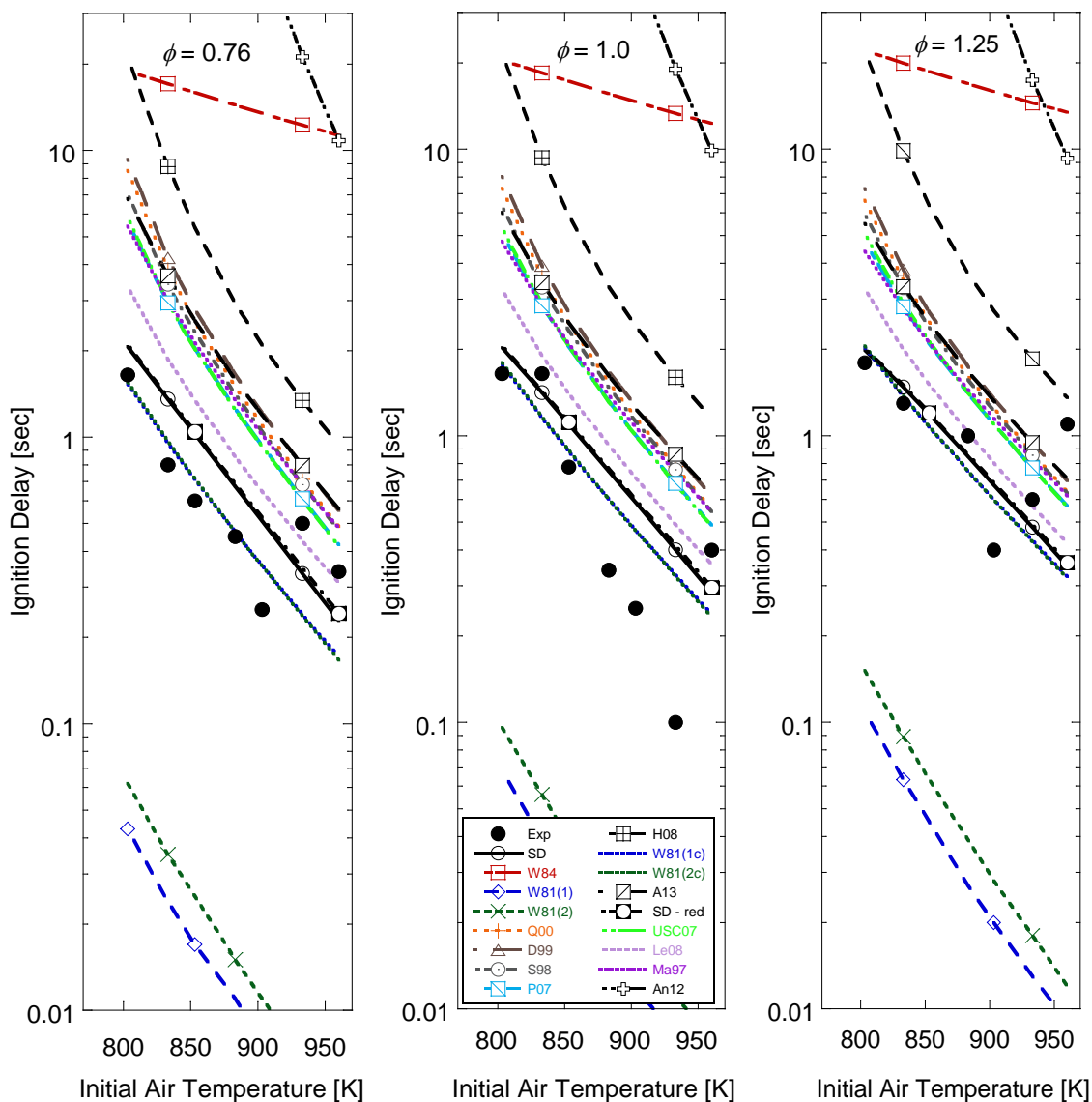


Figure 76: Comparison of Zero-Dimensional Simulations of Many Kinetic Mechanisms with Constant Volume Reactor Experimental Data from Werle [35, 262] for a Range of Equivalence Ratios and Initial Air Temperatures.

The comparison also included a reduced form of the full San Diego detailed mechanism (SD-red) that was formed by removing all the reactions not affecting the ignition delay at the 1 ms level.

This cut the mechanism down from 244 to 107 reactions and significantly decreased runtime. This sensitivity study followed a similar method as that for ozone described by Depcik, *et al.* [263]. Lastly, it also included a version of the 1981 one- and two-step Westbrook and Dryer mechanisms (WD(1c) and WD(2c), respectively) calibrated to Werle's propane ignition delay data [35] using the method outlined in Westbrook and Dryer's 1981 study [141]. This involved adjustment of the activation energies, pre-exponentials, and concentration exponents.

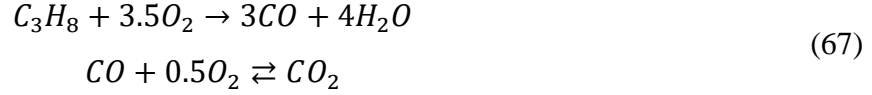
The comparison of these mechanisms is shown in Figure 76. It is immediately clear that although the general trend of increasing temperature and decreasing ignition delay is the same, there is a wide range of results. The most accurate across the range of equivalence ratios and temperatures were the full and reduced San Diego mechanisms and the calibrated one- and two-step Westbrook and Dryer mechanisms. The 1984 Westbrook and Dryer detailed mechanism showed excessive error both in slope and ignition delay. The 2012 Andreis mechanism was also significant in error predicting ignition delays as much as two orders of magnitude longer than the majority of mechanisms and the data. Most mechanisms were within an order of magnitude of the data and each other with the San Diego and calibrated Westbrook and Dryer mechanisms being most consistently within the experimental data scatter.

It is also worth noting that the 1981 one- and two-step mechanisms published by Westbrook and Dryer were initially significantly in error (more than an order of magnitude) as well. It was only with the aforementioned calibration that the mechanism was brought more in line with the experimental data. The resulting calibrated one-step Westbrook and Dryer mechanism is:



$$k_1 = 1.3497 \times 10^{10} e^{(-30/R_u \cdot T)} \cdot [C_3H_8]^{0.1000} \cdot [O_2]^{1.6474} \quad (66)$$

Similarly, the calibrated two-step Westbrook and Dryer mechanism is:



$$\begin{aligned}
k_1 &= 2.1548 \times 10^{10} e^{(-30/R_u \cdot T)} \cdot [C_3H_8]^{0.1} \cdot [O_2]^{1.65} \\
k_2 &= 10^{14.6} e^{(-40/R_u \cdot T)} \cdot [CO]^1 \cdot [H_2O]^{0.5} \cdot [O_2]^{0.25} \\
k_{-2} &= 5 \times 10^8 e^{(-40/R_u \cdot T)} \cdot [CO_2]^1
\end{aligned}
\tag{68}$$

The full detailed and reduced San Diego mechanisms [152] are also in a form easily accommodated by most available programs using CHEMKIN or related formats. They are also the more technically complete methods of modeling propane oxidation consisting of a large selection of intermediate reactions while still undergoing constant revision and updating. They will, however, demand the greatest computational time as every included reaction is another equation that must be solved to convergence at every reacting cell at every time step. The attractive alternative is to rely on a much simpler mechanism relying on just one or two reactions (like those provided by Westbrook and Dryer [141]) to reduce computational time.

The ignition delay comparison suggests first that the full San Diego mechanism [152] best matches the experimental data presented by Werle [35, 262]. This agrees with a similar finding by Benezech on premixed hydrocarbon flame speeds [253]. It further suggests that reducing the full detailed San Diego mechanism [152] had minimal effect on its error despite cutting more than half the reactions out – the full and reduced mechanisms are practically overlapped in terms of ignition delays. The comparison also suggests that while the use of a global mechanism will incur a nonzero increment in error, it is still within the scatter of the available experimental data. For these reasons, the full and reduced San Diego mechanisms, as well as the global one-step mechanism will be carried forward into the Computational Fluid Dynamics (CFD) simulations as the most promising prospects for modeling propane combustion.

IV. CFD Modeling With CONVERGE

A. Typical Model Parameters

Like most Computational Fluid Dynamics (CFD) packages, CONVERGE has a large array of model parameters that may be adjusted as the user deems necessary. The majority of these parameters have recommended defaults and are typically left at those settings. What follows is a discussion of the typical parameters that are either intrinsically important to the simulations in this research effort or were modified from their defaults.

1. Boundary and Initial Conditions

All transient partial differential equations require a series of conditions defining their value on the geometric boundaries at the beginning of the simulation. Without these conditions, a unique solution cannot be determined. Several types of boundary conditions are available in CONVERGE. Those used in this effort include wall, inflow, outflow, and symmetry boundaries.

The default wall boundary condition includes several subconditions. The velocity wall condition defaults to a “Law of Wall” definition that uses a logarithmic curve fit method to calculate the velocity at the wall through a boundary layer even when boundary layer fineness is low [28]. The temperature wall condition includes several options in addition to the default “Law of Wall.” These options are the specified value (Dirichelet condition) simply prescribing a constant temperature, zero normal gradient (Neumann condition) defining zero heat transfer between the wall and fluid, a convective boundary allowing definition of a convective heat transfer, and a general heat flux boundary using a constant heat flux value [28]. Wall roughness and turbulence parameters may also be set, however, in this research effort they were kept at their default settings.

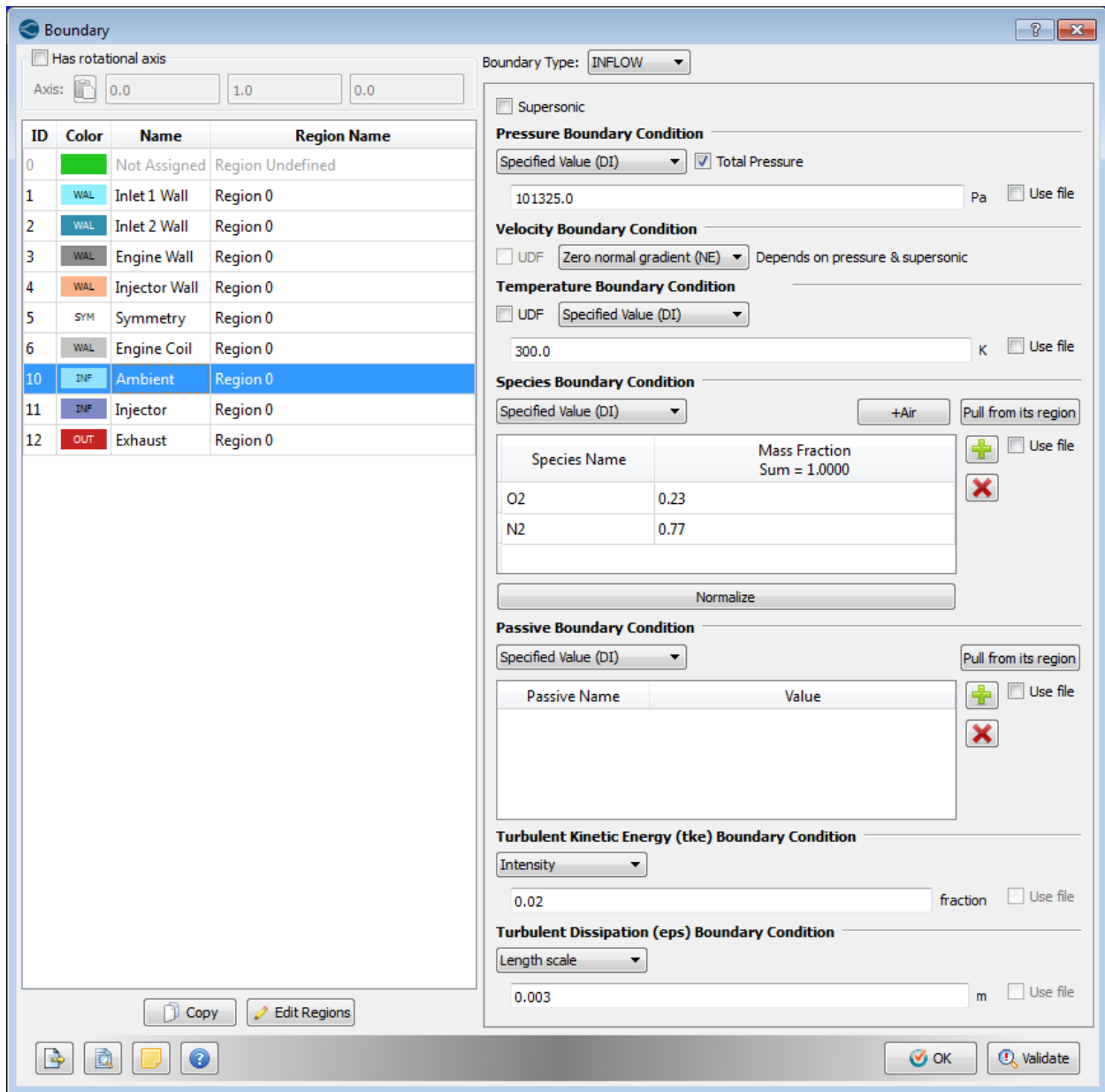


Figure 77: A Typical Inflow Boundary Condition Using Air at a Pressure of 1 atm, No Prescribed Velocity, and a Temperature of 300 K. Turbulent Kinetic Energy (TKE) and Turbulent Dissipation (ϵ) Are Shown at Default Settings. CONVERGE Studio Software

The default inflow boundary condition also includes many subconditions (shown in Figure 77) allowing definition of pressure, velocity, temperature, and species. The pressure inflow condition was typically set at a specified value (Dirichelet condition) but a zero normal gradient condition is also available. Fixing a specified pressure automatically sets the velocity boundary to be a zero normal gradient (Neumann condition). Hence, a boundary with a known pressure does

not have a prescribed constant boundary velocity and vice versa. The temperature inflow condition is also typically prescribed though a zero normal gradient option is also available. The species inflow boundary was defined by prescribing the known species mass fractions at the boundary, the sum of which must equal one. The default outflow boundary condition is much like the default inflow condition. Pressure and velocity may be specified or defined by a zero normal gradient. Temperatures and species at an outflow condition are, however, defined by backflow conditions. In a nominally-operating outflow, boundary flow is leaving the domain. In some cases the working fluid may temporarily flow *into* the domain from an outflow boundary. Should this occur, CONVERGE needs temperature and species values to model the inflow.

Lastly, the symmetry boundary condition may reduce computational runtime by exploiting surfaces of symmetry. In the case of a cylindrical pipe for instance, it may be useful to cut the pipe in halves, quarters, or some smaller radial fraction under the assumption that the flow will be radially symmetrical through the pipe. For a circular cross-section that should be a reasonable assumption. The symmetry conditions sets a slip velocity boundary (the fluid at the boundary may have a nonzero velocity) and all other conditions are given a zero normal gradient condition. Initial conditions are considered by defining the initial conditions of the domain's enclosed region. Here the user specifies the initial velocity, temperature, pressure, species, and turbulence.

2. Turbulence Model CFD Parameters

Selection of a turbulence model was done via the Converge Studio interface by first allowing selection of a base turbulence model between Reynolds Averaged Navier Stokes (RANS) or a Large Eddy Simulation (LES). A review of the literature in modeling combustion in general (discussed earlier in Chapter III Section C-2) suggested a LES turbulence model would be more accurate.

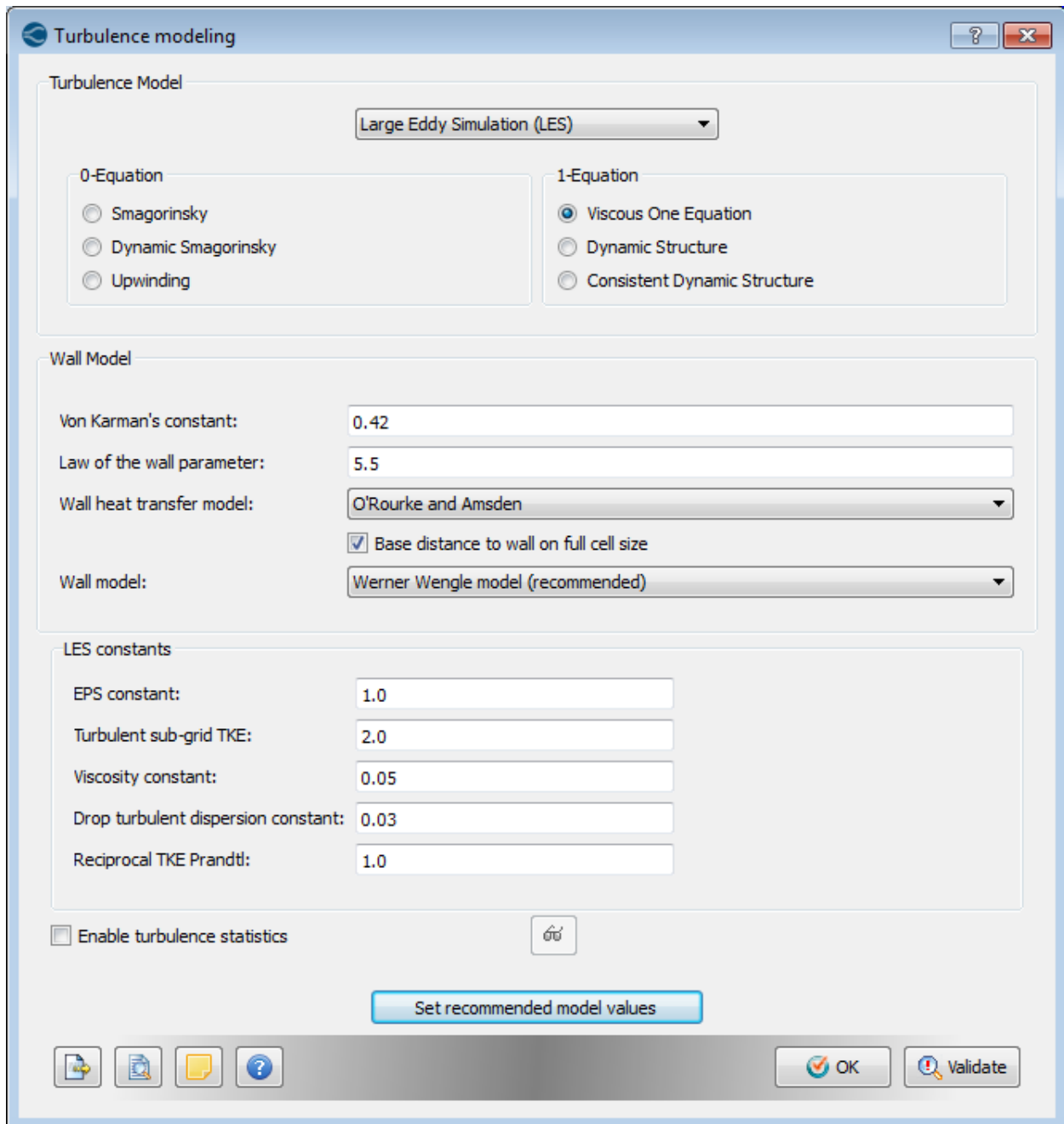


Figure 78: Converge Studio's Turbulence Modeling Interface Showing Recommended Default Constant Values for the Viscous One Equation LES Model

The default Viscous One Equation LES model was chosen in absence of a clear advantage to the alternatives. Recall that the Viscous One Equation Model uses the additional transport equation for a sub-grid turbulent kinetic energy (TKE) to model the stress tensor and thus the local turbulent viscosity and local stress tensor:

$$\tau_{ij} = -2\nu_t \overline{S_{ij}} + \frac{2}{3}k\delta_{ij} \quad \text{and} \quad \nu_t = C_k k^{0.5} \Delta$$

$$\text{where} \quad k = \frac{1}{2}(\overline{u_i u_i} - \overline{u_i} \overline{u_i}) \quad (69)$$

with a tuning constant, C_k . In this model, the sub-grid dissipation is similarly tunable [28]:

$$\varepsilon = C_\varepsilon \frac{k^{1.5}}{\Delta} \quad (70)$$

This involves defining several constants that were left at the default values recommended by the Converge Studio software (shown in Figure 78).

3. Combustion Model CFD Parameters

The CONVERGE package offers several combustion modeling options that have advantages for different types of simulations as discussed in the Converge Theory Manual [28]. The SAGE detailed chemistry was recommended as it is the ‘general’ combustion model typically used with detailed kinetic mechanisms (like those discussed in detail in Chapter III). This involves setting several constants including the minimum cell temperature (defaulting to 600 K) and the minimum fuel species mole fraction (defaulting to 1×10^{-8}) below which the chemical mechanism is not active. The package also includes NO_x and soot emissions modeling options but these were not employed because NO_x and soot emissions were not expected to significantly affect the heat release, pressure, and flow parameters. Future work can include comparing the emissions generated with this engine versus comparable sized pulsejets and ramjets.

4. Adaptive Mesh Refinement (AMR)

For the majority of their existence, CFD solvers have used static meshes. In other words, as a transient CFD simulation proceeds in time, the mesh fineness and, therefore, the resolution and gridsize was constant. For many applications, this can be sufficient. Meshes are designed to be finest (have the smallest grid sizes) typically near walls, obstacles, and regions of general

importance. Incorporating a fine mesh at walls is related to the importance of wall boundary layers, as well as their influence on the formation of flow structures like turbulent eddies. In flows with significant variation in these flow structures or movement of a region of interest, a static mesh requires a large area to be meshed finely with much of this area being unnecessary until the flow structure of interest passes through it. A good example is the classic Karman vortex street. In a static mesh, the entire path width of the vortex street must have a fine mesh whether there is a vortex there or not. This has a significant effect on computational cost.

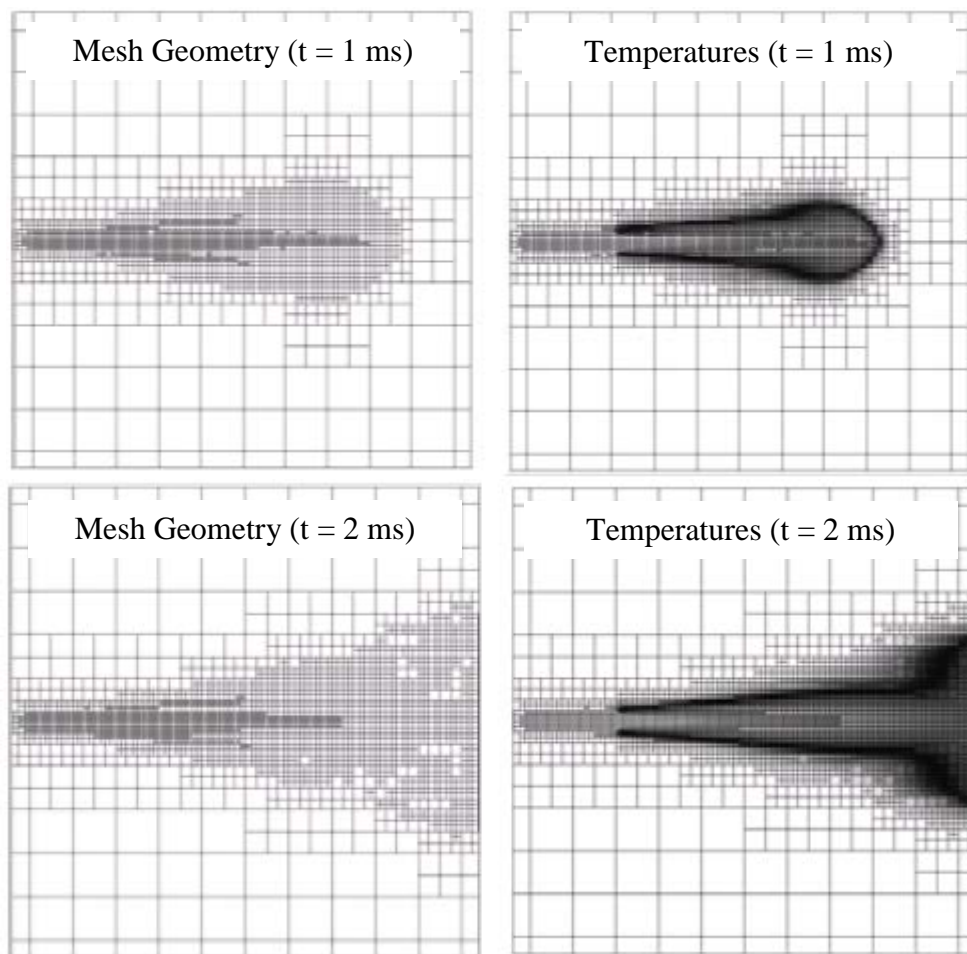


Figure 79: An Example of Adaptive Mesh Refinement Applied to a High Pressure Burning Spray in an Ambient Temperature of 1000 K. The Temperature Range (Represented in Grayscale) Shows a Maximum Temperature (in Black) of Approximately 2800 K. Referenced From CONVERGE 2.2.0 Theory Manual [28]

An alternative to the static mesh is one which is adaptive. An adaptive mesh polls a local point property of the flow (such as velocity, temperature, species concentration, etc...) and compares it with the cells around it. If the difference is large enough (greater than some value configurable by the user), then the cell is considered to be “under-resolved” [28] and this cell is subdivided into equal smaller cells. In CONVERGE, all cells are three-dimensional cubes; hence, equal halving of one cube results in eight (2^3) smaller cubes taking its place. It should be noted that if a cell is against a boundary, the boundary surface cuts into the cube. In other words, the default shape of a cell is a cube, but may take other smaller shapes as bounded cells are ‘sliced’ by the model geometry.

The primary advantage to this approach is to minimize the number of cells needed to simulate the phenomenon of interest. In the case of a Karman vortex street, elements need only form with significant fineness around the vortices as they propagate downstream of their source. The mesh does not propagate, but as a vortex moves downstream so too does the gradient necessitating subdivision of the grid. In short, adaptive mesh refinement (AMR) creates mesh fineness only when needed and can remove it when it becomes unnecessary. That second point highlights another important advantage of the AMR scheme – for simulations with limited available memory (and mesh size), cells that are no longer needed in one area can be recovered for use in another area. This allows the user to limit the simulation to a maximum number of cells while allowing the scheme to subdivide cells as necessary. In three-dimensional simulations, it is relatively easy to build a simulation that exceeds the memory available by simply demanding too much mesh fineness. Limiting the number of cells can prevent that from occurring.

It should be noted that the advantage of AMR is to speed up a CFD simulation by means of reducing the total number of cells that must be solved to convergence before moving to the next

timestep and repeating the process. Using AMR can reduce the number of cells in a simulation suggesting that more fineness could be added to increase local resolution while maintaining the same number of total cells and amount of system memory needed to run it. The reader should be cautioned however, that this strategy may actually *increase* simulation runtime if the new minimum grid size is smaller than the previous minimum grid size. This is a direct result of the Courant-Friedrichs-Lewy (CFL) Condition (shown earlier as Equation (13)) for convergence. The CONVERGE software uses the local flow speed and grid size to determine the maximum time step that will still converge. Therefore, assuming the flow speed is greatest in the region of minimum grid size and remains unchanged between the old and new models, the time step will be directly related to the minimum grid size. Hence, while it may be attractive to use these extra cells to further refine an area where the flow is at its fastest, doing so is likely to decrease the time step requiring more overall time steps to complete the simulation and may require more computational time despite using the same maximum number of cells. In practice this may only be an issue for high-speed injectors where fineness of the CFD mesh and high speed are colocated but not for adding fineness around walls where speeds are low.

B. Modeling of Nonreactive Mixing Flow

Prior to starting on the full engine simulation, it was necessary to build proficiency in the CONVERGE software. To do so, a series of simulations were built of a mixing box supplying air to a single-cylinder engine in the KU Sustainable Fuel and Transportation Laboratories Engine Test Cell. The mixing box takes in a controlled amount of engine exhaust gases and mixes them with fresh air supplied by a filtered chamber via a long duct to damp pressure vibrations to the engine. The method of using exhaust gas mixed with intake air is referred to as Exhaust Gas Recirculation (EGR) and is primarily used to control the emissions output of internal combustion engines. The simulations supported this research effort by testing species mixing in a three-dimensional CFD simulation and comparing the simulations' results with experimental data gathered in the engine test cell to gauge its accuracy and utility in doing so for a more complex set of conditions like the pressure jet engine. These simulations involved no chemical kinetics – all gases were considered chemically inert.

1. Exhaust Gas Recirculation (EGR)

With the current dependency on fossil fuel sources and transportation's influence on greenhouse gas emissions, there is an industry push towards higher internal combustion engine efficiencies. At the same time, modern spark ignition (SI) and compression ignition (CI) internal combustion engines must conform to emissions regulations that require the reduction of emissions of undesired species like carbon monoxide (CO), various hydrocarbons (HC), and nitrogen oxides (NO_x). Overall, lean combustion (excess O₂) is desirable to achieve greater thermal efficiencies because it takes advantage of a larger ratio of specific heats during the expansion process. Moreover, oxidation catalysts downstream of the engine work effectively in a lean environment to mitigate HC and CO emissions. However, a lean environment provides the right conditions for

NO_x species formation (i.e., relatively high temperatures and excess oxygen). Once NO_x is formed, a complex aftertreatment system is necessary to convert it back to benign species [264]. Hence, while other emissions can be readily converted catalytically while striving for improved fuel economy, it is more economical to prevent NO_x formation than to catalyze it afterward. As a result, in-cylinder NO_x control becomes a requirement of the engine calibrator.

The primary method of mitigating NO_x emissions is to reduce the temperature of combustion while maintaining a lean mixture with Exhaust Gas Recirculation (EGR). This process redirects a portion of the engine exhaust from the main exhaust stream to mix with the intake air and enter the cylinder in later intake cycles. A significant component of EGR is steam (H₂O), which serves to increase the heat capacity of the mixture during combustion. While this reduces engine power, it has proven effective at reducing NO_x emissions while maintaining thermal efficiency and brake specific fuel consumption (BSFC). These effects have been widely studied experimentally [265-268] and modeled [269-271].

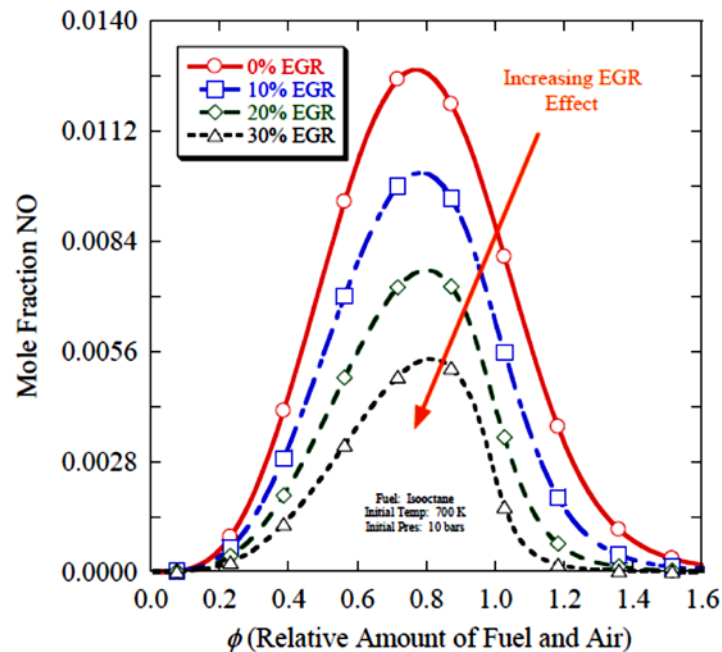


Figure 80: Trend of Exhaust Gas Recirculation (EGR) and Equivalence Ratio, ϕ , on Production of NO in Ideal Isooctane Combustion (Initial Temperature of 700 K and Initial Pressure of 9.87 atm) [34]

While the use of EGR has some simple global effects on the combustion process, an analysis that is more detailed is required to study the effects of mixing uniformity. For instance, it is known that if the distribution of EGR in the engine cylinder is poor, its capability to limit the production of NO_x is significantly reduced [272]. Moreover, to efficiently implement EGR in an engine design, the EGR/air charge must be both well-mixed and uniform from cylinder-to-cylinder [273]. If it is not, one or more cylinders could operate at a suboptimal EGR level resulting in lost power or high NO_x emissions at the same engine condition (speed, load, air flow, etc.).

The control of EGR mixing is also essential in the operation of new engine designs relying on homogeneous charge compression ignition (HCCI). This relies on both uniformity of the air/fuel charge and precise control of low temperature combustion using EGR [274-276]. Furthermore, the combustion characteristics of an HCCI engine are highly dependent on the supply methods of the EGR gas [277, 278], which suggest the need for computational fluid dynamics (CFD) analysis of the inlet air and EGR mixing process.

With respect to simulating the mixing process, a three-dimensional (3-D) CFD analysis is necessary for several reasons. Not only is the development of turbulence due to the mixing flow important to in-cylinder combustion characteristics (heat release rate, combustion efficiency, emissions formation, etc.) [279], but these effects are significantly 3-D in nature and may not be easily or accurately reduced to a two-dimensional (2-D) simulation. This is further exacerbated by the 3-D geometry of a typical mixing box. The presence of inlets, outflows, and sensor protrusions must be simulated in their precise 3-D locations and dimensions. These protrusions are likely to shed 3-D flow structures that will affect the flow turbulence that may not be otherwise captured by a 2-D analysis.

However, the use of a 3-D simulation significantly increases the computational time for the same level of mesh fineness. In recent years, a new technique has been employed to reduce computational time while preserving an adequate mesh size – Adaptive Mesh Refinement (AMR). Recall, this method checks local fluid conditions (velocity, temperature, etc.) and compares the condition with surrounding cells. If the difference between cells is greater than a user-defined value, the cell is subdivided. The advantage of this method is that the mesh is free to change as the simulation proceeds and this keeps the simulation detail only as fine as is immediately necessary. This is known to significantly reduce computational time [280] and more readily enables 3-D simulations of fluid flows.

Based on this understanding, this report investigates the EGR mixing process as it applies to a single cylinder engine test cell with a cooled-EGR system. The EGR is cooled with an oil cooler and two Direct Current (DC) fans. Mixing is achieved by using a small rectangular box in which clean air and engine exhaust are mixed prior to engine intake. The test data used in the current study was obtained during the completion and validation of a prior student's masters thesis. The data collected from the tests agreed with literature; thus, showing that the system is suitable for testing the engine with cooled EGR. To model the mixing quality of the test cell's EGR/air mixing box, a 3-D CFD model employing AMR was used. The results of the CFD model at full load and no load are compared with the test cell data to infer possible improvements to the test cell design and validate the setup.

2. Single-Cylinder Engine Stand and EGR Mixing Box

The engine utilized in testing is a single-cylinder, compression ignition, naturally aspirated Yanmar L100V [281]. This engine was originally part of an engine-generator package that has been converted for engine testing. It is capable of producing a maximum torque of 21 N-m at 2800

rpm. The shaft of the engine is coupled to a Dyne Systems Dymond Series 12 Alternating Current dynamometer, which is capable of providing 21.1 ft-lbs of torque and 12 hp at a maximum speed of 7,500 rpm. Between the dynamometer and engine is a Futek torque transducer (model #TRS-605), which can measure up to 200 N-m with an error of $\pm 0.2\%$ at full load.

In addition to the torque transducer, various sensors are installed in the test cell, intake, and exhaust to monitor pressure, temperature, and relative humidity. The room pressure is measured with an Omega barometric pressure sensor (model #EWS-BP-A) and the temperature and humidity are measured using an Omega sensor (model #EWS-RH). The volumetric flow-rate of the intake air is measured with a combination of a Meriam laminar flow element (model #50MW20-2) and an Omega differential pressure transducer (model #PX277-30D5V). The pressure in the EGR/air mixing box, immediately before the intake valve, and in the exhaust is measured with Omega pressure transducers (model #PX329) while the temperatures at these locations are found with Omega type-K thermocouples (model #KQXL). The temperature of the EGR is measured immediately before entering the mixing box with another type-K thermocouple.

The pressure inside the cylinder is measured using a Kistler pressure transducer (model #6052C). The pressure signal is associated with the crank angle of the engine through a combination of a Kistler encoder (model #2614B1), signal converter (model #2614B2), and pulse multiplier (model #2614B4).

All mentioned sensors are read and monitored by National Instruments (NI) hardware. The low-speed environmental sensors, along with the torque transducer are measured by a NI compact re-configurable Input/Output (cRIO) controller (model #cRIO-9104) with an eight-slot chassis (model #cRIO-9114). Various modules are used to measure the appropriate signals. The in-

cylinder pressure data and crank angle is monitored by a dedicated rack-mounted computer with a NI PCIe-7841R Field-Programmable Gate Array (FPGA) card.

Emissions data is obtained with a Vetronix five gas analyzer (model #PXA-1100). This analyzer can measure HC, CO, carbon dioxide (CO₂), diatomic oxygen (O₂), and NO_x. To record the data from the Vetronix, a laptop with TechView software installed is used. The particulate matter is collected with an AVL Smoke Meter (model #415S).

To calculate the amount of EGR in the intake, two CO₂ Meter CO₂ sensors (model #ICB-33) are used. One is located in the exhaust, the other is in the intake of the engine, downstream of the mixing box. The amount of EGR can be found by dividing the CO₂ measurement in the intake by the exhaust measurement. The CO₂ sensors are monitored by a laptop with DAS100, a proprietary program developed by CO₂ Meter, the manufacturer of the sensors.

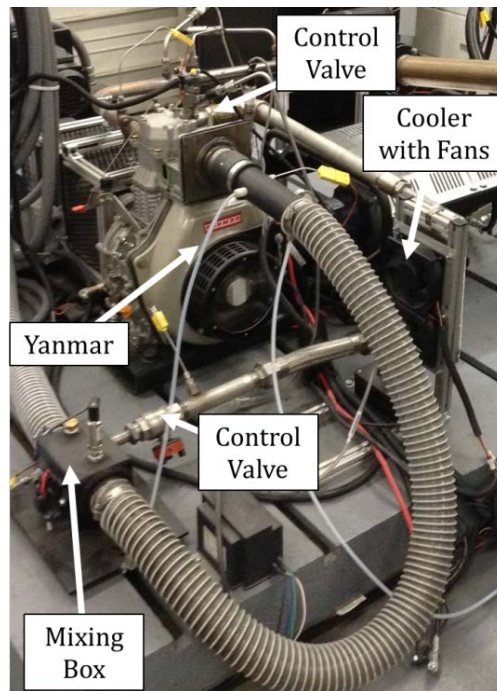


Figure 81: Set-up of the EGR and Mixing Box of the Single-Cylinder Engine Test Cell. The Mixing Box for EGR is Located in the Lower Left Corner.

The EGR enters the mixing box upstream of the engine intake through a system consisting of a control valve, piping, oil cooler, and fans as shown in Figure 1. The EGR enters the system

from the main exhaust near the exhaust valve on the engine, where the EGR is hottest. As the EGR flows from the engine to the mixing box, it enters an oil cooler (NSN #2930-01-156-8665), which sits in front of two 12 VDC computer case cooling fans. These fans cool the EGR to a temperature closer to that of ambient.

To increase the amount of EGR that enters the intake beyond 10%, the pressure differential between the intake and the exhaust needed to be increased. In order to do so, a valve is located upstream of the mixing box in the intake stream. By closing the valve slightly, the pressure in the intake and the mixing box decreases due to the throttling, which increases the pressure differential between the mixing box and exhaust. This increases the amount of EGR that enters the intake to approximately 25% for all loads

Four EGR rates were evaluated in the engine test with full load sweeps. This includes the EGR rates of 0%, 10%, 20%, and 25% at the loads of 0%, 25%, 50%, 75%, and 100% (corresponding to 0.5 N-m, 4.5 N-m, 9.0 N-m, 13.5 N-m, and 16.75 N-m on the Yanmar at 3,600 rpm). After a change in the operation of the engine, such as changing the EGR rate or the loading on the engine, the engine was allowed to come to steady state by observing the downstream temperature and the intake CO₂ measurement. When both of these items changed by less than 1% over a minute, the engine was considered to be at steady state.

Upon reaching steady state, emission data was collected for five minutes at one Hz. Engine performance data, such as temperatures and pressures, was collected for two minutes at ten Hz. The in-cylinder pressure data was measured over 60 consecutive thermodynamic cycles, and the measurements were averaged to provide the pressure traces.

The results of the cooled EGR tests that are indicated here matched that of literature. This includes a reduction in NO_x emission levels as the rate of EGR increases. Moreover, the increase

in mixing by adding EGR led to higher turbulence within the cylinder and resulted in a decrease of PM, CO, and HC emissions. On the other hand, BSFC increased with greater amounts of EGR. The complete results and analysis can be found in a previous study, but for the purpose of this paper, the 25% EGR test data is used [282].

3. CFD Model Parameters of EGR Mixing Flow

The mixing box model was built using CONVERGE's graphical user-interface software, CONVERGE UI. The user defines what type of analysis will be performed (steady state, transient, incompressible, compressible, etc.) and then defines the geometric region(s) using simple surfaces stitched together to form a single closed-volume shape. The faces of that shape are then used to define separate boundaries (walls, inlets, outflows, etc.). Once the boundaries are defined, their initial and boundary conditions are set (e.g., "Dirichelet" fixed conditions like mass flow rate, pressure, and temperature).

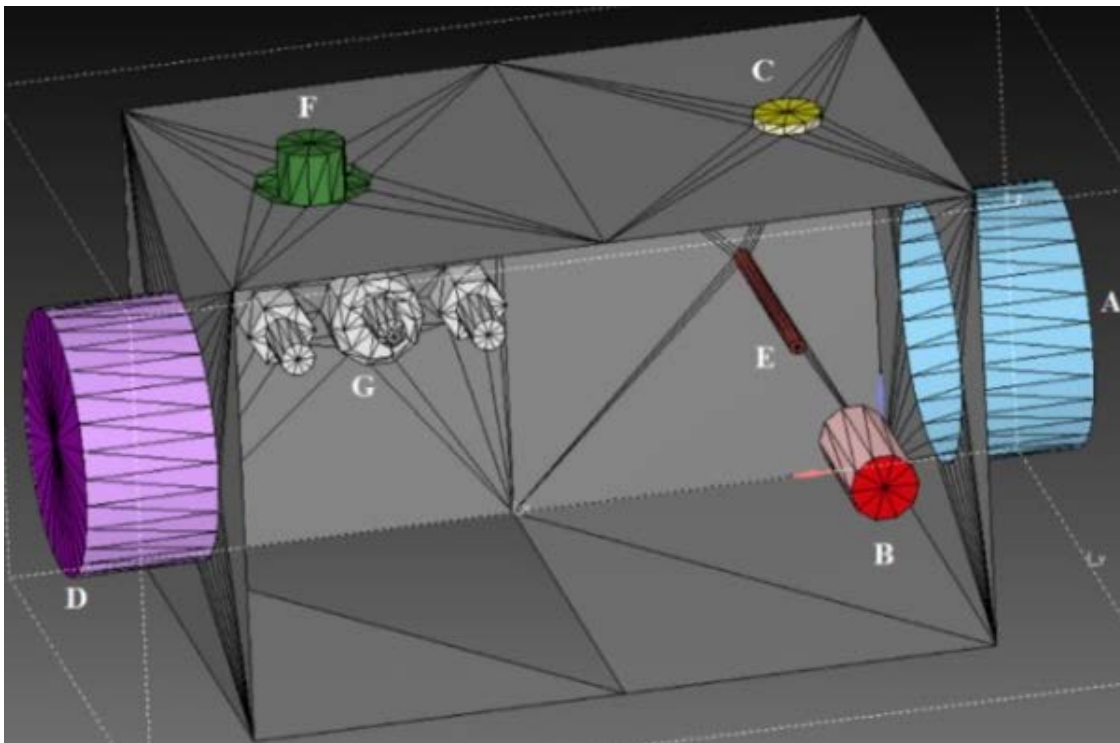


Figure 82: Single Cylinder Engine Test Stand Mixing Box CFD Model Domain Geometry (With Side Removed) and Associated Boundaries

Next, the turbulence model parameters are chosen, for instance, Reynolds Averaged Navier Stokes (RANS) or Large Eddy Simulation (LES) and associated sub-parameters. Lastly, the grid parameters are chosen, such as what size to set the fixed grid to on each boundary and (if desired) what levels of adaptive meshing are allowed.

The mixing box geometry was defined with eight components as shown in Figure 82. They are the wall geometry, (A) the air inlet, (B) the EGR inlet, (C) the (unused) secondary gas inlet, (D) the mixture outlet, (E) a fixed thermocouple, (F) a pressure sensor, and (G) a Bosch temperature and pressure sensor (used for other efforts). The initial boundary conditions of the simulations are included in Table 5 and initial species concentrations (defined only at the intake boundaries) are included in Table 6. Note that ‘Neu’ denotes a Neumann condition where the initial or boundary conditions are not fixed [25].

Table 5: Initial Fluid Conditions for Engine Cases

Load	Boundary	Mass Flow	Pressure	Temperature
		g/sec	Pa	K
100%	Air In	5.10	Neu.	300.4
	EGR In	1.77	Neu.	305.6
	Mix Out	Neu.	89,750	310.4
0%	Air In	5.20	Neu.	298.3
	EGR In	1.80	Neu.	301.6
	Mix Out	Neu.	89,970	307.1

Table 6: Initial Species Conditions for Engine Cases

Load	Boundary	yH ₂ O	yO ₂	yN ₂	yCO ₂	yCO
		%	%	%	%	%
100%	Air In	1.28	23.0	75.7	0.00	0.00
	EGR In	4.99	12.0	73.4	9.48	0.12
	Mix Out	1.28	23.0	75.7	0.00	0.00
0%	Air In	1.19	23.0	75.8	0.00	0.00
	EGR In	5.00	16.5	73.2	5.15	0.16
	Mix Out	1.19	23.0	75.8	0.00	0.00

The model geometric meshing parameters are included in Table 7. The base grid for the model was 0.01 m. This represents a starting grid of cubes and is the coarsest setpoint for any part

of the mesh. Each time a base grid element is ‘scaled’ it is segmented into eight equally-sized smaller elements. A grid element with 0.01 m sides scaled once will become eight cubes of the same total volume with sides of length 0.005 m. This forms the “fixed embedding” part of the mesh that is further refined at each time step using the solver’s adaptive meshing. The AMR was allowed to sub-grid up to an additional four layers finer than the fixed embedding with a local sub-grid speed of 0.4 m/s. The meshes for all four models were limited to 200,000 elements.

Table 7: Fixed Embedding Parameters Used for CFD Simulations of Mixing Box

Boundary	Scale	N _{LAYERS}	Grid Size
			mm
Box Walls	1	2	5.000
Air In Walls	2	3	2.500
EGR In Walls	2	3	2.500
Gas In Walls	2	3	2.500
Mix Out Walls	2	3	2.500
Thermocouple	4	2	0.625
Pressure Probe	3	2	1.250
Bosch Probe	3	2	1.250

4. Comparison of CFD Model Results to Experimental Data

A total of four CFD tests were run: two to match data at the no engine load condition with two at the full engine load condition. All of the data used employed 25% EGR. At both load cases, the default RANS and LES models were used for comparative purposes. Each model had the same starting grid with a total of 32,186 cells. Within 60 time-steps (around $t = 0.25$ ms) this reached 200,000 cells.

The time-history of the number of cells for each model is included in Figure 83. The RANS simulations showed a continuous decrease in number of cells following the initial transient flows of air and EGR entering the mixing box and eventually reached a minimum at about 20 ms. The LES simulations, however, remained at or near the maximum of 200,000 cells, indicating the sub-grid criteria chosen may be too sensitive to variations in cell-to-cell velocity. Since one intent of

the simulations was to maintain uniformity of the fixed embedding and AMR grid settings for comparative purposes, the authors' did not re-adjust the LES initial grid parameters. Overall, the number of cells in each model was effectively constant after 100 ms.

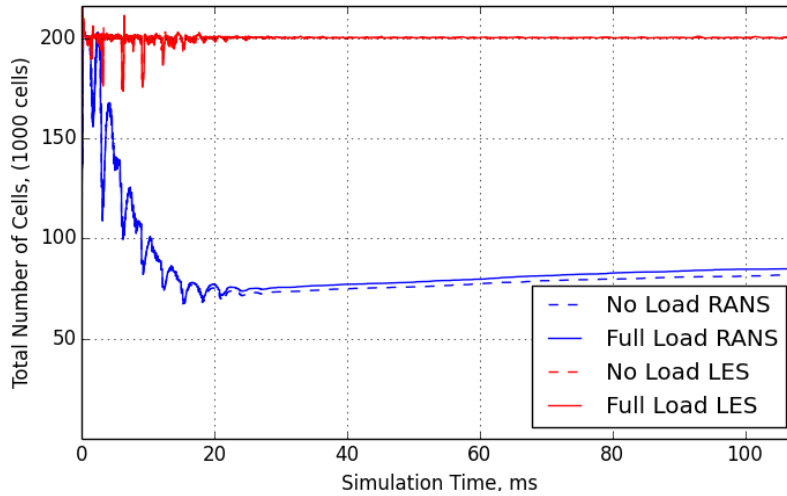


Figure 83: Total Number of Cells in Each CFD Model Showing AMR Varying with Time

Table 8: Comparison of Experimental Data to LES and RANS CFD Models (t = 400 ms)

Data	Mass Flow	T _{MIX}	P _{AIR}	P _{EGR}	Runtime
	g/sec	K	Pa	Pa	hrs
Engine Case 1: 100% Load, 25% EGR					
Exp.	6.890 ±0.015	310.4 ±0.04	90590 ±1174	101550 ±1300	n/a
LES	6.998	301.4	89740	89802	68.5
RANS	6.997	301.1	89766	89844	24.0
Engine Case 2: 0% Load, 25% EGR					
Exp.	6.868 ±0.016	307.1 ±0.04	90940 ±904	100268 ±1302	n/a
LES	6.866	299.4	89989	90240	58.0
RANS	6.879	299.3	89983	90024	22.5

Table 9: LES and RANS Model Percent Error Comparison

Data	Mass Flow	T _{MIX}	P _{AIR}	P _{EGR}
Engine Case 1: 100% Load, 25% EGR				
LES	1.57	2.91	0.94	11.6
RANS	1.56	2.99	0.91	11.5
Engine Case 2: 0% Load, 25% EGR				
LES	0.04	2.53	1.05	10.0
RANS	0.16	2.57	1.05	10.2

It is clear from Figure 3 that the AMR scheme was able to reduce the number of cells in the model as it was permitted based on how the sub grid criteria was influenced the turbulent model solver. And while LES models are generally expected to increase in computational time as compared to RANS models, the growth in run time of the LES model is likely also affected by the higher number of cells.

All mass-averaged parameters were at a quasi-steady state after approximately 400 ms of simulation. As indicated in Table 8 and Table 9, the mass flow rate of the mixture as it leaves the mixing box matched the actual mass flow rate within a few percent. At no load, the mass flow rate predicted by both the RANS and LES models matched within a fraction of a percent. The LES model was marginally closer, but this potential advantage was not seen at the full engine load condition suggesting that at least from the perspective of experimental data validation, there is not a significant advantage between conventional RANS or LES models except in computational time. However, the reader is cautioned that the turbulent flow structures which form in a Large Eddy Simulation are purely subgrid phenomena in a RANS model. These structures did not appear to affect the experimentally determined parameters, but they may affect others, such as the level of turbulence in the flow that cannot be easily measured experimentally.

There was some variation in the actual pressures at the inlets, but the error remained low. It should be noted that these pressures are mass-averaged over their respective boundaries and while this makes sense in a CFD simulation, it is not an exact representation of where the experimental pressures were measured. The simulation did not demonstrate a large variation of pressures throughout the mixing box; hence, if there is any phenomena that may account for this underprediction, it may occur outside of the mixing box. For example, the air into the mixing box was measured upstream of the mixing box; hence, the pressure drop between these two locations

would lower the pressure. In addition, the EGR pressure is measured in the exhaust upstream of the junction of the exhaust and EGR. It is likely that with the decrease in temperature and the length of pipe for flow of EGR, there is a pressure drop in the EGR system. Currently, there is no way to measure pressure of the EGR as it enters the mixing box.

There was not a significant difference between the RANS and LES predictions for either the air or the EGR inlet boundary pressures. This suggests that turbulent flow structures did not affect the inlet conditions nor were any observed in the visualized data.

Temperatures also showed some variation; however, this may be a result of the difference between mass-averaged temperatures at the inlet and outlet boundaries in comparison to where the temperatures were experimentally measured with thermocouples. The models predict some flow separation around the thermocouple and elevated temperatures as compared to those actually leaving the mixing box. It should also be noted that the simulation was adiabatic in nature – there was no simulated heat transfer to the cooler walls of the mixing box that may be expected to slightly reduce the simulation temperature further. However, the experimental temperature differential was 10.0 K at full load and 8.8 K at no load; therefore, the effect of heat transfer was expected to be low. Again, there was not a significant difference between the RANS and LES predictions for mixture outflow temperature.

The visualized data for the mole fraction (indicating mixing quality) of CO₂ from each of the four models is shown for no engine load and full engine load in Figure 84 and Figure 85, respectively. It is immediately clear that the greatest difference between the RANS and LES models is an additional accumulation of cells where the EGR intake flow contacts the wall of the mixing box. In both cases, the AMR scheme successfully added cells along the mixing areas where the incoming EGR and air flows meet.

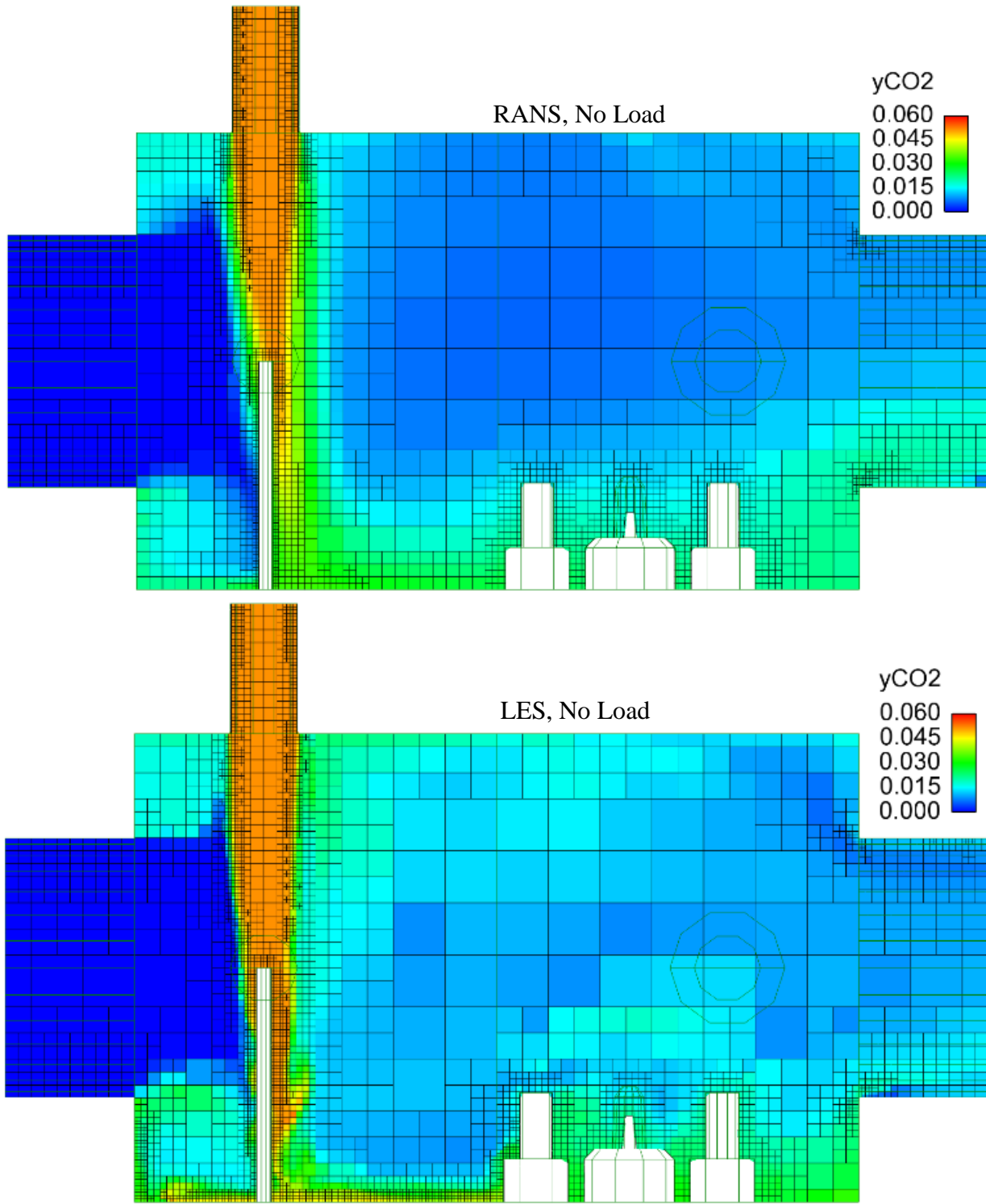


Figure 84: No Load Models - CO₂ Mixing at Quasi-Steady State (t = 400 ms), 25% EGR

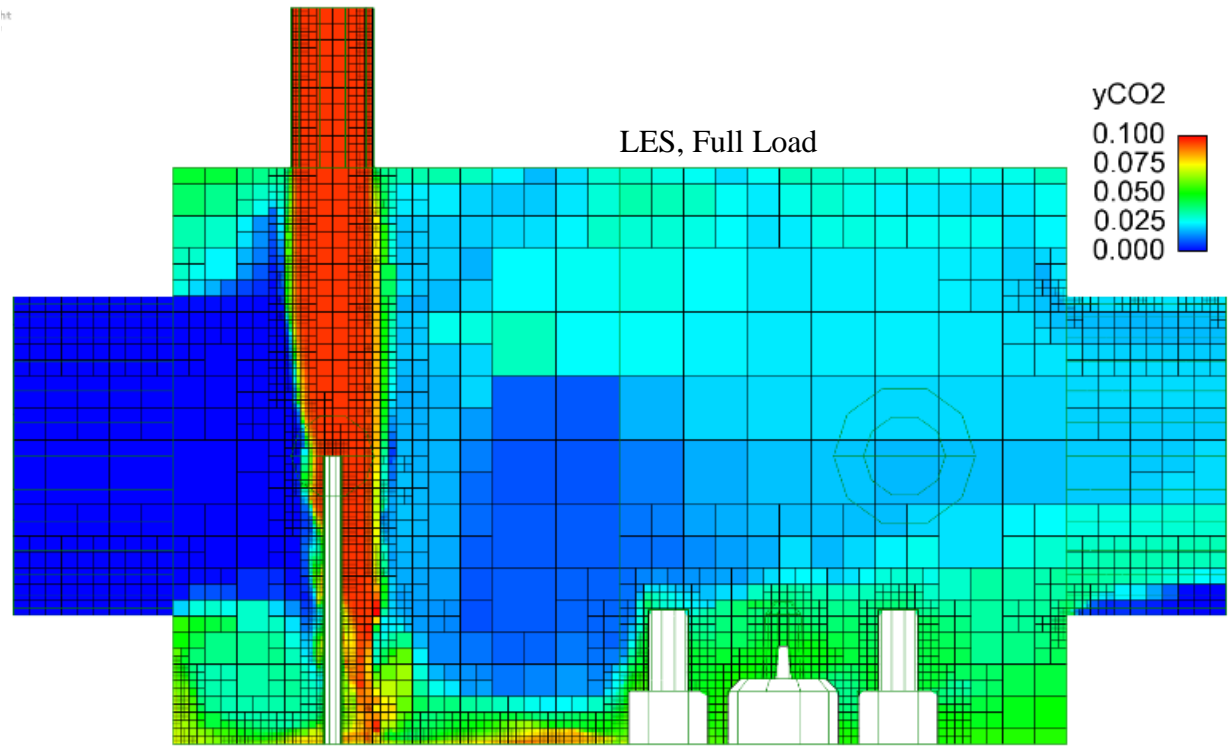
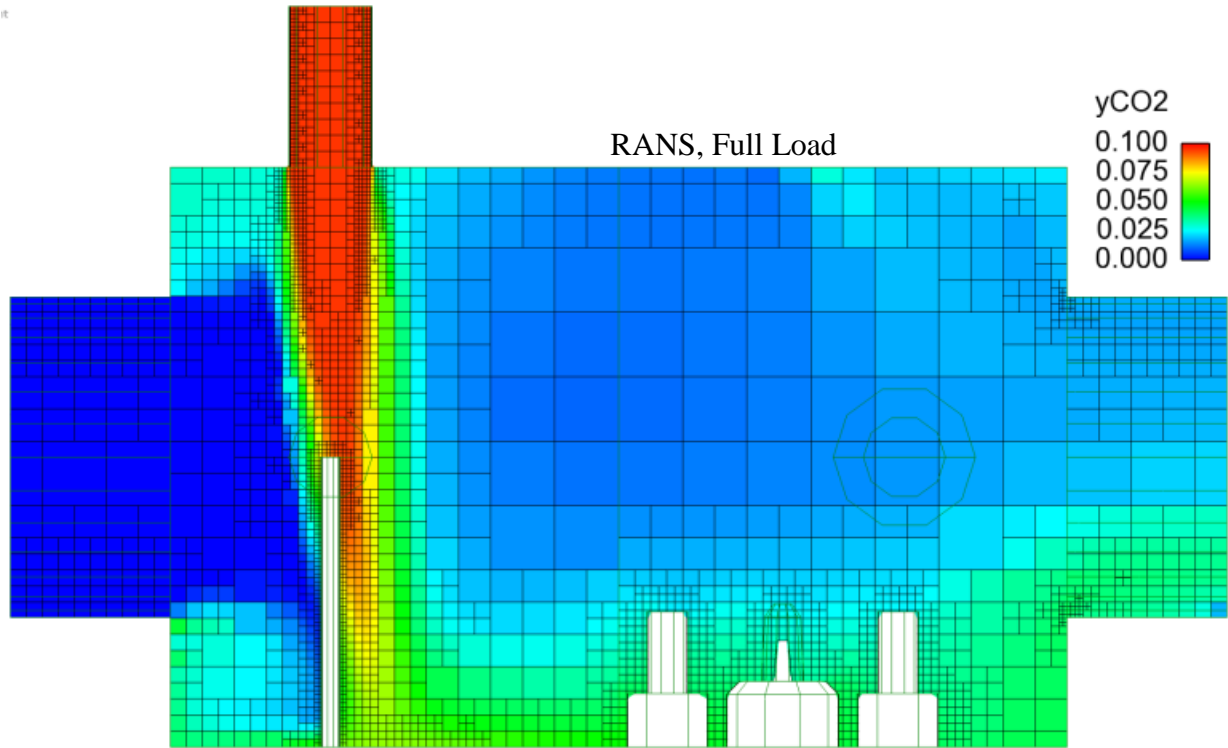


Figure 85: Full Load Models - CO₂ Mixing at Quasi-Steady State (t = 400 ms), 25% EGR

The no load RANS and LES models suggest a maximum CO₂ variation across the mixture exit of 10680 ppm and 7450 ppm, respectively. At full load, the RANS and LES CO₂ variations were 18270 ppm and 29940 ppm, respectively. The large variation in the LES model is due to the flow separation from the lower lip of the exit duct where the CO₂ mole fraction is nearly zero. Ignoring that zone, the variation in the LES model drops to 10800 ppm. Considering the CO₂ mole fractions entering the mixing box at no load and full load were 51500 and 94800 ppm, respectively, this shows a significant improvement in the mixture uniformity. Another EGR-specific species, CO (not pictured), entered the mixing box at up to 1600 ppm and left at less than 440 ppm. Further information and animations are publicly available at <http://depcik.faculty.ku.edu/simovies>.

Comparing the models at no load and full load, there appear to be only a few notable differences. As expected, there is more CO₂ in the exhaust at full load. This is also reflected in the greater mixture variation – the mixing box is less capable of producing a uniform flow field and mixture. Neither the RANS nor the LES model showed any significant advantage with respect to matching experimental data except in simulation runtime. However, if the LES model is accurate at full load, there may be significant flow separation due to the outflow lip. This may not appear in the RANS model as the separation developed from a turbulent recirculation around the bottom section of the outflow duct lip. A RANS-based simulation would not necessarily be expected to capture this phenomena. Although this is not expected to continue into the engine, it may be prudent to add a flow-straightening section to the outflow duct prior to feeding the mixed flow into the engine. This measure could ensure that any additional turbulent energy due to EGR and the mixing box only minimally affects the combustion mechanics in the engine. This would allow the authors to investigate singular parameter effects on combustion (e.g., EGR constituents not

including turbulence) illustrating how 3-D CFD simulations provide a valuable understanding of the mixing process.

The mixing box showed significant blending capabilities at reducing the mole fraction of EGR species and producing a generally uniform flow. At no engine load, the exit flow was most uniform for the LES model with this version predicting a reduction in CO₂ concentration of 85.5% as compared to when it enters the mixing box EGR port. At full load, the CO₂ concentration demonstrated a predicted reduction of 80.7% based on the RANS model. The reader is reminded that although no significant advantage was found between the RANS and LES models with regard to matching experimental data, it was possible to readily validate the level of turbulence. The blending capability of the mixing box geometry may be significantly affected by the level of turbulence. Further research may be done to validate the effect of turbulence on mixing of EGR species with air in addition to the effect of this turbulence on combustion and engine parameters. A LES model is expected to more accurately predict the turbulent structures that form around the thermocouple and sensor protrusions despite the added computational time required.

The AMR scheme was successfully employed to reduce the computational time necessary to run the simulation. It was clear, however, that uniformity of the AMR parameters (specifically the sub-grid criteria) did not produce the same grid in both RANS and LES models. Instead, it appears to be more sensitive for the LES model, which may be a result of the formation of large eddies in the mixing flow and along the wall. The result of this asymmetry in the grid geometry meant that the AMR scheme provided a significant benefit in reducing the computational time of the RANS model over the LES model in addition to the usual expected difference. Therefore, it should be possible to reduce the computational time of the LES model by adjusting the AMR sub-grid to a higher value making it less sensitive to cell-to-cell variation in velocity.

Further research could be performed to reduce the boundary pressure error by directly measuring pressure at the air and EGR inlets to the mixing box. These measurements are made at a significant distance, but the velocities through the feed ducts were assumed to be low enough that total pressure losses would be minimal. Further CFD simulations could also be run in order to provide more insight on the use of AMR between RANS and LES to determine an appropriate method of matching criteria between them in an effort to produce more equivalent grid geometries. At present, however, the greatest difference between the RANS and LES models is purely related to computational time as opposed to any quantifiable parameter like pressure or temperature. Lastly, for a more complete understanding of the differences between the RANS and LES algorithms, future work should include a comparison of these simulations against a measured flow velocity profile. This could be accomplished using laser Particle Image Velocimetry techniques.

C. Modeling of Quiescent Premixed Propane/Air Combustion

With a real world mixing flow modeled, it was then necessary to test modeling of combustion beyond the zero-dimensional simulations, particularly the application of chemical kinetics in the CONVERGE package. The simplest model available for which there was experimental data was chosen as the test geometry – the constant volume spherical chamber studied extensively by Razus, *et al.* [41-47]. These works are discussed in more detail in Chapter III, Section B-4. The chamber involves use of a quiescent (zero velocity) mixture of propane and air at some prescribed initial temperature and pressure. CFD simulations were performed for a range of equivalence ratios to match flame speeds and temperatures to Razus's data.

1. Chemical Kinetic Mechanisms

A total of two kinetic mechanisms were tested for comparison in CONVERGE – the detailed San Diego Mechanism (version published in 2005) [152] and a reduced form of this same mechanism (removing reactions with minimal effect on ignition delay). The calibrated form of Westbrook and Dryer's 1981 one-step global mechanism [141] could not be integrated into the solver in time for publication but is the focus of continued work. These mechanisms are discussed in detail and in the context of other propane and related kinetic mechanisms in Chapter III Section C-1. The actual mechanisms are included in full detail in Appendix A.

The detailed San Diego mechanism was considered the most complete and, therefore, likely the most accurate model of propane/air combustion (following the literature search in Chapter III). However, this mechanism is lengthy, requiring the most computational time and was not run for the whole range of equivalence ratios, just as a check at the stoichiometric equivalence ratio ($\phi = 1$). The reduced mechanism, however, ran significantly faster and was tested across the range of equivalence ratios between $\phi = 0.60$ and $\phi = 2.0$.

The global mechanism was employed using the built in User-Defined Function (UDF) in the CONVERGE package allowing the user to define an alternation combustion mechanism. In this case this means a mechanism that does not strictly adhere to the format of an Arrhenius or Kooij equation as in most detailed mechanisms. The calibrated global mechanism was tested across the same equivalence ratios as the reduced mechanism.

2. Spherical Chamber Model Geometry and Simulation Parameters

A constant-volume spherical chamber was chosen for its simplicity, symmetry, and the extensive available experimental data; i.e., primarily adiabatic flame temperatures and flame speeds for a variety of initial conditions. The spherical chamber was defined with a diameter of 0.10 m to match that used by Razus [44]. A thin slice of the sphere was used with symmetrical boundary conditions defined everywhere but the outer wall. This computational domain is shown in Figure 86 with symmetrical boundaries shown in red and the fixed wall boundary shown in grey.

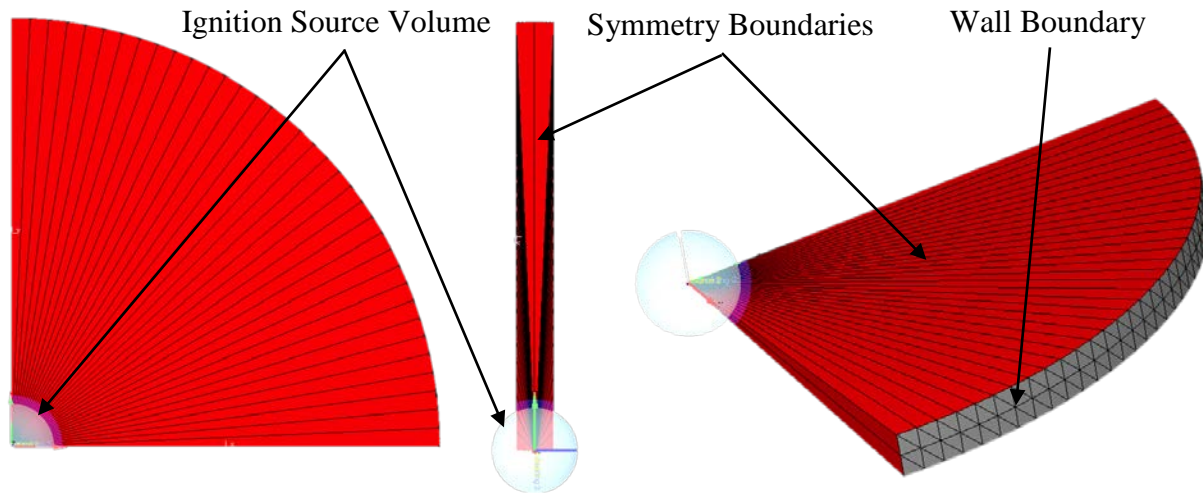


Figure 86: Multiple Views of the Computational Domain for Constant Volume Spherical Reactor Simulations of Premixed Propane/Air Combustion Showing Thin Slice Geometry and Symmetry and Wall Boundary Conditions

The mixture inside this domain was given initial conditions at standard temperature (300 K) and pressure (1 atm). Extensive studies on the effects of initial temperature and pressure have already been done and this effort was only meant to match existing data (discussed in Chapter III, Section B). Moreover, as the pressure jet engine will operate near standard temperature and pressure, these conditions best approximate the combustion process inside the engine (albeit with the effects of flow speed and turbulence minimized). The premixed propane and air conditions were set by defining the mole fractions of propane, oxygen, and nitrogen (0.060, 0.197, and 0.743, respectively corresponding to an equivalence ratio of $\phi = 1.1$). A source term at the center of the sphere was added to instigate ignition of the mixture. This was defined as 5.0 mJ of energy added to a spherical region of 0.005 m radius over a 0.5 ms duration. These parameters were arrived at after much experimentation (using the model) by attempting to minimize the energy put into the system such that as soon as ignition occurred the source term would stop. Allowing the energy source term continue longer than necessary artificially heated the center zone and could affect flame temperatures and flame speeds. Therefore, these conditions approximately represented the minimum energy necessary to cause sustained ignition in the simulation and are significantly larger than that considered to be the ideal minimum ignition energy of 0.48 mJ [48].

The simulations were run using the recommended settings for a Large Eddy Simulation (as discussed earlier). This included the selection of the 1-Equation viscous turbulence model, as well as an initial turbulent kinetic energy of $1 \text{ m}^2/\text{s}^2$ and a turbulent dissipation rate of $10 \text{ m}^2/\text{s}^3$. The base grid was set to one-tenth the radius of the sphere. That is, the maximum coarseness of the grid was set to 0.005 m or ten elements along the radius. A layer of fixed embedding was set to scale down twice in the region of the ignition source term making the grid size 0.00125 m. The adaptive meshing was set to a maximum of 100,000 cells and allowed to scale five times making

the minimum possible grid size as low as 0.00016 m. The local propane concentration was used as the criteria for allowing the adaptive meshing to reduce the local grid size. This was intended to keep the grid size the smallest where the flame front was propagating.

3. Simulation Results and Comparison to Experimental Data

The collection of simulations performed in the small slice of a spherical chamber produced a wide array of data, much of which was compared to available experimental data. These results compare the predictions of the full detailed 2005 San Diego mechanism (including nitrogen chemistry) and a reduced form of this mechanism (neglecting nitrogen chemistry as well as many other reactions). The calibrated Westbrook and Dryer one-step mechanism could not be included as the external user defined function to integrate it into the simulation produced compiling errors that could not be fixed in time for publication. This will be pursued in later work.

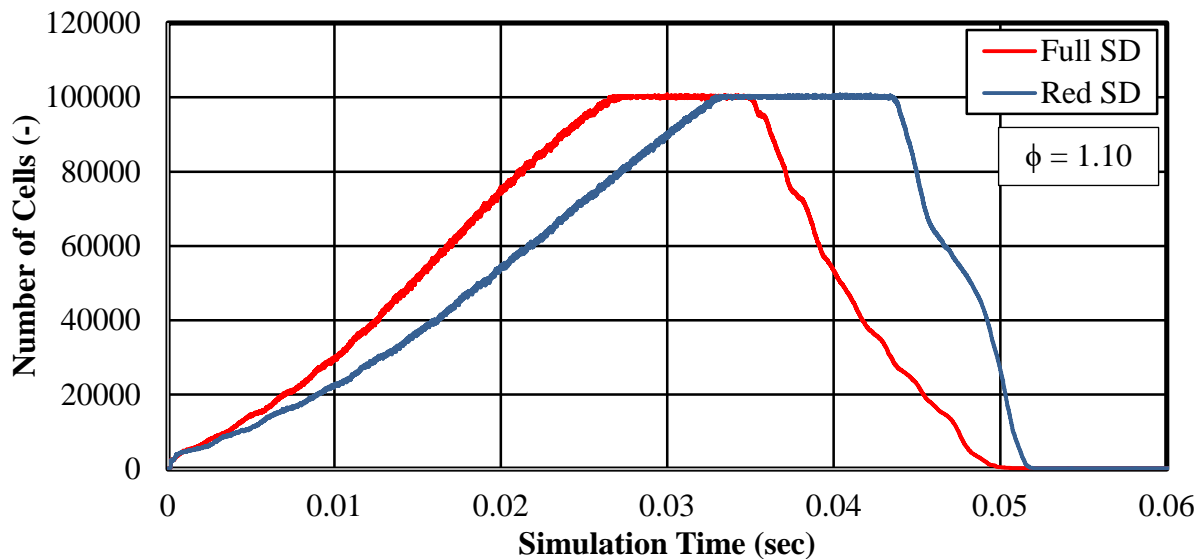


Figure 87: Time History of the Number of Cells in Spherical Chamber Simulations Comparing Adaptive Meshing of Different Kinetic Mechanisms (Full and Reduced San Diego Mechanisms)

The time history of the total number of cells in each simulation at an equivalence ratio of 1.10 is shown in Figure 87. This illustrates the result of the reduction of the full San Diego mechanism indirectly on the adaptive meshing scheme as it affects the local properties of the

mixture during flame propagation. It is clear, however, that in both, the adaptive meshing was capable of adding fineness as the flame propagated up to the posted limit of 100,000 cells until the flame impinged on the wall and no longer drove the adaptive meshing. At that point, cells could be removed to speed up the end of the simulation. This appeared to happen earlier for the full mechanism, potentially as a result of the nitrogen chemistry or the other removed reactions, but both appeared to complete around the same time (approximately 50 ms).

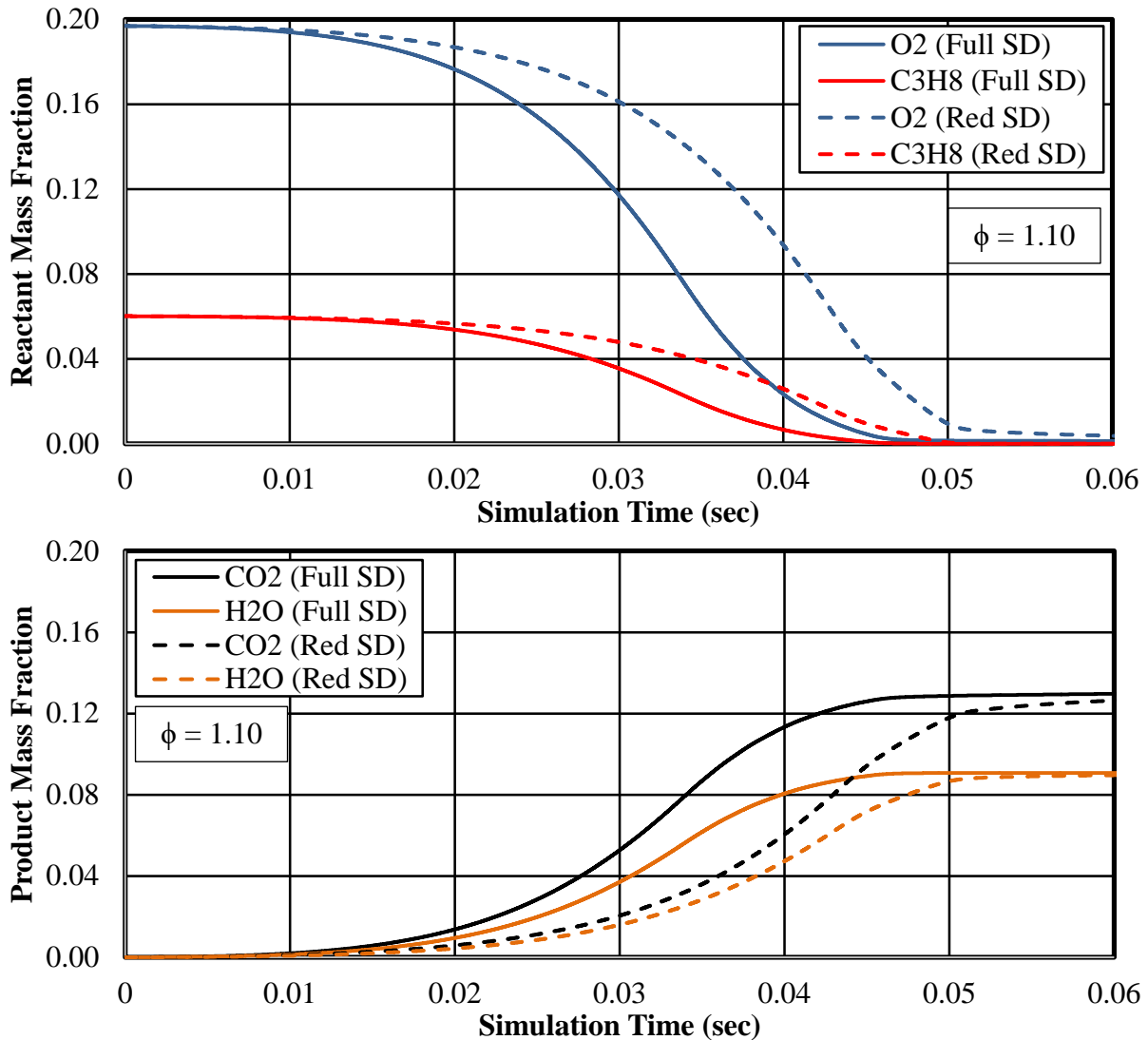


Figure 88: Time Histories of the Main Reaction Species Mass Fractions in Spherical Chamber Simulations Comparing the Response of Different Kinetic Mechanisms (Full and Reduced San Diego Mechanisms)

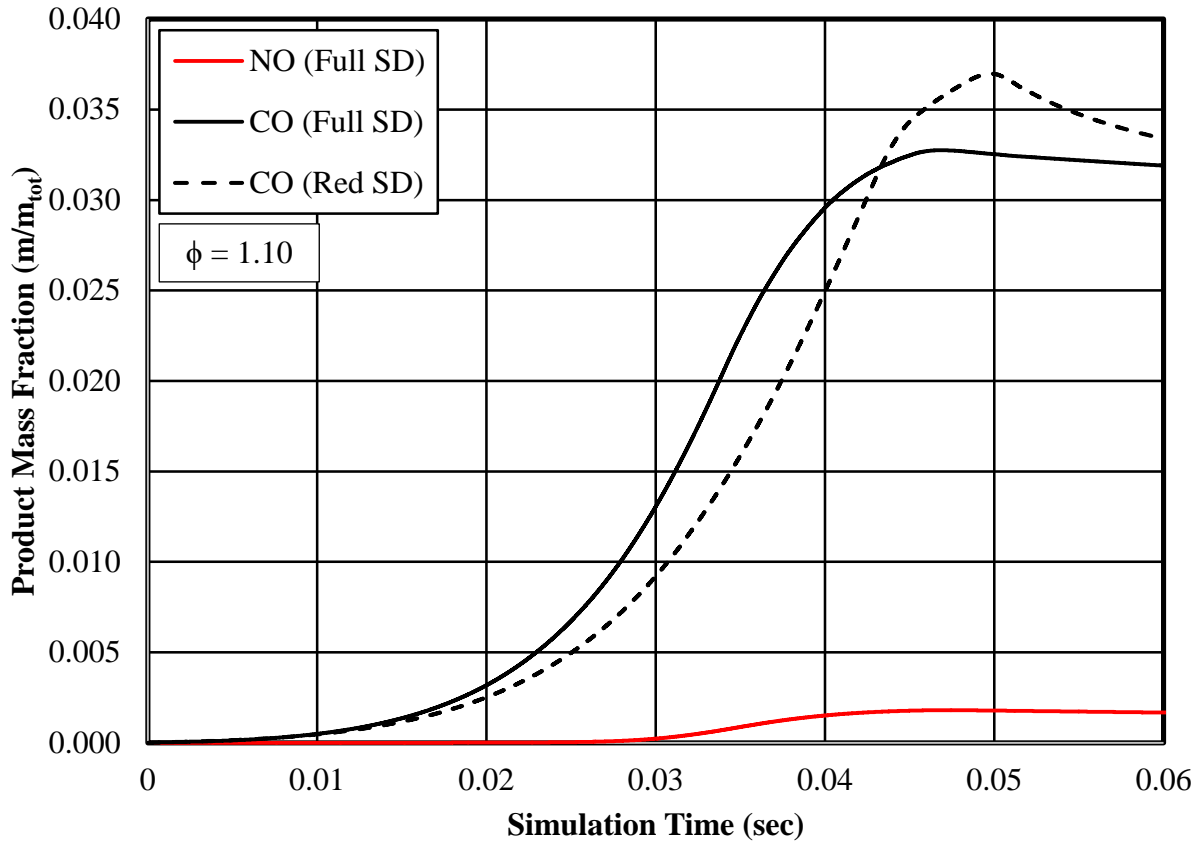


Figure 89: Time Histories of the Secondary Reaction Species Mass Fractions (NO and CO) in Spherical Chamber Simulations Comparing the Response of Different Kinetic Mechanisms (Full San Diego and Reduced San Diego Mechanisms)

A comparison between the chemical species profiles resulting from the full and reduced San Diego mechanisms is included in Figure 88. The most obvious difference is a slight delay of less than 10 ms in the overall process of oxidation in the reduced mechanism. The steady-state magnitudes (essentially the end species mass fractions once combustion was completed) remained largely unaffected. The reduced mechanism does show a small amount of residual oxygen at the end of primary (flame front-driven) combustion which seems to be oxidizing remaining species slowly due to the residual temperature in the chamber. The delay is also apparent in the production of other species, namely carbon monoxide (CO), shown in Figure 89. In this case, the reduced mechanism shows some overshoot of the CO production of the full mechanism though trending back toward the same steady state. This plot also illustrates the comparatively low concentration

of NO (and by extension, NO₂) that forms as a result of the oxidation process. The reduced mechanism does not include nitrogen chemistry so NO production cannot be compared between the two simulations.

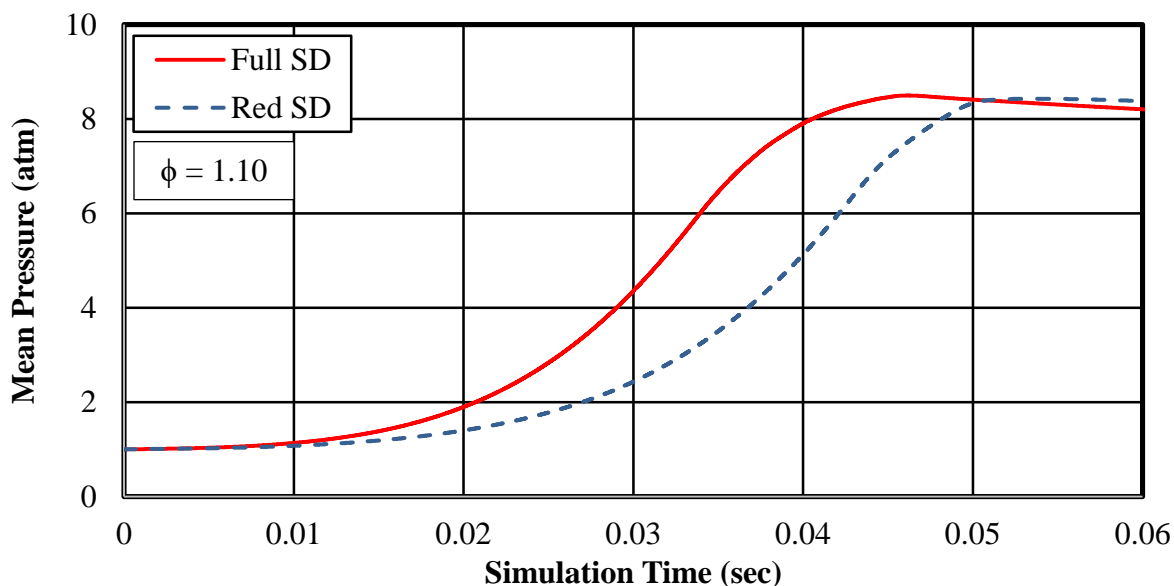


Figure 90: Time Histories of the Mean Chamber Pressure in Spherical Chamber Simulations Comparing the Response of Different Kinetic Mechanisms (Full San Diego and Reduced San Diego Mechanisms)

The mean pressure inside the chamber is plotted for both mechanisms in Figure 90. This pressure trace also shows the slight delay in the reduced mechanism seen in the species mass fractions, though the rate of pressure rise and the maximum pressure reached appear to both be largely unaffected. The peak pressure reached in the full San Diego simulation (8.50 atm, 0.861 MPa, 125 psi) is within the range of peak pressures recorded by Razus, *et al.* in their studies using a spherical chamber. The reduced mechanism simulation is also close, reaching a peak chamber pressure of 8.43 atm (0.854 MPa, 124 psi). The studies published by Razus, *et al.* recorded peak pressures from the same initial conditions as low as 0.77 MPa (7.6 atm, 112 psi) [41] to as high as 0.91 MPa (8.98 atm, 132 psi) [43].

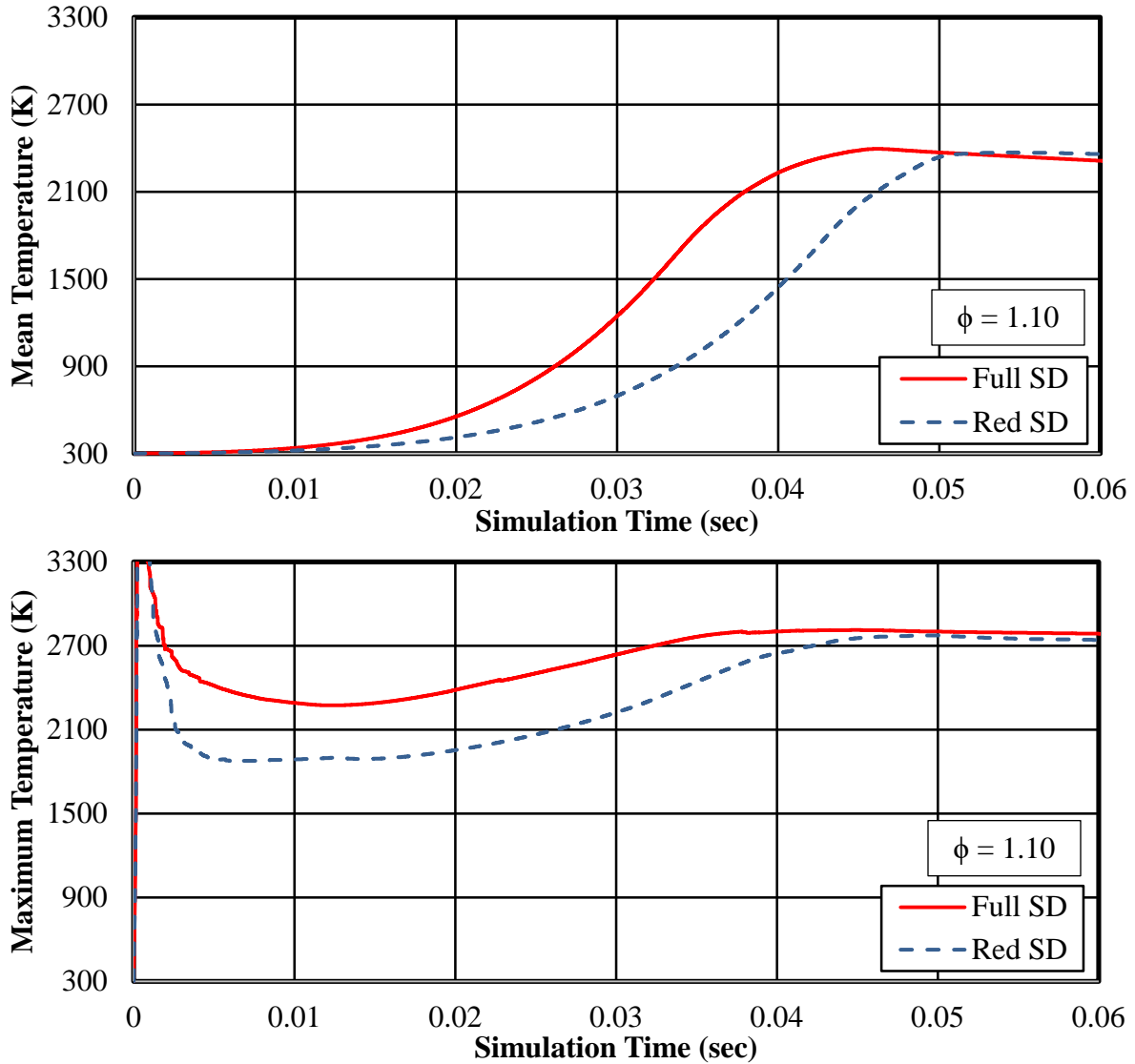


Figure 91: Time Histories of the Mean and Maximum Temperature in Spherical Chamber Simulations Comparing the Response of Different Kinetic Mechanisms (Full San Diego and Reduced San Diego Mechanisms)

Plots comparing the mean and maximum temperatures for the full and reduced mechanism simulations are included in Figure 91. The mean temperature (a mass-averaged temperature over the chamber’s closed domain) shows the same reduced mechanism delay as seen in the pressure and species concentrations. This delay is also apparent in the maximum temperature, as well as a reduction in the temperature of almost 400 K. This reduction in the flame temperature as the flame propagates could explain part of the delay as a lower temperature would be associated with a

reduction in the reaction rate of the kinetic mechanism. Nevertheless, the steady state temperatures are closer, ending within approximately 40 K of each other.

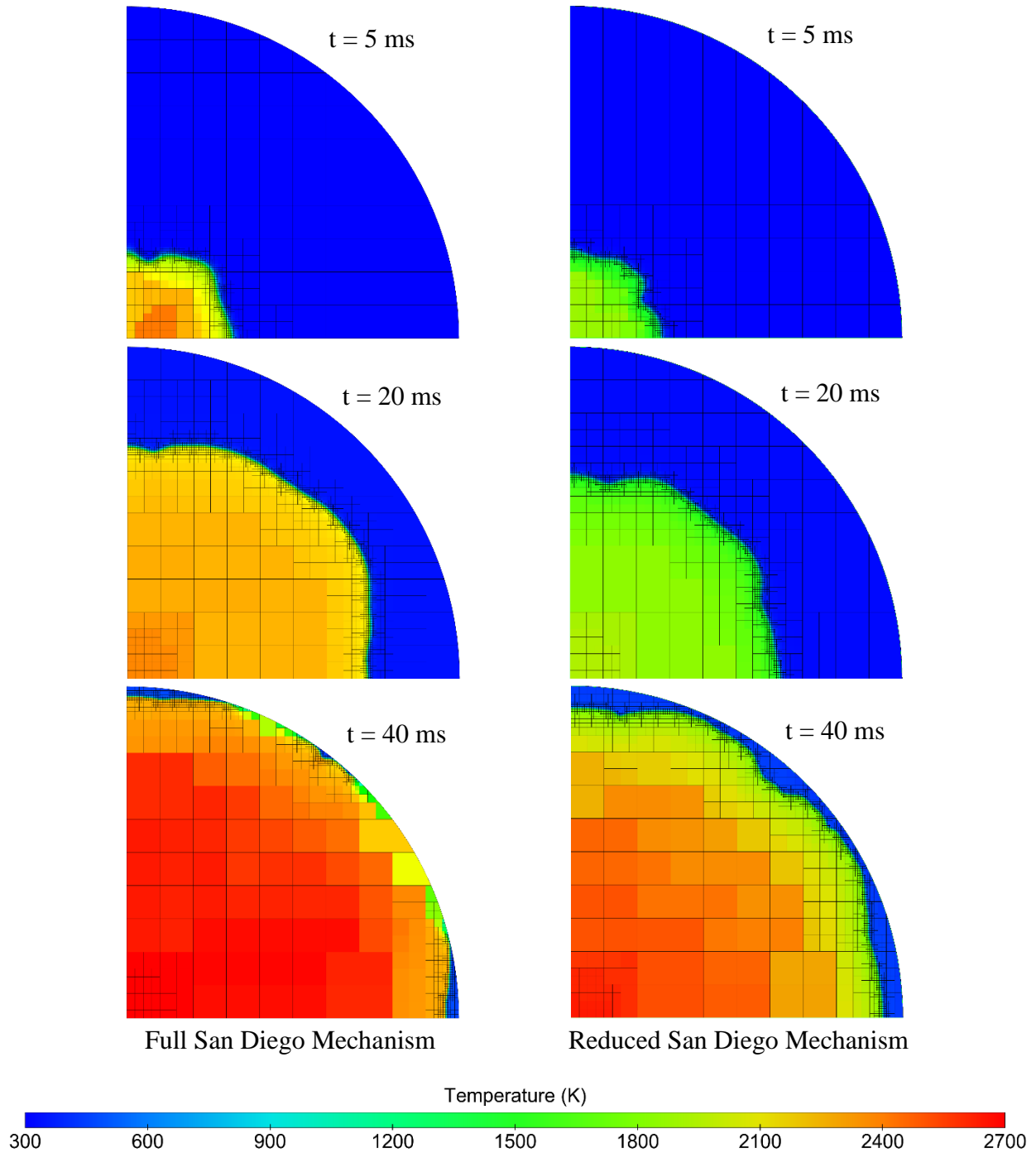


Figure 92: Spherical Chamber Simulation Temperature Distributions using the Full San Diego Mechanism (Left) and the Reduced San Diego Mechanism (Right) at 5 ms, 20 ms, and 40 ms (Equivalence Ratio of $\phi = 1.10$)

A comparison of the temperature distributions resulting from the CFD simulations of the two mechanisms at an equivalence ratio of $\phi = 1.10$ is shown in Figure 92. It is immediately apparent that both simulations do not show an idealized spherical flame propagation and instead appear to include some flame front wrinkling. This is most likely a result of the use of a large eddy simulation (LES) turbulence model (discussed earlier in this chapter) as opposed to the faster Reynolds-Averaged Navier Stokes (RANS) model. Early RANS simulations did show a very spherical flame front, but findings from the literature review recommended including the effects of turbulence as they can affect flame speed.

The increase in both the mean and maximum temperature discussed in regard to Figure 91 is also apparent in these distributions. Although both simulations appeared to show a flame front temperature of approximately 1500-1700 K, the full San Diego Mechanisms resulted in higher temperatures behind the flame front sooner than the reduced San Diego Mechanism. This suggests that while the primary fuel, propane, and other faster-oxidizing species included in the reduced mechanism are still accurately modeled, the slower-reacting species that were removed may play a role in releasing more secondary energy after the flame front has passed. This may account for the maximum temperature deficit seen in Figure 91 while also accounting for some delay in species production and oxidation.

The flame front temperature seen in the simulations is significantly below the accepted adiabatic flame temperature of propane oxidation with air (approximately 2270 K), but falls within the range of often-cited experimental flame measurements published by Law [36] and Mizomoto [99]. The peak temperature in the chamber is actually higher than the adiabatic flame temperature that may be the result of the elevated pressures in the chamber artificially raising the fluid temperature in addition to that from the energy release of the fuel.

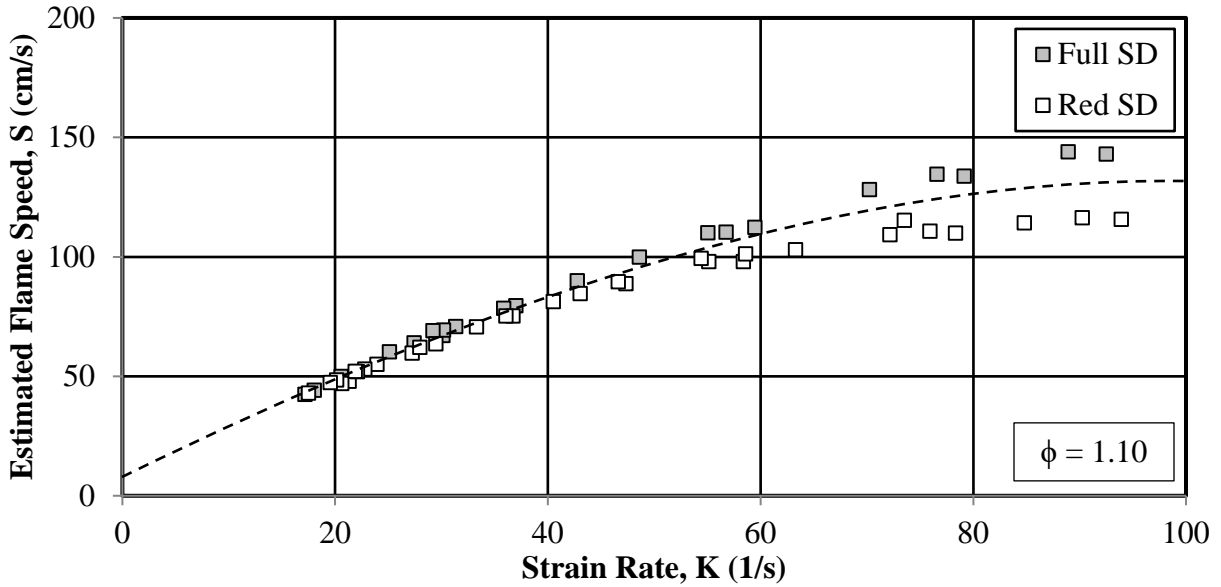
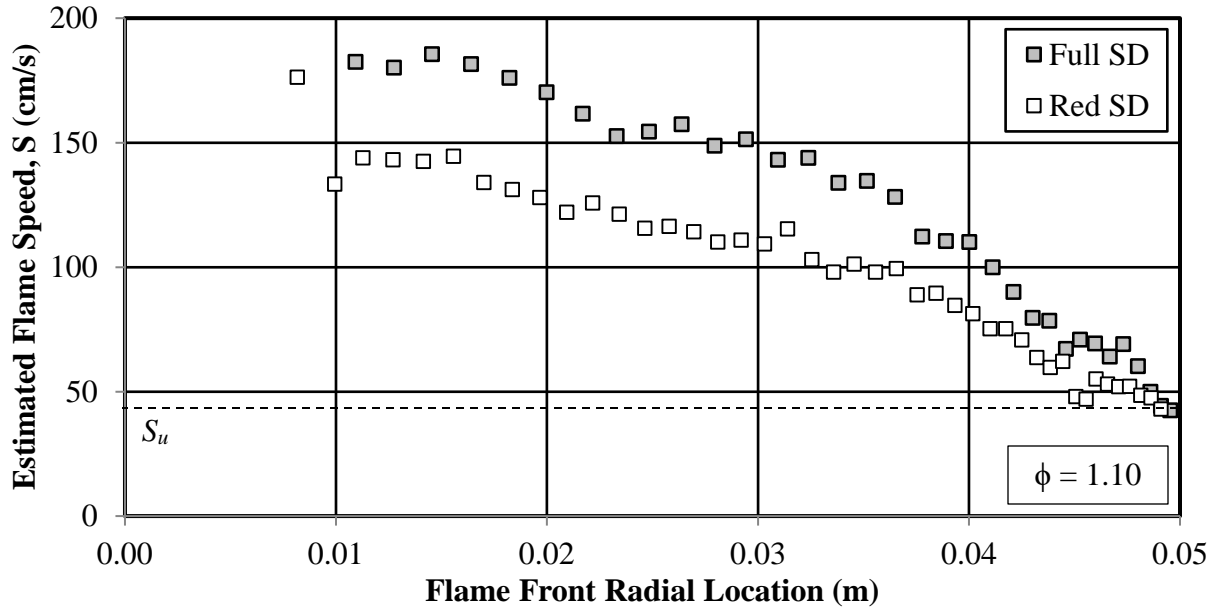


Figure 93: Determination of Laminar Flame Speed, S_u , as the Flame Front Progressed Through Spherical Chamber Including Estimation of Local Strain Rate.

Flame speeds were calculated for each simulation manually by recording the radial location of the flame front (along a line 45 degrees off the horizontal axis) as a function of time. The local flame speed was calculated based on the change in radial location and the time between measurements. This raw measurement of flame speeds, however, includes the effects of flame stretch as pointed out by Law [36]. Law's experiments and subsequent ones using flames

impinging on walls or other flames countered this corruption of the laminar flame speed by calculating the local flame stretch and taking the laminar flame speed at the point of minimum stretch. In their experiments, this usually occurs where the flame reaches the stagnation point impinging on the plate. A further improvement was to extrapolate the flame speed trend with stretch (as shown in Figure 93). Unfortunately, this ‘improved’ method did not result in laminar flame speeds that matched experimental data. However, the older method did. It is unclear why the simulation data had a higher slope of flame speed with flame stretch than seen in published experimental data. It may be a limitation of the computational approach (perhaps in grid fineness) either in the flame impinging on the chamber wall or in the estimation of flame stretch.

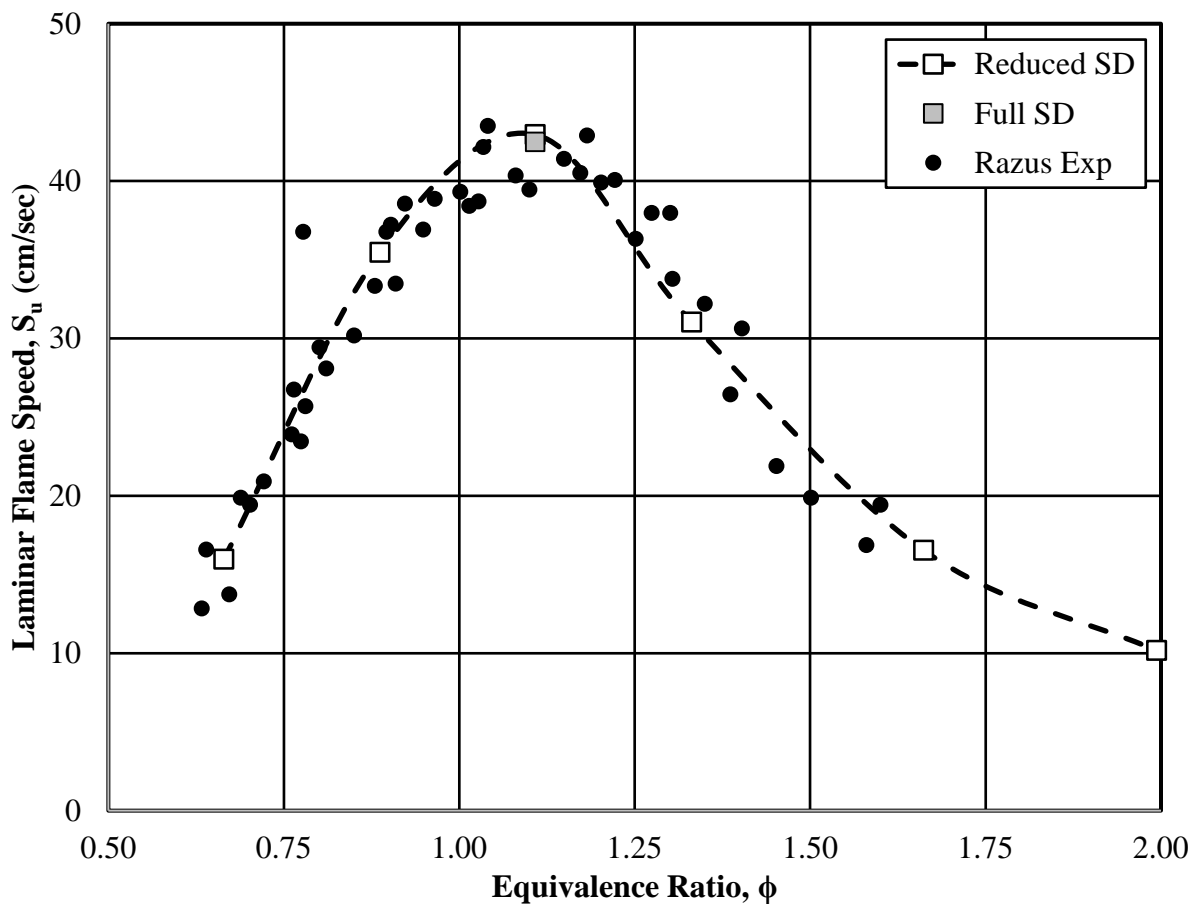


Figure 94: Variation of Laminar Flame Speed Across a Range of Lean and Rich Equivalence Ratios in Spherical Chamber Simulations Comparing the Response of Different Kinetic Mechanisms (Full and Reduced San Diego) to Experimental Data Published by Razus [44]

Nevertheless, using the flame speed at the wall (as opposed to extrapolating to zero flame stretch) produced results that matched experimental flame speeds published by Razus [44] for the full range of that data set. This is shown graphically in Figure 94. It is immediately clear that the laminar flame speeds calculated in this manner for simulations of an adiabatic, spherical chamber match closely to the experimental data from the same architecture across a wide range of equivalence ratios. This suggests the possibility of using such a simulation to expand on Razus, et al. and other studies on the dynamics of flames. And with the further study of other chemical kinetic mechanisms (for instance, oxidation of other fuels and blends of those fuels) there appears to be a strong opportunity to match experimental data to computational predictions beyond those of the simple closed form solutions used so far. Much of Razus's experiments [41-47] for instance, could be repeated computationally using that data to validate simulations and provide greater insight into what occurs inside the spherical chamber yet cannot otherwise be measured except as mean chamber properties.

D. Pressure Jet Engine CFD Model Parameters

With modeling of mixing flow and static combustion completed, it was time to model the pressure jet engine. The engine design requires several new considerations concerning the engine's unique geometry and parameters pertaining to running the CFD model. Simulations of the pressure jet engine were performed using the University of Kansas Advanced Computing Facility (KU ACF) server cluster running CONVERGE 2.2.0 Super (the 'Super' denoting a super license architecture allowing parallel computation on a single license) and the OpenMPI 1.6.5 message passing interface. Simulations were performed requesting 8 threads and limited to 200,000 cells and 12GB of memory. The complete parameters used (a series of formatted input files) to run the CONVERGE solver are included in Appendix B-0

1. Pressure Jet Model Geometry

The pressure jet engine requires several geometric boundary definitions. Because the engine relies heavily on acoustic tuning, this geometry is of critical importance. The geometry includes the locations and sizes of the inlet stages and their wall thicknesses, as well as the dimensions of the engine head, core, and exit nozzle. The model datum was set at the intersection of the two orthogonal centerlines meeting at the center of the engine core with the XY plane forming a symmetry boundary to reduce computational time. The X-axis was set down the engine exhaust path centerline with positive values marching toward the exit. The Y-axis was set down the intake centerline with positive values marching toward the injector (the y-location decreases to zero as it reaches the engine core). The Z-axis then forms the engine height dimension measured from the central symmetry plane. This section describes the ideal dimensions of the engine (neglecting manufacturing error) and the necessary extra boundaries.

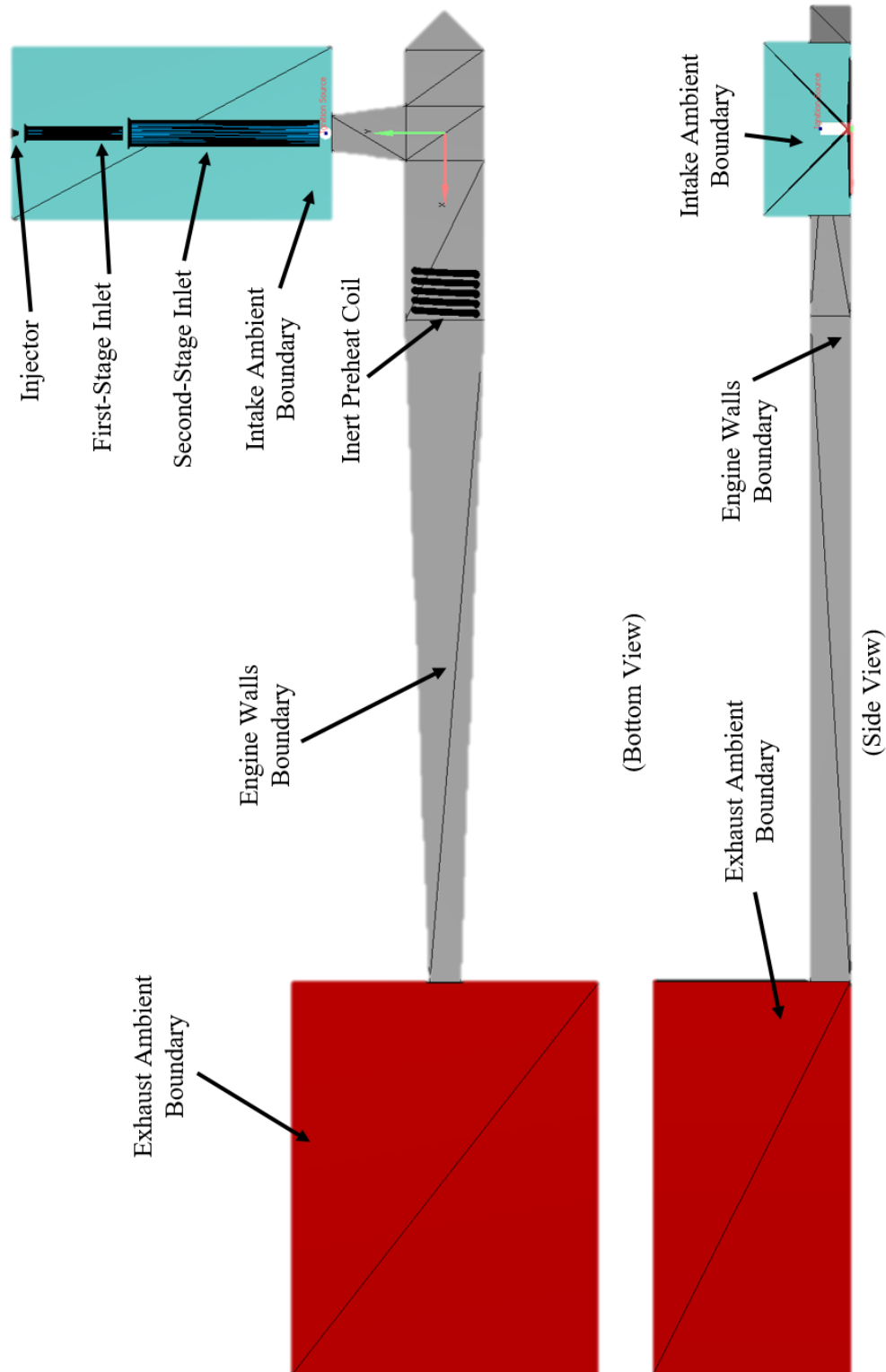


Figure 95: Pressure Jet Engine CFD Model Geometry with the Symmetry Boundary Hidden. Intake Ambient Boundary in Blue, Engine Walls Boundary in Gray, and Exhaust Ambient Boundary in Red. Injector and Inlet Geometry are within the Intake Ambient Boundaries. The Inert Preheat Coil (Active Only as a Flow Obstruction) is Also Included. Images Output from CONVERGE Studio Software [283]

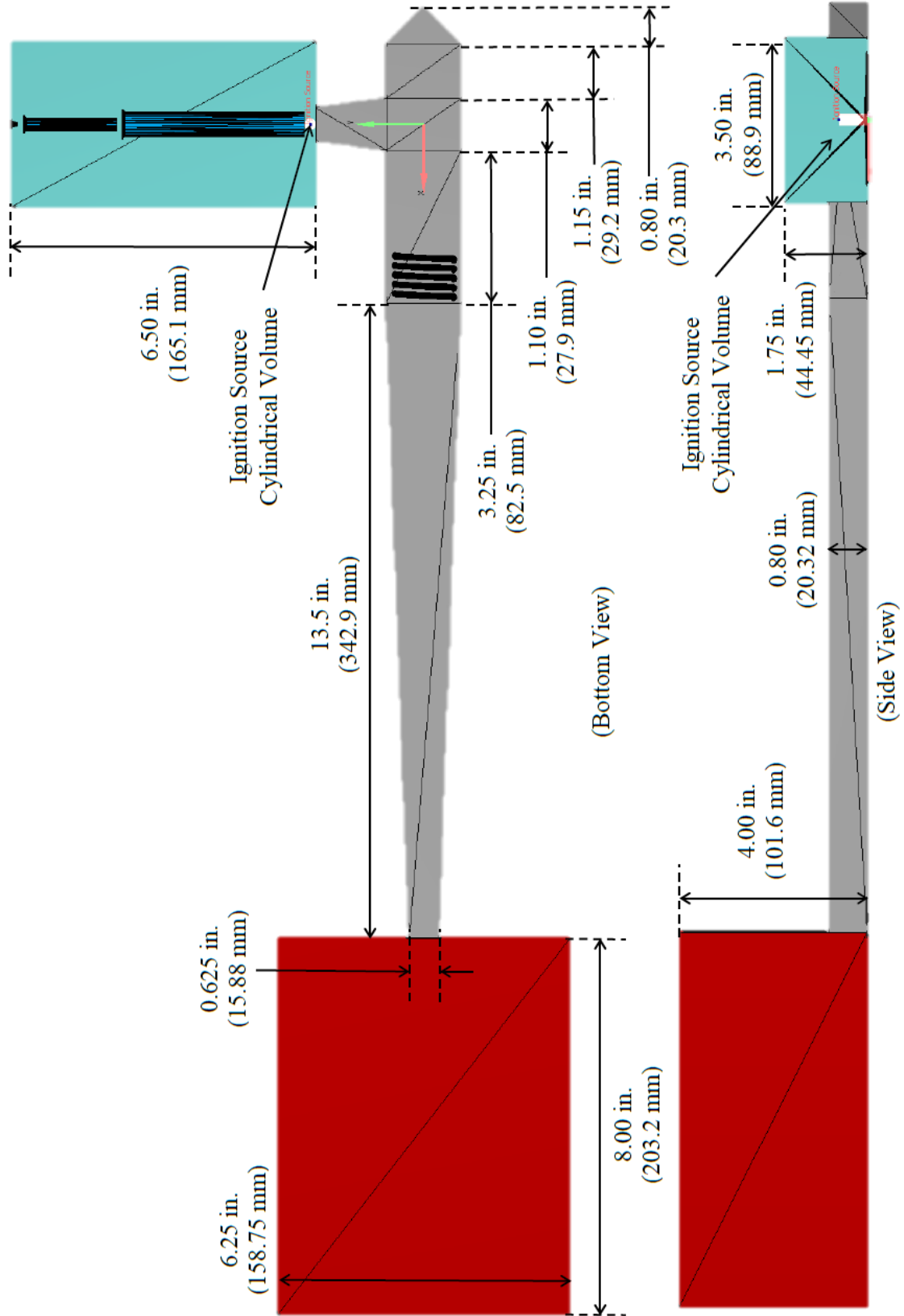


Figure 96: Engine and Boundary Geometric Dimensions (Bottom and Side Views with Symmetry Boundary Hidden)

As in the physical engine, the core engine geometry is rectangular, including the third-stage inlet. With the exception of the third-stage inlet, the engine chamber (including the head, core, and exit nozzle) has a continuously level, flat edge intended to allow the best sideward profile for imaging in the physical experiment. The first- and second-stage inlets are circular and flared to increase their inlet efficiency. This general geometry is shown in Figure 95 while major dimensions are shown in Figure 96.

The intake ambient volume extends two third-stage inlet hydraulic diameters ($ID_3 = 0.70$ in. = 17.8 mm) horizontally and vertically from the inlet. The exhaust ambient volume also extends horizontally and vertically by factors of the exit size. The physical engine's exhaust has an exit area of one square inch, set by a total height of 1.6 in. (40.64 mm) and a width of 0.625 in. (15.88 mm) corresponding to a hydraulic diameter of 0.90 in. Note that the symmetry plane splits the engine height in half so the exit height in the model geometry is 0.8 in. (20.32 mm). Comparatively, the computational exhaust volume totals ten exhaust widths wide, and four exhaust heights tall (from the symmetry plane), a total area of 25 in.² (161.3 cm²). Recall, the actual exhaust area of the engine being modeled is much smaller – just 0.5 in.² (3.23 cm²) which equates to 1/50th the computational ambient exhaust area. The exhaust volume is five exhaust heights long.

These figures also show the comparatively small ignition source which is represented geometrically as a stationary cylinder 0.25 in. (6.35 mm) in diameter and 0.63 in. (16 mm) tall positioned between the second- and third-stage inlets corresponding to the location where the physical engine is started with a small, handheld butane torch. The ignition source does not affect the flow until 100 ms (approximately the earliest the engine was considered to be sufficiently full of mixed fuel and air) when heat is added to the cylindrical volume that rapidly increases the local temperature resulting in spontaneous combustion.

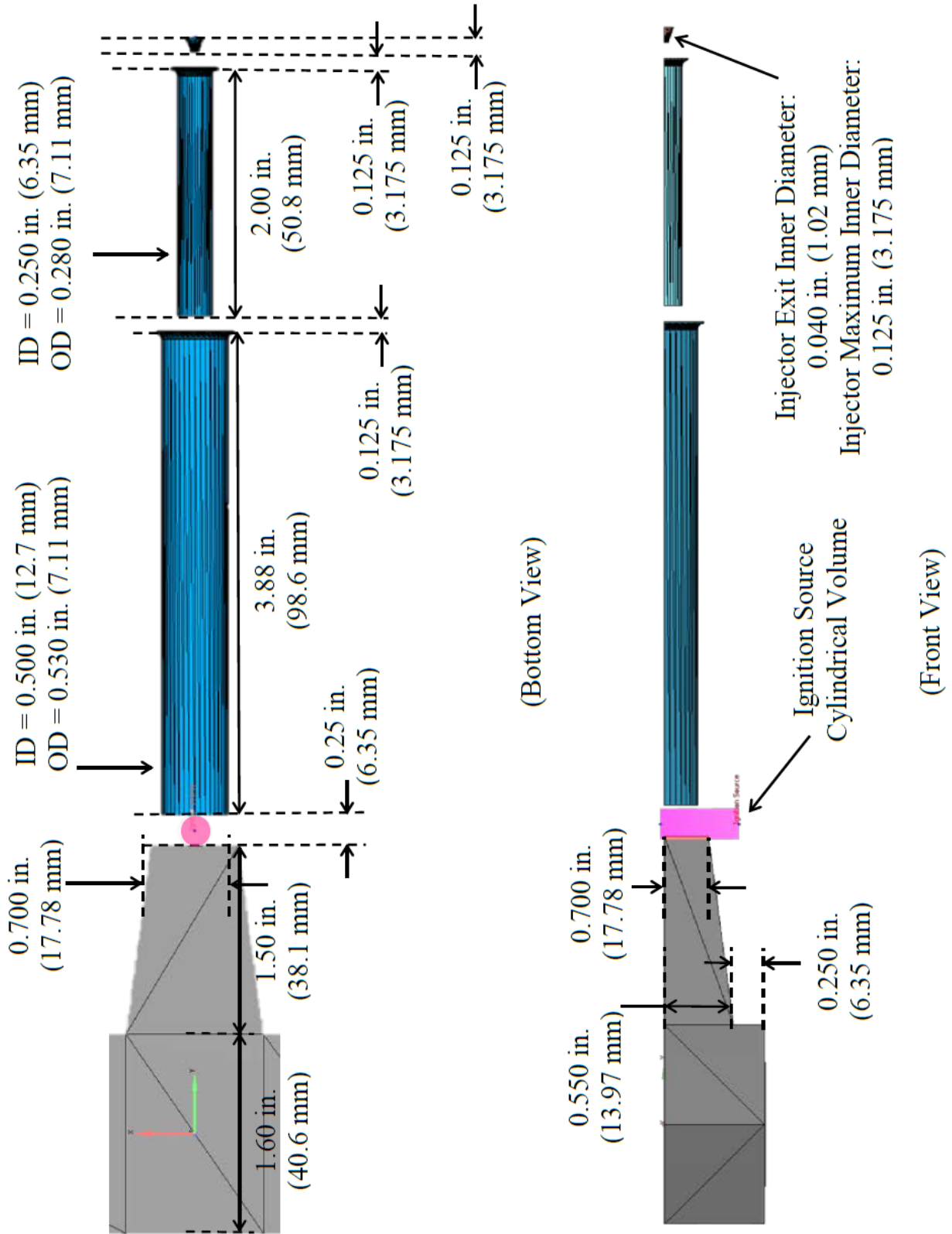


Figure 97: Engine Injector and Inlet Geometric Dimensions (Bottom and Front Views with Intake and Exhaust Ambient Boundaries and Symmetry Boundary Hidden) Including the Ignition Source Volume

This ignition volume is further visible in Figure 97, which also provides further detail to the roughly-tuned inlet geometry. The reader is reminded that these dimensions follow first from early closed-form approximations (Chapter II, Section B) and later from iterative bench testing of the physical engine intended to maximize the resonance (judged by the resultant noise level), heat (judged by incandescence and temperature), and stability. Of particular importance is the location of the inlets with respect to both the injector and the back wall of the engine core (from which the resonating pressure waves are formed). These locations were found by finely adjusting their linear position while the engine was in operation. Moving the inlets by as little as 0.1 in. (2.54 mm) was enough to disrupt the engine's resonance.

2. Pressure Jet Model CFD Parameters

The CFD model parameters are generally separated into two types – global properties tied to the entire computational domain (what the CONVERGE software refers to as the ‘region’) and properties introduced by boundary conditions. The boundaries were shown graphically earlier in Figure 95 and the inlet geometry in more detail in Figure 97.

The pressure jet model was defined as a transient, compressible gas simulation with combustion modeling, and a source/sink to enact ignition. The grid was defined with both fixed embedding (tied to the defined geometry) and adaptive meshing (tied to local temperature and propane concentration). The default Prandtl (ratio of kinematic viscosity to thermal diffusivity) of and Schmidt numbers (ratio of kinematic viscosity to mass diffusivity) of 0.90 and 0.78, respectively, were used. The numerical tolerances were also left at their default values: 1×10^{-4} for momentum, density transport, species, and specific internal energy, and 1×10^{-8} for pressure. Mass-averaged parameters were written to data files at every calculated time step while full 3-D distributions (used to generate data visualizations) were written every 0.1 ms. The engine region

was initialized with air (defined as mass fractions of 23% O₂ and 77% N₂) at standard temperature (300 K) and pressure (101,325 Pa) at zero velocity and initialized the default levels of turbulent kinetic energy (1.0 m²/sec²) and turbulent dissipation (10.0 m²/sec³).

The turbulence model was a Large Eddy Simulation (LES) using the default Viscous 1-Equation model and default recommended constants for a wall model and the LES. The combustion model for the reduced mechanisms relied on CONVERGE's built-in SAGE detailed chemistry solver. Again, default settings were used including a minimum cell temperature (used to define which cells were hot enough to require combustion modeling) of 600 K and a minimum fuel species mole fraction of 1×10^{-8} . The ignition source was determined based on the butane torch's published heat output of 2500 btu/hr (732.2 J/s). Assuming the energy is released over a 50 ms time interval (from 0.100 sec to 0.150 sec simulation time) this resulted in 36.6 J. The maximum temperature of the ignition source volume was limited to 1970 K.

The base grid size was set to 50 mm in all three dimensions (x , y , and z). This is the fundamental grid from which all others are subdivided and as such represents the coarsest grid level. In practice, this coarseness is only seen on the furthest edges of the ambient boundaries. Fixed embedding reduced this base grid on the engine walls to a scale of 5 for two layers. That means the base grid of 50 mm cubes is subdivided five times (to a new size of 1.56 mm) and extends two layers of this new size from the wall. The injector has the finest grid size being subdivided from the base seven times to a size of 0.39 mm. This was the coarsest grid that could still resolve the injector area. Testing of simulations with a further subdivision (to a size of 0.195 mm) showed better modeling of the supersonic injection, but this excessively increased the time to solve a time step. The first- and second-stage inlets (like the engine walls) were subdivided five times to a size of 1.56 mm. Lastly, the engine coil required slightly more definition, being

subdivided six times to a size of 0.78 mm). The AMR scheme was sensitive to the local temperature (with an embedding value of 2.5 K and scale of 7) and propane mass fraction (with an embedding value of 0.001 and a scale of 6). The grid was limited to 200,000 cells intending to reduce computational time. Estimates from test simulations using more cells than this resulted in prohibitively long runtimes on the order of months.

The boundary conditions were set as follows. The wall boundary type (using a law of wall definition for velocity and temperature) with an initial boundary temperature of 300 K was used for the injector, inlet, and engine walls. It was also applied to the internal engine core intended to act purely as a flow obstruction matching the physical engine to approximate the effect on the internal flow of an operational fuel heating coil. A symmetry boundary was defined along the centerline plane of symmetry to reduce computational time. The intake ambient volume boundary was defined as an intake boundary with air at a specified pressure (110,000 Pa) and temperature (300 K). The elevated pressure was necessary to reach a favorable equivalence ratio in the engine for continuous operation. The velocity condition was defined with a zero normal gradient (von Neumann) condition. The exhaust volume was defined as an outflow boundary with air also at standard pressure (101,325 Pa) and temperature (300 K) for backflow conditions. Lastly, the injector was defined as an inflow condition set to match measurements for operation of the engine. The pressure at the boundary was set to 50 psi (344,738 Pa) and an elevated temperature following the decoupled preheat coil of 420 °F (488.7 K) measured on the engine test stand (discussed in Chapter V, Section B). The resulting pressure differential ($P_{INJ}/P_0 = 3.13$) is more than sufficient to choke the injector flow. Lastly, the species defined at the boundary were set to a mass fraction of 100% propane. This resulted in a hot, gaseous, pure propane injection via a choked orifice as is used on the physical engine.

3. The Validity of a Symmetry Boundary Assumption

The BGX prototype (like the original Gluhareff pressure jet) engine geometry exhibits an inherent plane of symmetry which was exploited in the CFD simulations to reduce the time necessary to complete a simulation run. Modeling the engine in this way effectively reduces the number of cells to solve to convergence in half and is frequently used in computational works where the geometry being studied has a reasonable plane of symmetry through which little to no flow transits.

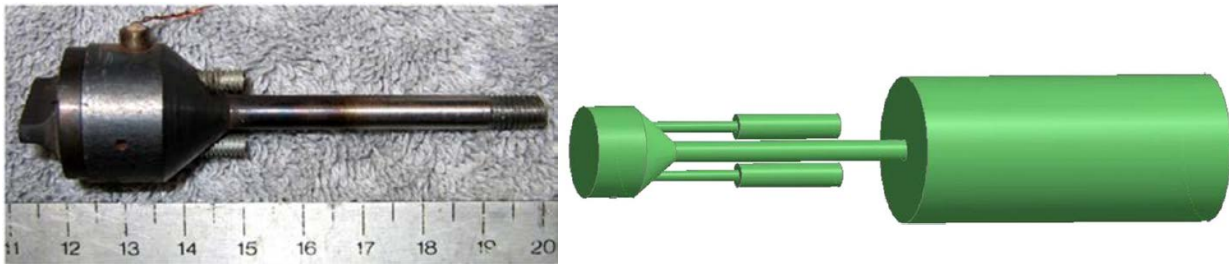


Figure 98: Example 8 cm Long Subscale Valveless Pulsejet Engine and Corresponding 3D CFD Domain Analyzed by Geng [30, 32]

Linear pulsejets and ramjets with circular cross-sections have made this sort of simplifying assumption before to allow computational analysis in two-dimensions (See Benelli, *et al* [284], Zhonghua [285], and Qian, *et al* [286]) or even one-dimension (see Ponizy, *et al* [287], Keller, *et al* [288], and Wan, *et al* [289] for instance). Most modern jet studies either modeled a thin slice of radial symmetry (see Zheng [33]) or the full 3D domain (see Geng [6, 30-32, 290], Isac, *et al* [291], and Möller and Lindlölm [292]). Meng, *et al* [293] recently published an extensive review of the state of the art in pulse combustion modeling and current challenges in research and development which summarizes many of these efforts in more detail. The latter is best capable of capturing the full 3D flow irregularities which are not necessarily symmetrical in nature allowing investigation of engines without a radial or even central plane of symmetry. This approach, however, likely requires more computational time.

These studies were primarily concerned with engines that have a single, straight, axis of symmetry. The flow through the pressure jet design is different, including a right angle turn of the flow (with some fluid expected to initially flow forward as opposed to downstream toward the exit). As a result, the engine has two perpendicular centerline axes – one for the intake flow and the other for the exhaust flow. The most similar common case is that of fluid pipe flow studies through a 90° bend. This concept has been studied extensively and the use of symmetry conditions in computational efforts is similarly varied.

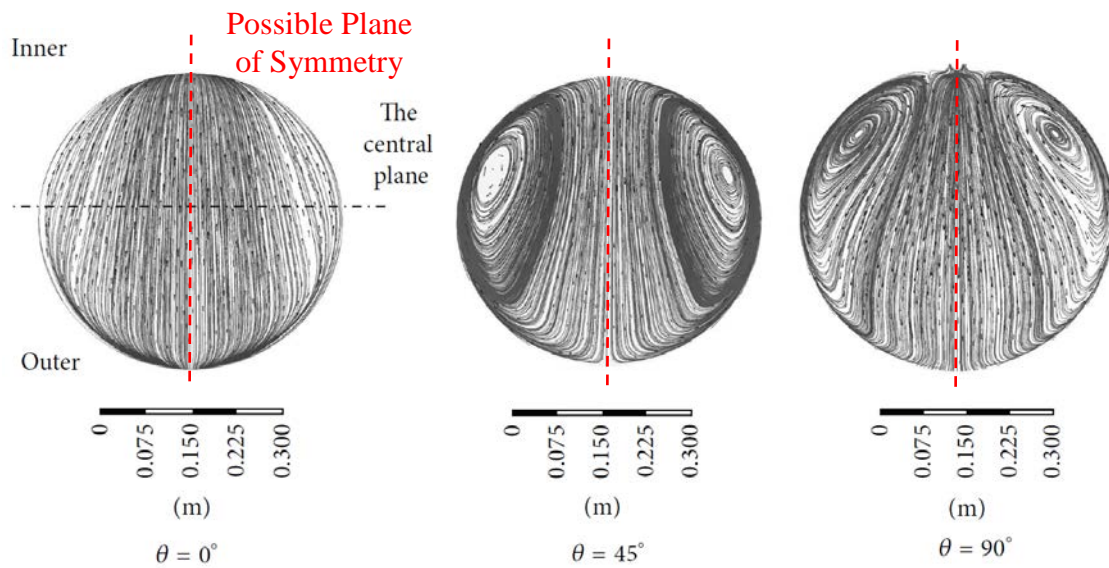


Figure 99: Symmetrical Flow Circulation in Circular Pipe Flow Through a 90° Bend as Shown in Full 3D CFD Simulations by Wang, et al [294] (Re = 20,000)

Pipe flows through a 90° bend have long been known to result in fluid circulation of some kind [294-304] likely as a result of centripetal acceleration of the fluid through the turn. Where studies appear to differ is in the patterns of circulation that form under different circumstances. A recent study by Wang [294], for instance, used no symmetry assumptions and produced circulation flow patterns which exhibited clear symmetry about a possible flat plane for a range of Reynolds numbers between 5,000 and 20,000.

This flow pattern (shown in Figure 99) is indicative of “Dean Flow” named for William Dean who first discovered and characterized the phenomena [303, 304]. This type of flow is characterized by the Dean number, D_n :

$$D_n = Re \sqrt{\frac{d}{2R}} \quad (71)$$

Which involves the fluid Reynolds number, Re , the pipe constant diameter, d , and the pipe’s radius of curvature, R . Qualitatively, this represents the strength of secondary flow (like the circulation shown above) through the pipe turn [302]. The inclusion of the Reynolds number accounts for the role of inertial and viscous forces with a Reynolds number of approximately 400 signifying the transition from laminar to turbulent flow [301]. The phenomena was directly studied by Ilori, et al [301] as recently as 2015 with a 3D CFD analysis. This study (which did not rely on a symmetry assumption) showed that secondary flow exhibited symmetry for larger bend radii but this was less evident in tighter turns.

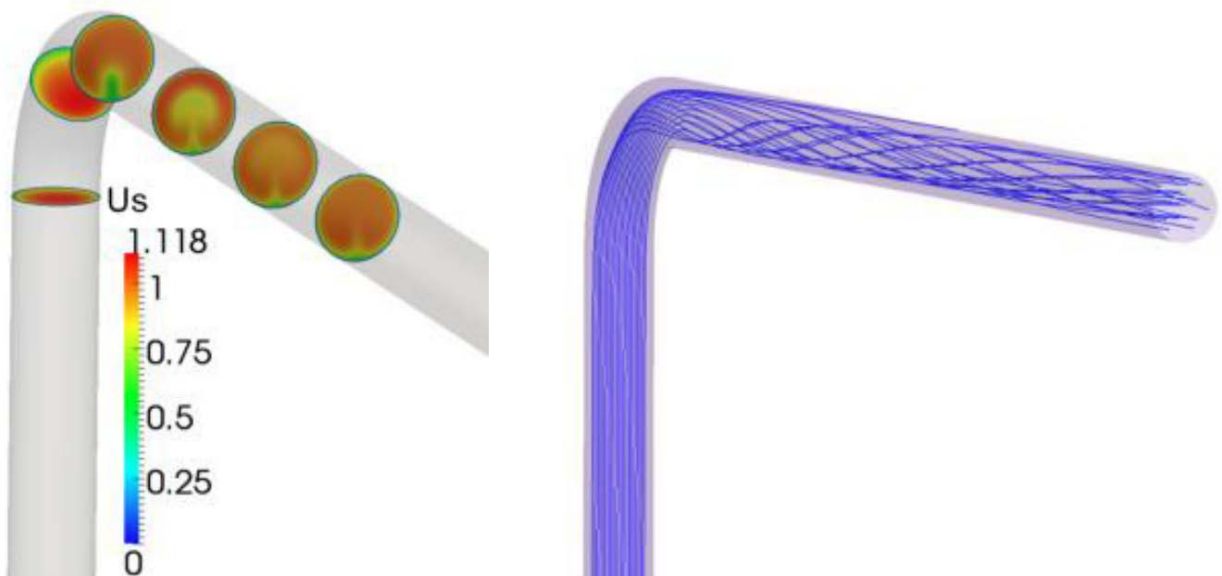


Figure 100: Computational Simulation by Kim [297] of a Fluid Pipe Flow Experiment Published by Sudo [305] Exhibiting Three-Dimensional Turbulent Swirl ($Re = 60,000$)

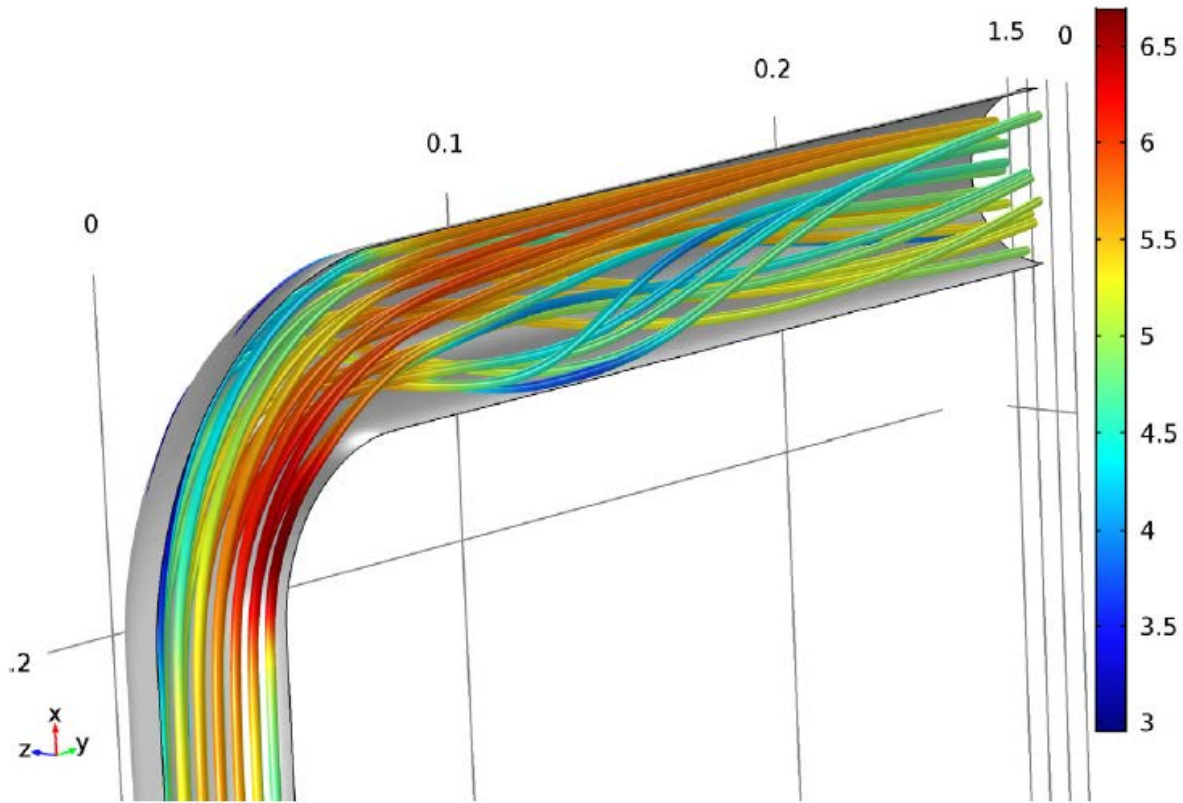


Figure 101: High Reynolds Number ($Re = 545,000$) Turbulent Pipe Flow with a Symmetry Plane Boundary Assumption in COMSOL Multiphysics Solver [296]

Another recent CFD turning pipe flow study by Kim (also without a symmetry assumption) tested different turbulence models. The simulation shown in Figure 100 appears to show good symmetry in cross-sectional visualizations of fluid speed, U_s , however, streamlines through the pipe show a swirling fluid which could not be captured accurately by a symmetrical boundary condition. A similar pipe flow used as an educational example for the COMSOL Multiphysics Solver [296] instead applied a symmetrical boundary condition and produced the similar streamline paths shown in Figure 101. The use of a symmetrical boundary condition in this case has biased the flow in such a way that what is likely a full-volume swirl phenomena (as shown in Figure 100 and experimentally validated) is instead represented as split swirling cores mirrored on either side of the symmetry boundary. The example is possibly misrepresenting the flow in the pipe as having

two mirrored swirls which may in reality be an artifact of the symmetry assumption. Modeling the pipe in quarters could erroneously predict four of these mirrored swirling cores downstream of the 90° pipe bend.

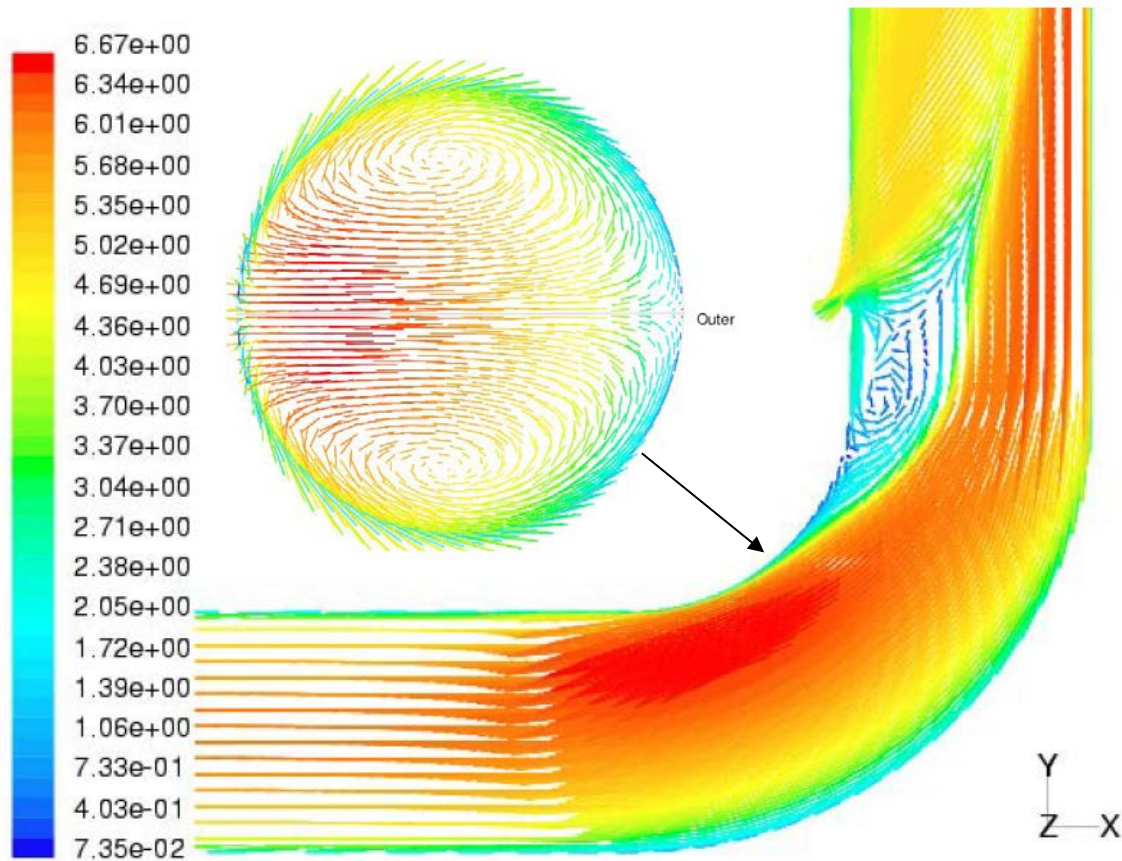


Figure 102: Symmetry Plane Velocity Vector Distribution from a CFD Simulation of Liquid Water Pipe Flow by Homicz (Re = 54,000) Showing *Assumed* Mirrored Recirculation Through the Pipe [300]

Nevertheless, studies like Homicz's [300] for Sandia National Laboratories in 2004 are able to produce useful results and qualitative study of corrosion and erosion in simulating this type of flow with a symmetry assumption. Flow downstream of the bend was not discussed in detail, where more regular full-volume swirl would likely appear. The study was generally more occupied with comparing turbulence models and wall effects but successfully produced flow separation on the leeward side of the pipe bend.

So it is clear that although the symmetry plane assumption does limit some aspects of the relevance and validity of the resulting flow field, it does not wholly invalidate the model or its utility. The use of a symmetry plane also does not prevent the formation of circulation patterns. We should simply be cautious in assuming that such flow structures are actually mirrored across the symmetrical plane in reality. Keeping this in mind, it was considered acceptable to trade this potential for error in exchange for a significant reduction in the simulation runtime subject to future research taking the successful simulations presented here and modeling them without the symmetry assumption to show what effect it has.

V. Experimental Setup

A. Engine Manufacturing Process

The engines are designed to be folded in a method reminiscent of classical Origami papercraft using a sheet of 302 stainless steel with a thickness of 0.005 in. This material was chosen for several reasons. First, this is similar to the 321 stainless steel used by Eugene Gluhareff in the original pressure jet design (albeit at a greater thickness). Second, the sheet can be easily bent into the necessary shapes to form the engine geometry allowing rapid prototyping of the engine's components. Lastly, it has many desirable material properties – it can withstand high temperatures, it is weldable, does not rust easily, and is readily available.

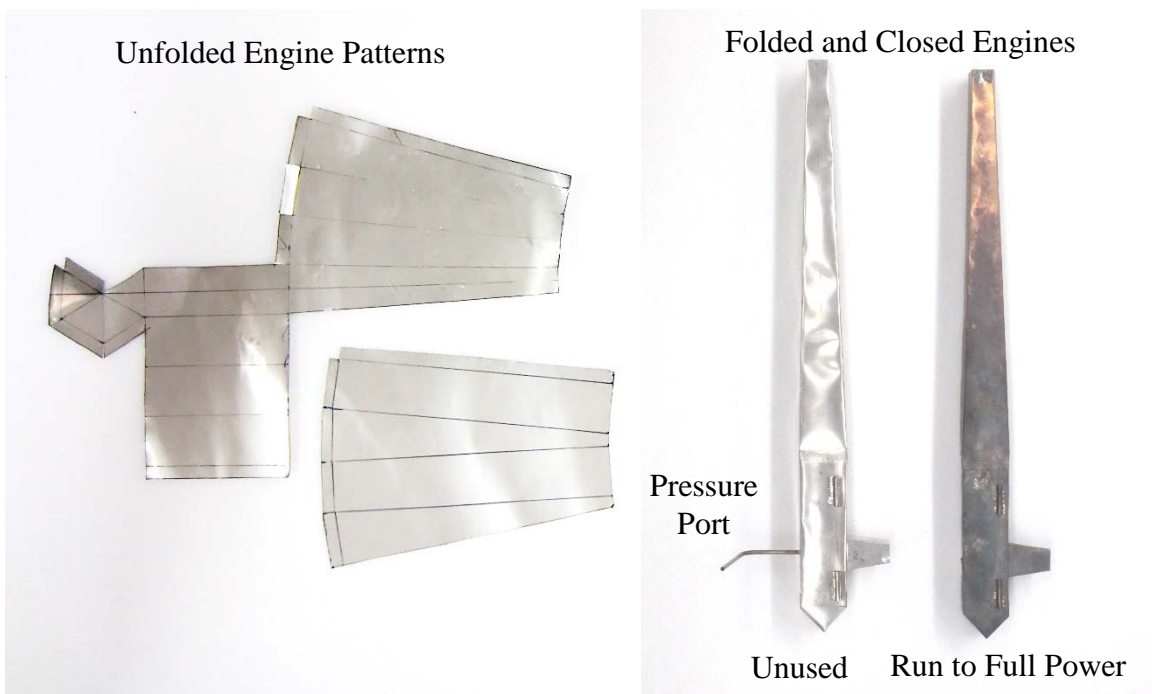


Figure 103: Example Scale Pressure Jet Engine Unfolded Patterns (Left) and Folded and Closed Engines (Right)

The process of making an engine involved first laying out the unfolded footprint in four pieces – the third-stage inlet, the engine head, the main combustion chamber, and the exhaust

nozzle. These components are shown in their flat forms in Figure 103. Arranging the layout in this way allows some minor mass-production of parts with some level of interchangeability such that, for instance, a short combustor can be tested with nozzles of various lengths. The stainless steel was thin enough to be cut with conventional scissors leaving clean edges. Edges were bent on an aluminum tool with a sharp right edge that produced crisp folds in the stainless steel sheet.

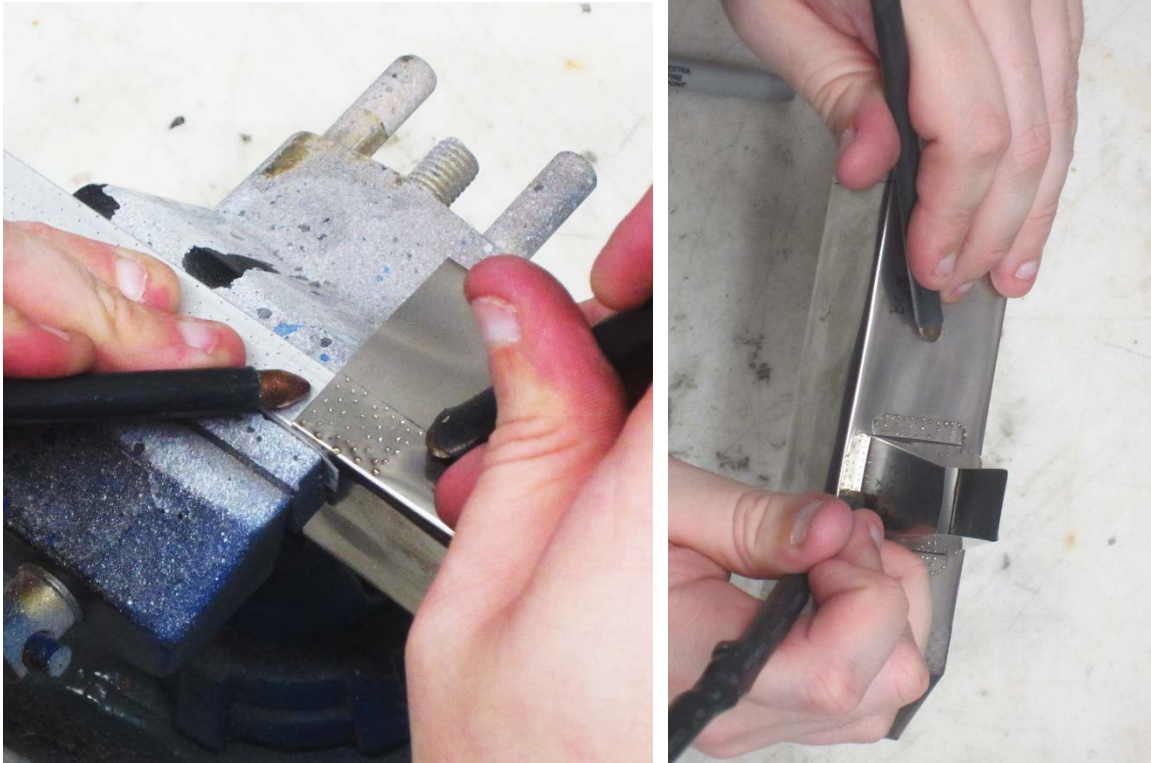


Figure 104: Engine Assembly Method Using Thin Sheet Steel Spot Welder. Closing Engine Core (Left) and Attaching Third-Stage Inlet (Right) Showing Use of the Grounding Contact and Welding Contact

The sheet metal seams were closed and bonded using an electrical arc spot welder as shown in Figure 104. No readily available bonding materials (resins, tapes, etc...) were known to withstand temperatures in excess of 2000 °F leaving spot welding as the only remaining possibility. Gluhareff's production engines were carefully TIG-welded for the same reasons. Spot welds were placed approximately every 1/16th in. in a diagonal offset pattern. All edge flaps were cut to ½ in. in length after testing of the engine with ¼ in. flaps were prone to fatigue. No such fatigue problems

were encountered after increasing the size of the flaps to ½ in. Closing the engines was done over a cantilevered aluminum tool. Aluminum was chosen because it is conductive enough for current flow but has comparatively poor weldability allowing easy removal of the welded part even if a fraction of the spot welds tack the engine to the tool. The tool was small enough such that when the engine was finally closed, the tool could be pulled back out of the engine nozzle.



Figure 105: The Inert “Dummy” Heating Coil Made of 1/8th in. Stainless Steel Rod Stock Prior to Installation in an Engine (Left) and as Installed in the Engine (Right)

Early testing of the engine showed that the use of a “dummy” inert heating coil (shown in Figure 105) had a significant effect on the maximum injection pressure possible. The inclusion of such a coil allowed the injection pressure to be raised by 5 - 10 psi which directly increased thrust. Therefore, the effect of the coil on the processes occurring in the chamber of the original Gluhareff Pressure Jet engine cannot be ignored. For this reason, an inert representation of the heating coil was included in the engine. It is not expected to perfectly recreate the heat transfer of the original engine (which used this coil to preheat fuel for injection) but simply to affect the flow like a rudimentary flame holder in conventional ramjets.

B. Engine Test Stand

The completed engine was mounted to an engine test stand designed to allow variation of the first- and second-stage inlet lengths and locations. This was accomplished using a length of 1 in. aluminum T-slot extrusion as a main rail and a set of four movable platforms. A diagram of the overall setup is shown in Figure 106.

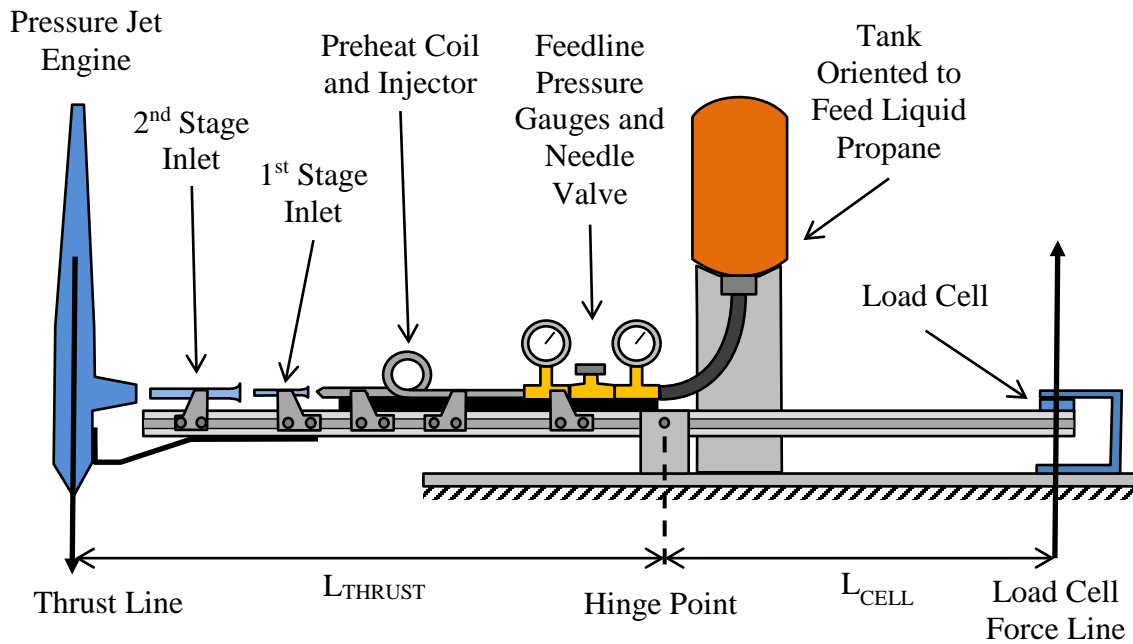


Figure 106: Side View Diagram of the Proposed Engine Test Stand (Not to Scale)

The first platform attaches to the propane injector allowing it to be adjusted between runs without changing the locations of the engine or inlets. This effectively allows adjustment of the sensitive spacing between the first-stage inlet and the injector that affects the level of initial air entrainment. The second and third platforms hold the first- and second-stage inlets, respectively. Lastly, the fourth platform allows attachment of the engine chamber with the final third-stage inlet permanently installed on the engine (as was also done on the original pressure jet). This arrangement allows the location of the engine, first- and second-stage inlets to be moved during engine operation while the propane injector is held in a fixed position as the reference datum. This

method enables fine-tuning of the engine's acoustic lengths in search of an optimum condition for an arbitrary configuration. This "sonic lock" condition is expected to result in maximum chamber pressure, thrust, and engine efficiency.

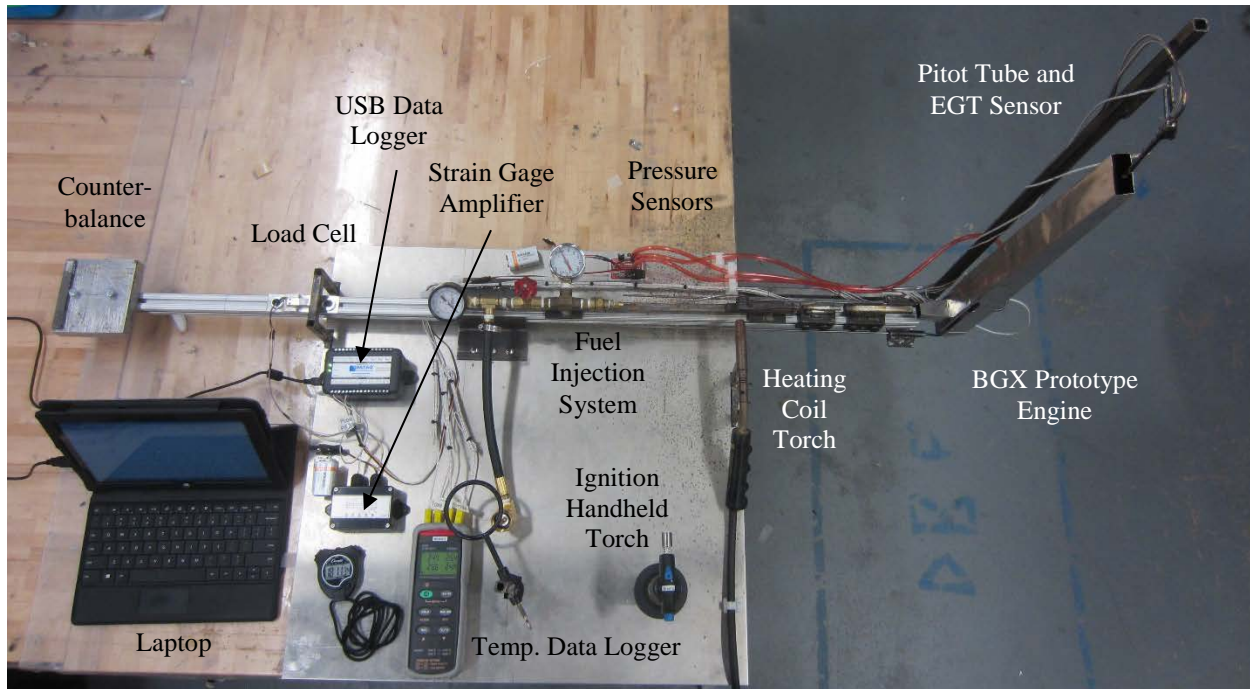


Figure 107: The Completed Engine Test Stand

The engine stand was also designed with instrumentation and reduction of error in mind. The main rail pivots on a movable hinge (via the side t-slot rails) so the hinge point can be adjusted as necessary to balance the weight distribution of the engine, inlets, and other hardware. A small counterbalance was also used to remove some static load from the load cell to bring it closer to its true zero load condition prior to firing the engine. The engine is oriented to produce downward thrust (to allow the hot exhaust upward away from the ground). The main rail is free to pivot due to this thrust force except for the resistance of a load cell to measure the force. Precise measurement of the moment arm between the thrust line (movable during operation), the hinge location, and the load cell (fixed at the opposite end) is necessary to convert the load cell's measurement to the actual engine thrust force via basic statics.

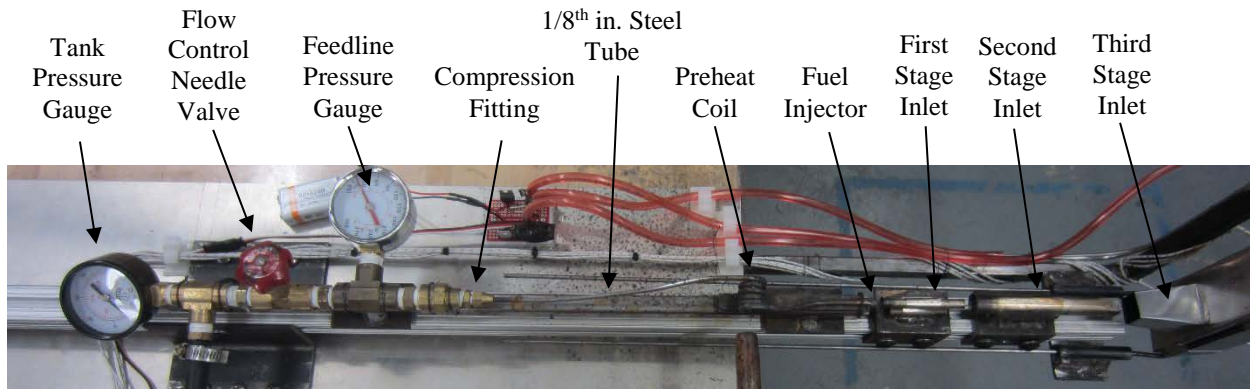


Figure 108: Thrust Stand Injection Rail Assembly As Installed on the Engine Test Stand

The only equipment not attached to the rail are the propane and propane accessories. The fuel feed line leaves the rail in a perpendicular direction near the hinge point to minimize any contamination in the thrust data from the stiffness of the feed line. The propane tank attaches to the feedline via an unregulated 1 in. -20 threaded female disposable propane tank fitting attached to a ¼ in. NPT (National Pipe Thread) elbow. The elbow connects to the thrust stand injector assembly using a ¼ in. NPT hose barb fitting plugged into an off-the-shelf propane extension hose cut to length and secured with a 9 – 16 mm stainless steel hose clamp. The propane hose’s fitting connects to a brass T-fitting that has a Winters brand PEM205 steel analog pressure gauge on one end (capable of reading up to 300 psi) and a needle valve on the end toward the injector. The needle valve is used to regulate the fuel flow to the injector and therefore the engine while the pressure gauge is used to record the available tank pressure. A second identical pressure gauge on the opposite end of the needle valve is used to record the injection pressure for matching to CFD simulations. This assembly is shown installed on the stand in Figure 108.

Following that is a brass compression fitting and the combination injector and heating coil formed out of 1/8th in. stainless steel tubing. The tubing was flared on one end to accommodate the compression fitting, wrapped around a ½ in. steel rod to form a 4-turn coil, and the injector formed from the remaining open end. The injector was formed using the necessary 0.040 in. diameter drill stock inserted into the tubing and the sides hammered down with a ball peen hammer

and flat punch tool until the edges were closed. The drill stock was then removed leaving an opening with an inner diameter fitted to the drill stock. The injector assembly was then fixed to a steel rail via steel safety wire. The rail was welded to two L-bracket pieces which bolted to the T-slot rail holding the entire assembly in place.

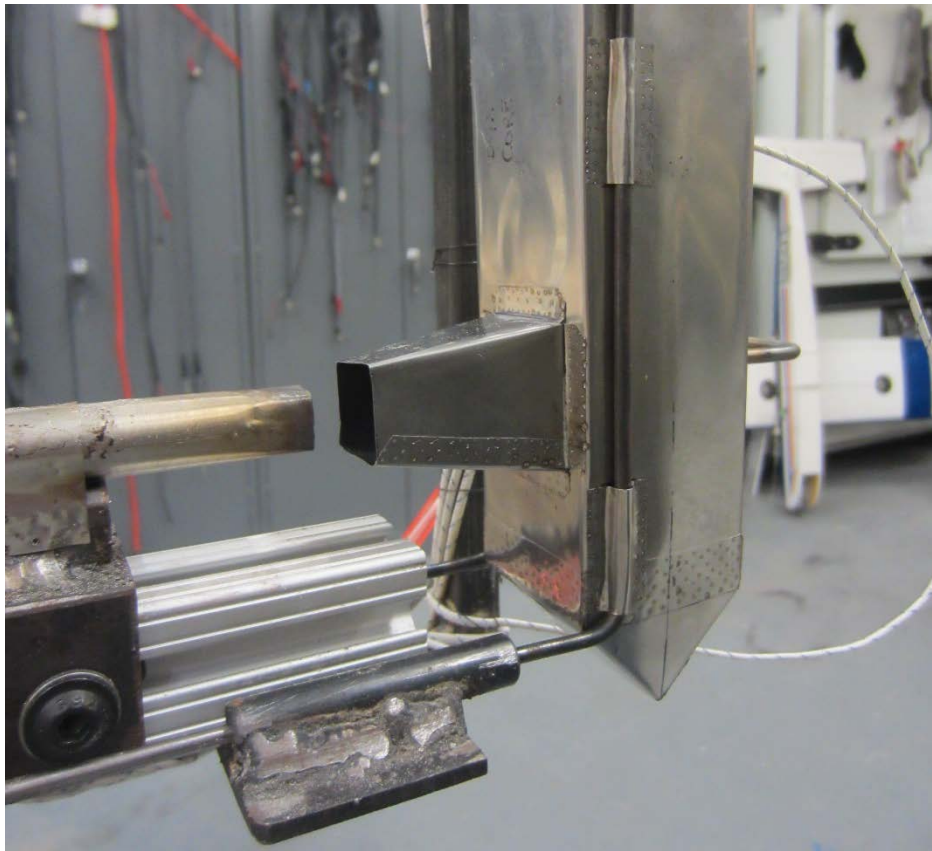


Figure 109: Engine Core Method of Attachment to the T-Slot Rail System

While the injector, first stage inlet, and second stage inlet are mounted directly to the T-slot rail, the engine core is attached via a separate rail. This rail consists of two 1/8th in. steel rods bent upward that fit inside a set of four slots added to the sides of the engine core held in place via a friction fit. The twin rods attach to the T-slot rail via two steel tubes welded to a plate, which bolts to the T-slot. The plate was fixed to the T-slot rail during operation while fine adjustments were made using the steel rods.

C. Instrumentation and Data Logging

The engine test stand includes support for pressure and temperature measurements, as well as fuel tank weight. Data was logged using a standalone DI-155 USB data logger manufactured by DATAQ Instruments. This data logger is capable of recording up to eight analog signals at 1,000 Hz [306] and was mounted to the engine stand's base plate with enough wiring lead length to not interfere with the free movement of the main rail or engine. Data was logged as raw voltages to be processed afterward with relations to convert the voltages into SI engineering units (Newtons, Pascals, etc...). Tank and feed line pressures were manually recorded as read from analog gauges. The weight of the propane tank was measured before and after a test run allowing a rough estimate of the engine's fuel flow rate enabling estimation of the engine's thrust specific fuel consumption.

1. Pressure Sensors and Voltage Relation

Three engine pressure measurements were taken in the form of constant location time-histories. The first is in the chamber (expected to be the maximum pressure in the engine). It was measured specifically at the stagnation point where the inlet flow impinges on the engine's back wall. This wall is also of particular interest because it is where the reflected pressure waves (which are expected to drive tuning and therefore "sonic lock" resonance) are initially formed. It was measured differential to the ambient air conditions in the lab at approximately 1 atm and 65 °F (291 K). The remaining two pressures were measured differentially via a conventional pitot tube at the nozzle exit providing the exhaust dynamic pressure. By assuming an exhaust density this produces an approximate measurement of exhaust speed and (for a given nozzle geometry) mass flow rate. This leads to a calculation of momentum thrust to compare with the load cell. The ambient atmospheric pressure was recorded for each test.

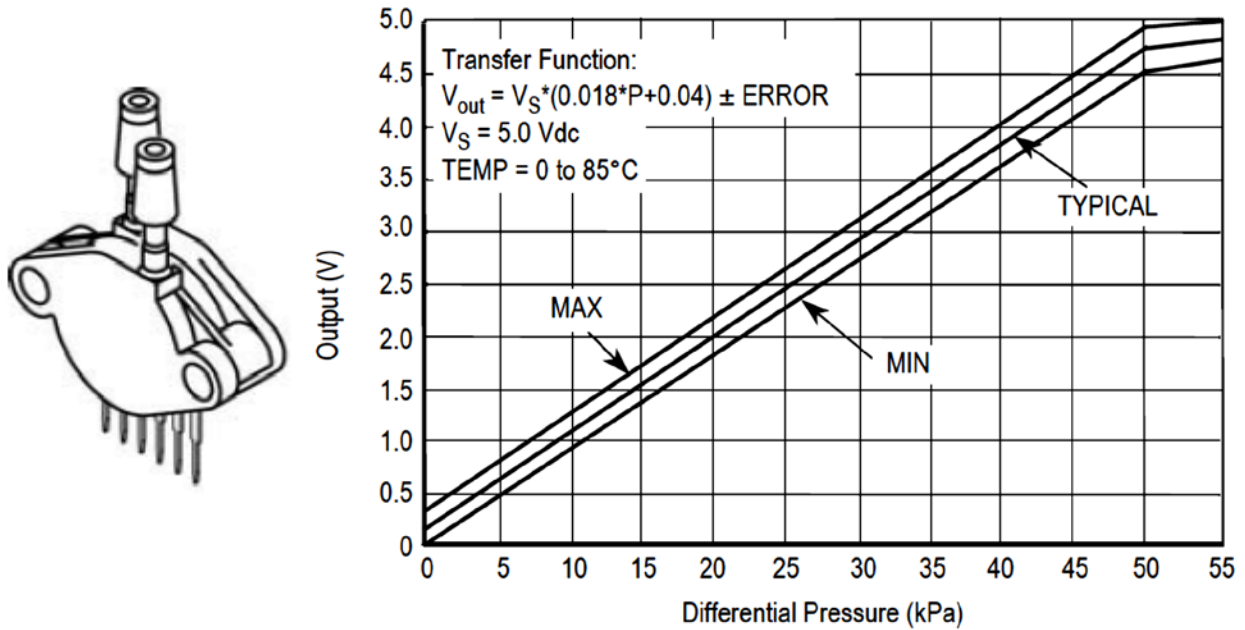


Figure 110: Physical Configuration and Output Voltage to Differential Pressure Relation for the MPX5050DP Pressure Transducer [307]

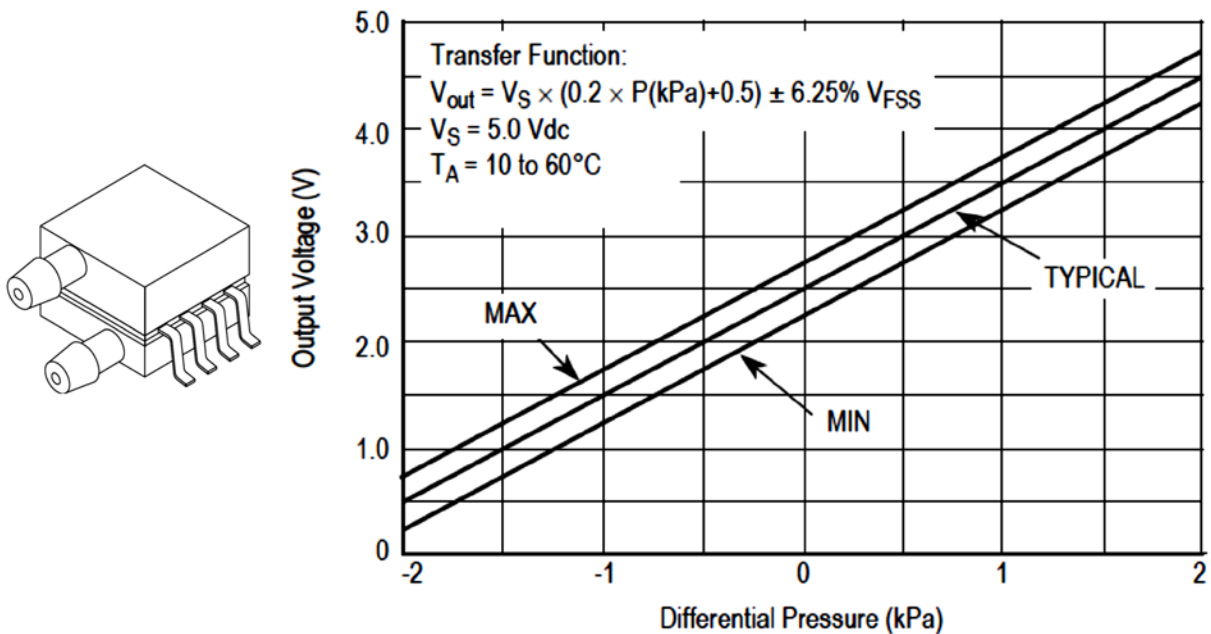


Figure 111: Physical Configuration and Output Voltage to Differential Pressure Relation for the MPXV7002DP Pressure Transducer [308]

The core pressure sensor (shown in Figure 110) is the Freescale Semiconductor MPX5050DP dual-port differential pressure transducer. The primary reason it was chosen was for its built-in signal amplifier outputting a 0-5 V DC analog data signal that is subsequently recorded

by the DATAQ data logger. It has an operating differential pressure between 0 and 7.25 psi (50,000 Pa) and an nominal response time (the time necessary to travel from 10% to 90% signal voltage) of 1 ms.

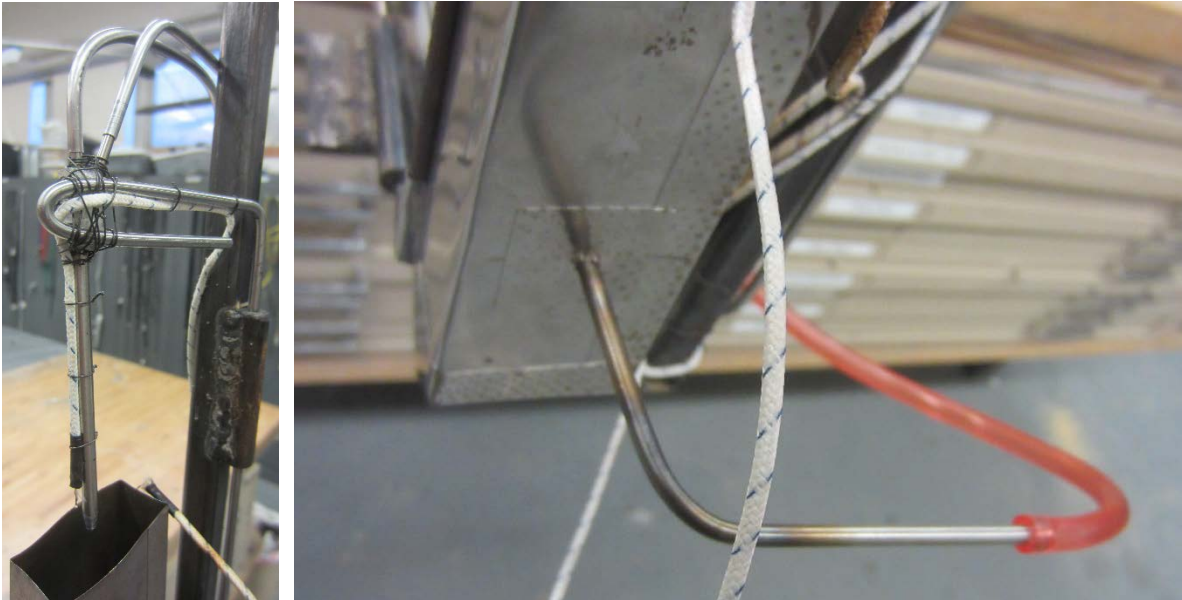


Figure 112: Engine Exhaust Pitot Tube Mounting Location with Coincident Exhaust Gas Temperature (EGT) Thermocouple (Shown at Left) and Engine Core Total Pressure Port with Stainless Steel Tube (Shown at Right) Prior to Firing

The pitot pressure sensor and pitot tube are sold together intended for use in measuring the airspeed of remote control aircraft. The set is specifically meant for integration into the Ardupilot Mega autopilot system. The pressure sensor used is the Freescale Semiconductor MPXV7002DP (shown in Figure 111) and operates slightly differently than the core pressure sensor. Although it outputs a signal between 0 and 5 V DC (readable by the DATAQ data logger), it has an offset of approximately 2.5 V DC and a much lower range ($\pm 2,000$ Pa, ± 0.29 psi). This is because high subsonic speeds actually produce a relatively low pressure differential. For reference, a pressure differential of 0.1 psi (~ 690 Pa) at sea level standard density corresponds to a speed of 75 mph or 110 ft/sec (120.7 km/hr or 33.5 m/s). This transducer also has a nominal response time of 1 ms.

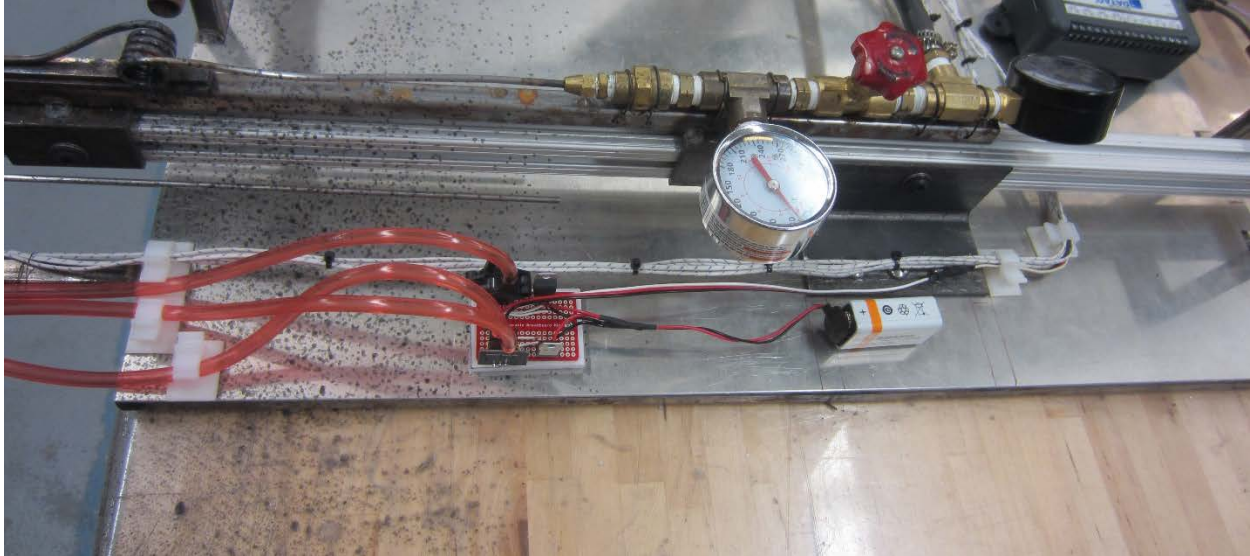


Figure 113: Location of Core and Pitot Pressure Transducers as Installed on the Pressure Jet Engine Test Stand

In regard to installation, two matters are of primary concern, both of which are related to the proximity of the transducer to the engine. The transducers must be as close as possible to the point of measure to reduce the time necessary for a pressure wave to reach the transducer element. Further length from the point of measure is also naturally expected to cause some level of signal attenuation. Ideally, the transducers would be mounted with no lead length. This would yield the fastest response time possible with the least pressure signal attenuation. Unfortunately this condition also results in the maximum temperature the transducer could encounter – a worst case at the engine core of approximately 2000 °F (1366 K). The transducers are intended to operate at temperatures no higher than 185 °F (358 K) for the MPX5050DP and 140 °F (333 K) for the MPXV7002DP. Beyond these temperatures, the temperature compensation error grows significantly and at temperatures beyond 257 °F (398 K) for the MPX5050DP and 212 °F (373 K) for the MPXV7002DP damage to the transducers may occur. [307, 308]

Therefore, it is clear that the transducers must be located as close to the engine as possible to reduce signal loss but far enough away that radiant and convective heat transfer does not produce

significant signal error or physical damage. This tradeoff resulted in the locations shown in Figure 113. Both transducers are soldered to a project circuit board that feeds them individually with a constant 5 V DC signal via a Texas Instruments UA7815C model 5 V DC regulator and an off-the-shelf alkaline 9 V DC battery. The board is held to the thrust stand via a foam plate standoff (to prevent shorting of soldered leads) and two machine screws through the stand's aluminum top sheet. Silicone fuel line hose with an inner diameter of 1/8th in. is used to connect the pressure transducers to the 1/8th in. outer diameter stainless steel tube that can withstand the high temperatures where the pressures are recorded.

2. Temperature Sensors and Camera Equipment

Four temperatures were recorded using Type K thermocouples and an independent temperature data logger. The temperature inside the chamber was measured near the pressure measurement. A second temperature measurement was made at the engine exhaust coincident to the Pitot tube's location. This provides an exhaust gas temperature during the engine's operation. The remaining two temperatures were measured on the engine surface – one over the center of the engine and the other on the surface of the nozzle. These two temperatures are used as data anchor points allowing temperature contours to be drawn from images of the engine in operation. The response times of the thermocouples was expected to be much slower than that of the pressure transducers and were used only for quasi-periodic analysis.

The thermocouples are standard Type-K with a glass braid and wire bead to withstand high temperatures and the typical two-pronged connector used for connection to digital thermometers. The temperatures were recorded using a Sper Scientific model 800024 4-channel datalogging thermometer at the maximum data rate of 1 Hz. The internal memory can store up to 16,000 points of data for each channel logged [309]. Data is then transferred to a computer via a proprietary

RS232 serial connector and saved using the manufacturer's "Computer Linking Software." A standalone logger (instead of integrating the thermocouples with the DATAQ logger) was used for several reasons. Thermocouples require expensive compensation circuits and their signals must then be amplified in order to be recorded as a typical DC voltage like that expected by the DATAQ logger. The use of four thermocouples rapidly increases the cost and complexity of such an architecture. Instead, the datalogging thermometer does all of this natively saving time, cost, and complexity.



Figure 114: Sper Scientific 800024 4-Channel Datalogging Thermometer with Four Labeled Type-K Thermocouples Corresponding to Different Locations On and In The Pressure Jet Engine (Temperatures are in deg F and Shown Reading Room Temperature)



Figure 115: Thermocouple Installation Methods: Core Surface “Pocket” and Internal Core (Left), Nozzle Exit Surface “Pocket” (Middle), and Coincident to Pitot Probe (Right)

Thermocouples were fixed to the Pitot tube armature with ample slack (to minimize mechanical interference with the load cell thrust data). The surface temperature thermocouples’ wire beads (the point at which the thermocouple measures local temperature) were fit into small stainless steel “pockets” spot-welded to the outer surface of the engine. These pockets served to restrain the bead against the surface of the engine at the point of interest. They were located on the side of the engine opposite the side being imaged such that the additional wall thickness and thermocouples did not affect the images. This relies on the assumption that the plane of symmetry (exploited in the CFD model geometry) does actually hold and that the surface temperature is the same on both sides. In practice only minimal variation was seen from one side to the other. Most variation was seen instead along the engine length.

A Canon PowerShot ELPH 300 HS “Point and Shoot” camera (confirmed to be sensitive to at least some portion of the IR-spectrum) was used to capture video of the engine startup,

operation, and shutdown in the interest of correlating image intensity to engine surface temperature. The camera was mounted to a tripod and video was recorded in both visible light and through a Neewer-brand IR-pass filter. The IR-pass filter blocks the majority of visible light wavelengths while passing wavelengths above 720 nm. This had several advantages. First, it was found to reduce the amount of overexposure of the engine glowing at full temperature allowing better resolution of regions immediately around the highest temperatures. The filter also had the effect of darkening unwanted parts of the image (background areas) to the point that they were not detectable in the video. This was particularly helpful in processing images from the video to correlate image intensity to surface temperature.

It should be noted that the 720 nm filter does pass a small amount of visible red light. Testing of an IR-pass filter which blocked wavelengths up to 760 nm (the next option available) appeared to pass no visible light. However, it also showed too much attenuation of the image and its use would result in an unnecessary reduction of data.

3. Load Cell and Calibration

The test stand's thrust measurement was made using a load cell scavenged from an off-the-shelf electronic desk scale with a maximum mass of 1000 g and a resolution of 0.1 g. The load cell was mounted on one end via resin epoxy to an adjustable plate allowing the load cell's movement along the thrust stand's T-slot rail. The opposite free end of the load cell bears the force of engine thrust against a 0.5" square steel tube welded arch piece that stands above the rail. Downward thrust force from the engine is transferred to upward force against this arch and a downward force on the load cell.

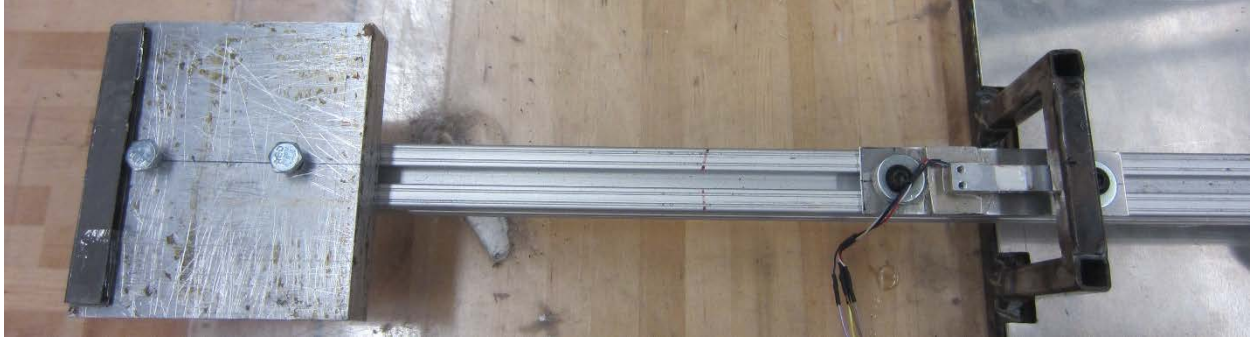


Figure 116: Aluminum Block Counterbalance (Left) and Load Cell (Right) Mounted on T-Slot Rail with the Load Cell Force Applied by Steel Arch

Because the fulcrum of the engine stand is not at the system center of gravity, without a counterbalance the load cell would bear significant rest load. To prevent this unnecessary corruption of data an aluminum block was mounted to the end of the t-slot rail opposite the engine to unload the load cell for all but less than 1 g of force prior to operation as shown in Figure 116. This effectively moves the rail system’s center of gravity nearly to the fulcrum point.

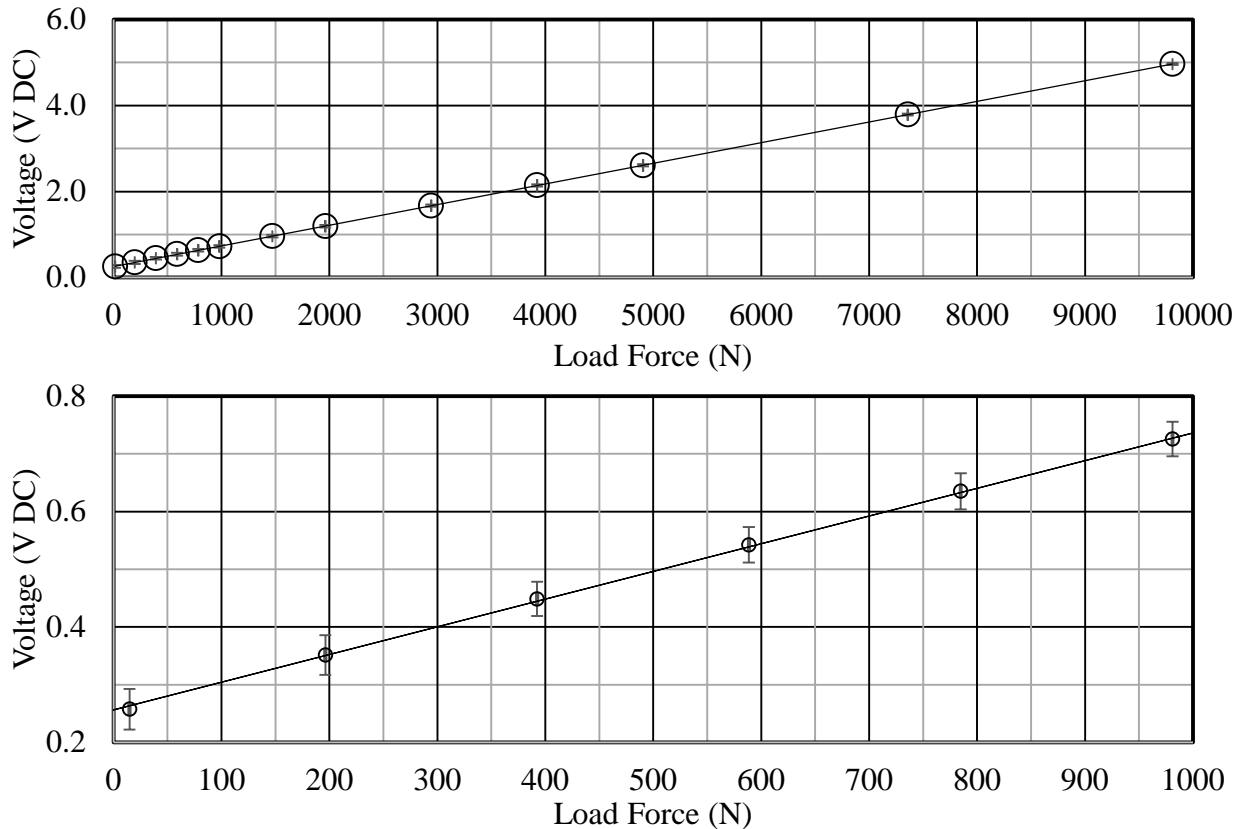


Figure 117: Engine Stand Load Cell Calibration Curve Full Range (Top) and Zoomed in to the Below 1000 N Range (Bottom)

The load cell was calibrated with all sensors and hoses installed by placing calibrated masses on the engine centerline and recording the resulting steady-state voltage reading from the load cell via the data logger. The resulting calibration curve checking the relationship between load cell voltage (output by the strain gage amplifier) and applied force on the thrust line is included in Figure 117. It is clear that the test data from the load cell as installed showed strong linearity at both low load levels and up to the maximum rated load. Each data point was taken as the mean of at least five seconds of data recorded at the maximum single-channel data rate used in testing – 3,333 Hz. One standard deviation from these means varied from as high as 0.035 V DC to as low as 0.023 V DC and are represented by error bars in Figure 117. Furthermore, because the engine was not moved after it was tuned to the locations used to model the engine in CFD (see Chapter IV-D) this also accounts for the difference in distance between the thrust line and the load cell's location. As a result, using this curve, the recorded voltage was related directly to the engine's thrust force.

D. Pressure Jet Engine Procedures

The following section briefly details the procedures for safe startup, operation, and shutdown of the prototype Brayton-Gluhareff Cycle Pressure Jet Engine. Because the engine involves the coincident use of propane fuel (a heavier-than-air gas), open flames, high pressures, and extremes of both high and low temperatures, great care must be taken to prevent gaseous fuel leaks and contact with surfaces at extreme temperatures. Operation should be performed in an area with proper ventilation or outdoors, and with ready access to a fire extinguisher.

Care should be taken around all the fuel lines, the sources of open flame (preheat coil as well as the engine's inlet and exhaust), and significant radiant heating. The latter is typically unexpected. Because the engine operates at a relatively high core temperature (to the point of glowing brightly in the visible spectrum) it radiates a significant amount of heat. Any people should wear appropriate safety equipment and observe from a safe distance of at least a few feet. Close proximity to the engine's exhaust and radiant heat is enough to roast or burn grilled foods like hot dogs and marshmallows. The "sonic lock" resonance also produces a significant amount of loud noise, hence, proper hearing protection is required.

1. Pressure Jet Engine Startup Procedure

The prototype engine startup involves several steps. Production Gluhareff pressure jet engines are less complicated to start and operate essentially just requiring an open fuel flow and a brief point of ignition. The test stand apparatus and separation of the prototype engine's preheat coil from its chamber adds some steps to this otherwise simple process.

First, fuel flow is initiated by slightly opening the tank valve. This sends cold, liquid propane through the heating coil and out the nozzle. Keeping the fuel flow low at this stage prevents bulk liquid propane from spraying out of the nozzle. Instead a small amount of boiled,

cold gas is injected into the engine. Second, the preheat torch flow is started and sparked to ignition. This applies direct heat to the preheat coil and allows the next step - increasing injection feedline pressure to full (50 psi) by opening the feedline valve and verifying pressure on the installed pressure gauge. At this point a nominal amount of fuel is continuously being injected into the engine. Assuming the inlets are in their proper locations, this injection of fuel is already being mixed with air as it heads toward the engine chamber. As soon as the injection pressure is set, it is ready to be started. Therefore, the last step is to use a butane pencil torch to touch off the fuel/air mixture at the third-stage inlet.

If the conditions are right, the mixture will immediately ignite signified by a loud bang followed by a low, rising rumble. Within a few seconds, the engine should reach a quasi-periodic state of operation exhibiting combustion oscillations consistent with the pressure jet engine design. If the injection pressure is too high, the flame will blow out. Future work will study methods of preventing blow out at higher injection pressures, but this is outside the scope of the current effort. If the inlet locations are not in their proper tuned locations, the oscillation will either not occur or may occur with a rolling beat frequency. Fine adjustment of the inlet locations is necessary to reach a steady oscillation.

2. Pressure Jet Engine Operating Procedure

The Gluhareff Pressure Jet was capable of throttling itself by adjusting the nozzle injection pressure and so too is the prototype pressure jet engine tested here. Testing of the engine is performed at the highest injection pressure possible without causing the flame to blow out. Once started, there is little involved in actually operating the engine other than monitoring the data output and audible signature of the oscillations. With practice it is possible to hear whether the oscillation is 'healthy' or not. An 'unhealthy' oscillation sounds irregular and therefore prone to blow out or

in some cases exhibits a harmonic “beat.” Fine adjustment of the injection pressure or inlet locations may help to alleviate an ‘unhealthy’ oscillation.

3. Pressure Jet Engine Shutdown Procedure

Shutting the engine down is comparatively simple. Because the engine operates solely on the injection pressure, operation can be stopped almost immediately by simply closing the valve on the fuel flow line. This stops the flow of fuel to the engine inlets that also stops the flow of extra air into the engine and within a few combustion oscillations, the flame is extinguished. All that remains is to close fuel flow to the preheat torch as well. This should be done immediately. Alternatively, the preheat torch may be ‘turned down’ by reducing fuel flow to the torch and then closing the engine injector fuel flow. This may be of some concern because when fuel is not flowing through the preheat coil, the heat provided by the torch instead is absorbed by the coil. A few seconds of direct heat in this way will cause the coil to glow and may significantly reduce its fatigue life, hence, it should be avoided. Within a few seconds the engine surface will cool to a safe temperature. However, the inert coil will retain a significant amount of heat (its thermal mass being much larger than its surface area) and should be avoided for several more minutes until it has cooled.

E. MATLAB Image Processing Analysis

While pressures can often be compared with those generated by CFD simulations, the thin walls of the engine and the temperatures allow a unique opportunity to match the CFD with experiments. Test images taken of the engine in operation were imported into MATLAB and edited using the Image Processing Toolbox to produce contours of estimated temperature based on the steel's incandescence. While this method has been used for centuries by blacksmiths and metallurgists to estimate the temperature of metals in industrial applications [310-314], the inclusion of a few anchoring temperatures serve to calibrate the contours.

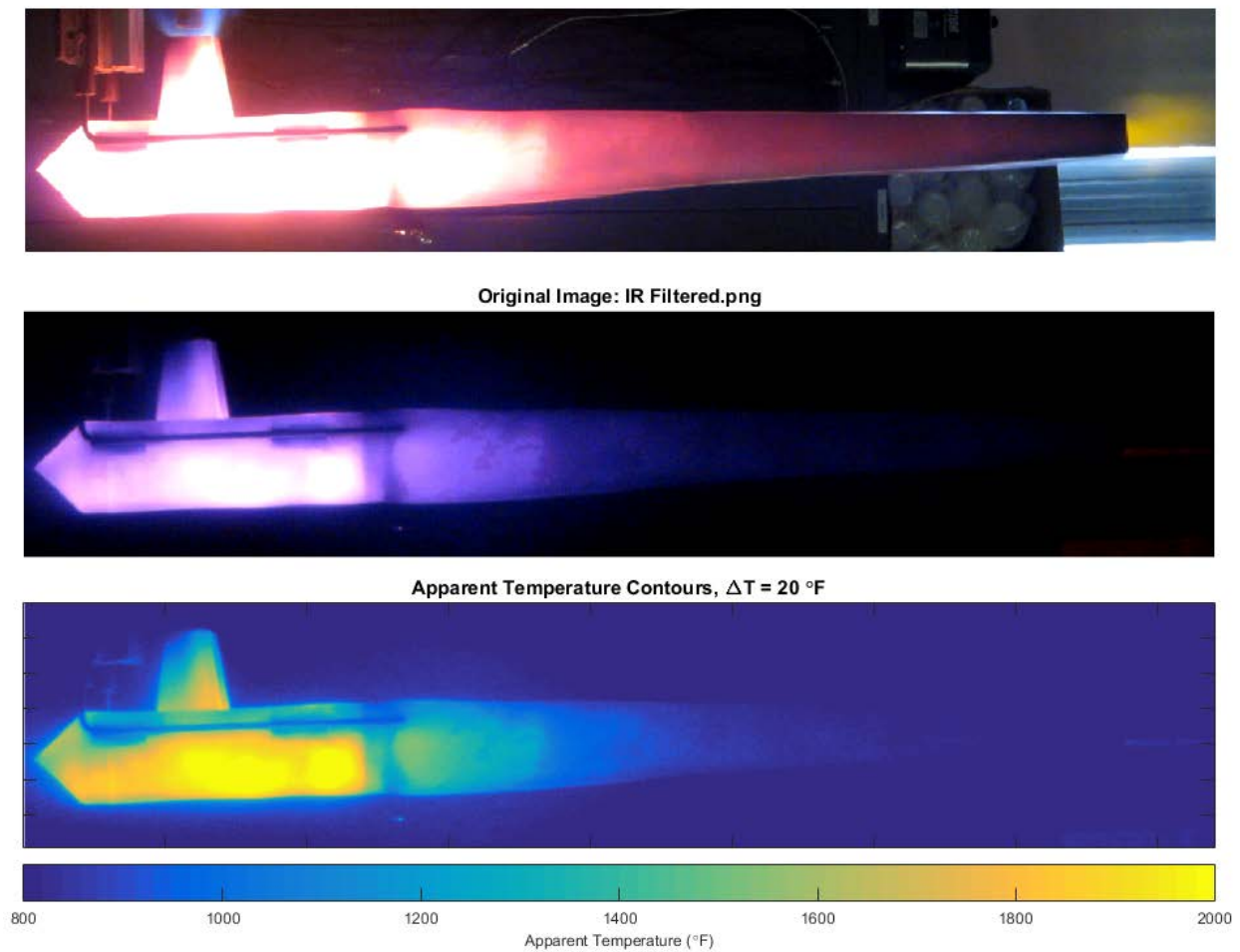


Figure 118: Comparison of the Engine (Injection Pressure of 50 psi) in Visible Light (Top), Through a 720 nm IR-Pass Filter (Middle) and the Filtered Image (Bottom) Processed in MATLAB to Generate Apparent Temperature Contours at a Resolution of $\Delta T = 20^\circ\text{F}$

In short, because the engine operates with a temperature high enough to glow, any conventional video camera can capture this phenomena and MATLAB's image processing toolbox can take the data and produce the same level of detail found in expensive thermal cameras. There are thermal cameras that can produce temperature contours in the range of the engine's operation (up to approximately 2000 °F), but none can compete with the resolutions or speeds available to conventional visible light cameras. An example of an early test of this method is shown in Figure 118. It is important to note that because these contours are not explicitly measured temperature contours, they will be referred to as "Apparent Temperature Contours." They are measurements of light intensity correlated to temperature. The MATLAB source code used to generate these contours is included in Appendix C-2.

The procedure used in the code relies on two experimental thermocouple measurements – one at the maximum temperature and one at the minimum temperature. These values are manually entered into the code prior to generating the temperature contours. The color image is cropped (to reduce computational time) and read into MATLAB via the Image Processing Toolbox's `imread()` function. This function saves the image into a 3-D array – a set of three 2-D arrays of red, green, and blue light intensity. The `rgb2gray()` function is then used to convert this data into a single combined array of grayscaled light intensity.

At this point the data is polled for a maximum and minimum value. If the image is under- and over-exposed in different regions, these integer values, I , will be off-scale high ($I = 255$) and low ($I = 0$) respectively. To convert this integer array to floating point values relatable to temperatures, the following fitting function was used to match the measured maximum and minimum temperatures, T_{MAX} and T_{MIN} :

$$T_{APP} \equiv I \left(\frac{T_{MAX} - T_{MIN}}{I_{MAX} - I_{MIN}} \right) + T_{MIN} \quad (72)$$

It is worth noting that this scaling function cannot explicitly guarantee matching of temperatures across the entire range between T_{MAX} and T_{MIN} , just that the bounds of the data will. This was considered acceptable because the combination of light intensity and color can be qualitatively related to approximate temperature [310-314]. As a result, this curve fitting method was considered reasonable on the basis that grounding the data set's bounds should bring intermediate temperatures within an acceptable level of experimental error, potentially better than relying on rough interpretations of the brightness and color.

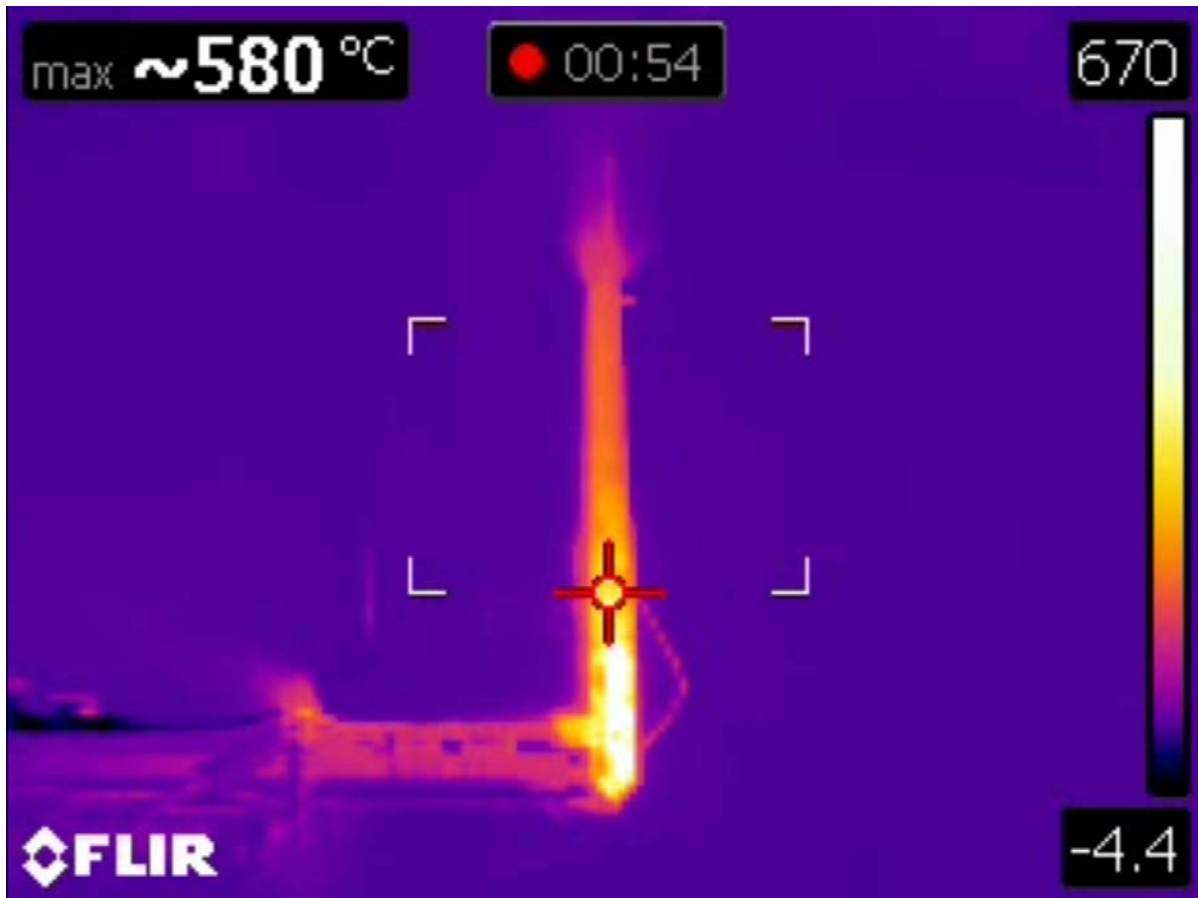


Figure 119: FLIR E-40 Image of Engine in Operation

An E-40 model Forward Looking Infrared (FLIR) Camera was briefly borrowed to test its ability to resolve temperatures during engine operation in comparison to the use of a conventional

visible camera and IR filter. The resulting image is shown in Figure 119. It is immediately clear that although the FLIR camera offers instantaneous, real-time image processing like that performed in MATLAB, it lacks the available resolution of the visible light camera. The FLIR camera has a resolution of 160 x 120 pixels while the Canon ELPH 300 HS has a resolution of 1920 x 1080 pixels when recording video. And despite having a relatively high upper temperature limit (officially listed as 650 °C), it is not as high as the available Type-K thermocouples. This means the images from the FLIR camera are fundamentally unable to capture the maximum surface temperature of the engine. As a result, the FLIR camera was not used to analyze the engine's surface temperature distribution in favor of contact measurement via type-K thermocouples and a visible/IR spectrum camera.

VI. Computational and Experimental Results

A. Computational Data Results

The following section details the output results of the final three-dimensional, transient, engine simulation using the reduced San Diego propane kinetic mechanism described in Chapter III-C while building on the incremental results of prior simulations discussed in Chapter IV. Relevant still images of the CONVERGE simulations visualized with EnSight 10.0 for CONVERGE are included where appropriate. Animations of many images showing propagation through time are available by request. The results are separated into major sections and their progressions through the simulation domain are discussed.

1. Simulation Parameters

There are several things to consider when reading the visualizations and plots in the sections that follow. The engine flow is largely driven by an injection event that remains constant throughout the operation of the engine as in any conventional ramjet. There are no opening or closing events to model (as in a conventional piston engine or valved pulse-jet). On the original Gluhareff Pressure Jets and on the BGX prototype engine, all control of the fuel/air mixture in the engine core is achieved through purely aerodynamic means. This control is affected via variations in the local pressure, velocity, and to some extent fuel/air mixture or more conveniently, equivalence ratio. The injection flow enters the inlet structure almost immediately and enters the engine shortly thereafter. At 25 ms, a 1 ms duration ignition event is started that releases 35 J of energy at the entrance to the third-stage inlet. This effectively models the butane torch used to ignite the physical BGX prototype engine. Following that is the startup transient phase which finally results in a quasi-periodic oscillation as the normal operating state.

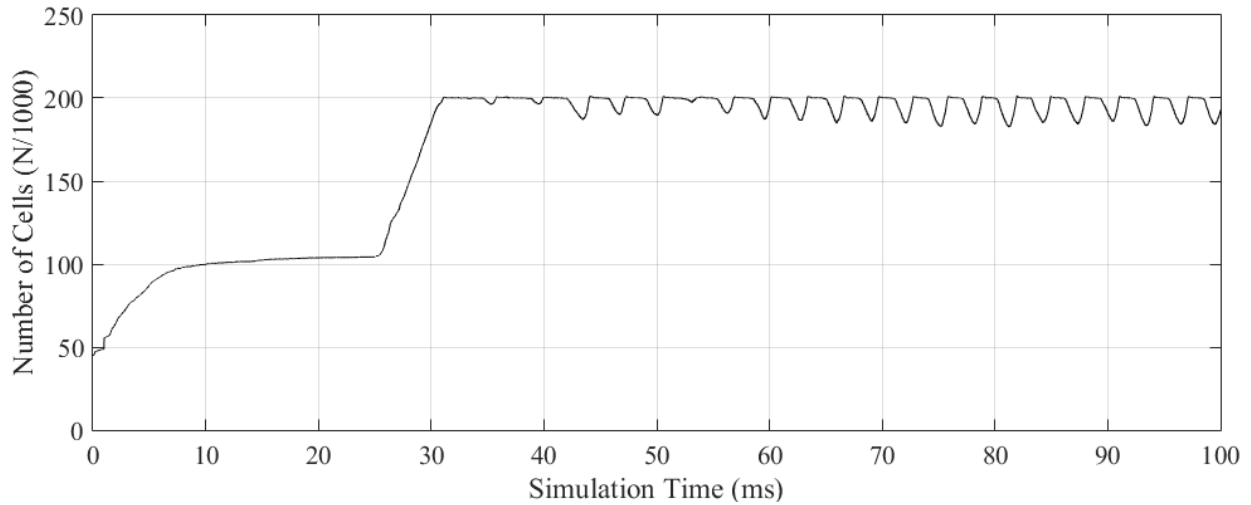


Figure 120: Time History of the Total Number of Cells in the Engine Simulation

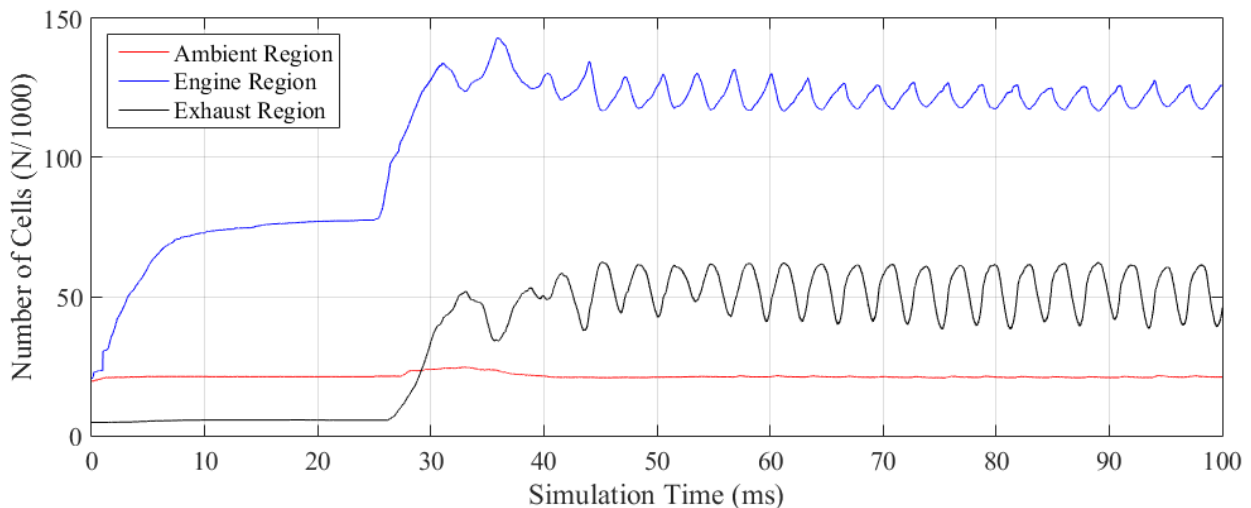


Figure 121: Time History of the Number of Cells in Each Region of the Engine Simulation

CONVERGE's built-in adaptive meshing scheme was used to build the simulation mesh as the simulation proceeded based on local velocity and propane concentration. The simulation was limited to 200,000 cells after which the solver's adaptive meshing scheme reduces the sensitivity to local parameters until the cell count is below the maximum. This is clearly shown in Figure 120 for the whole simulation domain and in Figure 121 separated by individual regions. As the simulation starts and the engine begins to fill with fuel and air, the number of cells in the engine region rises to a steady state of around 75,000 cells. Meanwhile the number of cells in the ambient region (including the inlet structures) and the exhaust region are largely constant. Following the

ignition event, there is immediately a sharp increase in the number of cells in the engine as combustion spreads and local velocity gradients increase. Shortly thereafter, the exhaust region also sees an increase in cells as the first exhaust flow begins to leave the engine. The ambient region was largely unaffected. The quasi-periodic state oscillatory condition signifying the operating condition of the engine is also clear in these plots – the velocity oscillations are driving an oscillation in the required number of cells.

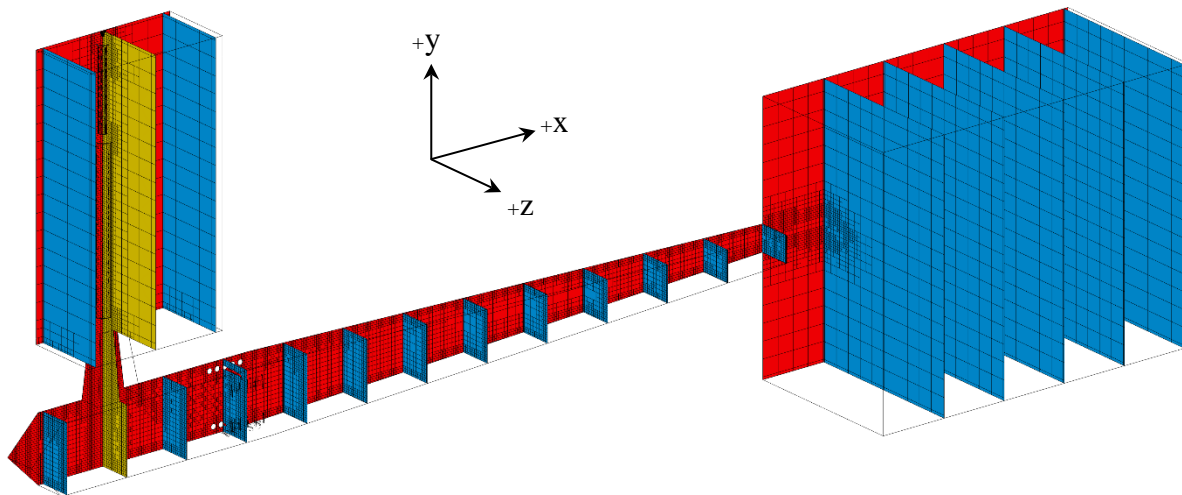


Figure 122: Definitions of the Common Planar Cross-Sections Seen in CFD Data Visualizations in the Following Sections

There are several common planar slices through the 3D simulation domain (shown in Figure 122) used to help visualize the data generated by the CFD solver. The first slice (shown in red) is through the XY symmetry plane of the domain where it is assumed the simulation is mirrored to reduce computational runtime. The next (shown in yellow) is a single YZ slice through the inlet axis. This is generally used to visualize the flow through the inlet structure. Lastly, this single slice is repeated throughout the simulation domain at a 40 mm spacing resulting in 13 slices throughout the engine chamber. These slices are shown in blue but when used in visualizations, also include the slice shown in yellow. The axes denoting positive directions are also shown for reference purposes.

2. Pressure Distributions

The pressure in two regions (engine chamber and exhaust) was initialized to one standard atmosphere – 101,325 Pa (14.70 psi, 1 atm) while the inlet region was initialized to a pressure slightly higher – 110,000 Pa (15.95 psi, 1.09 atm). This differential was necessary to reach the desired equivalence ratio in the chamber for ignition. Prior simulations using one atmosphere in all three regions were capable of ignition but at significantly higher equivalence ratios and did not exhibit desired characteristics like the Kadenacy effect discussed in Chapter I-A. Potential reasons for this and resulting opportunities for further study are discussed with the conclusions in Chapter VII. The injector has a pressure boundary set to 344,738 Pa (50.00 psi, 3.40 atm) to match the pressure recorded from the engine test stand. This boundary drives the fuel injection process and the majority of the pre-ignition mixing flow. This section details the pressure distributions throughout the engine prior to ignition, during ignition, and during quasi-periodic operation of the engine, particularly their effect on flow through the engine that drives further mixing of fuel and air, ultimately resulting in proper operation of the engine.

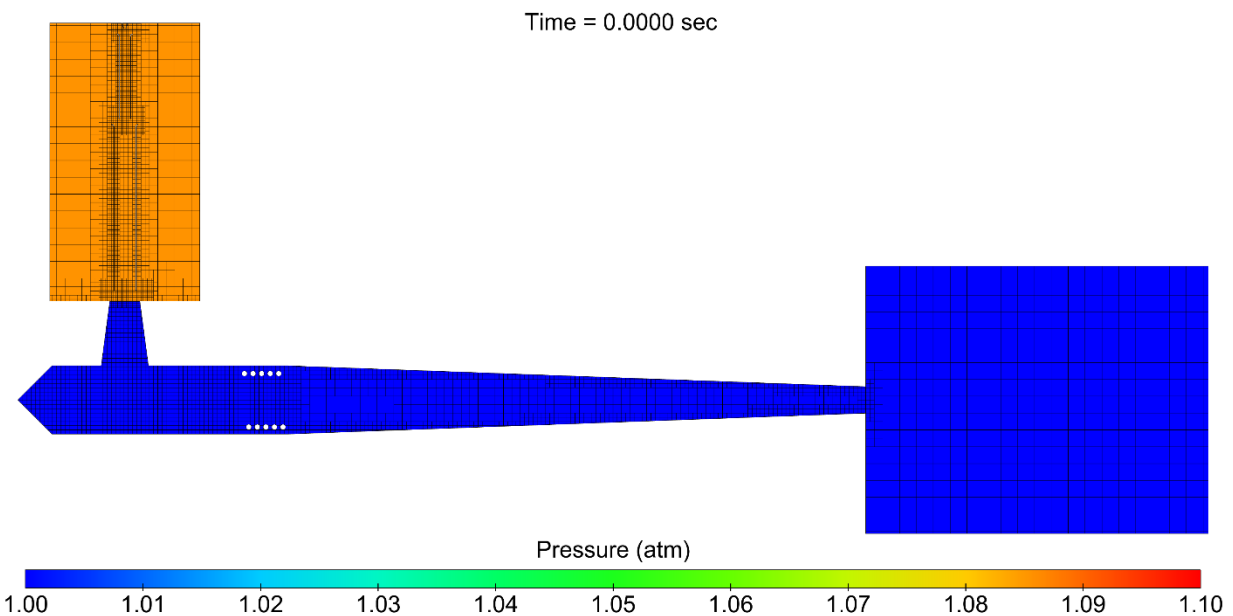


Figure 123: Initial Pressure Distribution (XY Symmetry Plane, t = 0 ms)

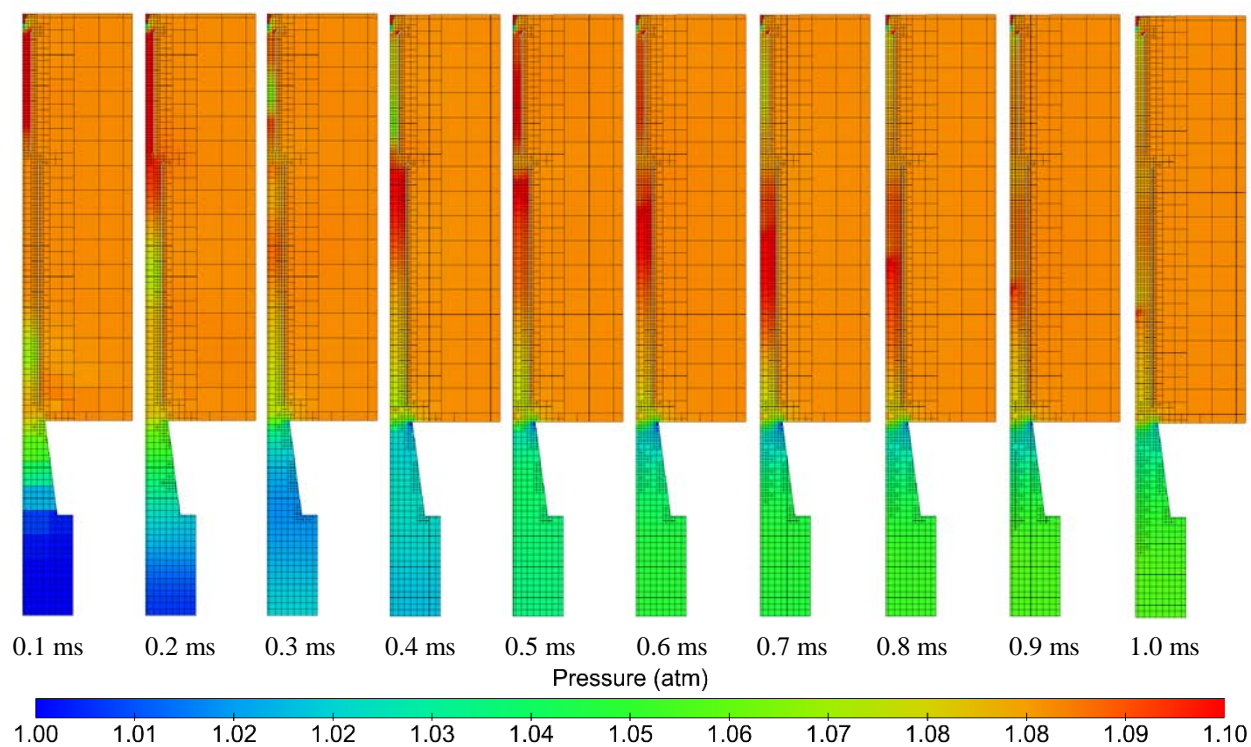


Figure 124: Pressure Wave Propagation through Engine Inlet Structures During Initial Injection (YZ Plane at Origin, $t = 0.1 - 1.0$ ms)

The initial pressure distribution (in atmospheres) is shown in Figure 123. Also visible is the initial grid showing the coarseness of the base grid and the inclusion of fixed embedding around the inlets. As the simulation progresses, more mesh fineness forms around the injection flow as well as the engine core interior and inert coil. The pressure bounds are limited to 1.00 atm and 1.10 atm to illustrate the propagation of pressure waves in the flow as opposed to the domain bounds. The minimum pressure tended to fluctuate around 1 atm while the maximum was steady at the injection pressure of 3.40 atm (344,738 Pa, 50 psi). Immediately following this initial condition, it is clear that the pressure wave caused by the initiation of fuel injection not only propagates through the ambient air region but is also captured by the inlet system. This exhibited a response similar to that expected from classical acoustics with the pressure wave propagating through the inlet pipes and reflecting back.

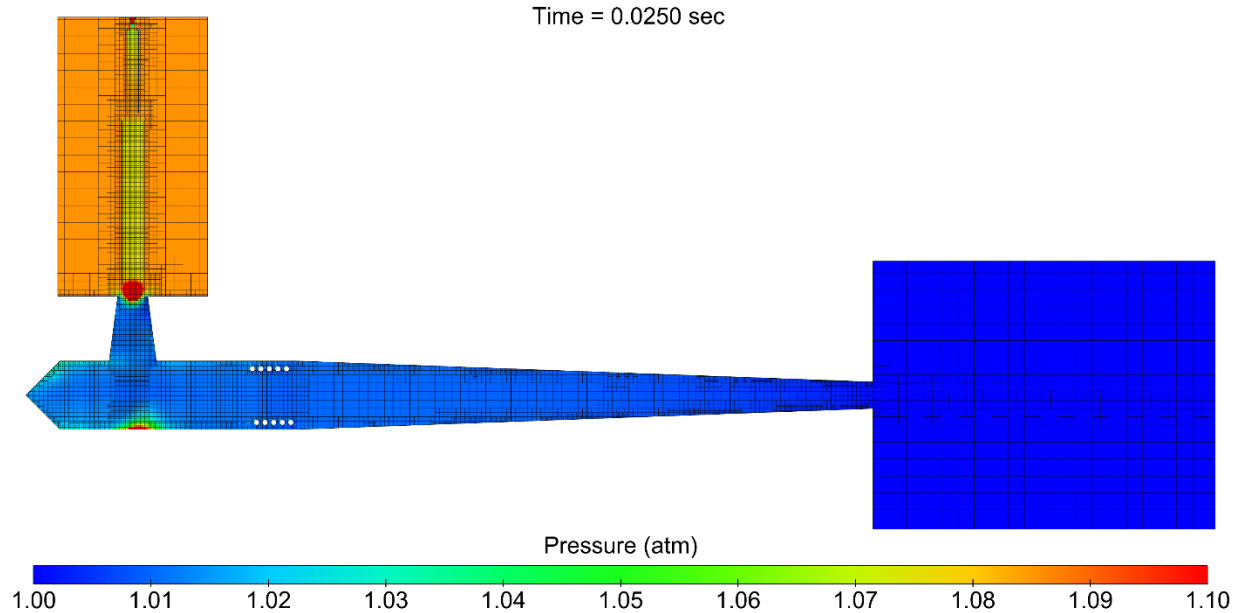


Figure 125: Pressure Distribution at Ignition (XY Symmetry Plane, $t = 25.0$ ms)

At the instant of ignition, the pressure in the engine core is slightly above atmospheric pressure and shows a generally decreasing trend toward the nozzle exit consistent with increasing speed and the fluid normalizing to the exhaust pressure condition of one atmosphere. This distribution is shown in Figure 125. There are a few notable differences. First, a slight high pressure zone appears to form in the engine head where swirling recirculation of the injected fuel/air mixture was expected. A second stronger high pressure zone occurs where the injecting fuel/air mixture impinges on the back wall and may be attributed to the stagnation point of the injecting flow. These two phenomena are expected to form on Gluhareff's original engine designs as well. The stagnation region where the flow impinges on the engine wall is also where the core pressure sensor is measured. Lastly, the point of ignition (centrally-located at the third-stage inlet) shows a significant increase in pressure consistent with the acoustic pressure wave beginning to propagate radially from the point of ignition. As the simulation proceeds, this pressure wave continues to propagate radially outward from the point of ignition both into the engine core and back into the ambient region and inlet structure.

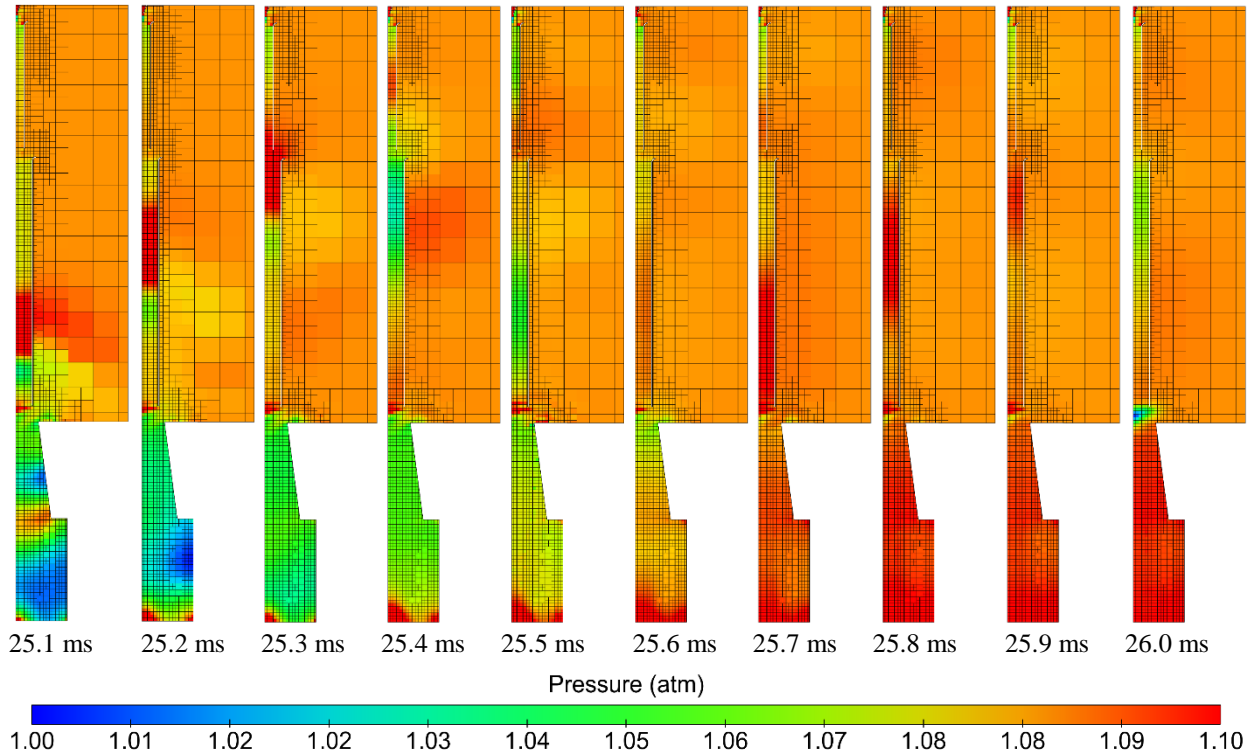


Figure 126: Pressure Wave Propagation through Engine Inlet Structures Immediately Following Ignition (YZ Plane, $t = 25.1 - 26.0$ ms)

This radial acoustic propagation is clear through the inlet structure as well as the portion that reflects inside the engine core though the latter is more diffused and attenuated. This is shown in a series of images at a 0.1 ms timestep visualized in atmospheres of pressure in Figure 126. The propagation exhibits generally the same response as what occurred when the simulation started with a similar acoustic shock propagating from the injector nozzle; however, stronger and resulting in a sustained chamber pressure likely due to the onset of early combustion. The waves were observed to propagate through the inlet tubes and reflect off the open ends. This brief transient response eventually damped out to a low amplitude quasi-periodic oscillation by 40 ms simulation time (15 ms following the start of ignition). Following the end of the initial ignition event (at 26.0 ms) the local high pressure at the ignition point immediately reverses to a low pressure zone as the pressure differential between the ambient and core drives a new flow of clean air into the third-stage inlet and toward the engine core.

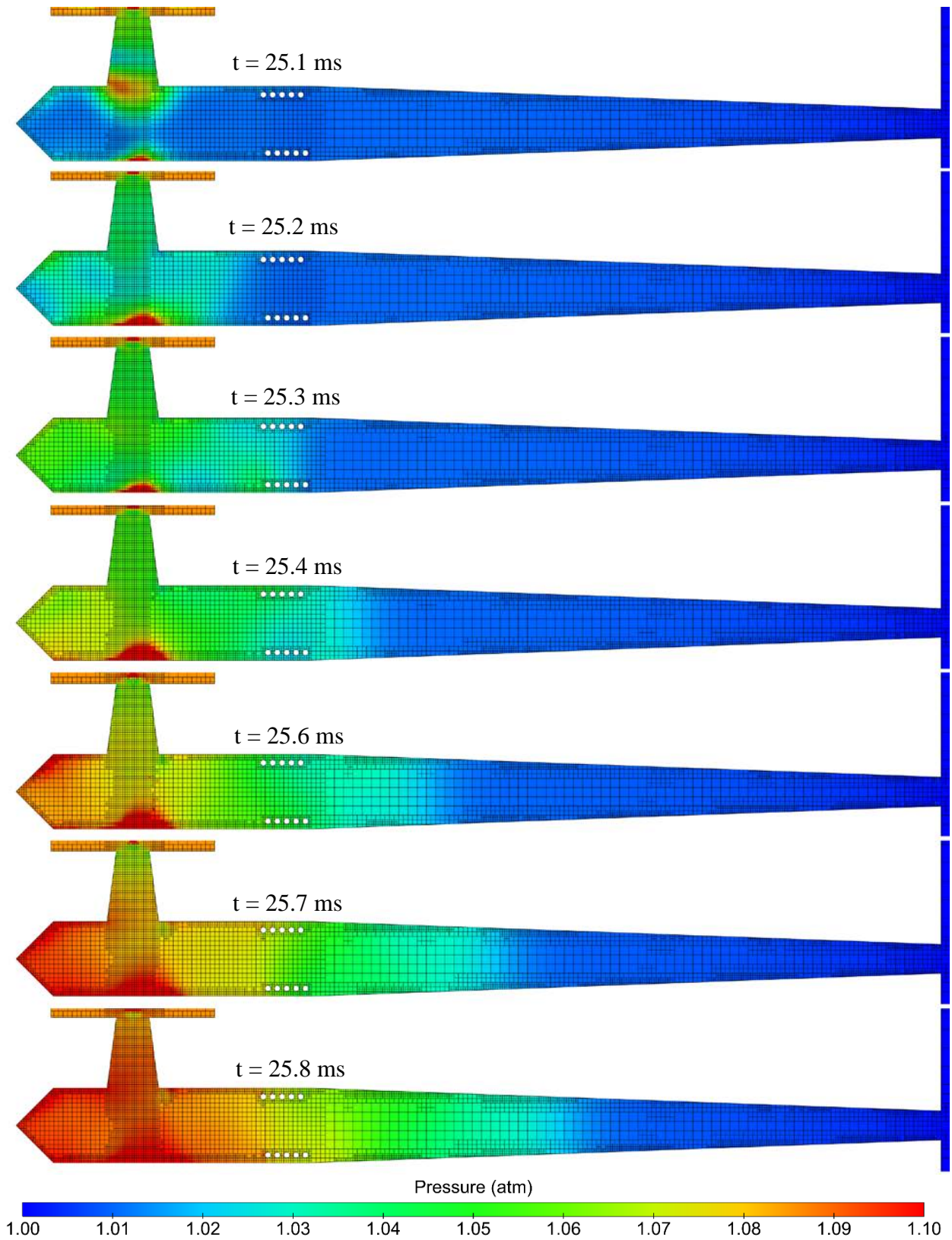


Figure 127: Pressure Wave Propagation Through Engine Core Immediately Following Ignition (XY Symmetry Plane, $t = 25.1 - 25.7$ ms)

This pressure wave propagation extends throughout the engine core as well. The core's pressure distribution immediately following the ignition event is shown in Figure 127. The ignition event at 25.0 ms immediately sends a pressure wave into the engine core. This wave diffuses and weakens significantly to approximately 1.05 atm (106 kPa, 15.4 psi) upon reaching the exit of the third-stage inlet and spreading into the larger engine core volume. Sometime between 25.1 and 25.2 ms, the wave reaches the back wall and begins its reflection. It should be noted at this point that although the time stepping in this diagrams is coarse compared to the propagation of pressure waves, the simulation time step stabilized around 2.0×10^{-6} to 3.0×10^{-6} sec but limited disk space for output files necessitated limiting their output rate to once every 0.1 ms (1.0×10^{-4} sec). Nevertheless, there is ample temporal resolution to observe the propagation and reflection of this initial pressure wave. The remainder of the wave is likely diffused by destructive interference from multiple reflections inside the chamber off the forward nose section and the other engine walls. There is essentially no discernable pressure wave by 25.4 ms except the pressure gradient propagating down the engine nozzle.

By this time, pressures in the engine core are beginning to rise beyond the simple wave reflection from the initial ignition transient. Although the 1.0 ms ignition event has not yet ended this suggests combustion is beginning to spread into the engine and release extra energy into the engine core. This appears to increase the pressure at the stagnation zone on the back wall as well as the pressure throughout the engine core. No other acoustic oscillations like those expected to drive the engine's production of usable thrust force were observed to this point in time.

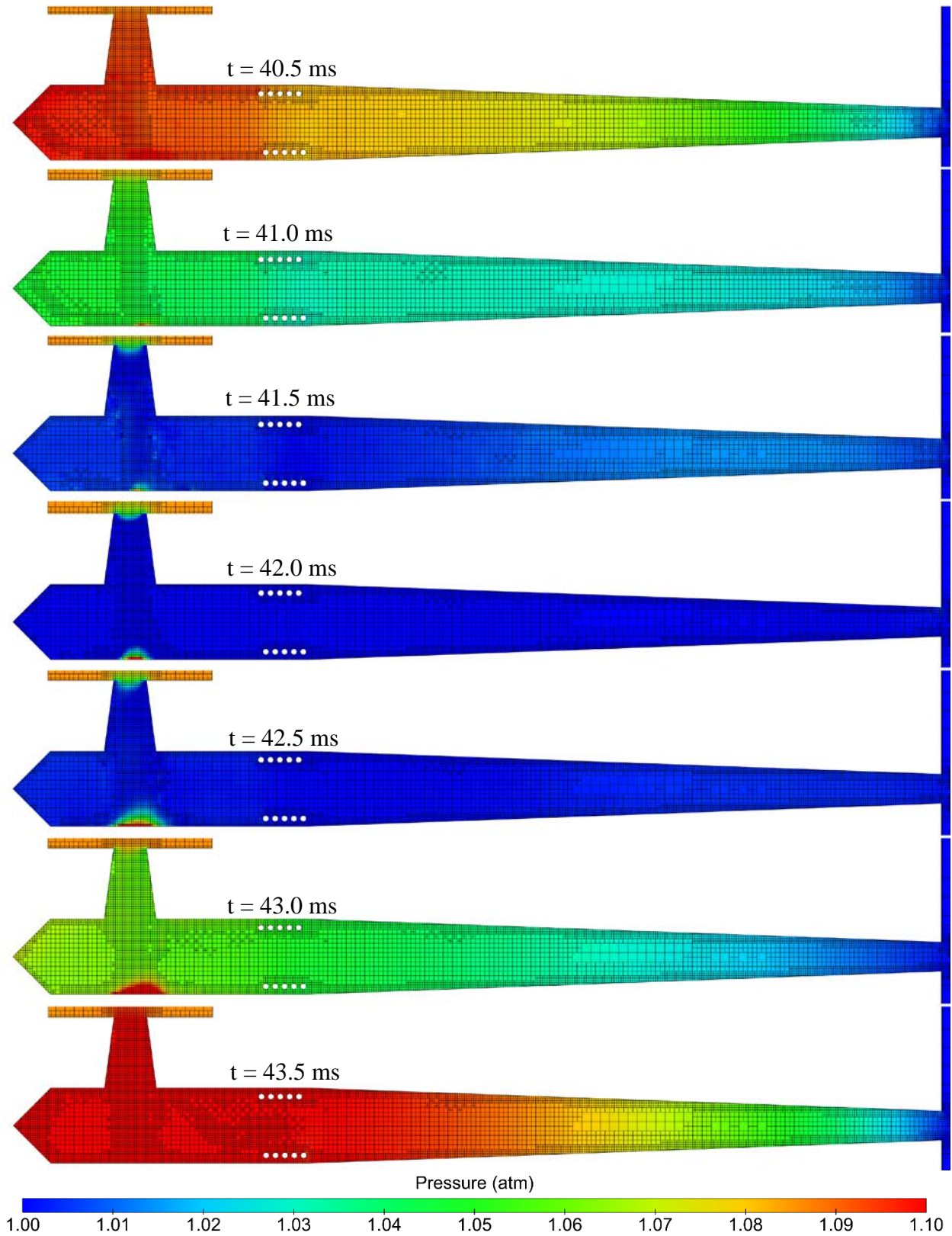


Figure 128: Pressure Distributions Showing Engine Startup Transient Exhibiting the Kadenacy Effect (XY Symmetry Plane, $t = 40.5 - 43.5$ ms)

After the initial ignition transient, the engine reaches a quasi-periodic condition which exhibits the “Kadenacy Effect” as can be seen in the visualizations of the pressure distributions. This effect (discussed in more detail in Chapter I-A) is a mode of operation commonly observed in pulse jets by which the oscillating high and low pressure waves exhaust hot gases and shortly thereafter draw in a fresh charge of air for combustion. It is a cycle by which pulse jets “breathe” and is the basis of their operation. Although the Gluhareff “Pressure Jet” is not a pulse jet (it is technically a pressurized ramjet), it may still operate on some of the same principles as pulse jets, particularly exploiting a similar effect.

This early transient cycle lasts approximately 3.5 ms from peak chamber pressure, to minimum pressure, and back as shown in Figure 128. At 40.0 ms simulation time (not shown), the chamber resembles the distribution at 43.5 ms closely. There is a high pressure in the third-stage inlet and engine core beyond that of the ambient conditions which diminishes as it spreads to the nozzle exit. Pressure begins to drop throughout the engine in the next frame (40.5 ms) and the low pressure at the nozzle exit begins to propagate forward. As the pressure drops below the ambient condition, it is clear there is some flow back into the engine as the stagnation pressure on the engine wall starts to rise despite the low chamber pressure (see 41.5 – 42.5 ms). This return of the inlet flow brings in more air with the fuel to augment combustion that drives an increase in the chamber pressure. This begins to raise the chamber pressure above the ambient pressure (see 43.0 and 43.5 ms) where the cycle then repeats. The effects of this pressure cycle on the local velocity and temperature distributions is discussed in Sections 3 and 4, respectively and are clearly beginning to produce usable pressure ratios that may generate measurable thrust forces. The cycle settles by 60 - 70 ms to a frequency of approximately 350 Hz (seven cycles in 20 ms).

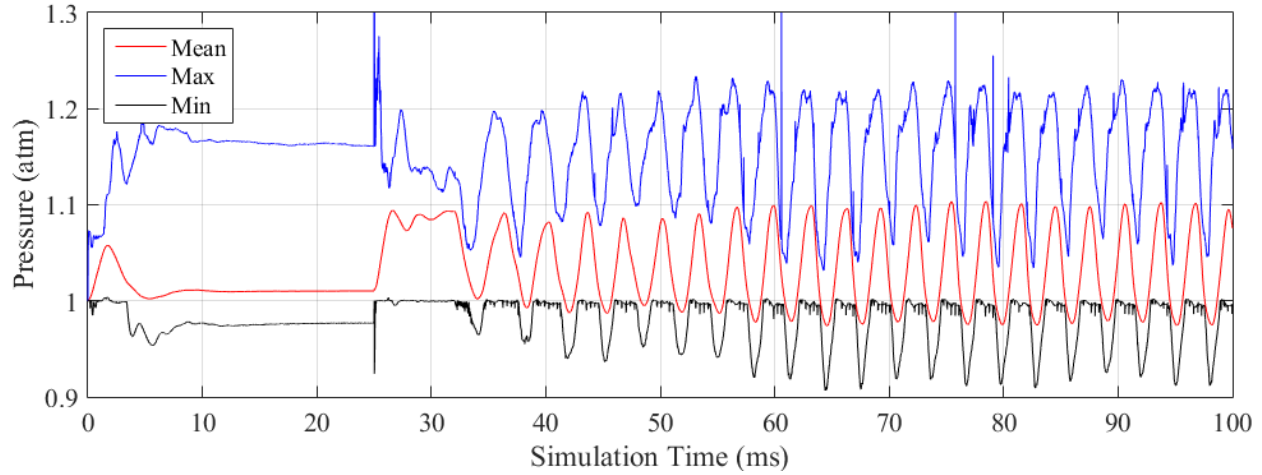


Figure 129: Engine Chamber Mean (Mass Averaged), Maximum, and Minimum Pressure Time Histories through Full Simulation Time Domain

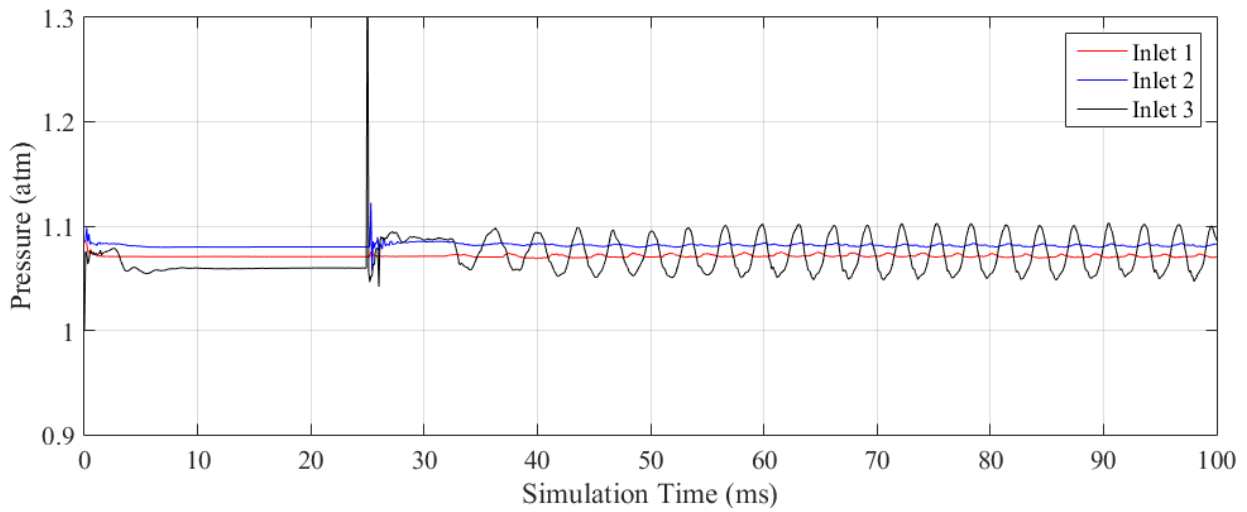


Figure 130: Engine First-, Second-, and Third-Stage Inlet Pressure Time Histories

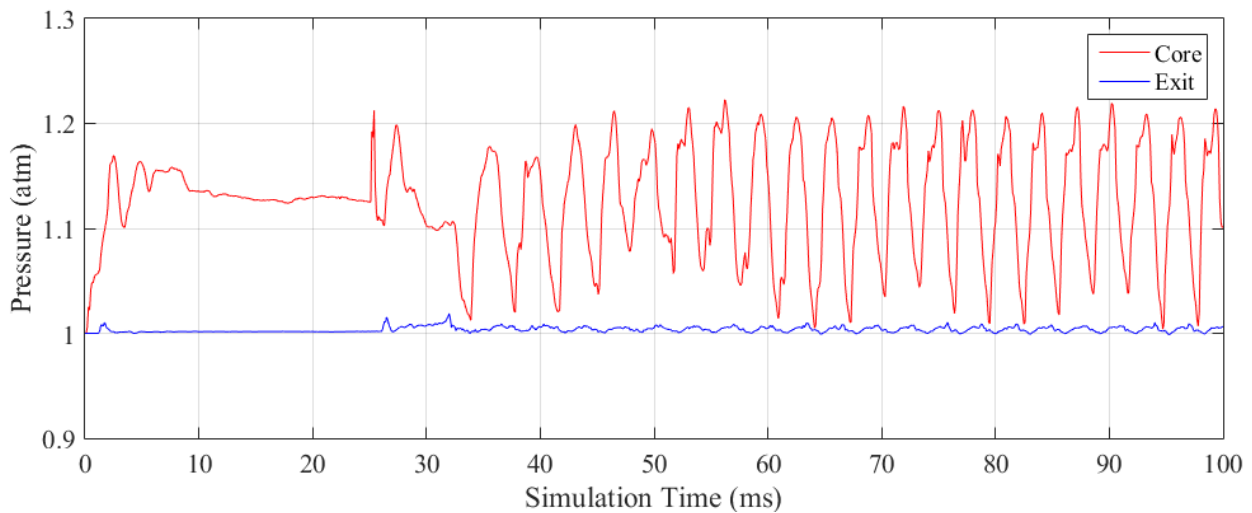


Figure 131: Engine Core Total Pressure Port and Nozzle Exit Location Time Histories

The simulation overall pressure statistics are plotted for the engine region in Figure 129 showing the mass averaged mean pressure as well as the maximum and minimum pressure variations with time. From this data, it appears that the initial injection flow results in an erratic pressure response that eventually damps to a pre-ignition steady-state. This steady state is perturbed at 25 ms when the ignition event sends a new pressure wave through the engine chamber and eventually starts the engine. This propagation occurs for approximately 7 ms when the chamber pressure drops and drawing in the first significant charge of fuel and air for combustion. Beyond this point, unsteady oscillations begin to emerge in the engine and by 60 – 70 ms, the engine has reached its quasi-periodic state with an approximately 0.10 atm mean amplitude with minima and maxima of approximately 0.92 and 1.22 atm, respectively.

Likewise, the inlet pressures (measured in the CFD simulation along the inlet centerline axis) are plotted with each other in Figure 130. The first and second inlets are weakly affected by the quasi-periodic oscillation resulting from the engine's core with the first inlet seeing an incrementally lower local pressure. The third-stage inlet sees a much high amplitude of 0.05 atm tracking the oscillation.

Lastly, the engine core and nozzle exit pressures are plotted with each other. These measurements from the simulation correspond to the same measurements made on the engine test stand with one change – the exit pressure is not directly recorded on the test stand, but is part of the exhaust speed measurement via Pitot tube system. The core pressure reading at the stagnation location, however is intended to match the experimental data as closely as possible. The amplitude of this data under quasi-periodic operation was approximately 0.20 atm from a minimum pressure of approximately 1.01 atm to a maximum of approximately 1.21 atm. The exit pressure weakly oscillates around 1 atm.

3. Velocity Magnitudes

The distribution of velocity magnitudes in all regions was initialized to zero with any resultant velocities caused by the pressure differential between the injection and the surrounding quiescent air. The high speed injection of preheated propane gas was expected to entrain ambient air and promote mixing of the fuel-rich core. This flow of fuel and air into the engine was also expected to fill the engine chamber with a mixture favorable to combustion and start any major flow patterns that would drive the fluid through the engine and out the nozzle, eventually to produce measurable thrust forces. Some recirculation or stagnation of the mixture is expected in the forward nose section of the engine as this is thought to act as a forward flame holder in stabilizing combustion. This section details the resulting flow of the injecting fuel stream and air throughout the simulation domain prior to ignition, during ignition, and during the engine's operation as well as any relevant flow structures that form. Of particular note is what role, if any, the inert heating coil's shape and blockage has on the flow both inside the engine core and leading outward through the engine nozzle.

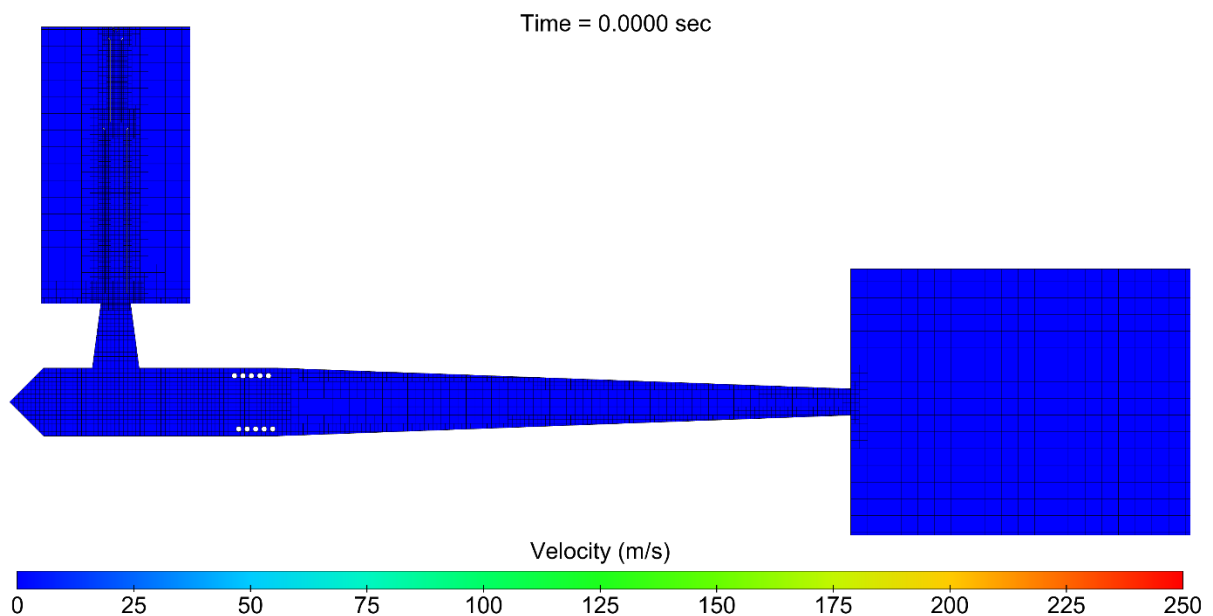


Figure 132: Initial Velocity Distribution (XY Symmetry Plane, t = 0 ms)

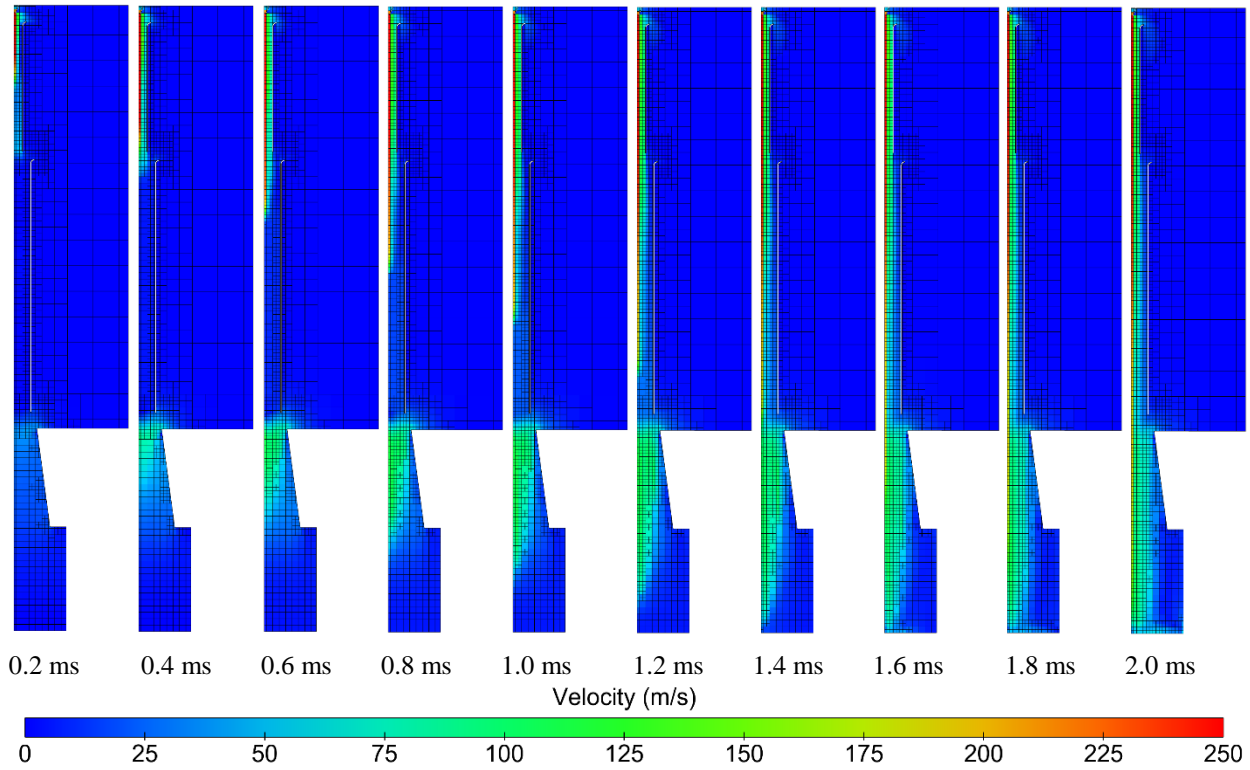


Figure 133: Velocity Distribution in Inlet Structures During Initial Injection (YZ Plane at Origin, $t = 0.2 - 2.0$ ms)

The velocity distribution following the initiation of fuel injection into the inlet structures is shown in Figure 133. It is largely characterized by the high velocity fuel stream directed axisymmetrically through the inlet stages. As the fuel stream continues through the inlet stages, it progressively slows from the initial injection speed of 280.5 m/s (919 ft/s) to around 50 m/s (164 ft/s) in the core. Here the flow appears to begin circulating around the square cross-section. Another flow feature is notable at this point – the entrainment of air into the inlet stages. This effect appears at the first stage inlet where the injection speed is the highest and the cross-sectional area is the lowest but is less evident at the second-stage inlet. It is strong at the third-stage inlet reaching 106 m/s (348 ft/s) at 1 ms (prior to the injection flow reaching the inlet) and increasing to 174 m/s (571 ft/s) at 2 ms (when the injection flow enters the inlet). This early entrainment is likely a result of the region pressure differential as opposed to the injection charge.

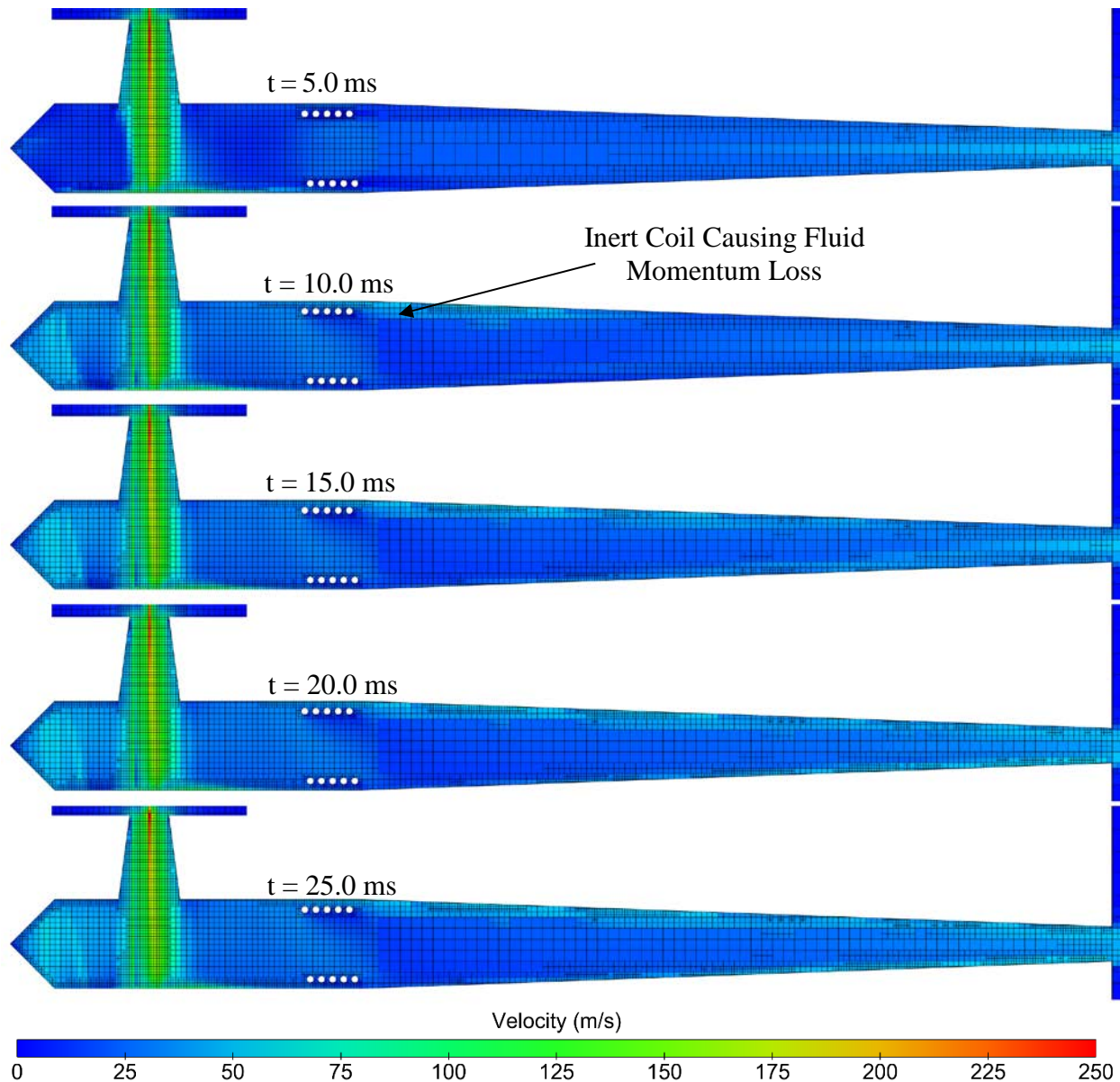


Figure 134: Velocity Distribution and Streamlines through Engine Core Immediately Prior to Ignition (XY Symmetry Plane, $t = 5.0 - 25.0$ ms)

The velocity distribution through the engine core reaches a pre-ignition quasi-periodic state by approximately 15 ms and is largely indistinguishable from the distribution at the time of ignition (25 ms) as shown in on the symmetry plane in Figure 134 and through multiple cross section planes in Figure 135. The distribution appears to suggest a weak recirculation zone in the nose of the engine forward of the third stage inlet, as well as around the sidewalls of the engine. It does not, however, appear to have a simple two-dimensional recirculation. Instead, the streamlines

suggest that the incoming flow spreads radially from the stagnation point and upon encountering the side walls and head of the engine, curl around these walls toward the plane of symmetry. Under ideal circumstances it may resemble a toroidal shape; however, in this case the flow is restricted by the rectangular cross-section of the engine core. The reader is reminded that the symmetrical boundary may limit the swirl in these areas to phenomena that are symmetrical. A simulation without this limitation should more conclusively describe this flow structure.

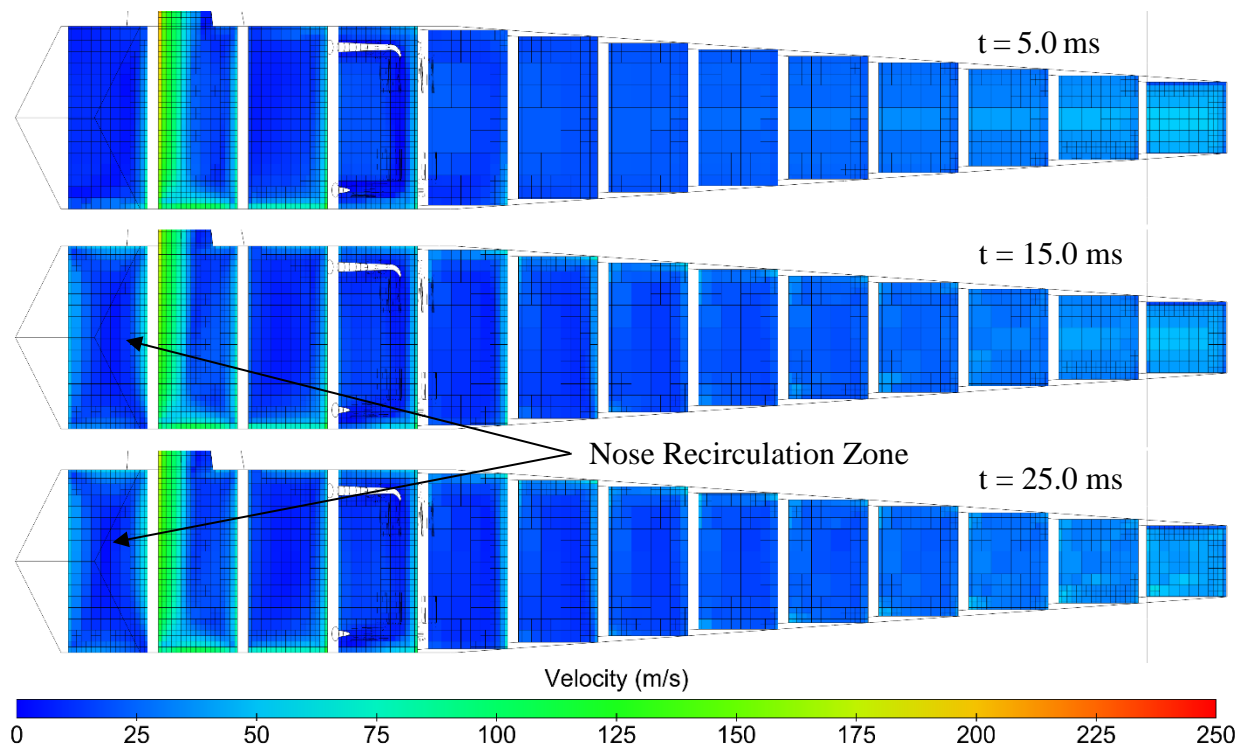


Figure 135: Velocity Distribution through Engine Core Immediately Prior to Ignition Showing Multiple Cross-Sections (Multiple YZ Planes at 0.04 m Intervals)

This phenomena is further suggested by the cross-sectional velocity profiles in Figure 135, particularly the one forwardmost which shows higher speeds along the periphery and low speeds in the center. A separate phenomenon is also worth noting. Aft of the inlet, it is apparent some fluid momentum loss is occurring as a result of the inert coil blockage. While this is consistent with the idea of a conventional ramjet's flameholder, its capability as a flameholder is expected to be weakly significant as opposed to a driving component of the engine's design.

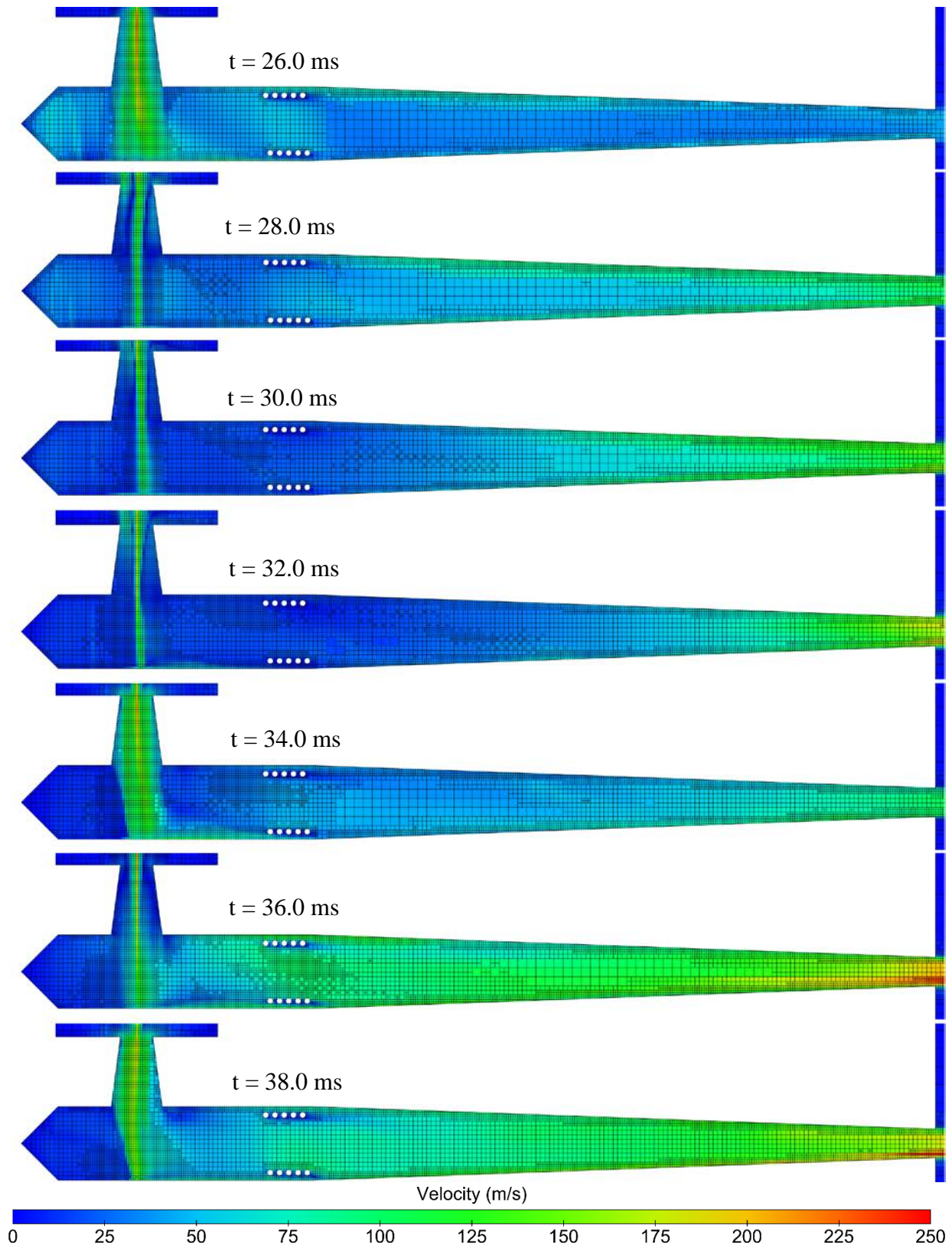


Figure 136: Velocity Magnitude Distributions of Engine Startup Transient (XY Symmetry Plane, $t = 26.0 - 38.0$ ms)

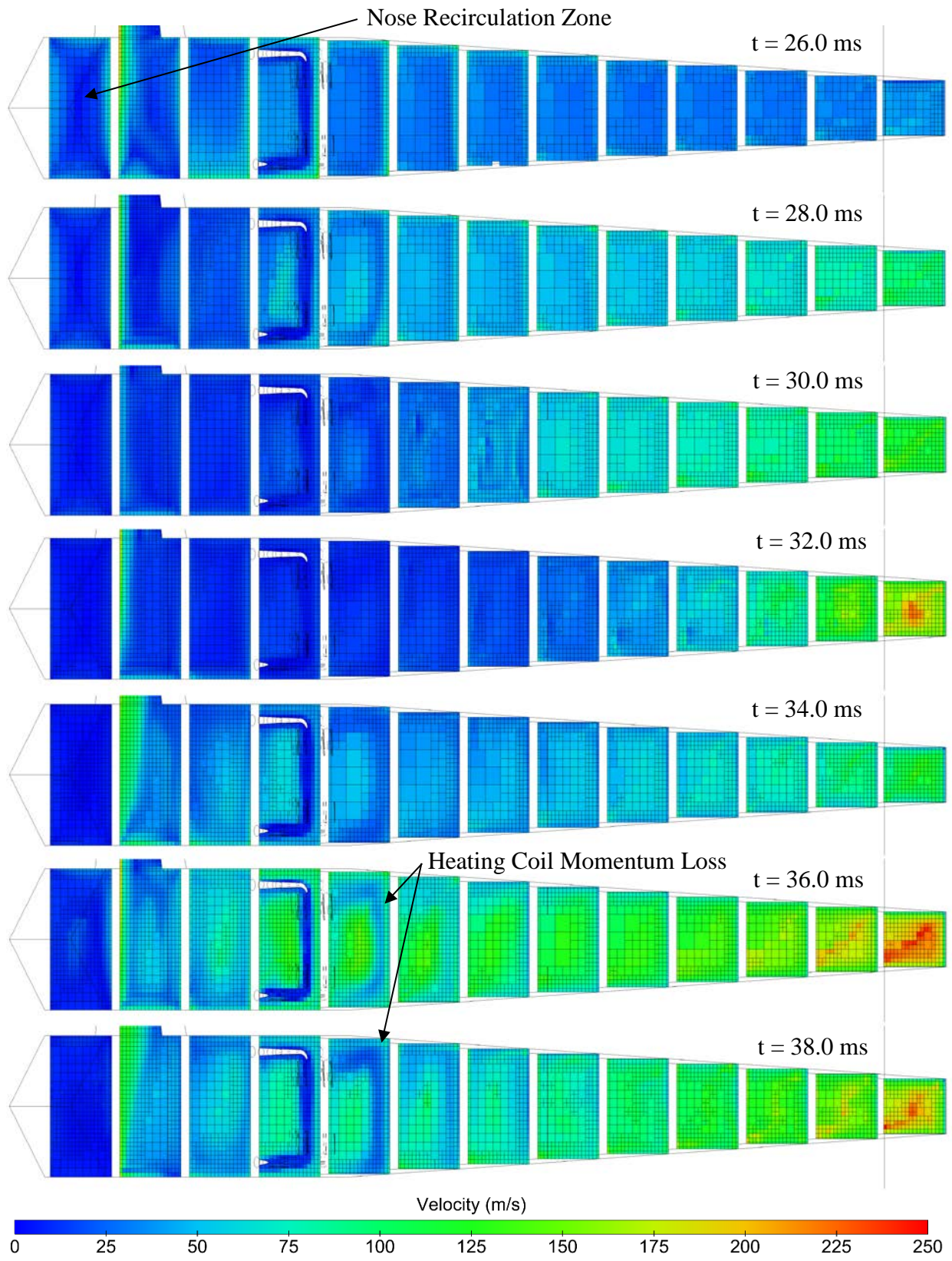


Figure 137: Velocity Magnitude Distributions of Engine Startup Transient (Multiple YZ Planes at 0.04 m Intervals, $t = 26.0 - 38.0$ ms)

The engine core's startup transient visualized through velocity magnitude distributions is shown on the centerline plane in Figure 136 and on cross-sectional planes (spaced 40 mm apart from the inlet axis) in Figure 137. While the startup transient is particularly chaotic, there are some notable features to consider. First, there still appears to be some recirculation in the engine both in the forward nose section and throughout the engine core. The nose recirculation appears to be significantly affected by the onset of combustion with the recirculation weakening until it begins to reappear at approximately 36 ms. The simulation shows persistent recirculation throughout the chamber that oscillating with the intake of air. The reader should note that this recirculation is likely not mirrored about the symmetry plane in reality and instead may be a full-volume swirl throughout the exhaust flow. This is a limitation of the symmetry plane assumption.

Second, immediately following the ignition source, there is still a high speed flow into the engine of around 125 m/s (410 ft/s). However, as combustion spreads, the temperature and pressure rises. This appears to cause less air entering the chamber and seems to have some effect on the core of the inlet flow though it still reaches the engine core. The remaining fluid in the engine is accelerated out the nozzle, which lowers the chamber pressure and allow the intake of air to resume. The momentum loss in the fluid due to the inert coil is also significant, reducing the local speed roughly by half immediately downstream of the coil and effectively to zero speed between coil sections. These conditions continue to vary while combustion spreads until the steady-state oscillatory condition is reached around 40 to 50 ms (15 to 25 ms after the start of ignition).

The simulation shows speeds at the nozzle exit still varying significantly with time but showing a general trend of increasing with time. Prior to ignition, the exit velocity through the center of the nozzle exit was approximately 44 m/s (144 ft/s). But as combustion spreads through the engine this rises to 221 m/s (725 ft/s) at 40 ms simulation time.

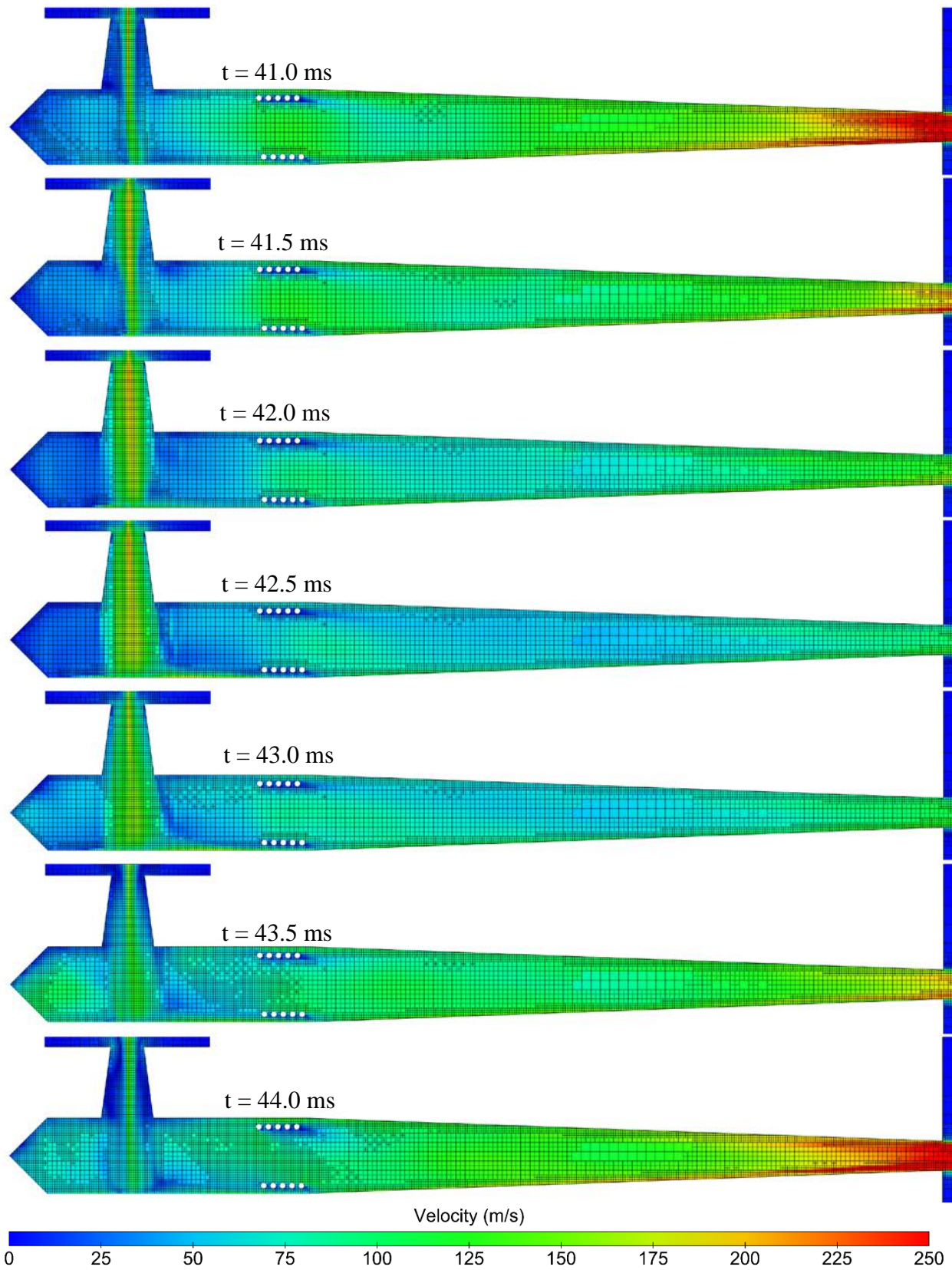


Figure 138: Quasi-Periodic Velocity Magnitude Distributions Showing the Kadenacy Effect (XY Symmetry Plane, $t = 41.0 - 44.0$ ms)

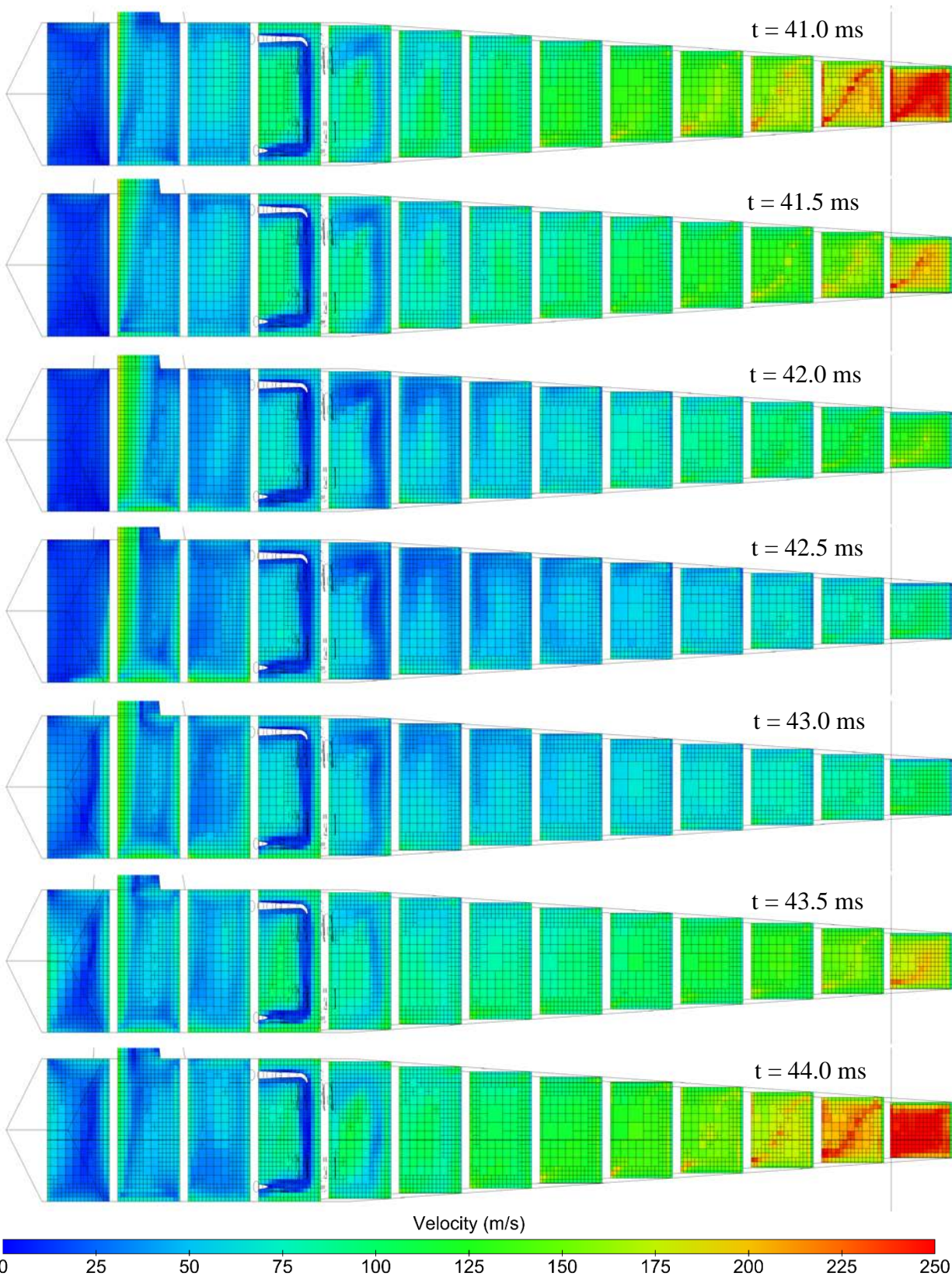


Figure 139: Quasi-Periodic Velocity Magnitude Distributions Showing the Kadenacy Effect (Multiple YZ Planes at 0.04 m Intervals, $t = 41.0 - 44.0$ ms)

As the engine begins to oscillate more regularly, the “Kadenacy Effect” discussed earlier in this Chapter as well as in Chapter I-A becomes more apparent. This is illustrated in velocity magnitude visualizations on the symmetry plane in Figure 138 and on a series of cross-sectional planes spaced 40 mm apart in Figure 139. It should first be noted that the recirculation throughout the engine during the startup transient was not seen to stop; however, in animations the strength of the circulation does appear to vary with the amount of inlet air entering the engine. When selecting individual frames showing the Kadenacy Effect in velocity magnitudes, the peak exit velocity appeared to lag behind the peak chamber pressure by approximately 0.5 ms, while the frequency did not appear to be significantly affected.

In terms of velocity magnitudes, the effect was signified by a reduction in chamber velocities, particularly in the forward nose section but coinciding with an increase in the velocity of the incoming flow. At this point the chamber pressure is decreasing of which the visualizations suggest this results in the engine drawing more air into the inlet while also reducing the exhaust speed from the maximum of nearly 300 m/s (984 m/s) to a minimum of approximately 100 m/s (328 ft/s). The velocity in the forward nose section quickly regains its recirculation speed even reaching a maximum of approximately 100 m/s (328 ft/s) before settling to around half that value. By then, the chamber pressure is rising again and the accelerating the flow out the nozzle. At no point does the circulation through the engine cease. Instead, it appears to be fed by the inlet flow in a manner similar to the way the fuel and air feeds the combustion process.

Lastly, the inert coil appears to continue having a momentum deficit effect on the flow throughout the engine cycle. This effect appeared strongest when the chamber pressure was highest and the velocity magnitude around the coil was the lowest. The effect on the flow downstream of the coil is nontrivial, but has largely diffused by three frames downstream (0.12 m).

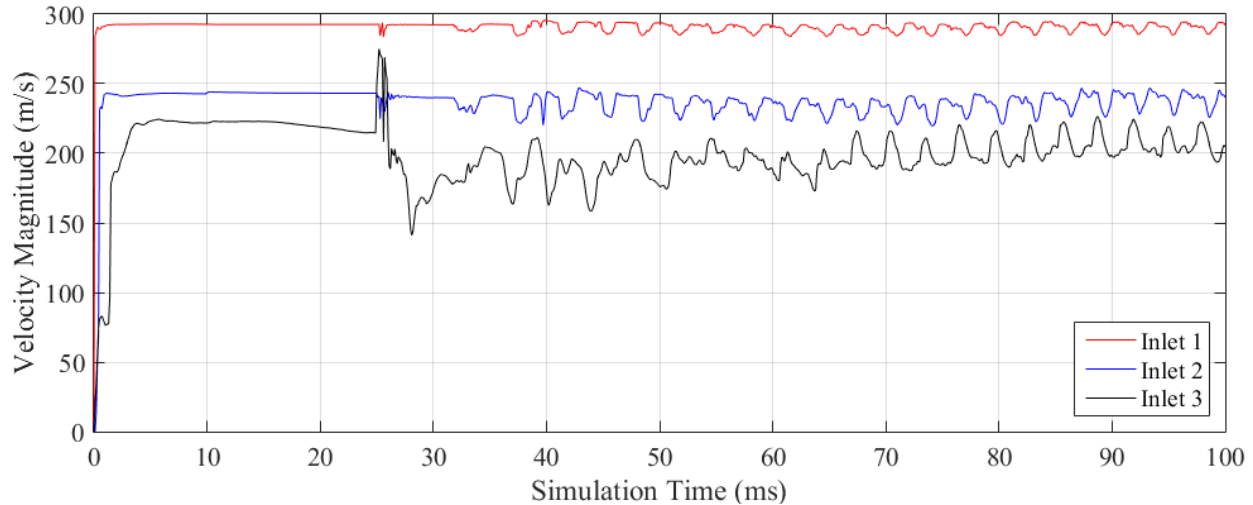


Figure 140: Engine First-, Second-, and Third-Stage Inlet Location Velocity Time Histories

The velocity magnitudes polled from the CFD distribution at the inlet centerline for all three inlet stages are plotted together in Figure 140. It is clear that the inlet speed diminishes significantly as the fuel/air mixture progresses through the inlet structures. This polled data from the simulation largely tracks the core of the fuel stream as it spreads and slows heading into the engine chamber. As a result, each progressive measurement shows a reduction in velocity magnitude.

Moreover, as the stream reaches the engine, it is more affected by the engine's oscillations, potentially because of the pressure waves propagating through the inlets. This effect is particularly erratic at the third-stage inlet but stabilizes by 70 ms. Stepping backward, the second stage inlet stabilizes much sooner, though to a lower amplitude, by 50 ms. The first stage inlet is only slightly affected and stabilizes to the lowest amplitude oscillation by approximately 40 ms.

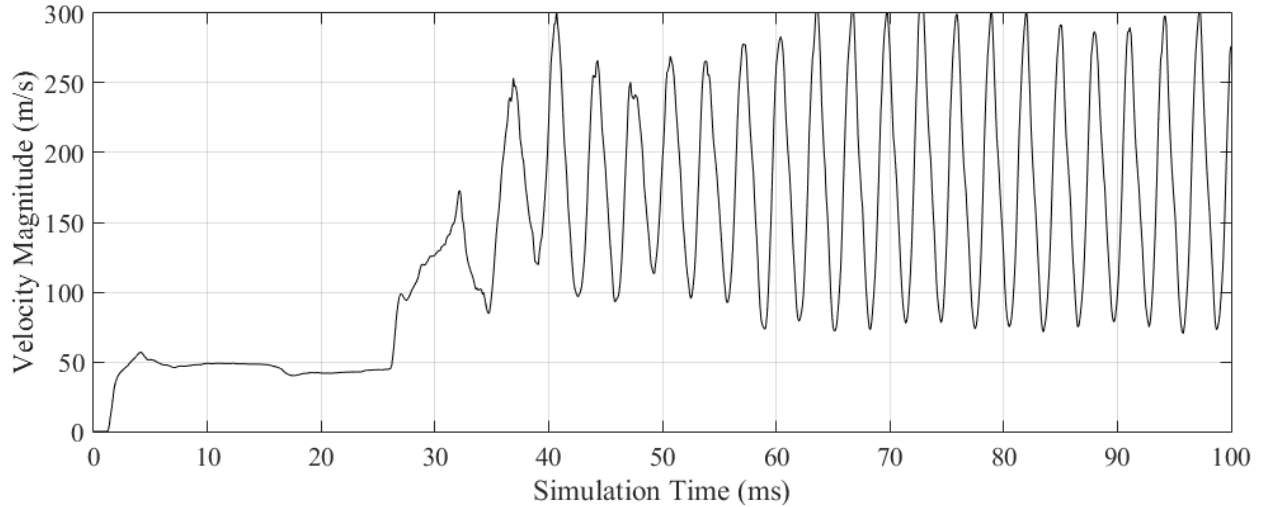


Figure 141: Engine Nozzle Exit Velocity Time History

The engine nozzle exit centerline velocity was also plotted from the velocity distributions as a time history in Figure 141. This simulation data is intended to match as closely as possible to the measurement of differential pressure from the exhaust Pitot tube on the engine test stand. When the simulation begins, the initiation of flow into the engine inlet soon causes flow out the engine exhaust at a speed of approximately 50 m/s (164 ft/s). Upon ignition, there is a brief delay until the exhaust speed doubles and eventually rises to triple the preignition exhaust speed. By this point, the ignition transient has begun and the pressure oscillations inside the engine begin driving the exhaust speed oscillations to a quasi-periodic peak-to-peak amplitude of 225 m/s (738 ft/s).

4. Temperature Distributions

The temperature distribution in all regions was initialized to standard temperature, 300 K (80.3 °F, 540 °R). The exception to this is the injection boundary which maintains a constant elevated temperature of 488.7 K (420.0 °F, 879.7 °R) as measured on the engine test stand due to the propane preheat prior to injection. This temperature is not enough to cause ignition for several reasons. First, the mixture is pure propane; hence, there is no oxygen for combustion until mixing with air occurs. This temperature is also far below the autoignition temperature of propane/air mixtures even at an ideal, stoichiometric mixture. Lastly, the simulation will not initiate chemical kinetic modeling until the local temperature exceeds 600 K (620.3 °F, 1080 °R). As a result, temperatures were expected to decrease from the injection until the ignition event at 25 ms. This section details the resulting temperature distributions of the mixture throughout the simulation domain prior to ignition, during ignition, and during the engine's operation. It should also be noted that kinetic modeling was only active in the engine chamber region to reduce simulation time. As a result, no combustion was modeled in the ambient or exhaust domains.

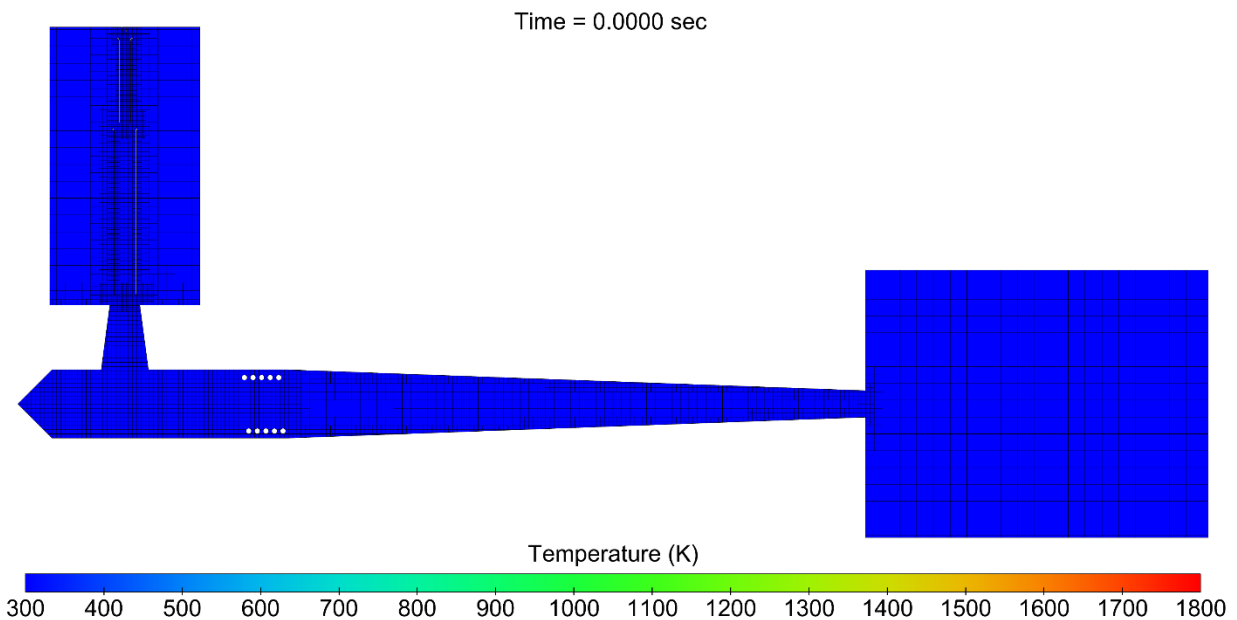


Figure 142: Initial Temperature Distribution (XY Symmetry Plane, t = 0 ms)

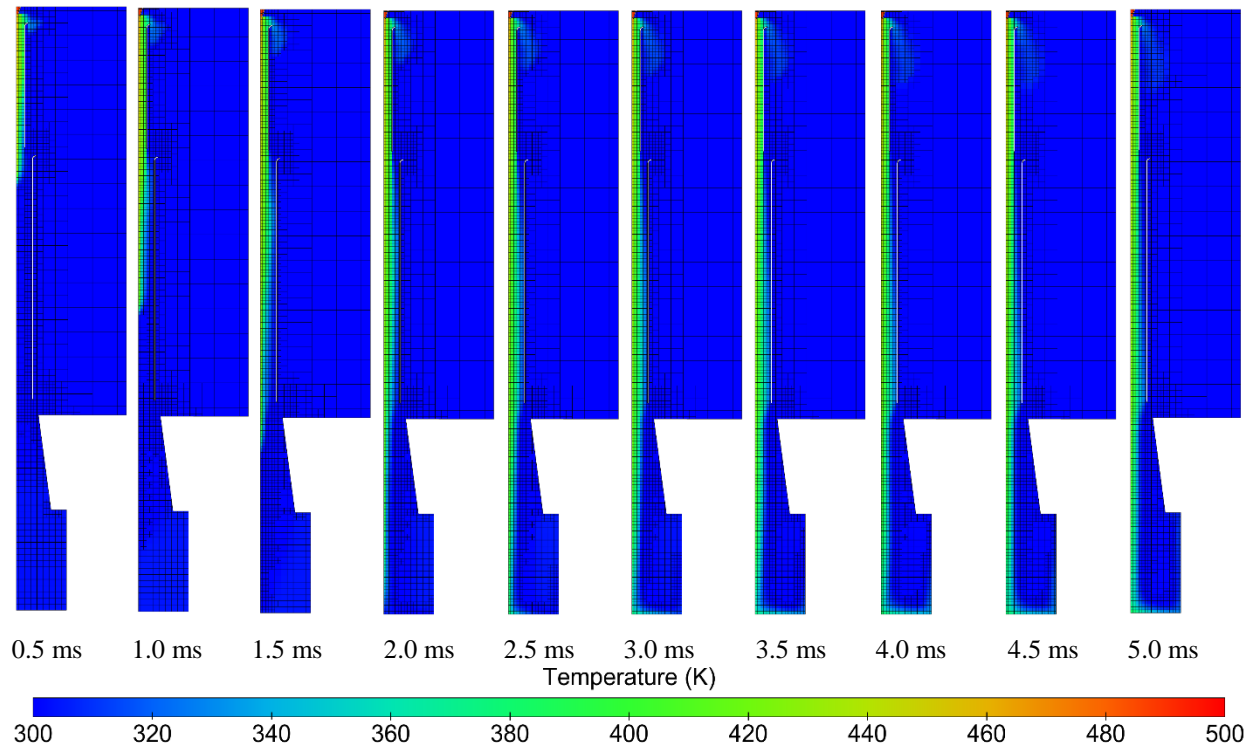


Figure 143: Temperature Distribution in Inlet Structures During Injection (YZ Plane at Origin, From Left to Right, $t = 0.5 - 5.0$ ms)

The temperature distribution of the injected fuel as it progressively mixes with the entrained intake air is shown in a series of cross-sectional slices through the inlet axis in Figure 143. The bounds on the temperature scale prior to ignition was limited to a maximum temperature of 500 K (440.0 °F, 900 °R) to better illustrate the local temperature changes. There was no reason to consider greater temperatures as there should be no temperature rise until the ignition source is activated at 25 ms. As a result, the temperature distribution is largely straightforward prior to ignition. The injection flow starts at the boundary temperature of 488.7 K and the core temperature quickly drops to 459 K (367 °F, 826 °R) at the first-stage inlet, 439 K (331 °F, 790 °R) at the second-stage inlet, 417 K (291 °F, 751 °R) at the third-stage inlet, and finally 382 K (228 °F, 688 °R) at the back wall stagnation point. The injection stream is clearly cooling toward the ambient temperature of 300 K.

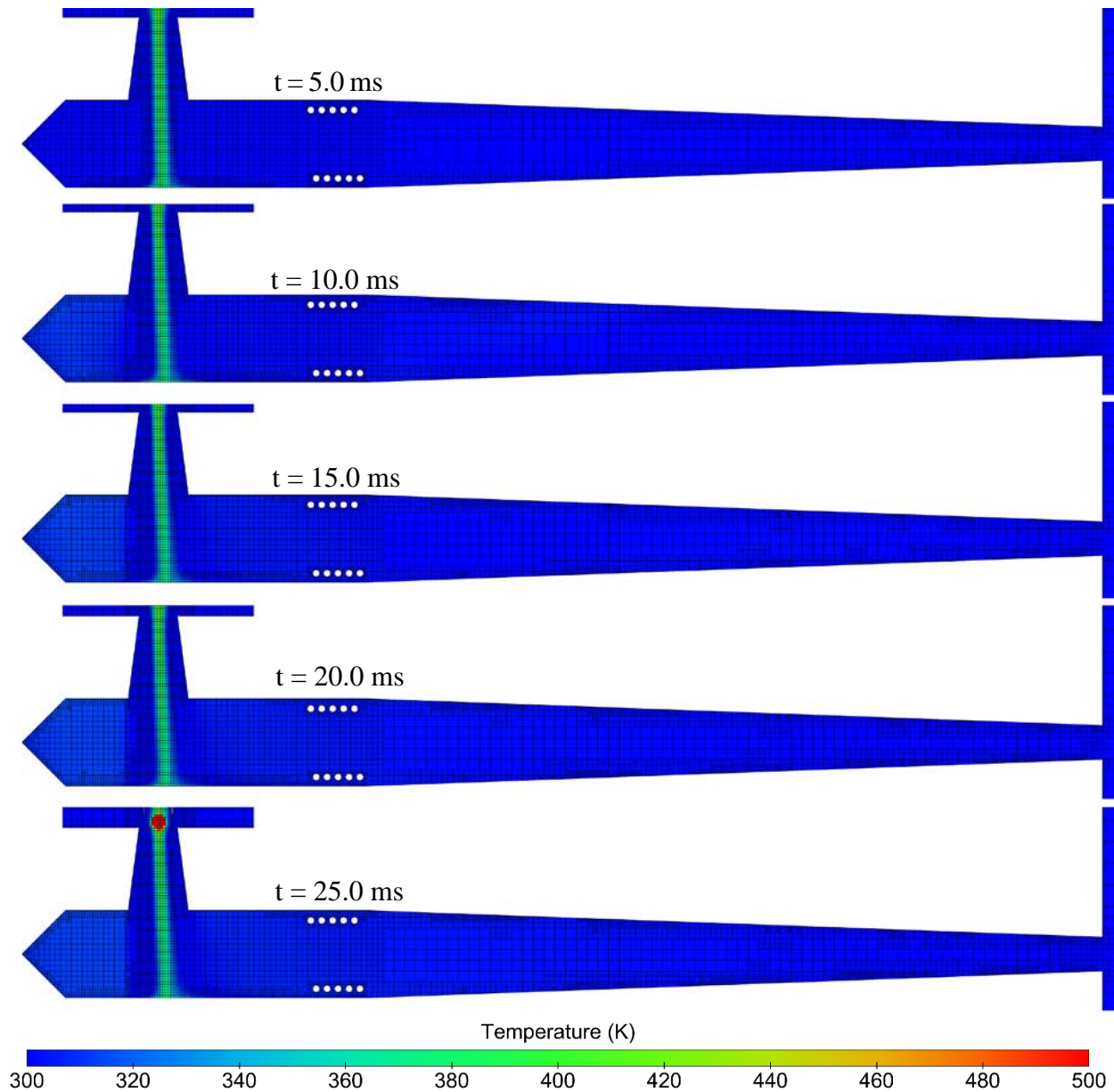


Figure 144: Temperature Distribution through Engine Core Immediately Prior to Ignition (XY Symmetry Plane, $t = 5.0 - 25.0$ ms)

The temperature distribution throughout the engine core (shown in Figure 144) is similarly conventional. As the simulation proceeds to the point of ignition (in the last frame), the only notable change is a slight temperature rise in the engine core, particularly in the forward recirculation zone. The fuel stream is surrounded by a jacket of cooler ambient air entering the engine that continues to cool the fuel/air mixture.

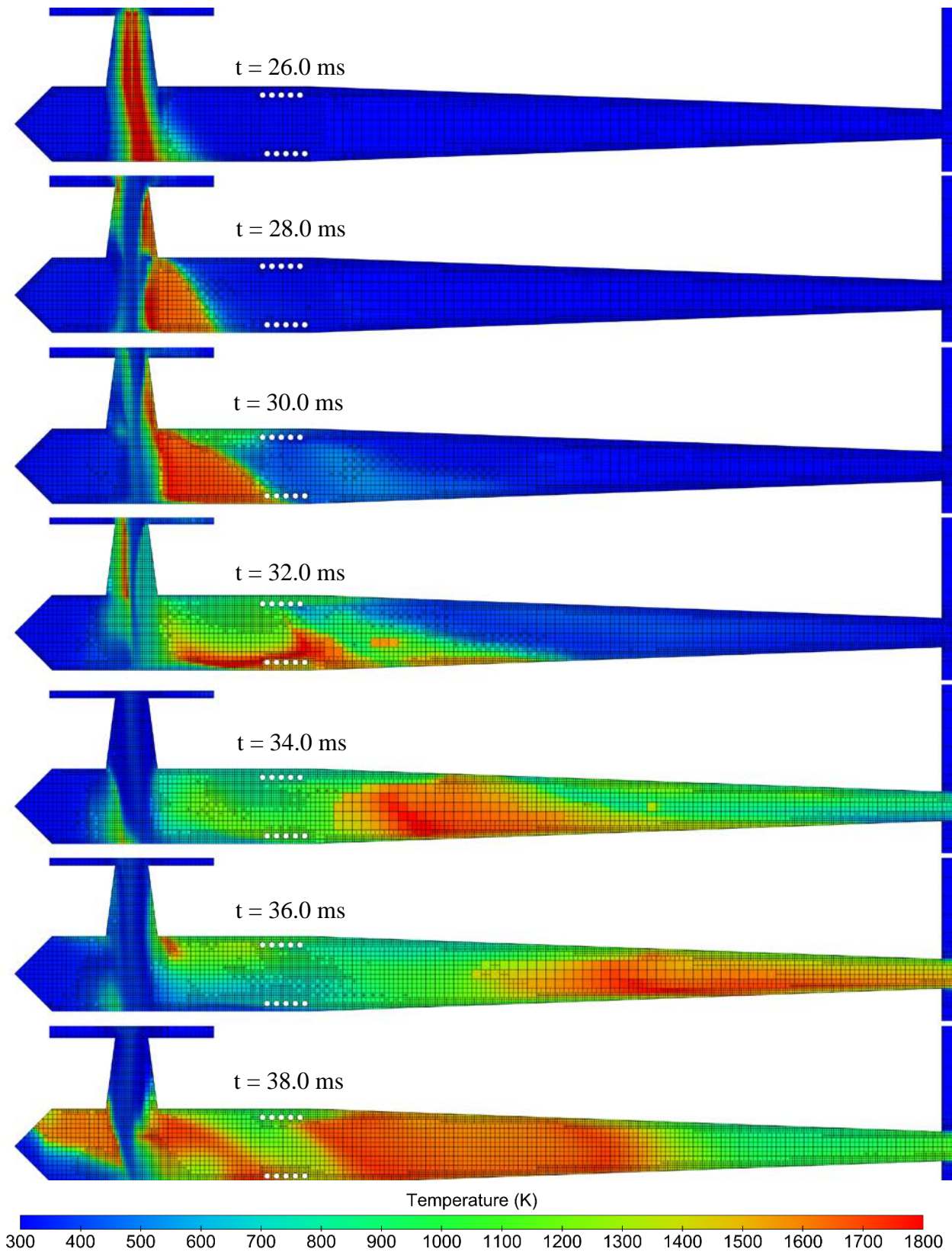
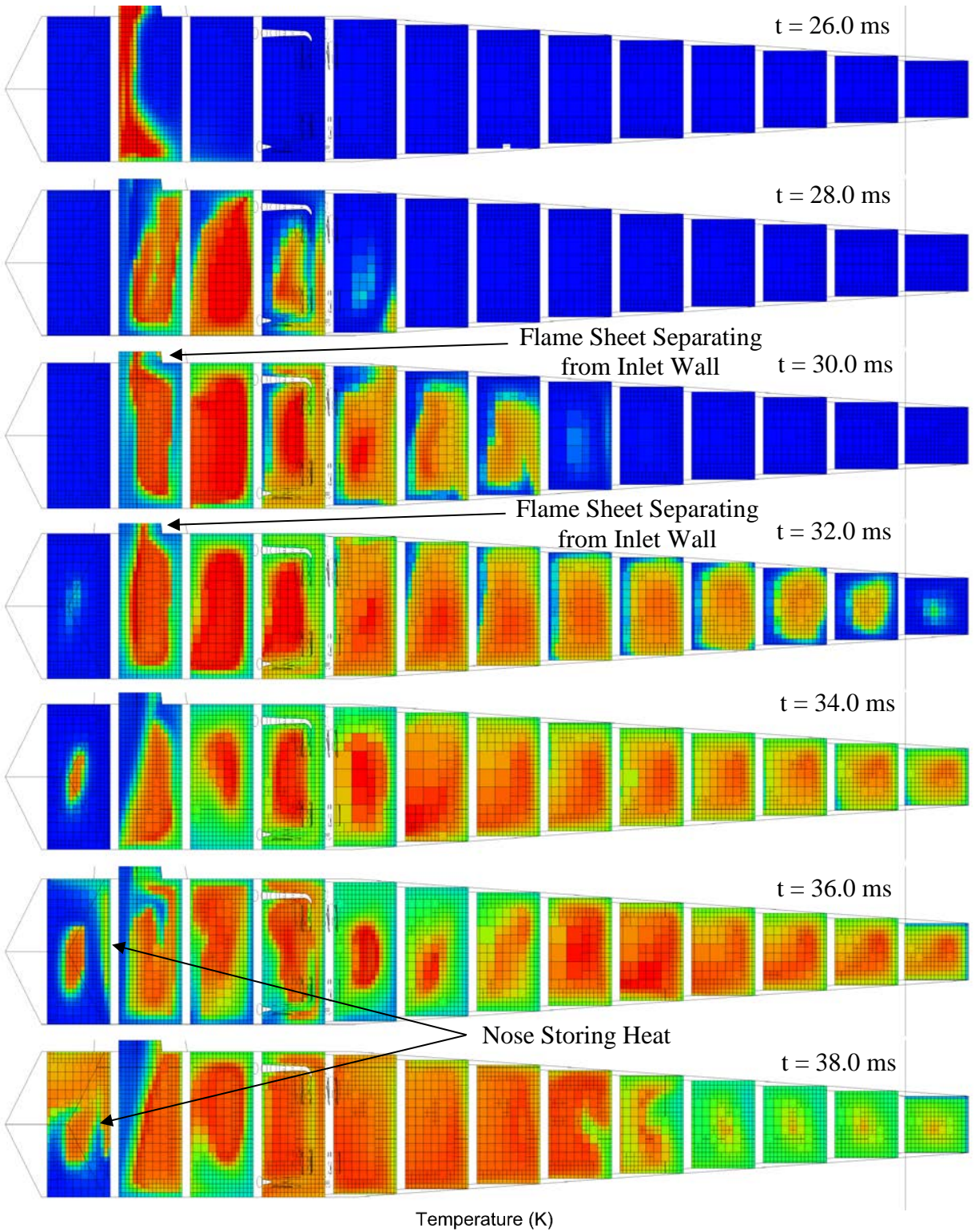


Figure 145: Temperature Distribution through Engine Core Immediately Following Ignition (XY Symmetry Plane, $t = 26.0 - 38.0$ ms)



Temperature (K)

300 400 500 600 700 800 900 1000 1100 1200 1300 1400 1500 1600 1700 1800

Figure 146: Temperature Distribution through Engine Core Following Ignition (Multiple YZ Planes at 0.04 m Intervals, $t = 26.0 - 38.0$ ms)

The temperature distribution throughout the engine during the initial startup transient is visualized along the centerline symmetry plane in Figure 145 and on cross-sectional planes spaced 40 mm apart in Figure 146. These two visualization help show both the progression of the flame front throughout the engine and how the flame front is affected by the recirculating flow. Starting at 26 ms (when the 1 ms ignition source ends and the flame is propagating under its own release of energy) the fuel/air injection flow is quickly surrounded in a high temperature jacket of combustion. Shortly thereafter, the slightly fuel-rich injection flow dominates again as the flame front circulates around the outside of the engine core and propagates aftward. As more fuel continues to enter the core, the temperature continues to rise and push toward the nozzle exit still heavily influenced by the recirculating flow.

At 32 ms (just 6 ms after ignition), the temperature begins to rise in the forward recirculation zone. The symmetry planes seems to show the cooler injection flow dominating the temperature distribution along the inlet axis with only minor variation. Comparing to the cross-section views, however, reveals the more nuanced reality the simulation predicts. The recirculation flow appears to oscillate with the air intake, particularly coming through the third-stage inlet. The cooler fuel/air stream is not stagnant. Instead it is constantly mixing with the incoming air which itself is affected by the local pressure (see distributions in Section 2) and the recirculation flow appears to drive a significant amount of it, as well as the heat release and temperature rise. It is not until late in this transient that the highest temperatures are reached along the plane of symmetry, but the core of the recirculation flow reaches peak temperature early on. The lower temperatures seen at the plane of symmetry are also evident on the wall boundaries of the engine through the length of the core and nozzle.

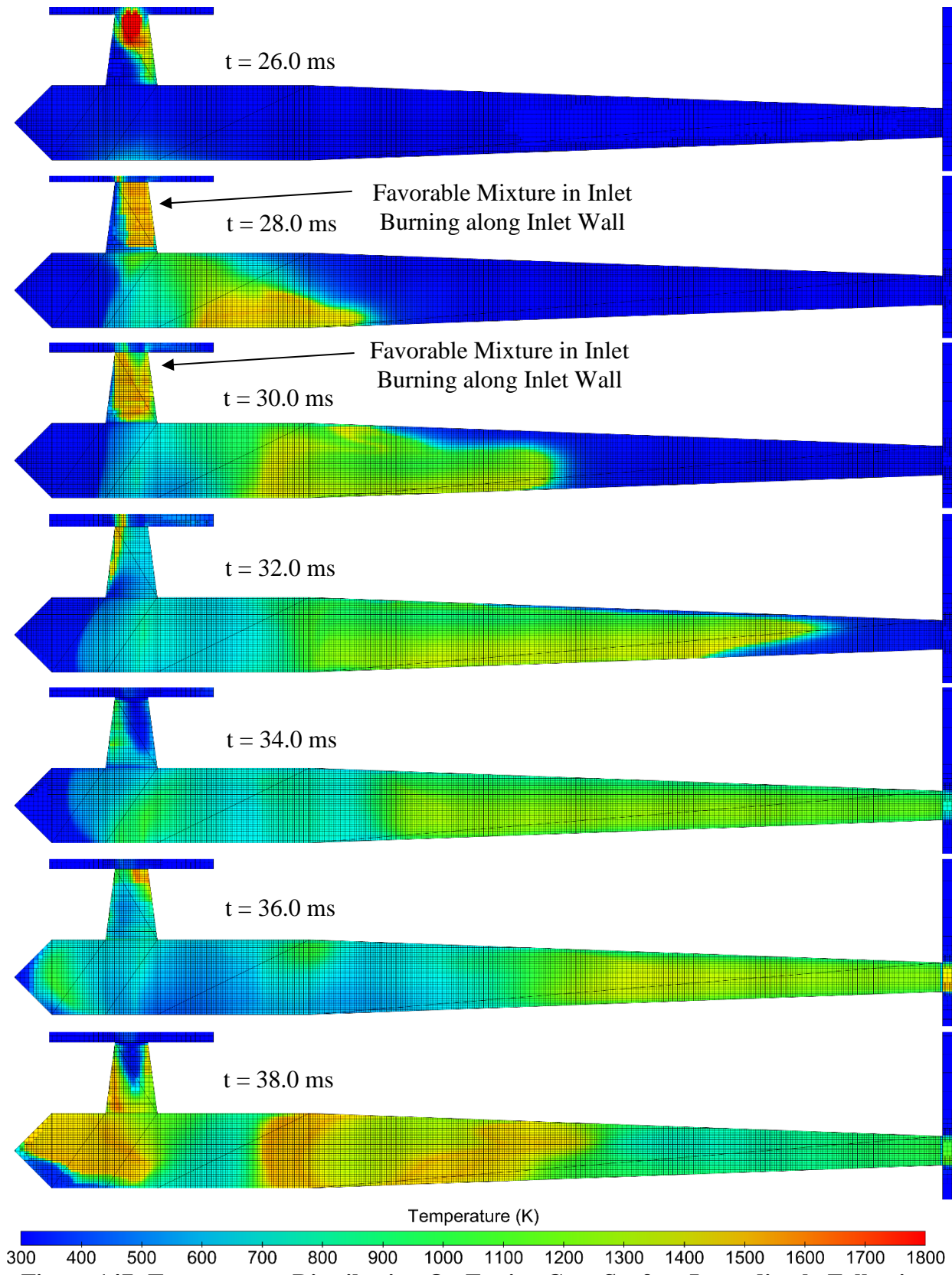


Figure 147: Temperature Distribution On Engine Core Surface Immediately Following Ignition (Engine Wall Boundary Surfaces, $t = 26.0 - 38.0$ ms)

This reduction of temperature on the wall boundary compared to the peak temperatures inside the core is most evident by visualizing the temperature distribution for the wall surfaces. This is shown for the same simulation time steps in Figure 147. Immediately following the ignition source, at 36 ms, there is a high local temperature zone trapped in the third stage inlet which appears to spread around the cooler, more fuel rich inlet flow. This suggests that early in the combustion process, the mixing of fuel and air at the inlet lip forms a region of fluid with a favorable mixture while the flame front begins to propagate downward into the engine core.

This is partially visible in Figure 146 at the 30 and 32 ms time steps where the high temperature region extends upward into the engine. In those frames, it appears the high temperature zone has separated from the inlet wall and may be feeding the core recirculation flow. So it seems at the earlier time steps (at 28 ms for instance) this zone of inlet combustion has not yet separated from the wall and/or been carried by the inlet flow into the engine core to help feed the combustion process. With that mechanism in mind, it seems at later time steps, there is an oscillatory phenomena that sets up between high and low temperatures on the inlet wall suggesting the shedding of a burning sheet, which is then replaced by cool air which mixes and eventually forms a new sheet of combustion in the same zone.

The remainder of the temperature distribution visualized on the engine wall is largely driven by the circulating flow around the edges of the engine volume. This helps illustrate how the flame front begins to heat up and burn inside the forward recirculation zone of the engine. At earlier time steps, the flame front is unable to push far forward of the inlet. However, by 36 ms, the high temperature flow is circulating upward into the forward region and begins filling the periphery that the circulation core (shown in Figure 146) has not yet heated to the point of combustion.

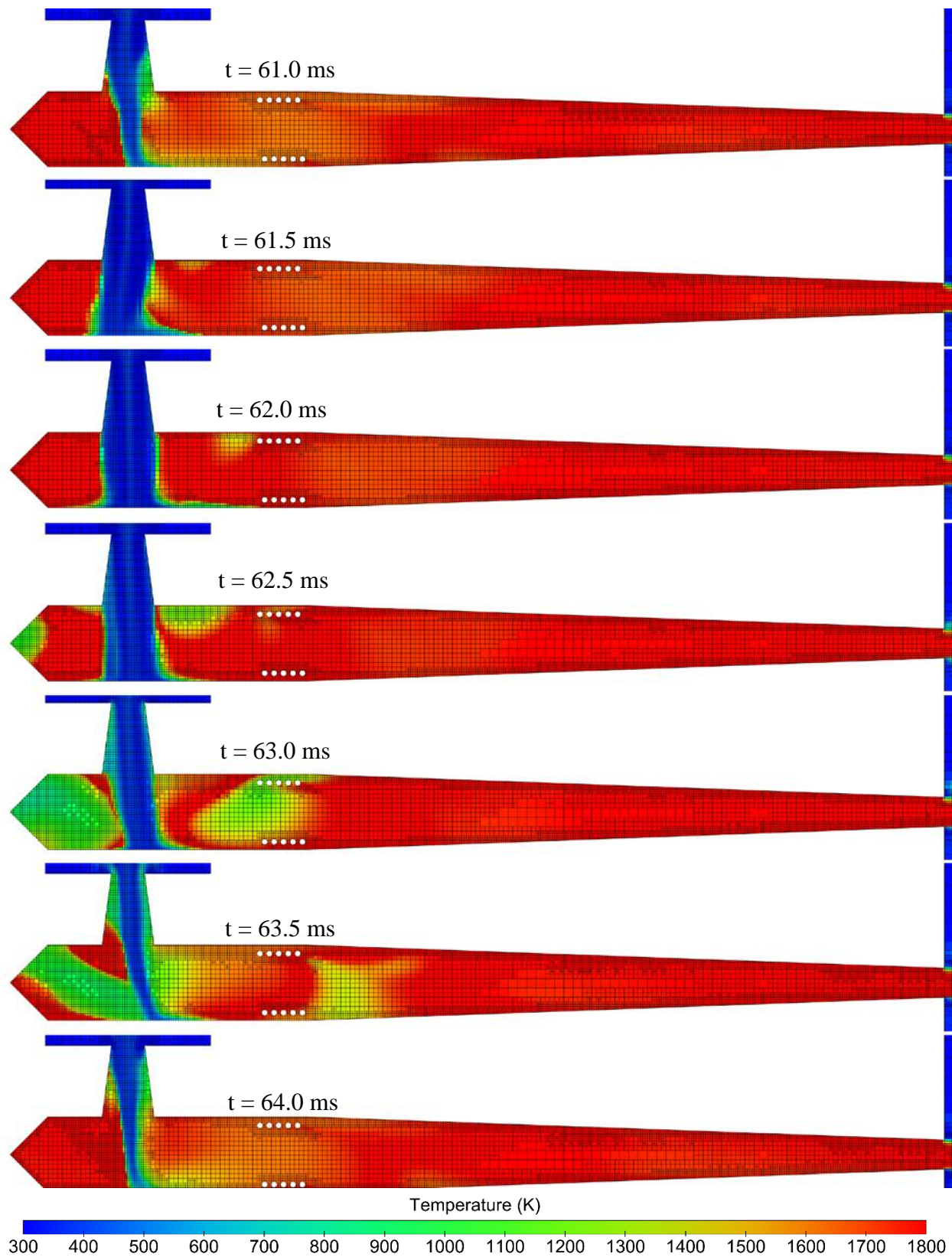


Figure 148: Quasi-Periodic Temperature Distributions Showing the Kadenacy Effect (XY Symmetry Plane, $t = 61.0 - 64.0$ ms)

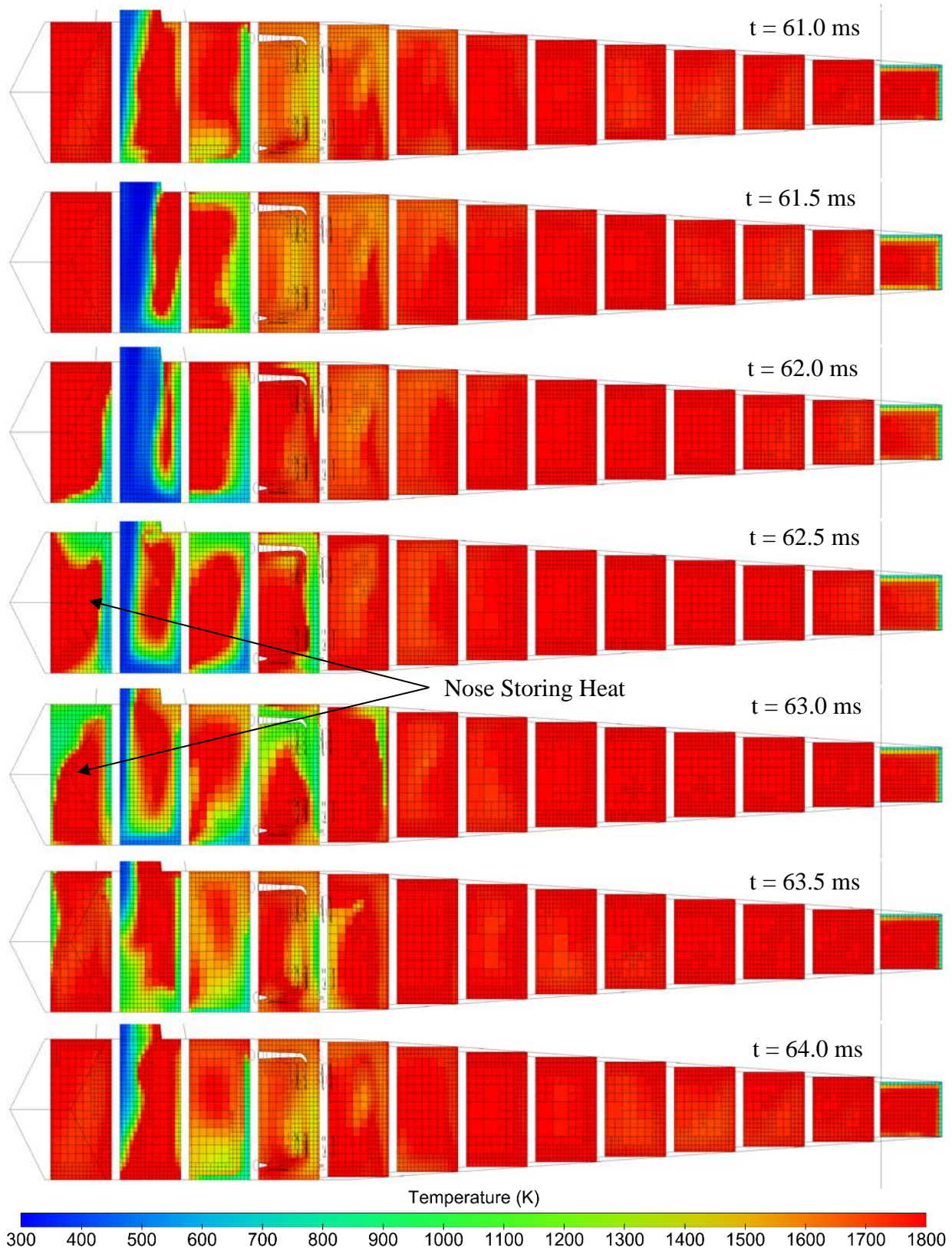


Figure 149: Quasi-Periodic Temperature Distributions Showing the Kadenacy Effect (Multiple YZ Planes at 0.04 m Intervals, $t = 61.0 - 64.0$ ms)

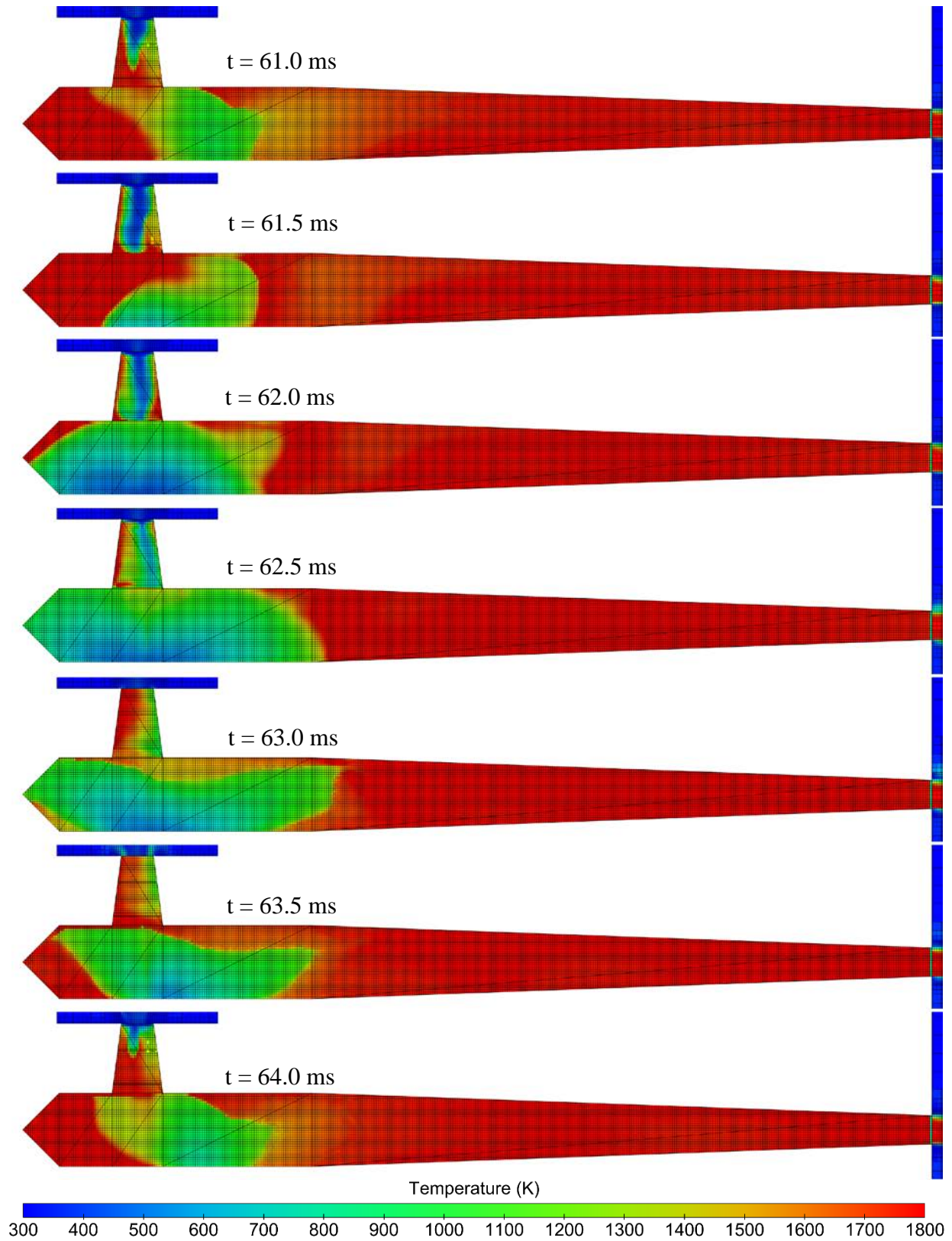


Figure 150: Quasi-Periodic Temperature Distributions on Engine Walls (Engine Wall Boundary Surfaces, $t = 61.0 - 64.0$ ms)

The quasi-periodic temperature distributions through the engine chamber visualized on the symmetry plane in Figure 148, on cross-sectional planes spaced 40 mm apart in Figure 149, and in this case, on the engine wall surfaces in Figure 150. It should be noted that the timesteps shown in these figures were taken much later than those for pressure and velocity for demonstration of the Kadenacy Effect in terms of temperatures. This is because the pressure and velocity profiles reached a nearly quasi-periodic condition as early as 40 ms. But the temperature profile at these times was not yet synchronized and stable due to the heating of the walls and ambient heat transfer. That did not occur until later. As a result, the visualizations for temperature were taken later, beginning at 61 ms as opposed to the 41 ms for pressure and velocity profiles.

These visualizations show an exhaust temperature distribution that is largely invariant with time despite the rapidly varying intake of comparatively cool fuel and air. This suggests that combustion occurring in the engine core is complete. The intake of a fresh charge of fuel and air is evident first in the cross-sectional planes almost immediately (entering at 61.0 ms and mixing into the core). It is then visibly affecting the chamber temperature in the symmetry plane both forward and aft of the inlet (from 62.5 ms onward). Meanwhile the temperature distribution around the engine walls shows the flow of the cooler fuel/air mixture around the periphery of the core (between 62.0 ms and 63.0 ms) before its own combustion reaches the wall and the flame spreads downstream (at 63.5 and 64.0 ms). The remnants of this flow burning the remaining unburnt fuel as it approaches the coil are similar to the start of the cycle shown at 61.0 ms. This process continues as the normal operating temperature profile of the engine.

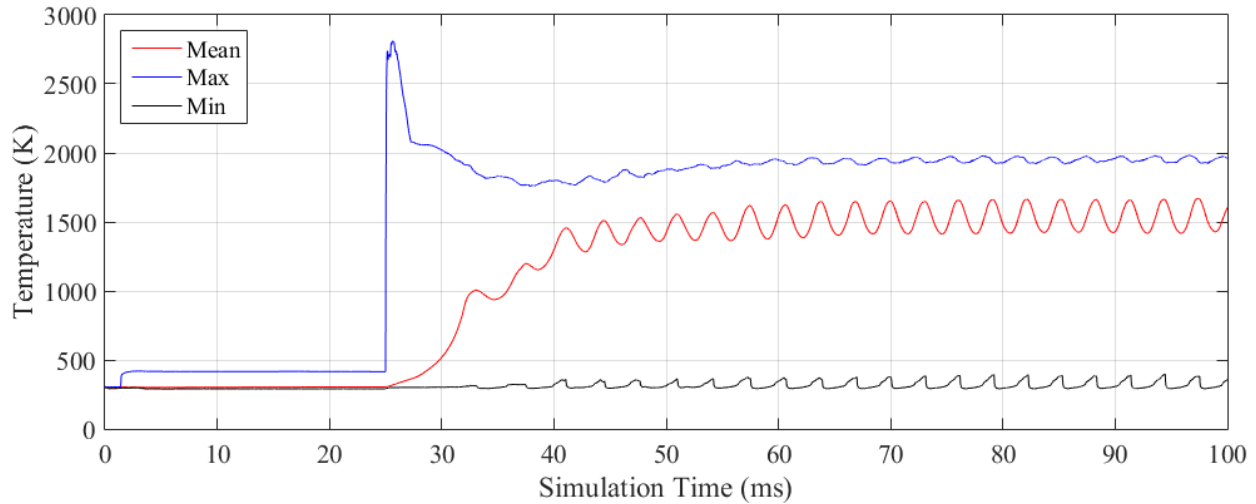


Figure 151: Simulation Mean (Mass Averaged), Maximum, and Minimum Temperatures in the Engine Chamber

A time history of the engine region’s mass-averaged (mean) temperature as well as the maximum and minimum temperatures in the chamber are plotted in Figure 151 over the entire simulation time domain from 0 to 100 ms. The flow inside the engine chamber never drops below the ambient temperature of 300 K (80.3 °F, 540 °R). The injection flow’s elevated temperature raises the maximum temperature of the chamber to a steady temperature of 416 K (289 °F, 749 °R) as it enters the engine. At the point of ignition, the maximum temperature (found at that time immediately around the ignition source) spikes to nearly 3000 K (4940 °F, 5400 °R) but soon stabilizes by 60 ms to a pproximately 2000 K (3140 °F, 3600 °R). Meanwhile, the mean chamber temperature rises to a quasi-periodic value oscillating around 1500 K (2240 °F, 2700 °R) with a minimum of approximately 1380 K (2024 °F, 2484 °R) and a maximum of approximately 1610 K (2438 °F, 2898 °R). The minimum temperature remained around 300 K (80.3 °F, 540 °R) though slightly affected by the temperature rises in the engine chamber.

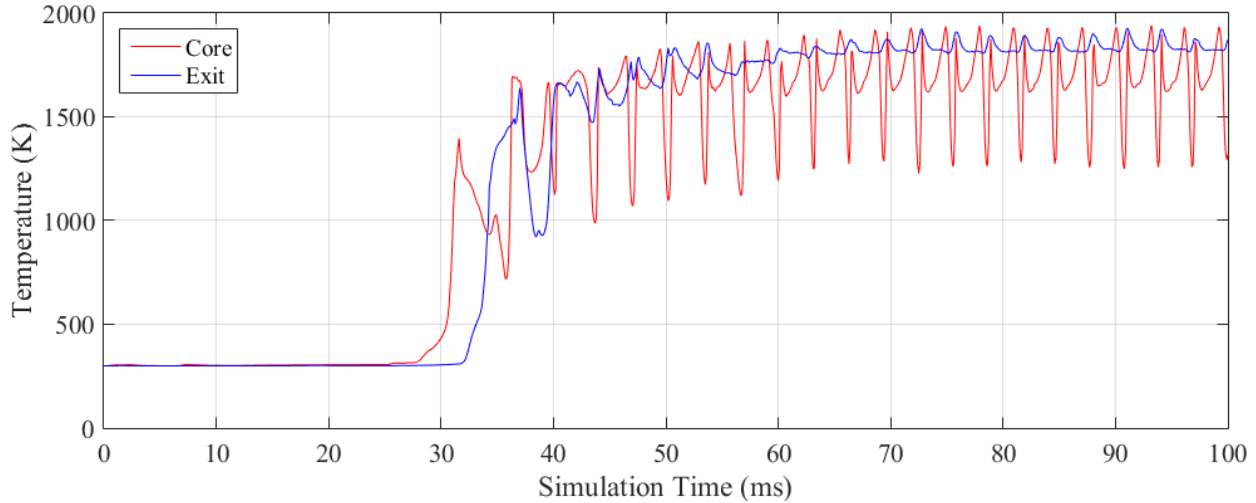


Figure 152: Engine Core and Exhaust Gas Temperatures

Lastly, the engine core and exit fluid temperatures were polled from the CFD distribution along the engine's centerline axis, the time histories of which are plotted over the entire simulation time domain in Figure 152. This data set is intended to match as closely as possible to the experimental measurements made inside the engine core (at the center of the inert coil) and coincident to the Pitot tube via thermocouples. Unfortunately, the nature of heat transfer and thermocouples all but prevents the ability to match temperatures at this fast a data rate (0.1 ms timestep or 10,000 Hz), but steady-state temperatures should be similar albeit lower since this adiabatic simulation does not account for heat loss to the surroundings.

This plot also illustrates the large swings in temperature the flow inside the engine chamber experiences between cycles. It also illustrates a significant lag in the core and exit temperatures behind the moment of ignition showing a delay of at least 5 ms for the core temperature and nearly 10 ms for the exit temperature as the flame front spreads through the engine. Beyond the erratic startup transient, a quasi-periodic state is reached by 70 ms with the exit temperature oscillating around 1700 K (2600 °F, 3060 °R) and the chamber temperature oscillating around an average of 1833 K (2840 °F, 3299 °R).

5. Equivalence Ratio and Species Distributions

The species distributions in all regions was initialized to that of standard dry air – mass fractions of oxygen and nitrogen of 0.23 and 0.77 respectively with no water content. The injection boundary is again the only exception with a mass fraction of gaseous propane, C_3H_8 , of 1.00. Because of this fuel-rich core to the injection flow, the equivalence ratio distribution is far outside the useful scale used to visualize the rest of the domain. As a result, the bounds of the visualizations of equivalence ratio distributions are limited to a maximum of 4.00, beyond which it was assumed combustion would be difficult to maintain. Some major species are also visualized to identify regions of oxidation and any level of unburnt propane the simulation suggests leaves the engine without burning. These species concentrations are visualized in mass fractions.

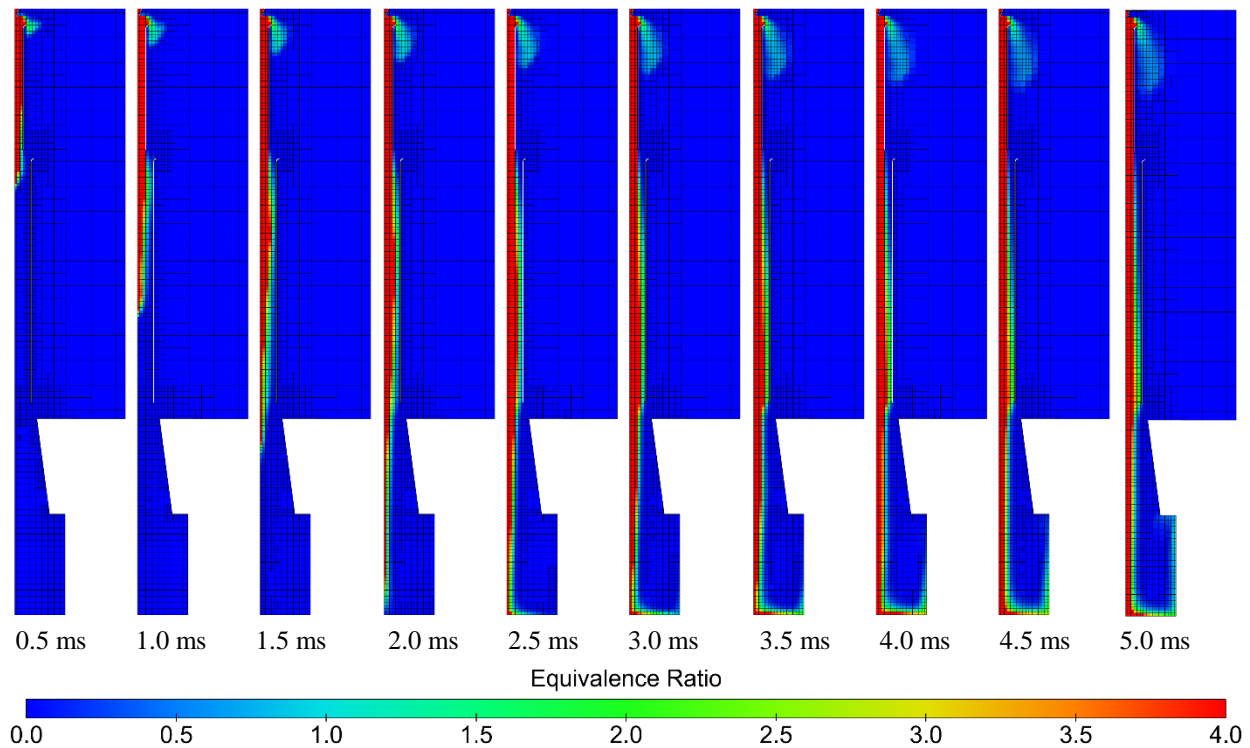


Figure 153: Equivalence Ratio Distribution in Inlet Structures During Initial Injection (YZ Plane at Origin, $t = 0.5 - 5.0$ ms)

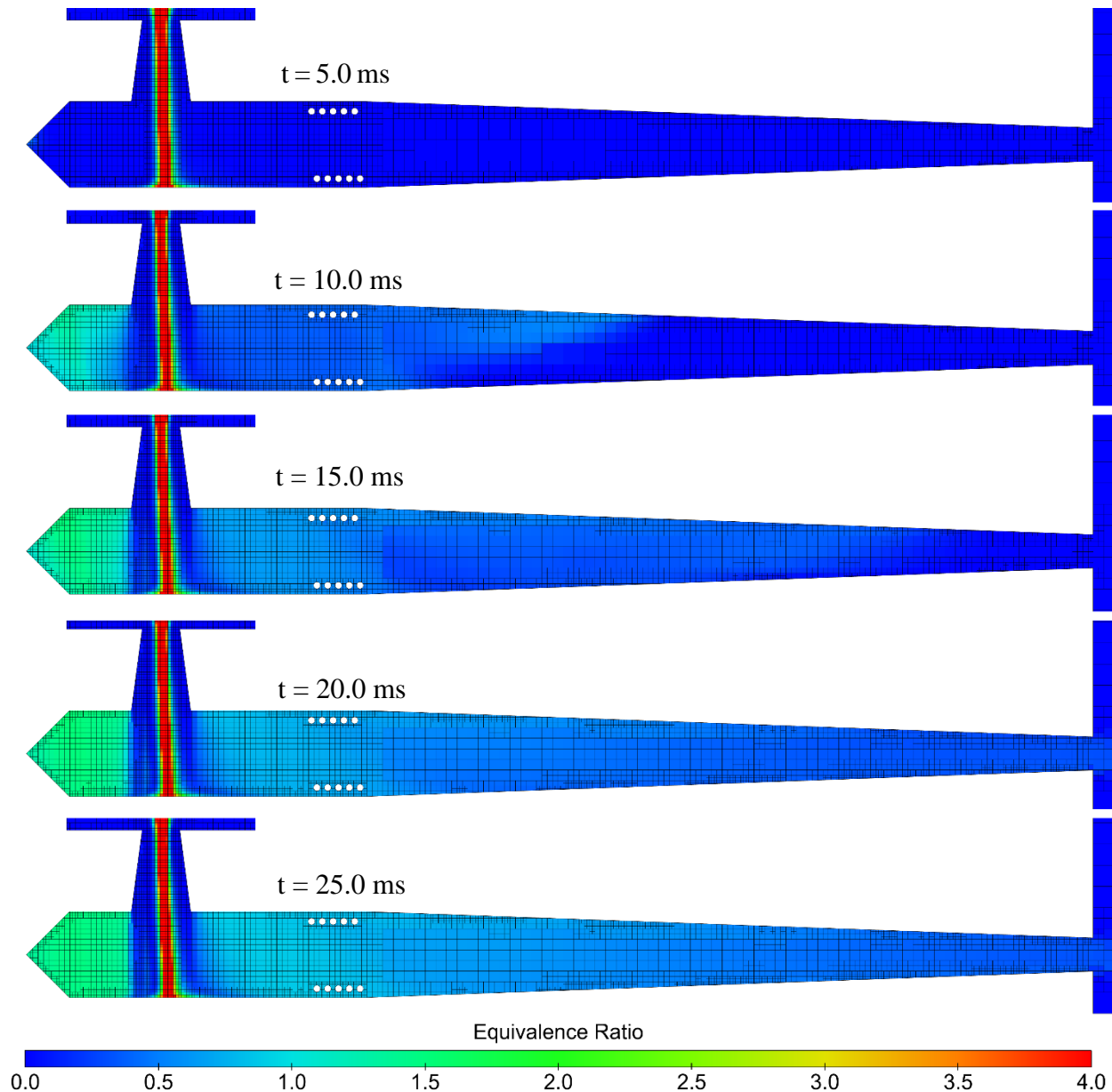


Figure 154: Equivalence Ratio Distribution and Streamlines through Engine Core Immediately Prior to Ignition (XY Symmetry Plane, $t = 5.0 - 25.0$ ms)

As the simulation begins, a stream of pre-heated propane gas is injected at high speed as was evident in the visualizations in Section 3. This is now also evident in the distributions of equivalence ratio up to a simulation time of 5 ms in Figure 153 and up to the point of ignition at 25 ms in Figure 154. Propane dominates the initial flow immediately leaving the nozzle, but the longer the simulation continues, more air is mixed with the fuel stream. It is clear, however, that

despite this early mixing, the core of this fuel/air stream remains too rich to burn effectively until it impinges on the back wall from approximately 2.5 ms onward. As the injecting fuel/air mixture continues to enter the engine, it is effectively split into two regions – part flows forward into the engine head recirculation zone and the rest flows aftward toward the nozzle exit. The mixture caught in the forward recirculation zone reaches an equivalence ratio between 1.0 and 2.0 by the time the ignition source appears at 25 ms. Further insight into the three-dimensional flow can be gained by checking the equivalence ratio distribution in cross-sectional planes.

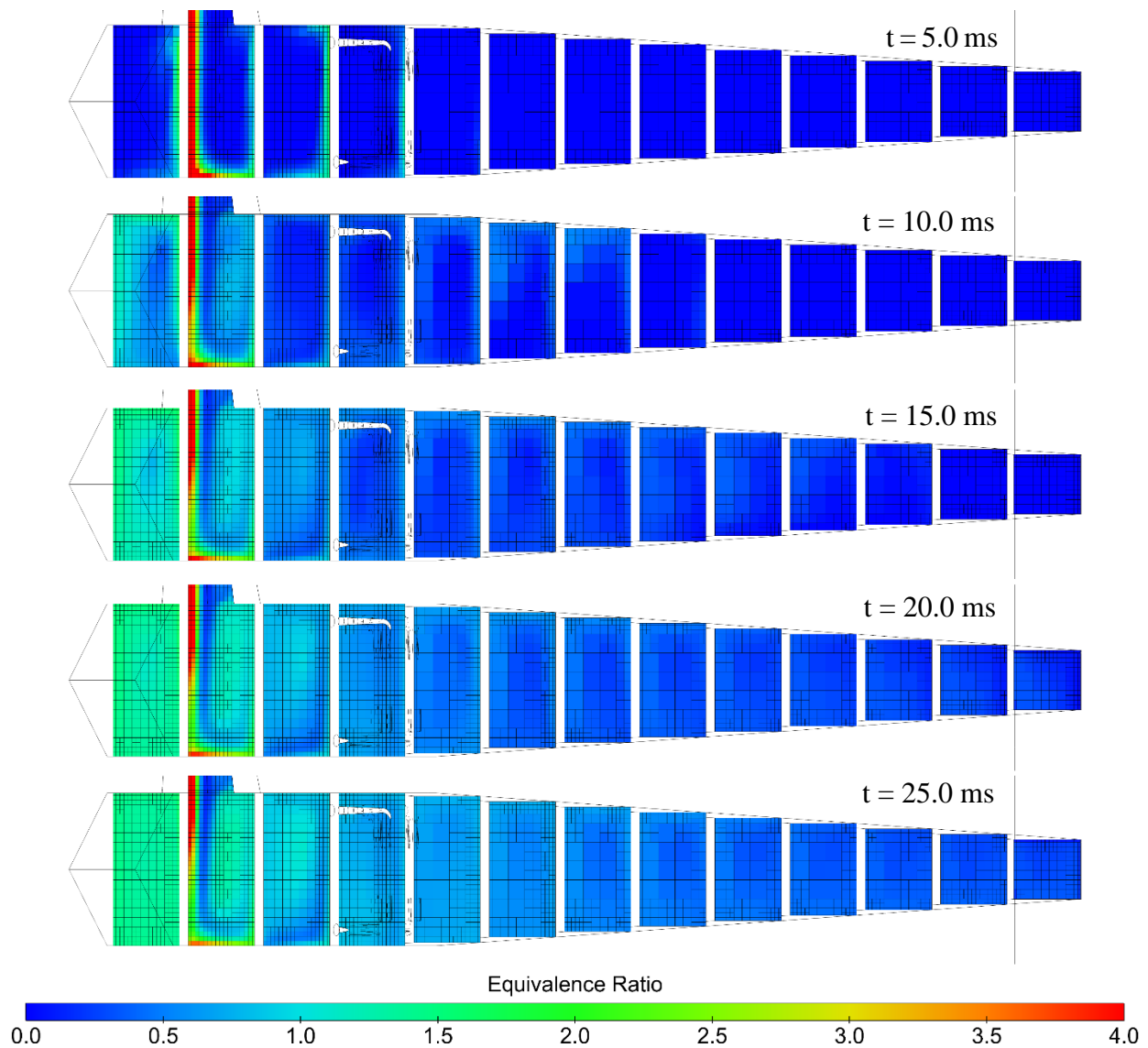


Figure 155: Equivalence Ratio Distribution through Engine Core Immediately Prior to Ignition (Multiple YZ Planes at 0.04 m Intervals, $t = 5.0 - 25.0$ ms)

The cross-sections shown in Figure 155 make it clear that there is significant recirculation around the walls of the engine core prior to ignition. The head of the engine (forward of the inlet) fills quickest reaching a steady equivalence ratio of 1.3 – 1.4 at the time of ignition. The recirculation remains most evident around the inlet where the final intake of fresh air is continuously being mixed with the incoming fuel/air mixture. In fact, from 10 ms onwards it is clear that the previously fuel-rich core is successfully being mixed except for the stagnation region where the flow impinges on the wall. As the flow continues out of the core and through the nozzle, the recirculation swirl is less evident potentially in part due to the blockage of the inert coil.

The equivalence ratio distribution from the coil onward shows a slight decrease as the flow reaches the nozzle. This could be due to several factors. Possibly the most likely is that the forward recirculation in the head of the engine is effectively trapping propane and air and so reaches an equilibrium mixture relatively early. Meanwhile, the engine nozzle has a much larger effective volume to fill with fuel before it reaches a steady state. Regardless, by 25 ms the engine is largely filled with a mixture of fuel and air that is within the range of propane autoignition and needs only to be touched off by the ignition source at the entrance to the third-stage inlet.

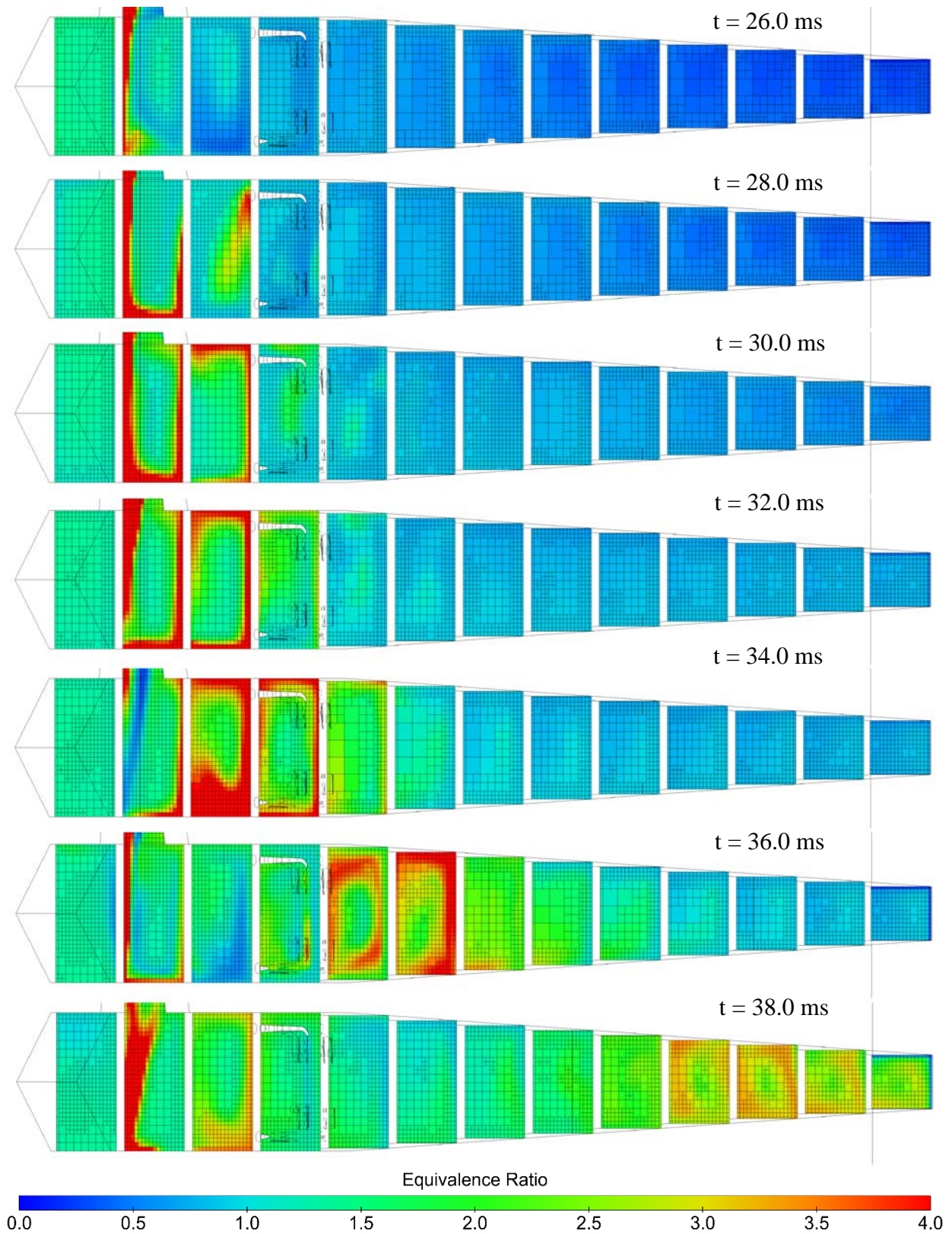


Figure 156: Equivalence Ratio Distribution through Engine Core Following Ignition (Multiple YZ Planes at 0.04 m Intervals, $t = 26.0 - 38.0$ ms)

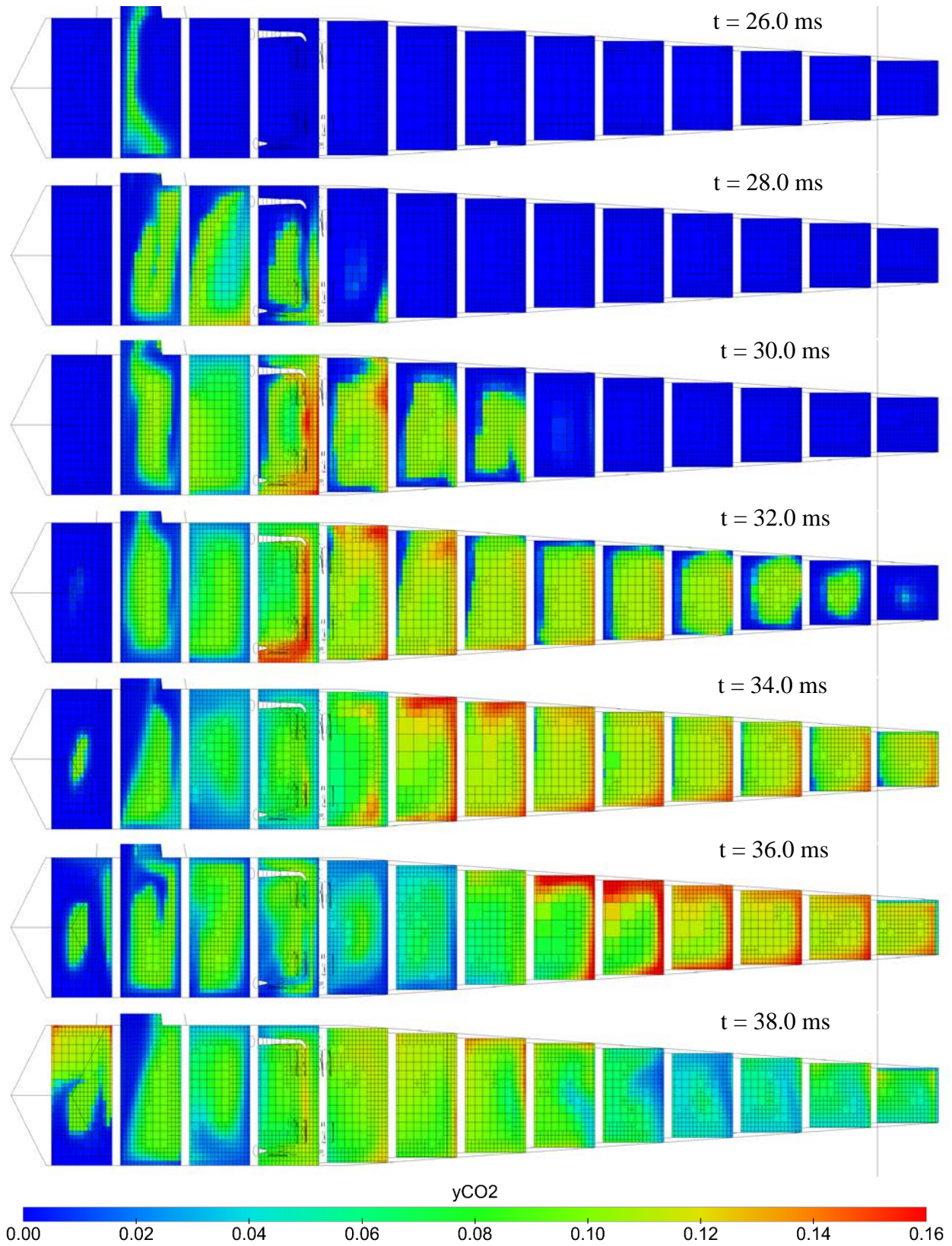


Figure 157: Carbon Dioxide Mass Ratio Distribution through Engine Core Following Ignition (Multiple YZ Planes at 0.04 m Intervals, $t = 26.0 - 38.0$ ms)

At the point of ignition, this equilibrium is violently disturbed by a 1.0 ms introduction of 35 J of energy at the entrance to the third stage inlet. The energy source term addition is enough to immediately raise the local temperature beyond the point of autoignition for the local propane/air mixture. The resulting pressure wave (seen in the visualizations in Section 2) appears to cause a brief disruption of the flow of clean air into the engine. This allows the engine core to receive a rich burst of fuel and air as the flame front begins to propagate through the rest of the core. The equivalence ratio distributions showing this process are included in Figure 156. The matching carbon dioxide mass ratio distributions are included in Figure 157 to allow direct comparison of the CO₂ production (and onset of the oxidation reaction) and equivalence ratio. The flow of clean air resumes some 6 ms later while the flame front from ignition slowly begins to spread (evidenced by the production of CO₂ and the temperature visualizations in Section 4).

Meanwhile this burst of rich fuel and air is flowing downstream toward the nozzle exit. It is clear from the final three time steps shown that the rich pulse is steadily mixing, burning, and accelerating as it moves aftward toward the nozzle exit. At a simulation time of 38 ms (now 12 ms since the ignition source was removed) a weaker fuel-rich pulse again enters the engine as a consequence of the startup Kadenacy effect seen in the earlier pressure distributions. It is not until 38 ms (on the first repetition of the cycle) that the flame begins to enter the forward recirculation zone. This intake, combustion, and exhaust cycle of the startup transient continues for 35 ms beyond ignition to a simulation time of 70 ms where a more steady oscillation is reached.

One final property of the flow which is difficult to visualize in still images is the continual circulation of both the equivalence ratio (and therefore species mass ratios) and the temperature distributions. This is more apparent in the animations made available on request from the author.

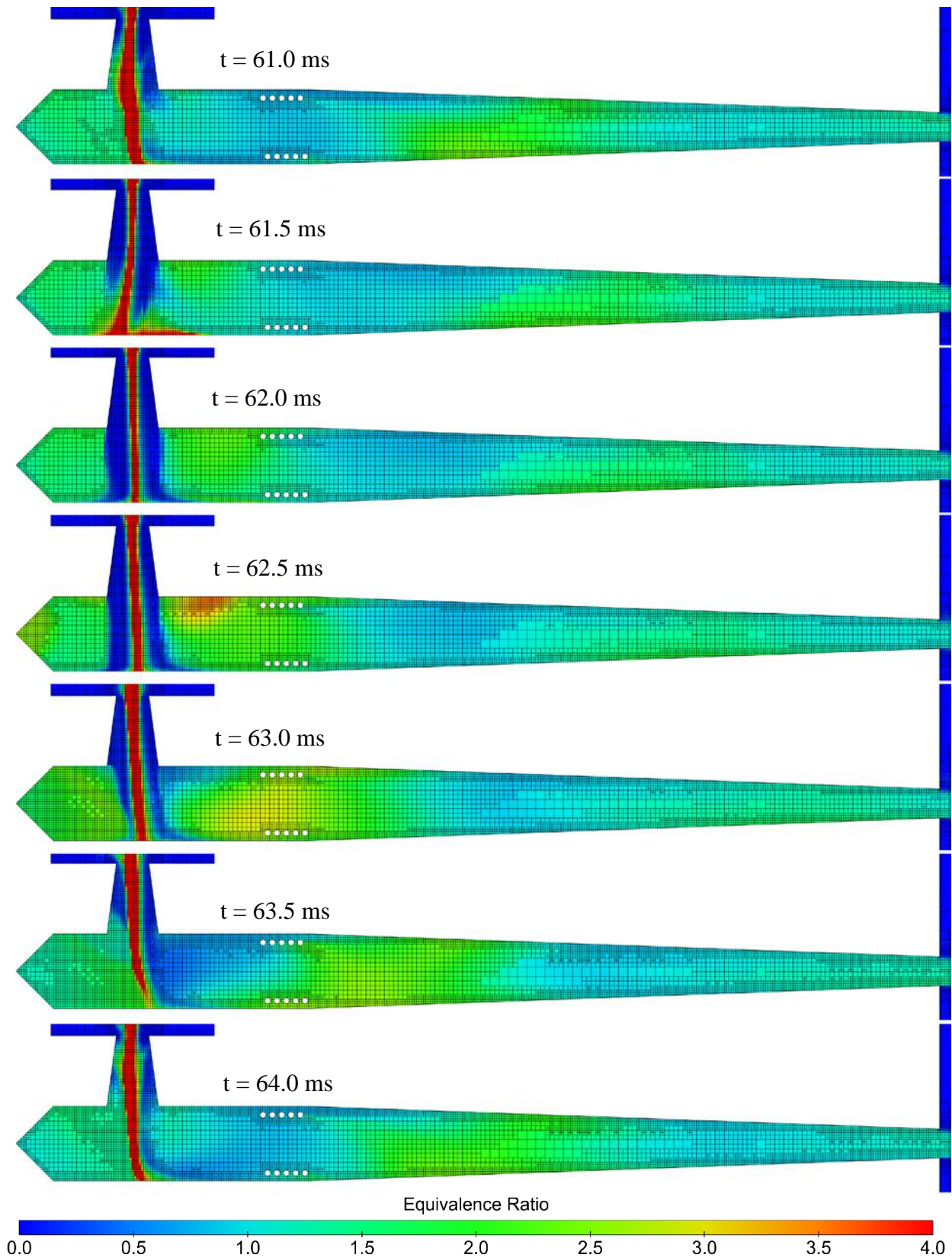


Figure 158: Quasi-Periodic Equivalence Ratio Distribution through Engine Core (XY Symmetry Plane, $t = 61.0 - 64.0$ ms)

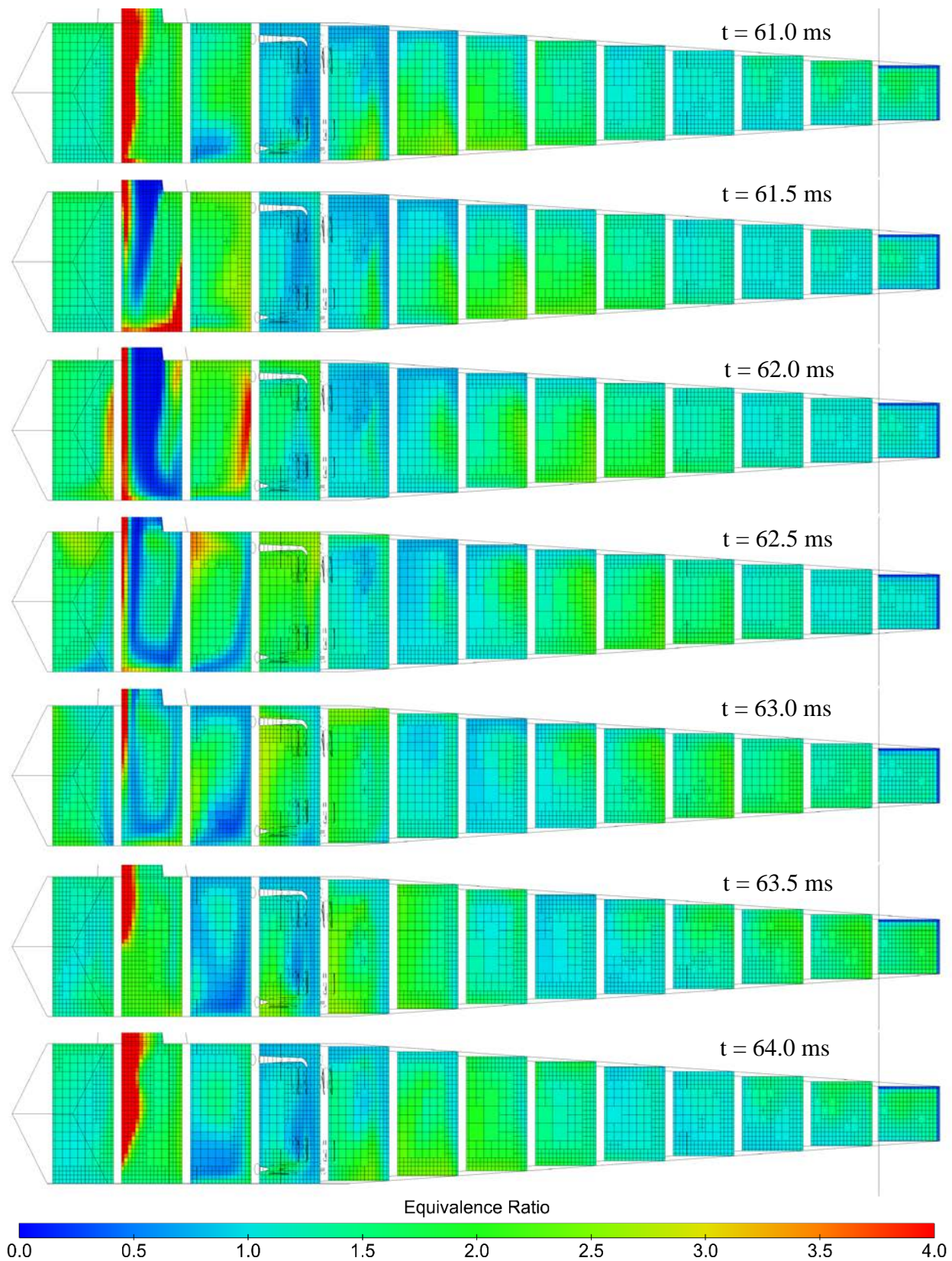


Figure 159: Quasi-Periodic Equivalence Ratio Distribution through Engine Core (Multiple YZ Planes at 0.04 m Intervals, $t = 61.0 - 64.0$ ms)

The equivalence ratio distribution throughout the engine chamber is visualized on the symmetry plane in Figure 158 and on a series of cross-sectional planes spaced 40 mm apart in Figure 159. These visualizations show a distribution of fuel and air that although periodic with the flow of clean intake air, remains largely steady around a slightly rich equivalence ratio with some regions reaching as high a ratio as twice that of stoichiometry. Only at the low point of the engine cycle (at 62.5 ms) is there any region not associated with the immediate injection flow that shows any higher. This region can be tracked through the engine chamber using the cross-sectional visualizations.

At the start of the cycle, engine chamber pressure is high which reduces the amount of clean air drawn into the engine. This allows a short charge of rich fuel/air mixture (an equivalence ratio slightly in excess of 4.0) which appears to circulate around the chamber periphery to both sides of the inlet as it continues to mix with the comparatively leaner fluid around it. By the low point of the cycle (62.5 ms) this rich burst is significantly diffused and has circulated around to the symmetry plane where it continues to circulate downward and out the engine as it continues to burn and become leaner. Meanwhile, the chamber pressure has reduced to a minimum and the engine is drawing in a large amount of air with the fuel. By the end of the cycle, the pressure has risen again due to the release of heat from combustion and the engine core has comparatively leaned except for the volume immediately around the inlet which is once again reducing the amount of air drawn into the engine with the fuel/air injection.

The equivalence ratio throughout the nozzle section is largely invariant with time except for the slow progression of a slightly rich pulse of fuel and air which appears to be continually replenished by the engine cycle.

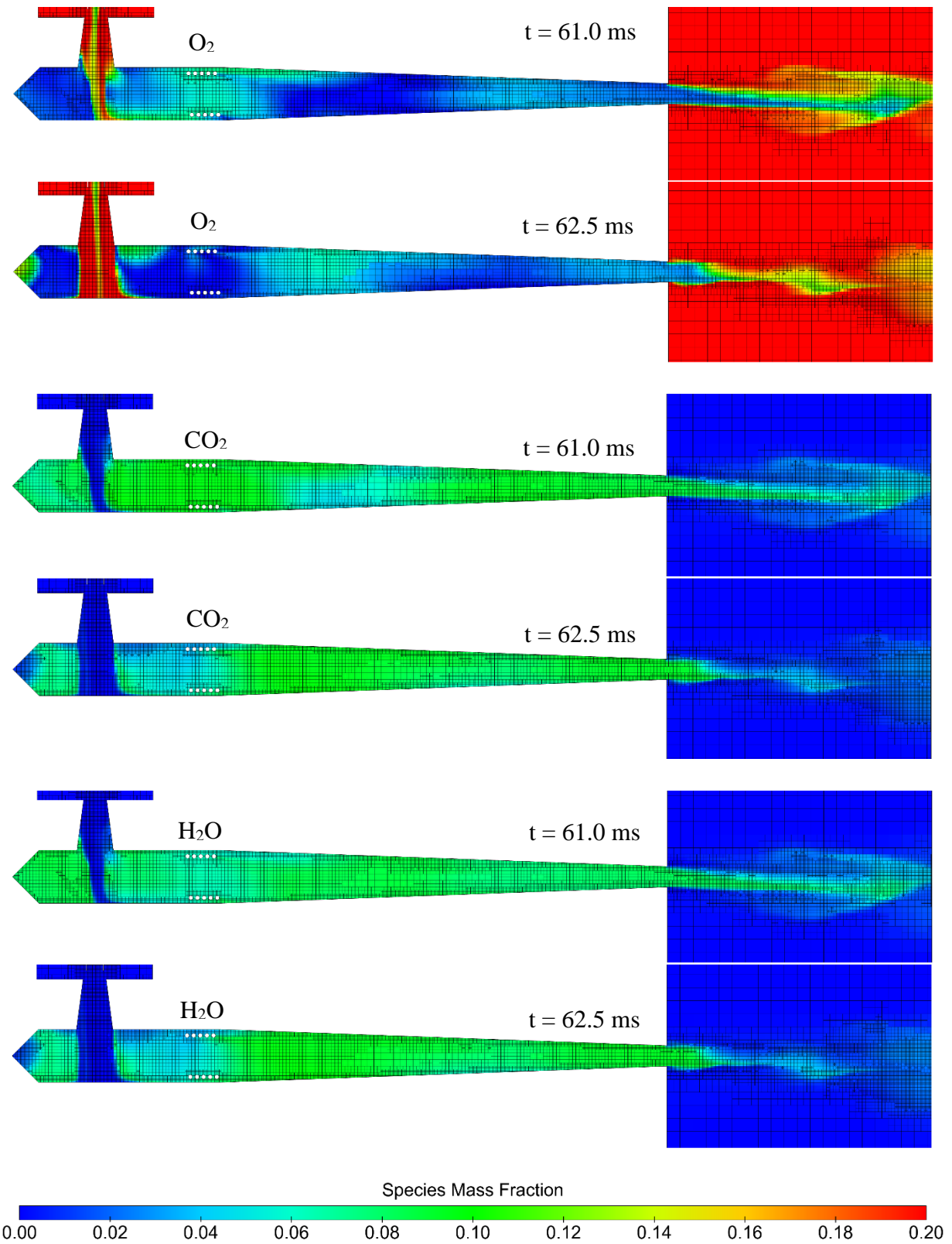


Figure 160: Comparison of Engine Quasi-Periodic O₂, CO₂, and H₂O Species Mass Fraction Distributions (XY Symmetry Plane, $t = 61.0$ and 62.5 ms)

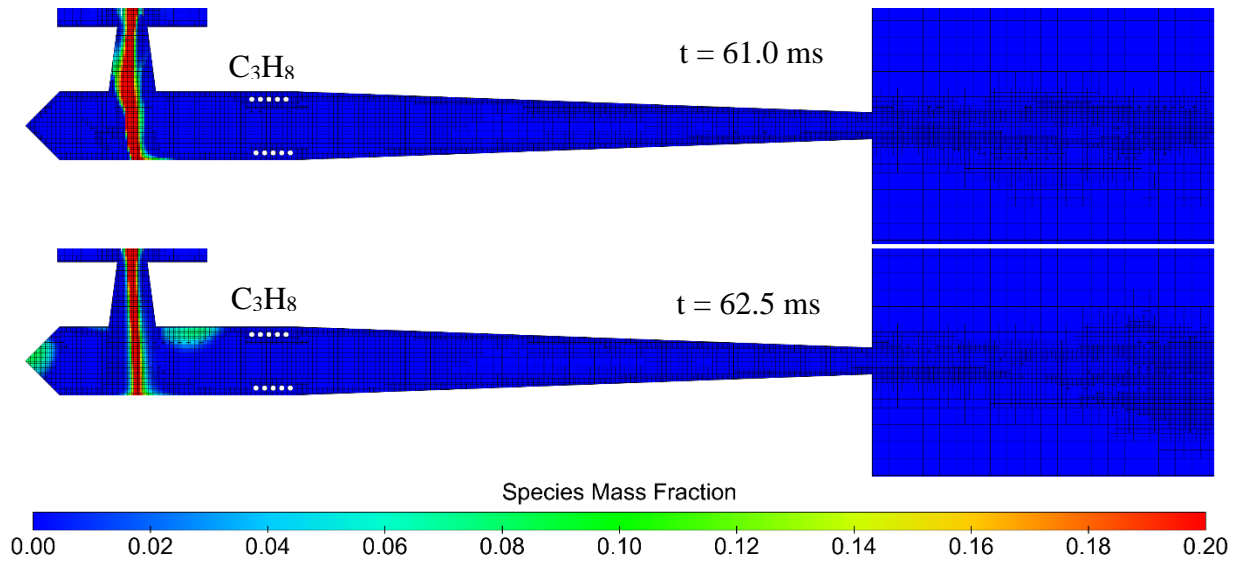


Figure 161: Engine Quasi-Periodic C₃H₈ Species Mass Fraction Distributions (XY Symmetry Plane, t = 61.0 and 62.5 ms)

The distributions of the major reaction species mass fractions are shown on the symmetry plane of the engine and exhaust regions at the start (61 ms) and midpoint (62.5 ms) of the engine cycle for O₂, CO₂, and H₂O in Figure 160 and C₃H₈ in Figure 161. These visualizations are directly complimentary in that regions with low C₃H₈ and low O₂ are likely regions to have produced the reaction products, CO₂, and H₂O. It is clear that the production of CO₂ and H₂O is largely unaffected by the engine cycle. There is some variation in the engine nose region and with the circulation of fresh air around the core at the midpoint of the engine cycle, but there is always a continuous stream of exhaust gases composed almost exclusively of reaction products. In fact, there is almost no unburnt propane leaving the engine and, compared to the products, very little unburnt oxygen. The propane mass fraction leaving the engine is on the order of 0.0001 and only along the engine wall. The presence of unburnt oxygen in the core and nozzle suggests, however, that this may be a result of the propane reacting quickly and oxidizing into lower hydrocarbons, which are then burning with the remaining air as it leaves the core and eventually the engine.

B. Experimental Data Results and Comparison to CFD

The following section details the results of the combined measurements of experimental data logged on the engine test stand using the Brayton-Gluhareff cycle Experimental (BGX) engine, both of which were described in detail in Chapter V. The results consist of time histories of measured pressures, temperatures, and thrust forces. The data was plotted in MATLAB r2015a to be compared with similar data predicted by the CFD simulation results detailed in the previous section. As before, these experimental results are separated into sections where their point measurements and (in the case of apparent temperatures) distributions are discussed. The experimental data and CFD predictions were matched as much as possible, but the reader is reminded that the nature of these two sources of data are fundamentally different with the experimental dataset being very large in the time domain but limited in specific measurements. Meanwhile, the CFD data is necessarily limited in the time domain (essentially reaching a quasi-periodic condition and ceasing further calculations to save time) but provides three-dimensional distributions of nearly any parameter albeit subject to many idealizations. Where these two datasets overlapped, comparisons between the experimental and computational were included in these results with final conclusions being drawn in Chapter VII. High speed data (thrust, core pressure, and exit velocity) were also subjected to a 10 ms moving average shown in many plots with the raw data. This is included only to show how the averaged response changed with time removing the higher-frequency cycle response.

1. Chamber Pressure

The engine chamber pressure was recorded at the maximum data rate of 10,000 Hz (split evenly among three channels at 3,333 Hz each) using a stainless steel tube located at the center of the inlet axis mounted flush to the back wall of the engine chamber. This location was expected to coincide with the stagnation, peak pressure inside the engine.

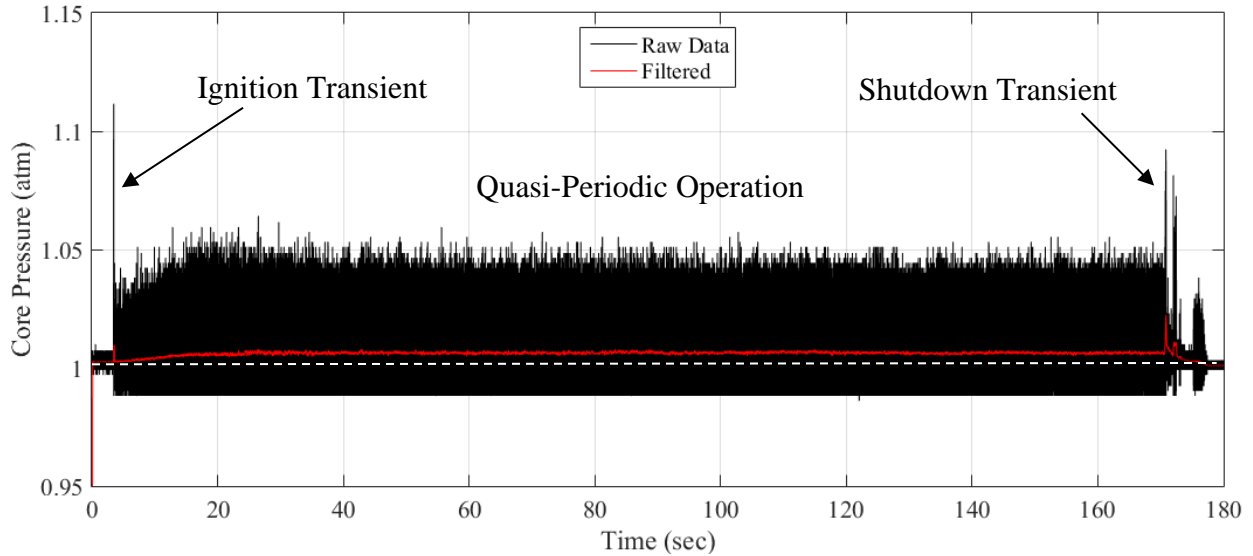


Figure 162: Engine Stand Core Stagnation Pressure Complete Time History

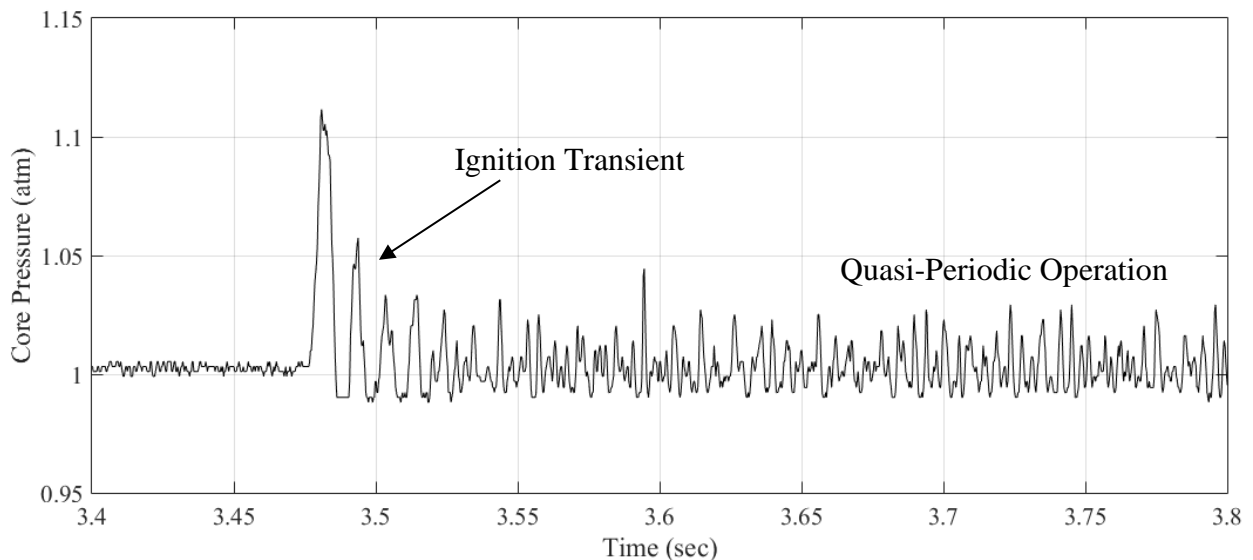


Figure 163: Engine Stand Core Stagnation Pressure Startup Transient (t = 3.4 - 3.8 sec)

The core stagnation pressure time history is shown over the entire recorded time frame in Figure 162 and zoomed into the startup transient region in Figure 163 to show oscillations due to the initial startup of the engine. It is clear that this brief startup transient, lasting less than 200 ms, produces a higher amplitude of 0.12 atm (12,341 Pa, 1.79 psi) than that seen in steady operation but lasting just a few cycles before damping to the quasi-periodic state which appeared to become more regular with time. The engine had reached a steady operation (in terms of the averaged core pressure) by 25 seconds into the engine run (approximately 21.5 seconds following ignition).

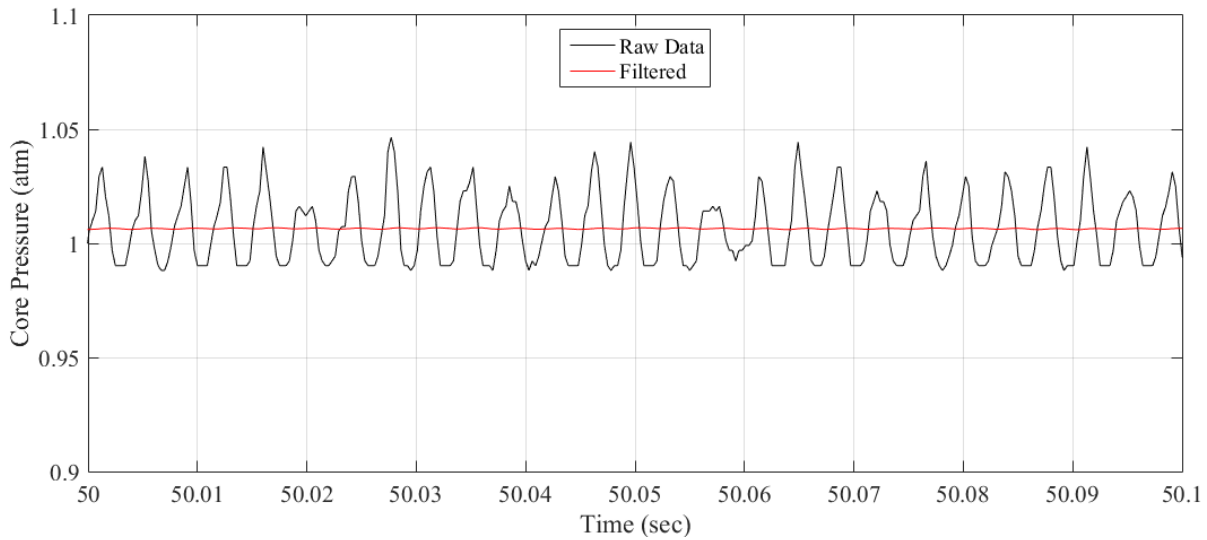


Figure 164: Engine Stand Core Stagnation Pressure Time History Zoomed In To Show Quasi-Periodic Engine Cycle

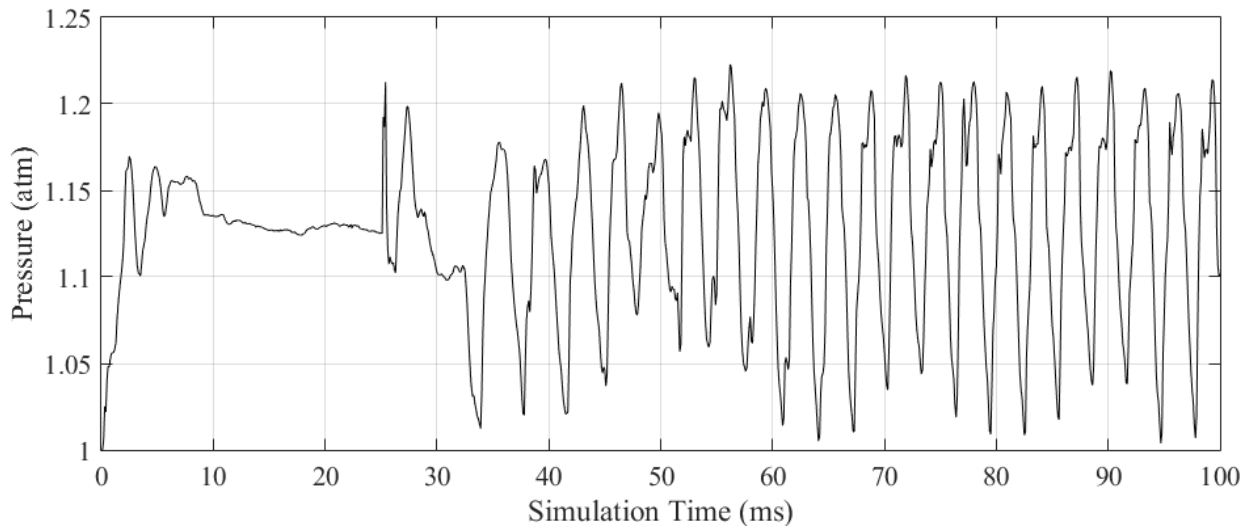


Figure 165: CFD Simulation Core Stagnation Pressure Time History

Core pressure oscillations (shown over a 100 ms sample of data in Figure 164) were observed at an amplitude of 0.058 atm (5,877 Pa, 0.852 psi) around the ambient 1 atm but biased toward higher pressures. The oscillations occurred at a frequency of approximately 300 Hz with little variation once the engine reached quasi-periodic operation. The amplitude was not as regular as the engine frequency, however, this did not appear to be indicative of actual irregularity in the engine's operation.

When compared to the much shorter dataset resulting from the main CFD simulation (repeated for more direct comparison in Figure 165), it is clear the same oscillatory response is seen. The startup transient is much shorter in the simulation; likely, a result of the lack of heat losses modeled in regard to the engine walls and the time necessary for the inert coil to reach its surrounding temperature. The operating frequency is close to that seen in the experimental data though slightly higher, showing a quasi-periodic frequency of up to 350 Hz. The amplitude is significantly larger in the simulation at approximately 0.10 atm (10,133 Pa, 1.47 psi) compared to the experimental amplitude of up to 0.058 atm (5,877 Pa, 0.852 psi). The simulation data is also oscillatory around the higher ambient pressure of 1.085 atm (110,000 Pa, 15.95 psi) necessary to reach a favorable equivalence ratio for engine startup. The experimental pressure data also shows a significantly more irregular amplitude while the CFD simulation predicts a more regular oscillation though with a mild beat frequency of approximately 55 Hz. Hence, the simulation and experimental data both show a qualitatively similar pressure response, which is also close in terms of operating frequency. Their respective offsets and amplitudes were likely affected by the different ambient pressure conditions.

2. Nozzle Exhaust Speed

The nozzle exhaust speed was measured at the centerline of the engine's nozzle at the exit face using a Pitot tube cantilevered off a fixed steel rail shown earlier in Chapter V. The two Pitot tube ports fed the two separate ports of a differential pressure gauge via stainless steel tube allowing measurement of the pressure differential between the Pitot tube's total and static ports. This change in pressure was related to the exhaust speed using the best available prediction of the exhaust density taken from the average exhaust density in the CFD simulation. This was estimated at 0.1745 kg/m^3 ($0.00034 \text{ slug/ft}^3$) and is the result of both the high exhaust gas temperatures and the mixture of combustion products as predicted by the CFD simulation. The exhaust velocity was then calculated by solving the Bernoulli equation for velocity as a function of pressure differential and this exhaust density. Exhaust speed data was also recorded at the maximum possible rate of 3,333 Hz on the same time datum used for the core pressure data.

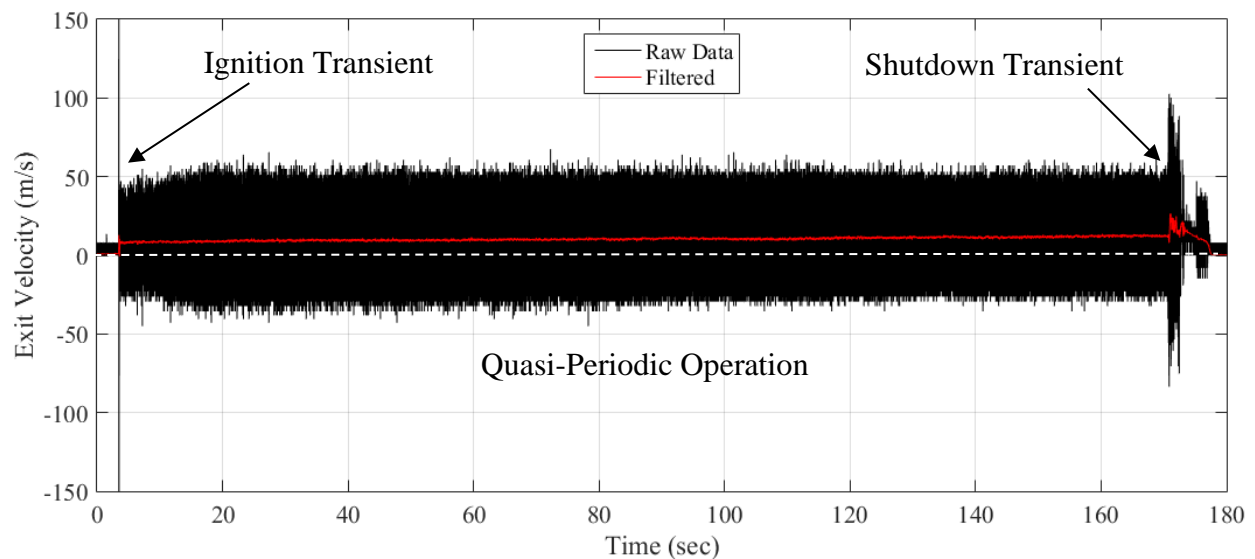


Figure 166: Engine Stand Pitot Tube Exhaust Speed Complete Time History

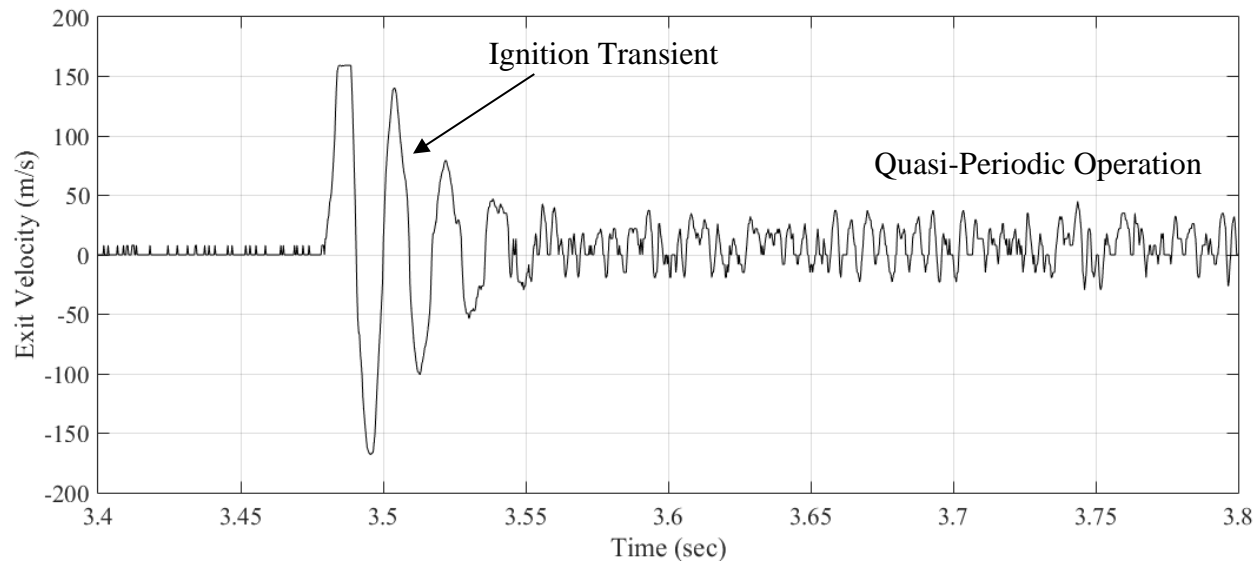


Figure 167: Engine Stand Pitot Tube Exhaust Speed Startup Transient (t = 3.4 – 3.8 sec)

The engine’s nozzle exhaust speed calculated from the Pitot tube data is shown over the entire data time frame in Figure 166 and zoomed into the startup transient region in Figure 167. There was again a large “noise” band between the startup and shutdown transients that exceeded the amplitude of the normal operation. This “noise” band is not actually noise but, instead is the typical, high frequency oscillatory response of the engine in quasi-periodic operation. The 10 ms moving average shown in Figure 166 illustrates the net positive exit velocity of approximately 10 m/s (32.8 ft/s) that abruptly starts with the ignition event and during shutdown becomes irregular and eventually drops to zero exit velocity. The operating velocity amplitude was up to 108 m/s (354 ft/s) reaching a maximum exit velocity of 67.5 m/s (221 ft/s) and a minimum of -45.1 m/s (148 ft/s). This is significantly less than the startup transient’s maximum amplitude of 327 m/s (1073 ft/s) spanning an exit velocity as high as 159 m/s (522 ft/s) and as low as -168 m/s (551 ft/s); however, this quickly damps to within the quasi-periodic amplitude within 60 ms from the onset of ignition.

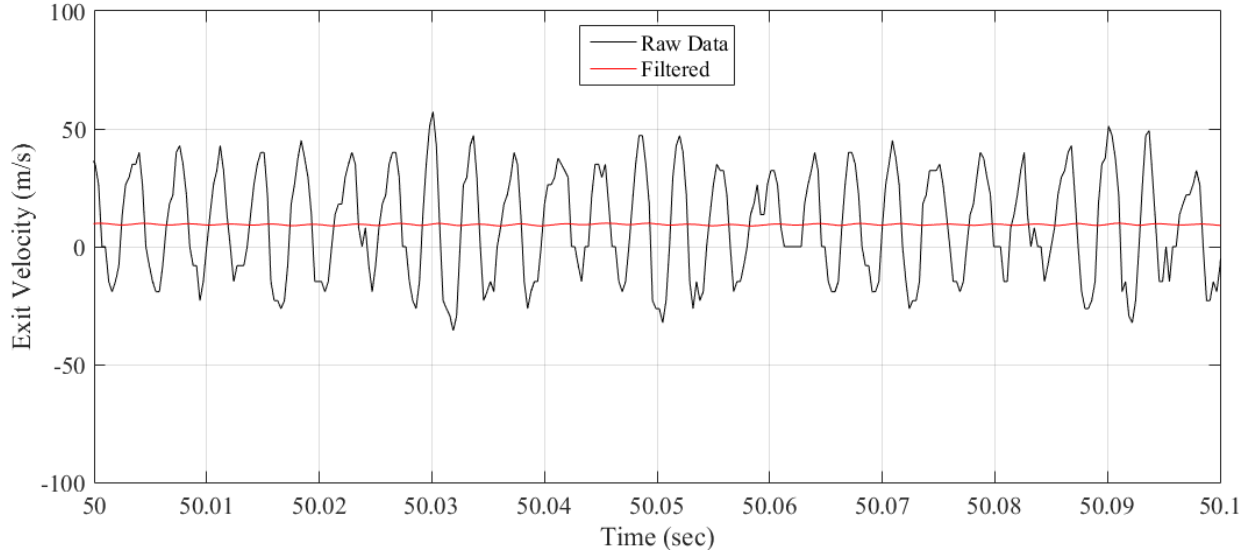


Figure 168: Engine Stand Pitot Exhaust Speed Time History Zoomed In To Show Quasi-Periodic Engine Cycle over 100 ms Timeframe

Like the core pressure data, the exhaust speed data (shown over a representative 100 ms timeframe in Figure 168) also shows a quasi-periodic oscillation with a frequency of up to 300 Hz. It is clear that the engine exhaust speed response was not ideally cyclical with significant possibly random variation throughout the engine's operation. The oscillations were more irregular than the chamber pressures with the frequency dropping as low as 250 Hz though exhibiting a rough beat frequency of approximately 50 Hz.

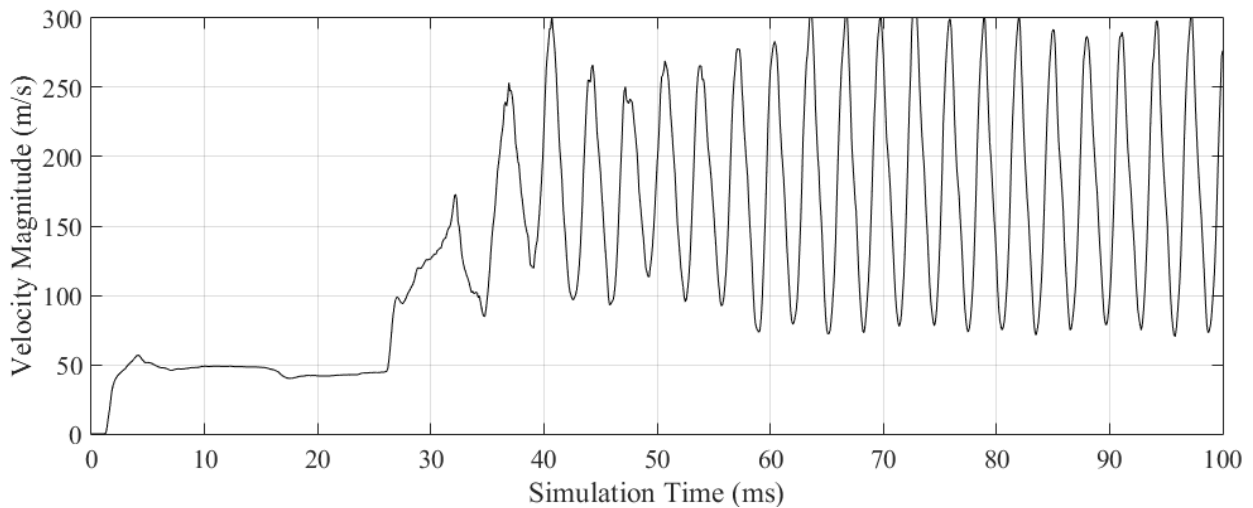


Figure 169: CFD Simulation Nozzle Exhaust Speed Time History

When compared to CFD simulation dataset (repeated for more direct comparison in Figure 169), it is again clear the same oscillatory response is seen. The exhaust speed CFD data again showed an increase in the operating frequency of up to 350 Hz being slightly higher than that seen in the experimental exhaust speeds (250 – 300 Hz). The exhaust speed also appears to have been affected by the difference between the experimental and computational ambient conditions. The 0.086 atm (8,675 Pa, 1.26 psi) pressure differential between the ambient and exhaust region pressures resulted in a CFD-predicted, nonreactive exhaust speed of approximately 50 m/s (164 ft/s) which appeared to be minimally affected by the fuel injection. Prior to ignition, the experimental exhaust speed measurements were negligible. The mean exhaust speed also appears to be affected with the CFD data predicted a mean speed of approximately 112 m/s (367 ft/s) compared to the actual mean speed measured on the engine stand of 24 m/s (78.7 ft/s). As a result, the qualitative response seen in the CFD simulation matched well while the actual quantitative matching was significantly affected by the simulated pressure differential.

3. Temperature Measurements and Apparent Temperature Distributions

Temperatures were recorded at several locations inside and on the surface of the engine and recorded at a much slower data rate of 1 Hz – the fastest possible using the available thermocouple recorder. As a result, the faster, high-resolution temperature response seen in the CFD predictions fundamentally could not be captured. This is also limited to some extent by the nature of heat transfer and the lag time necessary for a thermocouple and the engine surfaces to reach an equilibrium temperature with its surroundings. As a result, the experimental temperatures contained in this section are a much coarser dataset than those available from the CFD results and are only comparable to the quasi-periodic conditions.

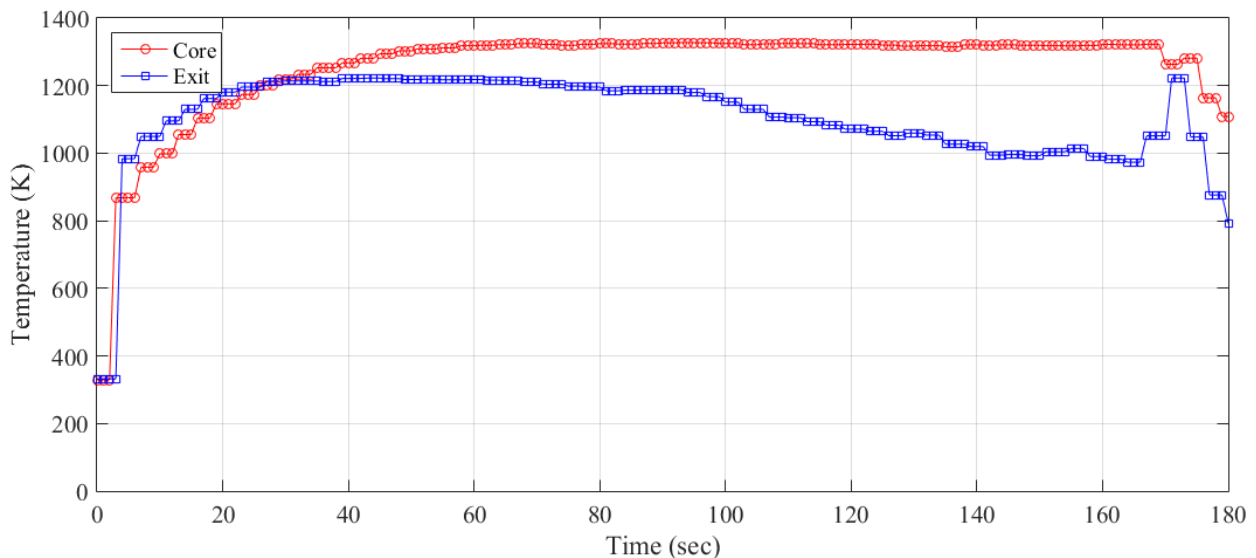


Figure 170: Engine Core and Exhaust Gas Temperature Time Histories as Measured via Engine Test Stand Thermocouples

The engine core and exhaust gas (“exit”) temperature data measured on the engine test stand are plotted over the entire run time frame in Figure 170. Following the ignition event and the resulting spike in temperature, the core temperatures steadily rose over a long period of time reaching a maximum of 1327 K (1929 °F) within 60 seconds of operation. Meanwhile, the exit temperature more quickly reached a lower plateau of 1212 K (1722 °F) at 28 seconds. This was held with little temperature loss until 94 seconds of operation when the exhaust temperature began

falling to approximately 1000 K (1340 °F). It is unclear what caused this drop in exit temperature as no corresponding change in the core pressure, thrust, or exhaust velocity was seen. The CFD predictions showed a mean quasi-periodic core temperature of 1680 K (2564 °F) and exit temperature of 1830 K (2834 °F). The engine was shutdown at approximately 170 sec, which briefly caused an extended flame to exit the engine nozzle to be subsequently sucked back into the engine as fuel flow ceased. This is thought to be the source of the shutdown transient's spike in exit temperature as the EGT thermocouple was briefly shrouded in an off-nominal exit flame. Furthermore, as the engine shut down, the approximate level of heat release in the core (evident by the brightness of the engine) quickly dropped as the remaining fuel in the injection line diminished. These two phenomena occurred largely simultaneously and is thought to be the cause of the atypical drop in core temperature and rise in the exit temperature.

For comparison, the core temperature in the simulation oscillated strongly with the engine cycle ranging as low as 1260 K (1808 °F) to as high as 1930 K (3014 °F) while the exit temperature was more steady with an amplitude of less than 100 K around the mean. This is significantly higher than the temperatures seen on the test stand, but to be expected for a number of reasons, not the least of which is the lack of heat losses modeled in the current adiabatic CFD simulation. No shutdown transient was modeled in the simulation for comparison.

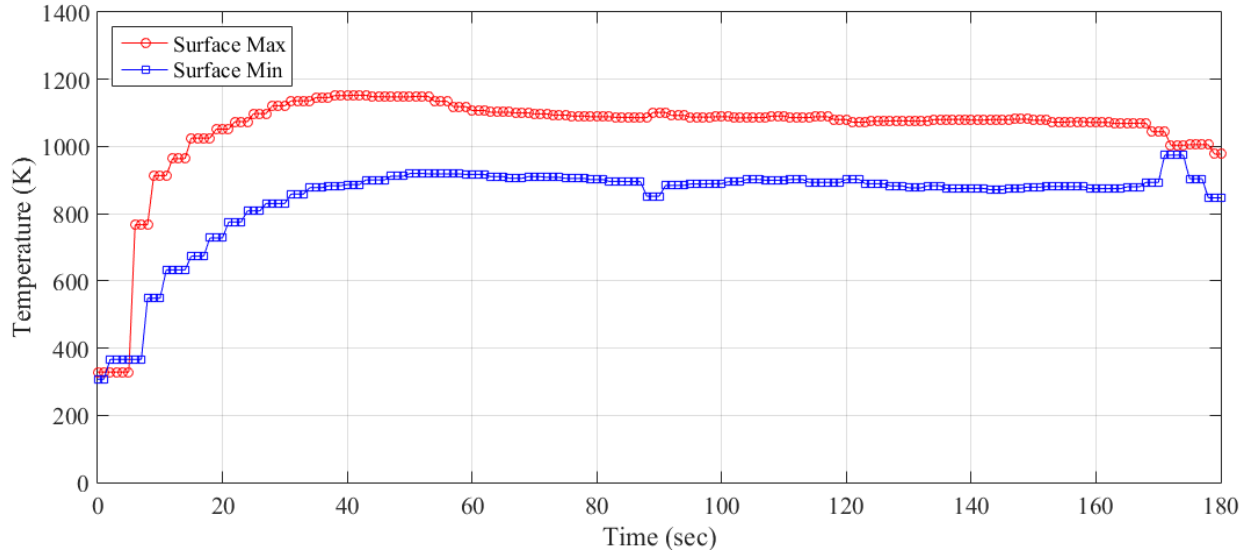


Figure 171: Engine Surface Temperature Time Histories as Measured via Engine Test Stand Thermocouples

The engine surface maximum and minimum temperature data measured on the engine test stand are similarly plotted over the entire run period in Figure 171. Again, following the initial ignition event, the maximum surface temperature (measured just downstream of the engine core) showed a similar, though delayed, sharp rise followed by a slower rise to a steady temperature of 1151 K (1612 °F) by 40 seconds of operation. Meanwhile, the minimum surface temperature showed a delayed and less-pronounced initial rise but with a similar rise to equilibrium temperature, reaching 920 K (1196 °F) by 50 seconds of operation. The maximum temperature showed a slight drop by 120 seconds to a temperature of 1080 K (1484 °F).

The CFD simulations, however showed significantly higher surface boundary temperatures of approximately 1800 K (2780 °F) which could be due to the absence of the multiple forms of heat transfer not accounted for in the adiabatic simulation. This could also be the cause of the slower time to reach a quasi-periodic state, as well as the slightly lower engine operating frequency. The simulation should, therefore, represent an upper bound on these properties.

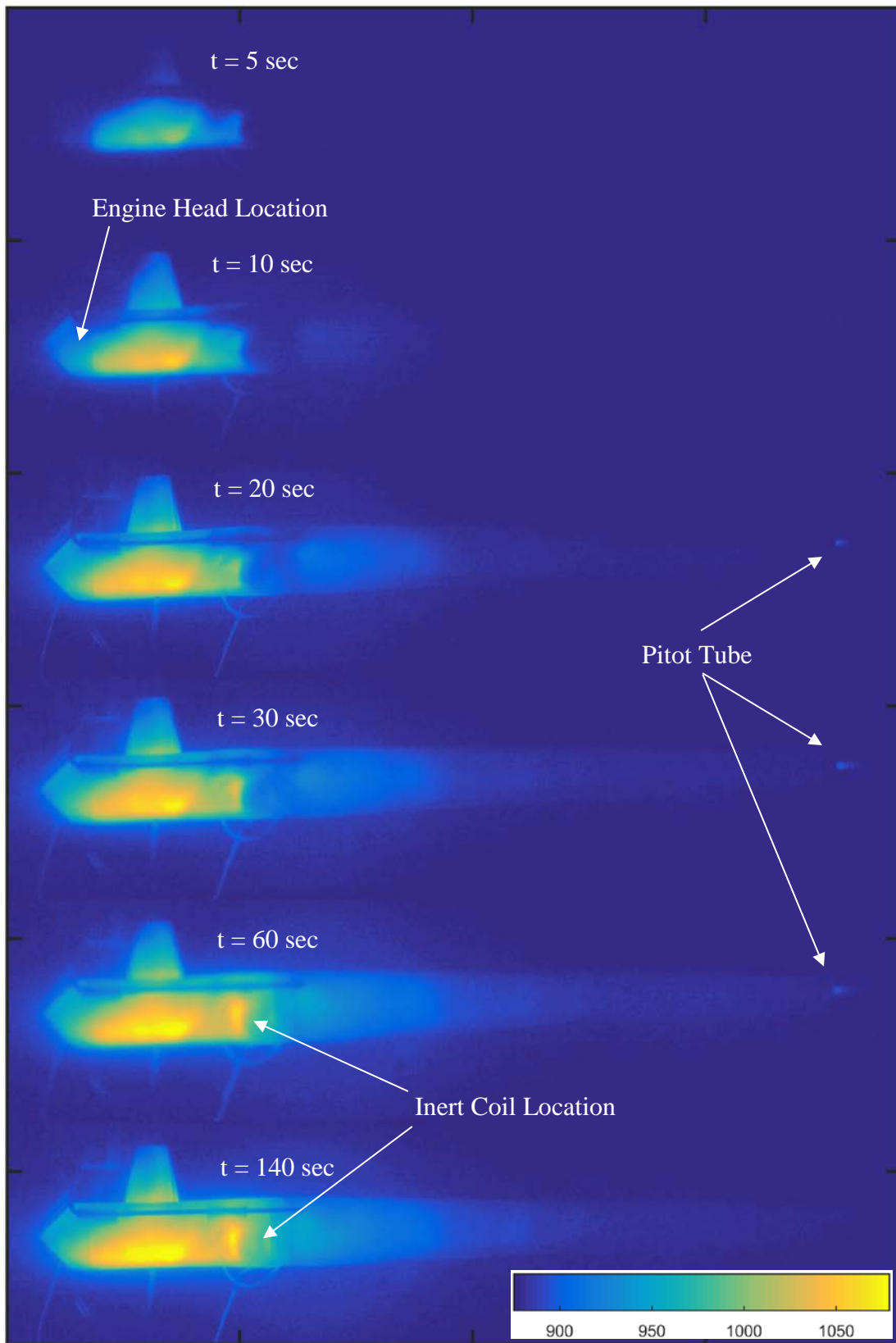


Figure 172: Engine Startup Apparent Temperature Distribution Contours via MATLAB (IR Filtered via 720 nm Filter, $\Delta T = 2.0$ K Contours, $T_{MAX} = 1079$ K, $T_{MIN} = 875$ K)

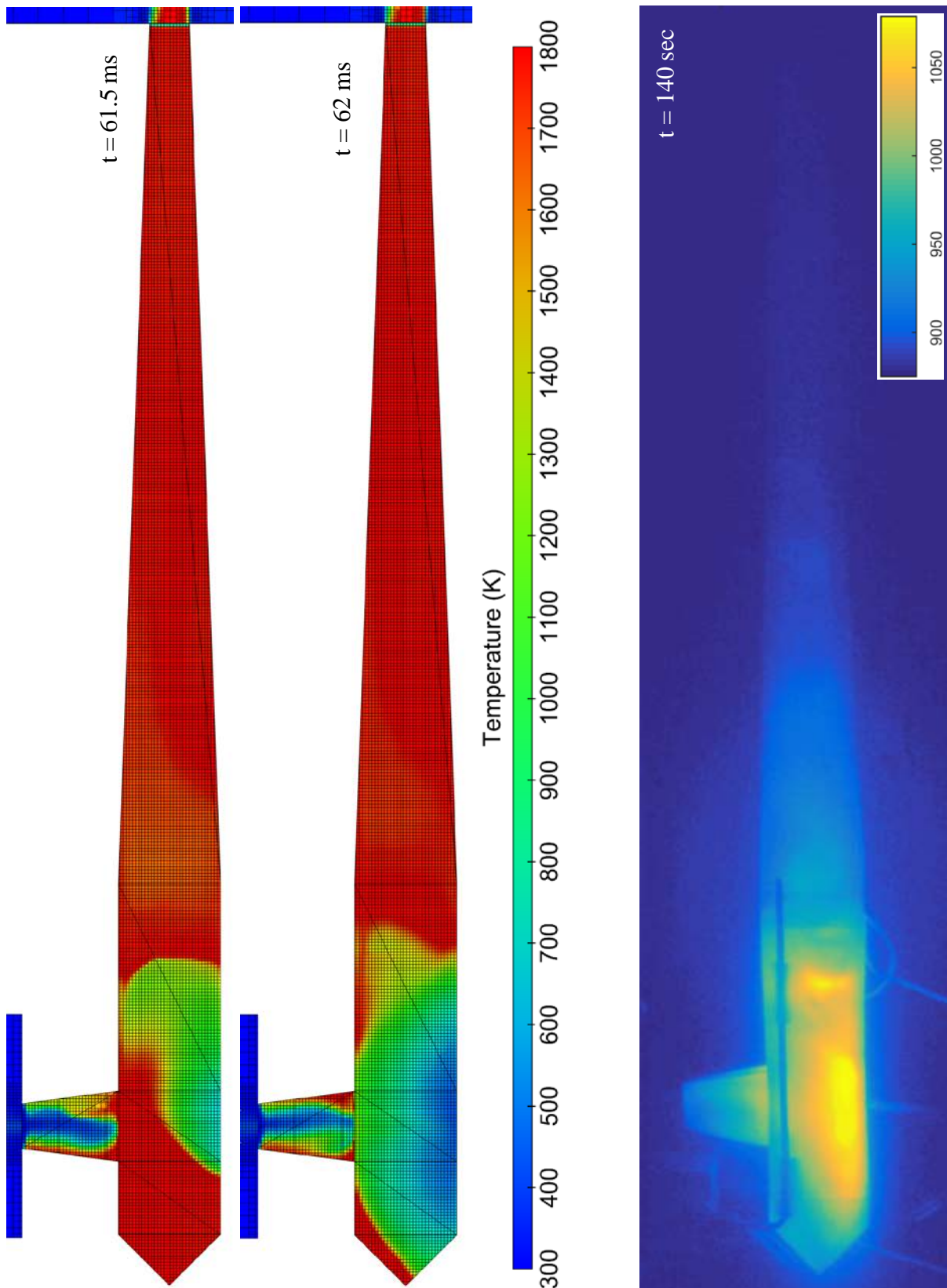


Figure 173: Comparison Between CFD Prediction of Engine Surface Temperatures (Left) and Apparent Temperatures via IR Filtering and MATLAB Contours (Right)

The engine surface temperature distribution during operation of the engine on the test stand is shown for a series of successive times in Figure 172. The images were taken from video recorded through the 720 nm IR-pass filter at a framerate of 23 Hz and a resolution of 1920x1080 pixels. The onset of ignition was seen to have an immediate response in the core pressure, exit velocity, and (in the next chapter) thrust force, but the surface temperatures rose on a much longer timescale. Through the IR filter, it took at least 3 seconds for the surface to heat to incandescence, releasing enough IR-spectrum light to be weakly captured on camera. By 5 seconds (shown in the image progression), it is clear that some heat is beginning to spread throughout the engine walls but is being stifled by the proximity of the inert coil. The highest local temperature is along the back wall and spreading around the walls back toward the inlet side of the chamber. This similar progression was seen at a much shorter timescale in the CFD simulations and are repeated in Figure 173 for comparison purposes with the resulting steady temperature distribution on the test stand.

By 10 seconds of operation, the engine walls downstream of the inert coil are beginning to absorb some heat from the flow. Meanwhile, the forward recirculation zone has also heated the forward engine walls. Heat also continues to spread through the engine surface (likely through wall conduction) to the inlet. By 20 seconds of operation, the cantilevered retaining rod is clearly visible against the brighter and hotter chamber. The nozzle wall temperatures continue to rise as well as the wall temperatures around the inert coil. This suggests that by 30 seconds, the inert coil is starting to reach its equilibrium temperature in the hot engine core. The Pitot tube at the nozzle exit is also visible as it is heated to the point of incandescence as well. The Pitot tube is eventually not visible by 95 seconds suggesting the exhaust temperature was steadily cooling during prolonged operation that reinforces the temperature data seen in Figure 170.

By 60 seconds of operation, it is clear that the inert coil is playing a role in the combustion inside the engine core. What role that is, exactly, is unclear, except that this time coincides with the point at which the engine core reaches its maximum steady temperature (as shown in Figure 170). This could be the point at which the coil reaches its equilibrium temperature with the core (despite the core temperature likely fluctuating with each cycle).

Lastly, the temperature distributions seen in the CFD simulation were not necessarily directly correlatable to the experimental measurements on the engine as a result of heat transfer effects. Specifically, this is related to the effect of the stainless steel sheet acting as a heat capacitor during engine cycles. When the relatively cold fuel enters the engine, it appears to locally drop the wall temperature down to 600 K. However, on the engine stand, this is where the walls show high temperatures. This suggests that the heat-sinking of the cooler fuel is not enough to draw more heat from the walls than is being stored as a result of the fuel's heat release – a phenomena not modeled in the CFD simulation. Nevertheless, the early spread of temperature and, therefore, heat through the engine chamber walls follows this similar path. This suggests that as the fuel burns in this same recirculation pattern, more heat is released against the back wall and successively less as it recirculates around the engine chamber before leaving through the nozzle. This effect is likely strongest with the inert coil that has more thermal mass in relation to its surface area than the engine walls and could explain why the engine coil reaches an equilibrium temperature later. Convective heat transfer could be the reason the nozzle walls stabilize to a lower temperature than that seen in the engine core. The hot gases in the core are at a lower speed and, thus, have more time to transfer heat to the walls. Alternatively, the hot gases in the nozzle have much less time to transfer heat to the walls as they accelerate out the nozzle. Heat transfer to the nozzle walls in this case may be driven more by wall conduction than by the exiting gases.

4. Load Cell Thrust, Estimated Fuel Consumption, and TSFC

Thrust force was measured via a load cell measuring the blocked force across a pivot due to the resulting couple moment induced by the engine's nozzle exhaust flow. The data was recorded at the same rate as the pressures (at the maximum of 3,333 Hz) and with the same time datum. Flow was initiated through the engine prior to the start of data recording so the only time the stand was touched was to stop fuel flow.

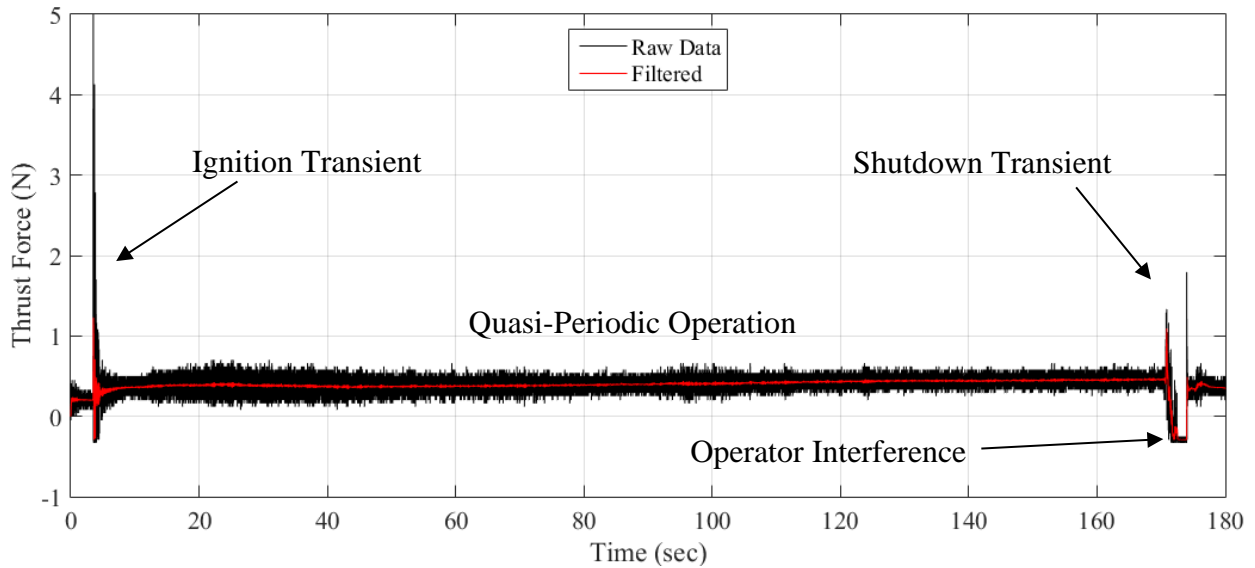


Figure 174: Engine Stand Load Cell Thrust Force Complete Time History

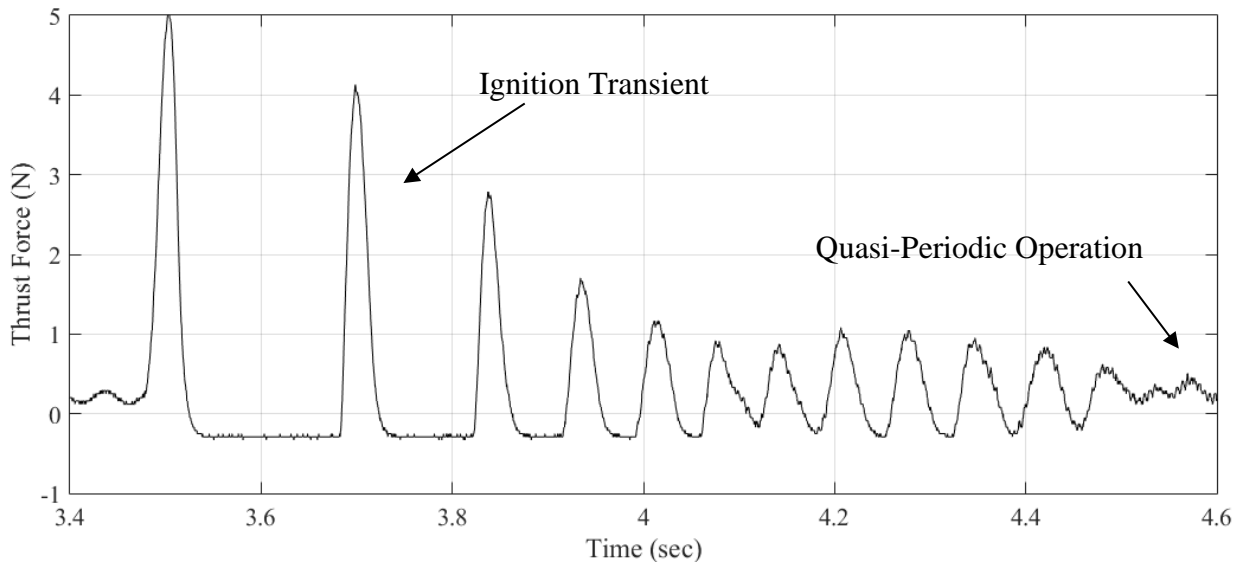


Figure 175: Engine Stand Load Cell Thrust Force Startup Transient

The engine stand's load cell thrust data is shown over the entire data time frame in Figure 174 and zoomed into the initial startup transient region in Figure 175. As seen in the core pressure and exit velocity time histories, the thrust time history is also characterized by large startup and shutdown transients with a significant high frequency band between them. Where the pressure and velocity histories showed largely consistent amplitude (with some random variation), the thrust history appears to show some longer-period variation, damping significantly by 60 seconds, and essentially reaching a quasi-periodic state by 120 sec. During shutdown, some interference by the operator was unavoidable as the fuel-flow is controlled by a needle valve located on the thrust stand. This accounts for the off-scale low "thrust force" registered just after 170 seconds when the engine was shutdown by closing the needle valve.

The startup transient thrust profile also reached the minimum (off-scale low) thrust reading caused by the load cell losing contact with the blocking bar. Nevertheless, the maximum positive force was still registered by the thrust stand, reaching as high as 5 N (18.0 oz.). This high initial transient rapidly damped to an intermediate transient with an amplitude of 1.33 N (4.79 oz.) at a frequency of 14 Hz. This lasts just seven cycles before finally damping out leaving the stabilizing quasi-periodic state. Closer inspection of the response shows higher frequency oscillations likely due to the engine's normal operation mixed with this intermediate transient as early as 4.1 seconds (0.64 seconds following ignition). It is therefore suspected that the intermediate transient is the result of the engine stand arm's impact on the blocking bar inducing a vibrational response in the T-slot arm itself that then took over half a second to damp back out.

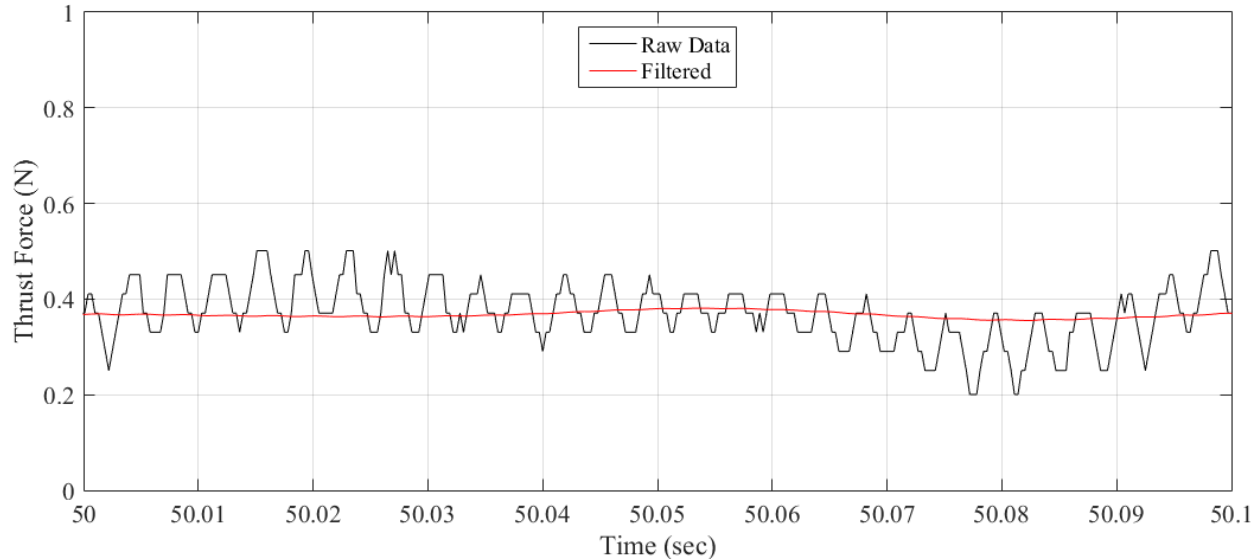


Figure 176: Engine Stand Load Cell Thrust Force Time History Zoomed In to Show Quasi-Periodic Engine Cycle

Nevertheless, once the engine reached a quasi-periodic oscillation, this was evident in the thrust data with a frequency of up to 300 Hz. It is clear, however, that the amplitude resolution is significantly lower than the resolution seen in the pressure and exhaust speed measurements. Nevertheless, the available resolution was sufficient to resolve the engine's cycle as it oscillates through an amplitude of 0.2 N (0.72 oz). It is unclear why there is an irregular, longer period of thrust oscillation occurring which drives the mean thrust from as low as 0.25 N (0.90 oz) and as high as 0.4 N (1.44 oz). It does not appear to correlate to any measured phenomena like the core pressure or the exhaust speed and the temperatures could not be recorded at a data rate high enough to match. This oscillation appears to have a short period though as the 10 ms moving average filter largely removed it from the time history.

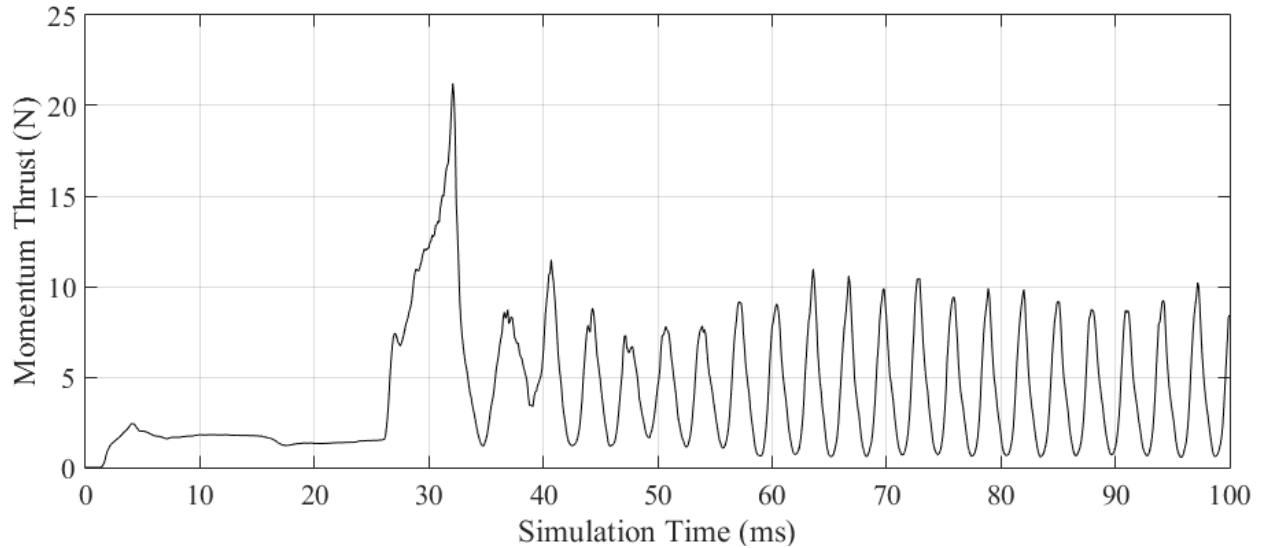


Figure 177: CFD Simulation Exhaust Density and Estimated Momentum Thrust Time History

There was no direct output of engine thrust force from the solver to compare to the experimental data. Instead, the simulation’s predicted momentum thrust time history was calculated based on the constant nozzle exit area (1.0 in.^2 , $6.45 \times 10^{-4} \text{ m}^2$), the exit centerline density time history, and the exit centerline velocity time history. The resulting plot of estimated momentum thrust is shown in Figure 177. It is immediately clear that the estimated thrust from the CFD simulations is significantly higher than that seen on the engine test stand experiments. This could be the result of a number of factors including the adiabatic idealization neglecting heat losses, as well as the high ambient pressure differential not present in the experiments. It is also unsurprising that the momentum thrust is heavily affected by the offset seen in the velocity time history considering the thrust calculation varies with the square of this exit velocity. Hence, the effect of the exit velocity offset is compounded here in the thrust estimation.

Nevertheless, the engine operating frequency is once again close to that of the actual engine ranging from 300 to 350 Hz as the engine cycle stabilizes. The simulation suggests an ideal quasi-periodic mean thrust force of 4.2 N (0.94 lbf, 15.1 oz). Although the experimental engine was unable to match this level of thrust, it serves as an upper bound to what may be possible with the

engine design at this size if operated on a vehicle at speed with an inlet scoop that could raise the inlet pressure to match the simulation. This concept was already tested by Gluhareff on an original pressure jet when installed on the tips of helicopter rotor blades to boost engine performance.

During this run shown, the engine was operated for 3.26 minutes. Unfortunately, there was not a method available for directly measuring the fuel flow rate or tank and injection pressures as a function of time. As a result, this fuel flow rate was calculated based on the recorded runtime and the measured change in the propane tank mass assuming the only lost mass is of fuel. During this runtime, the change in tank mass suggested that the injector delivered 66 g (2.33 oz) of liquid propane fuel. This resulted in an estimated average fuel flow rate of 0.337 g/sec (0.012 oz/sec, 2.67 lb_m/hr). This is significantly lower than that calculated from Gluhareff's G8-2-20 engine (the closest for which fuel consumption was known) having a fuel flow of 113 lb_m/hr. Nevertheless, these engines are not necessarily comparable based on their fuel flow rates due to the drastic differences in their size and thrust generation. Assuming an average thrust force of 0.40 N (0.09 lb_f), the BGX engine showed a thrust-specific fuel consumption (TSFC) of 29.7 kg/hr/kg (equivalent in lb_m/hr/lb_f). This allows comparison on equal terms and shows a different picture than the orders of magnitude reduction in fuel. The G8-2-20 engine had a static TSFC of just 4.8. His most efficient engine, the G8-2-130R had a TSFC of 0.78. The BGX prototype shown here is 6.2 times less efficient than the G8-2-20 suggesting that the engine is not yet optimized although it is clearly operating on the same principles. Gluhareff's own work to improve his engines' efficiency suggests that much fine-tuning of the design is necessary to optimize it. Even the G8-2-130 originally had a TSFC as high as 1.33 before the design was refined further. Finding ways to increase the chamber pressure should have significant effects on the engine TSFC and are a major part of the future work discussed in the next chapter.

5. The Effects of Radiative Heat Losses

The CFD simulation discussion so far was limited to an adiabatic model of the pressure jet engine during startup and quasi-periodic operation. This resulted in a wealth of data and qualitative findings but the absence of heat losses to the environment of an engine operating at temperatures high enough to reach incandescence is a nontrivial shortcoming. To that end, an approximation of the wall heat losses was included in a new series of simulations.

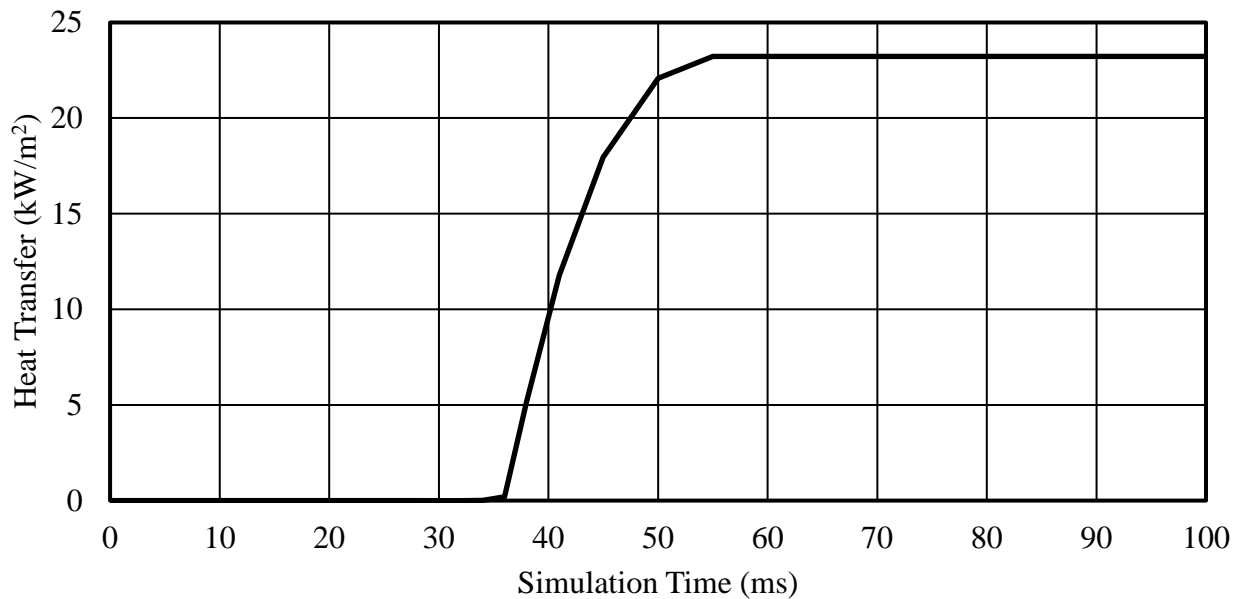


Figure 178: Blackbody Wall Heat Transfer per Unit Area History Used for Radiative Heat Loss CFD Simulations

The CONVERGE CFD solver allows the user to prescribe a wall heat loss term, q/A in units of W/m^2 either as a constant value or a time history read in from a file. Due to the high level of heat expected to be lost to the environment, the latter option was chosen such that the heat loss could be determined based on the experimental wall temperature measurement and the initial rise profile of the mean chamber temperature delayed by 10 ms from the start of ignition to correspond with the runaway rise of significant chamber temperature. Radiative heat transfer was expected to dominate the loss of heat to the ambient environment because the engine was operated in a still room (to minimize forced convective losses) and contact with the thrust stand was avoided (to

minimize conductive heat losses). Free convection was likely nontrivial as conduction to the immediate air may cause buoyant effects to result in a weakly rising flow along the engine walls. This free convective effect, however, was assumed to be much less than the effect of radiant heat losses. The resulting maximum heat transfer profile (applied to the engine chamber wall boundary and shown in Figure 178) was calculated based on the Stefan-Boltzmann Law for greybody radiation [315]:

$$\frac{q}{A} = \epsilon\sigma\Delta T^4 = \epsilon\sigma(T_W - T_{SUR})^4 \quad (73)$$

where q/A is the heat transfer per unit area (in W/m^2), σ is the Stefan-Boltzmann constant, $5.6703 \times 10^{-8} \text{ W}/\text{m}^2\text{-K}^4$, T_W and T_{SUR} are the wall and ambient surroundings temperatures (in K), respectively, and ϵ is a unitless empiricism denoting the “emissivity” of the wall material. That is, the fraction of the full energy emitted by an ideal “blackbody” for which $\epsilon = 1.0$ and the radiative energy is maximized. Typical values of ϵ are thus some fraction of unity. With no clear empirical data available to select a “best” value of ϵ for glowing stainless steel sheet at this thickness, a series of identical simulations were run with the heat transfer level scaled by emissivities between 0.3 and 0.9 to compare with the adiabatic simulation already presented earlier.

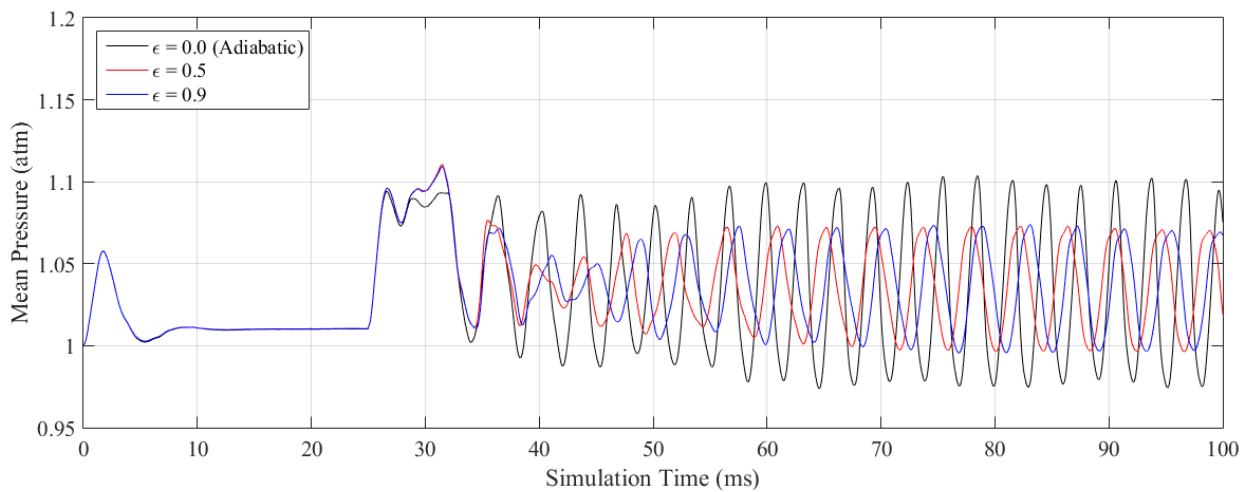


Figure 179: Effect of Wall Radiative Heat Losses on CFD Simulation Mass-Averaged Chamber Mean Pressure for Two Emissivities and Neglecting Heat Losses

The strongest effects of the heat loss on the engine operation were in regard to the engine temperatures, engine operating frequency, and the chamber pressure amplitude. The effect of wall heat losses on mean chamber pressure and by extension, the operating frequency is visible in Figure 179. Note that only two of the runs are shown here to reduce clutter and to show the general trend. The startup transient in pressure was significantly less pronounced and as the engine warmed up, the quasi-periodic mean pressure amplitude stabilized to a lower condition. There was some reduction in the time necessary to reach stable operation for lower emissivities (and thus lower heat loss) which makes sense considering that when less heat is lost to the surroundings, it is instead aggregately warming the fuel/air mixture and preparing it for combustion. So a slight trend of lower heat loss toward faster startup is to be expected.

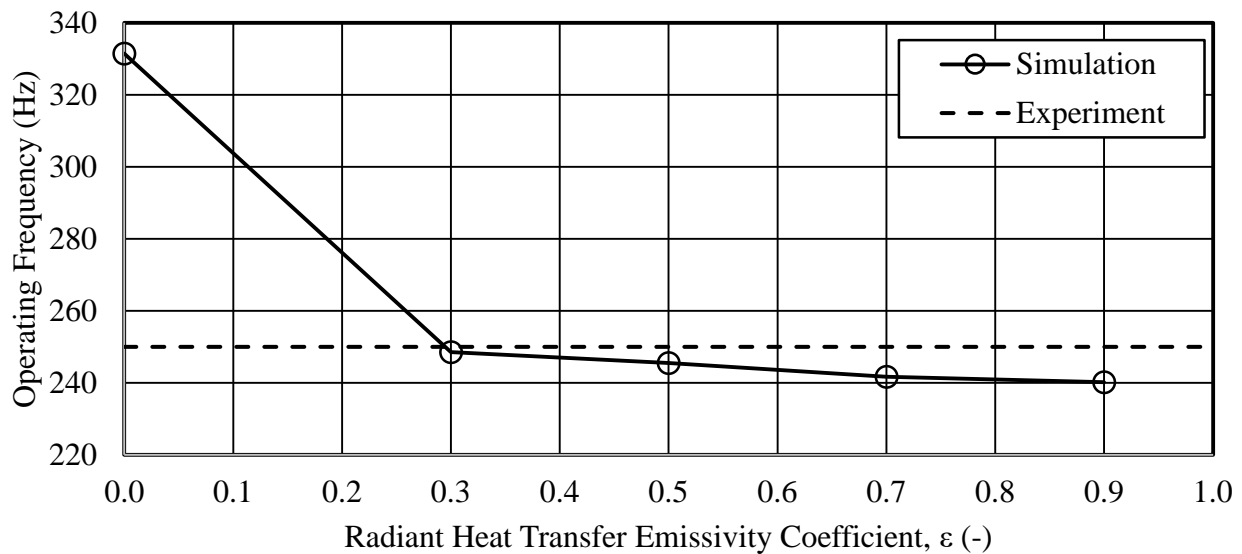


Figure 180: Effect of Wall Radiative Heat Losses on CFD Simulation Quasi-Periodic Operating Frequency for a Range of Emissivities

The engine operating frequency was calculated for each simulation run and in the experimental data based on the peak-to-peak time to complete multiple cycles. For the simulation runs, the times were taken from the end of the dataset and for the experimental data, a representative sampling was taken from the quasi-periodic range. The experimental frequency of

250 Hz matched well albeit slightly higher than the frequencies seen when accounting for heat losses, with a general trend of increasing frequency with lower heat losses eventually culminating in a high prediction for adiabatic operating frequency. This highlights the importance of heat losses in accurately capturing the operating frequency although the adiabatic simplification resulted in a minor error.

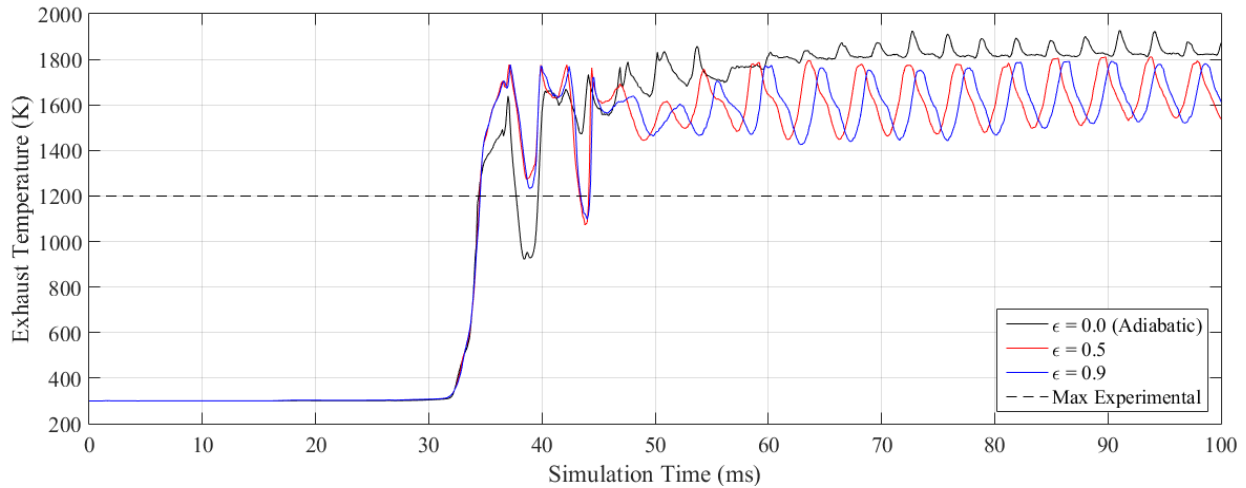


Figure 181: Effect of Wall Radiative Heat Losses on CFD Simulation Exhaust Gas Temperature (EGT) for Two Emissivities and Neglecting Heat Losses Compared to the Experimental EGT Measurement on Engine Test Stand

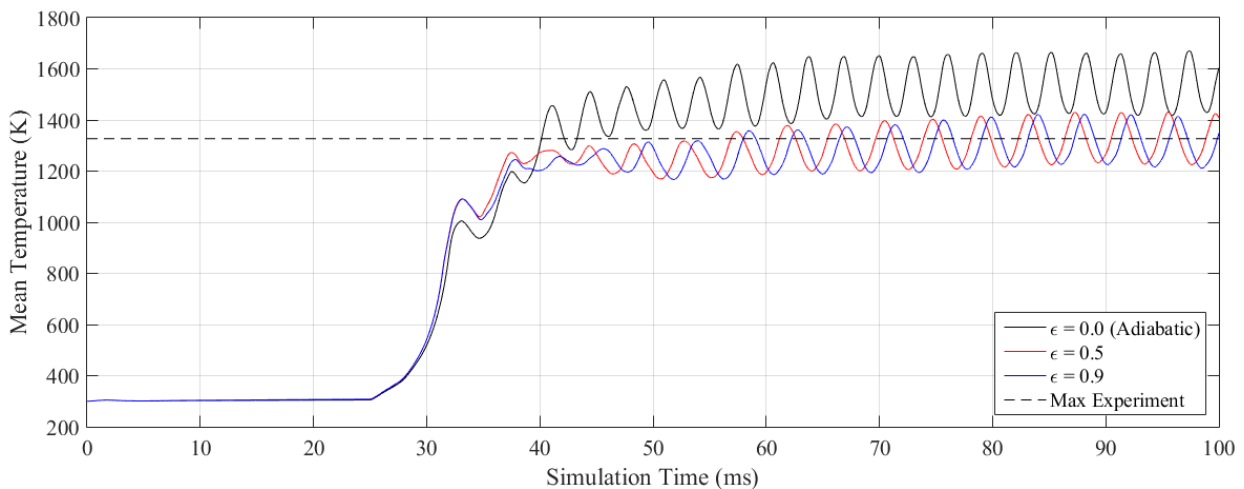


Figure 182: Effect of Wall Radiative Heat Losses on CFD Simulation Mass-Averaged Mean Chamber Temperature for Two Emissivities and Neglecting Heat Losses Compared to the Experimental Core Temperature Measurement on Engine Test Stand

The effect of wall radiative heat losses on the exit and mass-averaged mean chamber temperatures are shown in Figure 181 and Figure 182, respectively, for two emissivities and the adiabatic run, with a prescribed wall temperature. The exhaust temperature showed more significant swings though around a lower mean. Furthermore, as the engine warms up, this amplitude decreased around the mean suggesting a longer, subtle startup transient in regard to the wall heat losses around the nozzle. The mean temperature showed a similar trend, though the mass-averaging over the whole chamber appears to have averaged-out some of the longer transient as the engine warmed up. Nevertheless, there appeared to be a slight suppression of the mean temperature between 40 and 60 ms as the heat transfer was reaching its peak. By 80 ms, however, a stable quasi-periodic state was reached centered almost exactly around the experimental core temperature measurement where the simulation neglecting heat losses predicted a temperature approximately 200 K hotter.

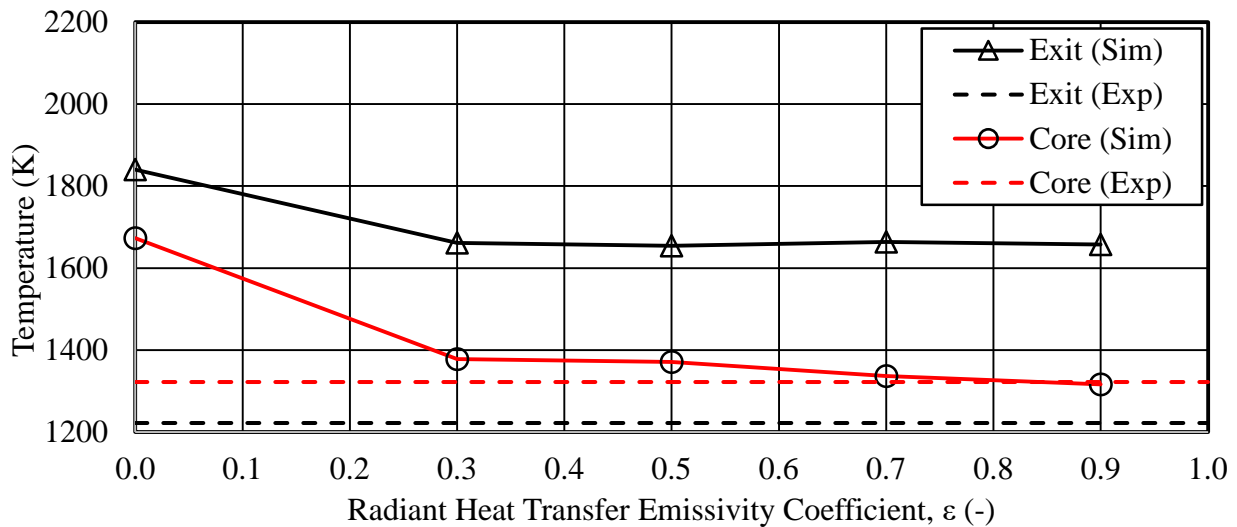


Figure 183: Effect of Wall Radiative Heat Losses on CFD Simulation Quasi-Periodic Mean Temperatures for a Range of Emissivities Compared to Experimental Data

The effect of heat losses on the exit and core temperatures for the full range of emissivities run is shown in Figure 183. This not only shows the improvement that accounting for heat losses make on matching engine temperature measurements, it also highlights a curious anomalous trend.

In the CFD simulation, the core temperature was lower than the exhaust temperature, however, the experimental measurements showed an opposite trend. This could be due to a combination of effects. First, the real engine walls have a nontrivial wall heat capacitance effect that could not be modeled in the current simulations. The wall heat capacitance is a means of the engine walls to store heat between cycles such that at the peak of the cycle's fluid temperature, the walls are absorbing heat released by the fuel combustion. And at the cycle's minimum fluid temperature, some heat is being transferred into the fuel. This could have the effect of stabilizing the core temperature. Along the nozzle walls, however, the hot, accelerating exhaust gases are less able to transfer heat to/from the walls being dominated by convective and radiative transfer on a shorter time frame than in the chamber. The gases are similarly less able to transfer heat to the thermocouple on the engine test stand. Ideally, the exhaust flow would be slowed to stagnation around the thermocouple bead to remove this source of error. But the EGT thermocouple's proximity to the exhaust Pitot tube would only shift that error to the exhaust velocity measurement. As a result, the exhaust thermocouple data could represent a lower bound on the actual exhaust temperature.

This could also be affected by the elevated ambient pressure condition exaggerating the flow out of the engine pushing some combustion processes further down the engine chamber in the simulation than they are really occurring on the thrust stand. In other words, there may be more heat release in the nozzle section predicted by the CFD simulation than is actually occurring on the test stand. This would follow from an excess of flow speed through the engine induced by the elevated pressure ratio blowing some of the combustion process further down the chamber than seen in reality and therefore could further explain the elevated temperatures in the nozzle.

6. Mass Flow Rate through the Engine

Lastly, the overall experimental mass flow rate through the engine was estimated based on the exhaust speed measured by the exhaust Pitot tube data, the known engine nozzle exit area (1.0 in.², 6.45 cm²) and a mean exhaust gas density taken from the CFD data as the best available approximation. The experimental mass flow rate, was then related proportionally to the exhaust speed as a limitation of the available experimental data. This was compared to the computational mass flow rate calculated by integrating the normal fluid momentum over the nozzle exit area. Mathematically that is:

$$\dot{m}_{exit} = \int_S ((\rho \vec{V})_{exit} \cdot \vec{n}) dS \quad (74)$$

where \dot{m}_{exit} is the total mass flow rate out of the engine (in kg/sec), ρ is the local fluid density (in kg/m³), and \vec{V} is the local velocity vector. These were taken from the cells (with varying sizes, dS) intersecting with and in the direction normal to a cross-sectional plane, S , located at the engine nozzle exit.

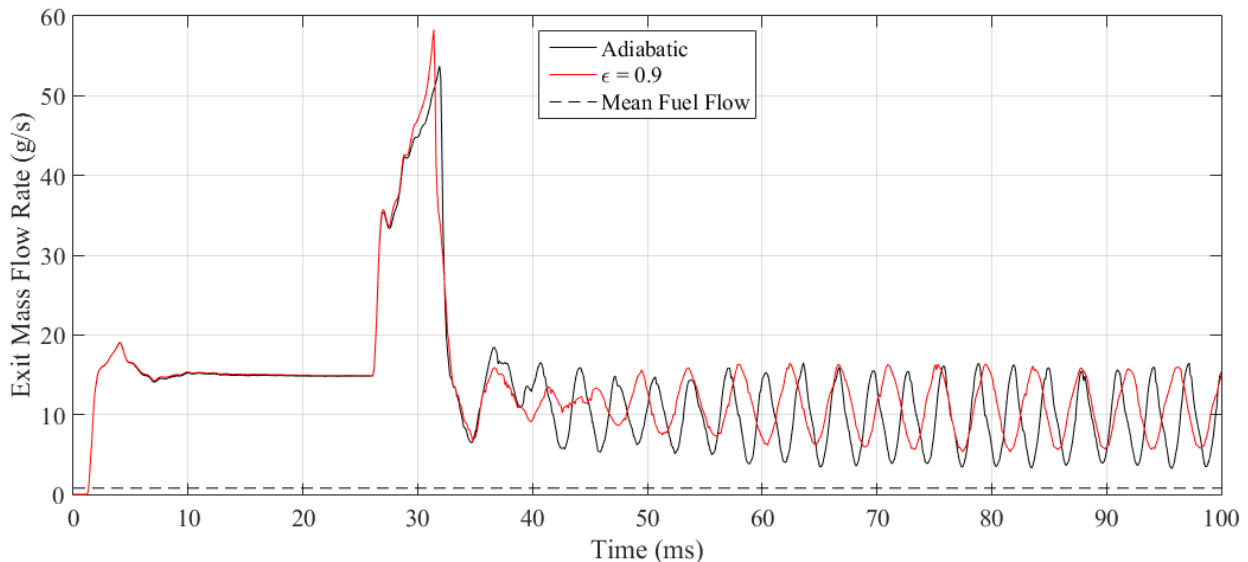


Figure 184: CFD Simulation (Adiabatic and with Radiative Heat Losses) Nozzle Exit Total Mass Flow Rate Time History In Comparison to Injection Fuel Flow Rate

The result of this integration is shown in Figure 184. It is first, immediately clear that fluid is flowing through the engine prior to ignition as evidenced by the approximately 30 g/s of total mass flow prior to ignition at 25 ms. The pressure differential between the ambient and exit boundary conditions is also likely playing a significant role in the engine's exit mass flow rate considering how low the constant injection fuel flow rate is. Some entrainment of air by the high speed fuel injection is expected by design but this is likely augmented significantly by the elevated ambient pressure condition discussed earlier.

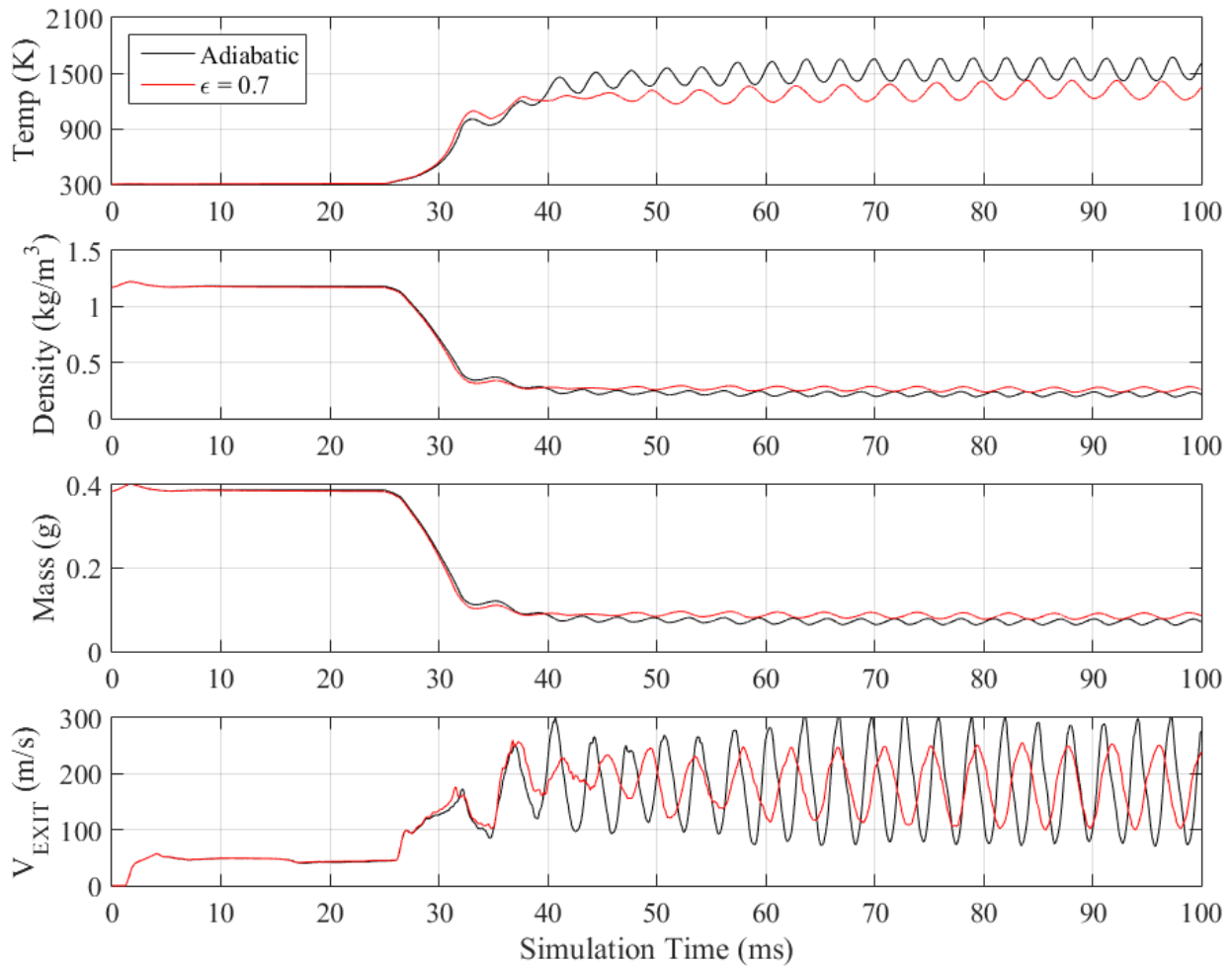


Figure 185: Chamber Region Mass-Averaged Density, Mass, and Temperature CFD Simulation Time Histories (Adiabatic and with Radiative Heat Losses)

Shortly following ignition, there is a large rise in the exit mass flow rate likely as a combined result of the initial startup chamber pressure and temperature transients. As the engine starts, initial ignition raises the chamber temperatures and pressures which increase the exhaust speed and lower the density inside the constant volume chamber. As the first cycle of fuel and air leave the engine, the low pressure chamber draws in more air raising the mass flow rate. After 30 ms, the density in the chamber is falling rapidly as the temperature rises and the pressures begin to oscillate driving the exit velocity oscillations. The combination of the stable velocity periodicity and the sharp fall in density results in this drop in mass flow rate as the engine warms up. A strip chart of these parameters for the adiabatic and a representative heat transfer simulation are included in Figure 185.

It is unclear if this spike in mass flow (essentially blowing clear the chamber's initial contents) is a true phenomenon in the physical engine or an artifact of the elevated ambient pressure condition. Nevertheless, its effect is gone by 50 ms of simulation time as stable operation is reached. The stable mass flow rate had a typical amplitude of approximately 13 g/s (~10 g/s including heat losses) between overall maxima and minima of 16.5 and 3.4 g/s, respectively (16.4 and 5.3 g/s with heat losses). This is compared to a constant fuel flow rate of 0.77 g/s. Because the minimum mass flow rate is actually lower in the adiabatic case despite the maxima being nearly equal, the mean exit total mass flow rate in the adiabatic simulation was just 9.5 g/s. All the cases accounting for heat transfer losses showed slightly higher exit mass flow rates between 10.6 and 11.2 g/s.

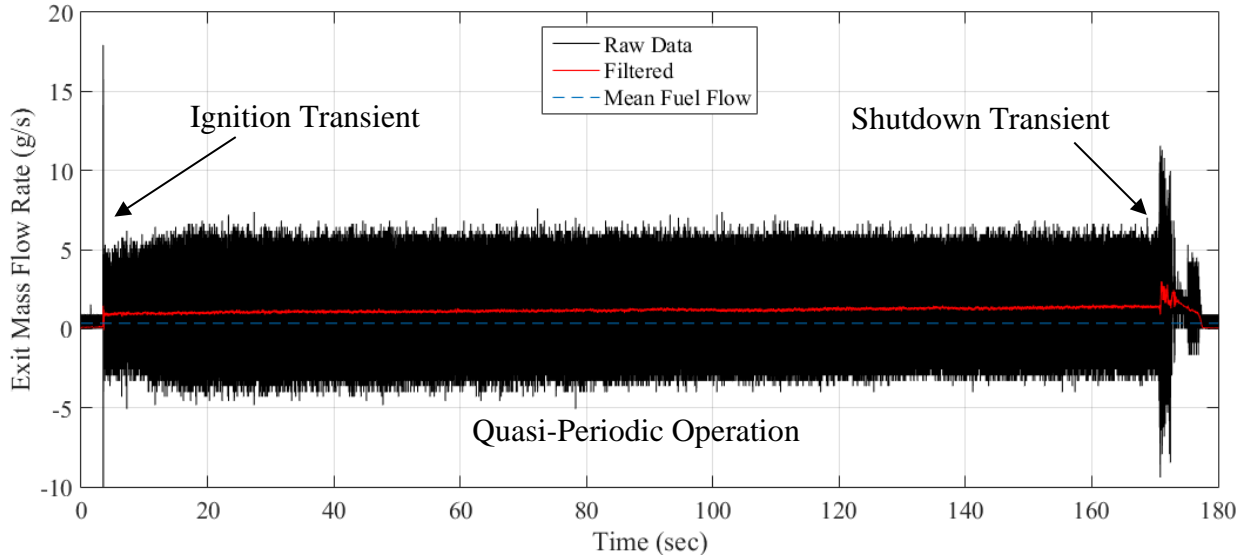


Figure 186: Engine Stand Pitot Tube-Based Exit Mass Flow Rate Complete Time History

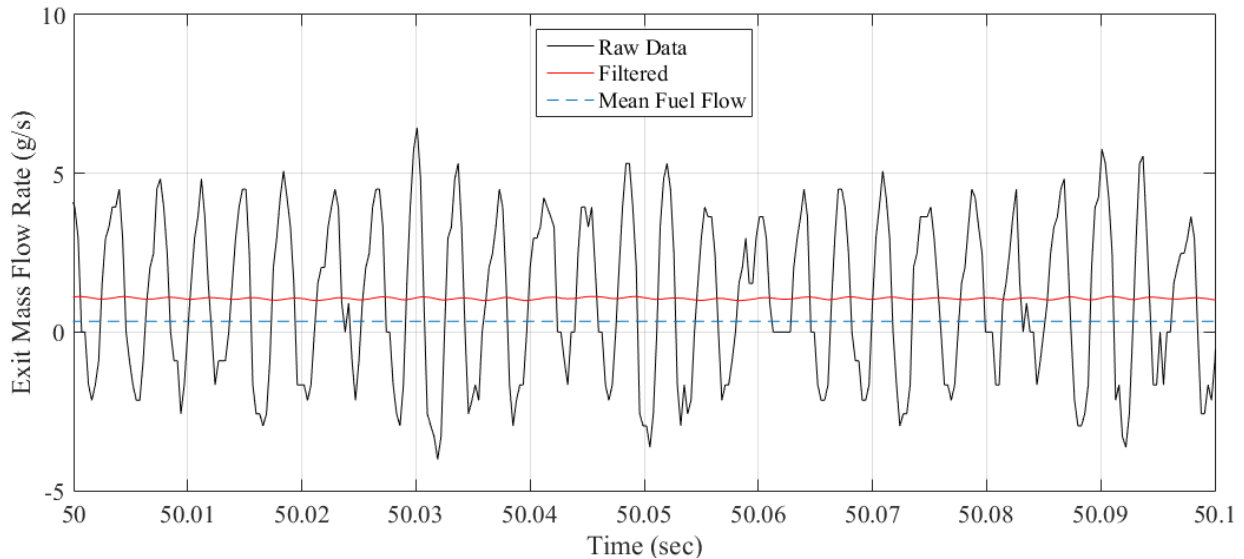


Figure 187: Engine Stand Pitot-Based Exit Mass Flow Rate Time History Zoomed In To Show Quasi-Periodic Engine Cycle over 100 ms Timeframe

For comparison, the experimental data was also sufficient to approximate the exit total mass flow rate. Because the mass flow rate calculation was essentially a scaling of the Pitot tube exhaust speed time history data, the mass flow rate time history looks much the same just scaled to units of mass flow rate (grams per second, g/s). The same startup and shutdown transients are again visible in Figure 186 placing bounds on a large “noise” band describing the quasi-periodic operation of the engine. Zooming into a 100 ms subset of this data (shown in Figure 187) shows

the same periodicity seen in the exhaust speed data. This exit mass flow rate exhibited the same frequency of approximately 250 Hz and had an amplitude up to approximately 10.5 g/s between maxima and minima of 7.6 g/s and -5.7 g/s respectively around a mean which rose slightly to 1.2 g/s as the engine warmed up. This is in comparison to the fuel flow rate of 0.34 g/s estimated on the engine thrust stand by measuring the mass of the propane fuel tank before and after a test run and recording the time the needle valve was open. These findings are significantly lower than those seen in the CFD data (including the runs accounting for radiative heat losses), likely as a result of the elevated ambient pressure condition “pumping” extra air through the engine. This would have the effect of significantly increasing the mean offset and also likely raising the amplitude as more air than usual would be drawn in during the intake phase of the engine cycle. Assuming a constant fuel flow rate, the fluid leaving the engine was as much as 95.5% air by mass with a mean of 71.9% air suggesting significant entrainment of air into the engine but which is also heavily dependent on the engine cycle.

VII. Conclusions and Future Research

A. Validity and Utility of Computational Models

In the area of computational modeling of real-world systems, there is a common adage on their ultimate application, “All models are wrong but some models are useful” [34]. As this chapter presents the ultimate conclusions of this research effort to revive the lost Brayton-Gluhareff cycle pressure jet engine, it is first necessary to discuss the limitations and applicability of the simulations with respect to the real-world data measureable on the engine test stand.

1. Relative Error of the Engine Simulation and Possible Sources of Error

The Computational Fluid Dynamics (CFD) engine simulation matched some experimental measurements well while others showed significant differences that prevent the simulation from representing a direct, exact model of the engine’s operation. In all possible cases, the general qualitative results matched expected response well. The Kadenacy Effect – the fundamental driving process found in valveless pulsejets – was clearly shown in both the CFD simulations and the experimental data. The maximum available data rate of 3,333 Hz on the engine test stand allowed sufficient speed to resolve the engine’s operating frequency. This frequency was observed on the test stand at around 300 Hz and in the idealized CFD simulations at slightly higher frequencies of 300 to 350 Hz. This frequency was observed in the CFD simulation pressure, velocity, and temperature distributions, as well as on the engine test stand in the pressure, velocity, and thrust force data with the temperature data being limited by the heat-transfer driven lag time to reach an equilibrium temperature and the thermocouple datalogger’s maximum refresh rate of 1 Hz. Both the engine simulation and the engine test stand data showed a high temperature engine

core and high temperature exhaust as shown in the IR-filtered images of the engine in operation used to compare with the CFD distributions.

Quantitative matching between the CFD simulation and the engine test stand was less promising. This was thought to be driven by three major factors. The first factor was the use of an elevated ambient pressure region (1.085 atm, 110,000 Pa, 15.95 psi) defined in the CFD simulation while the engine was operated near one atmosphere. Earlier simulations using a one atmosphere ambient region for the engine intake conditions resulted in the engine core mixture being too rich to sustain combustion beyond the initial ignition source. Despite trying reduced injection pressures, and some added fixed mesh fineness at the inlets, engine startup and continued operation was not observed until the ambient pressure region was raised to 110,000 Pa. This drove enough air into the engine that the distribution of fuel and air (represented in visualizations of equivalence ratio in Chapter VI, Section A-5) was favorable to self-sustained combustion.

Prior to ignition, this pressure differential drove an air flow into and out of the engine which artificially raised the mean chamber pressure and exhaust speed throughout the remainder of the simulation. As a result, this driving of the engine intake with extra air would be expected to further augment the combustion process raising the amplitudes of pressure and exhaust speeds and through more complete combustion, the heat release and resulting temperatures as well. This discrepancy between the CFD simulation and the engine test stand setup is not without a real-world counterpart. The original pressure jet engines built by Eugene Gluhareff featured a ram air scoop designed to capture extra air during operation at flight speeds and slow it to an elevated total pressure to augment engine performance. A plot of this effect on a production pressure jet engine was shown in Figure 10. As a result, assuming the simulation is accurate with the one atmosphere ambient

pressure, it could be a limitation of the kinetic model in capturing rich propane combustion that was possible on the engine test stand but not in the CFD simulation.

An alternative or potentially contributory explanation is the second major factor believed to affect the accuracy of the simulation's quantitative results – relatively low mesh fineness. Early simulations using much higher mesh fineness in the inlet regions were able to capture a major phenomena seen in reality – the shock diamonds that formed as a result of the under-expanded injection flow into the first-stage inlet. Unfortunately, use of a mesh fine enough to resolve those features was prohibitively slow even without using a kinetic mechanism. This is the result of the Courant-Friedrichs-Lewy (CFL) Condition for convergence of the simulation. This condition (discussed in Chapter IV, Section A-4) relates the local velocity and mesh size to the current simulation time step. The consequences of which result in a prohibitively small time step to most accurately capture the small size and high speed of the engine injector. With the available computing power, this pushed the time to complete a simulation from days to months and years.

The use of greater mesh fineness, particularly around the injector and inlets, would be expected to more accurately capture both the flow of ambient air entrained into the inlets and engine as well as the early mixing of fuel and air. If both of these phenomena were under-represented in the CFD model (potentially because of the low resolution limiting their effect to sub-grid modeling), that could cause the mixture to be too rich in the engine under the proper one atmosphere ambient pressure conditions.

The final effect not considered in the CFD simulations was that of heat losses from the engine as a result of conductive, convective, and radiative heat transfer. Contact area between the engine core and the metal thrust stand was kept to a minimum in an effort to minimize the effect of conductive heat losses from the engine as well as affecting the surface temperature distribution

any more than absolutely necessary. Conduction to the surrounding air was considered negligible. Hence, convective heat transfer was considered to have a negligible effect on the engine operation. The engine was tested indoors with an operating vent hood across the room but no noticeable room air currents were observed. Hence, forced convection was considered negligible. Free convection – the heat transfer from the engine to the cooler ambient air causing a local air density change and resulting in a buoyant rise of local air – could not be prevented. Potentially, the strongest source of heat loss – radiant heat transfer – was also not included in the CFD simulations. Considering the high surface temperatures (to the point of incandescence) and much cooler surrounding conditions, the radiant heat flux was considered to be the greatest source of heat loss from the engine and likely have the greatest effect on the engine cycle.

The CONVERGE solver did not have a means to model all these effects independently and there was not time prior to publication to include a combination of all these effects. The solver does have two heat transfer options for the temperature boundary condition – convection and heat flux. The convection boundary condition requires the user to select a far field ambient temperature and a convective heat transfer coefficient. Considering the potential for radiative heat transfer, this was considered an inaccurate approach. The remaining alternative (described earlier in Chapter VI, Section B-5) defines a heat flux in W/m^2 on the surface that could additively capture multiple effects like radiative heat flux, free convection heat flux, and the heat flux due to conduction to the surrounding air. The difficulty is in the feedback between surface temperature and heat flux as the engine heats up and the correlation between the engine wall heat capacitance which should drive the actual wall temperature which itself should then drive the wall heat transfer (conductive, convective, and/or radiative). This more in-depth analysis was not possible at this time. Instead a simpler approximation was made assuming a stable wall temperature that rapidly rose from the

ambient temperature following ignition. This significantly reduced errors in temperature measurements, particularly of the core and to a lesser extent the exhaust gas temperature as well as in predicting the engine's operating frequency – a dependency expected from a review of pulse jet studies published by Geng [6, 30-32, 290]. This same effect is also expected to affect the stability of the engine as suggested by studies on the stability of flames [96, 142, 143, 316, 317].

Modeling of the wall heat capacitance effects in addition to a distribution of wall heat losses (as a function of the surface temperature distribution) should further improve the simulations from the standpoint of heat loss effects. This would not be without significant difficulty, perhaps the greatest being the longer simulation runtime necessary to reach a “warmed-up” steady condition. It was clear from the experimental findings that the timescale for the walls and inert coil to reach a steady “thermal soak” temperature were on the order of 15 to 30 seconds at least compared to the engine's quasi-periodic operation at around 0.1 seconds.

2. Sources of Error on the Engine Test Stand

The experimental data is also not without its own limitations and sources of error. The majority of the project was completed with low cost as a significant driver of the available materials, equipment, and electronics. Consequentially, the availability of greater funding applied toward more sensitive sensors and faster data logging could produce data with greater resolution and less noise in addition to logging more channels of data. The latter opportunity would allow measurement of pressure and temperature distributions as opposed to a few point measurements. The comparatively low resolution and data rate was still sufficient to resolve the engine operating frequency and data amplitudes. Nevertheless, there is a strong opportunity to improve the precision of these findings with higher fidelity electronics. An increase in the data rate from 3,333 Hz to 10,000 Hz on each channel, for instance, could at least match the CFD data rate.

A further effect on the data is that of the lead length from the pressure port location to the pressure transducer where the pressure is measured by the transducers and converted to a voltage read by the data logger. The length was kept to a minimum but considering the speed of sound in air, each foot of lead length delays the pressure wave slightly more than 1 ms. This is a nontrivial effect for a data rate of 3.3 records per ms. Since the tubing had a tight fitting, the effect on the pressure amplitude was considered negligible. However, in the case of the Pitot tube, for instance, there are two small inner diameter changes that could slightly attenuate the pressure wave as it propagates toward the transducer.

Lastly, the CFD simulation assumes perfect, constant engine geometry and is unaffected by the minimized although nonzero, effect of the thermocouples, Pitot tube, and thrust stand in general. In practice, the engine was subject to some vibration on the engine stand as a result of the cantilevered mounting and periodicity of the thrust forces. Furthermore, the presence of heat and pressure differential inside the engine core resulted in some minor bulging of the engine core's original rectangular cross-section. This was not expected to have a significant influence on the engine cycle or overall engine performance. Other minor effects include potential physical interference caused by the core pressure port feed tube and thermocouple cables leading from the engine to the static frame of the test stand. Extra length was used to mitigate this effect and it did not appear to corrupt the thrust stand calibration data shown earlier in Figure 117, but this could still have a small effect on the data.

3. Effects of Engine Scaling on Pressure Jet Engines

Because Gluhareff was prolific in his life's work on the pressure jet engine, there is ample data on the capabilities of his engine design. This also includes the effect of scaling on how designs perform at small scales as low as 5 lb_f of thrust to large scales boasting a static thrust of 700 lb_f.

Nevertheless, through years of painstaking research and testing, Gluhareff was able to build a complete lineup of pressure jets between these bounds. Because their geometry is such an integral part of that performance, comparing them on that basis can make clear how they scale with size and now that trend can be extrapolated below the 5 lb_f thrust size.

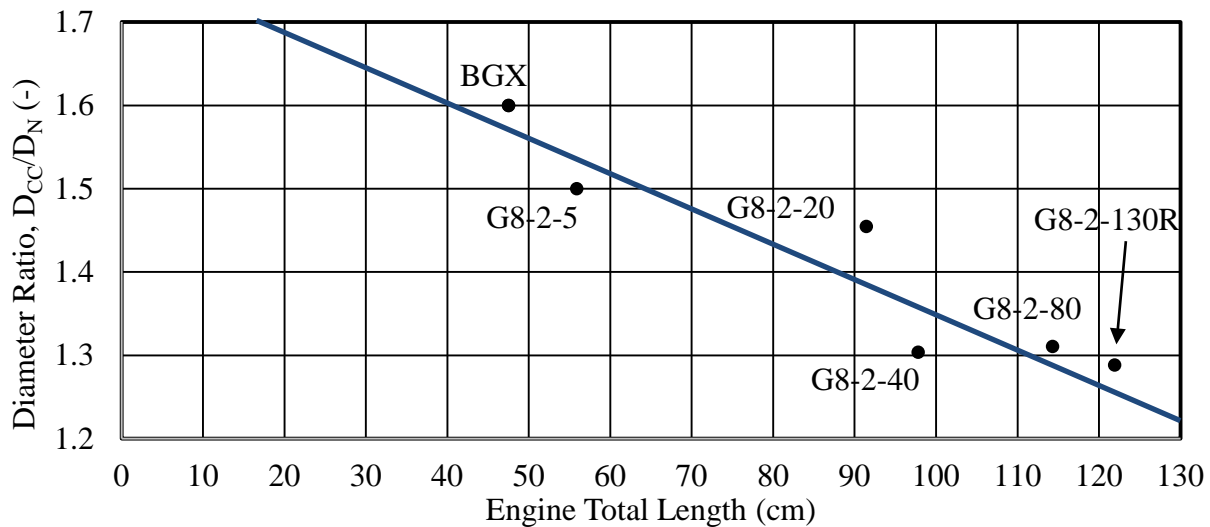


Figure 188: Pressure Jet Possible Geometric Scaling of Diameter Ratio (Combustion Chamber, D_{CC} to Nozzle Exit, D_N) with Total Engine Length

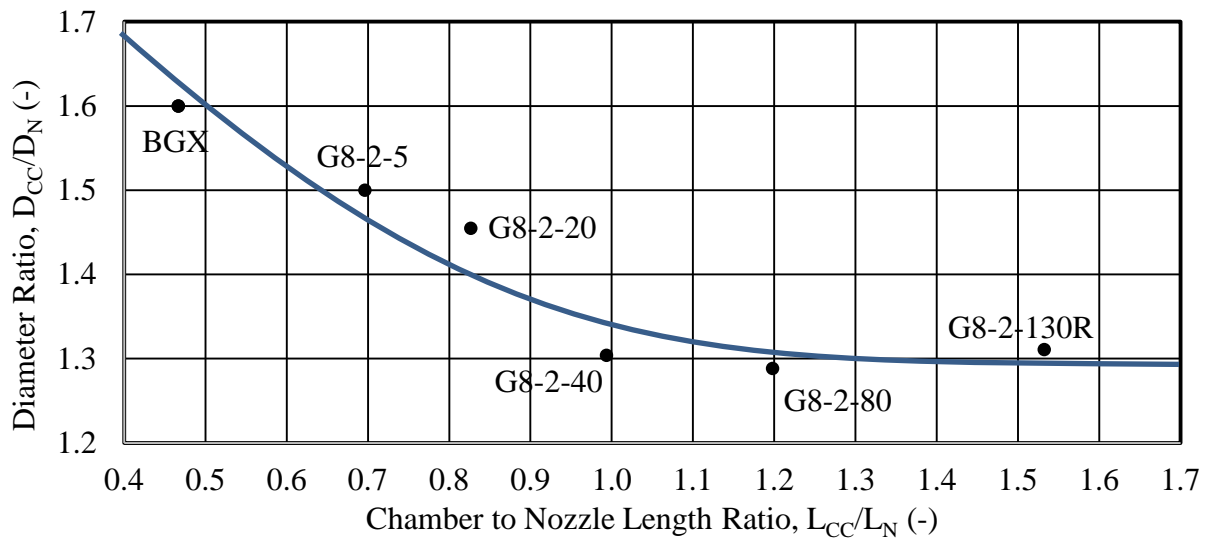


Figure 189: Pressure Jet Possible Geometric Scaling of Diameter Ratio with Length Ratio (Combustion Chamber, L_{CC} to Nozzle Exit, L_N)

In an attempt to draw some approximate conclusions from the scaling of the pressure jet engines Gluhareff designed and the geometry of the BGX prototype engine based on the same

principles, the general sizing parameters of the engines are plotted in a series of figures. These include some expected trends; however, these trends are expected to be subjective due to the low number of available data points. The scaling of the engine's combustion chamber and nozzle diameters with engine length is shown in Figure 188 and with the length broken down into a ratio of the combustion chamber and nozzle lengths in Figure 189. The engines always exhibited a larger combustion chamber diameter than nozzle exit diameter, though it appears that as the engines grew larger, this disparity (characterized by the chamber to nozzle diameter ratio, D_{CC}/D_N) decreased. This is visible in relation to both the engine total length and the split of that length between the chamber and nozzle.

Above the 40 lb_f (178 N) thrust scale, this diameter change appears to have stabilized around 1.3 with the chamber diameter being 30% larger than the nozzle. It makes sense that the nozzle diameter should always be smaller than the chamber since even Gluhareff's pressure jets did not produce a chamber pressure large enough to warrant a supersonic convergent/divergent nozzle. The relation between the chamber and nozzle lengths, however, does not stabilize. Beyond the G8-2-40 engine, the nozzle is actually shorter than the combustion chamber, a trend that appears to continue as the engines grew larger and produced more static thrust. In contrast, the smaller the engines got below the G8-2-40, the longer and thinner the nozzle got in relation to the combustion chamber. This trend appears to have continued down to the BGX's scale putting it in line with Gluhareff's original pressure jet lineage suggesting that application of the same principles and fine tuning on the engine stand was capable of producing an engine at least fitting with the proper geometric trends.

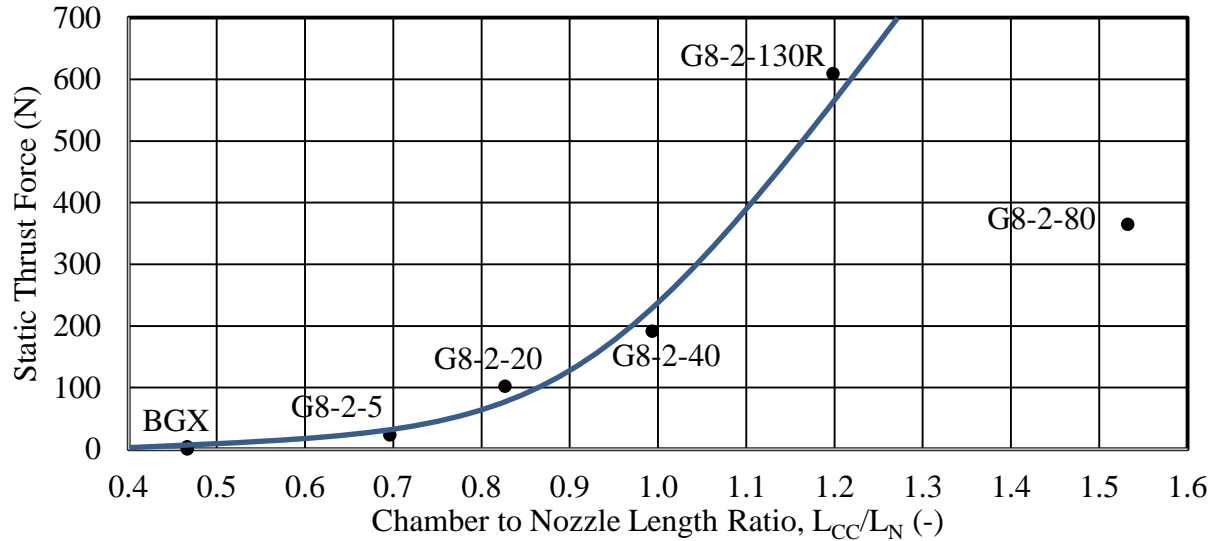


Figure 190: Pressure Jet Possible Scaling of Length Ratio (Combustion Chamber, L_{CC} to Nozzle Exit, L_N) with Static Thrust Force

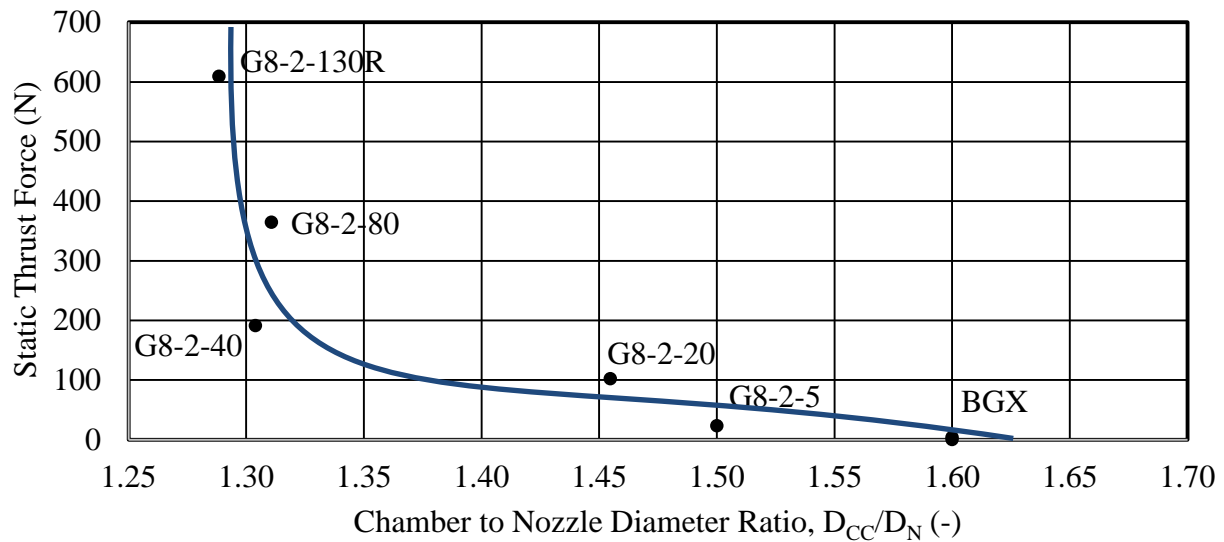


Figure 191: Pressure Jet Possible Scaling of Diameter Ratio (Combustion Chamber, D_{CC} to Nozzle Exit, D_N) with Static Thrust Force

The scaling of engine static thrust force with the length and diameter ratios are further shown in Figure 190 and Figure 191, respectively. These continue to illustrate the stabilization of the diameter ratio around 1.30 for larger engines and the continued reduction in nozzle length compared to the combustion chamber. The G8-2-80 engine is of particular note here as it stands significantly apart from the apparent trend set up by the rest of the pressure jet series. This can be traced back to its unusually short nozzle (or long combustion chamber) driving its chamber-to-

nozzle length ratio higher than that seen in the other engines. It is unclear why this was the case – there is no mention of the G8-2-80 engine as any form of outlier, and the diameter ratio is in better agreement with the thrust trends. The smaller engines appear to show a somewhat linear trend toward wider and shorter combustion chambers. However, prior to this research effort, this trend appeared to suggest that positive thrust below the scale of the G8-2-5 engine should diminish to zero around a length ratio of 0.60 and diameter ratio of 1.55. Although the thrust generated by the BGX engine was very small, it has proven that the engine’s principles can produce positive thrust at smaller scales than were previously suggested.

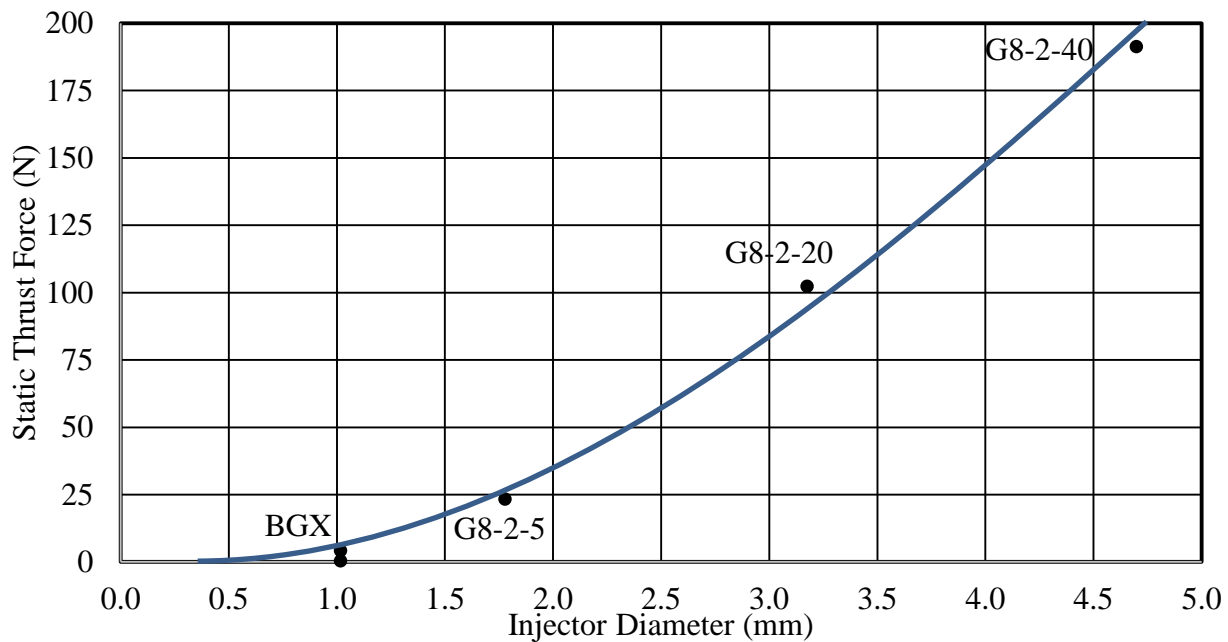


Figure 192: Pressure Jet Engine Trend of Static Thrust Scaling with Injector Diameter

Another significant driver of engine scaling was the primary driver used to determine the majority of the engine’s geometry – the selection of an injector diameter. As discussed in Chapter II, the choked fuel injector sets the fuel flow rate into the engine, sets the inlet areas to provide a slightly lean mixture of fuel and air to the engine core, and ultimately was used to scale the rest of the engine’s parameters. In short, the engine injector diameter sizes the rest of the engine. The trend of thrust with injector diameter is one that matches expectation – the smaller the injector, the

less thrust an engine will produce. Alternatively, the less thrust is needed from a pressure jet design, the smaller its injector should be. Below the size of the G8-2-40 engine, the trend of thrust with injector size appears to be linear with zero thrust predicted around a diameter of 1.25 mm. The fact that low but nonzero thrust was seen with a diameter of about 1 mm suggest that this trend is not necessarily completely linear at very small scales. It should be noted that both the CFD results and the experimental data from the BGX prototype are represented in these plots where there was significant disparity between their static thrust forces.

In general, the engines showed a slight reduction in TSFC (an improvement in engine efficiency) with increasing size and thrust forces with the G8-2-130R being a significant outlier with a TSFC of $0.78 \text{ lb}_m/\text{hr}/\text{lb}_f$, well below the $1.44 \text{ lb}_m/\text{hr}/\text{lb}_f$ of the original G8-2-130. Gluhareff noted one major reason for this improvement that had little to do with tuning or scaling – he changed the inlet design from an elliptical cross-section to a circular cross-section. He noted a reduction in the injection pressure needed to reach rated static thrust from 240 psi (16.3 atm, 1.66 MPa) to 170 psi (11.6 atm, 1.17 MPa) [15]. The elliptical cross-section was originally chosen to fit the engine's intake system inside the airfoil cross-section of a helicopter blade. However, by the time he had developed the G8-2-130, this application of his engine design was one of many opportunities and the elliptical choice was apparently holding the design back. Other than this modification, the effect of size on TSFC was relatively minor with a slight trend of lower efficiency with smaller engine scale. This was somewhat magnified by the BGX engine pushing to a minimum possible scale and apparently the lower-than-predicted static thrust, resulting in a TSFC of $29.8 \text{ lb}_m/\text{hr}/\text{lb}_f$. The CFD simulation's upper bound on performance pushed the TSFC at the same scale down to $6.5 \text{ lb}_m/\text{hr}/\text{lb}_f$. This was still high but more similar to the upward trend of 4 – 5 $\text{lb}_m/\text{hr}/\text{lb}_f$ seen on the other engines prior to the G8-2-130R's redesign improvements.

B. The Brayton-Gluhareff Cycle

The CFD simulation, and to a lesser extent, the experimental data, was also used to investigate the nature of the “Brayton-Gluhareff Cycle” (named as such for its relation to the conventional Brayton Cycle in a joint review of the engine and its history published by Barrett and Irina Gluhareff, the surviving daughter of the engine’s original inventor) [16]. Moreover, although the study presented a similar comparison of the Brayton and Brayton-Gluhareff cycle as shown in Chapter I, to date, no data to place bounds on the cycle were available.

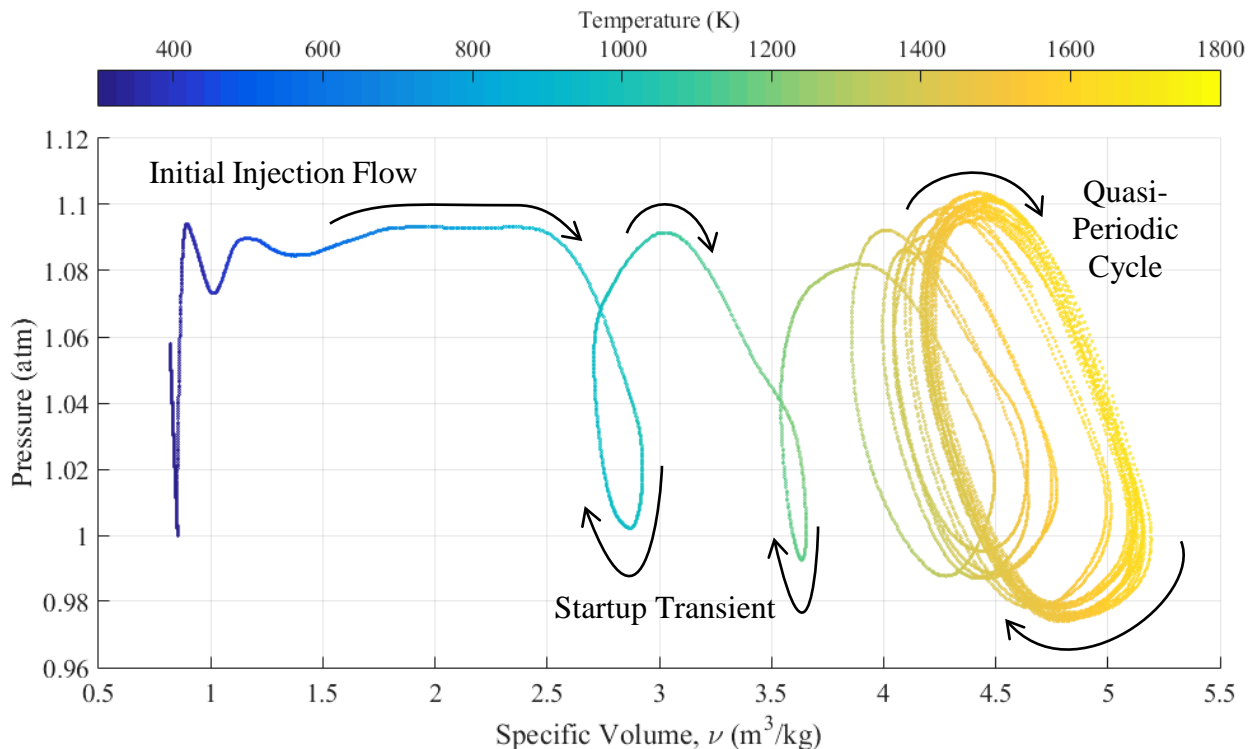


Figure 193: The Brayton-Gluhareff Pressurized Ramjet or “Pressure Jet” Engine Cycle Including Startup Transients as Calculated by Mass-Averaged Chamber Properties in the Engine CFD Simulation (P-v Diagram Colored by Temperature)

Toward that end, the CFD simulation in this study was used to build a typical Brayton cycle thermodynamic P-v diagram for the pressure jet engine. The resulting chart is shown in Figure 193. This was generated using the engine chamber region mass-averaged properties output by the CONVERGE solver. The full 100 ms simulation time domain was used to fill this plot of mean

chamber pressure against mean chamber specific volume. The path traced out was then colored by the mean (also mass-averaged) chamber temperature to illustrate the distribution of temperature as the engine reaches a quasi-periodic state of operation.

Several properties of this chart are worth mentioning. First, it is clear that mean temperature plays a role in the startup of the engine both in starting the engine via the first few irregular cycles and in stabilizing the engine to its final quasi-periodic condition. Next, as the engine warms during startup, it is clear that the mean chamber pressure cycle successively drops to lower maximum and minimum pressures. The maximum pressures appear to recover while the minimum pressures (coinciding with the start of new fuel and extra air intake thereby restarting the engine cycle) continue to drop to a steady condition as low as 0.97 atm (98,285 Pa, 14.3 psi).

This chart also shows a clear correlation between the mean chamber temperature and the mean chamber specific volume. Specifically, as the engine warms up to a quasi-periodic operation, it is clear that the specific volume generally increases as the temperature increases. This is at least consistent with trends suggested by the ideal gas law. It is worth noting, however, that application of the ideal gas law was *not* an assumption placed on the engine simulation or CONVERGE solver. Instead, the Redlich-Kwong equation of state (the default) was used because it “accounts for the non-ideal gas behavior that can be significant at high pressures and temperatures” [28, 283].

Another temperature correlation is also evident concerning the quasi-periodic engine cycle. Once the engine has stabilized, it is clear that the left, rising side of the cycle occurs at a relatively constant, lower temperature of approximately 1450 K until it nears the greatest mean chamber pressure. At that point, the temperature begins to noticeably rise up to 1670 K at which point the temperature is largely unaffected until it nears the cycle’s minimum pressure where cooler air and fuel begin mixing in the engine and restarting the cycle. It is worth noting that the rise and fall in

pressure appears to be significantly faster than the increases and decreases in specific density at the top and bottom of the cycle, respectively. This suggests that the pressure rise of combustion in the engine chamber is occurring at a faster time scale than the heat release due to combustion that raises the chamber temperature and is clearly affecting the fluid specific density.

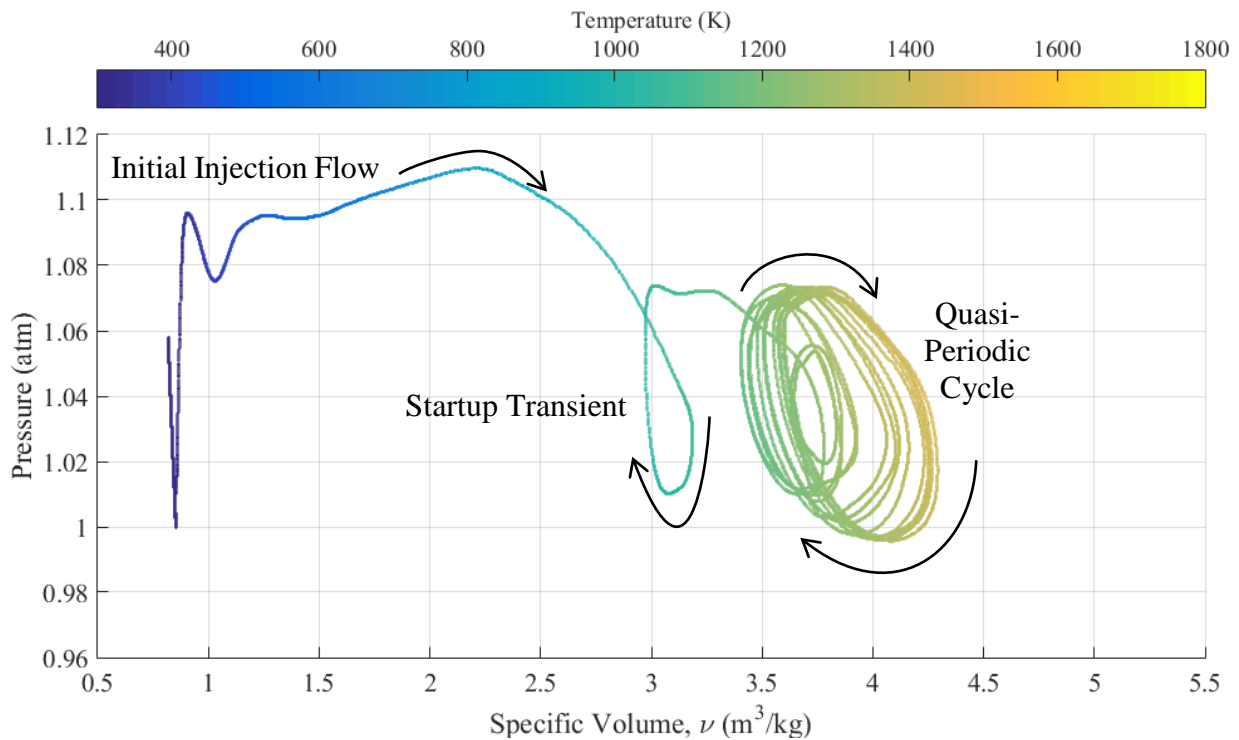


Figure 194: The Brayton-Gluhareff Pressurized Ramjet or “Pressure Jet” Engine Cycle Including Startup Transients as Calculated by Mass-Averaged Chamber Properties in the Engine CFD Simulation Accounting for Radiative Heat Losses (P-v Diagram Colored by Temperature, Emissivity of $\epsilon = 0.7$)

The engine cycle approximately accounting for some radiant heat losses is also included in Figure 194. The trends are much the same although, as one would expect, the inclusion of heat losses has significantly attenuated the engine’s cycle in terms of pressure, temperature, and specific volume. By extension, that means the inclusion of heat losses is decreasing the work output of the engine. This “wasted” heat is no longer being exploited by the engine and is therefore no longer part of the work output. Nevertheless, the cycle still exhibits quasi-periodicity and stabilizes to a repeatable engine cycle along a similar path as the adiabatic simulation.

1. Sonic Lock and Acoustic Tuning

That engine cycle response is largely the result of careful tuning necessary to set up a standing pressure wave in the inlet structure to draw in more air than normal entrainment would suggest. Gluhareff called this condition “Sonic Lock” [15, 18]. The tuning was done in two stages – closed-form approximation to determine the sizes of the inlets required to feed the engine with a favorable (slightly lean) mixture of fuel and air, followed by construction of the engine, the test stand, and repeated tests to find the location of these inlets that resulted in the most stable, hottest, and loudest response. In the absence of early thrust data, this qualitative response was used to fine-tune the inlet locations and engine location with respect to the injector until no discernable improvement was seen. Only small modifications were necessary after the closed-form approximations sized the engine. These included opening up the third-stage inlet slightly to let in extra air and extension of the nozzle length to minimize the flame exiting the engine (and therefore loss of fuel energy) accelerating flow out of the engine.

Once the engine dimensions were fixed and proper operation was verified, the geometry was carried over to the CFD simulation domain to match it. Due to time constraints, no ‘fine-tuning’ of the engine was done using CFD, just design to match the test conditions as closely as possible. Nevertheless, the engine’s oscillatory nature and even frequency closely matched those seen on the engine stand. Moreover, the stability of the engine once a quasi-periodic condition was reached was also evident in the simulations and in operation of the engine. The test run involved operation of the engine for over 3 minutes with no user adjustment to the fuel feedline and no discernable changes in the feedline pressure. This alone is a noteworthy accomplishment despite the engine’s comparatively low performance. Gluhareff reportedly worked on miniaturizing the engine design below the G8-2-5 scale but was unable to because of “instability.”

The new prototype engine design does not appear to suffer from any engine-tuning related instability problems. In fact, the only difficulty associated with operating the engine was related to locking down the engine's geometry despite its intent to shake loose. In one such test, the engine core was improperly located less than 0.25 in. (6.35 mm) further downstream of its intended location along the injection flow axis and was found to run unsteady and was seriously prone to irregular unstart events. Upon brief inspection, the engine core was returned to its intended location (matching the geometry described in Chapter IV, Section D-1) and stable operation was once again possible. This illustrates the sensitive nature of the "sonic lock" design and how critical it is to engine operation. Even slight misalignments can have cascading effects ultimately disallowing proper operation of the engine. It is therefore reasonable to conclude that further fine tuning and tighter control of the engine geometry should allow further increases in the engine's performance in the same way that careful tuning of the G8-2-130 engine was able to be improved into the G8-2-130R design with a 41% reduction in TSFC despite having the same rated thrust [15].

2. Engine Shape and Internal Flow

The stability of the BGX prototype design was intended to be a consequence of the square cross-section. Specifically, the hope was that small recirculation zones in the corners could work in concert with the larger recirculation zone in the engine head to effectively store fuel, heat, and potentially small flames at the low point of the engine cycle when extinction and/or blowout could unstart the engine. The design was largely chosen for its ease of construction with an early circular cross-section prototype suffering from extensive leaks in the chamber where curved parts were spot-welded together. The hope that the sharp corners would lend engine stability was thought to be a positive consequence of this design choice. At least part of this was suggested by the CFD simulation – that of the forward recirculation zone in the head of the engine. The second claim –

the stabilizing effect of flow in the corners of the engine – could not be satisfactorily verified due to the comparatively coarse mesh necessary to complete the engine simulation in a reasonable timeframe.

Nevertheless, the CFD simulation did elucidate something unexpected concerning the flow patterns inside the engine. To date, no published study exists to discuss the three-dimensional flow inside the Gluhareff pressure jet and how it affects the engine cycle. It is indeed possible that Eugene Gluhareff himself was not fully aware of the complex nature of the flow inside his own engine design. This is because it predates the widespread application of three-dimensional CFD and experimental visualization tools like those he would likely have seen working on the S-IVB stage of the Saturn V rocket for NASA [16] were likely outside his financial capability. The CFD simulation suggests that a twin-chambered recirculation, symmetrical about the engine's centerline symmetry plane that forms because of the injection flow spreading around the engine chamber's interior as it mixes and burns. This appears to be the driving mechanism behind the forward recirculation zone that seems to capture fuel, and to some extent heat, during the engine cycle. There is, however, some uncertainty as to whether this recirculation is a true representation of the actual pressure jet design or a consequence of the symmetry plane assumption as suggested by the literature on pipe flows discussed in more detail in Chapter IV, Section D-3. Future research (discussed in the next section) will include a study without this symmetry plane to verify to what extent the full engine domain continues to exhibit this recirculation, likely as a single full-volume swirl instead of a twin-cored phenomena.



Figure 195: Eugene M. Gluhareff Posing with his G8-2-130 Pressure Jet Engine

One final note on the engine design involves the Gluhareff pressure jet's engine nozzle "scarf" or cutout shown in Figure 195. Gluhareff claimed in conversations that this modification was the result of endurance testing on one of his prototype engines and had the effect of increasing engine performance, reducing noise, and resulted in smoother operation [318]. Since there exist very few publications on the engine and its design, it is then unsurprising that there exists no data proving these claims quantitatively. About the effect of the nozzle, Gluhareff himself wrote the following in the G8-2 Technical Handbook which was included with each engine he sold:

"The G8-2 Jet Engine is not a Pulse-Jet, it is a burner, and a resonating tail-pipe is detrimental, it reduces jet thrust. The end of the G8-2 Jets tail-pipe has a fishtail cut which dampens the tail-pipe's natural frequency. The change from straight to fishtail cut increased the thrust of the G8-2-15 by 3 lbs and reduced the noise level by about 1/2.

The resonance in the tail-pipe is detrimental to the intake system. The resonant frequency of the tail-pipe interferes (sic) with the frequency of the tuned intake, which operates on a higher frequency. A small hole in the side of the diffuser #5 is a sonic damper, it reduces noise and improves jet thrust."

engines assembled for this study. Unfortunately, no discernable change was seen in operation with or without the chevron cutout. This does not mean the chevron design has no merit, just that whatever benefit it does provide was too small to be noticeable either at this scale, low injection pressure, low performance, or any combination therein. Furthermore, whatever effect the chevrons had on the exit flow (typically involving mixing of the exhaust and ambient flow) may have been partially achieved by the square cross section because of the lower flow velocity at the nozzle corners. Construction of a new pressure jet matching Gluhareff's original drawings or surviving engines operated with and without the chevron would be needed to record data sufficiently showing what effect if any this cutout has on the engine and its operation. Computational modeling of that engine with and without the scarfed nozzle exit could further clarify those effects.

C. Future Research

One of the intended consequences of this effort was to lay the foundation for further research into the Brayton-Gluhareff cycle and the pressure jet engine. Because the subscale engine is not yet optimized, there is still significant room for further study both of the subscale engine and Gluhareff's original engine geometries.

1. Further CFD Modeling

The first aspect of this study with potential for future work is to continue improving the current base CFD simulation. Of primary interest is any means to reduce the ambient pressure condition to one atmosphere and still obtain combustion through the engine and reach quasi-periodic operation to reduce the disparity between the engine test stand data and the predictions from the CFD. It is possible this could be resolved by either adjusting boundary conditions or reducing the injector diameter and thus fuel flow for the same pressure. This may also be positively affected by increasing the mesh fineness and simply accepting the long runtime.

The problem of longer runtime could also be partially alleviated by completing the implementation of the Westbrook and Dryer one-step kinetic mechanism. The source code currently being used to attempt this is included in Appendix A-3. Instead, a reduced form of the San Diego mechanism was used since it did not require recompiling the solver to use, but even this lighter-weight version of the full San Diego mechanism would require substantially more computational time than a one-step mechanism. This would not prevent the CFL condition from driving the time step low, but could reduce the amount of time necessary to complete a time step allowing for greater mesh fineness for the same total computational time.

The next feature to be implemented is that of heat losses and their effect on the pressures, temperatures, exhaust speeds, ignition delay, and eventually overall engine operating frequency.

This would ideally include the effects of conductive, convective, and radiative heat transfer losses and (as much as possible) characterize the percent contribution of each to the overall surface heat flux. Ideally, such a study would also include simulations accounting for a few different levels of heat loss such that a trend between the adiabatic simulation and the matching simulation could be found for these effects.

An unrelated study could involve the accuracy of the symmetry plane assumption in the current CFD simulation. This assumption was used (as it is commonly used in many CFD simulations) to reduce simulation run time by directly cutting the solution domain in half. The flow through the engine, however, was heavily influenced by both the three-dimensional recirculation forced by the engine wall boundaries and the time-variant, quasi-periodic nature of the engine cycle in operation. It is possible that the symmetry assumption is weakly valid or invalid. A simulation not relying on this assumption could test this idea to determine what effect, if any, the removal of this assumption has on the engine performance and cycle.

Lastly, the end goal of this study is to effectively revive research into Eugene Gluhareff's original pressure jet engine design. The square cross-section and smaller scale were largely a consequence of rapid manufacturability and low cost necessary for this study. A study specifically intended to probe the original pressure jet design was considered prohibitively costly in terms of fuel, instrumentation, and manufacturing costs. Ideally, this research effort would be repeated with a full-scale version of Gluhareff's pressure jet engine (the 15 lb thrust, G8-2-15 engine for instance) by instrumenting the larger engine on a larger thrust stand and matching it to CFD simulations. In lieu of that, there is a small amount of overall performance data that could be roughly matched by a CFD simulation based on the same closed-form approximations discussed in Chapter II. A CFD simulation of a larger engine would also have an indirectly desirable effect

of alleviating some of the CFL condition's hinderance. The larger engine would have a larger injector, but the same tank pressure and injection pressure differential. Therefore, the injection velocity would be approximately the same as the smaller engine, but the grid size for the same relative fineness would be larger allowing for a larger time-step and faster overall simulation runtime. Most importantly, the results would be directly applicable to the original Gluhareff pressure jet engine design as opposed to related to them through a similar mechanism.

2. Modifications to Increase Performance

The most immediate area of possible future research is in "expanding the envelope" of the engine's performance. Eugene Gluhareff's original engine designs exhibited an increase in thrust proportional to an increase in the injection pressure. His engine typically reached rated thrust at injection pressures of 100 – 120 psi – around twice the injection pressures of the current prototype. It is currently limited at higher pressures by blowout – combustion is not adequately slowed in the combustion chamber above injection pressures around 50 – 60 psi. The G8-2-20 engine was producing approximately one third the rated static thrust under these conditions. As a result, pushing the injection pressure higher should have more than a proportional effect on the thrust generation and engine efficiency. Several modifications could be tested in an effort to increase this limit and therefore increase the thrust force using the same injection pressure and fuel mass flow rate.

One in particular that *was* tested was the inclusion of a dummy or inert internal heating coil. This resulted in a significant increase in maximum stable injection pressure possibly due to its fluid-mechanical function as a flameholder. The heating coil was designed to simply match the internal square geometry of the engine with a small standoff distance similar to that seen in Gluhareff's circular engines. Different coil geometries could be tested and compared based on

their maximum stable injection pressures. The coil, like conventional blockage-based flameholders, has two effects. First, the blockage area of the coil causes flow separation on the leeward side which reduces local velocity and fluid momentum. This reduction in velocity (augmented by the resulting turbulence) is what allows a nearby flame to adhere to the flameholder surface. The reduction in fluid momentum aft of the inert coil was clearly seen in velocity magnitude visualizations in Chapter VI, Section A-3. The second effect is related to the fluid momentum, but specifically its effect on the engine thrust. The coil's work as a flameholder necessarily produces a drag force that directly counteracts the engine's thrust. This is the cost of using a blockage-based flameholder. Flameholders of this kind and their drag forces are discussed by Farokhi [1] and Flack [2].

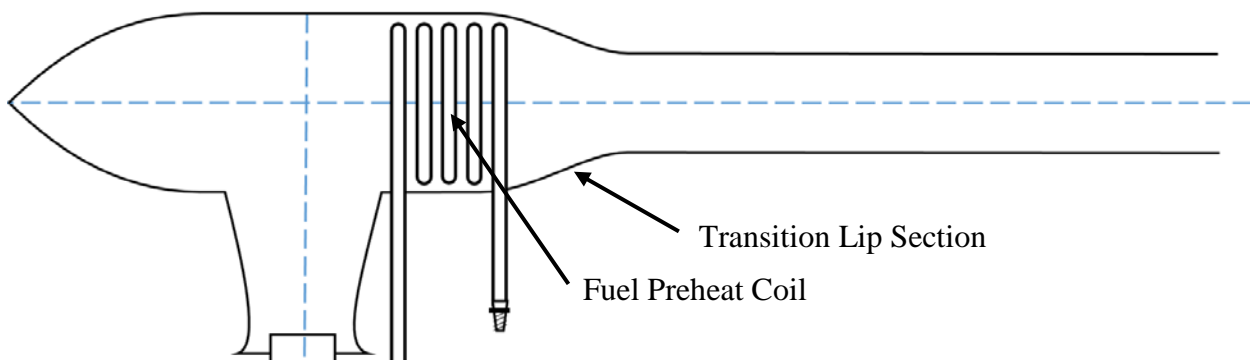


Figure 197: Gluhareff's Pressure Jet Engine Showing Transition Lip Section and Fuel Preheat Coil Location

An alternative means of flameholding may be hidden in Gluhareff's original designs. They used a linear slope between straight core and nozzle sections, shown in Figure 197. For the prototype engine, this linear slope was extended to the end of the nozzle. It is possible that this "feature" has reduced the maximum stable injection pressure compared to the shorter step that may hold back exhaust gases longer. Testing of a range of step lengths could reveal the influence of this effect. That effect is specifically one of pressure reflection as a means of flameholding instead of the lossier, drag-producing blockage. It is likely that the angled lip transition reflects the

pressure waves propagating outward from the core back inward which could reinforce the engine cycle's operation. This may be attenuated by the presence of the heating coil in direct proximity to this engine lip.

If this is found to be a significant effect, there is a common remedy found in some hobbyist pulse-jet engines – to wrap the preheat coil around the outside of the engine rather than fit it inside. This solution was likely considered unreasonable to Gluhareff for two possible reasons. First, the coil outside the engine would have increased the engine's drag profile and it was, after all, originally intended for mounting on the tip of helicopter rotor blades. The engine's external contours were, in fact, shaped the way they are for external profile drag reduction including the rounded nose section and the use of less-efficient elliptical inlets (to fit inside the outer moldlines of a helicopter blade's airfoil cross-section). When this became less of a concern, he changed the inlet shapes to a circular cross-section to exploit the greater inlet efficiency which contributed to the outstanding performance of the G8-2-130R compared to the rest of his designs. Secondly, the coil's primary goal is to preheat the fuel and extract extra energy from the fuel's phase change from a cold liquid to a hot gas. Completely surrounding the coil in high temperature combustion gases best realizes that goal of heat exchange. Placing the coil outside but still in contact with the chamber is expected to reduce the efficiency of that process. Still, the theoretical gains in performance by exploiting pressure as a mechanism for flameholding may outweigh the losses in reduced injection temperature which could be easily mitigated by increasing the length of the coil around the chamber. Doing so would expose the fuel to the chamber longer thereby making up some of the temperature lost to the surroundings. An external coil may even have some level of insulative effect on the engine reducing the amount of heat lost to the ambient environment as that wasted heat is instead absorbed by the fuel. The fuel should then lose less energy to the

surroundings than the bare chamber walls by merit of the fuel preheat coil's lower temperature differential. Testing this design modification with a CFD model verified with experimental data could confirm most, if not all of these possibilities.

A further source of study could probe the effect of injector diameter on a single engine size. The design of the BGX engine used in this study was largely driven by closed-form approximations based on the injector size and resulting expected fuel flow. In practice, these were at best a rough starting point and required substantial bench testing to reach a stable engine design producing positive static thrust. For this study, the injector size was not changed. It is unclear what effect exactly, reducing or enlarging the injector from this baseline size would have on the overall operation of the engine, the operating frequency, temperatures, and thrust. If the presented simulation is correct, the engine may be operating under rich conditions (perhaps too rich for the simulation kinetics to maintain combustion) and a smaller injector may feed less fuel to the engine. If the current injector were replaced with a precision-machined steel compression-fitting, multiple injectors could be tested with minimal changes to the thrust stand design.

The engine stand's needle valve flow control mechanism was chosen for its availability and low cost. Unfortunately, this made it difficult to feed a constant prescribed pressure. With very light application of torque, large swings in feed pressure could occur up to the maximum tank pressure of 150 psi. Testing at higher pressures should result in greater thrust considering the results produced by Gluhareff on his original engines [15, 16, 18, 19] so pushing to these higher pressures is desirable. Unfortunately, the only consumer propane regulators with any fine pressure control were intended for camping stoves and limited flow rate by limiting feed pressure to approximately 40 psi. The needle valve allowed pressures to exceed 40 psi, but control was less exact. Hence, if further study is going to push to higher pressures than 40 psi, it is recommended

that a more exact control of feedline pressure is found and a means of recording this pressure for data logging should the feed pressure change during operation.

Lastly, although the square cross-section was selected for ease of manufacturing and potentially to hold a stabilizing flame in small corner recirculation zones, this choice may have had a net negative impact on the engine's performance. It is possible that the square cross-section robs the flow of too much kinetic energy that may not be evident in terms of injection pressure but may result in a net loss of thrust for the same fuel injection. This could be tested by manufacturing an engine of the same scale but with a round cross-section. Alternatively, since this is potentially difficult to manufacture at small scale, one of Gluhareff's engines could be tested with the square design to quantify the related losses, if any.

3. Minimum Sizing for Ignition Delay and Supersonic Operation

Much of the engine sizing that is not driven directly by acoustics is thought to be driven by fuel/air and flame residence time inside the engine. This is important primarily because any unburnt fuel and air leaving the engine is wasted energy resulting in a higher than necessary fuel flow and an incremental increase in thrust-specific fuel consumption (TSFC) for the same level of thrust. Therefore, a nontrivial driver of the engine's core and nozzle volume and length are directly affected by this residence time. The residence time is affected by two factors – the mixture's ignition delay and the fluid speed inside the engine. The faster the fluid enters and exits the engine, the less time it spends inside the engine. Moreover, the faster the fuel/air mixture ignites, the less time it *needs* to be in the engine.

When the engine cycle and the design process is better understood, a study could be done to minimize the size of the engine based on the ignition delay and measures to increase residence time inside the engine. The latter could have the benefit of allowing the engine to push to higher

pressures allowing for increased engine performance. This, coupled with operation at minimum ignition delay could allow operation of the engine at speeds up to and exceeding the speed of sound, as long as the inlet is properly designed to feed the engine high pressure subsonic flow. Because the engine relies on the propagation of pressure waves throughout the engine, it is unlikely a supersonic flow pressure jet could be successful, but at least theoretically, there is no reason to believe the inlet pressure is limited by anything but ignition delay and residence time.

4. Preheat Coil Coking

A significant problem encountered with both the prototype engine and modern operation of Gluhareff's original engine is that of clogging or "coking" of the internal preheat coil. This is usually characterized by trouble starting the engine because of anemic injection pressure or in the late stages, no injection pressure at all. In early testing of the prototype engine, this coking was encountered and resulted in reduced heating of the fuel prior to injection. Eventually the fuel was not able to complete the state change to a hot gas and instead left the injector as an irregular mixture of liquid/gas spray. In an attempt to clear the clog, all immediately available solvents were tried including isopropyl alcohol, acetone, and carburetor cleaner. Ultrasonic cleaning was also tested on one of Gluhareff's original engines that had also suffered the coking problem. Unfortunately, none of these attempts cleared the coils. A final attempt to clear the coked prototype coil was made by running high pressure air (about 80 psi) through the coil while applying an external flame to melt or otherwise loosen the coking material. A glowing mass was observed to move through the coil under these conditions but shortly thereafter, it lodged and the coil ruptured. The coil was replaced with a new one for further testing and has since not been run long enough to expect significant coking to happen.

It is unclear what mechanism exactly is causing the coking but it is clear that the fuel undergoing a state change is resulting in deposits of some kind to form on the inner walls of the heating coil. Several possibilities could be explored. Consumer grades of propane are not actually chemically pure and instead include other hydrocarbons like propylene and polypropylene. The only truly pure source of propane is actually a refrigerant, R-290, and is prohibitively expensive for the operation of an engine. Polypropylene in some form could be a culprit as it is specifically chosen for its resistance to solvents.

A study to identify the actual material(s) clogging a known coked heating coil would be the first step to determining a method for cleaning it out. Moreover, this coking issue with propane in a heating coil does not appear to be common worldwide or even across the United States. It is possible that different propane blends from different parts of the country have different “contaminants” or perhaps just different levels of them. A comprehensive study of the different blends of propane available to the consumer for things like grills, camping stoves, and home heating may reveal trends that could bring light to the source of coking.

VIII. Appendices

A. Propane Chemical Kinetic Mechanism CHEMKIN Files

The following appendix lists the necessary CHEMKIN-format input files used to model chemical kinetics in the CONVERGE CFD solver. These files are specifically presented in the form of the mech.dat file necessary to run the reactive simulations in CONVERGE such that they could be used interchangeably with the rest of the CONVERGE input files listed in these appendices. These mechanisms are discussed in detail in Chapter III, Section C-1 in the context of the other propane kinetic mechanisms found in the literature. Considering the length of the mechanisms, all the mechanisms tested in Chapter III, Section D are not listed here but are instead available in digital format as they were used for analysis from the author via e-mail at Richard.Bramlette@gmail.com. The mechanisms used in the final engine simulation are repeated here.

1. Detailed Kinetic Mechanisms for Propane Oxidation

The detailed San Diego mechanism was chosen as the basis for modeling the chemical kinetics of propane oxidation because a review of the available literature (discussed in Chapter III, Section C-1) showed it to have the lowest error, specifically in terms of ignition delay and flame speeds. It was also the only propane mechanism being currently improved with the most recent experimental data whereas other mechanisms are either no longer developed and in some cases were no longer publicly available.

Mech.dat (Full San Diego Mechanism)

```

ELEMENTS
N H O C
END
SPECIES
N2                H                O2
OH                O                H2                H2O                HO2
H2O2             CO                CO2             HCO                CH3
CH4              CH2O             T-CH2          S-CH2             C2H4
CH3O             C2H5             C2H6           CH                C2H2
C2H4OOH         OC2H3OOH        C2H3           CH2CHO            C2H4O
HCCO             CH2CO           C2H            CH2OH             CH3OH
CH3CHO           CH3CO           C2H5OH         CH2CH2OH          CH3CHOH
CH3CH2O         C3H4            C3H3           C3H5              C3H6
C3H8             I-C3H7          N-C3H7         C3H6OOH           OC3H5OOH
!*****
****
!*****
***** Nitrogen Chemistry from San Diego
*****
!*****
****
NO                N                HCN                NCO                NH
HNCO             NH2                CN                HNO
N2O              N2H                NH3                NO2
END
REACTIONS
H+O2<=>OH+O      3.520e+16   -0.700   17069.79
H2+O<=>OH+H      5.060e+04   2.670    6290.63
H2+OH<=>H2O+H    1.170e+09   1.300    3635.28
H2O+O<=>2 OH     7.600e+00   3.840   12779.64
2 H+M<=>H2+M     1.300e+18   -1.000    0.00
H2/2.50/ H2O/12.00/ CO/1.90/ CO2/3.80/
H+OH+M<=>H2O+M  4.000e+22   -2.000    0.00
H2/2.50/ H2O/12.00/ CO/1.90/ CO2/3.80/
2 O+M<=>O2+M     6.170e+15   -0.500    0.00
H2/2.50/ H2O/12.00/ CO/1.90/ CO2/3.80/
H+O+M<=>OH+M    4.710e+18   -1.000    0.00
H2/2.50/ H2O/12.00/ CO/1.90/ CO2/3.80/
O+OH+M<=>HO2+M  8.000e+15   0.000    0.00

```

H2/2.50/ H2O/12.00/ CO/1.90/ CO2/3.80/			
H+O2(+M)<=>HO2(+M)	4.650e+12	0.440	0.00
H2/2.50/ H2O/16.00/ CO/1.20/ CO2/2.40/ C2H6/1.50/			
LOW / 5.750e+19 -1.400 0.00 /			
TROE/ 0.5 1e-30 1e+30 /			
HO2+H<=>2 OH	7.080e+13	0.000	294.93
HO2+H<=>H2+O2	1.660e+13	0.000	822.90
HO2+H<=>H2O+O	3.100e+13	0.000	1720.84
HO2+O<=>OH+O2	2.000e+13	0.000	0.00
HO2+OH<=>H2O+O2	2.890e+13	0.000	-497.13
2 OH(+M)<=>H2O2(+M)	7.400e+13	-0.370	0.00
H2/2.00/ H2O/6.00/ CO/1.50/ CO2/2.00/ CH4/2.00/ C2H6/3.00/			
LOW / 2.300e+18 -0.900 -1701.72 /			
TROE/ 0.735 94 1756 5182 /			
2 HO2<=>H2O2+O2	3.020e+12	0.000	1386.23
H2O2+H<=>HO2+H2	2.300e+13	0.000	7950.05
H2O2+H<=>H2O+OH	1.000e+13	0.000	3585.09
H2O2+OH<=>H2O+HO2	7.080e+12	0.000	1434.03
H2O2+O<=>HO2+OH	9.630e+06	2.000	3991.40
CO+O(+M)<=>CO2(+M)	1.800e+11	0.000	2384.08
H2/2.50/ H2O/12.00/ CO/2.00/ CO2/4.00/			
LOW / 1.550e+24 -2.790 4190.97 /			
CO+OH<=>CO2+H	4.400e+06	1.500	-740.92
CO+HO2<=>CO2+OH	2.000e+13	0.000	22944.55
CO+O2<=>CO2+O	1.000e+12	0.000	47700.05
HCO+M<=>CO+H+M	1.860e+17	-1.000	17000.48
H2/1.90/ H2O/12.00/ CO/2.50/ CO2/2.50/			
HCO+H<=>CO+H2	5.000e+13	0.000	0.00
HCO+O<=>CO+OH	3.000e+13	0.000	0.00
HCO+O<=>CO2+H	3.000e+13	0.000	0.00
HCO+OH<=>CO+H2O	3.000e+13	0.000	0.00
HCO+O2<=>CO+HO2	7.580e+12	0.000	409.89
HCO+CH3<=>CO+CH4	5.000e+13	0.000	0.00
H+HCO(+M)<=>CH2O(+M)	1.090e+12	0.480	-260.04
H2/2.00/ H2O/6.00/ CO/1.50/ CO2/2.00/ CH4/2.00/ C2H6/3.00/			
LOW / 1.350e+24 -2.570 424.95 /			
TROE/ 0.7824 271 2755 6570 /			
CH2O+H<=>HCO+H2	5.740e+07	1.900	2748.57
CH2O+O<=>HCO+OH	3.500e+13	0.000	3513.38
CH2O+OH<=>HCO+H2O	3.900e+10	0.890	406.31
CH2O+O2<=>HCO+HO2	6.000e+13	0.000	40674.00
CH2O+HO2<=>HCO+H2O2	4.110e+04	2.500	10210.33
CH4+H<=>H2+CH3	1.300e+04	3.000	8037.76
CH4+OH<=>H2O+CH3	1.600e+07	1.830	2782.03
CH4+O<=>CH3+OH	1.900e+09	1.440	8675.91
CH4+O2<=>CH3+HO2	3.980e+13	0.000	56890.54
CH4+HO2<=>CH3+H2O2	9.030e+12	0.000	24641.49
CH3+H<=>T-CH2+H2	1.800e+14	0.000	15105.16
CH3+H<=>S-CH2+H2	1.550e+14	0.000	13479.92
CH3+OH<=>S-CH2+H2O	4.000e+13	0.000	2502.39
CH3+O<=>CH2O+H	8.430e+13	0.000	0.00
CH3+T-CH2<=>C2H4+H	4.220e+13	0.000	0.00
CH3+HO2<=>CH3O+OH	5.000e+12	0.000	0.00
CH3+O2<=>CH2O+OH	3.300e+11	0.000	8941.20
CH3+O2<=>CH3O+O	1.100e+13	0.000	27820.03
2 CH3<=>C2H4+H2	1.000e+14	0.000	32002.87
2 CH3<=>C2H5+H	3.160e+13	0.000	14698.85

H+CH3(+M)<=>CH4(+M)	1.270e+16	-0.630	382.89
H2/2.00/ H2O/6.00/ CO/1.50/ CO2/2.00/ CH4/2.00/			
LOW /	2.470e+33	-4.760	2440.01 /
TROE/	0.783	74	2941 6964 /
2 CH3(+M)<=>C2H6(+M)	1.810e+13	0.000	0.00
H2/2.00/ H2O/6.00/ CO/1.50/ CO2/2.00/ CH4/2.00/ C2H6/3.00/			
LOW /	1.270e+41	-7.000	2762.91 /
TROE/	0.62	73	1.2e+03 /
S-CH2+OH<=>CH2O+H	3.000e+13	0.000	0.00
S-CH2+O2<=>CO+OH+H	3.130e+13	0.000	0.00
S-CH2+CO2<=>CO+CH2O	3.000e+12	0.000	0.00
S-CH2+M<=>T-CH2+M	6.000e+12	0.000	0.00
H2/2.40/ H2O/15.40/ CO/1.80/ CO2/3.60/			
T-CH2+H<=>CH+H2	6.020e+12	0.000	-1787.76
T-CH2+OH<=>CH2O+H	2.500e+13	0.000	0.00
T-CH2+OH<=>CH+H2O	1.130e+07	2.000	2999.52
T-CH2+O<=>CO+2 H	8.000e+13	0.000	0.00
T-CH2+O<=>CO+H2	4.000e+13	0.000	0.00
T-CH2+O2<=>CO2+H2	2.630e+12	0.000	1491.40
T-CH2+O2<=>CO+OH+H	6.580e+12	0.000	1491.40
2 T-CH2<=>C2H2+2 H	1.000e+14	0.000	0.00
CH+O<=>CO+H	4.000e+13	0.000	0.00
CH+O2<=>HCO+O	1.770e+11	0.760	-478.01
CH+H2O<=>CH2O+H	1.170e+15	-0.750	0.00
CH+CO2<=>HCO+CO	4.800e+01	3.220	-3226.58
CH3O+H<=>CH2O+H2	2.000e+13	0.000	0.00
CH3O+H<=>S-CH2+H2O	1.600e+13	0.000	0.00
CH3O+OH<=>CH2O+H2O	5.000e+12	0.000	0.00
CH3O+O<=>OH+CH2O	1.000e+13	0.000	0.00
CH3O+O2<=>CH2O+HO2	4.280e-13	7.600	-3537.28
CH3O+M<=>CH2O+H+M	7.780e+13	0.000	13513.38
H2/2.00/ H2O/6.00/ CO/1.50/ CO2/2.00/ CH4/2.00/			
C2H6+H<=>C2H5+H2	5.400e+02	3.500	5210.33
C2H6+O<=>C2H5+OH	1.400e+00	4.300	2772.47
C2H6+OH<=>C2H5+H2O	2.200e+07	1.900	1123.33
C2H6+CH3<=>C2H5+CH4	5.500e-01	4.000	8293.50
C2H6(+M)<=>C2H5+H(+M)	8.850e+20	-1.230	102222.75
H2/2.00/ H2O/6.00/ CO/1.50/ CO2/2.00/ CH4/2.00/ C2H6/3.00/			
LOW /	4.900e+42	-6.430	107169.93 /
TROE/	0.84	125	2219 6882 /
C2H6+HO2<=>C2H5+H2O2	1.320e+13	0.000	20469.89
C2H5+H<=>C2H4+H2	3.000e+13	0.000	0.00
C2H5+O<=>C2H4+OH	3.060e+13	0.000	0.00
C2H5+O<=>CH3+CH2O	4.240e+13	0.000	0.00
C2H5+O2<=>C2H4+HO2	7.500e+14	-1.000	4799.95
C2H5+O2<=>C2H4OOH	2.000e+12	0.000	0.00
C2H4OOH<=>C2H4+HO2	4.000e+34	-7.200	23000.00
C2H4OOH+O2<=>OC2H3OOH+OH	7.500e+05	1.300	-5799.95
OC2H3OOH<=>CH2O+HCO+OH	1.000e+15	0.000	43000.00
C2H5(+M)<=>C2H4+H(+M)	1.110e+10	1.037	36768.64
H2/2.00/ H2O/6.00/ CO/1.50/ CO2/2.00/ CH4/2.00/			
LOW /	3.990e+33	-4.990	40000.00 /
TROE/	0.168	1.2e+03	0 /
C2H4+H<=>C2H3+H2	4.490e+07	2.120	13360.42
C2H4+OH<=>C2H3+H2O	5.530e+05	2.310	2963.67
C2H4+O<=>CH3+HCO	2.250e+06	2.080	0.00
C2H4+O<=>CH2CHO+H	1.210e+06	2.080	0.00

2 C2H4<=>C2H3+C2H5	5.010e+14	0.000	64700.05
C2H4+O2<=>C2H3+HO2	4.220e+13	0.000	57623.09
C2H4+HO2<=>C2H4O+OH	2.230e+12	0.000	17189.29
C2H4O+HO2<=>CH3+CO+H2O2	4.000e+12	0.000	17007.65
C2H4+M<=>C2H3+H+M	2.600e+17	0.000	96568.12
H2/2.00/ H2O/6.00/ CO/1.50/ CO2/2.00/ CH4/2.00/			
C2H4+M<=>C2H2+H2+M	3.500e+16	0.000	71532.03
H2/2.00/ H2O/6.00/ CO/1.50/ CO2/2.00/ CH4/2.00/			
C2H3+H<=>C2H2+H2	4.000e+13	0.000	0.00
C2H3(+M)<=>C2H2+H(+M)	6.380e+09	1.000	37626.67
H2/2.00/ H2O/6.00/ CO/1.50/ CO2/2.00/ CH4/2.00/			
LOW / 1.510e+14 0.100 32685.95 /			
TROE/ 0.3 1e+30 1e-30 /			
C2H3+O2<=>CH2O+HCO	1.700e+29	-5.312	6503.11
C2H3+O2<=>CH2CHO+O	7.000e+14	-0.611	5262.43
C2H3+O2<=>C2H2+HO2	5.190e+15	-1.260	3312.62
C2H2+O<=>HCCO+H	4.000e+14	0.000	10659.66
C2H2+O<=>T-CH2+CO	1.600e+14	0.000	9894.84
C2H2+O2<=>CH2O+CO	4.600e+15	-0.540	44933.08
C2H2+OH<=>CH2CO+H	1.900e+07	1.700	999.04
C2H2+OH<=>C2H+H2O	3.370e+07	2.000	14000.96
CH2CO+H<=>CH3+CO	1.500e+09	1.430	2688.81
CH2CO+O<=>T-CH2+CO2	2.000e+13	0.000	2294.46
CH2CO+O<=>HCCO+OH	1.000e+13	0.000	2000.48
CH2CO+CH3<=>C2H5+CO	9.000e+10	0.000	0.00
HCCO+H<=>S-CH2+CO	1.500e+14	0.000	0.00
HCCO+OH<=>HCO+CO+H	2.000e+12	0.000	0.00
HCCO+O<=>2 CO+H	9.640e+13	0.000	0.00
HCCO+O2<=>2 CO+OH	2.880e+07	1.700	1001.43
HCCO+O2<=>CO2+CO+H	1.400e+07	1.700	1001.43
C2H+OH<=>HCCO+H	2.000e+13	0.000	0.00
C2H+O<=>CO+CH	1.020e+13	0.000	0.00
C2H+O2<=>HCCO+O	6.020e+11	0.000	0.00
C2H+O2<=>CH+CO2	4.500e+15	0.000	25095.60
C2H+O2<=>HCO+CO	2.410e+12	0.000	0.00
CH2OH+H<=>CH2O+H2	3.000e+13	0.000	0.00
CH2OH+H<=>CH3+OH	2.500e+17	-0.930	5126.91
CH2OH+OH<=>CH2O+H2O	2.400e+13	0.000	0.00
CH2OH+O2<=>CH2O+HO2	5.000e+12	0.000	0.00
CH2OH+M<=>CH2O+H+M	5.000e+13	0.000	25119.50
H2/2.00/ H2O/6.00/ CO/1.50/ CO2/2.00/ CH4/2.00/			
CH3O+M<=>CH2OH+M	1.000e+14	0.000	19120.46
H2/2.00/ H2O/6.00/ CO/1.50/ CO2/2.00/ CH4/2.00/			
CH2CO+OH<=>CH2OH+CO	1.020e+13	0.000	0.00
CH3OH+OH<=>CH2OH+H2O	1.440e+06	2.000	-838.91
CH3OH+OH<=>CH3O+H2O	4.400e+06	2.000	1505.74
CH3OH+H<=>CH2OH+H2	1.354e+03	3.200	3490.68
CH3OH+H<=>CH3O+H2	6.830e+01	3.400	7239.96
CH3OH+O<=>CH2OH+OH	1.000e+13	0.000	4684.51
CH3OH+HO2<=>CH2OH+H2O2	8.000e+13	0.000	19383.37
CH3OH+O2<=>CH2OH+HO2	2.000e+13	0.000	44933.08
CH3OH(+M)<=>CH3+OH(+M)	1.900e+16	0.000	91729.92
H2/2.00/ H2O/6.00/ CO/1.50/ CO2/2.00/ CH4/2.00/			
LOW / 2.950e+44 -7.350 95460.09 /			
TROE/ 0.414 2.8e+02 5.5e+03 /			
CH2CHO<=>CH2CO+H	1.047e+37	-7.189	44340.34
CH2CHO+H<=>CH3+HCO	5.000e+13	0.000	0.00

CH2CHO+H<=>CH2CO+H2	2.000e+13	0.000	0.00
CH2CHO+O<=>CH2O+HCO	1.000e+14	0.000	0.00
CH2CHO+OH<=>CH2CO+H2O	3.000e+13	0.000	0.00
CH2CHO+O2<=>CH2O+CO+OH	3.000e+10	0.000	0.00
CH2CHO+CH3<=>C2H5+CO+H	4.900e+14	-0.500	0.00
CH2CHO+HO2<=>CH2O+HCO+OH	7.000e+12	0.000	0.00
CH2CHO+HO2<=>CH3CHO+O2	3.000e+12	0.000	0.00
CH2CHO<=>CH3+CO	1.170e+43	-9.800	43799.95
CH3CHO<=>CH3+HCO	7.000e+15	0.000	81700.05
CH3CO(+M)<=>CH3+CO(+M)	3.000e+12	0.000	16700.05
H2/2.00/ H2O/6.00/ CO/1.50/ CO2/2.00/ CH4/2.00/ LOW / 1.200e+15 0.000 12500.00 /			
CH3CHO+OH<=>CH3CO+H2O	3.370e+12	0.000	-619.98
CH3CHO+OH<=>CH2CHO+H2O	3.370e+11	0.000	-619.98
CH3CHO+O<=>CH3CO+OH	1.770e+18	-1.900	2979.92
CH3CHO+O<=>CH2CHO+OH	3.720e+13	-0.200	3559.99
CH3CHO+H<=>CH3CO+H2	4.660e+13	-0.300	2989.96
CH3CHO+H<=>CH2CHO+H2	1.850e+12	0.400	5359.94
CH3CHO+CH3<=>CH3CO+CH4	3.900e-07	5.800	2200.05
CH3CHO+CH3<=>CH2CHO+CH4	2.450e+01	3.100	5729.92
CH3CHO+HO2<=>CH3CO+H2O2	3.600e+19	-2.200	14000.00
CH3CHO+HO2<=>CH2CHO+H2O2	2.320e+11	0.400	14900.10
CH3CHO+O2<=>CH3CO+HO2	1.000e+14	0.000	42200.05
C2H5OH(+M)<=>CH3+CH2OH(+M)	5.000e+15	0.000	82000.00
H2/2.00/ H2O/6.00/ CO/1.50/ CO2/2.00/ CH4/2.00/ LOW / 3.000e+16 0.000 58000.00 / TROE/ 0.5 1e-30 1e+30 /			
C2H5OH(+M)<=>C2H4+H2O(+M)	8.000e+13	0.000	65000.00
H2/2.00/ H2O/6.00/ CO/1.50/ CO2/2.00/ CH4/2.00/ LOW / 1.000e+17 0.000 54000.00 / TROE/ 0.5 1e-30 1e+30 /			
C2H5OH+OH<=>CH2CH2OH+H2O	1.810e+11	0.400	717.02
C2H5OH+OH<=>CH3CHOH+H2O	3.090e+10	0.500	-380.02
C2H5OH+OH<=>CH3CH2O+H2O	1.050e+10	0.800	717.02
C2H5OH+H<=>CH2CH2OH+H2	1.900e+07	1.800	5099.90
C2H5OH+H<=>CH3CHOH+H2	2.580e+07	1.600	2830.07
C2H5OH+H<=>CH3CH2O+H2	1.500e+07	1.600	3039.91
C2H5OH+O<=>CH2CH2OH+OH	9.410e+07	1.700	5460.09
C2H5OH+O<=>CH3CHOH+OH	1.880e+07	1.900	1820.03
C2H5OH+O<=>CH3CH2O+OH	1.580e+07	2.000	4450.05
C2H5OH+CH3<=>CH2CH2OH+CH4	2.190e+02	3.200	9619.98
C2H5OH+CH3<=>CH3CHOH+CH4	7.280e+02	3.000	7950.05
C2H5OH+CH3<=>CH3CH2O+CH4	1.450e+02	3.000	7650.10
C2H5OH+HO2<=>CH3CHOH+H2O2	8.200e+03	2.500	10799.95
C2H5OH+HO2<=>CH2CH2OH+H2O2	2.430e+04	2.500	15799.95
C2H5OH+HO2<=>CH3CH2O+H2O2	3.800e+12	0.000	24000.00
C2H4+OH<=>CH2CH2OH	2.410e+11	0.000	-2380.02
C2H5+HO2<=>CH3CH2O+OH	4.000e+13	0.000	0.00
CH3CH2O+M<=>CH3CHO+H+M	5.600e+34	-5.900	25299.95
H2/2.00/ H2O/6.00/ CO/1.50/ CO2/2.00/ CH4/2.00/ CH3CH2O+M<=>CH3+CH2O+M	5.350e+37	-7.000	23799.95
H2/2.00/ H2O/6.00/ CO/1.50/ CO2/2.00/ CH4/2.00/ CH3CH2O+O2<=>CH3CHO+HO2	4.000e+10	0.000	1099.90
CH3CH2O+CO<=>C2H5+CO2	4.680e+02	3.200	5380.02
CH3CH2O+H<=>CH3+CH2OH	3.000e+13	0.000	0.00
CH3CH2O+H<=>C2H4+H2O	3.000e+13	0.000	0.00
CH3CH2O+OH<=>CH3CHO+H2O	1.000e+13	0.000	0.00

CH3CHOH+O2<=>CH3CHO+HO2	4.820e+13	0.000	5020.08
CH3CHOH+O<=>CH3CHO+OH	1.000e+14	0.000	0.00
CH3CHOH+H<=>C2H4+H2O	3.000e+13	0.000	0.00
CH3CHOH+H<=>CH3+CH2OH	3.000e+13	0.000	0.00
CH3CHOH+HO2<=>CH3CHO+2 OH	4.000e+13	0.000	0.00
CH3CHOH+OH<=>CH3CHO+H2O	5.000e+12	0.000	0.00
CH3CHOH+M<=>CH3CHO+H+M	1.000e+14	0.000	25000.00
H2/2.00/ H2O/6.00/ CO/1.50/ CO2/2.00/ CH4/2.00/			
C3H4+O<=>C2H4+CO	2.000e+07	1.800	1000.00
CH3+C2H2<=>C3H4+H	2.560e+09	1.100	13643.88
C3H4+O<=>HCCO+CH3	7.300e+12	0.000	2250.00
C3H3+H(+M)<=>C3H4(+M)	3.000e+13	0.000	0.00
LOW / 9.000e+15 1.000 0.00 /			
TROE/ 0.5 1e+30 0 /			
C3H3+HO2<=>C3H4+O2	2.500e+12	0.000	0.00
C3H4+OH<=>C3H3+H2O	5.300e+06	2.000	2000.00
C3H3+O2<=>CH2CO+HCO	3.000e+10	0.000	2868.07
C3H4+H(+M)<=>C3H5(+M)	4.000e+13	0.000	0.00
LOW / 3.000e+24 -2.000 0.00 /			
TROE/ 0.8 1e+30 0 /			
C3H5+H<=>C3H4+H2	1.800e+13	0.000	0.00
C3H5+O2<=>C3H4+HO2	4.990e+15	-1.400	22428.06
C3H5+CH3<=>C3H4+CH4	3.000e+12	-0.320	-130.98
C2H2+CH3(+M)<=>C3H5(+M)	6.000e+08	0.000	0.00
LOW / 2.000e+09 1.000 0.00 /			
TROE/ 0.5 1e+30 0 /			
C3H5+OH<=>C3H4+H2O	6.000e+12	0.000	0.00
C3H3+HCO<=>C3H4+CO	2.500e+13	0.000	0.00
C3H3+HO2<=>OH+CO+C2H3	8.000e+11	0.000	0.00
C3H4+O2<=>CH3+HCO+CO	4.000e+14	0.000	41826.00
C3H6+O<=>C2H5+HCO	3.500e+07	1.650	-972.75
C3H6+OH<=>C3H5+H2O	3.100e+06	2.000	-298.28
C3H6+O<=>CH2CO+CH3+H	1.200e+08	1.650	327.44
C3H6+H<=>C3H5+H2	1.700e+05	2.500	2492.83
C3H5+H(+M)<=>C3H6(+M)	2.000e+14	0.000	0.00
H2/2.00/ H2O/6.00/ CO/1.50/ CO2/2.00/ CH4/2.00/ C2H6/3.00/			
LOW / 1.330e+60 -12.000 5967.97 /			
TROE/ 0.02 1097 1097 6860 /			
C3H5+HO2<=>C3H6+O2	2.660e+12	0.000	0.00
C3H5+HO2<=>OH+C2H3+CH2O	3.000e+12	0.000	0.00
C2H3+CH3(+M)<=>C3H6(+M)	2.500e+13	0.000	0.00
H2/2.00/ H2O/6.00/ CO/1.50/ CO2/2.00/ CH4/2.00/ C2H6/3.00/			
LOW / 4.270e+58 -11.940 9770.55 /			
TROE/ 0.175 1341 6e+04 1.014e+04 /			
C3H6+H<=>C2H4+CH3	1.600e+22	-2.390	11185.47
CH3+C2H3<=>C3H5+H	1.500e+24	-2.830	18618.55
C3H8(+M)<=>CH3+C2H5(+M)	1.100e+17	0.000	84392.93
LOW / 7.830e+18 0.000 64978.01 /			
TROE/ 0.76 1.9e+03 38 /			
C3H8+O2<=>I-C3H7+HO2	4.000e+13	0.000	47500.00
C3H8+O2<=>N-C3H7+HO2	4.000e+13	0.000	50932.12
C3H8+H<=>I-C3H7+H2	1.300e+06	2.400	4471.08
C3H8+H<=>N-C3H7+H2	1.330e+06	2.540	6761.47

C3H8+O<=>I-C3H7+OH	4.760e+04	2.710	2107.31
C3H8+O<=>N-C3H7+OH	1.900e+05	2.680	3718.45
C3H8+OH<=>N-C3H7+H2O	1.000e+10	1.000	1599.90
C3H8+OH<=>I-C3H7+H2O	2.000e+07	-1.600	-99.90
C3H8+HO2<=>I-C3H7+H2O2	9.640e+03	2.600	13917.30
C3H8+HO2<=>N-C3H7+H2O2	4.760e+04	2.550	16491.40
I-C3H7+C3H8<=>N-C3H7+C3H8	8.400e-03	4.200	8675.91
C3H6+H(+M)<=>I-C3H7(+M)	1.330e+13	0.000	1560.71
H2/2.00/ H2O/6.00/ CO/1.50/ CO2/2.00/ CH4/2.00/ C2H6/3.00/			
LOW /	8.700e+42	-7.500	4732.31 /
TROE/	1	1000	645.4 6844 /
I-C3H7+O2<=>C3H6+HO2	1.300e+11	0.000	0.00
N-C3H7(+M)<=>CH3+C2H4(+M)	1.230e+13	-0.100	30210.33
LOW / 5.490e+49 -10.000 35778.92 /			
TROE/	-1.17	251	1e-15 1185 /
H+C3H6(+M)<=>N-C3H7(+M)	1.330e+13	0.000	3260.04
H2/2.00/ H2O/6.00/ CO/1.50/ CO2/2.00/ CH4/2.00/ C2H6/3.00/			
LOW /	6.260e+38	-6.660	7000.48 /
TROE/	1	1000	1310 4.81e+04 /
N-C3H7+O2<=>C3H6+HO2	3.500e+16	-1.600	3500.00
N-C3H7+O2<=>C3H6OOH	2.000e+12	0.000	0.00
C3H6OOH<=>C3H6+HO2	2.500e+35	-8.300	22000.00
C3H6OOH+O2<=>OC3H5OOH+OH	1.500e+08	0.000	-7000.00
OC3H5OOH<=>CH2CHO+CH2O+OH	1.000e+15	0.000	43000.00
!*****			

!*****			
	Nitrogen	Chemistry	from San Diego

!*****			

O+N2<=>NO+N	1.470e+13	0.300	75286.81
N+O2<=>NO+O	6.400e+09	1.000	6285.85
N+OH<=>NO+H	3.800e+13	0.000	0.00
N2+CH<=>HCN+N	4.400e+12	0.000	21988.53
HCN+O<=>NCO+H	1.400e+06	2.100	6118.55
NCO+M<=>N+CO+M	3.100e+16	-0.500	48040.15
N2/1.50/ O2/1.50/ H2O/18.60/			
NCO+H<=>CO+NH	5.000e+13	0.000	0.00
NCO+O<=>NO+CO	4.700e+13	0.000	0.00
NCO+H2<=>HNCO+H	7.600e+02	3.000	3991.40
HCCO+NO<=>HNCO+CO	2.000e+13	0.000	0.00
HNCO+M<=>NH+CO+M	1.100e+16	0.000	86042.07
N2/1.50/ O2/1.50/ H2O/18.60/			
HNCO+H<=>NH2+CO	2.200e+07	1.700	3800.19
HNCO+O<=>NCO+OH	2.200e+06	2.110	11448.37
HNCO+O<=>NH+CO2	9.600e+07	1.410	8532.50
HNCO+OH<=>NCO+H2O	6.400e+05	2.000	2557.36
CN+H2<=>HCN+H	3.600e+08	1.550	3011.47
CN+H2O<=>HCN+OH	7.800e+12	0.000	7456.98
CN+OH<=>NCO+H	4.200e+13	0.000	0.00
CN+O2<=>NCO+O	7.200e+12	0.000	-418.26
NH+H<=>N+H2	1.000e+13	0.000	0.00
NH+O<=>NO+H	9.200e+13	0.000	0.00
NH+OH<=>HNO+H	4.000e+13	0.000	0.00

NH+OH<=>N+H2O	5.000e+11	0.500	2000.48
NH+O2<=>HNO+O	4.600e+05	2.000	6500.96
NH+NO<=>N2O+H	3.200e+14	-0.450	0.00
NH+NO<=>N2+OH	2.200e+13	-0.230	0.00
NH2+H<=>NH+H2	4.000e+13	0.000	3652.01
NH2+O<=>HNO+H	9.900e+14	-0.500	0.00
NH2+OH<=>NH+H2O	4.000e+06	2.000	1001.43
NH2+NO<=>N2+H2O	2.000e+20	-2.600	924.95
NH2+NO<=>N2H+OH	9.300e+11	0.000	0.00
NH3+M<=>NH2+H+M	2.200e+16	0.000	93451.24
NH3+H<=>NH2+H2	6.400e+05	2.390	10181.64
NH3+O<=>NH2+OH	9.400e+06	1.940	6465.11
NH3+OH<=>NH2+H2O	2.040e+06	2.040	566.44
N2H<=>N2+H	1.000e+08	0.000	0.00
N2H+H<=>N2+H2	1.000e+14	0.000	0.00
N2H+O<=>N2O+H	1.000e+14	0.000	0.00
N2H+OH<=>N2+H2O	5.000e+13	0.000	0.00
HNO+M<=>H+NO+M	1.500e+16	0.000	48757.17
N2/2.00/ O2/2.00/ H2/2.00/ H2O/10.00/			
HNO+H<=>NO+H2	4.400e+11	0.720	650.10
HNO+OH<=>NO+H2O	3.600e+13	0.000	0.00
NO+CH3=>HCN+H2O	8.300e+11	0.000	16085.09
NO+T-CH2<=>HNCO+H	2.900e+12	0.000	-597.51
NO+CH<=>HCN+O	1.100e+14	0.000	0.00
N2O(+M)<=>N2+O(+M)	8.000e+11	0.000	62619.50
LOW / 2.000e+14	0.000	56644.36	/
N2O+H<=>N2+OH	2.230e+14	0.000	16754.30
N2O+O<=>2 NO	2.900e+13	0.000	23159.66
N2O+OH<=>N2+HO2	2.000e+12	0.000	10000.00
NO2+M<=>NO+O+M	1.000e+16	0.000	65965.58
NO+HO2<=>NO2+OH	2.100e+12	0.000	-480.40
NO2+H<=>NO+OH	3.500e+14	0.000	1500.96
NO2+O<=>NO+O2	1.000e+13	0.000	599.90
END			

2. Reduced Kinetic Mechanisms for Propane Oxidation

The only reduced mechanism considered in this study was the reduced form of the San Diego mechanism discussed in Chapter III, Section C-1. This mechanism is simply a form of the full San Diego mechanism (listed in the prior section) with unwanted reactions removed. The removed reactions were chosen for their low influence on the resulting ignition delay and are discussed further in Chapter III, Section C-1.

mech.dat (Reduced San Diego)

```

ELEMENTS
N  AR HE H  O  C
END

SPECIES
N2          AR          HE          H          O2
OH          O          H2          H2O         HO2
H2O2       CO          CO2         HCO         CH3
CH4        CH2O         T-CH2      S-CH2      C2H4
CH3O       C2H5         C2H6       CH          C2H2
C2H4OOH   OC2H3OOH    C2H3       CH2CHO     C2H4O
HCCO      CH2CO       C2H        CH2OH      CH3OH
CH3CHO    CH3CO       C2H5OH     CH2CH2OH
CH3CHOH
CH3CH2O   C3H4        C3H3       C3H5       C3H6
C3H8     I-C3H7     N-C3H7     C3H6OOH
OC3H5OOH
END

REACTIONS
H+O2<=>OH+O          3.520e+16  -0.700  17069.79
!H2+O<=>OH+H        5.060e+04   2.670   6290.63

H2+OH<=>H2O+H       1.170e+09   1.300   3635.28

!H2O+O<=>2 OH        7.000e+05   2.330  14548.28

!2 H+M<=>H2+M        1.300e+18  -1.000    0.00

!      AR/0.50/ HE/0.50/ H2/2.50/ H2O/12.00/ CO/1.90/ CO2/3.80/
!H+OH+M<=>H2O+M     4.000e+22  -2.000    0.00

!      AR/0.38/ HE/0.38/ H2/2.50/ H2O/12.00/ CO/1.90/ CO2/3.80/
!2 O+M<=>O2+M       6.170e+15  -0.500    0.00

!      AR/0.20/ HE/0.20/ H2/2.50/ H2O/12.00/ CO/1.90/ CO2/3.80/
!H+O+M<=>OH+M       4.710e+18  -1.000    0.00

```

```

!      AR/0.75/ HE/0.75/ H2/2.50/ H2O/12.00/ CO/1.90/ CO2/3.80/
!O+OH+M<=>HO2+M                8.000e+15    0.000    0.00
!      AR/0.75/ HE/0.75/ H2/2.50/ H2O/12.00/ CO/1.90/ CO2/3.80/
!H+O2(+M)<=>HO2(+M)              4.650e+12    0.440    0.00
!      AR/0.70/ HE/0.70/ H2/2.50/ H2O/16.00/ CO/1.20/ CO2/2.40/ C2H6/1.50/
!      LOW / 5.750e+19  -1.400    0.00 /
!      TROE/ 0.5  1e-30  1e+30 /
HO2+H<=>2 OH                    7.080e+13    0.000    294.93
HO2+H<=>H2+O2                   1.660e+13    0.000    822.90
HO2+H<=>H2O+O                   3.100e+13    0.000    1720.84
HO2+O<=>OH+O2                   2.000e+13    0.000    0.00
!HO2+OH(+M)<=>H2O+O2(+M)        4.500e+14    0.000    10929.73
!      LOW / 2.890e+13  0.000  -497.13 /
!      TROE/ 1  1  1e+07  1e+07 /
2 OH(+M)<=>H2O2(+M)              9.550e+13   -0.270    0.00
      AR/0.70/ HE/0.40/ H2/2.50/ H2O/6.00/ CO/1.50/ CO2/2.00/
      LOW / 2.760e+25  -3.200  0.000 /
      TROE/ 0.57  1e+30  0 /
!2 HO2(+M)<=>H2O2+O2(+M)         1.940e+11    0.000   -1408.94
!      LOW / 1.030e+14  0.000  11042.07 /
!      TROE/ 1  1  1e+07  1e+07 /
H2O2+H<=>HO2+H2                 2.300e+13    0.000    7950.05
H2O2+H<=>H2O+OH                 1.000e+13    0.000    3585.09
!H2O2+OH(+M)<=>H2O+HO2(+M)       7.590e+13    0.000    7272.94
!      LOW / 1.740e+12  0.000  1434.03 /
!      TROE/ 1  1  1e+07  1e+07 /
H2O2+O<=>HO2+OH                 9.630e+06    2.000    3991.40
!CO+O(+M)<=>CO2(+M)              1.800e+11    0.000    2384.08

```

```

!      AR/0.70/ HE/0.70/ H2/2.50/ H2O/12.00/ CO/2.00/ CO2/4.00/
!
!      LOW / 1.550e+24 -2.790 4190.97 /
!
!      TROE/      1      1      1e+07      1e+07 /
CO+OH<=>CO2+H      4.400e+06      1.500 -740.92
CO+HO2<=>CO2+OH      2.000e+13      0.000 22944.55
!CO+O2<=>CO2+O      1.000e+12      0.000 47700.05
HCO+M<=>CO+H+M      1.860e+17      -1.000 17000.48
      H2/1.90/ H2O/12.00/ CO/2.50/ CO2/2.50/
!HCO+H<=>CO+H2      5.000e+13      0.000      0.00
!HCO+O<=>CO+OH      3.000e+13      0.000      0.00
!HCO+O<=>CO2+H      3.000e+13      0.000      0.00
HCO+OH<=>CO+H2O      3.000e+13      0.000      0.00
HCO+O2<=>CO+HO2      7.580e+12      0.000      409.89
HCO+CH3<=>CO+CH4      5.000e+13      0.000      0.00
!H+HCO(+M)<=>CH2O(+M)      1.090e+12      0.480 -260.04
!
!      AR/0.70/ H2/2.00/ H2O/6.00/ CO/1.50/ CO2/2.00/ CH4/2.00/ C2H6/3.00/
!
!      LOW / 1.350e+24 -2.570 424.95 /
!
!      TROE/ 0.7824      271      2755      6570 /
CH2O+H<=>HCO+H2      5.740e+07      1.900 2748.57
CH2O+O<=>HCO+OH      3.500e+13      0.000 3513.38
CH2O+OH<=>HCO+H2O      3.900e+10      0.890 406.31
CH2O+O2<=>HCO+HO2      6.000e+13      0.000 40674.00
CH2O+HO2<=>HCO+H2O2      4.110e+04      2.500 10210.33
CH4+H<=>H2+CH3      1.300e+04      3.000 8037.76
CH4+OH<=>H2O+CH3      1.600e+07      1.830 2782.03
!CH4+O<=>CH3+OH      1.900e+09      1.440 8675.91
CH4+O2<=>CH3+HO2      3.980e+13      0.000 56890.54
CH4+HO2<=>CH3+H2O2      9.030e+12      0.000 24641.49

```

!CH3+H<=>T-CH2+H2	1.800e+14	0.000	15105.16
!CH3+H<=>S-CH2+H2	1.550e+14	0.000	13479.92
!CH3+OH<=>S-CH2+H2O	4.000e+13	0.000	2502.39
CH3+O<=>CH2O+H	8.430e+13	0.000	0.00
CH3+T-CH2<=>C2H4+H	4.220e+13	0.000	0.00
CH3+HO2<=>CH3O+OH	5.000e+12	0.000	0.00
CH3+O2<=>CH2O+OH	3.300e+11	0.000	8941.20
CH3+O2<=>CH3O+O	1.100e+13	0.000	27820.03
!2 CH3<=>C2H4+H2	1.000e+14	0.000	32002.87
!2 CH3<=>C2H5+H	3.160e+13	0.000	14698.85
!H+CH3(+M)<=>CH4(+M)	1.270e+16	-0.630	382.89
! AR/0.70/ H2/2.00/ H2O/6.00/ CO/1.50/ CO2/2.00/ CH4/2.00/			
! LOW / 2.470e+33 -4.760 2440.01 /			
! TROE/ 0.783 74 2941 6964 /			
2 CH3(+M)<=>C2H6(+M)	1.810e+13	0.000	0.00
AR/0.70/ H2/2.00/ H2O/6.00/ CO/1.50/ CO2/2.00/ CH4/2.00/ C2H6/3.00/			
LOW / 1.270e+41 -7.000 2762.91 /			
TROE/ 0.62 73 1.2e+03 /			
!S-CH2+OH<=>CH2O+H	3.000e+13	0.000	0.00
!S-CH2+O2<=>CO+OH+H	3.130e+13	0.000	0.00
!S-CH2+CO2<=>CO+CH2O	3.000e+12	0.000	0.00
!S-CH2+M<=>T-CH2+M	6.000e+12	0.000	0.00
! H2/2.40/ H2O/15.40/ CO/1.80/ CO2/3.60/			
!T-CH2+H<=>CH+H2	6.020e+12	0.000	-1787.76
!T-CH2+OH<=>CH2O+H	2.500e+13	0.000	0.00
!T-CH2+OH<=>CH+H2O	1.130e+07	2.000	2999.52
!T-CH2+O<=>CO+2 H	8.000e+13	0.000	0.00
!T-CH2+O<=>CO+H2	4.000e+13	0.000	0.00

!T-CH2+O2<=>CO2+H2	2.630e+12	0.000	1491.40
!T-CH2+O2<=>CO+OH+H	6.580e+12	0.000	1491.40
!2 T-CH2<=>C2H2+2 H	1.000e+14	0.000	0.00
!CH+O<=>CO+H	4.000e+13	0.000	0.00
!CH+O2<=>HCO+O	1.770e+11	0.760	-478.01
!CH+H2O<=>CH2O+H	1.170e+15	-0.750	0.00
!CH+CO2<=>HCO+CO	4.800e+01	3.220	-3226.58
!CH3O+H<=>CH2O+H2	2.000e+13	0.000	0.00
!CH3O+H<=>S-CH2+H2O	1.600e+13	0.000	0.00
!CH3O+OH<=>CH2O+H2O	5.000e+12	0.000	0.00
!CH3O+O<=>OH+CH2O	1.000e+13	0.000	0.00
CH3O+O2<=>CH2O+HO2	4.280e-13	7.600	-3537.28
CH3O+M<=>CH2O+H+M	7.780e+13	0.000	13513.38
AR/0.70/ H2/2.00/ H2O/6.00/ CO/1.50/ CO2/2.00/ CH4/2.00/			
!C2H6+H<=>C2H5+H2	5.400e+02	3.500	5210.33
!C2H6+O<=>C2H5+OH	1.400e+00	4.300	2772.47
!C2H6+OH<=>C2H5+H2O	2.200e+07	1.900	1123.33
!C2H6+CH3<=>C2H5+CH4	5.500e-01	4.000	8293.50
!C2H6(+M)<=>C2H5+H(+M)	8.850e+20	-1.230	102222.75
! AR/0.70/ H2/2.00/ H2O/6.00/ CO/1.50/ CO2/2.00/ CH4/2.00/ C2H6/3.00/			
! LOW / 4.900e+42 -6.430 107169.93 /			
! TROE/ 0.84 125 2219 6882 /			
!C2H6+HO2<=>C2H5+H2O2	1.320e+13	0.000	20469.89
!C2H5+H<=>C2H4+H2	3.000e+13	0.000	0.00
!C2H5+O<=>C2H4+OH	3.060e+13	0.000	0.00
!C2H5+O<=>CH3+CH2O	4.240e+13	0.000	0.00
C2H5+O2<=>C2H4+HO2	7.500e+14	-1.000	4799.95
!C2H5+O2<=>C2H4OOH	2.000e+12	0.000	0.00

C2H4OOH<=>C2H4+HO2	4.000e+34	-7.200	23000.00
C2H4OOH+O2<=>OC2H3OOH+OH	7.500e+05	1.300	-5799.95
OC2H3OOH<=>CH2O+HCO+OH	1.000e+15	0.000	43000.00
C2H5(+M)<=>C2H4+H(+M)	1.110e+10	1.037	36768.64
AR/0.70/ H2/2.00/ H2O/6.00/ CO/1.50/ CO2/2.00/ CH4/2.00/			
LOW /	3.990e+33	-4.990	40000.00 /
TROE/	0.168	1.2e+03	0 /
C2H4+H<=>C2H3+H2	4.490e+07	2.120	13360.42
C2H4+OH<=>C2H3+H2O	5.530e+05	2.310	2963.67
C2H4+O<=>CH3+HCO	2.250e+06	2.080	0.00
C2H4+O<=>CH2CHO+H	1.210e+06	2.080	0.00
2 C2H4<=>C2H3+C2H5	5.010e+14	0.000	64700.05
C2H4+O2<=>C2H3+HO2	4.220e+13	0.000	57623.09
C2H4+HO2<=>C2H4O+OH	2.230e+12	0.000	17189.29
C2H4O+HO2<=>CH3+CO+H2O2	4.000e+12	0.000	17007.65
!C2H4+M<=>C2H3+H+M	2.600e+17	0.000	96568.12
! AR/0.70/ H2/2.00/ H2O/6.00/ CO/1.50/ CO2/2.00/ CH4/2.00/			
!C2H4+M<=>C2H2+H2+M	3.500e+16	0.000	71532.03
! AR/0.70/ H2/2.00/ H2O/6.00/ CO/1.50/ CO2/2.00/ CH4/2.00/			
C2H3+H<=>C2H2+H2	4.000e+13	0.000	0.00
!C2H3(+M)<=>C2H2+H(+M)	6.380e+09	1.000	37626.67
! AR/0.70/ H2/2.00/ H2O/6.00/ CO/1.50/ CO2/2.00/ CH4/2.00/			
! LOW /	1.510e+14	0.100	32685.95 /
! TROE/	0.3	1e+30	1e-30 /
C2H3+O2<=>CH2O+HCO	1.700e+29	-5.312	6503.11
C2H3+O2<=>CH2CHO+O	7.000e+14	-0.611	5262.43
C2H3+O2<=>C2H2+HO2	5.190e+15	-1.260	3312.62
C2H2+O<=>HCCO+H	4.000e+14	0.000	10659.66

!C2H2+O<=>T-CH2+CO	1.600e+14	0.000	9894.84
!C2H2+O2<=>CH2O+CO	4.600e+15	-0.540	44933.08
C2H2+OH<=>CH2CO+H	1.900e+07	1.700	999.04
!C2H2+OH<=>C2H+H2O	3.370e+07	2.000	14000.96
CH2CO+H<=>CH3+CO	1.500e+09	1.430	2688.81
CH2CO+O<=>T-CH2+CO2	2.000e+13	0.000	2294.46
CH2CO+O<=>HCCO+OH	1.000e+13	0.000	2000.48
CH2CO+CH3<=>C2H5+CO	9.000e+10	0.000	0.00
!HCCO+H<=>S-CH2+CO	1.500e+14	0.000	0.00
!HCCO+OH<=>HCO+CO+H	2.000e+12	0.000	0.00
!HCCO+O<=>2 CO+H	9.640e+13	0.000	0.00
!HCCO+O2<=>2 CO+OH	2.880e+07	1.700	1001.43
!HCCO+O2<=>CO2+CO+H	1.400e+07	1.700	1001.43
!C2H+OH<=>HCCO+H	2.000e+13	0.000	0.00
!C2H+O<=>CO+CH	1.020e+13	0.000	0.00
!C2H+O2<=>HCCO+O	6.020e+11	0.000	0.00
!C2H+O2<=>CH+CO2	4.500e+15	0.000	25095.60
!C2H+O2<=>HCO+CO	2.410e+12	0.000	0.00
!CH2OH+H<=>CH2O+H2	3.000e+13	0.000	0.00
!CH2OH+H<=>CH3+OH	2.500e+17	-0.930	5126.91
!CH2OH+OH<=>CH2O+H2O	2.400e+13	0.000	0.00
!CH2OH+O2<=>CH2O+HO2	5.000e+12	0.000	0.00
!CH2OH+M<=>CH2O+H+M	5.000e+13	0.000	25119.50
! AR/0.70/ H2/2.00/ H2O/6.00/ CO/1.50/ CO2/2.00/ CH4/2.00/			
CH3O+M<=>CH2OH+M	1.000e+14	0.000	19120.46
AR/0.70/ H2/2.00/ H2O/6.00/ CO/1.50/ CO2/2.00/ CH4/2.00/			
CH2CO+OH<=>CH2OH+CO	1.020e+13	0.000	0.00
!CH3OH+OH<=>CH2OH+H2O	1.440e+06	2.000	-838.91

!CH3OH+OH<=>CH3O+H2O	4.400e+06	2.000	1505.74
!CH3OH+H<=>CH2OH+H2	1.354e+03	3.200	3490.68
!CH3OH+H<=>CH3O+H2	6.830e+01	3.400	7239.96
!CH3OH+O<=>CH2OH+OH	1.000e+13	0.000	4684.51
!CH3OH+HO2<=>CH2OH+H2O2	8.000e+13	0.000	19383.37
CH3OH+O2<=>CH2OH+HO2	2.000e+13	0.000	44933.08
CH3OH(+M)<=>CH3+OH(+M)	1.900e+16	0.000	91729.92
AR/0.70/ H2/2.00/ H2O/6.00/ CO/1.50/ CO2/2.00/ CH4/2.00/			
LOW /	2.950e+44	-7.350	95460.09 /
TROE/	0.414	2.8e+02	5.5e+03 /
CH2CHO<=>CH2CO+H	1.047e+37	-7.189	44340.34
!CH2CHO+H<=>CH3+HCO	5.000e+13	0.000	0.00
!CH2CHO+H<=>CH2CO+H2	2.000e+13	0.000	0.00
!CH2CHO+O<=>CH2O+HCO	1.000e+14	0.000	0.00
CH2CHO+OH<=>CH2CO+H2O	3.000e+13	0.000	0.00
CH2CHO+O2<=>CH2O+CO+OH	3.000e+10	0.000	0.00
!CH2CHO+CH3<=>C2H5+CO+H	4.900e+14	-0.500	0.00
CH2CHO+HO2<=>CH2O+HCO+OH	7.000e+12	0.000	0.00
CH2CHO+HO2<=>CH3CHO+O2	3.000e+12	0.000	0.00
CH2CHO<=>CH3+CO	1.170e+43	-9.800	43799.95
CH3CHO<=>CH3+HCO	7.000e+15	0.000	81700.05
!CH3CO(+M)<=>CH3+CO(+M)	3.000e+12	0.000	16700.05
! AR/0.70/ H2/2.00/ H2O/6.00/ CO/1.50/ CO2/2.00/ CH4/2.00/			
! LOW /	1.200e+15	0.000	12500.00 /
! TROE/	1	1	1e+07 1e+07 /
!CH3CHO+OH<=>CH3CO+H2O	3.370e+12	0.000	-619.98
CH3CHO+OH<=>CH2CHO+H2O	3.370e+11	0.000	-619.98
!CH3CHO+O<=>CH3CO+OH	1.770e+18	-1.900	2979.92

!CH3CHO+O<=>CH2CHO+OH	3.720e+13	-0.200	3559.99
!CH3CHO+H<=>CH3CO+H2	4.660e+13	-0.300	2989.96
!CH3CHO+H<=>CH2CHO+H2	1.850e+12	0.400	5359.94
!CH3CHO+CH3<=>CH3CO+CH4	3.900e-07	5.800	2200.05
!CH3CHO+CH3<=>CH2CHO+CH4	2.450e+01	3.100	5729.92
CH3CHO+HO2<=>CH3CO+H2O2	3.600e+19	-2.200	14000.00
!CH3CHO+HO2<=>CH2CHO+H2O2	2.320e+11	0.400	14900.10
!CH3CHO+O2<=>CH3CO+HO2	1.000e+14	0.000	42200.05
!C2H5OH(+M)<=>CH3+CH2OH(+M)	5.000e+15	0.000	82000.00
! AR/0.70/ H2/2.00/ H2O/6.00/ CO/1.50/ CO2/2.00/ CH4/2.00/			
! LOW / 3.000e+16 0.000 58000.00 /			
! TROE/ 0.5 1e-30 1e+30 /			
!C2H5OH(+M)<=>C2H4+H2O(+M)	8.000e+13	0.000	65000.00
! AR/0.70/ H2/2.00/ H2O/6.00/ CO/1.50/ CO2/2.00/ CH4/2.00/			
! LOW / 1.000e+17 0.000 54000.00 /			
! TROE/ 0.5 1e-30 1e+30 /			
!C2H5OH+OH<=>CH2CH2OH+H2O	1.810e+11	0.400	717.02
!C2H5OH+OH<=>CH3CHOH+H2O	3.090e+10	0.500	-380.02
!C2H5OH+OH<=>CH3CH2O+H2O	1.050e+10	0.800	717.02
!C2H5OH+H<=>CH2CH2OH+H2	1.900e+07	1.800	5099.90
!C2H5OH+H<=>CH3CHOH+H2	2.580e+07	1.600	2830.07
!C2H5OH+H<=>CH3CH2O+H2	1.500e+07	1.600	3039.91
!C2H5OH+O<=>CH2CH2OH+OH	9.410e+07	1.700	5460.09
!C2H5OH+O<=>CH3CHOH+OH	1.880e+07	1.900	1820.03
!C2H5OH+O<=>CH3CH2O+OH	1.580e+07	2.000	4450.05
!C2H5OH+CH3<=>CH2CH2OH+CH4	2.190e+02	3.200	9619.98
!C2H5OH+CH3<=>CH3CHOH+CH4	7.280e+02	3.000	7950.05
!C2H5OH+CH3<=>CH3CH2O+CH4	1.450e+02	3.000	7650.10

!C2H5OH+HO2<=>CH3CHOH+H2O2	8.200e+03	2.500	10799.95
!C2H5OH+HO2<=>CH2CH2OH+H2O2	2.430e+04	2.500	15799.95
C2H5OH+HO2<=>CH3CH2O+H2O2	3.800e+12	0.000	24000.00
!C2H4+OH<=>CH2CH2OH	2.410e+11	0.000	-2380.02
C2H5+HO2<=>CH3CH2O+OH	4.000e+13	0.000	0.00
!CH3CH2O+M<=>CH3CHO+H+M	5.600e+34	-5.900	25299.95
! AR/0.70/ H2/2.00/ H2O/6.00/ CO/1.50/ CO2/2.00/ CH4/2.00/			
!CH3CH2O+M<=>CH3+CH2O+M	5.350e+37	-7.000	23799.95
! AR/0.70/ H2/2.00/ H2O/6.00/ CO/1.50/ CO2/2.00/ CH4/2.00/			
CH3CH2O+O2<=>CH3CHO+HO2	4.000e+10	0.000	1099.90
!CH3CH2O+CO<=>C2H5+CO2	4.680e+02	3.200	5380.02
!CH3CH2O+H<=>CH3+CH2OH	3.000e+13	0.000	0.00
!CH3CH2O+H<=>C2H4+H2O	3.000e+13	0.000	0.00
!CH3CH2O+OH<=>CH3CHO+H2O	1.000e+13	0.000	0.00
!CH3CHOH+O2<=>CH3CHO+HO2	4.820e+13	0.000	5020.08
!CH3CHOH+O<=>CH3CHO+OH	1.000e+14	0.000	0.00
!CH3CHOH+H<=>C2H4+H2O	3.000e+13	0.000	0.00
!CH3CHOH+H<=>CH3+CH2OH	3.000e+13	0.000	0.00
!CH3CHOH+HO2<=>CH3CHO+2 OH	4.000e+13	0.000	0.00
!CH3CHOH+OH<=>CH3CHO+H2O	5.000e+12	0.000	0.00
!CH3CHOH+M<=>CH3CHO+H+M	1.000e+14	0.000	25000.00
! AR/0.70/ H2/2.00/ H2O/6.00/ CO/1.50/ CO2/2.00/ CH4/2.00/			
!C3H4+O<=>C2H4+CO	2.000e+07	1.800	1000.00
!CH3+C2H2<=>C3H4+H	2.560e+09	1.100	13643.88
!C3H4+O<=>HCCO+CH3	7.300e+12	0.000	2250.00
!C3H3+H(+M)<=>C3H4(+M)	3.000e+13	0.000	0.00
! LOW / 9.000e+15 1.000 0.00 /			
! TROE/ 0.5 1e+30 0 /			

!C3H3+HO2<=>C3H4+O2	2.500e+12	0.000	0.00
!C3H4+OH<=>C3H3+H2O	5.300e+06	2.000	2000.00
!C3H3+O2<=>CH2CO+HCO	3.000e+10	0.000	2868.07
!C3H4+H(+M)<=>C3H5(+M)	4.000e+13	0.000	0.00
! LOW / 3.000e+24 -2.000	0.00 /		
! TROE/ 0.8 1e+30	0 /		
C3H5+H<=>C3H4+H2	1.800e+13	0.000	0.00
C3H5+O2<=>C3H4+HO2	4.990e+15	-1.400	22428.06
C3H5+CH3<=>C3H4+CH4	3.000e+12	-0.320	-130.98
!C2H2+CH3(+M)<=>C3H5(+M)	6.000e+08	0.000	0.00
! LOW / 2.000e+09 1.000	0.00 /		
! TROE/ 0.5 1e+30	0 /		
C3H5+OH<=>C3H4+H2O	6.000e+12	0.000	0.00
!C3H3+HCO<=>C3H4+CO	2.500e+13	0.000	0.00
!C3H3+HO2<=>OH+CO+C2H3	8.000e+11	0.000	0.00
!C3H4+O2<=>CH3+HCO+CO	4.000e+14	0.000	41826.00
C3H6+O<=>C2H5+HCO	3.500e+07	1.650	-972.75
C3H6+OH<=>C3H5+H2O	3.100e+06	2.000	-298.28
C3H6+O<=>CH2CO+CH3+H	1.200e+08	1.650	327.44
C3H6+H<=>C3H5+H2	1.700e+05	2.500	2492.83
C3H5+H(+M)<=>C3H6(+M)	2.000e+14	0.000	0.00
AR/0.70/ H2/2.00/ H2O/6.00/ CO/1.50/ CO2/2.00/ CH4/2.00/ C2H6/3.00/			
LOW / 1.330e+60 -12.000	5967.97 /		
TROE/ 0.02 1097	1097 6860 /		
C3H5+HO2<=>C3H6+O2	2.660e+12	0.000	0.00
C3H5+HO2<=>OH+C2H3+CH2O	3.000e+12	0.000	0.00
C2H3+CH3(+M)<=>C3H6(+M)	2.500e+13	0.000	0.00
AR/0.70/ H2/2.00/ H2O/6.00/ CO/1.50/ CO2/2.00/ CH4/2.00/ C2H6/3.00/			

```

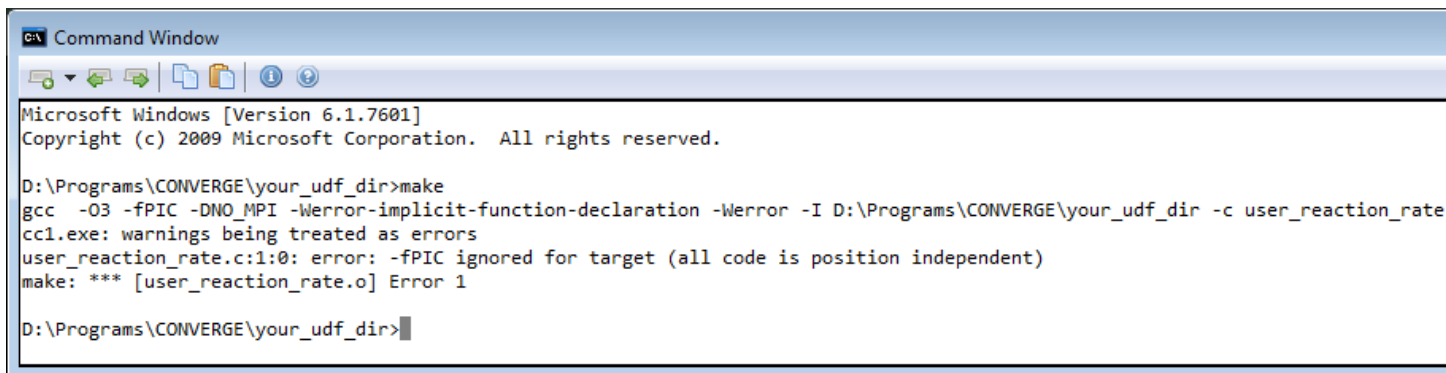
LOW / 4.270e+58 -11.940 9770.55 /
TROE/ 0.175 1341 6e+04 1.014e+04 /
C3H6+H<=>C2H4+CH3 1.600e+22 -2.390 11185.47
!CH3+C2H3<=>C3H5+H 1.500e+24 -2.830 18618.55
C3H8(+M)<=>CH3+C2H5(+M) 1.100e+17 0.000 84392.93
LOW / 7.830e+18 0.000 64978.01 /
TROE/ 0.76 1.9e+03 38 /
C3H8+O2<=>I-C3H7+HO2 4.000e+13 0.000 47500.00
C3H8+O2<=>N-C3H7+HO2 4.000e+13 0.000 50932.12
C3H8+H<=>I-C3H7+H2 1.300e+06 2.400 4471.08
C3H8+H<=>N-C3H7+H2 1.330e+06 2.540 6761.47
C3H8+O<=>I-C3H7+OH 4.760e+04 2.710 2107.31
C3H8+O<=>N-C3H7+OH 1.900e+05 2.680 3718.45
C3H8+OH<=>N-C3H7+H2O 1.000e+10 1.000 1599.90
!C3H8+OH<=>I-C3H7+H2O 2.000e+07 -1.600 -99.90
C3H8+HO2<=>I-C3H7+H2O2 9.640e+03 2.600 13917.30
C3H8+HO2<=>N-C3H7+H2O2 4.760e+04 2.550 16491.40
I-C3H7+C3H8<=>N-C3H7+C3H8 8.400e-03 4.200 8675.91
C3H6+H(+M)<=>I-C3H7(+M) 1.330e+13 0.000 1560.71
AR/0.70/ H2/2.00/ H2O/6.00/ CO/1.50/ CO2/2.00/ CH4/2.00/ C2H6/3.00/
LOW / 8.700e+42 -7.500 4732.31 /
TROE/ 1 1000 645.4 6844 /
I-C3H7+O2<=>C3H6+HO2 1.300e+11 0.000 0.00
N-C3H7(+M)<=>CH3+C2H4(+M) 1.230e+13 -0.100 30210.33
LOW / 5.490e+49 -10.000 35778.92 /
TROE/ -1.17 251 1e-15 1185 /
H+C3H6(+M)<=>N-C3H7(+M) 1.330e+13 0.000 3260.04
AR/0.70/ H2/2.00/ H2O/6.00/ CO/1.50/ CO2/2.00/ CH4/2.00/ C2H6/3.00/
LOW / 6.260e+38 -6.660 7000.48 /

```

TROE/	1	1000	1310	4.81e+04 /		
N-C3H7+O2<=>C3H6+HO2			3.500e+16	-1.600	3500.00	
N-C3H7+O2<=>C3H6OOH			2.000e+12	0.000	0.00	
C3H6OOH<=>C3H6+HO2			2.500e+35	-8.300	22000.00	
C3H6OOH+O2<=>OC3H5OOH+OH			1.500e+08	0.000	-7000.00	
OC3H5OOH<=>CH2CHO+CH2O+OH			1.000e+15	0.000	43000.00	
END						

3. Global Westbrook and Dryer One-Step Mechanism Code for Propane Oxidation

The following C code was edited from an example “user-defined function” (UDF) provided by Convergent Science, Inc. (CSI) in the interest of integrating the calibrated global Westbrook and Dryer one-step mechanism. Typically, this UDF is accounted for by recompiling the solver with this updated version of `user_reaction_rate.c` replacing the stock example included in the public version of the solver. Recompiling the solver involves using a “make” function available from CSI in the UDF example library. Running the make function typically would output a new recompiled file the solver can use, `libconverge_udf.so` as long as no errors are encountered. Unfortunately, this final step was not accomplished in time for publication due to errors in the make function’s process. The error output is shown below. Following publication, work will continue debugging this issue and proceeding with the global mechanism to reduce runtime and potentially increase mesh fineness. In the interest of presenting results in time, CFD simulations were run using the reduced San Diego mechanism. Future work will then involve comparing the results of the reduced mechanism with the global mechanism when it can be properly integrated into the solver and validated with the spherical chamber data.



```
C:\ Command Window
Microsoft Windows [Version 6.1.7601]
Copyright (c) 2009 Microsoft Corporation. All rights reserved.

D:\Programs\CONVERGE\your_udf_dir>make
gcc -O3 -fPIC -DNO_MPI -Werror-implicit-function-declaration -Werror -I D:\Programs\CONVERGE\your_udf_dir -c user_reaction_rate
cc1.exe: warnings being treated as errors
user_reaction_rate.c:1:0: error: -fPIC ignored for target (all code is position independent)
make: *** [user_reaction_rate.o] Error 1

D:\Programs\CONVERGE\your_udf_dir>
```

`user_reaction_rate.c`

```
#include <math.h>
#include <stdio.h>
#include <string.h>
#include <stdlib.h>
```

```

#include "const_shared.h"
#include "structures_shared.h"
#include "prototype_shared.h"
#include "common_shared.h"
#include "user_header.h"
#include "safe_prototypes.h"
#include "parsing.h"
#include "tools_shared.h"

/*****
*****/
/* user_reaction_rate(int jj,double *sage_x,struct mechanism_definition
*mechanism,double totconc,double avgMW, double q_tot) */
/* calculates the reaction rate of user defined reactions
*/
/* these reactions do not fit into standard Arrhenius format
*/
/*****
*****/
//Westbrook and Dryer 1981 One-Step Global Reaction Mechanism for Propane
Oxidation
void user_reaction_rate(int jj,double *sage_x,struct mechanism_definition
*mech,int user_index, double totconc, double *q_tot)
{
    double temp;
    double pres;
    double R_gc;
    double A_WD81;
    double E_WD81;

    temp = mech->temp;
    pres = mech->pres;
    R_gc = 8.31430; //Universal Gas Constant
    A_WD81 = 8.6e11; //Preexponential Constant
    E_WD81 = 30000.0; //Activation Energy
    CE_C3H8 = 0.10; //Propane Concentration Exponent
    CE_O2 = 1.65; //Oxygen Concentration Exponent

    if(user_index==1) //User Reaction Number from Mech.dat
    {
        //Get Curve-Fit Concentrations of Propane and Oxygen using Constant
        Concentration Exponents
        //Note: sage_x[isp] is the concentration of species denoted by isp
        counter as listed in mech_check.out
        CFC_C3H8 = pow(sage_x[1],CE_C3H8);
        //Curve-Fit Concentration of Propane, [C3H8]^CE_C3H8
        CFC_O2 = pow(sage_x[2],CE_O2);
        //Curve-Fit Concentration of Oxygen, [O2]^CE_O2

        //Calculate Reaction Rate, q_tot
        //Note: In C, the * notation indicates a pointer to reduce
        computation time
        *q_tot *= A_WD81*exp(-E_WD81/(R_gc*temp))*CFC_C3H8*CFC_O2;
        //Global One-Step Reaction Mechanism Reaction Rate
    }
}
}

```

B. Complete CFD Model Input Parameters

The following section lists the complete input files used to run the CONVERGE solver for all three simulations discussed in the dissertation. They are separated below into sections for each simulation with each individual file starting with the filename in bold centered on the first line of the file text. If the text of these input files is copied to recreate the simulations, this filename line should be deleted. Lastly, all simulations use the same gas.dat and therm.dat files. These are lookup tables necessary for the simulation to run and are listed at the end of the mixing flow simulation input files. Due to their length, they are not repeated in the other sections. Nevertheless, they are still necessary to repeat a run of the spherical chamber or the BGX prototype engine.

1. Nonreactive Mixing Flow Simulations

The following files were used to run the Engine Stand Mixing Box simulations. A total of four simulations were run: ESMB1 – 0% Load LES, ESMB2 – 0% Load RANS, ESMB3 – 100% Load LES, and ESMB4 – 100% Load RANS. The differences between these cases are primarily in the boundary conditions (defined in the boundary.in file) and turbulence models (defined in the turbulence.in file) used. All other settings (fixed embedding, adaptive meshing, etc...) were held constant between simulations. The input files which changed from one simulation to the next are listed first for each simulation with the remaining common files listed thereafter. Two files were omitted due to their length and commonality between all simulations in this dissertation - therm.dat and gas.dat (lengthy databases provided with the solver).

boundary.in (ESMB1 – 0% Load, LES)

```
#!/csi_version=1.4.1
#=====

12  # Number of boundaries defined
#-----
1      BoxWalls
WALL      ST
roughness 0.0      0.5
velocity  la      0.0 0.0 0.0
pressure  ne      0.0
temperature la    300.0
species   ne      0.0
passive   ne      0.0
tke       ne      0.0
eps       ne      0.0
region    0
#-----
2      AirInWalls
WALL      ST
roughness 0.0      0.5
velocity  la      0.0 0.0 0.0
pressure  ne      0.0
temperature la    300.0
species   ne      0.0
passive   ne      0.0
tke       ne      0.0
eps       ne      0.0
region    0
#-----
3      EgrInWalls
WALL      ST
roughness 0.0      0.5
velocity  la      0.0 0.0 0.0
pressure  ne      0.0
temperature la    300.0
species   ne      0.0
passive   ne      0.0
tke       ne      0.0
eps       ne      0.0
region    0
#-----
4      GasInWalls
WALL      ST
roughness 0.0      0.5
velocity  la      0.0 0.0 0.0
pressure  ne      0.0
temperature la    300.0
species   ne      0.0
passive   ne      0.0
tke       ne      0.0
eps       ne      0.0
region    0
#-----
5      MixOutWalls
WALL      ST
```

```

roughness    0.0      0.5
velocity     la       0.0 0.0 0.0
pressure     ne       0.0
temperature  la       300.0
species      ne       0.0
passive      ne       0.0
tke          ne       0.0
eps          ne       0.0
region       0
#-----
6           AirIn
INFLOW
velocity     ma       0.0051
pressure     ne       0.0
temperature  di       298.3
species      di       3
H2O          0.0119
O2           0.2302
N2           0.7579
passive      di       0
tke          in       0.02
eps          le       0.003
region       0
#-----
7           EgrIn
INFLOW
velocity     ma       0.00177
pressure     ne       0.0
temperature  di       301.6
species      di       5
O2           0.1645
N2           0.7324
CO           0.0016
CO2          0.0515
H2O          0.05
passive      di       0
tke          in       0.02
eps          le       0.003
region       0
#-----
8           GasIn
WALL        ST
roughness    0.0      0.5
velocity     la       0.0 0.0 0.0
pressure     ne       0.0
temperature  la       300.0
species      ne       0.0
passive      ne       0.0
tke          ne       0.0
eps          ne       0.0
region       0
#-----
9           MixOut
OUTFLOW
velocity     ne       0.0 0.0 0.0
pressure     di       89970.0 0.0
temperature  ne       0.0

```

```

species      ne      0.0
passive      ne      0.0
tke          ne      0.0
eps          ne      0.0
temperature  backflow di 307.1
species      backflow di 3
H2O          0.0119
O2           0.2302
N2           0.7579
passive      backflow di 0
tke          backflow in 0.02
eps          backflow le 0.003
region      0
#-----
10           BoschProbe
WALL         ST
roughness    0.0      0.5
velocity     la       0.0 0.0 0.0
pressure     ne       0.0
temperature  la       300.0
species      ne       0.0
passive      ne       0.0
tke          ne       0.0
eps          ne       0.0
region      0
#-----
11           Thermcpl
WALL         ST
roughness    0.0      0.5
velocity     la       0.0 0.0 0.0
pressure     ne       0.0
temperature  la       300.0
species      ne       0.0
passive      ne       0.0
tke          ne       0.0
eps          ne       0.0
region      0
#-----
12           PressProbe
WALL         ST
roughness    0.0      0.5
velocity     la       0.0 0.0 0.0
pressure     ne       0.0
temperature  la       300.0
species      ne       0.0
passive      ne       0.0
tke          ne       0.0
eps          ne       0.0
region      0

```

turbulence.in (ESMB1 – 0% Load, LES)

```

#!csi_version=1.4.1
#=====

11          turbmodel          Turbulence model flag
(RANS):1=k-eps, 2=rng k-eps, 3 rapid distortion rng k-eps.
0.09        cmu                Turbulent viscosity
coefficient. Typically 0.09 for k-eps and 0.0845 for rng k-eps.
1.0         rpr_tke            Reciprocal TKE Prandtl
number. Typically 1.0 for k-eps, 1.39 for rng k-eps.
1.44        ceps1              Turbulent dissipation (eps)
constant. Typically 1.44 for k-eps, 1.42 for rng k-eps..
1.92        ceps2              Turbulent dissipation (eps)
constant. Typically 1.92 for k-eps, 1.68 for rng k-eps.
-1.0        ceps3              Turbulent dissipation (eps)
constant. Typically -1.0.
0.77        rpr_eps            Reciprocal turbulent
dissipation (eps) Prandtl number. Typically 0.7692 for k-eps, 1.39 rng k-eps
0.012       beta              RNG k-epsilon constant.
Typically 0.012.
4.38        eta0              RNG k-epsilon constant.
Typically 4.38.
0.0         c_s                Turbulent spray source
constant. Typically 0 to 1.5.
0.03        c_ps              Drop turbulent dispersion
constant. Typically 0 to 0.16.
2.0         c_tke_les          LES sub-grid estimate
constant. Typically 2.0.
0.05        c_tke_visc_les     LES Viscosity coefficient.
1.0         c_eps_les          Turbulent LES dissipation
constant. Typically 1.0.
1           wall_model         LES wall model: 0=standard
law of the wall, 1=Werner and Wengle (recommended).
114.0       re_crit           Law of the wall critical
Reynolds number
0.15        clw               Law of the wall constant
0.42        law_kappa         Von Karmen's constant.
5.5         law_b             Law of wall parameter
10          heatmodel         Wall heat transfer model:
0=O'Rourke , 1=Han and Reitz, 2=Angelberger.

```

Boundary.in (ESMB2 – 0% Load, RANS)

```
#!/csi_version=1.4.1
#=====

12  # Number of boundaries defined
#-----
1      BoxWalls
WALL      ST
roughness 0.0      0.5
velocity  la      0.0 0.0 0.0
pressure  ne      0.0
temperature la    300.0
species   ne      0.0
passive   ne      0.0
tke       ne      0.0
eps       ne      0.0
region    0
#-----
2      AirInWalls
WALL      ST
roughness 0.0      0.5
velocity  la      0.0 0.0 0.0
pressure  ne      0.0
temperature la    300.0
species   ne      0.0
passive   ne      0.0
tke       ne      0.0
eps       ne      0.0
region    0
#-----
3      EgrInWalls
WALL      ST
roughness 0.0      0.5
velocity  la      0.0 0.0 0.0
pressure  ne      0.0
temperature la    300.0
species   ne      0.0
passive   ne      0.0
tke       ne      0.0
eps       ne      0.0
region    0
#-----
4      GasInWalls
WALL      ST
roughness 0.0      0.5
velocity  la      0.0 0.0 0.0
pressure  ne      0.0
temperature la    300.0
species   ne      0.0
passive   ne      0.0
tke       ne      0.0
eps       ne      0.0
region    0
#-----
5      MixOutWalls
WALL      ST
```

```

roughness    0.0      0.5
velocity     la       0.0 0.0 0.0
pressure     ne       0.0
temperature  la       300.0
species      ne       0.0
passive      ne       0.0
tke          ne       0.0
eps          ne       0.0
region       0
#-----
6           AirIn
INFLOW
velocity     ma       0.0051
pressure     ne       0.0
temperature  di       298.3
species      di       3
H2O          0.0119
O2           0.2302
N2           0.7579
passive      di       0
tke          in       0.02
eps          le       0.003
region       0
#-----
7           EgrIn
INFLOW
velocity     ma       0.00177
pressure     ne       0.0
temperature  di       301.6
species      di       5
O2           0.1645
N2           0.7324
CO           0.0016
CO2          0.0515
H2O          0.05
passive      di       0
tke          in       0.02
eps          le       0.003
region       0
#-----
8           GasIn
WALL        ST
roughness    0.0      0.5
velocity     la       0.0 0.0 0.0
pressure     ne       0.0
temperature  la       300.0
species      ne       0.0
passive      ne       0.0
tke          ne       0.0
eps          ne       0.0
region       0
#-----
9           MixOut
OUTFLOW
velocity     ne       0.0 0.0 0.0
pressure     di       89970.0 0.0
temperature  ne       0.0

```

```

species      ne      0.0
passive      ne      0.0
tke          ne      0.0
eps          ne      0.0
temperature  backflow di 307.1
species      backflow di 3
H2O          0.0119
O2           0.2302
N2           0.7579
passive      backflow di 0
tke          backflow in 0.02
eps          backflow le 0.003
region      0
#-----
10           BoschProbe
WALL         ST
roughness    0.0      0.5
velocity     la      0.0 0.0 0.0
pressure     ne      0.0
temperature  la      300.0
species      ne      0.0
passive      ne      0.0
tke          ne      0.0
eps          ne      0.0
region      0
#-----
11           Thermcpl
WALL         ST
roughness    0.0      0.5
velocity     la      0.0 0.0 0.0
pressure     ne      0.0
temperature  la      300.0
species      ne      0.0
passive      ne      0.0
tke          ne      0.0
eps          ne      0.0
region      0
#-----
12           PressProbe
WALL         ST
roughness    0.0      0.5
velocity     la      0.0 0.0 0.0
pressure     ne      0.0
temperature  la      300.0
species      ne      0.0
passive      ne      0.0
tke          ne      0.0
eps          ne      0.0
region      0

```

turbulence.in (ESMB2 – 0% Load, RANS)

```
#!csi_version=1.4.1
#=====

2                turbmodel                Turbulence model flag
(RANS):1=k-eps, 2=rng k-eps, 3 rapid distortion rng k-eps.
0.09            cmu                        Turbulent viscosity
coefficient. Typically 0.09 for k-eps and 0.0845 for rng k-eps.
1.0             rpr_tke                    Reciprocal TKE Prandtl
number. Typically 1.0 for k-eps, 1.39 for rng k-eps.
1.44            ceps1                      Turbulent dissipation (eps)
constant. Typically 1.44 for k-eps, 1.42 for rng k-eps..
1.92            ceps2                      Turbulent dissipation (eps)
constant. Typically 1.92 for k-eps, 1.68 for rng k-eps.
-1.0            ceps3                      Turbulent dissipation (eps)
constant. Typically -1.0.
0.77            rpr_eps                    Reciprocal turbulent
dissipation (eps) Prandtl number. Typically 0.7692 for k-eps, 1.39 rng k-eps
0.012           beta                      RNG k-epsilon constant.
Typically 0.012.
4.38            eta0                      RNG k-epsilon constant.
Typically 4.38.
0.0             c_s                        Turbulent spray source
constant. Typically 0 to 1.5.
0.03            c_ps                       Drop turbulent dispersion
constant. Typically 0 to 0.16.
2.0             c_tke_les                  LES sub-grid estimate
constant. Typically 2.0.
0.05            c_tke_visc_les             LES Viscosity coefficient.
1.0             c_eps_les                  Turbulent LES dissipation
constant. Typically 1.0.
1               wall_model                 LES wall model: 0=standard
law of the wall, 1=Werner and Wengle (recommended).
114.0           re_crit                    Law of the wall critical
Reynolds number
0.15            clw                        Law of the wall constant
0.42            law_kappa                  Von Karmen's constant.
5.5             law_b                      Law of wall parameter
10             heatmodel                   Wall heat transfer model:
0=O'Rourke , 1=Han and Reitz, 2=Angelberger.
```

boundary.in (ESMB3 – 100% Load, LES)

```
#!/csi_version=1.4.1
#=====

12 # Number of boundaries defined
#-----
1      BoxWalls
WALL   ST
roughness 0.0      0.5
velocity  la      0.0 0.0 0.0
pressure  ne      0.0
temperature la    300.0
species   ne      0.0
passive   ne      0.0
tke       ne      0.0
eps       ne      0.0
region    0
#-----
2      AirInWalls
WALL   ST
roughness 0.0      0.5
velocity  la      0.0 0.0 0.0
pressure  ne      0.0
temperature la    300.0
species   ne      0.0
passive   ne      0.0
tke       ne      0.0
eps       ne      0.0
region    0
#-----
3      EgrInWalls
WALL   ST
roughness 0.0      0.5
velocity  la      0.0 0.0 0.0
pressure  ne      0.0
temperature la    300.0
species   ne      0.0
passive   ne      0.0
tke       ne      0.0
eps       ne      0.0
region    0
#-----
4      GasInWalls
WALL   ST
roughness 0.0      0.5
velocity  la      0.0 0.0 0.0
pressure  ne      0.0
temperature la    300.0
species   ne      0.0
passive   ne      0.0
tke       ne      0.0
eps       ne      0.0
region    0
#-----
5      MixOutWalls
WALL   ST
```

```

roughness    0.0      0.5
velocity     la       0.0 0.0 0.0
pressure     ne       0.0
temperature  la       300.0
species      ne       0.0
passive      ne       0.0
tke          ne       0.0
eps          ne       0.0
region       0
#-----
6           AirIn
INFLOW
velocity     ma       0.0052
pressure     ne       0.0
temperature  di       300.4
species      di       3
H2O          0.0128
O2           0.23
N2           0.7572
passive      di       0
tke          in       0.02
eps          le       0.003
region       0
#-----
7           EgrIn
INFLOW
velocity     ma       0.0018
pressure     ne       0.0
temperature  di       305.6
species      di       5
O2           0.1204
N2           0.7337
CO           0.0012
CO2          0.0948
H2O          0.0499
passive      di       0
tke          in       0.02
eps          le       0.003
region       0
#-----
8           GasIn
WALL        ST
roughness    0.0      0.5
velocity     la       0.0 0.0 0.0
pressure     ne       0.0
temperature  la       300.0
species      ne       0.0
passive      ne       0.0
tke          ne       0.0
eps          ne       0.0
region       0
#-----
9           MixOut
OUTFLOW
velocity     ne       0.0 0.0 0.0
pressure     di       89750.0 0.0
temperature  ne       0.0

```

```

species      ne          0.0
passive      ne          0.0
tke          ne          0.0
eps          ne          0.0
temperature  backflow di 310.4
species      backflow di 3
H2O          0.0023
O2           0.2095
N2           0.7882
passive      backflow di 0
tke          backflow in 0.02
eps          backflow le 0.003
region      0
#-----
10           BoschProbe
WALL         ST
roughness    0.0          0.5
velocity     la           0.0 0.0 0.0
pressure     ne           0.0
temperature  la           300.0
species      ne           0.0
passive      ne           0.0
tke          ne           0.0
eps          ne           0.0
region      0
#-----
11           Thermcpl
WALL         ST
roughness    0.0          0.5
velocity     la           0.0 0.0 0.0
pressure     ne           0.0
temperature  la           300.0
species      ne           0.0
passive      ne           0.0
tke          ne           0.0
eps          ne           0.0
region      0
#-----
12           PressProbe
WALL         ST
roughness    0.0          0.5
velocity     la           0.0 0.0 0.0
pressure     ne           0.0
temperature  la           300.0
species      ne           0.0
passive      ne           0.0
tke          ne           0.0
eps          ne           0.0
region      0

```

turbulence.in (ESMB3 – 100% Load, LES)

```
#!/csi_version=1.4.1
#=====

11          turbmodel          Turbulence model flag
(RANS):1=k-eps, 2=rng k-eps, 3 rapid distortion rng k-eps.
0.09        cmu                Turbulent viscosity
coefficient. Typically 0.09 for k-eps and 0.0845 for rng k-eps.
1.0         rpr_tke            Reciprocal TKE Prandtl
number. Typically 1.0 for k-eps, 1.39 for rng k-eps.
1.44        ceps1              Turbulent dissipation (eps)
constant. Typically 1.44 for k-eps, 1.42 for rng k-eps..
1.92        ceps2              Turbulent dissipation (eps)
constant. Typically 1.92 for k-eps, 1.68 for rng k-eps.
-1.0        ceps3              Turbulent dissipation (eps)
constant. Typically -1.0.
0.77        rpr_eps            Reciprocal turbulent
dissipation (eps) Prandtl number. Typically 0.7692 for k-eps, 1.39 rng k-eps
0.012       beta              RNG k-epsilon constant.
Typically 0.012.
4.38        eta0              RNG k-epsilon constant.
Typically 4.38.
0.0         c_s                Turbulent spray source
constant. Typically 0 to 1.5.
0.03        c_ps              Drop turbulent dispersion
constant. Typically 0 to 0.16.
2.0         c_tke_les          LES sub-grid estimate
constant. Typically 2.0.
0.05        c_tke_visc_les     LES Viscosity coefficient.
1.0         c_eps_les          Turbulent LES dissipation
constant. Typically 1.0.
1           wall_model         LES wall model: 0=standard
law of the wall, 1=Werner and Wengle (recommended).
114.0       re_crit           Law of the wall critical
Reynolds number
0.15        clw               Law of the wall constant
0.42        law_kappa         Von Karmen's constant.
5.5         law_b             Law of wall parameter
10          heatmodel         Wall heat transfer model:
0=O'Rourke , 1=Han and Reitz, 2=Angelberger.
```

boundary.in (ESMB4 – 100% Load, RANS)

```
#!/csi_version=1.4.1
#=====

12  # Number of boundaries defined
#-----
1      BoxWalls
WALL      ST
roughness 0.0      0.5
velocity  la      0.0 0.0 0.0
pressure  ne      0.0
temperature la    300.0
species   ne      0.0
passive   ne      0.0
tke       ne      0.0
eps       ne      0.0
region    0
#-----
2      AirInWalls
WALL      ST
roughness 0.0      0.5
velocity  la      0.0 0.0 0.0
pressure  ne      0.0
temperature la    300.0
species   ne      0.0
passive   ne      0.0
tke       ne      0.0
eps       ne      0.0
region    0
#-----
3      EgrInWalls
WALL      ST
roughness 0.0      0.5
velocity  la      0.0 0.0 0.0
pressure  ne      0.0
temperature la    300.0
species   ne      0.0
passive   ne      0.0
tke       ne      0.0
eps       ne      0.0
region    0
#-----
4      GasInWalls
WALL      ST
roughness 0.0      0.5
velocity  la      0.0 0.0 0.0
pressure  ne      0.0
temperature la    300.0
species   ne      0.0
passive   ne      0.0
tke       ne      0.0
eps       ne      0.0
region    0
#-----
5      MixOutWalls
WALL      ST
```

```

roughness    0.0      0.5
velocity     la       0.0 0.0 0.0
pressure     ne       0.0
temperature  la       300.0
species      ne       0.0
passive      ne       0.0
tke          ne       0.0
eps          ne       0.0
region       0
#-----
6           AirIn
INFLOW
velocity     ma       0.0052
pressure     ne       0.0
temperature  di       300.4
species      di       3
H2O          0.0128
O2           0.23
N2           0.7572
passive      di       0
tke          in       0.02
eps          le       0.003
region       0
#-----
7           EgrIn
INFLOW
velocity     ma       0.0018
pressure     ne       0.0
temperature  di       305.6
species      di       5
O2           0.1204
N2           0.7337
CO           0.0012
CO2          0.0948
H2O          0.0499
passive      di       0
tke          in       0.02
eps          le       0.003
region       0
#-----
8           GasIn
WALL        ST
roughness    0.0      0.5
velocity     la       0.0 0.0 0.0
pressure     ne       0.0
temperature  la       300.0
species      ne       0.0
passive      ne       0.0
tke          ne       0.0
eps          ne       0.0
region       0
#-----
9           MixOut
OUTFLOW
velocity     ne       0.0 0.0 0.0
pressure     di       89750.0 0.0
temperature  ne       0.0

```

```

species      ne      0.0
passive      ne      0.0
tke          ne      0.0
eps          ne      0.0
temperature  backflow di 310.4
species      backflow di 3
H2O          0.0023
O2           0.2095
N2           0.7882
passive      backflow di 0
tke          backflow in 0.02
eps          backflow le 0.003
region      0
#-----
10           BoschProbe
WALL         ST
roughness    0.0      0.5
velocity     la       0.0 0.0 0.0
pressure     ne       0.0
temperature  la       300.0
species      ne       0.0
passive      ne       0.0
tke          ne       0.0
eps          ne       0.0
region      0
#-----
11           Thermcpl
WALL         ST
roughness    0.0      0.5
velocity     la       0.0 0.0 0.0
pressure     ne       0.0
temperature  la       300.0
species      ne       0.0
passive      ne       0.0
tke          ne       0.0
eps          ne       0.0
region      0
#-----
12           PressProbe
WALL         ST
roughness    0.0      0.5
velocity     la       0.0 0.0 0.0
pressure     ne       0.0
temperature  la       300.0
species      ne       0.0
passive      ne       0.0
tke          ne       0.0
eps          ne       0.0
region      0

```

turbulence.in (ESMB4 – 100% Load, RANS)

```

#!csi_version=1.4.1
#=====

2                               turbmodel                               Turbulence model flag
(RANS):1=k-eps, 2=rng k-eps, 3 rapid distortion rng k-eps.
0.09                             cmu                               Turbulent viscosity
coefficient. Typically 0.09 for k-eps and 0.0845 for rng k-eps.
1.0                               rpr_tke                               Reciprocal TKE Prandtl
number. Typically 1.0 for k-eps, 1.39 for rng k-eps.
1.44                             ceps1                               Turbulent dissipation (eps)
constant. Typically 1.44 for k-eps, 1.42 for rng k-eps..
1.92                             ceps2                               Turbulent dissipation (eps)
constant. Typically 1.92 for k-eps, 1.68 for rng k-eps.
-1.0                             ceps3                               Turbulent dissipation (eps)
constant. Typically -1.0.
0.77                             rpr_eps                               Reciprocal turbulent
dissipation (eps) Prandtl number. Typically 0.7692 for k-eps, 1.39 rng k-eps
0.012                             beta                               RNG k-epsilon constant.
Typically 0.012.
4.38                             eta0                               RNG k-epsilon constant.
Typically 4.38.
0.0                               c_s                               Turbulent spray source
constant. Typically 0 to 1.5.
0.03                             c_ps                               Drop turbulent dispersion
constant. Typically 0 to 0.16.
2.0                               c_tke_les                               LES sub-grid estimate
constant. Typically 2.0.
0.05                             c_tke_visc_les                               LES Viscosity coefficient.
1.0                               c_eps_les                               Turbulent LES dissipation
constant. Typically 1.0.
1                               wall_model                               LES wall model: 0=standard
law of the wall, 1=Werner and Wengle (recommended).
114.0                             re_crit                               Law of the wall critical
Reynolds number
0.15                             clw                               Law of the wall constant
0.42                             law_kappa                               Von Karmen's constant.
5.5                             law_b                               Law of wall parameter
10                             heatmodel                               Wall heat transfer model:
0=O'Rourke , 1=Han and Reitz, 2=Angelberger.

```

The remaining files listed in this section are common to each of the four simulations. If recreating the simulations, each of the remaining files will be needed for each simulation.

amr.in

```

#!csi_version=1.4.1
#=====

100                amr_cycle_steady                Number of cycles between
AMR calculations.
200000            amr_max_cells                    Maximum number of cells in
the entire domain
1                amr_min_cells                    Minimum number of cells in
the entire domain
#=====
# Amr Group 1
#-----
1                amr_num_regions                Number of AMR regions
0                amr_active_region                Active AMR region
##### Velocity #####
1                amr_vel_flag                    Enable AMR based on velocity
conditions.
4                amr_embed_vel_scale                Maximum embedding level
for velocity.
0.1              amr_vel_sgs_embed                Sub-grid velocity above
which a cell will be embedded.
PERMANENT                Temporal type and cyclic
period
-999999.0          amr_vel_start_time                Time to start the AMR
-999999.0          amr_vel_end_time                Time to end the AMR
50                amr_parcel_embed                Maximum number of parcels
in a cell before CONVERGE embeds a cell using AMR.
##### Temperature #####
0                amr_temp_flag                    Enable AMR based on
temperature conditions.
3                amr_embed_temp_scale                Maximum embedding level
for temperature.
2.5              amr_temp_sgs_embed                Sub-grid temperature above
which a cell will be embedded.
PERMANENT                Temporal type and cyclic
period
-999999.0          amr_temp_start_time                Time to start the AMR
-999999.0          amr_temp_end_time                Time to end the AMR
##### Species data #####
0                amr_species_flag                Enable AMR based on species
conditions.
3                amr_embed_species_scale                Maximum embedding level
for species.
1                amr_num_species                Number of species to
trigger AMR
NOT_USED          species_name                    Species name
PERMANENT                Temporal type and cyclic
period
1.0e-6           amr_species_sgs_embed                Minimum mass fraction of
the species that will trigger AMR
0.0              amr_species_start_time                Time to start the AMR
10.0            amr_species_end_time                Time to end the AMR

```

```

##### Passive data #####
0          amr_passive_flag          Enable AMR based on passives
conditions.
3          amr_embed_passive_scale    Maximum embedding level
for passives.
1          amr_num_passive            Number of passives to
trigger AMR
NOT_USED   passive_name              Passive name
PERMANENT  Temporal type and cyclic
period
1.0e-6     amr_passive_sgs_embed      Minimum mass fraction of
the passive that will trigger AMR
0.0        amr_passive_start_time     Time to start the AMR
10.0       amr_passive_end_time       Time to end the AMR
#=====
# Boundary data
#-----
0          amr_num_bounds             Number of boundary on which
CONVERGE will use AMR.

```

embedded.in

```
#!/csi_version=1.4.1
#=====

#-----
# BoxWalls@
#-----
BOUND          embedded_type
1              boundary_id          Boundary identifier (from
boundary.in) that defines the boundary on which embedding is to be added.
1              embed_scale          Defines the level of
refinement for embedding. Represents the value of n in  $dx\_base/2^n$ .
2              num_embed           Number of layers of
embedding (at the specified embed_scale) to be added to the boundary.
PERMANENT                                           Temporal type and cyclic
period
-999999.0          start_time          Time when embedding starts.
Not used when temporal_type is PERMANENT
-999999.0          end_time           Time when embedding ends.
Not used when temporal_type is PERMANENT
#=====
# AirInWalls@
#-----
BOUND          embedded_type
2              boundary_id          Boundary identifier (from
boundary.in) that defines the boundary on which embedding is to be added.
2              embed_scale          Defines the level of
refinement for embedding. Represents the value of n in  $dx\_base/2^n$ .
3              num_embed           Number of layers of
embedding (at the specified embed_scale) to be added to the boundary.
PERMANENT                                           Temporal type and cyclic
period
-999999.0          start_time          Time when embedding starts.
Not used when temporal_type is PERMANENT
-999999.0          end_time           Time when embedding ends.
Not used when temporal_type is PERMANENT
#=====
# EgrInWalls@
#-----
BOUND          embedded_type
3              boundary_id          Boundary identifier (from
boundary.in) that defines the boundary on which embedding is to be added.
2              embed_scale          Defines the level of
refinement for embedding. Represents the value of n in  $dx\_base/2^n$ .
3              num_embed           Number of layers of
embedding (at the specified embed_scale) to be added to the boundary.
PERMANENT                                           Temporal type and cyclic
period
-999999.0          start_time          Time when embedding starts.
Not used when temporal_type is PERMANENT
-999999.0          end_time           Time when embedding ends.
Not used when temporal_type is PERMANENT
#=====
# GasInWalls@
#-----
BOUND          embedded_type
```

```

4          boundary_id          Boundary identifier (from
boundary.in) that defines the boundary on which embedding is to be added.
2          embed_scale          Defines the level of
refinement for embedding. Represents the value of n in dx_base/2^n.
3          num_embed            Number of layers of
embedding (at the specified embed_scale) to be added to the boundary.
PERMANENT          Temporal type and cyclic
period
-999999.0          start_time    Time when embedding starts.
Not used when temporal_type is PERMANENT
-999999.0          end_time      Time when embedding ends.
Not used when temporal_type is PERMANENT
#=====
# MixOutWalls@
#-----
BOUND          embedded_type
5          boundary_id          Boundary identifier (from
boundary.in) that defines the boundary on which embedding is to be added.
2          embed_scale          Defines the level of
refinement for embedding. Represents the value of n in dx_base/2^n.
3          num_embed            Number of layers of
embedding (at the specified embed_scale) to be added to the boundary.
PERMANENT          Temporal type and cyclic
period
-999999.0          start_time    Time when embedding starts.
Not used when temporal_type is PERMANENT
-999999.0          end_time      Time when embedding ends.
Not used when temporal_type is PERMANENT
#=====
# Thermcpl@
#-----
BOUND          embedded_type
11         boundary_id          Boundary identifier (from
boundary.in) that defines the boundary on which embedding is to be added.
4          embed_scale          Defines the level of
refinement for embedding. Represents the value of n in dx_base/2^n.
1          num_embed            Number of layers of
embedding (at the specified embed_scale) to be added to the boundary.
PERMANENT          Temporal type and cyclic
period
-999999.0          start_time    Time when embedding starts.
Not used when temporal_type is PERMANENT
-999999.0          end_time      Time when embedding ends.
Not used when temporal_type is PERMANENT
#=====
# Bosch
#-----
BOUND          embedded_type
10         boundary_id          Boundary identifier (from
boundary.in) that defines the boundary on which embedding is to be added.
3          embed_scale          Defines the level of
refinement for embedding. Represents the value of n in dx_base/2^n.
2          num_embed            Number of layers of
embedding (at the specified embed_scale) to be added to the boundary.
PERMANENT          Temporal type and cyclic
period

```

```

-999999.0          start_time          Time when embedding starts.
Not used when temporal_type is PERMANENT
-999999.0          end_time            Time when embedding ends.
Not used when temporal_type is PERMANENT
#=====
# Press
#-----
BOUND              embedded_type
12                 boundary_id        Boundary identifier (from
boundary.in) that defines the boundary on which embedding is to be added.
3                 embed_scale        Defines the level of
refinement for embedding. Represents the value of n in dx_base/2^n.
2                 num_embed          Number of layers of
embedding (at the specified embed_scale) to be added to the boundary.
PERMANENT          Temporal type and cyclic
period
-999999.0          start_time          Time when embedding starts.
Not used when temporal_type is PERMANENT
-999999.0          end_time            Time when embedding ends.
Not used when temporal_type is PERMANENT

```

gridscale.in

```
#!/csi_version=1.4.1
```

```
#=====
```

```
0 num_gridscale
```

initialize.in

```
#!/csi_version=1.4.1
#=====

1          numregions          Number of regions
#-----
# MixingBoxRegion
#-----
0          region_id
300.0     temp_init           Initial temperature in the
region (K)
101325.0  pres_init          Initial absolute pressure
in the region (Pa)
1.0       tke_init           Initial turbulent kinetic
energy in the region (m^2/s^2)
10.0     eps_init           Initial tke dissipation
rate in the region (m^2/s^3)
3          numspeciesinit     Number of initialized
species mass fractions to follow. All others set to 0.0.
H2O 0.0023      Name of species and mass
fraction
O2 0.2095      Name of species and mass
fraction
N2 0.7882      Name of species and mass
fraction
0          numpassiveinit     Number of initialized
passive. Names and values should follow.
```

inputs.in

```
#!/csi_version=1.4.1
#=====

surface.dat          surface_filename      The name of surface data
file.
0                   rstrtflg              Flag to indicate if the
simulation is a restart or new run: 0=new run, 1=restart.
1                   rstrtnum              Number added to output
files to identify different restarts.
1                   num_restart_files     Number of restart files to
be saved.
1                   restart_embed_flag    AMR restart embedding flag:
0=do not write AMR embedding to restart file, 1=write AMR embedding to restart
file.
0                   mapflag               Flag to allow mapping in
initial conditions: 0=do not map, 1=map (requires map.in and a data file).
0                   ga_flag               Flag to activate genetic
algorithm: 0=do not use GA, 1=activate GA.
0                   ga_individual         Genetic algorithm individual
number.
0                   ga_generation         Genetic algorithm generation
number.
0                   nohydro               Flag to indicate run type:
0=solve full hydrodynamics (typical), 1=no hydrodynamics--used to check grid.
6                   parallel_scale        Parallel blocks level.
100                 load_cyc              Number of cycles between
load balancing.
1                   reread_input          Flag to indicate whether
or not to re-read inputs, 0=do not re-read, 1=re-read each time step.
0                   screen_print_level    Screen print level
0                   crank_flag            Flag to indicate time
units: 0=seconds, 1=crank angles (used for transient engine simulations).
0.0                 start_time            Start time, in sec.  or
crank angles.
5.0                 end_time              End time, in sec.  or crank
angles.
0.01                twrite_post           Time interval for writing
3D output (s/crank angle/cycle).
10.0                twrite_transfer       Time interval for writing
heat transfer output data (s/crank angle/cycle).
1e-006              twrite_restart        Time interval for writing
restart output (s/crank angle/cycle).
1e-008              twrite_files          Time interval for writing
text data files (s/crank angle/cycle).
0                   wall_output_flag      Flag to write wall output:
0=do not generate wall output, 1=generate wall output.
0                   transfer_flag         Flag to generate FEA heat
transfer data: 0=do not generate FEA data, 1=generate FEA data.
1                   mixing_output_flag    Flag to generate mixing
related output: 0=do not generate output, 1=generate output.
1                   inter_regions_flow_flag Flag to generate inter
region flow output: 0=do not generate output, 1=generate output.
0                   dynamic_flag          Dynamic output options.
1                   timeflag              Flag for variable time-
step: 0=constant time-step (dt) 1=variable time-step (recommended).
```

1e-005	dtstart	Time-step (dt) at the start of the simulation (s).
1e-005	dt	Fixed time-step(s)--only used if timeflag=0.
0.001	dt_max	Maximum time-step (dt).
1e-008	dt_min	Minimum time-step (dt).
1.5	mult_dt_spray	Multiplier used in calculating maximum time-step based on spray.
9999.0	mult_dt_evap	Multiplier used in calculating maximum time-step based on evaporation.
0.5	mult_dt_chem	Multiplier used in calculating time-step based on chemical heat release.
0	dt_coll_mesh_flag	Flag for limiting time-step based on collision mesh: 1=use collision mesh dt limiter, 0=do not use.
1e-012	mult_dt_coll_mesh	Multiplier used in calculating dt_coll_mesh.
1.0	max_cfl_u	Maximum cfl number based on velocity.
2.0	max_cfl_nu	Maximum cfl number based on viscosity.
50.0	max_cfl_mach	Maximum cfl number based on speed of sound.
0.5	fv_upwind_factor_global	Blending factor for finite volume cells. 1.0=first order upwind, 0.5=second order central.
0.5	fv_upwind_factor_mom	Blending factor for momentum finite volume cells. 1.0=first order upwind, 0.5=second order central.
2	fd_order_convect	Order of upwinded finite difference convective stencils.
0	fd_skewness_convect	Skewness of upwinded finite difference convective stencils.
2	fd_order_diff	Order of central finite difference stencils.
1.0	impl	Fraction of the solver that is implicit
30	itmax	Maximum iterations allowed for solving transport equations using an iterative method.
500	itmax_pres	Maximum iterations allowed for solving the pressure equation using an iterative method.
500	itmax_pres_ideal	Ideal number of iterations for pressure equation used to determine time-step control.
1	multigrid_flag	Pressure solver flag: 0 =pressure is solved by SOR, 1=pressure is solved by multigrid method.
15	num_multigrid_relaxations	Maximum number of iterations at each multigrid level.
0.0001	tol_u	Convergence tolerance for the momentum equation.
0.0001	tol_sie	Convergence tolerance for the energy equation.
1e-005	tol_p	Convergence tolerance for the pressure equation.
0.0001	tol_density_transport	Convergence tolerance for the density transport equation.
0.0001	tol_species	Convergence tolerance for species.
0.0001	tol_passive	Convergence tolerance for passives.

0.001	tol_tke	Convergence tolerance for
the turbulent kinetic energy equation.		
0.001	tol_eps	Convergence tolerance for
the turbulent dissipation equation.		
10.0	mult_piso	Convergence tolerance for
PISO iterations.		
0.7	omega_presrat	Under relaxation used in
solving PISO density (pres_rat).		
1.0	omega_u	Under relaxation used in
solving momentum equation.		
1.0	omega_sie	Under relaxation used in
solving specific internal energy (sie) equation.		
1.3	omega_p	Under/over relaxation used
in solving pressure equation.		
0.2	omega_p_steady	Under/over relaxation used
in solving steady pressure.		
1.0	omega_density_transport	Under relaxation used in
solving density transport equation.		
1.0	omega_species	Under relaxation used in
solving species.		
1.0	omega_passive	Under relaxation used in
solving passive.		
0.7	omega_tke	Under relaxation used in
solving tke.		
0.7	omega_eps	Under relaxation used in
solving eps.		
9	max_piso	Maximum number of PISO
iterations.		
2	min_piso	Minimum number of PISO
iterations.		
1.0	conserve	Fraction of the momentum
equation in conservative form.		
1	strict_conserve_flag	
1	rc_flag	Flag for rhie-chow model:
0 =no rhie-chow, 1 =Rhie-Chow.		
1	finitevol_flag	Flag to indicate numerical
scheme:0= finite difference scheme, 1=finite volume scheme.		
1	momentum_solver	Flag to solve momentum:
0=do not solve momentum equation, 1=solve momentum equation.		
1	compressible_flag	Compressible flag:
0=incompressible flow, 1=compressible flow.		
0	phase_flag	Phase flag: 0=gas_phase,
1=liquid_phase,3=gas-liquid phase (VOF).		
0	vof_hric_flag	VOF flag for hric numerical
scheme. 0= do not use hric, 1=use hric		
0	liquid_prop_flag	Liquid properties flag:
0=liquid properties from liquid.dat, 1=constant liquid prop.		
-999999.0	liquid_density	Constant liquid density
(kg/m^3).		
-999999.0	liquid_visc	Constant liquid dynamic
viscosity (N s/m^2).		
-999999.0	liquid_cond	Constant liquid conductivity
(W/m K).		
-999999.0	liquid_c	Constant liquid specific
heat (J/kg K).		
-999999.0	liquid_surf_ten	Constant liquid surface
tension (N/m).		

0	eos_flag	Equation of state: 0=ideal gas, 1=Redlich-Kwong.
133.0	crit_temp	Critical temperature used for Redlich-Kwong (K).
3.77e+006.0	crit_pres	Critical pressure used for Redlich-Kwong (Pa).
1	energy_solver	Flag to solve energy: 0=do not solve energy equation, 1=solve energy equation.
1	species_solver	Flag to solve species: 0=do not solve species equation, 1=solve species equation.
0.9	prandtl	Turbulent Prandtl number.
0.78	schmidt	Turbulent Schmidt number.
0	steady_solver	Flag to indicate transient or steady, 0=transient, 1=steady pressure based, 2=steady density based.
5000	min_cycles_steady	Minimum number of cycles for steady calculations.
10.0	min_temp	Minimum temperature allowed in the domain (K).
60000.0	max_temp	Maximum temperature allowed in the domain (K).
10.0	max_visc	Maximum turbulent dynamic viscosity allowed in the domain (N s/m ²).
0.0	gravity_x	Gravity in X-direction (m/s ²).
0.0	gravity_y	Gravity in Y-direction (m/s ²).
0.0	gravity_z	Gravity in Z-direction (m/s ²).
0	spray_flag	Flag to activate spray modeling: 0=do not use spray model, 1=use (requires spray.in).
1	turb_flag	Flag to activate turbulence modeling: 0=do not use turbulence model, 1=use (requires turbulence.in).
0	comb_flag	Flag to activate combustion modeling: 0=do not use combustion model, 1= use (requires combust.in).
0	source_flag	Flag to activate user-specifies sources: 0=do not use sources, 1=use (requires source.in).
0.01	dx_base	Maximum cell size (dx) in X-direction (m).
0.01	dy_base	Maximum cell size (dy) in Y-direction (m).
0.01	dz_base	Maximum cell size (dz) in Z-direction (m).
0	grid_scale_file_flag	0=do not use gridscale.in, 1=use gridscale.in.
0	grid_scale	Value of n in dx_base/2 ⁿ (only used if grid_scale_file_flag=0).
1	amr_flag	Flag to activate AMR: 0=do not use AMR, 1=use AMR (requires amr.in).
1	embedded_flag	Flag to activate fixed embedding: 0=do not use fixed embedding, 1=use (requires embedded.in).
0	events_flag	Flag to activate events: 0=do not use events, 1= use (requires events.in)
0	composite_flag	Flag to activate composite species: 0=do not use composite species, 1=use (requires a composite.in)
0	wallvalue_flag	Flag to activate wall initial values: 0=do not use, 1=use (requires wallvalue.in).

0 udf_flag Flag to allow user-defined
functions: 0=do not use, 1=use (requires udf.in).

post.in

```
#!/csi_version=1.4.1
#=====

<cells>
density
pressure
temp
velocity
vorticity
xcen[0]
xcen[1]
xcen[2]
idreg
mfrac(H2O)
mfrac(O2)
mfrac(N2)
mfrac(CO2)
mfrac(CO)
eps
tke
tur_length
tur_velocity
visc
```

mech.dat

```
elements  
  n o c h  
end
```

```
species  
  n2 o2 co co2 h2o  
end
```

```
reactions  
end
```

surface.dat

366 366 726
1 0 0 0
2 0 0.09 0
3 0.14 0.09 0
4 0.14 0 0
5 0 0 0.09
6 0 0.09 0.09
7 0.14 0.09 0.09
8 0.14 0 0.09
9 -0.025 0.045 0.045
10 -0.025 0.045 0.02
11 0 0.045 0.02
12 -0.025 0.0501977922704 0.0205463099817
13 0 0.0501977922704 0.0205463099817
14 -0.025 0.0551684160769 0.0221613635589
15 0 0.0551684160769 0.0221613635589
16 -0.025 0.0596946313073 0.0247745751406
17 0 0.0596946313073 0.0247745751406
18 -0.025 0.0635786206369 0.028271734841
19 0 0.0635786206369 0.028271734841
20 -0.025 0.0666506350946 0.0325
21 0 0.0666506350946 0.0325
22 -0.025 0.0687764129074 0.0372745751406
23 0 0.0687764129074 0.0372745751406
24 -0.025 0.0698630473842 0.0423867884183
25 0 0.0698630473842 0.0423867884183
26 -0.025 0.0698630473842 0.0476132115817
27 0 0.0698630473842 0.0476132115817
28 -0.025 0.0687764129074 0.0527254248594
29 0 0.0687764129074 0.0527254248594
30 -0.025 0.0666506350946 0.0575
31 0 0.0666506350946 0.0575
32 -0.025 0.0635786206369 0.061728265159
33 0 0.0635786206369 0.061728265159
34 -0.025 0.0596946313073 0.0652254248594
35 0 0.0596946313073 0.0652254248594
36 -0.025 0.0551684160769 0.0678386364411
37 0 0.0551684160769 0.0678386364411
38 -0.025 0.0501977922704 0.0694536900183
39 0 0.0501977922704 0.0694536900183
40 -0.025 0.045 0.07
41 0 0.045 0.07
42 -0.025 0.0398022077296 0.0694536900183
43 0 0.0398022077296 0.0694536900183
44 -0.025 0.0348315839231 0.0678386364411
45 0 0.0348315839231 0.0678386364411
46 -0.025 0.0303053686927 0.0652254248594
47 0 0.0303053686927 0.0652254248594
48 -0.025 0.0264213793631 0.061728265159
49 0 0.0264213793631 0.061728265159
50 -0.025 0.0233493649054 0.0575
51 0 0.0233493649054 0.0575
52 -0.025 0.0212235870926 0.0527254248594
53 0 0.0212235870926 0.0527254248594
54 -0.025 0.0201369526158 0.0476132115817

55 0 0.0201369526158 0.0476132115817
56 -0.025 0.0201369526158 0.0423867884183
57 0 0.0201369526158 0.0423867884183
58 -0.025 0.0212235870926 0.0372745751406
59 0 0.0212235870926 0.0372745751406
60 -0.025 0.0233493649054 0.0325
61 0 0.0233493649054 0.0325
62 -0.025 0.0264213793631 0.028271734841
63 0 0.0264213793631 0.028271734841
64 -0.025 0.0303053686927 0.0247745751406
65 0 0.0303053686927 0.0247745751406
66 -0.025 0.0348315839231 0.0221613635589
67 0 0.0348315839231 0.0221613635589
68 -0.025 0.0398022077296 0.0205463099817
69 0 0.0398022077296 0.0205463099817
70 0.165 0.045 0.045
71 0.14 0.045 0.02
72 0.165 0.045 0.02
73 0.14 0.0501977922704 0.0205463099817
74 0.165 0.0501977922704 0.0205463099817
75 0.14 0.0551684160769 0.0221613635589
76 0.165 0.0551684160769 0.0221613635589
77 0.14 0.0596946313073 0.0247745751406
78 0.165 0.0596946313073 0.0247745751406
79 0.14 0.0635786206369 0.028271734841
80 0.165 0.0635786206369 0.028271734841
81 0.14 0.0666506350946 0.0325
82 0.165 0.0666506350946 0.0325
83 0.14 0.0687764129074 0.0372745751406
84 0.165 0.0687764129074 0.0372745751406
85 0.14 0.0698630473842 0.0423867884183
86 0.165 0.0698630473842 0.0423867884183
87 0.14 0.0698630473842 0.0476132115817
88 0.165 0.0698630473842 0.0476132115817
89 0.14 0.0687764129074 0.0527254248594
90 0.165 0.0687764129074 0.0527254248594
91 0.14 0.0666506350946 0.0575
92 0.165 0.0666506350946 0.0575
93 0.14 0.0635786206369 0.061728265159
94 0.165 0.0635786206369 0.061728265159
95 0.14 0.0596946313073 0.0652254248594
96 0.165 0.0596946313073 0.0652254248594
97 0.14 0.0551684160769 0.0678386364411
98 0.165 0.0551684160769 0.0678386364411
99 0.14 0.0501977922704 0.0694536900183
100 0.165 0.0501977922704 0.0694536900183
101 0.14 0.045 0.07
102 0.165 0.045 0.07
103 0.14 0.0398022077296 0.0694536900183
104 0.165 0.0398022077296 0.0694536900183
105 0.14 0.0348315839231 0.0678386364411
106 0.165 0.0348315839231 0.0678386364411
107 0.14 0.0303053686927 0.0652254248594
108 0.165 0.0303053686927 0.0652254248594
109 0.14 0.0264213793631 0.061728265159
110 0.165 0.0264213793631 0.061728265159
111 0.14 0.0233493649054 0.0575

112 0.165 0.0233493649054 0.0575
113 0.14 0.0212235870926 0.0527254248594
114 0.165 0.0212235870926 0.0527254248594
115 0.14 0.0201369526158 0.0476132115817
116 0.165 0.0201369526158 0.0476132115817
117 0.14 0.0201369526158 0.0423867884183
118 0.165 0.0201369526158 0.0423867884183
119 0.14 0.0212235870926 0.0372745751406
120 0.165 0.0212235870926 0.0372745751406
121 0.14 0.0233493649054 0.0325
122 0.165 0.0233493649054 0.0325
123 0.14 0.0264213793631 0.028271734841
124 0.165 0.0264213793631 0.028271734841
125 0.14 0.0303053686927 0.0247745751406
126 0.165 0.0303053686927 0.0247745751406
127 0.14 0.0348315839231 0.0221613635589
128 0.165 0.0348315839231 0.0221613635589
129 0.14 0.0398022077296 0.0205463099817
130 0.165 0.0398022077296 0.0205463099817
131 0.025 0.115 0.045
132 0.0315 0.09 0.045
133 0.0315 0.115 0.045
134 0.0302586104634 0.09 0.0411793958601
135 0.0302586104634 0.115 0.0411793958601
136 0.0270086104634 0.09 0.0388181326441
137 0.0270086104634 0.115 0.0388181326441
138 0.0229913895366 0.09 0.0388181326441
139 0.0229913895366 0.115 0.0388181326441
140 0.0197413895366 0.09 0.0411793958601
141 0.0197413895366 0.115 0.0411793958601
142 0.0185 0.09 0.045
143 0.0185 0.115 0.045
144 0.0197413895366 0.09 0.0488206041399
145 0.0197413895366 0.115 0.0488206041399
146 0.0229913895366 0.09 0.0511818673559
147 0.0229913895366 0.115 0.0511818673559
148 0.0270086104634 0.09 0.0511818673559
149 0.0270086104634 0.115 0.0511818673559
150 0.0302586104634 0.09 0.0488206041399
151 0.0302586104634 0.115 0.0488206041399
152 0.025 0.045 0.045
153 0.0265 0 0.045
154 0.0265 0.045 0.045
155 0.0262135254916 5.39871995854e-020 0.0441183221216
156 0.0262135254916 0.045 0.0441183221216
157 0.0254635254916 8.73531238867e-020 0.0435734152256
158 0.0254635254916 0.045 0.0435734152256
159 0.0245364745084 8.73531238867e-020 0.0435734152256
160 0.0245364745084 0.045 0.0435734152256
161 0.0237864745084 5.39871995854e-020 0.0441183221216
162 0.0237864745084 0.045 0.0441183221216
163 0.0235 1.124819837e-035 0.045
164 0.0235 0.045 0.045
165 0.0237864745084 -5.39871995854e-020 0.0458816778784
166 0.0237864745084 0.045 0.0458816778784
167 0.0245364745084 -8.73531238867e-020 0.0464265847744
168 0.0245364745084 0.045 0.0464265847744

169 0.0254635254916 -8.73531238867e-020 0.0464265847744
170 0.0254635254916 0.045 0.0464265847744
171 0.0262135254916 -5.39871995854e-020 0.0458816778784
172 0.0262135254916 0.045 0.0458816778784
173 0.1044 0 0.045
174 0.1044 0.0082 0.045
175 0.10271934955 3.16724904235e-019 0.0398274897798
176 0.10271934955 0.0082 0.0398274897798
177 0.0983193495505 5.12471660135e-019 0.0366307026566
178 0.0983193495505 0.0082 0.0366307026566
179 0.0928806504495 5.12471660135e-019 0.0366307026566
180 0.0928806504495 0.0082 0.0366307026566
181 0.0884806504495 3.16724904235e-019 0.0398274897798
182 0.0884806504495 0.0082 0.0398274897798
183 0.0868 6.59894304371e-035 0.045
184 0.0868 0.0082 0.045
185 0.0884806504495 -3.16724904235e-019 0.0501725102202
186 0.0884806504495 0.0082 0.0501725102202
187 0.0928806504495 -5.12471660135e-019 0.0533692973434
188 0.0928806504495 0.0082 0.0533692973434
189 0.0983193495505 -5.12471660135e-019 0.0533692973434
190 0.0983193495505 0.0082 0.0533692973434
191 0.10271934955 -3.16724904235e-019 0.0501725102202
192 0.10271934955 0.0082 0.0501725102202
193 0.1024 0.0102 0.045
194 0.101101315562 0.0102 0.0410030602844
195 0.0977013155617 0.0102 0.0385328156892
196 0.0934986844383 0.0102 0.0385328156892
197 0.0900986844383 0.0102 0.0410030602844
198 0.0888 0.0102 0.045
199 0.0900986844383 0.0102 0.0489969397156
200 0.0934986844383 0.0102 0.0514671843108
201 0.0977013155617 0.0102 0.0514671843108
202 0.101101315562 0.0102 0.0489969397156
203 0.0989 0.0102 0.0475
204 0.0982697560814 0.0102 0.0455603086674
205 0.0978652475842 0.0202 0.0458542012936
206 0.0966197560814 0.0102 0.0443615134962
207 0.0964652475842 0.0202 0.0448370417544
208 0.0945802439186 0.0102 0.0443615134962
209 0.0947347524158 0.0202 0.0448370417544
210 0.0929302439186 0.0102 0.0455603086674
211 0.0933347524158 0.0202 0.0458542012936
212 0.0923 0.0102 0.0475
213 0.0928 0.0202 0.0475
214 0.0929302439186 0.0102 0.0494396913326
215 0.0933347524158 0.0202 0.0491457987064
216 0.0945802439186 0.0102 0.0506384865038
217 0.0966197560814 0.0102 0.0506384865038
218 0.0964652475842 0.0202 0.0501629582456
219 0.0982697560814 0.0102 0.0494396913326
220 0.0956 0.0222 0.0475
221 0.0984 0.0202 0.0475
222 0.097 0.0222 0.0475
223 0.0967326237921 0.0222 0.0466771006468
224 0.0960326237921 0.0222 0.0461685208772
225 0.0951673762079 0.0222 0.0461685208772

226 0.0944673762079 0.0222 0.0466771006468
227 0.0942 0.0222 0.0475
228 0.0944673762079 0.0222 0.0483228993532
229 0.0947347524158 0.0202 0.0501629582456
230 0.0951673762079 0.0222 0.0488314791228
231 0.0960326237921 0.0222 0.0488314791228
232 0.0978652475842 0.0202 0.0491457987064
233 0.0967326237921 0.0222 0.0483228993532
234 0.025 0.045 0.092
235 0.0315 0.045 0.09
236 0.0315 0.045 0.092
237 0.0302586104634 0.0488206041399 0.09
238 0.0302586104634 0.0488206041399 0.092
239 0.0270086104634 0.0511818673559 0.09
240 0.0270086104634 0.0511818673559 0.092
241 0.0229913895366 0.0511818673559 0.09
242 0.0229913895366 0.0511818673559 0.092
243 0.0197413895366 0.0488206041399 0.09
244 0.0197413895366 0.0488206041399 0.092
245 0.0185 0.045 0.09
246 0.0185 0.045 0.092
247 0.0197413895366 0.0411793958601 0.09
248 0.0197413895366 0.0411793958601 0.092
249 0.0229913895366 0.0388181326441 0.09
250 0.0229913895366 0.0388181326441 0.092
251 0.0270086104634 0.0388181326441 0.09
252 0.0270086104634 0.0388181326441 0.092
253 0.0302586104634 0.0411793958601 0.09
254 0.0302586104634 0.0411793958601 0.092
255 0.07 0 0
256 0.07 0.09 0
257 0.07 0 0.09
258 0.07 0.09 0.09
259 0.12 0 0.045
260 0.12 0.0083 0.045
261 0.1168 3.39384076392e-019 0.0394574374158
262 0.1168 0.0083 0.0394574374158
263 0.1104 3.39384076392e-019 0.0394574374158
264 0.1104 0.0083 0.0394574374158
265 0.1072 4.79923130452e-035 0.045
266 0.1072 0.0083 0.045
267 0.1104 -3.39384076392e-019 0.0505425625842
268 0.1104 0.0083 0.0505425625842
269 0.1168 -3.39384076392e-019 0.0505425625842
270 0.1168 0.0083 0.0505425625842
271 0.084 0 0.045
272 0.084 0.0083 0.045
273 0.0808 3.39384076392e-019 0.0394574374158
274 0.0808 0.0083 0.0394574374158
275 0.0744 3.39384076392e-019 0.0394574374158
276 0.0744 0.0083 0.0394574374158
277 0.0712 4.79923130452e-035 0.045
278 0.0712 0.0083 0.045
279 0.0744 -3.39384076392e-019 0.0505425625842
280 0.0744 0.0083 0.0505425625842
281 0.0808 -3.39384076392e-019 0.0505425625842
282 0.0808 0.0083 0.0505425625842

283 0.0776 0.021 0.045
284 0.0808 0.0083 0.045
285 0.0808 0.021 0.045
286 0.080188854382 0.0083 0.0431190871927
287 0.080188854382 0.021 0.0431190871927
288 0.078588854382 0.0083 0.0419566191479
289 0.078588854382 0.021 0.0419566191479
290 0.076611145618 0.0083 0.0419566191479
291 0.076611145618 0.021 0.0419566191479
292 0.075011145618 0.0083 0.0431190871927
293 0.075011145618 0.021 0.0431190871927
294 0.0744 0.0083 0.045
295 0.0744 0.021 0.045
296 0.075011145618 0.0083 0.0468809128073
297 0.075011145618 0.021 0.0468809128073
298 0.076611145618 0.0083 0.0480433808521
299 0.076611145618 0.021 0.0480433808521
300 0.078588854382 0.0083 0.0480433808521
301 0.078588854382 0.021 0.0480433808521
302 0.080188854382 0.0083 0.0468809128073
303 0.080188854382 0.021 0.0468809128073
304 0.1136 0.021 0.045
305 0.1168 0.0083 0.045
306 0.1168 0.021 0.045
307 0.116188854382 0.0083 0.0431190871927
308 0.116188854382 0.021 0.0431190871927
309 0.114588854382 0.0083 0.0419566191479
310 0.114588854382 0.021 0.0419566191479
311 0.112611145618 0.0083 0.0419566191479
312 0.112611145618 0.021 0.0419566191479
313 0.111011145618 0.0083 0.0431190871927
314 0.111011145618 0.021 0.0431190871927
315 0.1104 0.0083 0.045
316 0.1104 0.021 0.045
317 0.111011145618 0.0083 0.0468809128073
318 0.111011145618 0.021 0.0468809128073
319 0.112611145618 0.0083 0.0480433808521
320 0.112611145618 0.021 0.0480433808521
321 0.114588854382 0.0083 0.0480433808521
322 0.114588854382 0.021 0.0480433808521
323 0.116188854382 0.0083 0.0468809128073
324 0.116188854382 0.021 0.0468809128073
325 0 0 0
326 0.1035 0.045 0.09
327 0.1035 0.045 0.088
328 0.105619911362 0.0515244163004 0.09
329 0.105619911362 0.0515244163004 0.088
330 0.111169911362 0.0555567273309 0.09
331 0.111169911362 0.0555567273309 0.088
332 0.118030088638 0.0555567273309 0.09
333 0.118030088638 0.0555567273309 0.088
334 0.123580088638 0.0515244163004 0.09
335 0.123580088638 0.0515244163004 0.088
336 0.1257 0.045 0.09
337 0.1257 0.045 0.088
338 0.123580088638 0.0384755836996 0.09
339 0.123580088638 0.0384755836996 0.088

340 0.118030088638 0.0344432726691 0.09
341 0.118030088638 0.0344432726691 0.088
342 0.111169911362 0.0344432726691 0.09
343 0.111169911362 0.0344432726691 0.088
344 0.105619911362 0.0384755836996 0.09
345 0.105619911362 0.0384755836996 0.088
346 0.1146 0.045 0.098
347 0.121 0.045 0.088
348 0.121 0.045 0.098
349 0.119777708764 0.0487618256147 0.088
350 0.119777708764 0.0487618256147 0.098
351 0.116577708764 0.0510867617043 0.088
352 0.116577708764 0.0510867617043 0.098
353 0.112622291236 0.0510867617043 0.088
354 0.112622291236 0.0510867617043 0.098
355 0.109422291236 0.0487618256147 0.088
356 0.109422291236 0.0487618256147 0.098
357 0.1082 0.045 0.088
358 0.1082 0.045 0.098
359 0.109422291236 0.0412381743853 0.088
360 0.109422291236 0.0412381743853 0.098
361 0.112622291236 0.0389132382957 0.088
362 0.112622291236 0.0389132382957 0.098
363 0.116577708764 0.0389132382957 0.088
364 0.116577708764 0.0389132382957 0.098
365 0.119777708764 0.0412381743853 0.088
366 0.119777708764 0.0412381743853 0.098
9 10 12 6
9 12 14 6
9 14 16 6
9 16 18 6
9 18 20 6
9 20 22 6
9 22 24 6
9 24 26 6
9 26 28 6
9 28 30 6
9 30 32 6
9 32 34 6
9 34 36 6
9 36 38 6
9 38 40 6
9 40 42 6
9 42 44 6
9 44 46 6
9 46 48 6
9 48 50 6
9 50 52 6
9 52 54 6
9 54 56 6
9 56 58 6
9 58 60 6
9 60 62 6
9 62 64 6
9 64 66 6
9 66 68 6
9 68 10 6

10 11 13 2
10 13 12 2
12 13 15 2
12 15 14 2
14 15 17 2
14 17 16 2
16 17 19 2
16 19 18 2
18 19 21 2
18 21 20 2
20 21 23 2
20 23 22 2
22 23 25 2
22 25 24 2
24 25 27 2
24 27 26 2
26 27 29 2
26 29 28 2
28 29 31 2
28 31 30 2
30 31 33 2
30 33 32 2
32 33 35 2
32 35 34 2
34 35 37 2
34 37 36 2
36 37 39 2
36 39 38 2
38 39 41 2
38 41 40 2
40 41 43 2
40 43 42 2
42 43 45 2
42 45 44 2
44 45 47 2
44 47 46 2
46 47 49 2
46 49 48 2
48 49 51 2
48 51 50 2
50 51 53 2
50 53 52 2
52 53 55 2
52 55 54 2
54 55 57 2
54 57 56 2
56 57 59 2
56 59 58 2
58 59 61 2
58 61 60 2
60 61 63 2
60 63 62 2
62 63 65 2
62 65 64 2
64 65 67 2
64 67 66 2
66 67 69 2

66 69 68 2
68 69 11 2
68 11 10 2
72 70 74 9
74 70 76 9
76 70 78 9
78 70 80 9
80 70 82 9
82 70 84 9
84 70 86 9
86 70 88 9
88 70 90 9
90 70 92 9
92 70 94 9
94 70 96 9
96 70 98 9
98 70 100 9
100 70 102 9
102 70 104 9
104 70 106 9
106 70 108 9
108 70 110 9
110 70 112 9
112 70 114 9
114 70 116 9
116 70 118 9
118 70 120 9
120 70 122 9
122 70 124 9
124 70 126 9
126 70 128 9
128 70 130 9
130 70 72 9
71 72 74 5
71 74 73 5
73 74 76 5
73 76 75 5
75 76 78 5
75 78 77 5
77 78 80 5
77 80 79 5
79 80 82 5
79 82 81 5
81 82 84 5
81 84 83 5
83 84 86 5
83 86 85 5
85 86 88 5
85 88 87 5
87 88 90 5
87 90 89 5
89 90 92 5
89 92 91 5
91 92 94 5
91 94 93 5
93 94 96 5
93 96 95 5

95 96 98 5
95 98 97 5
97 98 100 5
97 100 99 5
99 100 102 5
99 102 101 5
101 102 104 5
101 104 103 5
103 104 106 5
103 106 105 5
105 106 108 5
105 108 107 5
107 108 110 5
107 110 109 5
109 110 112 5
109 112 111 5
111 112 114 5
111 114 113 5
113 114 116 5
113 116 115 5
115 116 118 5
115 118 117 5
117 118 120 5
117 120 119 5
119 120 122 5
119 122 121 5
121 122 124 5
121 124 123 5
123 124 126 5
123 126 125 5
125 126 128 5
125 128 127 5
127 128 130 5
127 130 129 5
129 130 72 5
129 72 71 5
133 131 135 7
135 131 137 7
137 131 139 7
139 131 141 7
141 131 143 7
143 131 145 7
145 131 147 7
147 131 149 7
149 131 151 7
151 131 133 7
132 133 135 3
132 135 134 3
134 135 137 3
134 137 136 3
136 137 139 3
136 139 138 3
138 139 141 3
138 141 140 3
140 141 143 3
140 143 142 3
142 143 145 3

142 145 144 3
144 145 147 3
144 147 146 3
146 147 149 3
146 149 148 3
148 149 151 3
148 151 150 3
150 151 133 3
150 133 132 3
152 154 156 11
152 156 158 11
152 158 160 11
152 160 162 11
152 162 164 11
152 164 166 11
152 166 168 11
152 168 170 11
152 170 172 11
152 172 154 11
154 153 156 11
156 153 155 11
156 155 158 11
158 155 157 11
158 157 160 11
160 157 159 11
160 159 162 11
162 159 161 11
162 161 164 11
164 161 163 11
164 163 166 11
166 163 165 11
166 165 168 11
168 165 167 11
168 167 170 11
170 167 169 11
170 169 172 11
172 169 171 11
172 171 154 11
154 171 153 11
174 173 176 10
176 173 175 10
176 175 178 10
178 175 177 10
178 177 180 10
180 177 179 10
180 179 182 10
182 179 181 10
182 181 184 10
184 181 183 10
184 183 186 10
186 183 185 10
186 185 188 10
188 185 187 10
188 187 190 10
190 187 189 10
190 189 192 10
192 189 191 10

192 191 174 10
174 191 173 10
193 174 194 10
194 174 176 10
194 176 195 10
195 176 178 10
195 178 196 10
196 178 180 10
196 180 197 10
197 180 182 10
197 182 198 10
198 182 184 10
198 184 199 10
199 184 186 10
199 186 200 10
200 186 188 10
200 188 190 10
200 190 201 10
201 190 202 10
202 190 192 10
202 192 193 10
193 192 174 10
221 203 205 10
205 203 204 10
205 204 207 10
207 204 206 10
207 206 209 10
209 206 208 10
209 208 211 10
211 208 210 10
211 210 213 10
213 210 212 10
213 212 215 10
215 212 214 10
215 214 229 10
229 214 216 10
229 216 218 10
218 216 217 10
218 217 232 10
232 217 219 10
232 219 221 10
221 219 203 10
220 222 223 10
220 223 224 10
220 224 225 10
220 225 226 10
220 226 227 10
220 227 228 10
220 228 230 10
220 230 231 10
220 231 233 10
220 233 222 10
222 221 223 10
223 221 205 10
223 205 224 10
224 205 207 10
224 207 225 10

225 207 209 10
225 209 226 10
226 209 211 10
226 211 227 10
227 211 213 10
227 213 215 10
227 215 228 10
228 215 230 10
230 215 229 10
230 229 231 10
231 229 218 10
231 218 233 10
233 218 232 10
233 232 222 10
222 232 221 10
208 195 196 10
208 196 210 10
210 196 197 10
210 197 212 10
212 197 198 10
195 208 206 10
195 206 194 10
194 206 204 10
193 194 204 10
193 204 203 10
193 203 202 10
203 219 202 10
202 219 201 10
201 219 217 10
201 217 200 10
200 217 216 10
200 216 199 10
216 214 199 10
199 214 198 10
212 198 214 10
236 234 238 8
238 234 240 8
240 234 242 8
242 234 244 8
244 234 246 8
246 234 248 8
248 234 250 8
250 234 252 8
252 234 254 8
254 234 236 8
235 236 238 4
235 238 237 4
237 238 240 4
237 240 239 4
239 240 242 4
239 242 241 4
241 242 244 4
241 244 243 4
243 244 246 4
243 246 245 4
245 246 248 4
245 248 247 4

247 248 250 4
247 250 249 4
249 250 252 4
249 252 251 4
251 252 254 4
251 254 253 4
253 254 236 4
253 236 235 4
7 258 256 1
3 7 256 1
148 258 6 1
148 150 258 1
150 132 258 1
258 132 256 1
132 134 256 1
256 134 136 1
256 136 2 1
136 138 2 1
2 138 140 1
2 140 142 1
2 142 6 1
6 142 144 1
144 146 6 1
6 146 148 1
6 27 2 1
29 27 6 1
29 6 31 1
33 31 6 1
33 6 35 1
37 35 6 1
6 39 37 1
41 39 6 1
6 5 41 1
43 41 5 1
45 43 5 1
45 5 47 1
49 47 5 1
49 5 51 1
51 5 53 1
55 53 5 1
55 5 57 1
57 5 1 1
57 1 59 1
61 59 1 1
61 1 63 1
65 63 1 1
65 1 67 1
67 1 69 1
11 69 1 1
11 1 2 1
11 2 13 1
15 13 2 1
15 2 17 1
17 2 19 1
21 19 2 1
21 2 23 1
25 23 2 1

25 2 27 1
1 255 2 1
2 255 256 1
256 255 4 1
256 4 3 1
157 255 1 1
157 1 159 1
159 1 161 1
161 1 163 1
163 1 5 1
163 5 165 1
167 165 5 1
169 167 5 1
169 5 257 1
169 257 171 1
153 171 257 1
153 257 255 1
155 153 255 1
155 255 157 1
7 3 85 1
85 3 83 1
81 83 3 1
81 3 79 1
77 79 3 1
77 3 75 1
73 75 3 1
73 3 71 1
71 3 4 1
129 71 4 1
129 4 127 1
125 127 4 1
125 4 123 1
121 123 4 1
121 4 119 1
117 119 4 1
4 8 117 1
115 117 8 1
115 8 113 1
111 113 8 1
111 8 109 1
107 109 8 1
107 8 105 1
103 105 8 1
101 103 8 1
101 8 7 1
101 7 99 1
97 99 7 1
97 7 95 1
95 7 93 1
91 93 7 1
91 7 89 1
87 89 7 1
87 7 85 1
258 239 6 1
239 258 237 1
237 258 235 1
239 241 6 1

241 243 6 1
6 243 245 1
6 245 5 1
245 247 5 1
247 249 5 1
249 251 5 1
5 251 257 1
251 253 257 1
253 235 257 1
257 235 258 1
260 259 262 10
262 259 261 10
262 261 264 10
264 261 263 10
264 263 266 10
266 263 265 10
266 265 268 10
268 265 267 10
268 267 270 10
270 267 269 10
270 269 260 10
260 269 259 10
272 271 274 10
274 271 273 10
274 273 276 10
276 273 275 10
276 275 278 10
278 275 277 10
278 277 280 10
280 277 279 10
280 279 282 10
282 279 281 10
282 281 272 10
272 281 271 10
283 285 287 10
283 287 289 10
283 289 291 10
283 291 293 10
283 293 295 10
283 295 297 10
283 297 299 10
283 299 301 10
283 301 303 10
283 303 285 10
285 284 287 10
287 284 286 10
287 286 289 10
289 286 288 10
289 288 291 10
291 288 290 10
291 290 293 10
293 290 292 10
293 292 295 10
295 292 294 10
295 294 297 10
297 294 296 10
297 296 299 10

299 296 298 10
299 298 301 10
301 298 300 10
301 300 303 10
303 300 302 10
303 302 285 10
285 302 284 10
304 306 308 10
304 308 310 10
304 310 312 10
304 312 314 10
304 314 316 10
304 316 318 10
304 318 320 10
304 320 322 10
304 322 324 10
304 324 306 10
306 305 308 10
308 305 307 10
308 307 310 10
310 307 309 10
310 309 312 10
312 309 311 10
312 311 314 10
314 311 313 10
314 313 316 10
316 313 315 10
316 315 318 10
318 315 317 10
318 317 320 10
320 317 319 10
320 319 322 10
322 319 321 10
322 321 324 10
324 321 323 10
324 323 306 10
306 323 305 10
307 260 262 10
307 262 309 10
309 262 311 10
264 311 262 10
307 305 260 10
260 305 323 10
323 270 260 10
323 321 270 10
270 321 319 10
270 319 268 10
317 268 319 10
268 317 266 10
317 315 266 10
315 313 266 10
264 266 313 10
264 313 311 10
286 272 274 10
286 274 288 10
276 288 274 10
290 288 276 10

276 292 290 10
278 292 276 10
294 292 278 10
278 296 294 10
278 280 296 10
298 296 280 10
280 300 298 10
282 300 280 10
300 282 302 10
302 282 272 10
302 272 284 10
286 284 272 10
327 326 329 12
329 326 328 12
329 328 331 12
331 328 330 12
331 330 333 12
333 330 332 12
333 332 335 12
335 332 334 12
335 334 337 12
337 334 336 12
337 336 339 12
339 336 338 12
339 338 341 12
341 338 340 12
341 340 343 12
343 340 342 12
343 342 345 12
345 342 344 12
345 344 327 12
327 344 326 12
348 346 350 12
350 346 352 12
352 346 354 12
354 346 356 12
356 346 358 12
358 346 360 12
360 346 362 12
362 346 364 12
364 346 366 12
366 346 348 12
347 348 350 12
347 350 349 12
349 350 352 12
349 352 351 12
351 352 354 12
351 354 353 12
353 354 356 12
353 356 355 12
355 356 358 12
355 358 357 12
357 358 360 12
357 360 359 12
359 360 362 12
359 362 361 12
361 362 364 12

361 364 363 12
363 364 366 12
363 366 365 12
365 366 348 12
365 348 347 12
335 349 351 12
335 351 333 12
353 333 351 12
331 333 353 12
353 355 331 12
329 331 355 12
355 357 329 12
327 329 357 12
357 359 327 12
327 359 345 12
361 345 359 12
345 361 343 12
343 361 363 12
363 341 343 12
363 365 341 12
339 341 365 12
365 347 339 12
337 339 347 12
347 349 337 12
335 337 349 12
7 330 258 1
258 330 328 1
330 7 332 1
332 7 334 1
336 334 7 1
7 8 336 1
338 336 8 1
338 8 340 1
340 8 342 1
342 8 257 1
342 257 344 1
326 344 257 1
326 257 258 1
326 258 328 1
4 259 8 1
8 259 269 1
269 267 8 1
8 267 189 1
8 189 257 1
257 189 187 1
187 281 257 1
257 281 279 1
279 277 257 1
255 257 277 1
277 275 255 1
255 275 273 1
273 179 255 1
255 179 177 1
255 177 4 1
4 177 263 1
263 261 4 1
4 261 259 1

265 173 267 1
267 173 191 1
267 191 189 1
173 265 263 1
173 263 175 1
177 175 263 1
183 273 271 1
271 281 183 1
183 281 185 1
187 185 281 1
273 183 181 1
181 179 273 1

2. Reactive Constant Volume Bomb Simulations

The following files were common to all the constant volume bomb simulations presented in Chapter IV, Section C with two exceptions. Not listed among these files is the mech.dat file necessary to model the chemical kinetics of combustion. That file is the CHEMKIN-formatted input file containing the list of all reactions part of the mechanism. The two versions of mech.dat are listed in full in Appendices A1 and A2. The other exception is a simple modification to the initialize.in file which defines the chamber's initial conditions, specifically the initial mass fractions of oxygen (O_2), nitrogen (N_2), and propane (C_3H_8) to match the desired equivalence ratio. As mentioned in the prior section, the gas.dat and therm.dat files are also not included due to their length considering no modification was made and they are typically provided with or are integrated into the CFD solver being used.

amr.in

```

#!csi_version=2.2.0
#=====

100                amr_cycle_steady                Number of cycles between
AMR calculations.
100000            amr_max_cells                    Maximum number of cells in
the entire domain.
1                amr_min_cells                    Minimum number of cells in
the entire domain.
#=====
# Amr Group 1
#-----
1                amr_num_regions                Number of AMR regions.
0                amr_active_region                Active AMR region.
##### Velocity #####
0                amr_vel_flag                    Enable AMR based on velocity
conditions.
3                amr_embed_vel_scale                Maximum embedding level
for velocity.
1.0              amr_vel_sgs_embed                Minimum velocity above
which a cell will be embedded.
PERMANENT                Temporal type and cyclic
period.
-999999.0          amr_vel_start_time                Time to start the AMR.
-999999.0          amr_vel_end_time                Time to end the AMR.
50                amr_parcel_embed                Maximum number of parcels
in a cell before CONVERGE embeds a cell using AMR.
##### Temperature #####
0                amr_temp_flag                    Enable AMR based on
temperature conditions.
3                amr_embed_temp_scale                Maximum embedding level
for temperature.
20.0              amr_temp_sgs_embed                Minimum temperature above
which a cell will be embedded.
PERMANENT                Temporal type and cyclic
period.
-999999.0          amr_temp_start_time                Time to start the AMR.
-999999.0          amr_temp_end_time                Time to end the AMR.
##### Void fraction #####
0                amr_void_flag                    Enable AMR based on Void
fraction conditions.
3                amr_embed_void_scale                Maximum embedding level
for Void fraction.
0.001            amr_void_sgs_embed                Minimum VOF above which a
cell will be embedded.
PERMANENT                Temporal type and cyclic
period.
-999999.0          amr_void_start_time                Time to start the AMR.
-999999.0          amr_void_end_time                Time to end the AMR.
##### Species data #####
1                amr_species_flag                Enable AMR based on species
conditions.
5                amr_embed_species_scale                Maximum embedding level
for species.

```

```

1                amr_num_species                Number of species to
trigger AMR.
C3H8                species_name                Species name.
0.00025            amr_species_sgs_embed        Minimum mass fraction of
the species that will trigger AMR.
PERMANENT                Temporal type and cyclic
period.
-999999            amr_species_start_time        Time to start the AMR.
-999999            amr_species_end_time        Time to end the AMR.
##### Passive data #####
0                amr_passive_flag                Enable AMR based on passives
conditions.
3                amr_embed_passive_scale        Maximum embedding level
for passives.
1                amr_num_passive                Number of passives to
trigger AMR.
NOT_USED            passive_name                Passive name.
1.0e-6            amr_passive_sgs_embed        Minimum mass fraction of
the passive that will trigger AMR.
PERMANENT                Temporal type and cyclic
period.
0.0                amr_passive_start_time        Time to start the AMR.
10.0              amr_passive_end_time        Time to end the AMR.
#=====
# Boundary data
#-----
0                amr_num_bounds                Number of boundary on which
CONVERGE will use AMR.

```

boundary.in

```
#!/csi_version=2.2.0
#=====

2  # Number of boundaries defined
#-----
1      Wall
WALL      FIXED      Stationary
roughness  0.0        0.5
velocity   Law_of_wall 0.0 0.0 0.0
pressure   Neumann     0.0
temperature Law_of_wall 300.0
species    Neumann     0.0
passive    Neumann     0.0
tke        Neumann     0.0
eps        Dirichlet  0.0
region     0
#-----
2      Symmetry
SYMMETRY
region     0
```

combust.in

```
#!/csi_version=2.2.0
#=====

C3H8          fuel_name          Fuel species name.
0.25          omega_combust_steady Under-relaxation for
steady-state combustion.
1            sage_flag          SAGE detailed chemistry
model flag: 0=no SAGE model, 1=activate SAGE model.
0            sage_ode_solver     0=CVODES with dense
solver (recommended for up to 100 species); 1=CVODES with preconditioned
iterative solver.
600.0        sage_tcut         Minimum cell temperature
(K) for SAGE activation.
1e-008       sage_hcmin        Minimum HC+CO species
mole fraction for SAGE activation.
PERMANENT    Temporal type and cyclic
period.
-999999.0    sage_tstart       SAGE start time in
seconds or crank angles.
-999999.0    sage_tend        SAGE end time in seconds
or crank angles.
0            sage_region_flag   0=SAGE is not region
dependent, 1=SAGE is region dependent.
0            sage_solve_temp    SAGE temperature
solution flag. 0=do not re-solve temperature unless its change exceeds
sage_delta_temp, 1=always re-solve temperature.
2.0          sage_delta_temp    Magnitude of the
temperature change (K), above which temperature will be re-solved in SAGE.
1            sage_analyt_jac    Flag to determine if
Jacobian matrix is solved analytically in the SAGE solver: 0=solve Jacobian
matrix numerically, 1=solve Jacobian matrix analytically.
0.0001       sage_rel_tol       Relative iteration error
for each species in the SAGE solver.
1e-014       sage_abs_tol       Absolute iteration error
for each species in the SAGE solver.
1.0          sage_reac_mult     Scaling factor of
reaction rates in the SAGE solver.
0            sage_dmr_flag       Use dynamic mechanism
reduction (sage_dmr.in is required).
0            multizone_flag     0=do not use multi zone
model, 1=use multi zone model.
2            multizone_bin_dim   Dimension of multizone.
5.0          multizone_tol_temp Temperature bin size (K)
for multizone chemistry.
0.05         multizone_tol_phi  Equivalence ratio bin
size for multizone chemistry.
1            multizone_nox_flag  0=default, 1=improves
the accuracy of NOx emissions prediction in the multizone model.
0            multizone_output_flag 0=no additional output
for multizone chemistry, 1=activate additional output for multizone
chemistry.
0            multizone_hr_map_flag Use heat release
mapping.
0            ceq_flag           CEQ equilibrium solver
flag: 0=no CEQ, 1=activate CEQ, 2=activate CEQ with mixing time scale.
```

0	ceq_subsp_flag	Define CEQ species
subset (ceq_species.in is required).		
600.0	ceq_tcut	Minimum cell temperature
(K) for CEQ activation.		
1e-014	ceq_hcmin	Minimum HC+CO species
mole fraction for CEQ activation.		
0	ctc_flag	Characteristic Time
Combustion (CTC) model flag: 0=no CTC model, 1=activate CTC model.		
-999999.0	ctc_init_time	Time for CTC model
initialization(s/deg).		
1	ctc_mult_scale	Multi-scale CTC model
flag: 0=single scale CTC model, 1=multi-scale CTC model.		
0.2	tau_fraction	Multi-scale CTC time-
scale fraction.		
0.1	cm2	CTC turbulent time-scale
constant.		
7680000000.0	denomc	CTC chemical time-scale
constant.		
1000.0	tchop	Transition temperature
(K) for Shell/CTC models.		
0	shell_flag	Shell ignition model
flag: 0=no Shell model, 1=activate conserving Shell model, 2=activate		
original Shell model.		
125000.0	af04	Shell model ignition
delay parameter.		
0	nox_flag	Extended Zeldovich NOx
model flag: 0=no NOx model, 1=activate NOx model.		
0	soot_hiroy_flag	Hiroyasu/NSC soot model
flag: 0=no soot model, 1=activate soot model.		
350.0	soot_asf	Soot formation pre-
exponential factor (1/(s bar^0.5)).		
12500.0	soot_esf	Soot formation
activation energy parameter (cal/gmol).		
2.5e-006	soot_diam	Soot particle diameter
(cm).		
1.0	soot_oxid_fac	Soot oxidation model
factor.		
2.0	soot_density	Soot density (g/cm^3).
0	soot_form_flag	0=use the sum of the
hydrocarbon species as the soot formation species, 1=use C2H2 as the soot		
formation species.		
0	soot_mauss_mr_flag	Particle Moment
Rate(PMR) soot model flag: 0=no PMR model, 1=active PMR model.		
2	mauss_num_mom	Number of moments to be
solved.		
2.25	surfacegrowth_model	Describes the surface
reactions soot dependence:-1=no surface reactions, 0.0=function of number		
density, 2.0=function of surface area, 2.25= d**2.25(typical for diesel),		
3.0=function of soot volume.		
0.3	alpha_corrector	Part of sites on soot
surface available for surface reactions.		
0	soot_sectrate_flag	Particle Size Mimic(PSM)
soot model flag:0=no PSM model, 1=active PSM model.		
20	num_sootsections	Number of section(soot
volume fraction) to be solved.		
5	num_subsections	Number of sub-sections
for each section.		

2.0	sgmodell1	Describes the surface reactions soot dependence in the range of PAH to sgSizeLimit.
2.25	sgmodell2	Describes the surface reactions soot dependence in the range of sgSizeLimit to biggestSoot.
0.95	alphacorr1	Part of sites on soot surface available for surface reactions in the range of PAH to sgSizeLimit.
0.3	alphacorr2	Part of sites on soot surface available for surface reactions in the range of sgSizeLimit to biggestSoot.
0	custom_soot_precursor_flag	0=Don't use soot precursor; 1=Use soot precursor (soot_precursor.dat is required).
0	soot_condensation_flag	Condensation submodel flag for both Mauss and PSM model.
1.0	hr_time	Heat release rate time (s/crank).
0	mix_frac_flag	0=do not calculate mixture fraction, 1=calculate mixture fraction.
0	mix_frac_var_flag	0=do not calculate mixture fraction variance, 1=calculate mixture fraction variance.
2.0	c_chi	Constant used in modeling of the scalar dissipation in the mixture fraction variance calculation.
0	g_eqn_flag	G-Eqn model flag: 0=no model, 1=equil. inside flame, 2=sage outside flame and equil. inside flame, 3=sage inside and outside flame.
-0.1	g_eqn_init_value	Initial G-value.
1	g_eqn_grad_g_flag	0= Explicit method; 1=Sussman method.
0	laminar_flamespeed_flag	Laminar flamespeed flag: 0=constant, 1=Metghalchi, 2=Gulder.
-999999.0	constant_laminar_flamespeed	Constant laminar flamespeed (m/s).
298.0	laminar_flamespeed_temp_ref	Reference temperature.
101325.0	laminar_flamespeed_pres_ref	Reference pressure.
0.2632	met_bm	Metghalchi constant 1 (m/s).
-0.8472	met_b2	Metghalchi constant 2 (m/s).
1.13	met_equiv_ratio	Metghalchi ref. equivalence ratio.
0.0	g_eqn_dilution	Metghalchi dilution species mass fraction.
0.4658	gulder_omega	Gulder coefficient for calculating laminar flame speed.
-0.326	gulder_eta	Gulder coefficient for calculating laminar flame speed.
4.48	gulder_xi	Gulder coefficient for calculating laminar flame speed.
1.2	g_eqn_temp_exponent	Temperature exponent constant.
-0.26	g_eqn_pres_exponent	Pressure exponent constant.
0	g_eqn_turb_flamespeed_flag	Turbulent flame-speed calculation flag:0= don't use g_prime, 1=use_g_prime.
0.78	st_a4	Constant for turbulent flame speed calculation(a4).

2.0	st_b1	Constant for turbulent
flame speed calculation(b1).		
1.0	st_b3	Constant for turbulent
flame speed calculation(b3).		
2.0	g_prime_cs	Constant used for
calculating g_prime equation dissipation.		
3000.0	tcut_g_eqn	Temperature above which
G is initialized.		
0	g_eqn_spark_flag	Flag for g_eqn kernel
ignition model: 0= don't use, 1= use kernel igniton model.		
0.3	spark_eff	Spark efficiency used
for kernel model.		
100	g_eqn_num_kernel_init	Number of spark kernels
initialized for kernel model.		
80.0	karlovitz_ig	Karlovitz ignition
number.		
0	g_eqn_unburned_temp_flag	0= Don't transport
unburned temperature; 1= Transport unburned temperature.		
0	ecfm3z_flag	Flag for ECFM3Z model.
0=off, 1=on.		
CYCLIC 720		Temporal type and cyclic
period.		
-999999.0	ecfm3z_tstart	ECFM3Z model starting
time.		
-999999.0	ecfm3z_tend	ECFM3Z model ending
time.		
0	ecfm3z_region_flag	1=Region based the
ECFM3Z model (ecfm3z_region.in required).		
2.0	ecfm3z_mix_betam	Mixing constant.
48.0	ecfm3z_cetaneno	Fuel cetane number of
ignition delay prediction.		
1.6	cfm_stretch_alpha	Constant for turbulent
stretch introduced the surface density production term.		
0.54	cfm_itnfs_factor	ITNFS model constant.
1.0	cfm_destruct_beta	Constant for the surface
density destruction term.		
2	auto_ignition_flag	Auto-ignition model
1=single stage ignition 2=double stages ignition.		
2e-005	auto_ignition_tc	Fuel consumption
characteristic time in the ignition model.		
0	li_spark_flag	Laminar ignition (LI)
spark model.		
CYCLIC 720		Temporal type and cyclic
period.		
-999999.0	li_spark_tstart	LI model starting time.
0.002	li_init_kernel_diameter	Initial flame kernel
diameter.		
0	li_spark_locate_x	LI spark location x
coordinate.		
0	li_spark_locate_y	LI spark location y
coordinate.		
0	li_spark_locate_z	LI spark location z
coordinate.		
7.0	li_src_factor	Constant for surface
density source from LI spark model.		
1	ecfm3z_post_ceq_flag	Enable CEQ solver for
burned zone.		

0	ecfm3z_reinit_flag	1=Variables in the
ECFM3Z model will be initialized for multiple cycle simulation		
(ecfm3z_reinit.in required).		
0	rif_flag	Flag for RIF model 0 is
off, 1 is on.		
1	rif_solver_flag	RIF Solver option.
1	rif_nproc_flamelet	Number of processors for
each flamelet.		
1e-005	rif_init_zmin	Minimum Z-value to
initialize flamelet.		
0.0	rif_unburned_temp_offset	Offset in unburnt
temperature (K).		
2.0	rif_flmt_c_chi	Flamelet scalar
dissipation constant.		
2.0	rif_cfd_c_chi	CFD scalar dissipation
constant.		
1000.0	rif_chi_clip	Max allowed value for
scalar dissipation rate.		
1	num_rif_flamelets	Number of flamelets.
4	rif_grid_type	Grid in the Z
coordinate, Default set to 4 to use Hyperbolic grid.		
100	rif_num_zgrids	Number of Z grids,
Default set to 100.		
0	rif_pdf_flag	0 is beta pdf, 1 is
clipped Gaussian pdf.		
0	rif_transport_species_flag	0= all the species will
be transported, 1= only species listed below will be transported.		
0	num_rif_transport_species	Number of RIF species
will be transported.		
1	num_rif_bc0	Number of species on
boundary 0 (oxidizer side).		
O2 0.00000	bc0_rif	List of species names
and species mass fractions for the oxidizer.		
0	num_rif_bc1	Number of species on
boundary 1 (fuel side).		
700.0	rif_fuel_temp	Gaseous phase fuel
temperature (K).		

embedded.in

```
#!/csi_version=2.2.0
#=====

#-----
#  Embedding 3
#-----
SPHERE                embedded_type
0.0 0.0 0.0           x_center           The center point of the
spherical shaped embedding.
0.006                 radius             The radius of the
sphere.
2                     embed_scale       Defines the level of
refinement for embedding. Represents the value of n in  $dx\_base/2^n$ .
PERMANENT              Temporal type and cyclic
period.
-999999.0              start_time        Time when embedding
starts. Not used when temporal_type is PERMANENT.
-999999.0              end_time          Time when embedding
ends. Not used when temporal_type is PERMANENT.
```

initialize.in

```
#!/csi_version=2.2.0
#=====

1          numregions          Number of regions
#-----
# Chamber
#-----
0          region_id
0          stream_id          A unique integer
identifier that represents a collection of regions.
0          solid_flag          0=Regions in this
stream_id are associated with the fluid phase, 1=Regions are associated with
the solid.
0.0 0.0 0.0          vel_init          Initial velocity in the
region (m/s).
300.0          temp_init          Initial temperature in
the region (K).
101325.0          pres_init          Initial absolute
pressure in the region (Pa).
1          tke_init          Initial turbulent
kinetic energy in the region (m^2/s^2).
10          eps_init          Initial tke dissipation
rate in the region (m^2/s^3).
3          numspeciesinit          Number of initialized
species mass fractions to follow. All others set to 0.0.
O2 0.19687          name          Name of species and mass
fraction
N2 0.74303          name          Name of species and mass
fraction
C3H8 0.0601          name          Name of species and mass
fraction
0          numpassiveinit          Number of initialized
passive. Names and values should follow.
```

inputs.in

```
#!/csi_version=2.2.0
#=====

"surface.dat"          surface_filename      The name of surface data
file.
1                      rstrtflg          Flag to indicate if the
simulation is a restart or new run: 0=new run, 1=restart.
2                      rstrtnum          Number added to output
files to identify different restarts.
1                      num_restart_files   Number of restart files
to be saved.
1                      restart_embed_flag   AMR restart embedding
flag: 0=do not write AMR embedding to restart file, 1=write AMR embedding to
restart file.
0                      mapflag            Flag to allow mapping in
initial conditions: 0=do not map, 1=map (requires map.in and a data file).
0                      ga_flag            Flag to enable genetic
algorithm output: 0=do not use GA output, 1=activate GA output.
0                      ga_individual       Genetic algorithm
individual number.
0                      ga_generation       Genetic algorithm
generation number.
0                      nohydro            Flag to indicate run
type: 0=solve full hydrodynamics (typical), 1=no hydrodynamics--used to check
grid.
6                      parallel_scale      Parallel blocks level.
100                   load_cyc            Number of cycles between
load balancing.
1                      reread_input        Flag to indicate whether
or not to re-read inputs, 0=do not re-read, 1=re-read each time step.
0                      screen_print_level  Screen print level.
0                      crank_flag         Flag to indicate time
units: 0=seconds, 1=crank angles (used for transient engine simulations).
0.0                   start_time          Start time, in sec. or
crank angles.
1.0                   end_time            End time, in sec. or
crank angles. If gti_flag is on in boundary.in, keyword GT can be used.
0.0001                twrite_post         Time interval for
writing 3D output (s/crank angle/cycle).
10.0                  twrite_transfer      Time interval for
writing heat transfer output data (s/crank angle/cycle).
0.0001                twrite_restart      Time interval for
writing restart output (s/crank angle/cycle).
1e-008                twrite_files        Time interval for
writing text data files (s/crank angle/cycle).
0                      wall_output_flag    Flag to write wall
output: 0=do not generate wall output, 1=generate wall output.
0                      transfer_flag       Flag to generate FEA
heat transfer data: 0=do not generate FEA data, 1=generate FEA data.
1                      mixing_output_flag  Flag to generate mixing
related output: 0=do not generate output, 1=generate output.
2                      species_output_flag  Flag for output of
species standard deviation.
```

0	inter_regions_flow_flag	Flag to generate inter region flow output: 0=do not generate output, 1=total mass-flux output, 2=mass-flux output for each specified species ('regions_flow.in').
0	dynamic_flag	Dynamic output options.
1	timeflag	Flag for variable time-step: 0=constant time-step (dt) 1=variable time-step (recommended).
0.0001	dtstart	Time-step (dt) at the start of the simulation (s).
1e-008	dt	Fixed time-step(s)--only used if timeflag=0.
0.01	dt_max	Maximum time-step (dt).
1e-008	dt_min	Minimum time-step (dt).
1.5	mult_dt_spray	Multiplier used in calculating maximum time-step based on spray.
9999.0	mult_dt_evap	Multiplier used in calculating maximum time-step based on evaporation.
0.5	mult_dt_chem	Multiplier used in calculating time-step based on chemical heat release.
0	dt_coll_mesh_flag	Flag for limiting time-step based on collision mesh: 1=use collision mesh dt limiter, 0=do not use.
1e-012	mult_dt_coll_mesh	Multiplier used in calculating dt_coll_mesh.
1.0	max_cfl_u	Maximum cfl number based on velocity.
2.0	max_cfl_nu	Maximum cfl number based on viscosity.
50.0	max_cfl_mach	Maximum cfl number based on speed of sound.
0.5	fv_upwind_factor_global	Blending factor for finite volume cells. 1.0=first order upwind, 0.5=second order central.
0.5	fv_upwind_factor_mom	Blending factor for momentum finite volume cells. 1.0=first order upwind, 0.5=second order central.
2	fd_order_convect	Order of upwinded finite difference convective stencils.
0	fd_skewness_convect	Skewness of upwinded finite difference convective stencils.
2	fd_order_diff	Order of central finite difference stencils.
1.0	impl	Fraction of the solver that is implicit.
0.0005	seal_tol	Sealing tolerance.
0	random_seed	Random seed number.
30	itmax	Maximum iterations allowed for solving transport equations using an iterative method.
500	itmax_pres	Maximum iterations allowed for solving the pressure equation using an iterative method.
500	itmax_pres_ideal	Ideal number of iterations for pressure equation used to determine time-step control.
1	multigrid_flag	Pressure solver flag: 0 =pressure is solved by SOR, 1 =pressure is solved by multigrid method.
15	num_multigrid_relaxations	Maximum number of iterations at each multigrid level.
0.0001	tol_u	Convergence tolerance for the momentum equation.
0.0001	tol_sie	Convergence tolerance for the energy equation.

0.0001	tol_rad	Convergence tolerance
for the radiation transport equation.		
1e-008	tol_p	Convergence tolerance
for the pressure equation.		
0.0001	tol_density_transport	Convergence tolerance
for the density transport equation.		
0.0001	tol_species	Convergence tolerance
for species.		
0.0001	tol_passive	Convergence tolerance
for passives.		
0.001	tol_tke	Convergence tolerance
for the turbulent kinetic energy equation.		
0.001	tol_eps	Convergence tolerance
for the turbulent dissipation equation.		
10.0	mult_piso	Convergence tolerance
for PISO iterations.		
0.7	omega_presrat	Under relaxation used in
solving PISO density (pres_rat).		
1.0	omega_u	Under relaxation used in
solving momentum equation.		
1.0	omega_sie	Under relaxation used in
solving specific internal energy (sie) equation.		
1.0	omega_rad	Under relaxation used in
solving radiation transport equation.		
1.3	omega_p	Under/over relaxation
used in solving pressure equation.		
0.2	omega_p_steady	Under/over relaxation
used in solving steady pressure.		
1.0	omega_density_transport	Under relaxation used in
solving density transport equation.		
1.0	omega_species	Under relaxation used in
solving species.		
1.0	omega_passive	Under relaxation used in
solving passive.		
0.7	omega_tke	Under relaxation used in
solving tke.		
0.7	omega_eps	Under relaxation used in
solving eps.		
9	max_piso	Maximum number of PISO
iterations.		
2	min_piso	Minimum number of PISO
iterations.		
1.0	conserve	Fraction of the momentum
equation in conservative form.		
1	strict_conserve_flag	
1	rc_flag	Flag for rhie-chow
model: 0 =no rhie-chow, 1 =Rhie-Chow.		
1	finitevol_flag	Flag to indicate
numerical scheme:0= finite difference scheme, 1=finite volume scheme.		
1	momentum_solver	Flag to solve momentum:
0=do not solve momentum equation, 1=solve momentum equation.		
1	gas_compressible_flag	Gas compressibility
flag: 0=incompressible gas flow, 1=compressible gas flow.		
0	liquid_compressible_flag	Liquid compressibility
flag: 0=incompressible liquid flow, 1=compressible liquid flow.		
0	eos_flag	Equation of state:
0=ideal gas, 1=Redlich-Kwong, 2=Redlich-Kwong-Soave, 3=Peng-Robinson.		

0	real_gas_prop_flag	0=Thermodynamic quantities are only function of T, 1=Thermodynamic quantities are only function of both T and P.
6.0	max_reduced_pres	The maximum reduced pressure for the departure function tables.
133.0	crit_temp	Critical temperature used for Redlich-Kwong (K).
3770000.0	crit_pres	Critical pressure used for Redlich-Kwong (Pa).
0.035	acentric_factor	Acentric factor of air (used for advanced equations of state).
1	energy_solver	Flag to solve energy: 0=do not solve energy equation, 1=solve energy equation.
1	species_solver	Flag to solve species: 0=do not solve species equation, 1=solve species equation.
0.9	prandtl	Turbulent Prandtl number.
0.78	schmidt	Turbulent Schmidt number.
0	steady_solver	Flag to indicate transient or steady, 0=transient, 1=steady pressure-based, 2=steady density-based, 3=steady density-based on local cell time-steps.
5000	min_cycles_steady	Minimum number of cycles for steady calculations.
10.0	min_temp	Minimum temperature allowed in the domain (K).
60000.0	max_temp	Maximum temperature allowed in the domain (K).
10.0	max_visc	Maximum turbulent dynamic viscosity allowed in the domain (N s/m ²).
0.0	gravity_x	Gravity in X-direction (m/s ²).
0.0	gravity_y	Gravity in Y-direction (m/s ²).
0.0	gravity_z	Gravity in Z-direction (m/s ²).
0	spray_flag	Flag to activate spray modeling: 0=do not use spray model, 1=use (requires spray.in).
1	turb_flag	Flag to activate turbulence modeling: 0=do not use turbulence model, 1=use (requires turbulence.in).
1	comb_flag	Flag to activate combustion modeling: 0=do not use combustion model, 1= use (requires combust.in).
1	source_flag	Flag to activate user-specifies sources: 0=do not use sources, 1=use (requires source.in).
0.005	dx_base	Maximum cell size (dx) in X-direction (m).
0.005	dy_base	Maximum cell size (dy) in Y-direction (m).
0.005	dz_base	Maximum cell size (dz) in Z-direction (m).
0	grid_scale_file_flag	0=do not use gridscale.in, 1=use gridscale.in.
0	grid_scale	Value of n in dx_base/2 ⁿ (only used if grid_scale_file_flag=0).

```

1          amr_flag          Flag to activate AMR:
0=do not use AMR, 1=use AMR (requires amr.in).
1          embedded_flag    Flag to activate fixed
embedding: 0=do not use fixed embedding, 1=use (requires embedded.in).
0          events_flag      Flag to activate events:
0=do not use events, 1= use (requires events.in).
0          composite_flag    Flag to activate
composite species: 0=do not use composite species, 1=use (requires a
composite.in).
0          wallvalue_flag    Flag to activate wall
initial values: 0=do not use, 1=use (requires wallvalue.in).
0          udf_flag          Flag to allow user-
defined functions: 0=do not use, 1=use (requires udf.in).
0          supercycle_flag   Supercycle flag. 0= do
not use Supercycle, 1=use Supercycle.
0          vof_flag          Flag to activate Volume
Of Fluid method(VOF): 0=do not use VOF, 1=use (requires vof.in).
0          fsi_flag          Flag to activate Fluid
Structure Interaction(FSI) method: 0=do not use FSI, 1=use (requires fsi.in).
0          radiation_flag    Flag to activate
radiation: 0=do not use radiation, 1= use (requires radiation.in).

```

post.in

```
#!/csi_version=2.2.0
#=====
```

```
<cells>
density          Cell density (Kg/m^3).
pressure         Cell pressure (N/m^2).
temp            Cell temperature (K).
velocity        All three components of cell velocity (m/s).
vorticity       Vorticity (generates 3 separate scalar components)
(1/s).
idreg           Cell region identification number.
equiv_ratio     Cell equivalence ratio.
lambda         Cell relative air-fuel ratio.
react_lambda    Cell lambda value for the combustion reaction
excluding CO2 and H2O.
react_ratio     Cell equivalence ratio that does not include CO2 and
H2O in the calculation.
bound_temp      Temperature at wall boundary (K).
massfrac(N2O)   Mass fraction of species, species name must appear
exactly as in "mech.dat" or "species.in".
massfrac(NO2)   Mass fraction of species, species name must appear
exactly as in "mech.dat" or "species.in".
massfrac(NO)    Mass fraction of species, species name must appear
exactly as in "mech.dat" or "species.in".
massfrac(H2O)   Mass fraction of species, species name must appear
exactly as in "mech.dat" or "species.in".
massfrac(CO2)   Mass fraction of species, species name must appear
exactly as in "mech.dat" or "species.in".
massfrac(CO)    Mass fraction of species, species name must appear
exactly as in "mech.dat" or "species.in".
massfrac(C3H8)  Mass fraction of species, species name must appear
exactly as in "mech.dat" or "species.in".
massfrac(N2)    Mass fraction of species, species name must appear
exactly as in "mech.dat" or "species.in".
massfrac(O2)    Mass fraction of species, species name must appear
exactly as in "mech.dat" or "species.in".
eps            Cell turbulence dissipation rate (m^2/s^3).
tke           Cell turbulent kinetic energy (m^2/s^2).
visc          Cell viscosity, including the turbulent component (N-
s/m^2).
```

source.in

```
#!/csi_version=2.2.0
#=====

#-----
# Source 2
#-----
ENERGY          source equation          Source equation (ENERGY,
U-EQ, V-EQ, W-EQ, TKE, EPS, [species], [passive], USER, POROUS).
1              source_type              Source type (0 = Per
unit volume per time; 1 = Total value of source; 2 = Pressure trace; 3 = Heat
release data).
0.0            source_unit_volume        Unit volume. Refer the
documentation for details.
0.007          source_value              Value.
SEQUENTIAL     period                   Temporal type and cyclic
period.
0.0            start_source              The start time, in
seconds or crank-angle-degrees, for the Source/Sink model.
0.0005         end_source                 The end time, in seconds
or crank-angle-degrees, for the Source/Sink model.
50000.0        max_value                  Maximum value for the
source.
SPHERE         source_shape              Source shape (BOX,
SPHERE, CYLINDER, REGION, LINE, CIRCLE).
0.0 0.0 0.0    x_center                   The center point of the
sphere.
0.005          radius                     The radius of the
sphere-shaped source.
0              moving                     0 = Stationary; 1 =
Prescribed velocity; 2 = Move with flow.
0.0 0.0 0.0    velocity                   Velocity vector of the
source.
0.0            max_displace               Distance for the maximum
displacement a source.
0              reset_source              Displacement control(0 -
2). Refer the documentation for details.
```

turbulence.in

```
#!/csi_version=2.2.0
#=====

11          turbmodel          Turbulence model flag
(RANS):0=Upwinding, 1=k-eps, 2=rng k-eps, 3=rapid distortion rng k-eps.
0.09        cmu                Turbulent viscosity
coefficient. Typically 0.09 for k-eps and 0.0845 for rng k-eps.
1.0         rpr_tke            Reciprocal TKE Prandtl
number. Typically 1.0 for k-eps, 1.39 for rng k-eps.
1.44        cept1              Turbulent dissipation
(eps) constant. Typically 1.44 for k-eps, 1.42 for rng k-eps.
1.92        cept2              Turbulent dissipation
(eps) constant. Typically 1.92 for k-eps, 1.68 for rng k-eps.
-1.0        cept3              Turbulent dissipation
(eps) constant. Typically -1.0 to 0.5.
0.77        rpr_eps            Reciprocal turbulent
dissipation (eps) Prandtl number. Typically 0.7692 for k-eps, 1.39 rng k-eps.
0.012       beta               RNG k-epsilon constant.
Typically 0.012.
4.38        eta0               RNG k-epsilon constant.
Typically 4.38.
0.0         c_s                Turbulent spray source
constant. Typically 0 to 1.5.
0.03        c_ps               Drop turbulent
dispersion constant. Typically 0 to 0.16.
2.0         c_tke_les          LES sub-grid estimate
constant. Typically 2.0.
0.05        c_tke_visc_les     LES Viscosity
coefficient.
1.0         c_eps_les           Turbulent LES
dissipation constant. Typically 1.0.
1           wall_model         LES wall model:
0=standard law of the wall, 1=Werner and Wengle (recommended).
11.4        re_crit            Law of the wall critical
Reynolds number.
0.15        clw                Law of the wall
constant.
0.42        law_kappa          Von Karman's constant.
5.5         law_b              Law of wall parameter.
10          heatmodel         Wall heat transfer
model: 0=O'Rourke , 1=Han and Reitz, 2=Angelberger.
0           turb_stat_flag     Select turbulent
statistics model (0=disabled).
-999999     turb_stat_start_time
-999999     mean_stat_end_time
0.0001      turb_stat_tol
```

3. Brayton-Gluhareff Cycle Pressure Jet Simulations

The following files were used to run the Brayton-Gluhareff Experimental (BGX) prototype engine presented in Chapter IV, Section D. As before, the mech.dat file necessary to model the chemical kinetics of combustion is not listed among these files. The mech.dat file representing the reduced San Diego mechanism listed in Appendix A2 was used to generate the output data discussed in Chapter VI, Section A. However, two versions of mech.dat are listed in full in Appendices A1 and A2 and either could be used (or any other mechanism in a valid mech.dat format). The reduced mechanism was chosen to reduce simulation runtime. Finally, as mentioned in the prior sections, the gas.dat and therm.dat files are not included due to their length considering they were unchanged from the default files and they are typically provided with or are integrated into the CFD solver being used.

amr.in

```
#!/csi_version=2.2.0
#=====

100                amr_cycle_steady                Number of cycles between
AMR calculations.
200000            amr_max_cells                    Maximum number of cells in
the entire domain.
1                amr_min_cells                    Minimum number of cells in
the entire domain.
#=====
# AmrGroup 1
#-----
3                amr_num_regions                Number of AMR regions.
1                amr_active_region                Active AMR region.
2                amr_active_region                Active AMR region.
0                amr_active_region                Active AMR region.
##### Velocity #####
1                amr_vel_flag                    Enable AMR based on velocity
conditions.
3                amr_embed_vel_scale                Maximum embedding level
for velocity.
1.0              amr_vel_sgs_embed                Minimum velocity above
which a cell will be embedded.
PERMANENT                                Temporal type and cyclic
period.
0.01            amr_vel_start_time                Time to start the AMR.
-999999.0       amr_vel_end_time                Time to end the AMR.
50              amr_parcel_embed                Maximum number of parcels
in a cell before CONVERGE embeds a cell using AMR.
##### Temperature #####
0                amr_temp_flag                    Enable AMR based on
temperature conditions.
5                amr_embed_temp_scale                Maximum embedding level
for temperature.
2.5             amr_temp_sgs_embed                Minimum temperature above
which a cell will be embedded.
SEQUENTIAL                                Temporal type and cyclic
period.
0.1            amr_temp_start_time                Time to start the AMR.
100.0          amr_temp_end_time                Time to end the AMR.
##### Void fraction #####
0                amr_void_flag                    Enable AMR based on Void
fraction conditions.
3                amr_embed_void_scale                Maximum embedding level
for Void fraction.
0.001          amr_void_sgs_embed                Minimum VOF above which a
cell will be embedded.
PERMANENT                                Temporal type and cyclic
period.
-999999.0       amr_void_start_time                Time to start the AMR.
-999999.0       amr_void_end_time                Time to end the AMR.
##### Species data #####
1                amr_species_flag                Enable AMR based on species
conditions.
```

```

3          amr_embed_species_scale      Maximum embedding level
for species.
1          amr_num_species              Number of species to
trigger AMR.
C3H8      species_name                 Species name.
0.001     amr_species_sgs_embed        Minimum mass fraction of
the species that will trigger AMR.
SEQUENTIAL                                Temporal type and cyclic
period.
0          amr_species_start_time      Time to start the AMR.
1          amr_species_end_time        Time to end the AMR.
##### Passive data #####
0          amr_passive_flag            Enable AMR based on passives
conditions.
3          amr_embed_passive_scale      Maximum embedding level
for passives.
1          amr_num_passive              Number of passives to
trigger AMR.
NOT_USED  passive_name                 Passive name.
1.0e-6    amr_passive_sgs_embed        Minimum mass fraction of
the passive that will trigger AMR.
PERMANENT                                Temporal type and cyclic
period.
0.0       amr_passive_start_time      Time to start the AMR.
10.0     amr_passive_end_time         Time to end the AMR.
#####
# Boundary data
#-----
0          amr_num_bounds              Number of boundary on which
CONVERGE will use AMR.

```

boundary.in

```
#!/csi_version=2.2.0
#=====

11  # Number of boundaries defined
#-----
1      Injector
INFLOW
velocity      Neumann      0.0 0.0 0.0
pressure      Dirichlet     [344738.0]
temperature   Dirichlet     488.7
species       Dirichlet     3
O2            0.0
N2            0.0
C3H8         1.0
passive       Dirichlet     0
tke           Intensity     0.2
eps           Length_scale 0.0001
region        0
#-----
2      Injector Wall
WALL          FIXED        Stationary
roughness     0.0          0.5
velocity      Law_of_wall   0.0 0.0 0.0
pressure      Neumann       0.0
temperature   Law_of_wall   300.0
species       Neumann       0.0
passive       Neumann       0.0
tke           Neumann       0.0
eps           Dirichlet     0.0
region        0
#-----
3      Inlet 1 Wall
WALL          FIXED        Stationary
roughness     0.0          0.5
velocity      Law_of_wall   0.0 0.0 0.0
pressure      Neumann       0.0
temperature   Law_of_wall   300.0
species       Neumann       0.0
passive       Neumann       0.0
tke           Neumann       0.0
eps           Dirichlet     0.0
region        0
#-----
4      Inlet 2 Wall
WALL          FIXED        Stationary
roughness     0.0          0.5
velocity      Law_of_wall   0.0 0.0 0.0
pressure      Neumann       0.0
temperature   Law_of_wall   300.0
species       Neumann       0.0
passive       Neumann       0.0
tke           Neumann       0.0
eps           Dirichlet     0.0
region        0
#-----
```

```

5          Sym_Inlet
SYMMETRY
region    0
#-----
6          Ambient
INFLOW
velocity  Neumann      0.0 0.0 0.0
pressure  Dirichlet    [110000.0]
temperature Dirichlet    300.0
species   Dirichlet    2
O2        0.23
N2        0.77
passive   Dirichlet    0
tke       Intensity    0.02
eps       Length_scale 0.003
region    0
#-----
7          Engine Wall
WALL      FIXED      Stationary
roughness 0.0        0.5
velocity  Law_of_wall  0.0 0.0 0.0
pressure  Neumann      0.0
temperature Law_of_wall  "EngineWallTemps.in"
species   Neumann      0.0
passive   Neumann      0.0
tke       Neumann      0.0
eps       Dirichlet    0.0
region    1
#-----
8          Engine Coil
WALL      FIXED      Stationary
roughness 0.0        0.5
velocity  Law_of_wall  0.0 0.0 0.0
pressure  Neumann      0.0
temperature Law_of_wall  "EngineWallTemps.in"
species   Neumann      0.0
passive   Neumann      0.0
tke       Neumann      0.0
eps       Dirichlet    0.0
region    1
#-----
9          Sym_Combustor
SYMMETRY
region    1
#-----
10         Sym_Exhaust
SYMMETRY
region    2
#-----
11         Outflow
OUTFLOW
velocity  Neumann      0.0 0.0 0.0
pressure  Dirichlet    101325.0 0.0
temperature Neumann      0.0
species   Neumann      0.0
passive   Neumann      0.0
tke       Neumann      0.0

```

```
eps          Neumann      0.0
temperature  backflow Dirichlet 300.0
species      backflow Dirichlet 2
O2           0.23
N2           0.77
passive      backflow Dirichlet 0
tke          backflow Intensity 0.02
eps          backflow Length_scale 0.003
region       2
```

combust.in

```
#!/csi_version=2.2.0
#=====

C3H8          fuel_name          Fuel species name.
0.25          omega_combust_steady Under-relaxation for
steady-state combustion.
1            sage_flag            SAGE detailed chemistry
model flag: 0=no SAGE model, 1=activate SAGE model.
0            sage_ode_solver      0=CVODES with dense solver
(recommended for up to 100 species); 1=CVODES with preconditioned iterative
solver.
600.0        sage_tcut           Minimum cell temperature
(K) for SAGE activation.
1e-008       sage_hcmin          Minimum HC+CO species mole
fraction for SAGE activation.
SEQUENTIAL   Temporal type and cyclic
period.
0.024       sage_tstart         SAGE start time in seconds
or crank angles.
999999.0    sage_tend           SAGE end time in seconds
or crank angles.
1            sage_region_flag    0=SAGE is not region
dependent, 1=SAGE is region dependent.
0            sage_solve_temp     SAGE temperature solution
flag. 0=do not re-solve temperature unless its change exceeds sage_delta_temp,
1=always re-solve temperature.
2.0         sage_delta_temp     Magnitude of the temperature
change (K), above which temperature will be re-solved in SAGE.
1            sage_analyt_jac     Flag to determine if
Jacobian matrix is solved analytically in the SAGE solver: 0=solve Jacobian
matrix numerically, 1=solve Jacobian matrix analytically.
0.0001      sage_rel_tol        Relative iteration error
for each species in the SAGE solver.
1e-014      sage_abs_tol        Absolute iteration error
for each species in the SAGE solver.
1.0         sage_reac_mult      Scaling factor of reaction
rates in the SAGE solver.
0            sage_dmr_flag       Use dynamic mechanism
reduction (sage_dmr.in is required).
1            multizone_flag      0=do not use multi zone
model, 1=use multi zone model.
2            multizone_bin_dim   Dimension of multizone.
5.0         multizone_tol_temp  Temperature bin size (K)
for multizone chemistry.
0.05        multizone_tol_phi   Equivalence ratio bin size
for multizone chemistry.
1            multizone_nox_flag  0=default, 1=improves the
accuracy of NOx emissions prediction in the multizone model.
0            multizone_output_flag 0=no additional output for
multizone chemistry, 1=activate additional output for multizone chemistry.
0            multizone_hr_map_flag Use heat release mapping.
0            ceq_flag           CEQ equilibrium solver
flag: 0=no CEQ, 1=activate CEQ, 2=activate CEQ with mixing time scale.
0            ceq_subsp_flag     Define CEQ species subset
(ceq_species.in is required).
```

600.0	ceq_tcut	Minimum cell temperature
(K) for CEQ activation.		
1e-014	ceq_hcmin	Minimum HC+CO species mole
fraction for CEQ activation.		
0	ctc_flag	Characteristic Time
Combustion (CTC) model flag: 0=no CTC model, 1=activate CTC model.		
-999999.0	ctc_init_time	Time for CTC model
initialization(s/deg).		
1	ctc_mult_scale	Multi-scale CTC model flag:
0=single scale CTC model, 1=multi-scale CTC model.		
0.2	tau_fraction	Multi-scale CTC time-scale
fraction.		
0.1	cm2	CTC turbulent time-scale
constant.		
7680000000.0	denomc	CTC chemical time-scale
constant.		
1000.0	tchop	Transition temperature (K)
for Shell/CTC models.		
0	shell_flag	Shell ignition model flag:
0=no Shell model, 1=activate conserving Shell model, 2=activate original Shell		
model.		
125000.0	af04	Shell model ignition delay
parameter.		
0	nox_flag	Extended Zeldovich NOx
model flag: 0=no NOx model, 1=activate NOx model.		
0	soot_hiroy_flag	Hiroyasu/NSC soot model
flag: 0=no soot model, 1=activate soot model.		
350.0	soot_asf	Soot formation pre-
exponential factor (1/(s bar^0.5)).		
12500.0	soot_esf	Soot formation activation
energy parameter (cal/gmol).		
2.5e-006	soot_diam	Soot particle diameter
(cm).		
1.0	soot_oxid_fac	Soot oxidation model
factor.		
2.0	soot_density	Soot density (g/cm^3).
0	soot_form_flag	0=use the sum of the
hydrocarbon species as the soot formation species, 1=use C2H2 as the soot		
formation species.		
0	soot_mauss_mr_flag	Particle Moment Rate(PMR)
soot model flag: 0=no PMR model, 1=active PMR model.		
2	mauss_num_mom	Number of moments to be
solved.		
2.25	surfacegrowth_model	Describes the surface
reactions soot dependence:-1=no surface reactions, 0.0=function of number		
density, 2.0=function of surface area, 2.25= d**2.25(typical for diesel),		
3.0=function of soot volume.		
0.3	alpha_corrector	Part of sites on soot
surface available for surface reactions.		
0	soot_sectrate_flag	Particle Size Mimic(PSM)
soot model flag:0=no PSM model, 1=active PSM model.		
20	num_sootsections	Number of section(soot
volume fraction) to be solved.		
5	num_subsections	Number of sub-sections for
each section.		
2.0	sgmodell	Describes the surface
reactions soot dependence in the range of PAH to sgSizeLimit.		

2.25	sgmodel2	Describes the surface reactions soot dependence in the range of sgSizeLimit to biggestSoot.
0.95	alphacorrl	Part of sites on soot surface available for surface reactions in the range of PAH to sgSizeLimit.
0.3	alphacorr2	Part of sites on soot surface available for surface reactions in the range of sgSizeLimit to biggestSoot.
0	custom_soot_precursor_flag	0=Don't use soot precursor; 1=Use soot precursor (soot_precursor.dat is required).
0	soot_condensation_flag	Condensation submodel flag for both Mauss and PSM model.
1.0	hr_time	Heat release rate time (s/crank).
1	mix_frac_flag	0=do not calculate mixture fraction, 1=calculate mixture fraction.
0	mix_frac_var_flag	0=do not calculate mixture fraction variance, 1=calculate mixture fraction variance.
2.0	c_chi	Constant used in modeling of the scalar dissipation in the mixture fraction variance calculation.
0	g_eqn_flag	G-Eqn model flag: 0=no model, 1=equil. inside flame, 2=sage outside flame and equil. inside flame, 3=sage inside and outside flame.
-0.1	g_eqn_init_value	Initial G-value.
1	g_eqn_grad_g_flag	0= Explicit method; 1= Sussman method.
0	laminar_flamespeed_flag	Laminar flamespeed flag: 0=constant, 1=Metghalchi, 2=Gulder.
0.0	constant_laminar_flamespeed	Constant laminar flamespeed (m/s).
298.0	laminar_flamespeed_temp_ref	Reference temperature.
101325.0	laminar_flamespeed_pres_ref	Reference pressure.
0.2632	met_bm	Metghalchi constant 1 (m/s).
-0.8472	met_b2	Metghalchi constant 2 (m/s).
1.13	met_equiv_ratio	Metghalchi ref. equivalence ratio.
0.0	g_eqn_dilution	Metghalchi dilution species mass fraction.
0.4658	gulder_omega	Gulder coefficient for calculating laminar flame speed.
-0.326	gulder_eta	Gulder coefficient for calculating laminar flame speed.
4.48	gulder_xi	Gulder coefficient for calculating laminar flame speed.
1.2	g_eqn_temp_exponent	Temperature exponent constant.
-0.26	g_eqn_pres_exponent	Pressure exponent constant.
0	g_eqn_turb_flamespeed_flag	Turbulent flame-speed calculation flag:0= don't use g_prime, 1=use_g_prime.
0.78	st_a4	Constant for turbulent flame speed calculation(a4).
2.0	st_b1	Constant for turbulent flame speed calculation(b1).
1.0	st_b3	Constant for turbulent flame speed calculation(b3).

2.0	g_prime_cs	Constant used for calculating
g_prime equation dissipation.		
3000.0	tcut_g_eqn	Temperature above which G
is initialized.		
0	g_eqn_spark_flag	Flag for g_eqn kernel
ignition model: 0= don't use, 1= use kernel igniton model.		
0.3	spark_eff	Spark efficiency used for
kernel model.		
100	g_eqn_num_kernel_init	Number of spark kernels
initialized for kernel model.		
80.0	karlovitz_ig	Karlovitz ignition number.
0	g_eqn_unburned_temp_flag	0= Don't transport unburned
temperature; 1= Transport unburned temperature.		
0	ecfm3z_flag	Flag for ECFM3Z model.
0=off, 1=on.		
CYCLIC 720		Temporal type and cyclic
period.		
-999999.0	ecfm3z_tstart	ECFM3Z model starting time.
-999999.0	ecfm3z_tend	ECFM3Z model ending time.
0	ecfm3z_region_flag	1=Region based the ECFM3Z
model (ecfm3z_region.in required).		
2.0	ecfm3z_mix_betam	Mixing constant.
48.0	ecfm3z_cetaneno	Fuel cetane number of
ignition delay prediction.		
1.6	cfm_stretch_alpha	Constant for turbulent
stretch introduced the surface density production term.		
0.54	cfm_itnfs_factor	ITNFS model constant.
1.0	cfm_destruct_beta	Constant for the surface
density destruction term.		
2	auto_ignition_flag	Auto-ignition model 1=single
stage ignition 2=double stages ignition.		
2e-005	auto_ignition_tc	Fuel consumption
characteristic time in the ignition model.		
0	li_spark_flag	Laminar ignition (LI) spark
model.		
CYCLIC 720		Temporal type and cyclic
period.		
-999999.0	li_spark_tstart	LI model starting time.
0.002	li_init_kernel_diameter	Initial flame kernel
diameter.		
0	li_spark_locate_x	LI spark location x
coordinate.		
0	li_spark_locate_y	LI spark location y
coordinate.		
0	li_spark_locate_z	LI spark location z
coordinate.		
7.0	li_src_factor	Constant for surface
density source from LI spark model.		
1	ecfm3z_post_ceq_flag	Enable CEQ solver for
burned zone.		
0	ecfm3z_reinit_flag	1=Variables in the ECFM3Z
model will be initialized for multiple cycle simulation (ecfm3z_reinit.in		
required).		
0	rif_flag	Flag for RIF model 0 is
off, 1 is on.		
1	rif_solver_flag	RIF Solver option.

1	rif_nproc_flamelet	Number of processors for
each flamelet.		
1e-005	rif_init_zmin	Minimum Z-value to
initialize flamelet.		
0.0	rif_unburned_temp_offset	Offset in unburnt temperature
(K).		
2.0	rif_flmt_c_chi	Flamelet scalar dissipation
constant.		
2.0	rif_cfd_c_chi	CFD scalar dissipation
constant.		
1000.0	rif_chi_clip	Max allowed value for
scalar dissipation rate.		
1	num_rif_flamelets	Number of flamelets.
4	rif_grid_type	Grid in the Z coordinate,
Default set to 4 to use Hyperbolic grid.		
100	rif_num_zgrids	Number of Z grids, Default
set to 100.		
0	rif_pdf_flag	0 is beta pdf, 1 is clipped
Gaussian pdf.		
0	rif_transport_species_flag	0= all the species will be
transported, 1= only species listed below will be transported.		
0	num_rif_transport_species	Number of RIF species will
be transported.		
1	num_rif_bc0	Number of species on
boundary 0 (oxidizer side).		
O2 0.00000	bc0_rif	List of species names and
species mass fractions for the oxidizer.		
0	num_rif_bc1	Number of species on
boundary 1 (fuel side).		
700.0	rif_fuel_temp	Gaseous phase fuel
temperature (K).		

embedded.in

```
#!/csi_version=2.2.0
#=====

#-----
# Engine Wall Surface

#-----
BOUND          embedded_type
7              boundary_id          Boundary identifier (from
boundary.in) that defines the boundary on which embedding is to be added.
2              embed_scale          Defines the level of
refinement for embedding. Represents the value of n in  $dx\_base/2^n$ .
1              num_embed            Number of layers of
embedding (at the specified embed_scale) to be added to the boundary.
PERMANENT      Temporal type and cyclic
period.
0.001          start_time            Time when embedding starts.
Not used when temporal_type is PERMANENT.
1.0            end_time              Time when embedding ends.
Not used when temporal_type is PERMANENT.
#-----
# Inlet 1 Wall Surface

#-----
BOUND          embedded_type
3              boundary_id          Boundary identifier (from
boundary.in) that defines the boundary on which embedding is to be added.
3              embed_scale          Defines the level of
refinement for embedding. Represents the value of n in  $dx\_base/2^n$ .
2              num_embed            Number of layers of
embedding (at the specified embed_scale) to be added to the boundary.
PERMANENT      Temporal type and cyclic
period.
-999999.0     start_time            Time when embedding starts.
Not used when temporal_type is PERMANENT.
-999999.0     end_time              Time when embedding ends.
Not used when temporal_type is PERMANENT.
#-----
# Inlet 2 Wall Surface

#-----
BOUND          embedded_type
4              boundary_id          Boundary identifier (from
boundary.in) that defines the boundary on which embedding is to be added.
3              embed_scale          Defines the level of
refinement for embedding. Represents the value of n in  $dx\_base/2^n$ .
2              num_embed            Number of layers of
embedding (at the specified embed_scale) to be added to the boundary.
PERMANENT      Temporal type and cyclic
period.
-999999.0     start_time            Time when embedding starts.
Not used when temporal_type is PERMANENT.
-999999.0     end_time              Time when embedding ends.
Not used when temporal_type is PERMANENT.
#-----
```

```

# Injector Wall Surface

#-----
BOUND          embedded_type
2              boundary_id          Boundary identifier (from
boundary.in) that defines the boundary on which embedding is to be added.
3              embed_scale          Defines the level of
refinement for embedding. Represents the value of n in dx_base/2^n.
2              num_embed            Number of layers of
embedding (at the specified embed_scale) to be added to the boundary.
PERMANENT      Temporal type and cyclic
period.
-999999.0      start_time            Time when embedding starts.
Not used when temporal_type is PERMANENT.
-999999.0      end_time              Time when embedding ends.
Not used when temporal_type is PERMANENT.
#-----
# Engine Coil Surface

#-----
BOUND          embedded_type
8              boundary_id          Boundary identifier (from
boundary.in) that defines the boundary on which embedding is to be added.
3              embed_scale          Defines the level of
refinement for embedding. Represents the value of n in dx_base/2^n.
2              num_embed            Number of layers of
embedding (at the specified embed_scale) to be added to the boundary.
SEQUENTIAL     Temporal type and cyclic
period.
0.001          start_time            Time when embedding starts.
Not used when temporal_type is PERMANENT.
1.0            end_time              Time when embedding ends.
Not used when temporal_type is PERMANENT.
#-----
# Core Fineness
#-----
BOX            embedded_type
0.0 0.0 0.0   x_center              Center point of the embedded
box.
0.1 0.0587 0.011 x_size            The half-size of the box.
2              embed_scale          Defines the level of
refinement for embedding. Represents the value of n in dx_base/2^n.
PERMANENT      Temporal type and cyclic
period.
0.0001        start_time            Time when embedding starts.
Not used when temporal_type is PERMANENT.
1.0            end_time              Time when embedding ends.
Not used when temporal_type is PERMANENT.
#-----
# Injection Fineness
#-----
CYLINDER      embedded_type
0.0 0.225 0.0 x_center              Center point of the first
end of a cylinder.
0.007         radius                Radius of the first end of
a cylinder.

```

```

0.0 0.215 0.0          x_center          Center point of the second
end of a cylinder.
0.007                  radius            Radius of the second end
of a cylinder.
3                      embed_scale       Defines the level of
refinement for embedding. Represents the value of n in dx_base/2^n.
PERMANENT              Temporal type and cyclic
period.
-999999.0              start_time        Time when embedding starts.
Not used when temporal_type is PERMANENT.
-999999.0              end_time          Time when embedding ends.
Not used when temporal_type is PERMANENT.
#-----
# Inlet 2 Fineness
#-----
BOX                    embedded_type
0.0 0.165 0.0058      x_center          Center point of the embedded
box.
0.01 0.0075 0.006    x_size            The half-size of the box.
3                      embed_scale       Defines the level of
refinement for embedding. Represents the value of n in dx_base/2^n.
PERMANENT              Temporal type and cyclic
period.
-999999.0              start_time        Time when embedding starts.
Not used when temporal_type is PERMANENT.
-999999.0              end_time          Time when embedding ends.
Not used when temporal_type is PERMANENT.
#-----
# Inlet 3 Fineness
#-----
BOX                    embedded_type
0.0 0.0625 0.0075    x_center          Center point of the embedded
box.
0.015 0.0075 0.008  x_size            The half-size of the box.
3                      embed_scale       Defines the level of
refinement for embedding. Represents the value of n in dx_base/2^n.
PERMANENT              Temporal type and cyclic
period.
-999999.0              start_time        Time when embedding starts.
Not used when temporal_type is PERMANENT.
-999999.0              end_time          Time when embedding ends.
Not used when temporal_type is PERMANENT.

```

enginewalltemps.in

```
TEMPORAL
SEQUENTIAL
second      temperature
0           300
0.025      300
0.028      310
0.032      358
0.034      445
0.035      514
0.036      622
0.037      793
0.038      937
0.041      1200
0.045      1400
0.050      1600
0.055      1700
0.060      1775
0.065      1800
0.100      1800
```

events.in

```
#!csi_version=2.2.0
#=====
# {CYCLIC N | SEQUENTIAL | PERMANENT}
# <REG_1 REG_2> <OPEN/CLOSE> <TIME>
SEQUENTIAL
0          1          OPEN          0.0
1          2          OPEN          0.0
```

gridscale.in

```
#!/csi_version=2.2.0  
#=====
```

```
1          num_gridscale  
0.0        gridscale_time  
-1         gridscale_value
```

initialize.in

```

#!csi_version=2.2.0
#=====

3                      numregions                      Number of regions
#-----
# Inlet
#-----
0                      region_id
0                      stream_id                      A unique integer identifier
that represents a collection of regions.
0                      solid_flag                      0=Regions in this stream_id
are associated with the fluid phase, 1=Regions are associated with the solid.
0.0 0.0 0.0           vel_init                          Initial velocity in the
region (m/s).
300.0                 temp_init                         Initial temperature in the
region (K).
110000.0              pres_init                         Initial absolute pressure
in the region (Pa).
1                      tke_init                        Initial turbulent kinetic
energy in the region (m^2/s^2).
10                     eps_init                        Initial tke dissipation
rate in the region (m^2/s^3).
2                      numspeciesinit                  Number of initialized
species mass fractions to follow. All others set to 0.0.
O2 0.23               name                             Name of species and mass
fraction
N2 0.77               name                             Name of species and mass
fraction
0                      numpassiveinit                 Number of initialized
passive. Names and values should follow.
#-----
# Combustor
#-----
1                      region_id
0                      stream_id                      A unique integer identifier
that represents a collection of regions.
0                      solid_flag                      0=Regions in this stream_id
are associated with the fluid phase, 1=Regions are associated with the solid.
0.0 0.0 0.0           vel_init                          Initial velocity in the
region (m/s).
300.0                 temp_init                         Initial temperature in the
region (K).
101325.0              pres_init                         Initial absolute pressure
in the region (Pa).
1                      tke_init                        Initial turbulent kinetic
energy in the region (m^2/s^2).
10                     eps_init                        Initial tke dissipation
rate in the region (m^2/s^3).
2                      numspeciesinit                  Number of initialized
species mass fractions to follow. All others set to 0.0.
O2 0.23               name                             Name of species and mass
fraction
N2 0.77               name                             Name of species and mass
fraction

```

```

0                               numpassiveinit           Number of initialized
passive. Names and values should follow.
#-----
# Exhaust
#-----
2                               region_id
0                               stream_id               A unique integer identifier
that represents a collection of regions.
0                               solid_flag             0=Regions in this stream_id
are associated with the fluid phase, 1=Regions are associated with the solid.
0.0 0.0 0.0                     vel_init              Initial velocity in the
region (m/s).
300.0                             temp_init           Initial temperature in the
region (K).
101325.0                          pres_init          Initial absolute pressure
in the region (Pa).
1                               tke_init             Initial turbulent kinetic
energy in the region (m^2/s^2).
10                               eps_init           Initial tke dissipation
rate in the region (m^2/s^3).
2                               numspeciesinit       Number of initialized
species mass fractions to follow. All others set to 0.0.
O2 0.23                           name                Name of species and mass
fraction
N2 0.77                           name                Name of species and mass
fraction
0                               numpassiveinit           Number of initialized
passive. Names and values should follow.

```

inputs.in

```
#!/csi_version=2.2.0
#=====

"surface.dat"          surface_filename          The name of surface data
file.
1                      rstrtflg                Flag to indicate if the
simulation is a restart or new run: 0=new run, 1=restart.
1                      rstrtnum                Number added to output
files to identify different restarts.
2                      num_restart_files        Number of restart files to
be saved.
1                      restart_embed_flag       AMR restart embedding flag:
0=do not write AMR embedding to restart file, 1=write AMR embedding to restart
file.
0                      mapflag                  Flag to allow mapping in
initial conditions: 0=do not map, 1=map (requires map.in and a data file).
0                      ga_flag                  Flag to enable genetic
algorithm output: 0=do not use GA output, 1=activate GA output.
0                      ga_individual            Genetic algorithm individual
number.
0                      ga_generation            Genetic algorithm generation
number.
0                      nohydro                  Flag to indicate run type:
0=solve full hydrodynamics (typical), 1=no hydrodynamics--used to check grid.
6                      parallel_scale           Parallel blocks level.
100                    load_cyc                 Number of cycles between
load balancing.
1                      reread_input             Flag to indicate whether
or not to re-read inputs, 0=do not re-read, 1=re-read each time step.
0                      screen_print_level       Screen print level.
0                      crank_flag               Flag to indicate time
units: 0=seconds, 1=crank angles (used for transient engine simulations).
0.0                    start_time               Start time, in sec. or
crank angles.
0.1                    end_time                 End time, in sec. or crank
angles. If gti_flag is on in boundary.in, keyword GT can be used.
0.0001                 twrite_post              Time interval for writing
3D output (s/crank angle/cycle).
10.0                   twrite_transfer          Time interval for writing
heat transfer output data (s/crank angle/cycle).
0.0001                 twrite_restart           Time interval for writing
restart output (s/crank angle/cycle).
1e-005                 twrite_files             Time interval for writing
text data files (s/crank angle/cycle).
0                      wall_output_flag         Flag to write wall output:
0=do not generate wall output, 1=generate wall output.
0                      transfer_flag            Flag to generate FEA heat
transfer data: 0=do not generate FEA data, 1=generate FEA data.
1                      mixing_output_flag       Flag to generate mixing
related output: 0=do not generate output, 1=generate output.
1                      species_output_flag      Flag for output of species
standard deviation.
0                      inter_regions_flow_flag  Flag to generate inter
region flow output: 0=do not generate output, 1=total mass-flux output, 2=mass-
flux output for each specified species ('regions_flow.in').
```

0	dynamic_flag	Dynamic output options.
1	timeflag	Flag for variable time-
step: 0=constant time-step (dt) 1=variable time-step (recommended).		
1e-006	dtstart	Time-step (dt) at the start
of the simulation (s).		
1e-006	dt	Fixed time-step(s)--only
used if timeflag=0.		
0.01	dt_max	Maximum time-step (dt).
1e-010	dt_min	Minimum time-step (dt).
1.5	mult_dt_spray	Multiplier used in
calculating maximum time-step based on spray.		
9999.0	mult_dt_evap	Multiplier used in
calculating maximum time-step based on evaporation.		
0.5	mult_dt_chem	Multiplier used in
calculating time-step based on chemical heat release.		
0	dt_coll_mesh_flag	Flag for limiting time-
step based on collision mesh: 1=use collision mesh dt limiter, 0=do not use.		
1e-012	mult_dt_coll_mesh	Multiplier used in
calculating dt_coll_mesh.		
1.0	max_cfl_u	Maximum cfl number based
on velocity.		
2.0	max_cfl_nu	Maximum cfl number based
on viscosity.		
50.0	max_cfl_mach	Maximum cfl number based
on speed of sound.		
1.0	fv_upwind_factor_global	Blending factor for finite
volume cells. 1.0=first order upwind, 0.5=second order central.		
1.0	fv_upwind_factor_mom	Blending factor for momentum
finite volume cells. 1.0=first order upwind, 0.5=second order central.		
2	fd_order_convect	Order of upwinded finite
difference convective stencils.		
0	fd_skewness_convect	Skewness of upwinded finite
difference convective stencils.		
2	fd_order_diff	Order of central finite
difference stencils.		
1.0	impl	Fraction of the solver
that is implicit.		
0.0005	seal_tol	Sealing tolerance.
0	random_seed	Random seed number.
30	itmax	Maximum iterations allowed
for solving transport equations using an iterative method.		
500	itmax_pres	Maximum iterations allowed
for solving the pressure equation using an iterative method.		
500	itmax_pres_ideal	Ideal number of iterations
for pressure equation used to determine time-step control.		
1	multigrid_flag	Pressure solver flag: 0
=pressure is solved by SOR, 1 =pressure is solved by multigrid method.		
15	num_multigrid_relaxations	Maximum number of iterations
at each multigrid level.		
0.0001	tol_u	Convergence tolerance for
the momentum equation.		
0.0001	tol_sie	Convergence tolerance for
the energy equation.		
0.0001	tol_rad	Convergence tolerance for
the radiation transport equation.		
1e-008	tol_p	Convergence tolerance for
the pressure equation.		

0.0001	tol_density_transport	Convergence tolerance for the density transport equation.
0.0001	tol_species	Convergence tolerance for species.
0.0001	tol_passive	Convergence tolerance for passives.
0.001	tol_tke	Convergence tolerance for the turbulent kinetic energy equation.
0.001	tol_eps	Convergence tolerance for the turbulent dissipation equation.
10.0	mult_piso	Convergence tolerance for PISO iterations.
0.7	omega_presrat	Under relaxation used in solving PISO density (pres_rat).
1.0	omega_u	Under relaxation used in solving momentum equation.
1.0	omega_sie	Under relaxation used in solving specific internal energy (sie) equation.
1.0	omega_rad	Under relaxation used in solving radiation transport equation.
1.3	omega_p	Under/over relaxation used in solving pressure equation.
0.2	omega_p_steady	Under/over relaxation used in solving steady pressure.
1.0	omega_density_transport	Under relaxation used in solving density transport equation.
1.0	omega_species	Under relaxation used in solving species.
1.0	omega_passive	Under relaxation used in solving passive.
0.7	omega_tke	Under relaxation used in solving tke.
0.7	omega_eps	Under relaxation used in solving eps.
9	max_piso	Maximum number of PISO iterations.
2	min_piso	Minimum number of PISO iterations.
1.0	conserve	Fraction of the momentum equation in conservative form.
1	strict_conserve_flag	
1	rc_flag	Flag for rhie-chow model: 0 =no rhie-chow, 1 =Rhie-Chow.
1	finitevol_flag	Flag to indicate numerical scheme:0= finite difference scheme, 1=finite volume scheme.
1	momentum_solver	Flag to solve momentum: 0=do not solve momentum equation, 1=solve momentum equation.
1	gas_compressible_flag	Gas compressibility flag: 0=incompressible gas flow, 1=compressible gas flow.
0	liquid_compressible_flag	Liquid compressibility flag: 0=incompressible liquid flow, 1=compressible liquid flow.
1	eos_flag	Equation of state: 0=ideal gas, 1=Redlich-Kwong, 2=Redlich-Kwong-Soave, 3=Peng-Robinson.
0	real_gas_prop_flag	0=Thermodynamic quantities are only function of T, 1=Thermodynamic quantities are only function of both T and P.

6.0	max_reduced_pres	The maximum reduced pressure for the departure function tables.
133.0	crit_temp	Critical temperature used for Redlich-Kwong (K).
3770000.0	crit_pres	Critical pressure used for Redlich-Kwong (Pa).
0.035	acentric_factor	Acentric factor of air (used for advanced equations of state).
1	energy_solver	Flag to solve energy: 0=do not solve energy equation, 1=solve energy equation.
1	species_solver	Flag to solve species: 0=do not solve species equation, 1=solve species equation.
0.9	prandtl	Turbulent Prandtl number.
0.78	schmidt	Turbulent Schmidt number.
0	steady_solver	Flag to indicate transient or steady, 0=transient,1=steady pressure-based, 2=steady density-based, 3=steady density-based on local cell time-steps.
5000	min_cycles_steady	Minimum number of cycles for steady calculations.
10.0	min_temp	Minimum temperature allowed in the domain (K).
60000.0	max_temp	Maximum temperature allowed in the domain (K).
10.0	max_visc	Maximum turbulent dynamic viscosity allowed in the domain (N s/m ²).
0.0	gravity_x	Gravity in X-direction (m/s ²).
0.0	gravity_y	Gravity in Y-direction (m/s ²).
0.0	gravity_z	Gravity in Z-direction (m/s ²).
0	spray_flag	Flag to activate spray modeling: 0=do not use spray model, 1=use (requires spray.in).
1	turb_flag	Flag to activate turbulence modeling: 0=do not use turbulence model, 1=use (requires turbulence.in).
1	comb_flag	Flag to activate combustion modeling: 0=do not use combustion model, 1= use (requires combust.in).
1	source_flag	Flag to activate user-specifies sources: 0=do not use sources, 1=use (requires source.in).
0.005	dx_base	Maximum cell size (dx) in X-direction (m).
0.005	dy_base	Maximum cell size (dy) in Y-direction (m).
0.005	dz_base	Maximum cell size (dz) in Z-direction (m).
1	grid_scale_file_flag	0=do not use gridscale.in, 1=use gridscale.in.
0	grid_scale	Value of n in dx_base/2 ⁿ (only used if grid_scale_file_flag=0).
1	amr_flag	Flag to activate AMR: 0=do not use AMR, 1=use AMR (requires amr.in).
1	embedded_flag	Flag to activate fixed embedding: 0=do not use fixed embedding, 1=use (requires embedded.in).
1	events_flag	Flag to activate events: 0=do not use events, 1= use (requires events.in).
0	composite_flag	Flag to activate composite species: 0=do not use composite species, 1=use (requires a composite.in).

```
0          wallvalue_flag          Flag to activate wall
initial values: 0=do not use, 1=use (requires wallvalue.in).
0          udf_flag                Flag to allow user-defined
functions: 0=do not use, 1=use (requires udf.in).
0          supercycle_flag        Supercycle flag. 0= do not
use Supercycle, 1=use Supercycle.
0          vof_flag                Flag to activate Volume Of
Fluid method(VOF): 0=do not use VOF, 1=use (requires vof.in).
0          fsi_flag                Flag to activate Fluid
Structure Interaction(FSI) method: 0=do not use FSI, 1=use (requires fsi.in).
0          radiation_flag          Flag to activate radiation:
0=do not use radiation, 1= use (requires radiation.in).
```

post.in

```
#!/csi_version=2.2.0
#=====
```

```
<cells>
mach                Cell Mach number.
density             Cell density (Kg/m^3).
pressure           Cell pressure (N/m^2).
grad_p[0]          Gradient of pressure in the cell in the i-th direction,
1 represents x, 2 is y, and 3 is z (N/m^3).
grad_p[1]          Gradient of pressure in the cell in the i-th direction,
1 represents x, 2 is y, and 3 is z (N/m^3).
grad_p[2]          Gradient of pressure in the cell in the i-th direction,
1 represents x, 2 is y, and 3 is z (N/m^3).
temp               Cell temperature (K).
velocity           All three components of cell velocity (m/s).
volume             Cell volume or cell pair volume if cell is paired (m^3).
vorticity          Vorticity (generates 3 separate scalar components)
(1/s).
idreg              Cell region identification number.
equiv_ratio        Cell equivalence ratio.
bound_flux         Heat flux at wall boundary (W/m^2).
bound_htc          Heat transfer coefficient at wall boundary (W/m^2-K).
bound_temp         Temperature at wall boundary (K).
massfrac(H2O)      Mass fraction of species, species name must appear
exactly as in "mech.dat" or "species.in".
massfrac(CO2)      Mass fraction of species, species name must appear
exactly as in "mech.dat" or "species.in".
massfrac(CO)       Mass fraction of species, species name must appear
exactly as in "mech.dat" or "species.in".
massfrac(O2)       Mass fraction of species, species name must appear
exactly as in "mech.dat" or "species.in".
massfrac(C3H8)     Mass fraction of species, species name must appear
exactly as in "mech.dat" or "species.in".
eps                Cell turbulence dissipation rate (m^2/s^3).
tke                Cell turbulent kinetic energy (m^2/s^2).
visc               Cell viscosity, including the turbulent component (N-
s/m^2).
```

sage_region.in

#!/csi_version=2.2.0

#=====

1	region_id	The regions for SAGE
calculations.	The region_id must be included in "initialize.in".	
SEQUENTIAL		Temporal type and cyclic
period.		
0.024	sage_tstart	Starting time for SAGE
calculation.		
9999.0	sage_tend	Ending time of SAGE
calculation.		

source.in

```
#!/csi_version=2.2.0
#=====

#-----
# Ignition Source

#-----
ENERGY          source equation          Source equation (ENERGY,
U-EQ, V-EQ, W-EQ, TKE, EPS, [species], [passive], USER, POROUS).
1              source_type              Source type (0 = Per unit
volume per time; 1 = Total value of source; 2 = Pressure trace; 3 = Heat release
data).
10.0           source_unit_volume        Unit volume. Refer the
documentation for details.
35.0           source_value              Value.
SEQUENTIAL                                          Temporal type and cyclic
period.
0.025         start_source                The start time, in seconds
or crank-angle-degrees, for the Source/Sink model.
0.026         end_source                  The end time, in seconds
or crank-angle-degrees, for the Source/Sink model.
1970.0        max_value                   Maximum value for the
source.
CYLINDER      source_shape                Source shape (BOX, SPHERE,
CYLINDER, REGION, LINE, CIRCLE).
0.0 0.06175 0.015  x1_center              Center point of the first
end of a cylinder.
0.003175      radius1                    Radius of the first end of
a cylinder for the cylinder-shaped source.
0.0 0.06175 -0.001 x2_center              Center point of the second
end of a cylinder.
0.003175      radius2                    Radius of the second end
of a cylinder for the cylinder-shaped source.
0              moving                     0 = Stationary; 1 =
Prescribed velocity; 2 = Move with flow.
0.0 0.0 0.0    velocity                  Velocity vector of the
source.
0.0           max_displace                Distance for the maximum
displacement a source.
0              reset_source               Displacement control(0 -
2). Refer the documentation for details.
```

turbulence.in

```
#!csi_version=2.2.0
#=====

11          turbmodel          Turbulence model flag
(RANS):0=Upwinding, 1=k-eps, 2=rng k-eps, 3=rapid distortion rng k-eps.
0.0845      cmu                Turbulent viscosity
coefficient. Typically 0.09 for k-eps and 0.0845 for rng k-eps.
1.0         rpr_tke            Reciprocal TKE Prandtl
number. Typically 1.0 for k-eps, 1.39 for rng k-eps.
1.42        ceps1              Turbulent dissipation (eps)
constant. Typically 1.44 for k-eps, 1.42 for rng k-eps.
1.68        ceps2              Turbulent dissipation (eps)
constant. Typically 1.92 for k-eps, 1.68 for rng k-eps.
-1.0        ceps3              Turbulent dissipation (eps)
constant. Typically -1.0 to 0.5.
1.39        rpr_eps            Reciprocal turbulent
dissipation (eps) Prandtl number. Typically 0.7692 for k-eps, 1.39 rng k-eps.
0.012       beta              RNG k-epsilon constant.
Typically 0.012.
4.38        eta0              RNG k-epsilon constant.
Typically 4.38.
0.0         c_s                Turbulent spray source
constant. Typically 0 to 1.5.
0.03        c_ps              Drop turbulent dispersion
constant. Typically 0 to 0.16.
2.0         c_tke_les          LES sub-grid estimate
constant. Typically 2.0.
0.05        c_tke_visc_les     LES Viscosity coefficient.
1.0         c_eps_les          Turbulent LES dissipation
constant. Typically 1.0.
1           wall_model         LES wall model: 0=standard
law of the wall, 1=Werner and Wengle (recommended).
11.4        re_crit           Law of the wall critical
Reynolds number.
0.15        clw               Law of the wall constant.
0.42        law_kappa         Von Karman's constant.
5.5         law_b             Law of wall parameter.
10          heatmodel         Wall heat transfer model:
0=O'Rourke , 1=Han and Reitz, 2=Angelberger.
0           turb_stat_flag     Select turbulent statistics
model (0=disabled).
-999999     turb_stat_start_time
-999999     mean_stat_end_time
0.0001      turb_stat_tol
```

C. MATLAB Source Codes

The Student Edition of MATLAB r2015a was used extensively throughout this research effort. It was used first to run the calculations necessary to estimate a scaled engine's approximate sizing. Although these parameters were not exact – they required some modification (discussed as the subject of Chapter II and in terms of tuning the engine in Chapter VII, Section B), construction of an engine at all would not have been possible without this first approximation. Next, the MATLAB Image Processing Toolbox was used to estimate approximate temperature distributions based on still images from video of the engine in operation filtered through an IR-pass filter. This process is discussed in more detail in Chapter V, Section E. Lastly, MATLAB's recently updated plotting tools were used to visualize mass-averaged and polled CFD data as well as data from the engine test stand due to its improved handling of large data sets compared to Microsoft Excel and even older versions of MATLAB. The source code for this was not included as it largely involved importing the large raw data set and simply repeating plot formatting code which is well-described in the MATLAB help files.

1. Brayton-Gluhareff Cycle Approximate Sizing

```
%Richard Bramlette
%Graduate Research Assistant
%University of Kansas
%27 July 2010

%PROGRAM TO DESIGN A GLUHAREFF PRESSURE JET ENGINES

%This program will allow the user to design and size a Gluhareff Pressure
%Jet engine based on the parameters available such as engine thrust, tank
%pressure, etc...

%Design Input Specifications
ID0 = 0.0400;           %Injector Inner Diameter (in.)
Pf = 74.700;           %Injector Feed Pressure (psia)
Tf = 420.00;           %Injector Feed Temp (deg F)
Tflame = 1670.0;       %Third Stage Flame Temp (deg F)

N0 = 0.9097;           %Injector Efficiency (per 1)
Ni = 0.6747;           %Inlet Efficiency (per 1)

phi3 = 0.9429;         %Third Stage Equivalency Ratio
phi2 = 0.8068;         %Second Stage Equivalency Ratio
phi1 = 0.3807;         %First Stage Equivalency Ratio
f_stoich = 15.500;     %Stoichiometric Air/Fuel Ratio for Fuel

F15 = 639;             %G8-2-15 Operating Frequency (Hz)
ID15 = 0.125;         %G8-2-15 Injector Inner Diameter (in.)

%Operating Conditions
Pamb = 14.700;         %Ambient Pressure (psia)
Tamb = 70.000;         %Ambient Temp (deg F)
g = 32.178;           %Acceleration Due To Gravity (ft/sec^2)
y_prop = 1.15;         %Ratio of Specific Heats for Propane
y_air = 1.40;          %Ratio of Specific Heats for Air
R_prop = 1130;         %Propane Gas Constant (ft-lbf/slug-R)
R_air = 1716;         %Air Gas Constant (ft-lbf/slug-R)

% Derived Specifications
%=====
A0 = pi*(ID0/2)^2;     %Injector Exit Area (sq.in.)
Tf = Tf + 459.67;      %Injector Temperature (Rankine)
Tamb = Tamb + 459.67;  %Ambient Temperature (Rankine)
rhoAMB = Pamb*144/(R_air*Tamb); %Ambient Density (slug/ft^3)
Tflame = Tflame + 459.67; %Third Stage Flame Temp (Rankine)

%=====
%                               Injection Nozzle Analysis
%=====
%Injector Mass Flow Rate (slug/sec)
yf = y_prop; Rf = R_prop;
mdot0_ideal = Pf*A0*sqrt((yf/(Rf*Tf))*(2/(yf+1))^(((yf+1)/(yf-1))));
mdot0 = N0*mdot0_ideal;
```

```

%Injector Exit Temperature (deg R)
y0 = yf;
T0 = Tf*(Pamb/Pf)^((y0-1)/y0);

%Injector Sound Speed (ft/sec)
R0 = Rf;
a0 = sqrt(y0*R0*T0);

%Injector Exit Density (slug/ft^3)
R0 = Rf; P0 = Pf;
rho0 = P0/(R0*T0);

%Injector Exit Speed (ft/sec)
V0 = N0*a0;

%Injector Dynamic Pressure (psia)
Q0 = (1/144)*(1/2)*rho0*V0^2;

%Injector Kinetic Energy (slug-ft^2/sec^2)
KE0 = (1/2)*mdot0*V0^2;

%Injector (and thus engine) Operating Frequency (Hz)
Fx = F15*(ID15/ID0);

%Injector Length (Unnecessary; Ignore)
L0 = 0;

%Save All Injector Data
Injector = [0; N0; Fx; mdot0; rho0; L0; A0; ID0; V0; y0; R0; T0-
459.67; a0; P0; Q0; 1; KE0];
InjectorG = [0; N0; Fx; mdot0*g; rho0*g; L0; A0; ID0; V0; y0; R0/g; T0;
a0; P0; Q0; 1; KE0*g];

%=====
%                               Air Intake System Analysis
%=====

% Sizing FIRST Stage Inlet
%=====
f1 = phil*f_stoich;           %Necessary fuel/air mixture
mdot1 = f1*mdot0;           %Total mass flow for fuel/air mixture
                               (slug/sec)

N1 = Ni;                     %Efficiency from Injector to First Stage (per
1)
KE1 = N1*KE0;                %First Stage Kinetic Energy (slug-ft^2/sec^2)
V1 = sqrt(2*KE1/mdot1);      %First Stage Inlet Speed (ft/sec)

rho1 = rhoAMB*(1-(1/f1)) + rho0*(1/f1); %Rule of Mixtures to find rho
A1 = 144*mdot1/(rho1*V1);    %First Stage Area needed to achieve mdot1
                               (in.^2)
ID1 = 2*sqrt(A1/pi);         %First Stage Inner Diameter needed for Area
                               (in.)

```

```

Q1 = (1/144)*(1/2)*rho1*V1^2;    %First Stage Dynamic Pressure (psia)
P1 = Pamb - Q1;                  %First Stage Static Pressure (psia) ***CHECK
THIS***

R1 = R_air*(1-(1/f1)) + R_prop*(1/f1);    %Rule of Mixtures to find R
y1 = y_air*(1-(1/f1)) + y_prop*(1/f1);    %Rule of Mixtures to find gamma
Tex = P1*144/(rho1*R1);                %Ideal Gas Law Temp (R) ***CHECK
THIS***

T1 = Tamb*(1-(1/f1)) + Tex*(1/f1);        %First Stage Temperature (R)
***CHECK THIS***

%R1 = Rf; y1 = yf; T1 = T0;    %Assuming Fuel Properties into First Stage
%R1 = R_air; y1 = y_air; T1 = Tamb;

a1 = sqrt(y1*R1*T1);                %Sound Speed in First Stage (ft/sec)
L1 = a1/(2*Fx);                      %First Stage Inlet Length (ft)

% Sizing SECOND Stage Inlet
%=====
f2 = phi2*f_stoich;                  %Necessary fuel/air mixture
mdot2 = f2*mdot0;                    %Total mass flow for fuel/air mixture
(slug/sec)

N2 = Ni^2;                            %Efficiency from Injector to Second Stage
(per 1)
KE2 = N2*KE0;                         %Second Stage Kinetic Energy (slug-
ft^2/sec^2)
V2 = sqrt(2*KE2/mdot2);               %Second Stage Inlet Speed (ft/sec)

rho2 = rhoAMB*(1-(1/f2)) + rho0*(1/f2);    %Rule of Mixtures to find rho
A2 = 144*mdot2/(rho2*V2);                 %Second Stage Area needed to achieve mdot2
(in.^2)
ID2 = 2*sqrt(A2/pi);                      %First Stage Inner Diameter needed for Area
(in.)

Q2 = (1/144)*(1/2)*rho2*V2^2;            %Second Stage Dynamic Pressure (psia)
P2 = Pamb - Q2;                          %Second Stage Static Pressure (psia) ***CHECK
THIS***

R2 = R_air*(1-(1/f2)) + R_prop*(1/f2);    %Rule of Mixtures to find R
y2 = y_air*(1-(1/f2)) + y_prop*(1/f2);    %Rule of Mixtures to find gamma
T2 = P2*144/(rho2*R2);                    %Second Stage Temperature (R) ***CHECK
THIS***

a2 = sqrt(y2*R2*T2);                      %Sound Speed in First Stage (ft/sec)
L2 = a2/(2*Fx);                          %Second Stage Inlet Length (ft)

% Sizing THIRD Stage Inlet
%=====
f3 = phi3*f_stoich;                      %Necessary fuel/air mixture for combustion
mdot3 = f3*mdot0;                        %Total mass flow for fuel/air mixture
(slug/sec)

```

```

N3 = Ni^3; %Efficiency from Injector to Third Stage (per
1)
KE3 = N3*KE0; %Third Stage Kinetic Energy (slug-ft^2/sec^2)

V3 = sqrt(2*KE3/mdot3); %Third Stage Inlet Speed (ft/sec)

rho3 = rhoAMB*(1-(1/f3)) + rho0*(1/f3); %Rule of Mixtures to find rho
A3 = 144*mdot3/(rho3*V3); %Third Stage Area needed to achieve mdot3
(in.^2)
ID3 = 2*sqrt(A3/pi); %First Stage Inner Diameter needed for Area
(in.)

Q3 = (1/144)*(1/2)*rho3*V3^2; %Third Stage Dynamic Pressure (psia)
P3 = Pamb - Q3; %Third Stage Static Pressure (psia) ***CHECK
THIS***

R3 = R_air*(1-(1/f3)) + R_prop*(1/f3); %Rule of Mixtures to find R
y3 = y_air*(1-(1/f3)) + y_prop*(1/f3); %Rule of Mixtures to find gamma
T3 = Tflame; %Third Stage Temperature (R) **ASSUMED**

a3 = sqrt(y3*R3*T3); %Sound Speed in First Stage (ft/sec)
L3 = a3/(4*Fx); %Third Stage Inlet Length (ft)

%Save All Inlet Data
Inlet1 = [1; N1; Fx; mdot1; rho1; L1; A1; ID1; V1; y1; R1; T1-459.67;
a1; P1; Q1; f1; KE1];
Inlet2 = [2; N2; Fx; mdot2; rho2; L2; A2; ID2; V2; y2; R2; T2-459.67;
a2; P2; Q2; f2; KE2];
Inlet3 = [3; N3; Fx; mdot3; rho3; L3; A3; ID3; V3; y3; R3; T3-459.67;
a3; P3; Q3; f3; KE3];

Inlet1G = [1; N1; Fx; mdot1*g; rho1*g; L1; A1; ID1; V1; y1; R1/g; T1;
a1; P1; Q1/144; f1; KE1*g];
Inlet2G = [2; N2; Fx; mdot2*g; rho2*g; L2; A2; ID2; V2; y2; R2/g; T2;
a2; P2; Q2/144; f2; KE2*g];
Inlet3G = [3; N3; Fx; mdot3*g; rho3*g; L3; A3; ID3; V3; y3; R3/g; T3;
a3; P3; Q3/144; f3; KE3*g];

Ln = L2*2; %Length of Nozzle/L2 = 2 (ft)
IDcc = L3/2; %Diameter of Combustor/L3 = 1/2 (in.)
Lcc = ((3.6988*ID0) + 0.8307)*L2*1.15; %Length of Combustor (ft)
%Note: Trend of ratio with injector ID and adding 15% for nose
%section (which was not included in trend calc).
IDn = (2/3)*IDcc; %IDn/IDcc = 0.66 (in.)
ID3f = ID3*(1.25); %Flared slope of 8 (in.)

%=====
% Organize Results
%=====

%Concatenate All Data
DATA = [Injector Inlet1 Inlet2 Inlet3];
DATA_G = [InjectorG Inlet1G Inlet2G Inlet3G];

%Write out designed specifications

```

```

fprintf('The Engine has been sized based on:\n')
fprintf('Injector Inner Diameter = %2.4f in.\n',ID0)
fprintf('Injector Feed Press.     = %4.1f psi\n',Pf)
fprintf('Injector Feed Temp.      = %4.1f deg F\n',Tf-459.67)
fprintf('Injector Efficiency       = %3.2f %%\n',N0*100)
fprintf('Inlet Efficiency           = %3.2f %%\n',Ni*100)
fprintf('Equivalency Ratios         = %1.4f %1.4f %1.4f\n',phi1,phi2,phi3)
fprintf('Stoich. Air/Fuel Ratio     = %3.2f\n',f_stoich)
fprintf('=====\n\n')
fprintf('Operating Frequency = %5.1f Hz\n\n',Fx)
fprintf('First Stage Inlet:\n')
fprintf('=====\n')
fprintf('Inner Diameter = %2.4f in.\n',ID1)
fprintf('Length         = %2.4f in.\n\n',L1*12)
fprintf('Second Stage Inlet:\n')
fprintf('=====\n')
fprintf('Inner Diameter = %2.4f in.\n',ID2)
fprintf('Length         = %2.4f in.\n\n',L2*12)
fprintf('Third Stage Inlet:\n')
fprintf('=====\n')
fprintf('Inner Diameter = %2.4f in.\n',ID3)
fprintf('Flared ID      = %2.4f in.\n',ID3f)
fprintf('Length         = %2.4f in.\n\n',L3*12)
fprintf('Combustion Chamber:\n')
fprintf('=====\n')
fprintf('Inner Diameter = %2.4f in.\n',IDcc*12)
fprintf('Length (w nose)= %2.4f in.\n\n',Lcc*12)
fprintf('Nozzle:\n')
fprintf('=====\n')
fprintf('Inner Diameter = %2.4f in.\n',IDn*12)
fprintf('Length         = %2.4f in.\n\n',Ln*12)

```

2. Temperature Contour Image Processing and Analysis (IMG2IR.m)

The following source code was used with the MATLAB 2015a Student License. It depends on the MATLAB Image Processing Toolbox to generate apparent temperature contours from IR-pass filtered still-images of the pressure jet engine in quasi-periodic operation. Maximum and minimum temperatures were experimentally measured with type-K thermocouples held to the engine external surface with a friction fit via an additional layer of sheet steel. The method is discussed in more detail in Chapter V-E.

```
%Richard Bramlette
%University of Kansas
%Ph.D Research
%
%IMG2IR - Code to Read in an Image of an Object Heated to Incandescence and
%Convert the Information to Apparent Temperature Contours Scaled Using
%Measurements of the Actual Maximum and Minimum Temperatures

%User Input Values
Tmax = 2000;           %Max Temperature in deg F
Tmin = 800;           %Min Temperature in deg F
dTContour = 20;       %Contour Step Size, deg F

t_start = cputime;
%Read in User-Selected Image File
[filename pathname filterindex] = uigetfile({'*.png;*.jpg;*.tif;*.gif'});
[image map alpha] = imread(filename);      %Read Image at filename
[X Y N] = size(image);                    %Get Image Size
fprintf('%s was read into memory (%i Pixels Tall, %i Pixels Wide)\n',...
        filename,X,Y')

%Convert Red/Green/Blue Image to Black/White
I = rgb2gray(image);                       %Note: BW is uint8 data
Imax = single(max(BW(:)));                 %Check Max Brightness
Imin = single(min(BW(:)));                 %Check Min Brightness

%Scale BW Data to Max and Min Temperature
Tapp = single(BW)*((Tmax - Tmin)/(Imax - Imin)) + Tmin;

%Plot Scaled Image Data Contours
figure(3)

subplot(2,1,1)
imshow(filename)                            %Show Original Image
title(sprintf('Original Image: %s',filename))

fprintf('Generating Contours of Apparent Temperature From Image File...\n')
```

```

subplot(2,1,2)
v = [Tmin:dTContour:Tmax];           %Array of Temp. Contour Values
[Cf,hf] = contourf(Tapp,v);         %Show Temperature Contours
if length(v) > 10                    %If more than 10 Contours,
    hf.LineColor = 'none';          %Turn Off Contour Lines
end

%Limit Plot to Image Size with no skew
axis([0 Y 0 X], 'equal')

%Flip Image Y-Axis and Remove Irrelevant Pixel Numbers on Axes
set(gca, 'ydir', 'reverse', 'XTickLabel', [], 'YTickLabel', [])

%Add Contour Plot Title, Colorbar, and Colorbar Title
title(sprintf('Apparent Temperature Contours, \\DeltaT = %2.0f \\circF',...
dTContour))
Cb = colorbar('southoutside');
Cb.Label.String = 'Apparent Temperature (\\circF)';

t_end = cputime;
t_run = t_end - t_start;
fprintf('Contour Image Processing Complete in %0.1f sec\\n', t_run)

```

D. Selected Original Production Gluhareff Engine Drawings

The following pages comprise the complete set of currently-available flat drawings originally sold by Eugene Gluhareff. These show the complete list of measurements drawn to scale by Eugene Gluhareff himself and copied from the best sources available. They include the complete list of parts necessary to build a pressure jet engine from raw sheet metal and tubing. The original engines were as much works of fine machine art as they were works of proper engineering. A skilled machinist and welder is recommended for attempting assembly of a new engine.

Included Jet Engine Plans:

G8-2-5

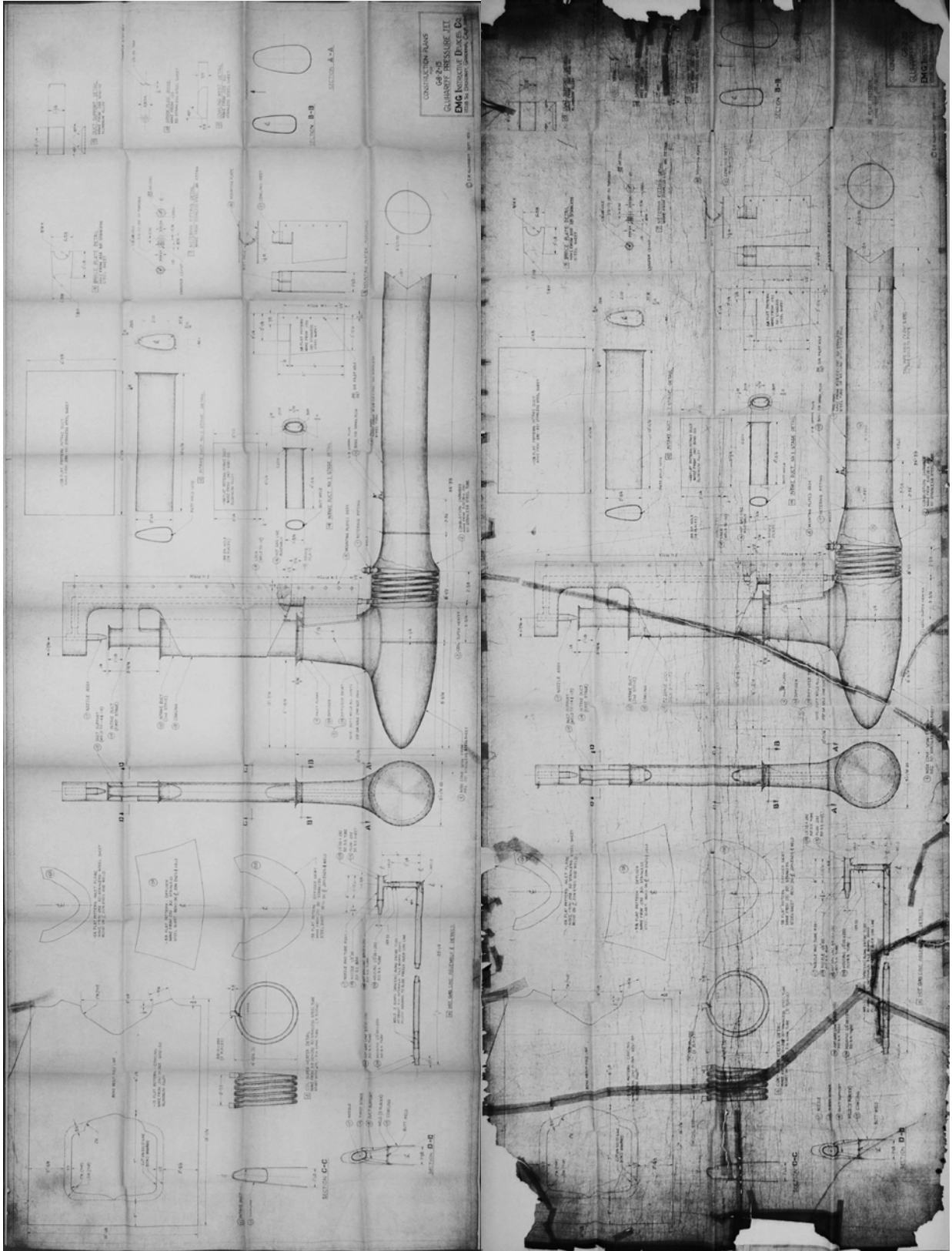
G8-2-15

G8-2-20

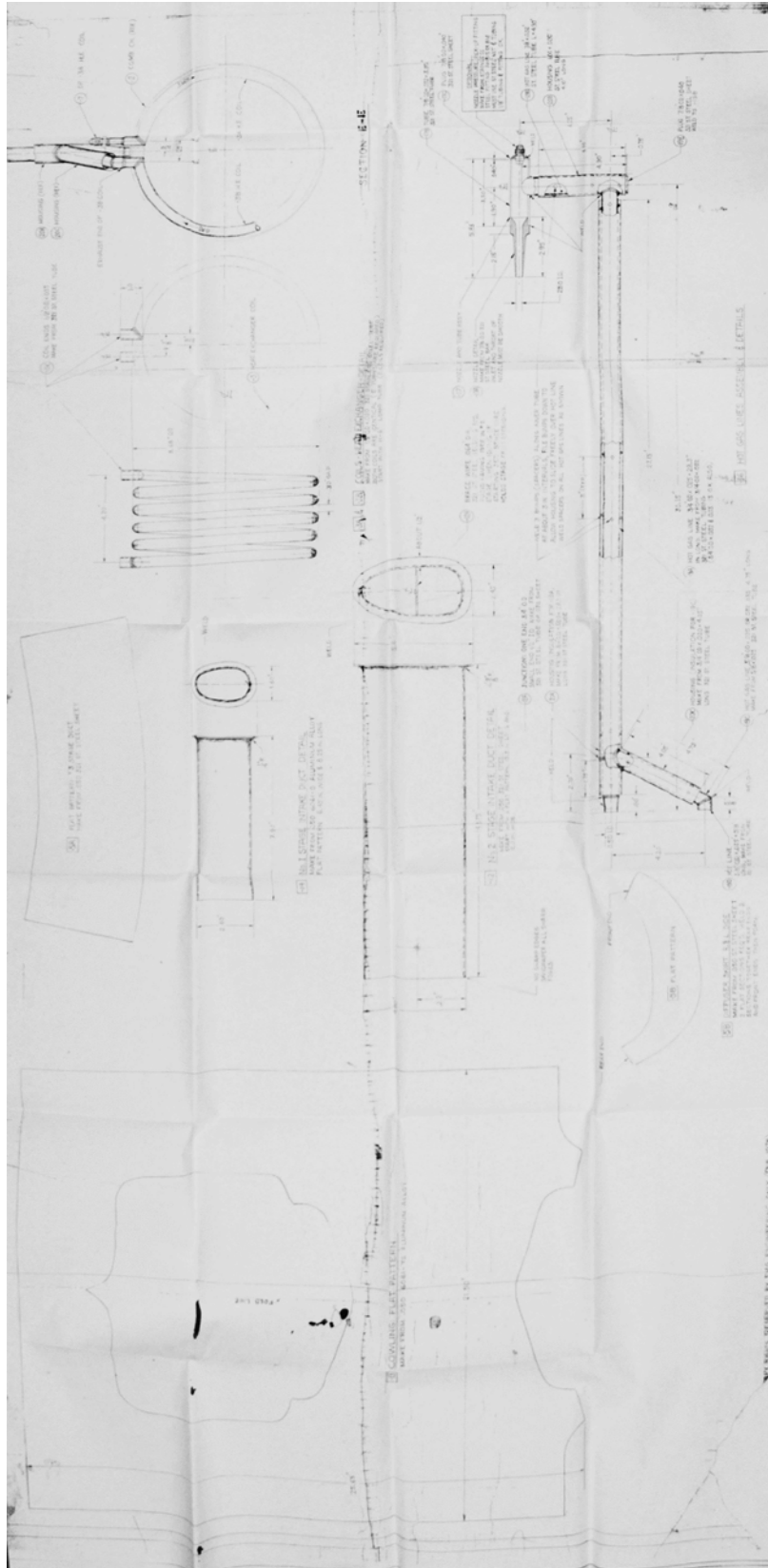
G8-2-40

G8-2-130 (in two parts)

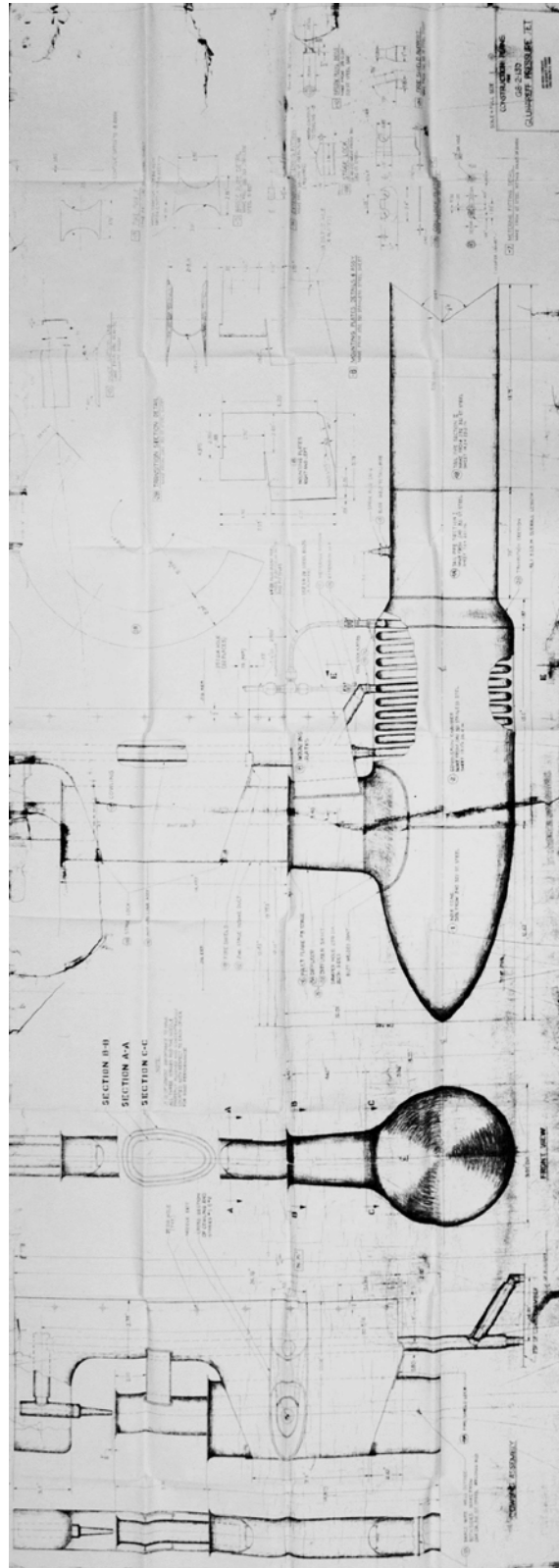
The images are intended for educational purposes only. Due to the folds in the plan sheets, some of the contours may be skewed. If you intend to scratch build a pressure jet engine based on plans, do so carefully and, if possible, work from a high resolution scan of these plans. Also included is the set of instructions on how to assemble the parts shown in these plans.



G8-2-15 (Left) and G8-2-20 (Right) Pressure Jet Engine Construction Plans



G8-2-130 Pressure Jet Engine Construction Plans (Part 1)



G8-2-130 Pressure Jet Engine Construction Plans (Part 2)

G8-2 Pressure Jet Assembly Instructions

EMG ENGINEERING CO.

18518 SOUTH BROADWAY • GARDENA, CALIFORNIA 90247

INSTRUCTIONS

To build the G8-2 Jet Engine correctly follow the directions for fabricating and assembling given here and on the construction plans.

It is not mandatory which parts you fabricate first, altho the following sequence is suggested. However, it is of the utmost importance in assembling to follow the specified procedure as stated here for best results.

Each part is numbered to correspond with the number on the price list, parts list, and on the construction plans.

1. The first part to be made should be the Nose Cone, part # 1.

If you do not have a spinning lathe the nose cone can be made from several conical rings as shown in Fig.#1a.



FIG. 1a

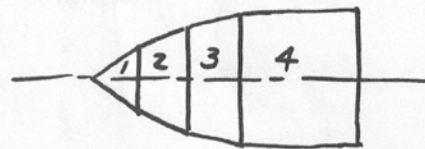


FIG. 1b

You can lay out the sizes of the rings right on the blueprint of nose cone. Ref. Fig. #1b. Welding all the rings together will result in a correct sized nose cone.

The welds must be filed to avoid excessive concentration of metal. Blobs of metal or a crude weld will eventually result in cracking from thermal fatigue.

2. The second part should be the Combustion Chamber, part # 2.

Follow the blueprint. If you have no spinning facilities the Combustion Chamber can be made by welding together a cylinder and a cone. See Fig#2a.

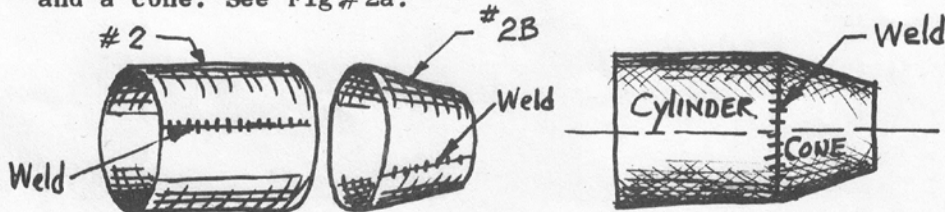


FIG. 2a

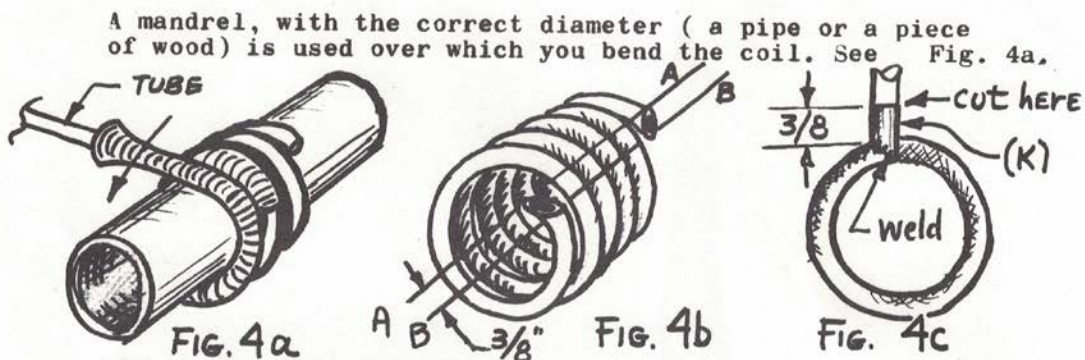
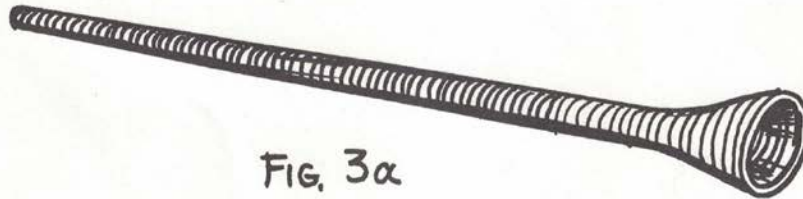
FIG. 2b

You can determine from the blueprint the size of the cylinder and the cone. See Fig. 2b.

- 1 -

3. The third part is the Heat Exchanger Coil, part # 3.

If you are bending your own coil use a wire Tube Bender for 3/8 O.D. tubing. Available in any hardware store. See Fig. 3a.

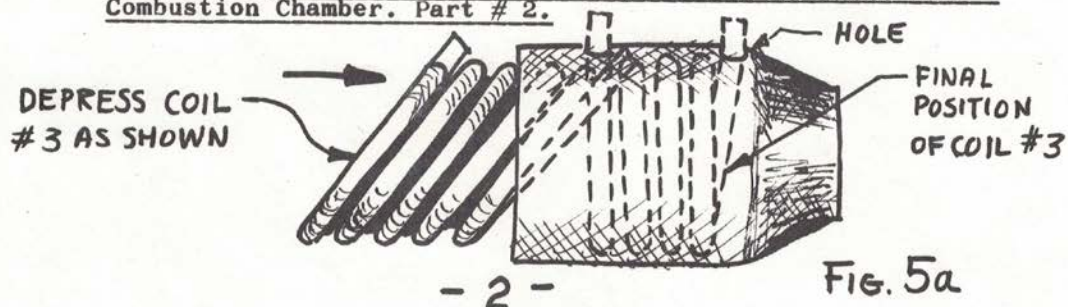


When the coil is bent to the proper outside diameter and has (5) five turns, cut off the excess ends at 45°, with 3/8 in. between lines A & B. See Fig. 4b. When the inlet and outlet ends are welded on, they will be in line and between lines A & B as shown. See blueprint.

Weld inlet and outlet (K) to the coil. Cut a 3/8 O.D. x .032 stainless steel tube at a 45° angle, and weld it to the 45° cut on the coil. See Fig. 4c. Make sure the weld is good and without any pin holes. This is a vital part and must have an excellent weld.

Weld both ends in a similar way. Then cut off the excess, resulting in two short stubs 3/8 in. high at 90° to the coil.

4. Fourth step. Assemble Heat Exchanger Coil, Part #3, and Combustion Chamber. Part # 2.

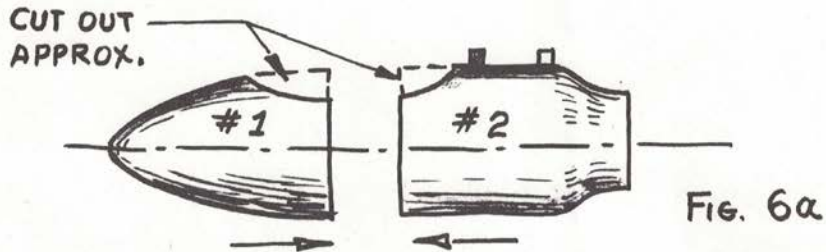


Squeeze the Coil as shown and slide it into the Combustion Chamber so that the Coil inlet and outlet ends fall into the 3/8 I.D. holes provided in the Combustion Chamber shell.

As the inlet & outlet stubs protrude through the Combustion Chamber holes keep pushing the Coil until it assumes its proper location as shown in dotted lines. See Fig. 5a.

DO NOT WELD Coil to the Combustion Chamber. It must be a good tight fit but free to expand and contract with temperature change of hot gas inside. Longitudinal expansion.

5. Step five. Weld Nose Cone, Part # 1, and Combustion Chamber, Part # 2.

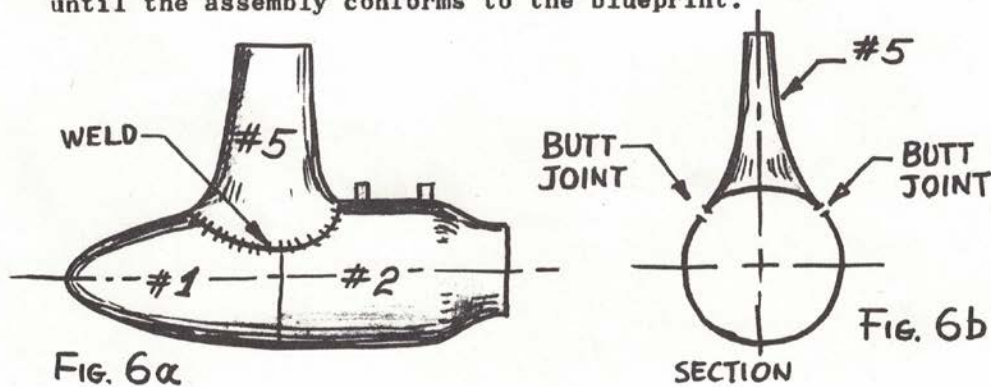


Cut out metal as shown to make a hole that would be approximately the size required to install part # 5. This is for an access hole while aligning and welding parts # 1 & 2.

Before welding tack every inch to assure concentricity, then weld. Straighten out the weld if deformed while the access hole exists.

6. Step six. Weld Diffuser part # 5 to the Nose Cone and Combustion Chamber assembly.

If you are making your own Diffuser, part # 5, note that it consists of a flat pattern 5A and 5B. Ref. blueprint. These parts must be welded together first and worked by forming until the assembly conforms to the blueprint.



When the Diffuser is completed place it on top of the Nose Cone - Combustion Chamber Assembly, over the access hole, locating properly its exact position and angle. Ref. blueprint.

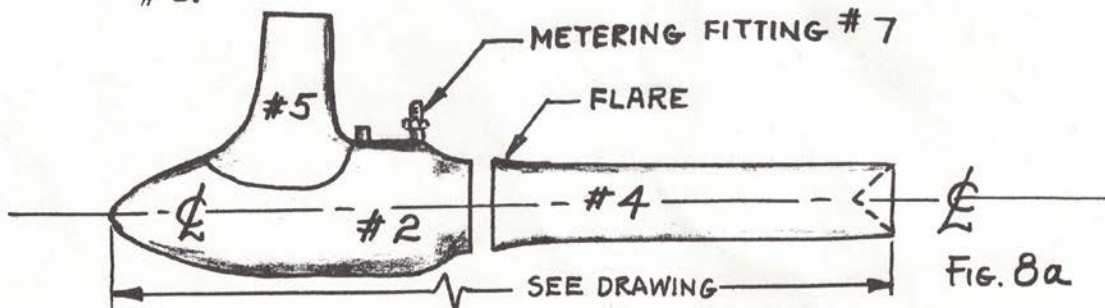
With a scribe scribe the outline of part # 5 on the assembly of parts # 1 & 2 as it saddles it. Then remove part # 5 and cut the hole exactly as scribed.

Make a butt joint close fitted all around. Tack every one inch and then weld. Straighten out the weld if it warps to maintain the desired shape by hammering. File the weld if needed to remove all bumps.

7. Step seven. Weld Metering Fitting part # 7 to the Heat Exchanger Coil Inlet. (ONE OR TWO COILS, DEPENDING ON MODEL)

Insert Metering Fitting part # 7 narrow end into 3/8 O.D. inlet like a cork. Then weld all around. Check for pin holes. Ref. blueprint.

8. Step eight. Weld Tail Pipe part # 4 to Combustion Chamber # 2.



The Tail-Pipe is made from a 3-1/2 in. O.D. OR 5" O.D. Steel tube. The end to be welded must be mated to correspond to the diameter of the end of Combustion Chamber. Sometimes a slight flaring of the Tail-pipe is required. See sketch 8a.

When aligning the Tail-pipe for welding to the Combustion Chamber, make sure that both pieces are on the same center-line and concentric with each other. Tack every inch of the circumference. then weld.

Measure 1N inches from the nose to the end of Tail-pipe, cut off the excess. Mark the fish-tail with scribe as per blueprint and cut.

9. Step nine. Weld stage No. 3 inlet Flare part # 6 to Diffuser part # 5, then weld Mounting Plates part # 8 and Brace Plate part # 9 to Mounting Plates Assembly.

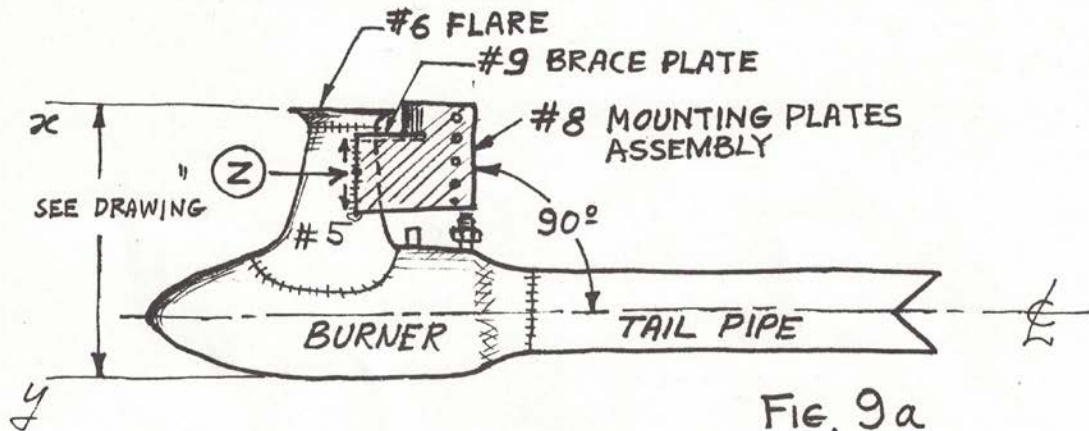


FIG. 9a

Match contour of Flare part # 6 to contour of Diffuser part # 5, by working one part or both until they are the same, matching cross section given on blueprint,

Cut top of Diffuser if needed to make overall distance between lines X & Y, SEE BLUEPRINT, AND Fig. 9a. Make absolutely sure that the top of Inlet Flare part # 6 is parallel to line Y-Y, or burner center-line.

It is very important that the both sides of the Inlet Flare be symmetrical in front view. The whole Diffuser assembly must be symmetrically mounted on burner.

To make a smooth entry file the weld joining parts #5 and # 6 inside and sand off all file marks, also sand off all sharp edges on Inlet Flare edge.

Weld Mounting Plates Assembly, part # 8 to Diffuser, part # 5 & # 6 assembly. Make sure that the mounting holes are located along a line perpendicular to the center line of burner. See Fig. 9a.

To avoid deformation of Diffuser when welding Mounting Plates # 8, follow this procedure. Locate Mounting Plates position on Diffuser as per blueprint. Tack Plates to Diffuser every 1/2 inch and on both sides.

Start welding at point Z half way of plate, as shown on Fig. 9a. Weld 1/2 inch at a time going in each direction, with time intervals to allow the weld to cool after every 1/2 in. of welding.

When welding is complete straighten out any deformation that may have resulted. Set plates parallel, and match the width of the tube you intend to mount the G8-2 Jet on.

Place The Brace Plate part # 9 in position on top of and between two parallel mounting plates # 8A. Ref. blueprint. Fuse edges of Mounting Plates and Brace Plate, also weld the corners to the Diffuser- Flare and the other corners to the curved part of the Mounting Plates Assembly. This provides a very stiff mounting means.

Weld Cowling Rest part # 21 and Sparkplug Boss part # 10, as per blueprint. Cowling Rest is a small steel bracket that is welded to the Mounting Plates Assembly, whose function is to locate and retain Cowling part # 13 in its proper relation to the Burner. (OPTIONAL)

Locate sparkplug position measuring from end of tail-pipe. Drill 3/8" ID. hole, place Boss part # 10 over it and weld, and with 1/4-32 tap chase the threads.

10. Step ten. Assemble Hot Gas Line, part # 16 and Nozzle, part # 17, then weld it to the burner.

Weld Nozzle part # 17A to a 3/8 O.D. tube part # 17B. Then weld plug part # 17C. Ref. blueprint. The new assembly becomes Nozzle Assembly part # 17, and set it aside.

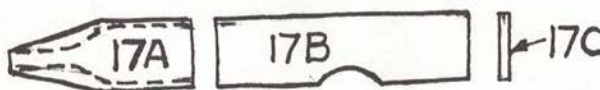


FIG. 10a

Assemble The Hot Gas Line part # 16. Start by welding together part # 19A and # 19B at 90° to each other. See Fig. 10b. and blueprint.

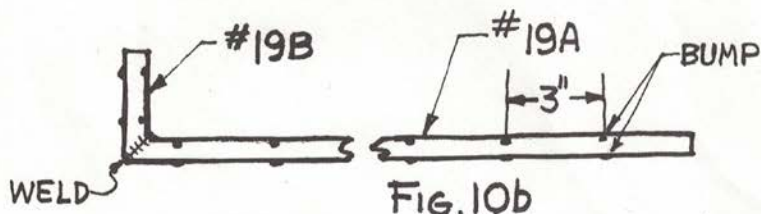


FIG. 10b

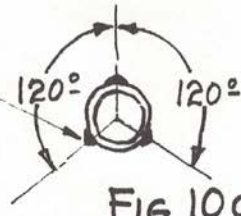


FIG. 10c

Weld clusters of 3 small bumps at 120° to each other and at 3 inch intervals, spaced along tube part # 19A and two clusters on tube 19B. Ref. blueprint.

These bumps serve as spacers that hold the outer tube (housing) parts # 20A & 20B from contacting the hot gas line. The air space between the two tubes acts as insulator which reduces the heat loss of gas in the line.

Slide the outer tube (housing) part # 20A over hot gas line part # 19A while filing down the restraining bumps, so that the housing slides freely all the way to the joint of part # 19B.

Weld bumps on part #19B, file and slide housing part #20B in a similar fashion. The two housings meet at 45° to each other. Then weld them together allowing the other ends to remain free, thus allowing the hot line to expand and contract unobstructed. SEE BLUEPRINT FOR ASSEMBLING HOT LINE FOR DIFFERENT MODELS.

Part # 17, that was laid aside, now weld it to the Hot Gas Line Assembly, part # 16, as shown on blueprint. Make sure you do not block the passage by inserting tube # 19B too deep into tube # 17B.

Weld open end of part # 16 to the open end of outlet of COIL #3 OR COILS that protrudes from the shell of the combustion chamber.

Make sure that the weld is good and without pin holes. It is a vital part. This tube carries hot Propane gas at 1,120°F and must be leak proof and strong.

This completes the fabrication of the Burner of G8-2 Jet.

COWLING ASSEMBLY

Cowling assembly is comprised of the following parts: # 12, # 13, # 14, # 15, & #18.

Cowling is the assembly of the first and second stage intake ducts, the part when assembled with the burner (just completed) constitutes a completed G8-2 Jet Engine.

11. Eleventh step. Fabricate second stage intake duct, part #12.

Form flat pattern #12A into an elliptical shape as shown on blueprint. To bend it over use a steel pipe or a wooden mandrel of proper contour. Weld at the wide end. Straighten out the duct and weld if deformed.

Flare one end of duct #12 by hammering over a steel pipe. File and sand inside of the flare and all sharp edges of flare rim. The entry must be smooth.

The length of duct #12 must be AS PER BLUEPRINT, the flat pattern provides more metal than is needed therefor measure and cut off the excess. Make sure the ends of the duct are perpendicular (90°) to the walls.

12. Twelfth step. Fabricate first stage intake duct, part # 14.

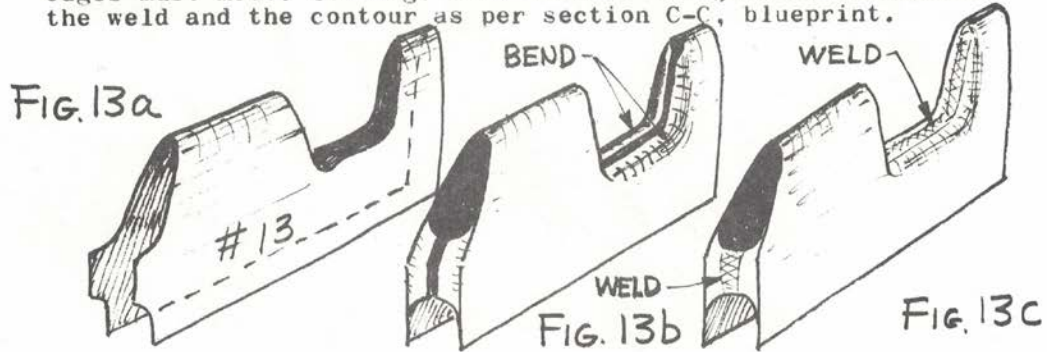
Bend flat pattern #14A into an elliptical shape and weld in the same way you constructed duct #12. Ref. to blueprint. Mark, position and weld two aluminum duct supports #15 to the first stage part #14. Ref. section D-D on blueprint.

Clean and polish inside of first stage and flare, and set aside.

13. Thirteenth step. Form cowling part #13

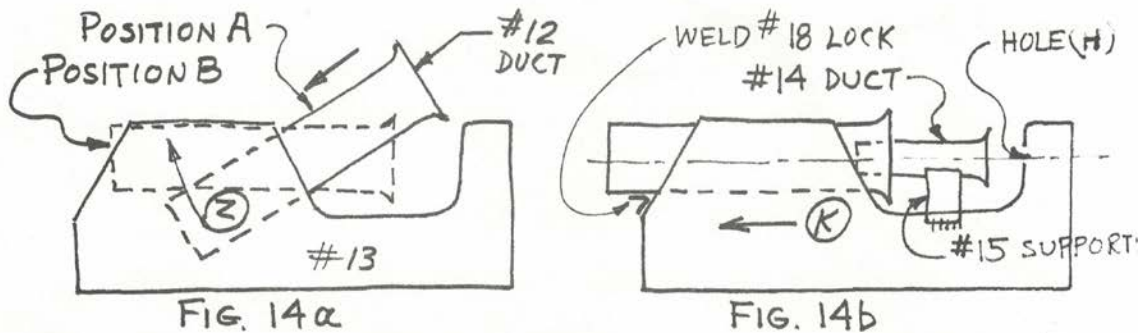
It is suggested that you make a wooden form to simplify the fabrication of the cowling part #13. Bend flat pattern #13A in half, see fig. 13a and section C-C and D-D, blueprint.

Place bent flat pattern #13A over the wooden form and fasten it to the wooden block with C clamps, then using rawhide hammer bend inward the edges of the cutout and the end. The edges must meet. See fig. 13b. Weld at the joints. Straighten the weld and the contour as per section C-C, blueprint.



14. Fourteenth step. Assemble first and second stage intake ducts with cowling part #13

Insert 2nd stage duct, part #12, as shown in fig. 14a, position A, by filing a hole in cowling, part #13, just enough to fit duct #12. Elongate the hole until it is possible to rotate duct #12 as shown, to assume a horizontal position, position "B". See fig. 14a, also section C-C, blueprint showing final position of duct part #12.



File the hole at the other end of cowling part #13 so that by pushing duct #12 in the direction "K" indicated Fig. 14b, the duct #12 will protrude from the cowling as shown Fig. 14b and will come to rest when flare of #12 contacts cowling #13.

Lock duct #12 and the cowling in this position by welding part #18 to duct #12 in two spots.

Weld First stage part #14 to cowling part #13. See fig. 14b. For ease of aligning and welding make a wooden mandrel that can be inserted into duct #12 and then duct #14 with proper alignment AND DISTANCE between flares. Weld duct supports #15 to cowling part #13. Remove the wooden mandrel.

Drill nozzle access hole (H) in cowling, Fig 14b. The hole must be concentric with 1st stage, part #14, and should be 1/2 in. diameter, for ease of nozzle insertion the hole must be filed elliptical.

Assembling the burner and cowling it is of the utmost importance that the 2nd stage, duct #12 be inserted 5/16 in. into the 3rd stage. See blueprint. The space between the two parts must be the same all around for best performance of G8-2 jet engine.

FIRST FIRING OF THE NEW ENGINE

The first firing is the most important firing, it must be conducted as prescribed.

Ignite the G8-2, by any means, electric or a match, start warming up the engine by opening the throttle gently and slowly, allowing all the parts to come to an even temperature.

Keep increasing the throttle, the engine will hum and the noise level will increase, don't quit now, keep opening the throttle, the engine will get red hot, don't get frightened, it is normal.

Slowly open to full throttle, the jet shell will be glowing orange and roaring, keep it up for about 30 seconds then you can shut it off by turning off the fuel, (throttle).

What you have done is to remove all the internal buildup of stress as a result of welding. Bring the whole engine to temperature slowly, thus annealing the metal and releasing all stress concentrations.

If the jet is fired fast without even warmup and gradual temperature increase, you may deform or break the unit.

After the first controlled firing you can fire any which way you want, it is then safe.

WARNING

Do not forget to use liquid Propane, not gas. If you do not have a tank with a liquid pick-up, turn your tank upside-down this way you will be getting liquid instead of gas.

E. G8-2 Pressure Jet Technical Handbook



REVISED 1985

TECHNICAL HANDBOOK

**AN AMAZING JET ENGINE
YOU CAN BUILD
IN YOUR OWN
SHOP!**

G8-2 GLUHAREFF PRESSURE JET ENGINE



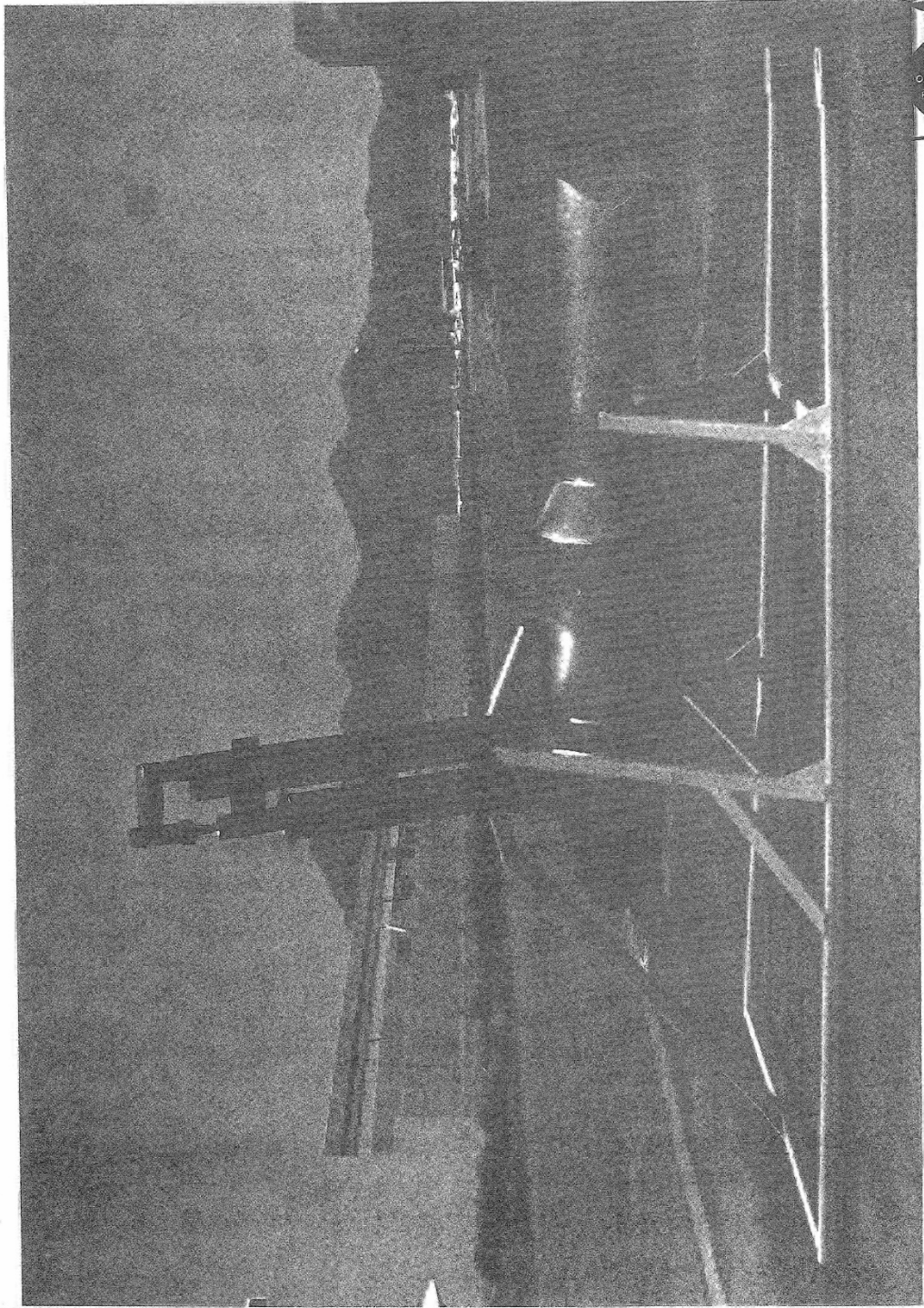
EMG ENGINEERING CO.

P.O. BOX 1368 HESPERIA, CA. 92345

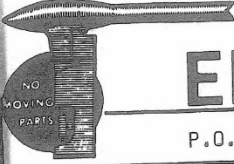
TABLE OF CONTENTS

Introduction	5
Basic Principle of The GB-2 Jet Engine	7
Model GB-2-5 Data.	8
Model GB-2-20 Data	9
Portable Demonstrator GB-2-15	9
Model GB-2-40 Data	10
Model GB-2-80 Data	11
Propane Tank Pressurization System.....	11
Schematic Diagram of GB-2 Fuel & Control	12
Model GB-2-130 Data	13
Model GB-2-130R Data	13
Mollier Diagram for Propane.....	14
Discussion of GB-2 Jet Engine	15
Firing Instructions for GB-2 Jet.....	22
Why The GB-2 Jet was Invented & Comparison	23
Helicopter Blade Tip Installation of GB-2 Jet....	26
MEG-1X Helicopter Data.....	29
MEG-2X Helicopter Data.....	30
GB-2-15 Static Performance.....	32
GB-2-15 Windtunnel Data.....	34
MEG-2X & 3X Hovering Flight Data.....	35
MEG 3X Flying Platform Data.....	37
Other Jet Helicopters Powered by GB-2-20 & 40....	42
GB-2 Glider Power.....	43-52
Icarus V Hang-Glider.....	45
MEG-600 Jet Plane	47
Whilling Aircraft Co's PJ-1	50
BD-5 Powered by two GB-2-130 Jets	51
Space Ranger Data.....	53
Jet Go-Karts.....	54
Jet Bicycles	56
Hovercrafts.....	57
Jet Museum Exhibit Los Angeles CA.	58
GTS-15 Teaching Test Stand for Colleges.....	59

G8-2-700 JET ENGINE



NO
DIVING
PARTS



EMG ENGINEERING CO.

P.O. Box 1368 Hesperia, California 92345

Phone 619-247-8519



Eugene M. Gluhareff,

MESSAGE FROM THE PRESIDENT

Eugene M. Gluhareff, president and founder of The EMG Engineering Company, invites you to become acquainted with the EMG products, and become one of the pleased users of the G8-2 Jet Engines. Join other inventors who pioneer in new applications of the G8-2 Jets, who achieved new products and established new records.

Write and tell us what you have powered with your G8-2 Jet Engine. What new and exciting accomplishments have you attained.

Send us photo, performance data, and a brief description. Include your name, address, and a passport photo of yourself. We will give you honorable mention in this Technical Hand Book and will pay you \$20 if we use your photo.

If you would like to see the G8-2 Jet firing, drop in for a free demonstration, but give us a call a day ahead. Phone: 619-247-8519

If you need an engine of a different size or thrust perhaps we can be of service to you by designing and building the engine to suit your project.

Eugene M. Gluhareff

- 3 -

A FEW WORDS ABOUT MR. E. M. GLUHAREFF

Eugene M. Gluhareff is a graduate Aeronautical Engineer from the Rensselaer Polytechnic Institute, Troy, New York Class of 1942. He is holding a lifetime federal pilots license. Trained to fly as a cadet in US. Army Aircorps. He is also a well known helicopter designer and inventor of jet engines. His extensive experience was acquired over twenty five years of association with many helicopter companies as designer project engineer and developer.

He was a part of the helicopter history since its beginning with Sikorsky Aircraft Corp. Bridgeport Conn. as Primary Design Engineer and Project Engineer working directly under Mr. Igor I. Sikorsky and with Mr. Igor A. Sikorsky Chief of Aerodynamics. There he participated in the design of many helicopters. Among many others projects he was a Project Engineer testing and Developing of the single bladed helicopter system. Also invented & developed Kerosene fueled Valveless Pulse Jet which he used in designing a Single Blade One-Man helicopter which he test flown himself in 1949. He also designed a Delta-Wing Convertiplane, with foldable Single Bladed Rotor turbine powered with tip Cold-Jet for for The USAF.

In 1950 moved to California and joined The American Helicopter Co. Manhattan Beach, CA. as Project Engineer on Top-Sergeant a Valve Pulse-Jet Powered Helicopter. Shortly he was promoted to Preliminary Design and designed the XH-26 One-Man Tip Jet powered helicopter for The USAF. In 1952 he joined Rotorcraft Corp. Glendale, CA. as a Design Engineer redesigning of two bladed Tip Rocket Powered One-Man Helicopter for The US. Navy The Pin-Wheel.

In 1953 organized his own company, The Gluhareff Helicopters Corp. in Manhattan Beach, CA. Invented a Valveless-Pulse-Jet using Propane as fuel Designed a Single Bladed One-Man Portable Helicopter using that jet. Participated in USAF Competition with another Co. In 1955 The G8-2 Pressure-Jet was under development. With it Mr. Gluhareff designed and build the two Portable Helicopters MEG-1X and MEG-2X and later the MEG-3X Flying Platform. All were successfully flown in Palm Springs in 1959. The company ran out of funds.

In 1960 joined The US. Navy at Naval Ordnance Test Station, China-Lake CA. as Aerospace Engineer GS-12 and worked up to GS-14 as Project Engineer on Rotary Drones. In Fall of 1963 he joined Douglass Aircraft Co. Missile & Space Division, Huntington Beach, CA. as design Engineer Scientist on Saturn Rocket. He has participated in the launching of 4 Saturn Rockets in charge of the sequence of events from firing to parking orbit. He also did performance data verification and orbit analysis. On termination of S-4 stage he was transferred to Long Beach division as Senior Design Engineer in Advanced Systems on Special Projects, researching and testing rocket engines for two years. Then transferred to The Ejection Seat Group, he became a Specialist in the design of Rocket Stabilization Systems for the Ejection Seats and Capsules for USAF.

In 1972 again organized his own co. The EMG Engineering Co. Gardena, CA. here he pioneered in development and inventing more powerful G8-2 jet engines beyond 15 lbs. of thrust.

In 1981 moved to Hesperia, CA. Surviving the Terminal Lung Cancer in 1982 now is well and has been designing more powerful Jet Engines up to 700 lbs. thrust and engaged in new designs of jets and helicopters.

INTRODUCTION

The G8-2 Technical Hand-Book presents Information, Photos, Theory, Description, Principles and Functions of The Gluhareff Pressure Jet Engine. It also presents the uses and applications of The G8-2 Jet Engine by The EMG Engineering and our customers.

The reader may notice a bit of history as one analyzes the data and graphs especially referring to the first engine the G8-2-13 It was this first engine that made The MEG-2X Portable One-Man Helicopter air borne.

The information presented here was accumulated over a period of many years of research and testing. Starting with the G8-2-13 producing only 13 lbs. Max. static thrust. As improvements were made the thrust reached 15 lbs. The G8-2-15 was evolved. Researching and developing new inventions the thrust was growing. In 1978 in Gardena The new G8-2-20 was borne. This engine produced 23 lbs. statically. However; the weight and size did not change, it remained 5 lbs. but the G8-2-20H the helicopter engine weighed 7 lbs with different C.G.

The S.F.C. the specific fuel consumption, is also continually improving with the increasing of jet thrust. As the improvements are achieved they are automatically incorporated into all the engines and drawings which are periodically updated.

In 1978 EMG Engineering had 5 different models of G8-2 jets which are as follows

G8-2-5	5.25	lbs	of	thrust	static.
G8-2-20	23.00	"	"	"	"
G8-2-40	43.00	"	"	"	"
G8-2-82	82.00	"	"	"	"
G8-2-130	130.00	"	"	"	"

In 1984 the following new engines emerged.

G8-2-350	350.00	"	"	"	"
G8-2-700	700.00	"	"	"	"

These jets are rated on the basis of static thrust. However; with a forward speed the jet thrust increases. This is due to the Ram-Air, provided the engine has a properly designed and leakproof airscoup. The dynamic S.F.C. at about 200 - 250 mph. drops to 1/3 of static S.F.C. value and lower at higher speed.

The G8-2 jets starts with a push of a button. It is 100% throttleable with a smooth throttle progression. Idle to max. thrust with instant response of throttle variation. The thrust curve is a straight line. The jet emits no smoke or visible flame in day time. It has ecologically clean and non-toxic exhaust that consists of Steam and carbon-dioxide. All engines are made of heat resistant 321 Stainless steel and Aluminum. The G8-2 jet has no moving parts for that it is very reliable and has extremely long life without maintenance.

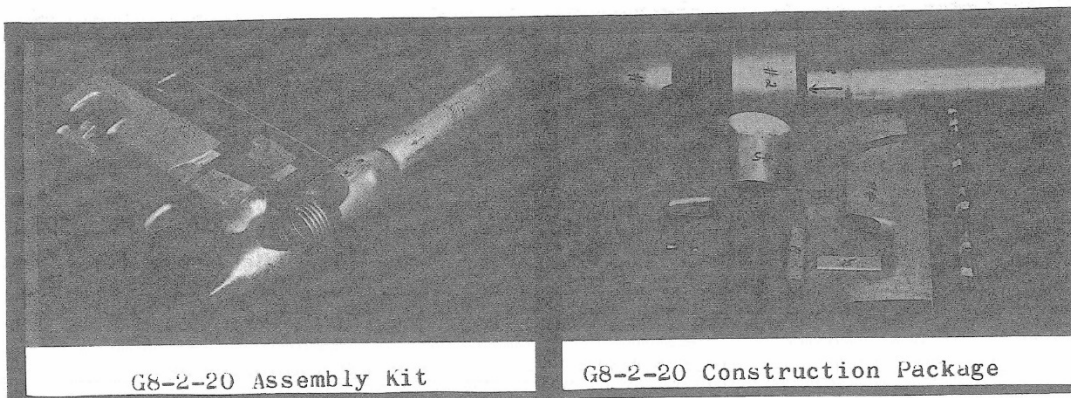
The tuning of the intakes is built in, the fuel-air ration is also automatically controlled all these features are built in and are as per the Construction Plans.

The G8-2 Jet consists of two main parts the BURNER and COWLING that houses first and second stages of the Intake System. The two parts are assembled on a Mounting-Bar which is provided with fully assembled and tested engines. The customer should test-verify the engine for thrust and how to handle it prior to mounting the Jet on his own installation. One also can copy the holes from the bar to your installation for proper location. Helicopter engines come with the Mounting-Bar others do not. The Round-Intake jets have no Mounting-Bar. In most cases the G8-2 is available in 3 ways.

1. Completely Assembled & Tested Jets.
2. Assembly Kits
3. Construction Packages

The completely Assembled engines, this is selfexplanatory. The Assembly Kits consists of finished parts and sub-assemblies. Some jets have one Heat Exchanger Coil some have two Coils. The Kits require less work for you, and what sub-assemblies are made are assembled in a jig thus, all parts are uniform and per print. To assemble a Kit one must take it to a Heliarc-welding place.

The Construction Package consists of pre-formed but unfinished parts. It is the least expensive way to get a G8-2 Jet Engine. However, it requires a lot of work on your part. The tools required to assemble the jet are; a hammer, two pair of metal snips, right and left hand. Several files, measuring instruments, Sand-Paper and a roll of masking tape to keep the parts together while taking to the welder. Welding must be done with a Heliarc Welding machine, and the welder must be an Aircraft Heliarc welder.



For a correct sequence and the method of assembling the G8-2 parts one must closely follow the Construction Plans and Instructions.

When you are ready to fire your own G8-2 jet for the first time it is very important to follow a prescribed way. Read carefully the instructions. If the engine was assembled by EMG you can fire it any way within the limits. Keep the fire out of second stage.

y

BASIC PRINCIPLE OF THE G8-2 JET

o

The G8-2 Jet Engine is an entirely new concept as compared to the conventional turbo-jet. It is not a Ram-Jet nor a Pulse-Jet. It is basically a burner with a sonic synchronized intake. Classically the G8-2 is a Pressure-Jet Engine.

The G8-2 Jet Engine was designed specifically around the fuel Liquid Propane. Primarily because it is a fuel with DOUBLE ENERGY compressive energy and heat of combustion. This resulted in simplification of the entire design.

Propane is safer than gasoline, readily available, easily stored and controlled and is inexpensive. Propane weighs 4.23 lbs per gallon, and releases about 21,690 BTU/lb when burned (oxidized).

When putting this fuel to work, and using both of these energies, the following is accomplished: The first energy, the inherent pressure in the fuel tank, when released, delivers the liquid fuel to the jet engine at high pressure, thus eliminating the fuel pump.

red
t
and
o

The Liquid Propane upon reaching the hot Heat-Exchanger coil in the engine combustion chamber, is vaporeized and super-heated and piped to the ejection nozzle, while still under high pressure.

From the nozzle, the hot-gas is injected into the 1 stage intake system at supersonic speed. The high velocity of the gas does the work of drawing-in the surrounding air into the intake system at predetermined fuel-air ratio of 15 to 1 by weight.

Thus, compressive energy release pumps the air into the jet burner, eliminating the need of a bulky air compressor and the motor to drive it.

The 2nd stage duct must be sonically tuned to the 3rd stage duct, in the ratio of 1/2 wave length in #2 stage, to 1/4 wave in the 3rd stage duct. This permits the G8-2 Jet to operate statically at rated thrust.

When the "fuel-air" mixture reaches the combustion chamber, it releases its second energy, "the heat of combustion", resulting in jet thrust.

ge

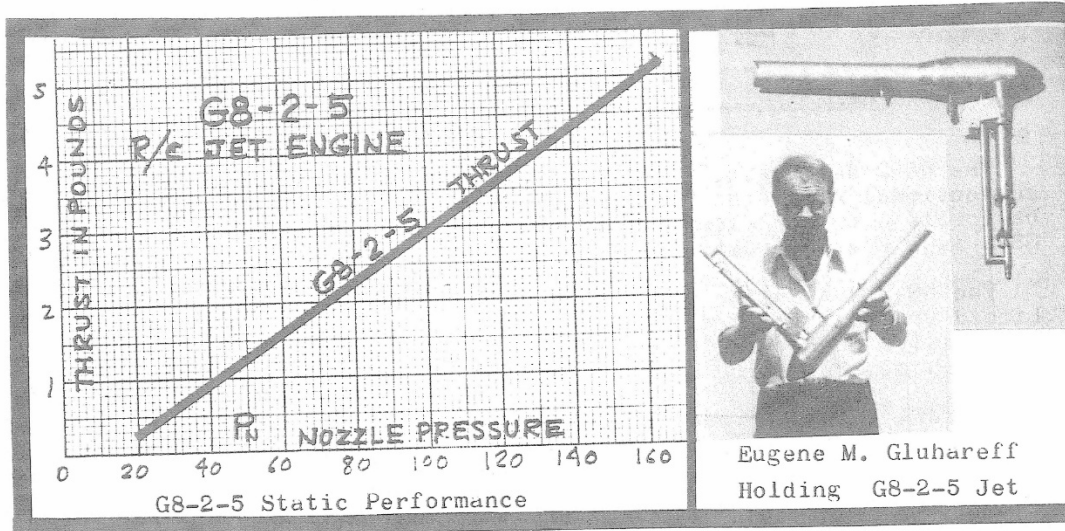
When the G8-2 Jet is operating dynamically, its thrust increases with forward speed due to ram-air. However, a good ram-air scoop is essential.

ts

The length of tail-pipe is such that all gas must expand inside the container. If the tail-pipe is shortened, a visible flame will appear, and jet thrust will decrease. The fish-tail cut and holes de-tune the tail-pipe. This cuts down noise level and increases jet thrust.

it
e
t

MODEL G8-2-5 JET ENGINE



SPECIFICATION

Max. Static Thrust	5.2 lbs.
Weight (Jet assembled).....	1.5 lbs.
S.F.C. Static.....	N/A (very low)
HP. Rating Static (equivalent HP)...	1.25 hp.
HP. Rating at 200 mph (gross hp)....	1.83 hp.

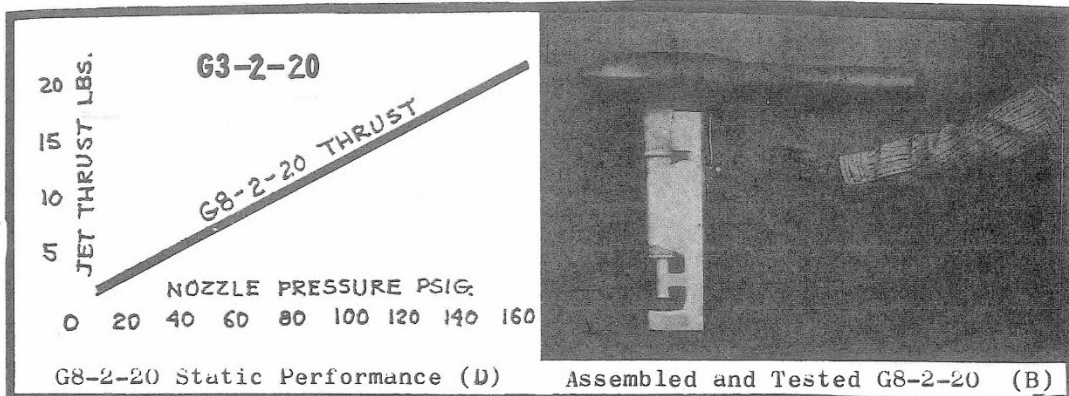
DIMENSION

Overall Length.....	22.0 in.
Overall Intake from \varnothing Burner.....	15.5 in.
Combustion Diameter.....	3.0 in.
Tail Pipe Diameter.....	2.0 in.

A significant breakthrough for R/C model airplane enthusiasts, this pressure-jet engine starts with a push of a button by R/C, it idles with a wind like a turbine, and can be stopped and restarted in the air by R/C.

For the first time ever, an operator without going near the plane can start the engine, taxi, take-off, fly and land, taxi back to the apron, park and shut-off the jet engine.

MODEL G8-2-20 JET ENGINE



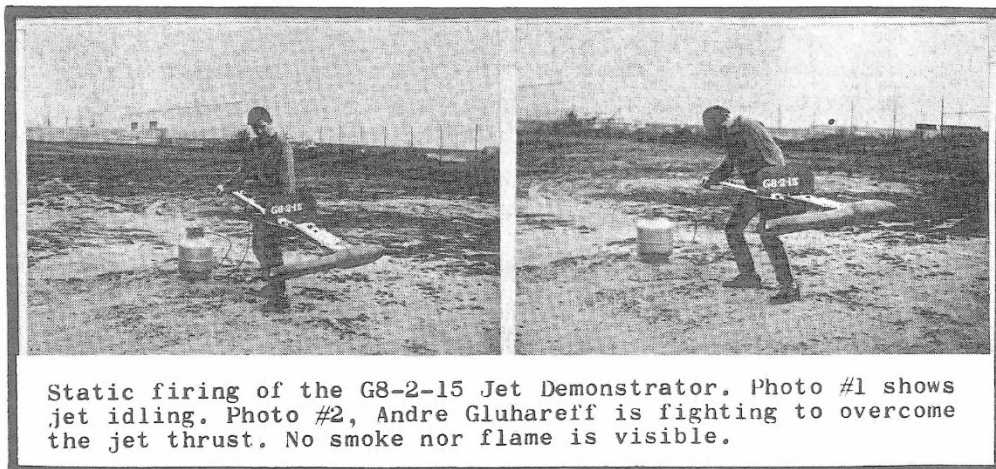
SPECIFICATION

Max. Static Thrust.....	23.5 lbs.
Weight Jet assembled.....	5.5 lbs.
S.F.C. Static	4.8 lbs/lb/hr
S.F.C. Dynamic at 200 MPH.....	1.67lbs/lb/hr actual
HP Rating Static (Equivalent HP.)...	5.0 hp.
HP Dynamic at 200 MPH (Gross HP.)...	12.2 hp.

DIMENSION

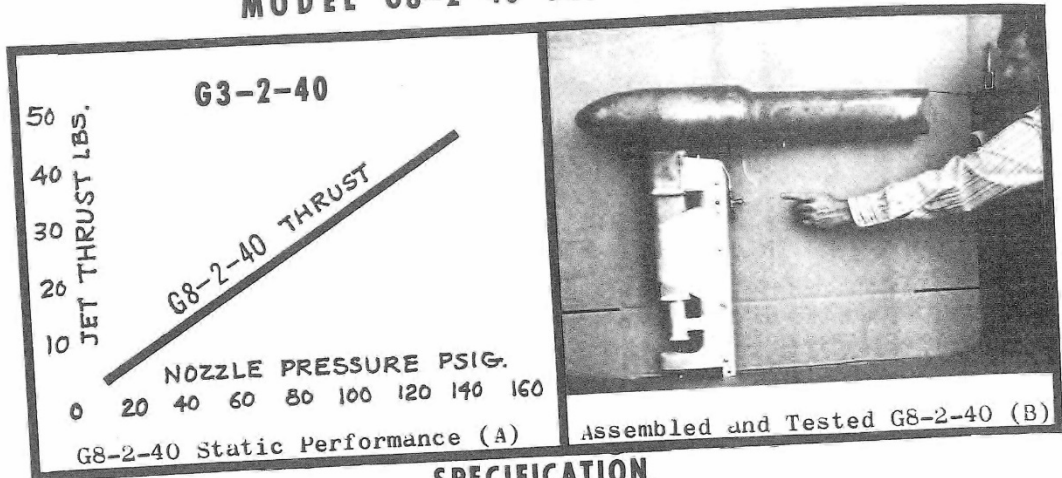
Overall Length.....	36.5 in.
Overall Intake from $\frac{1}{2}$ Burner.....	25.5 in.
Combustion Chamber Diameter.....	5.0 in.
Tail Pipe Diameter.....	3.5 in.

The G8-2-15 Jet Engine was featured on the cover of MECHANICS ILLUSTRATED MAGAZINE, January 1975 issue, story and many photos.



DEMONSTRATOR as shown above are available on request but with G8-2-20 Jet Engine instead of G8-2-15 which are obsolete and no longer manufactured by EMG.

MODEL G8-2-40 JET ENGINE

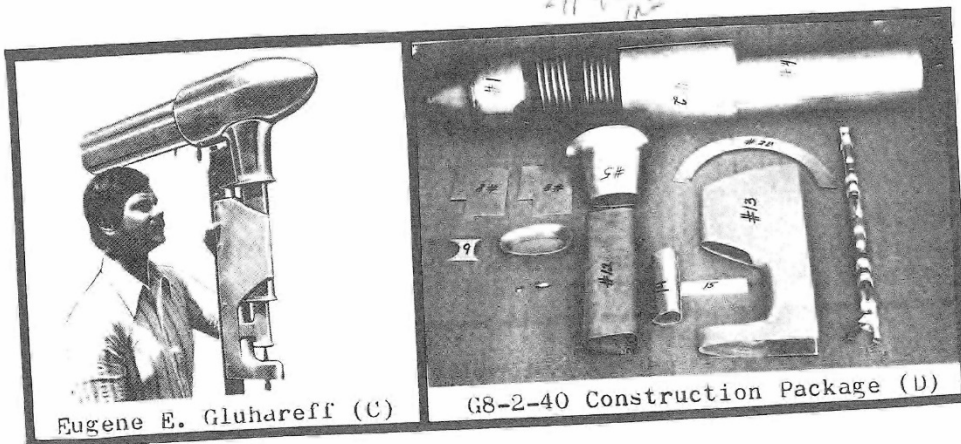


SPECIFICATION

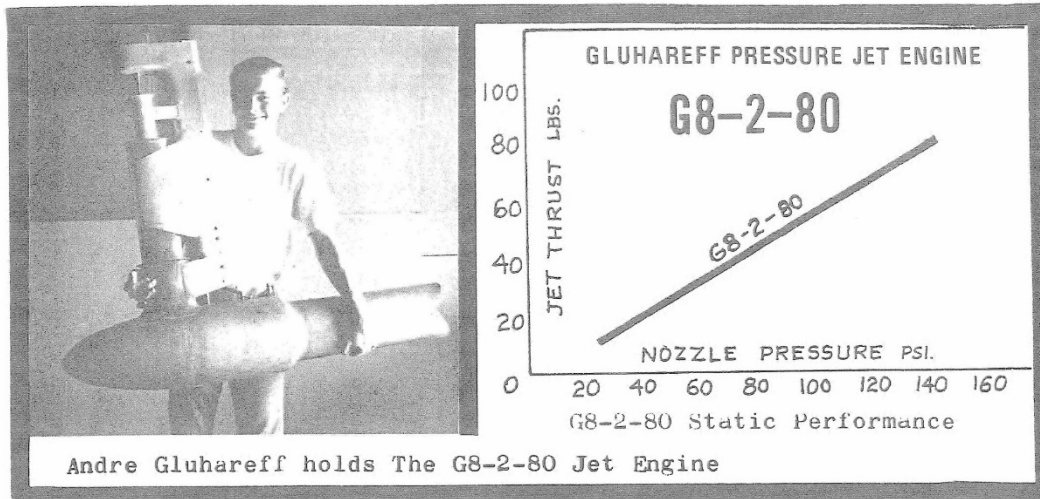
	G8-2-40	G8-2-80
Max. Static Thrust in LBS.	43.0	82.0 lbs.
Jet Weight Assembled.	11.0	21.0 lbs.
S.F.C. Static Value	4.6	4.2 lbs/lb/hr.
S.F.C. Dynamic Value	N/A	N/A
HP. Rating Static Equivalent HP.....	10.0	20.0 hp.
HP. Dynamic over 200 MPH Gross HP...	22.9	42.5 hp.

DIMENSION

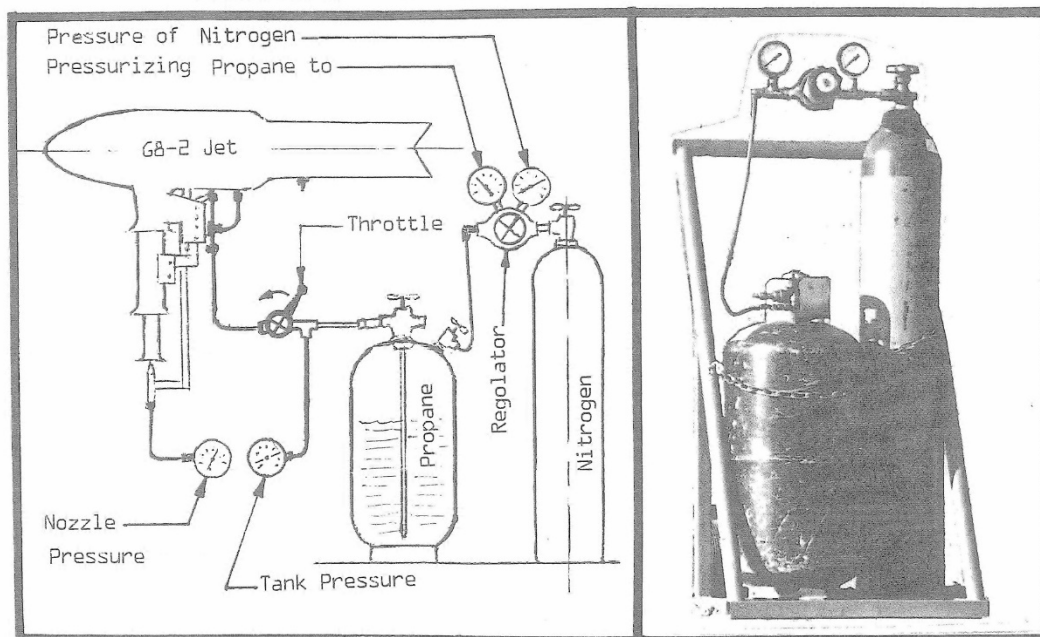
Overall Length in inches	38.5	45.0 inches
Overall Intake from ϕ of Burner..	27.5	36.0 inches
Combustion Chamber Diameter	6.5	8.5 inches
Tail-Pipe Diameter	5.0	6.5 inches



MODEL G8-2-80 JET ENGINE



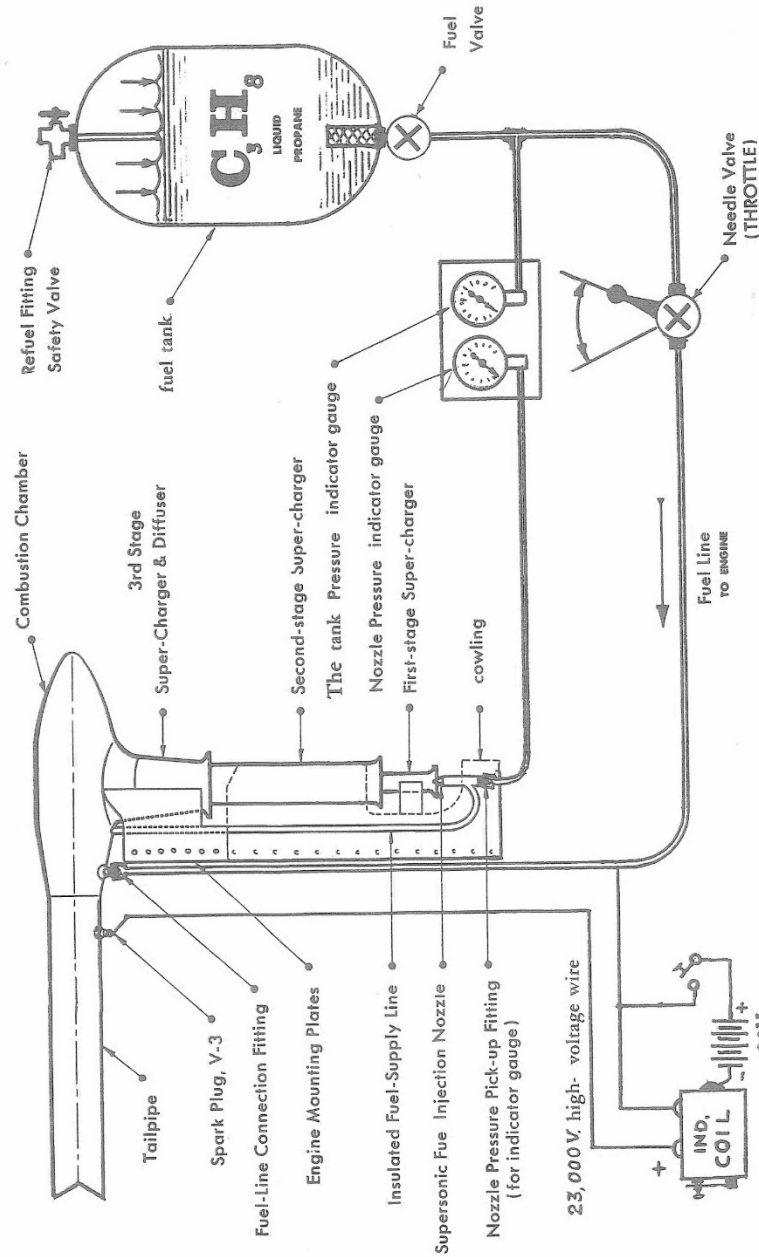
PROPANE TANK PRESSURIZATION



The schematic diagram above shows the proper way to pressurise the Propane tank and to keep the pressure in the tank constant while a test is run. This way the data obtained will be under proper conditions. One must keep in mind that the Propane-Tank has a pressure relief valve. It is usually preset at 375 psig by the State regulation DOT, Department of Transportation. If one will raise the pressure above that value the Propane Tank will leak beyond operators control. The leaking gas is flammable and may explode. The EMG recommends that operator do not go above the 300 psig mark, because the pressure valve is not exact it may start leaking at 350 psig. or below that value.

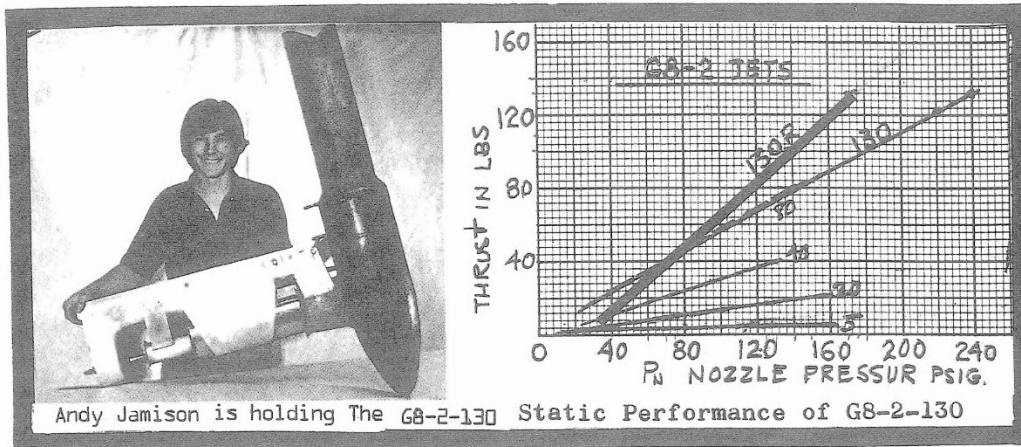
G8-2 SCHEMATIC DIAGRAM

THE G8-2 JET ENGINE FUEL SYSTEM



The engine was out of alignment the two lbs. thru the bar

MODEL G8-2-130 JET ENGINE



SPECIFICATION

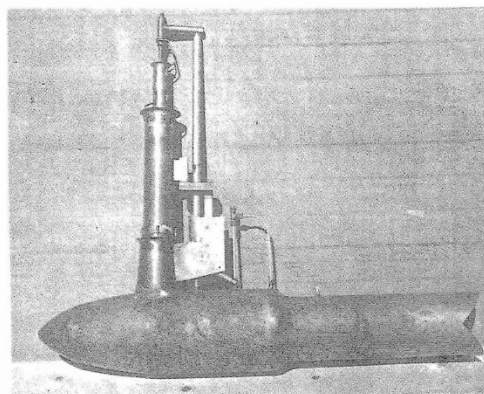
	G8-2-130	G8-2-130R
Max. Static Thrust in LBS.....	137.0	132.0 lbs.
Jet Weight, Assembled	24.5	23.0 lbs.
S.F.C. Static Value	1.33	0.78 lbs/lb/hr.
S.F.C. Dynamic Value	N/A	N/A
HP. Rating Static Equivalent HP.....	33.0	32.5 hp.
HP. Dynamic over 200 mph. Gross HP.....	73.0	73.0 hp.

DIMENSION

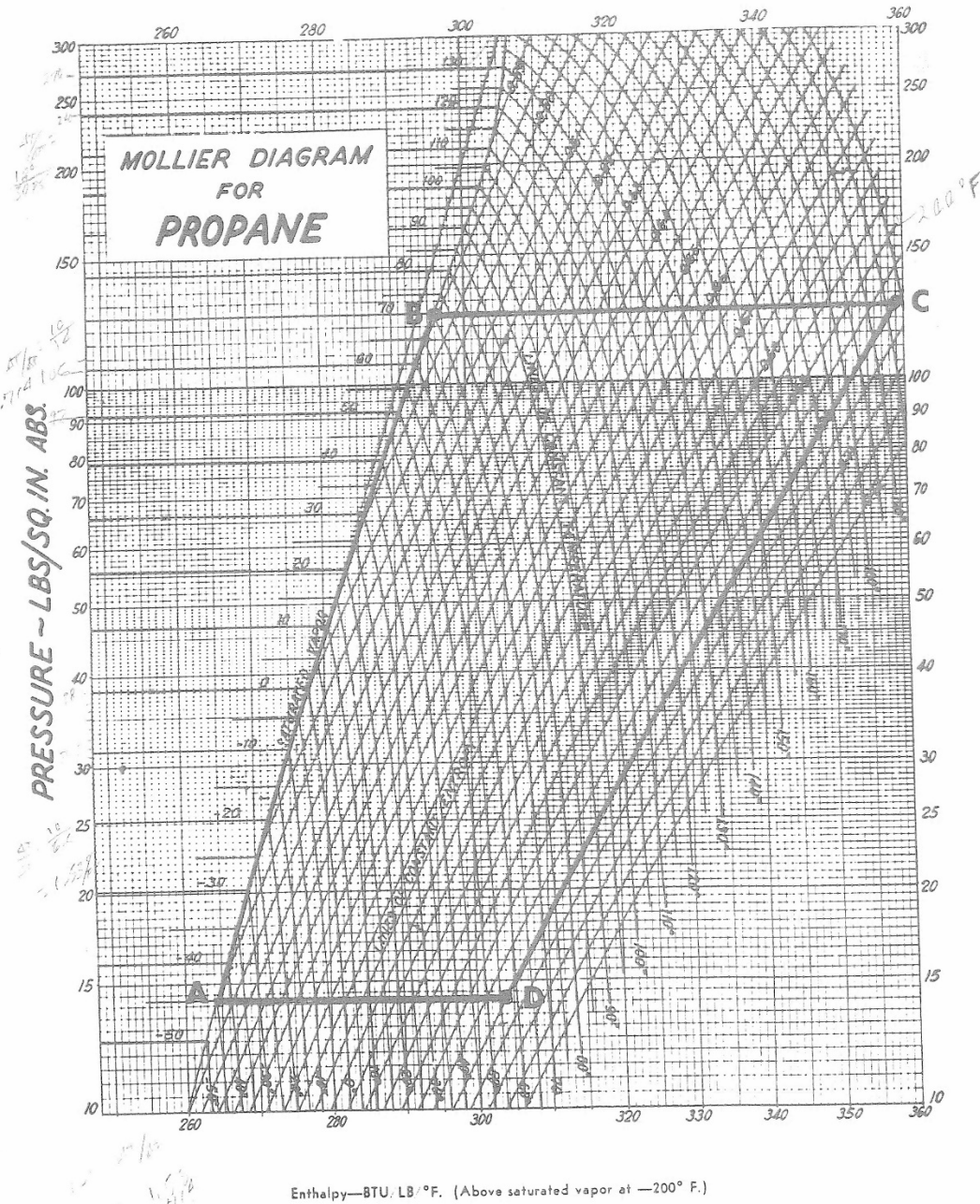
Overall Length inches	48.0	48.5 in.
Overall Intake from C of Burner	37.0	36.0 in.
Combustion Chamber Diameter inches	9.0	9.0 in.
Tail-Pipe Diameter	7.0	7.0 in.

MODEL G8-2-130R JET

The G8-2-130R photo left is a much better engine. Changes are: The Elliptical Intake was replaced by a Round Intake this knocked out many problems that people had such as the alignment of the second stage and the third stage. Now there is no problem, just insert the second stage into the third stage & the two bolts holding it and it is all done. The Improvements are: Jet weight is less, 23 lbs. The Nozzle pressure for 130 lbs. of static thrust is 170 psi. instead of the 240 psi. The S.F.C. = 0.78 lbs/lb/hr. The Mounting Bar was eliminated and all Aluminum Parts.



Mollier chart for propane.



t
c.
c.

is
ci
va
ta
pr
th
ta
re
at

th
ou
ga
tl
ex.

an
wh
flo
the
the
air

an
Noz
reg

can
in
noz

pai
the
tanl

] unti
foll

DISCUSSION OF THE G8-2 JET ENGINE

The basic motive power of The G8-2 Jet Engine is the FUEL in the tank. Propane is The Liquified Petroleum Gas (LPG), which is used in campers and trailers for cooking and heating. It comes in silver colored containers that are attached to the trailer frame.

The Propane in the tank is C_3H_8 , normally it is a liquid and it is under pressure of about 120 psig at ambient temperature. For clarification refer to The Mollier Chart page 14, follow the saturated vapor line until it intersects the ambient temperature line. Horizontally go to the left margin, there you will find the absolute tank pressure. From that value subtract 14.7 and the remainder will be the tank pressure in psig. Example: at 80° F ambient temperature, the tank pressure will be $143 - 14.7 = 128.3$ psig. When Propane burns it releases 21,690 BTU/lb. Propane weighs 4.23 lbs. per gallon and boils at -43.8° F.

Tank with a liquid pick-up, has a tube that goes to the bottom of the tank. Therefore, when the tank valve is open a liquid Propane flows out to the throttle. The tank pressure is registered on the right hand gauge, see Schematic Diagram page 12. When the operator opens the throttle valve, liquid fuel flows to the jet engine, when it enters the heat exchanger via #7 metering fitting.

Liquid Propane upon entering the heat exchanger coils is vaporized and super-heated. Absorbing the heat energy from the combustion chamber, which is at about 3,600° F. The hot Propane vapor at about 1200° F. flows under pressure from heat-exchanger through an insulated tube to the ejection nozzle, see page 12. There it is allowed to expand through the nozzle C to D (ref. Mollier Diagram), and enter the three stage air intake at supersonic speed.

The pressure in the heat-exchanger and at the nozzle is the same, and it is registered on the left hand gauge, and is referred to as the Nozzle Pressure, see page 12. The operator by moving the throttle can regulate the nozzle pressure with almost instant response.

When operating The G8-2 Jet statically, the nozzle pressure (P_n) can never exceed the tank pressure (P_t), because the boiling Propane in the tank is the original source of pressure. Consequently the max. nozzle pressure will be, the tank pressure less line friction (P_f).

$$\text{Maximum } P_n = P_t - P_f$$

If slightly higher nozzle pressure is desired, the tank can be painted black. This will increase the heat absorption, and increase the temperature of the Propane, which in turn will result in higher tank pressure. This increase may be about 40 psi.

If a much higher pressure is desired, then the tank must be heated until the desired tank pressure is reached. Ref. Mollier Diagram, follow saturated line A to B.

When whirling the G8-2 Jet Engine on a tip of helicopter blade the tank pressure is not too important, because the pressure built-up due to the centrifugal force (P_{cf}) acting on the fuel in the blade line is adding to the tank pressure. The nozzle pressure (P_n) will then be as follows;

$$P_n = P_t + P_{cf} - P_f$$

The three stage air intake is so designed that the ambient air is picked-up at each stage. Fuel mixes with air so that the fuel-air ratio of the gas entering the combustion chamber is maintained at about 15 to 1, by weight. In doing this work the Propane's inherent compressive energy is released as Kinetic Energy (KE).

The air is pumped in the following manner. The supersonic blast of Propane Vapor from the nozzle entering the first stage, creates a partial vacuum at the inlet, thus inducing ambient air (W_{a_1}).

The new mixture of the induced air and fuel in the first stage blasts into the second stage, creating a partial vacuum at the inlet of #2 stage, and inducing more air (W_{a_2}) into the second stage.

The same process is repeated at the inlet of the third stage, inducing final air (W_{a_3}). With the addition of (W_{a_3}) air to the mixture it becomes combustible, up to now it was too rich and would not burn.

The mixture then moves through the diffuser section, where the high velocity of gas is converted to pressure. This phenomenon is referred to as the pressure recovery by the diffuser. This is used to pressurize the combustion chamber, and to upgrade the combustion efficiency.

The junction of the diffuser and combustion chamber is called the diffuser-skirt. In this section the mixture is ignited and forms a stationary flame-front. This is defined as a point where the velocity of the flame propagation upstream is equal to the velocity of the gas mixture coming down.

The amount of air drawn in by each stage, and the total amount of air (by weight) can be determined by the use of the continuity equation, which is as follows;

$$(\eta_o M_o V_o) = (\eta_1 M_1 V_1) = (\eta_2 M_2 V_2) = (\eta_3 M_3 V_3)$$

NOZZLE 1st STAGE 2nd STAGE 3rd STAGE

η = Nozzle Efficiency, M = Mass Flow, V = Exit-Velocity

See sketch (A) page 17, or page 34 GTS-15 Technical Hand Book, "Intake System Analysis."

Due to the higher pressure in the combustion chamber, the hot gas is driven toward the tail-pipe completing its burning cycle. In the tail-pipe the gas accelerates and cools due to its expansion, and is ejected out. Thus the second energy of Propane, (the heat of combustion) is released resulting in jet thrust.

CALCULATE JET EXHAUST VELOCITY

The equation for jet thrust (T) is $T = M \times V_e$

M = mass of gas in slugs (W/g), V_e = exhaust gas velocity in ft./sec.
 $g = 32.2$ gravity constant.

EXAMPLE :

Calculate the jet exhaust velocity (V) for the G8-2-15 Jet Engine, producing 16 lbs. of static thrust.

1. Determine the weight-flow of fuel (G_f) lbs./sec. From graph (A) page 31 determine corresponding SFC = 6.5

$$G_f = \frac{T \times \text{SFC}}{t} = \frac{16 \times 6.5}{3600} = 0.0289 \text{ lbs./sec.}$$

2. Determine the weight-flow of air (G_a) lbs./sec. From graph (C) page 33 air-fuel ratio is 14.6 to 1.

$$G_a = G_f \times 14.6 = 0.422 \text{ lbs./sec.}$$

3. Determine the total weight-flow (G) lbs./sec.

$$G = G_f + G_a = 0.451 \text{ lbs./sec.}$$

4. Determine the total mass-flow (M) slugs/sec.

$$M = G/g = 0.451/32.2$$

5. Determine exhaust exit velocity (V_e) in ft./sec.

$$V_e = T/M = 16 \times 32.2 / 0.451 = 1,142 \text{ ft./sec.}$$

HORSE POWER VS JET THRUST

A question often asked is, WHAT IS THE HP RATING OF THE G8-2 JET? A Horse Power (HP) is a unit of power that we are familiar with. It applies to the internal combustion engine and a turbine, which produce shaft power (torque). When we refer to pure thrust engines we rate them in pounds of thrust.

The HP of the G8-2 Jet cannot be stated unless a specific condition is given. The HP of G8-2, or any jet engine that produces pure thrust statically, by calculation, is zero. We use the term, Equivalent Horse Power (HP_e). This means that the HP value is based on an empirical value determined by actual test. As compared to the internal combustion engine.

gas
the
nd is
mbus-

EXAMPLE

An actual test was conducted, a 12 hp rated internal combustion engine, with a fixed pitch propeller, produced a max. static thrust of 48 lbs. running at full power. Calculate the lbs. of thrust per hp.

$$\text{THRUST (T)} = 48/12 = 4 \text{ lbs. per HP.}$$

t./sec

The G8-2 Jet produces 40 lbs. of thrust statically, calculate its equivalent HP.

$$\text{EQUIVALENT (HP}_e\text{)} = 40/4 = 10 \text{ hp.}$$

ne,

For calculating the HP of the G8-2 Jet at any other condition, the equation is as follows;

$$\text{HP} = T \times V/550$$

mph

T = thrust in lbs., V = velocity in ft./sec. 550 = constant.

EXAMPLE

Calculate the HP of the G8-2-40 Jet at 400 mph. (V = 586 ft./sec.)

$$\text{HP} = 40 \times 586/550 = 42.7 \text{ hp.}$$

Calculate the HP of the same engine at 650 mph. (V = 954 ft./sec.)

$$\text{HP} = 40 \times 954/550 = 69.5 \text{ hp.}$$

The actual value of HP will be higher with a properly designed air scoop. It will increase the inlet pressure due to the ram-air effect. Increasing the thrust and lowering the S.F.C., means that you burn less fuel, and get more thrust. Allowing longer flight on a tank of fuel.

Page 34 presents a wind-tunnel data for the G8-2-15 Jet. It was tested with and without the air-scoop. Curve (B) shows jet thrust with the air-scoop on at 300 ft./sec. (205 mph). The curve (A) is static performance with air-scoop on. The results indicate that the jet is starving for air. The curve (C) shows static thrust without the air-scoop. Comparing the curve (B) with curve (C) shows that there is a 10% thrust gain with the scoop. This particular scoop had a substantial leakage of pressure.

-2 JET?
th. It

Due to very efficient burning there is no visible flame nor smoke. The exhaust gas is not toxic, it consists of steam, carbon-dioxide, and inert nitrogen. The exhaust blast of G8-2-15 is relatively cool, you can put your hand in it at 5 ft from the end of tail-pipe, and experience only a warm blast. If the tail-pipe is shortened a visible flame will appear, and thrust will drop.

ent
n empir
rnal

The noise level of the G8-2 Jet is considered low. The sound is mostly from the tail-pipe, it has a tendency to select and amplify its own natural frequency, from the noise source at the fluctuating flame front in the diffuser skirt.

The G8-2 Jet Engine is not a Pulse-Jet, it is a burner, and a resonating tail-pipe is detrimental, it reduces jet thrust. The end of the G8-2 Jets tail-pipe has a fishtail cut which dampens the tail-pipe's natural frequency. The change from straight to fishtail cut increased the thrust of the G8-2-15 by 3 lbs and reduced the noise level by about 1/2.

The resonance in the tail-pipe is detrimental to the intake system. The resonant frequency of the tail-pipe interferes with the frequency of the tuned intake, which operates on a higher frequency. A small hole in the side of the Diffuser #5 is a sonic damper, it reduces noise and improves jet thrust. (Refer to GTS-15 Technical Hand Book, page 46. " Sonic Tuning of the G8-2 Jet Engine).

The total compressive energy of Propane is released to the intake system as Kinetic Energy (KE). This energy is responsible for pumping air and to maintain combustion chamber pressure. The total Kinetic Energy can be calculated as heat energy, by the area enclosed by A, B, C, and D. (see Mollier Chart page 14).

Liquid Propane in the tank is under pressure which is applied at the metering fitting #7 at point (B) on Mollier Chart. The heat Energy (B) to (C) increasing its Enthalpy, is transferred to the fuel in the Heat-Exchanger Coils #3, to vaporize and dry. Energy released at the nozzle #17, expanding gas follows the line of constant Entropy (C) to (D), is Kinetic Energy (KE). (D) to (A) this energy is released in the intake stages as Heat Energy. (A) to (B) energy transferred to Propane in the tank as heat, from the ambient air, or by heating the tank when more pressure is needed.

The simplicity of the G8-2 Jet Engine, and its similarity to the Turbo-Jet Engine in performance, resulted in great demand and popularity in schools and colleges, which lead to the development of The GTS-15 Teaching Test Stand. This audio-visual educational device simplifies the teaching of the principles of jet propulsion. (Refer, pages 54-55, or to The GTS-15 Technical Hand Book which is primarily for jet performance calculation and lab. use).

INSTALLATION INSTRUCTIONS

The completely assembled G8-2 Jet is mounted on a mounting-bar, the assembly consists of 3 parts, the Burner Assy. part (A), Cowling Assy. part (B), and a Mounting-Bar. (see page 21) The Mounting-Bar serves two purposes, one is to hold the parts (A) and (B) together with proper positioning of parts and proper stage alignment, the second is for transportation.

The jets are test fired while on the mounting-bar. You may incorporate the mounting-bar into your design, or substitute your own mounting-bar, using the original bar as a jig to drill new mounting holes. To disassemble the G8-2 Jet Engine into the burner (A), cowling (B) and the mounting-bar, one must remove the bolts. However, a sequential procedure must be followed in disassembling or assembling.

First remove the screws or bolts holding the cowling, thus loosening it from the mounting-bar. Apply slight pressure to the cowling pulling the #2 stage out of #3 stage and lift, (see fig. A). When cowling clears the #3 stage, slide it toward the burner while it is sliding off the nozzle, until it is free. Finally remove bolts holding the burner assembly and then mounting-bar and separate them.

d
il-

tem.
icy

ok,

ake
ping
c
A,

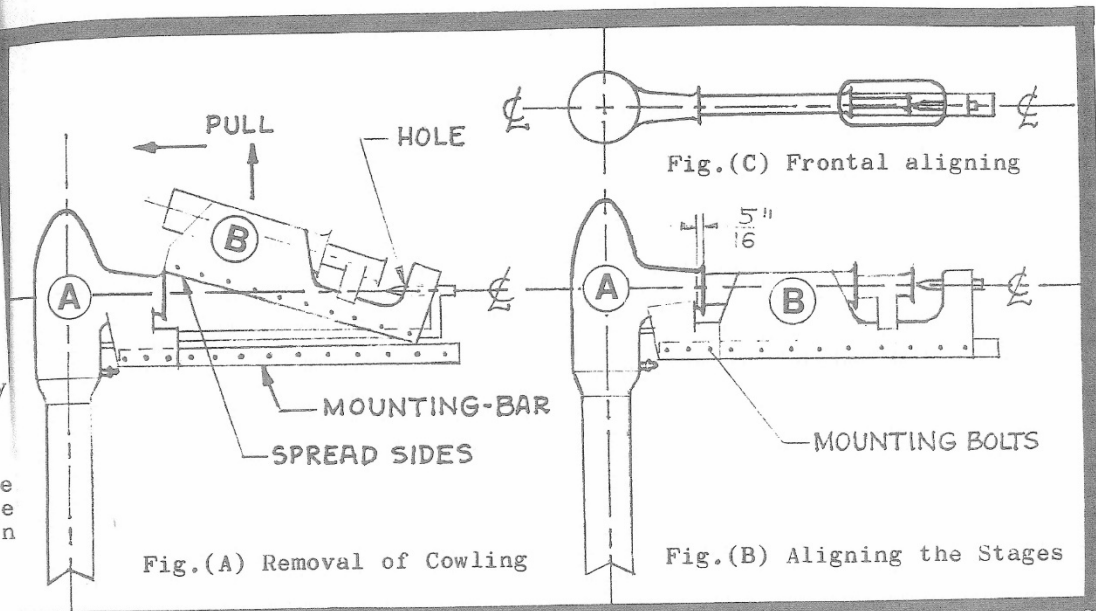
at
energy
the
the
) to
in the
propane
k when

the
pula-
he

fer,
rily

ar,
wling
Bar
her
e

incor-
vn
nting
cowling
a seque
g.



To assemble the G8-2 Jet, one made by you from a construction package or assembly kit, follow the same procedure as above, but in reverse.

All stages must fit one into the other as concentrically as possible. The air-gap between the two mating stages must be the same all around, this applies to stages 1 and 2, and 2 and 3.

The nozzle should be positioned to blast through the center of #1 stage, and aim at the exact center of #3 stage in both planes. To check this alignment one must mount the burner assy. on to the mounting-bar, then position the nozzle at the approx. location where it will be when the cowling assy. is mounted.

Use a rod or wire that fits exactly into the nozzle orifice, it should be long enough to reach inside the #3 stage. If the alignment is not correct, bend the nozzle to aim as stated above. Remove the rod and install the cowling assy. All 3 stages and the nozzle must be on the center-line, see fig. (C). If the stages and nozzle are not properly aligned, it will result in ear splitting shrills. Recheck the alignment and correct.

FIRST FIRING OF A NEW JET

The first firing is the most important firing, it must be followed as directed. The new G8-2 Jet Engine must be heated gradually to its maximum temperature. This initial heating releases all the internal stress concentrations as a result of welding and hammering. If the gradual heating is not carried out, the engine may be permanently deformed or cracked. After the first controlled firing as directed, the G8-2 Jet can be fired any way you wish, then it is safe.

Firing of the G8-2 Jet is extremely simple. Open valve on fuel tank, crack the throttle, and push the ignition button, the jet will light-up with a weak puff. Allow heat-exchanger coils to warm-up for 6-8 seconds then use the throttle as you wish. More throttle more jet thrust.

FIRST FIRING DIRECTIONS

Prior to firing the G8-2 Jet see the schematic diagram on page 12. Carefully check your fuel lines and ignition wires, make sure all nuts are tightened properly. Also check how securely your jet is fastened, would it tear itself loose or not? Then read the instructions below.

Ignite the G8-2 Jet by pushing the ignition button, at the same time crack the throttle gently to about 10 - 15 psi nozzle pressure. If the electric ignition is not available use a match at the tail-pipe. As the fuel-air mixture ignites, slowly increase the nozzle pressure to about 25 psi and let the engine warm-up for 5 -10 seconds, at this point the jet engine is idling.

CAUTION:

Do not allow the fire in #2 stage, fire will deform the #2 stage duct and may melt the aluminum cowling. If this occurs immediately push the throttle and increase the nozzle pressure, this will blow the fire into the combustion chamber, where it belongs.

When the engine is idling properly, wait for it to get red-hot and allow all parts to come to an even temperature. Then start opening the throttle slowly to its maximum position. The noise will change from a hum to a roar and the thrust will go up. Make sure the engine is properly secured and will not tear itself loose. Do NOT be frightened by the red-hot engine it is quite normal. Keep it firing at maximum throttle setting for about 30 seconds. Then shut it off just by turning off the fuel (throttle). This terminates the first firing of your jet.

Maximum jet thrust output depends on the gas pressure in the fuel tank, higher the pressure, higher the jet thrust. By painting the fuel tank flat black the tank pressure may be raised as much as 40 psi.

DO NOT use any pressure regulators on your fuel tank. If you have one on, remove it. The fuel line must be direct, tank to throttle and then to jet.

NOTE; use Liquid Propane not gas. If you do not have a tank with a liquid pick-up, turn your tank upsidedown, in this way you will supply the jet with Liquid Propane instead of gas.

in
ab
th

to
Je

ho
ha
fu

a '
CO
su:
was

for
eng
the

bet
Als
the
not

and
Hel
be
to
lac

ROC

dan
exp
Thi
Con
mea
the
lys
sur

WHY THE G8-2 JET ENGINE WAS INVENTED

BY

EUGENE M. GLUHAREFF

Whenever there is a discussion regarding the G8-2 Jet Engine invariably the question is asked: "How and Why did the G8-2 Jet come about? The reader of this article will probably ask the same question therefore, I shall anticipate this and provide the explanation.

The engine was invented due to necessity. It took about five years to develop a 1.25 lb thrust working prototype, to the present G8-2-15 Jet Engine and in 1978 a 23 lbs of thrust.

It may seem unusual to take five years for a relatively simple job, however, Propane is a new fuel and the "know how" on its application had to be acquired experimentally step by step. Insufficient amount of funds slowed it down considerably.

The idea that instigated this development was my ambition to build a "FLYING MOTORCYCLE", or in other words, a "PORTABLE ONE-MAN HELICOPTER", a field heretofore untouched due to the non-existence of a suitable blade-tip powerplant. I was convinced that blade-tip power was the only solution to this problem.

Consequently, my next problem was to find a suitable powerplant for installation on a helicopter blade-tip. Examining available jet engines, such as RAM-JET, PULSE-JET, VALVELESS PULSE JET, I realized that there were no suitable engines to do the job.

At this point the usual question asked is, "What is the difference between the above mentioned jets and rockets and the G8-2 Jet Engine? Also, "Why some of the above jets cant be used". The answer is that they can be used but they are not practical for the job, the goal would not be reached.

I feel that prior to further discussion as to why the existing jets and rockets are not suited for the job of powering a Portable One-Man Helicopter. Disadvantages of each of the above mentioned jets should be pointed out this will familiarize the reader so that he will be able to recognize the features of the G8-2 Jet Engine, that the others are lacking, and its essential superiority and simplicity.

ROCKET ENGINE

Rocket engines, mono-propellant or bi-propellant are inherently dangerous because their thrust is a result of a continuous controlled explosion. The specific fuel consumption of rockets is extremely high. This is due to the fact that all of the fuel must be carried on board. Contrary to air-breathing jet engines with fuel-air ratio of 15, which means that for 1 lb of fuel on board, 15 lbs of air is picked-up from the atmosphere. In starting a rocket on a blade-tip with a poor catalyst or if not igniting instantly, this will spew raw fuel into the surrounding atmosphere, which in most cases is toxic or incendiary.

Thus not a desired feature for rotary aircraft. Refueling also requires trained personnel and the cost of most rocket fuels is prohibitive. The average S.F.C. = 36 lbs/lb/hr. The attractive feature of tip-rockets is that it is small, simple, and lightweight. As an example to fly a rocket powered flying-belt using Hydrogene Peroxide (H_2O_2) as fuel, the cost is about \$45 for about 20 seconds.

RAM JET ENGINE

Ram-jet is known to be the simplest jet engine but it is the hungriest on the list of S.F.C. The Ram-Jets average S.F.C. = 12 lbs/lb/hr. in the subsonic range. Furthermore, ram-jet does not operate statically and it has to move through the air at a relatively high speed before it can be ignited.

The ram-jet's propulsive efficiency and thrust is solely a function of ram-air pressure which in subsonic region is low. Moreover, ram-jets frontal projected area is the largest in comparison with other types of jets for the same thrust. Therefore, the ram-jet has a very high profile drag at high speed while at low speed it does not work.

The combustion cycle of a ram-jet is considered to be that of a simple low pressure burner. Ram-jet uses ordinary gasoline, kerosene or jet fuels, resulting in smoke, fire, and toxic product of combustion. This is mostly carbon-monoxide (CO). The advantages of Ram-Jet is simplicity and no moving parts.

PULSE JET ENGINE

The Pulse-Jet is a member of the jet family that operates on an explosion cycle. In other words, its thrust is a result of a series of explosions which are controlled by sonic synchronization of the inlet valve to the resonant natural frequency of the tail-pipe. The length of the tail-pipe is equal to $1/4$ of the sonic wave length.

The Pulse-Jet operates best statically, its thrust decreases with forward speed, due to its high drag and desynchronizing effect of the ram-air on the valve. (At mach number $M = 0.6$ the jet thrust is almost zero). The Pulse-Jet is long, bulky and heavy it requires auxiliary starting equipment such as air compressor, motor, and a big storage tank because the jet does not start every time.

The throttleability of Pulse-Jet is about 20% at the top (between 80 and 100% only). The average S.F.C. = 6.0 lbs/lb/hr. The biggest disadvantage of the Pulse-Jet is its valve which is completely unreliable, heavy and has a very short life. Consequently, as the valve disintegrates the jet thrust drops. The noise level of the Pulse-Jet is extremely high because the jet performance depends on the compression of the sonic wave to reignite the fuel-air mixture each cycle.

VALVELESS PULSE JET

The Valveless Pulse-Jet is merely a pulse-jet without the valve. This is accomplished by matching the natural frequency of the tail-pipe to the natural frequency of the intake. However, the elimination of the valve does not alter the jet operational cycle in any way. It improves the engine by making it more reliable, lighter and longer-lasting.

The elimination of the leaky valve improves the propulsive efficiency, it also improves the S.F.C. = 5.0 lbs/lb/hr This also allows a more complete combustion thus reducing the toxic exhaust fumes, as compared to the pulse-jet. The toxic exhaust fumes of the pulse-jet are considerably less if compared to the ram-jet. This is the result of changing from low compression burning cycle of ram-jet to the explosion cycle of the pulse-jet.

The configuration of the Valveless Pulse-Jet differs from the standard pulse-jet by having a longer intake duct, and overall length becomes 1/2 of the sonic operating wave length, but all other operational characteristics of the pulse-jet are retained.

PRESSURE JET ENGINE

A Pressure-Jet is a ram-jet to which the air for combustion is supplied under pressure. Consequently the ram-air is no longer of any use. Pressurization of the combustion chamber allows the burning cycle to take place under higher pressure, thus greatly improving the propulsive efficiency which results in much greater thrust and lower S.F.C.

The average value of S.F.C. = 2.0 lbs/lb/hr for the Pressure-Jet. The burner unit is usually small, has low aerodynamic profile drag and also low weight. This is a very attractive quality. However, the compressed air must be supplied by a compressor which in turn requires its own power source. Therefore, rendering the system complex, heavy and high-priced. Consequently evaluating the over-all system and considering the machinery involved, the over-all S.F.C. the system is no longer attractive.

Upon analyzing the existing types of jet engines I came to the conclusion there were no jet engines that were practical. It was necessary for me to invent one. Since I had several patents on Pulse-Jets and Jet Helicopters, this contemplated task was not a new one.

The new engine would have the following qualities; Lightweight, no moving parts, low fuel consumption, requiring no auxiliary starting equipment, work well statically and at high speed, start without fail every time with a push of a button, minimum noise, smoke, flame, and one without the toxic exhaust fumes. All of the above mentioned jets use gasoline, kerosene, and J.P. fuels which have toxic exhaust gas, smoke and flame.

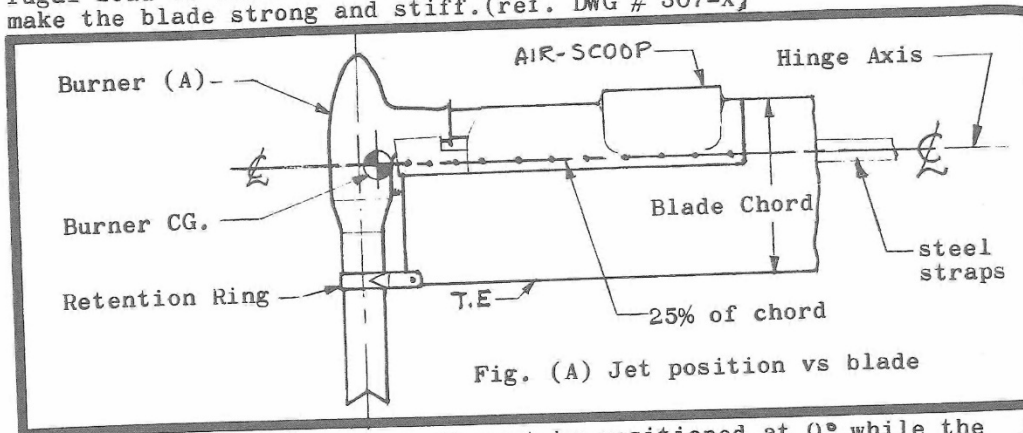
Weighing all the factors, I felt that the fuel was the No 1. item and the jet must be designed for use with a particular fuel. Then, into that were incorporated the phenomena of desired characteristics, and so, Propane was selected and the G8-2 type jet was invented.

Now in 1978 with larger thrust units such as the G8-2-130, based on data obtained from Space-Ranger the S.F.C. = 0.78 lbs/lb/hr. in static operation, and no machinery.

HELICOPTER BLADE-TIP INSTALLATION

To install the G8-2 Jet on a helicopter blade-tip, whether the MEG-1X, MEG-2X, MEG-3X or others, certain specific requirements must be carried out.

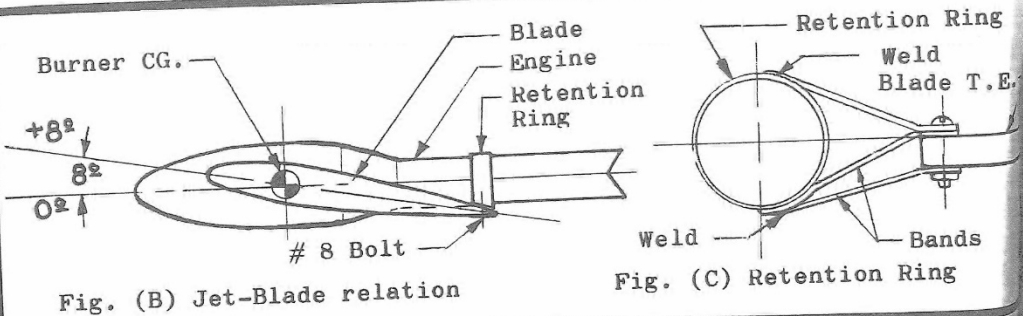
The c.g. of the burner assembly (A) must be located on 25% of the blade chord. The jet mounting plates must be bolted directly to the load carrying straps. The steel straps run on top and bottom of the blade on 25% of chord, transmitting directly the jet centrifugal load to the root-fitting. (see photo B page 32) Steel straps make the blade strong and stiff. (ref. DWG # 307-X)



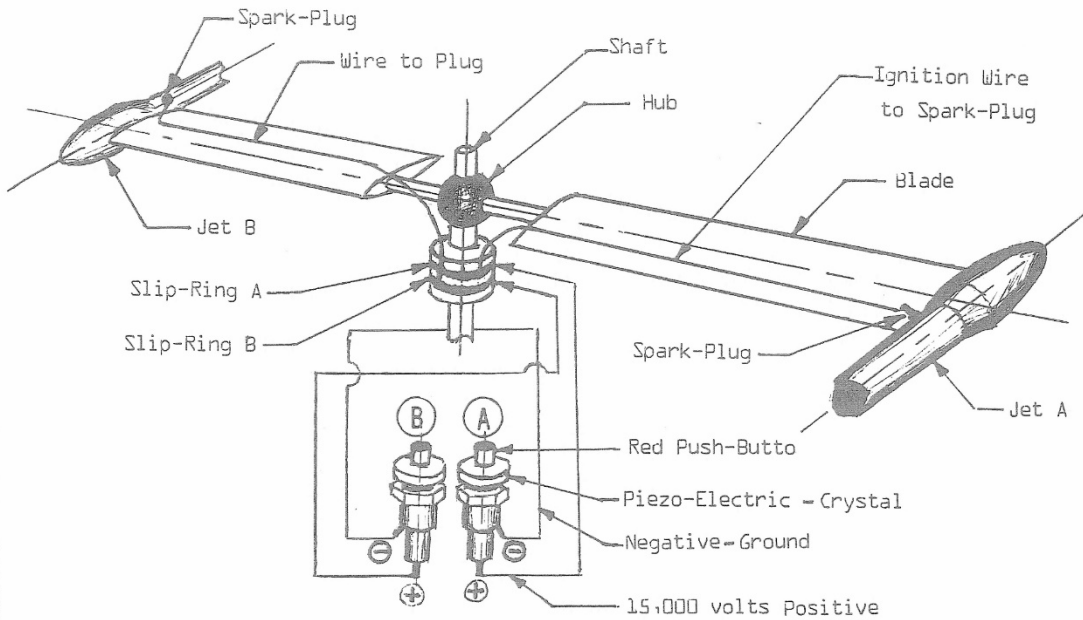
To minimize the jet drag it must be positioned at 0° while the blade is at $+8^\circ$ (see Fig. B). Also ref. to DWG # 301-X, To accomplish this twist, # 3 stage must be turned 8° prior to welding it to the combustion chamber. (when ordering a G8-2-15 or G8-2-20 for helicopter use, please specify 8° twist).

The tail-pipe being subjected to the centrifugal force, must be attached to the trailing edge (T.E.) with a retention ring. This ring must fit loosely over the tail-pipe, allowing it to slide freely; it may move $1/4$ to $1/2$ inch. Tail-pipe expands longitudinally from the heat inside. (see Fig. A & C).

The retention ring must be made of normalized 4130 steel band, and welded to the holding bands with Heliarc, with all welds to carry the load in shear.



TIP-JET IGNITION



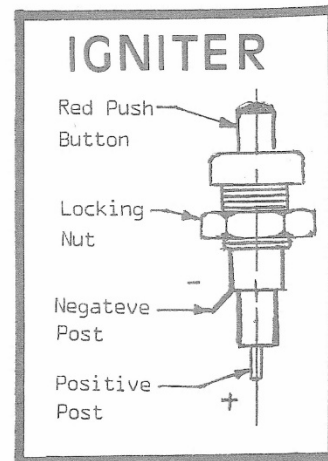
The diagram above illustrates a typical helicopter ignition system powered by two tip jets. The system has two Igniters A and B individual system for each jet.

The diagram above illustrates a typical ignition for a helicopter with two blades and two tip jets. The system has two Igniters A and B an individual system for each jet.

When the RED BUTTON is pushed a 15,000 volt charge goes to a SLIP-RING where it is transferred through a brush to a rotating part. From slip-ring the charge travels to the spark-plug through a high voltage wire in the blade. The spark ignites the gas in the combustion chamber and jet is on. The current returns to the Igniter via metal structure that serves as ground thus closing the circuit. Consequently when button A is pressed the jet A is ignited, press button B the B jet is ignited stationary or rotating rotor.

One Igniter can be used for two jets but the slip-ring must be split in two, one half for each jet so igniting one jet at a time. To avoid electric leakage the high-tension wire must be well protected.

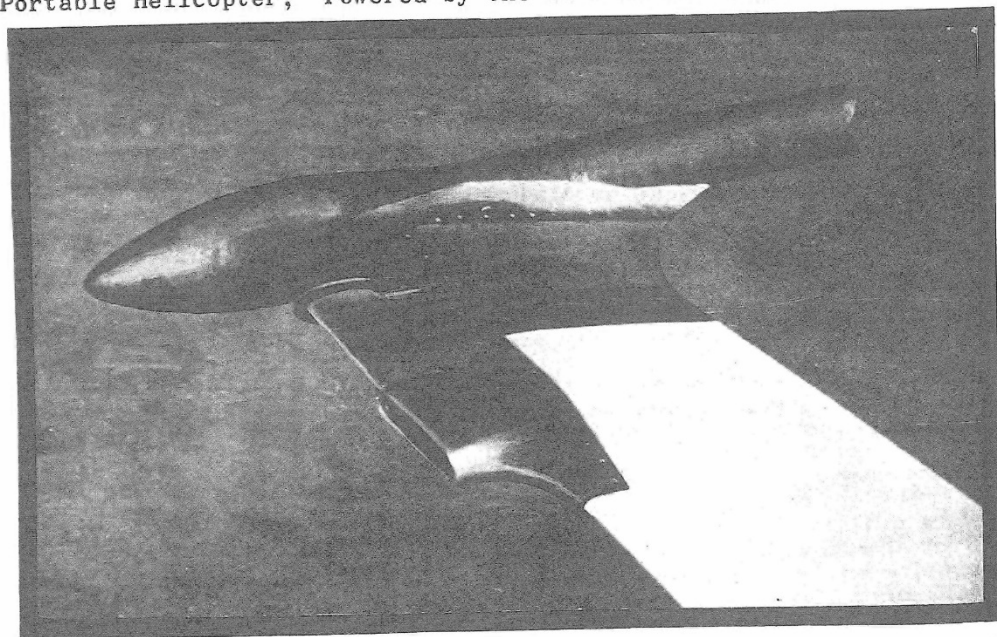
The IGNITER is a Piezo-electric crystal when it is hit it produces the 15,000 volts suitable to ignite the jet. It always works, weighs under 2 oz. There is no need for a battery.



MEG-1X HELICOPTER

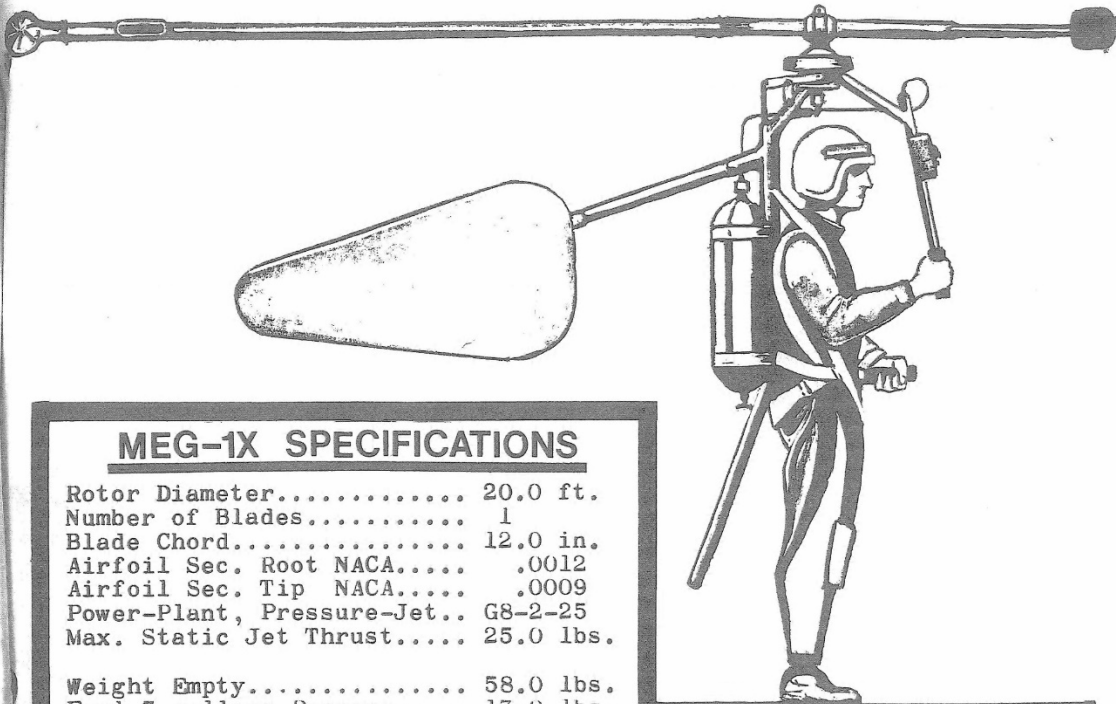


E.M. Gluhareff Harness Flight Testing MEG-1X Single Bladed One-Man Portable Helicopter, Powered by one G8-2-25 Jet Engine.



The G8-2-25 Installation on MEG-1X Blade-Tip. This is the Improved version, not the original. Above installation is similar to the G8-2-15 installation on MEG-3X blade-tip.

MEG-1X HELICOPTER



MEG-1X SPECIFICATIONS

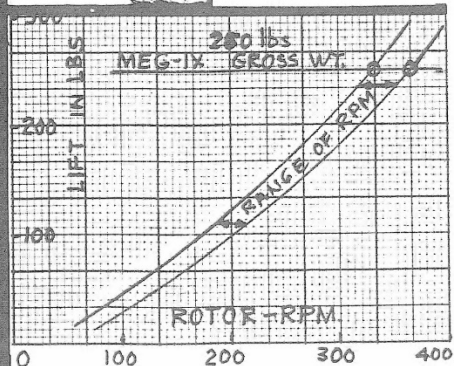
Rotor Diameter..... 20.0 ft.
 Number of Blades..... 1
 Blade Chord..... 12.0 in.
 Airfoil Sec. Root NACA..... .0012
 Airfoil Sec. Tip NACA..... .0009
 Power-Plant, Pressure-Jet.. G8-2-25
 Max. Static Jet Thrust..... 25.0 lbs.

Weight Empty..... 58.0 lbs.
 Fuel 3 gallons Propane..... 13.0 lbs.
 Gross Weight..... 260.0 lbs.

Flight RPM 335-370
 Hovering Flight Duration... 18.0 min.
 Fuel used per minute..... 0.72 lbs.

First test flight (harness) Feb. 1956
 Total Flight Time..... 70-90 hr.
 Test Pilots; E.M. Gluhareff
 Robert Farrington

No Vibration, Excellent Control
 Response and extremely Stable.



The MEG-1X, a single bladed portable one-man helicopter, is not a conventional machine but it has many advantages. It is simple in design, has low operating cost, has only one jet to feed and very low construction cost due to its simplicity. The reason the MEG-1X does not flip over is that its rotor is on a hinge, allowing the blade to flap. Consequently a hinge transmits no moment.

oved
e

MEG-2X HELICOPTER



Los Angeles Mirror News
DESIGNER GLUHAREFF & HELICOPTER

In the race to build the world's smallest helicopter, the lead was claimed last week by Aeronautical Engineer Eugene Gluhareff. Weight of the contraption: 68 lbs., and Gluhareff thinks he can eventually lower it to 45 lbs.

MEG-2X SPECIFICATIONS

Rotor Diameter.....	20.0 ft.
Number of Blades.....	2
Blade Chord.....	12.0 in.
Airfoil Sec. Root NACA.....	.0012
Airfoil Sect. Tip NACA.....	.0009
Power-Plant, Pressure-Jet..	G8-2-13
Max.Jet Thrust (Static)....	13.0 lbs.
Weight Empty.....	68.0 lbs.
Fuel 3 gallons, Propane....	13.0 lbs.
Gross Weight.....	270.0 lbs.
Flight RPM.....	300-340 actual
Hovering Flight Duration..	12.0 min. act.
Fuel used per minute.....	0.54 lbs.
Forward Speed Max.....	65.0 mph.
Hovering Ceiling.....	4500.0 ft. calculated
Service Ceiling.....	17000.0 ft. calculated
First Flight (hovering)....	Oct. 1956
Forward Flight in wind cond.	25-35 mph.
Forward Flight Duration....	18.0 min. actual
Total Flight Time.....	170. hours plus
Test Pilots; E.M. Gluhareff	
Robert Farrington	



EUGENE M. GLUHAREFF

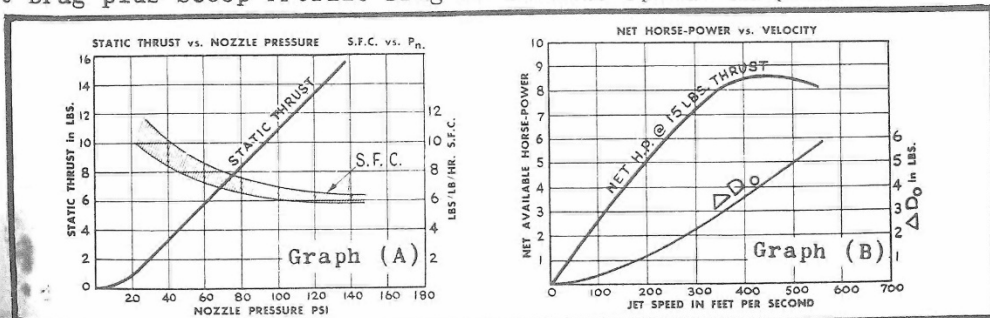
MEG-2X Portable One-Man Helicopter, piloted by E.M. Gluhareff

The original MEG-2X Helicopter as shown above was powered by two G8-2-13 Jets on each blade-tip. The helicopter became airborne in hovering at about 300 RPM and 6.5 blade pitch angle lifting 270 lbs. (see graph page 35). The jet speed at 300 RPM is 315 ft./sec. and its thrust was 13 lbs. With two jets the total thrust was $2 \times 13 = 26$ lbs (ref. page 35). The horse power to fly was 14.9 hp. (Gross HP).

$$HP = T \times V/550 = 26 \times 315/550 = 14.9 \text{ hp.}$$

The Graph (A) below, illustrates a typical G8-2-15 static performance, also shown is the S.F.C curve vs Thrust and Nozzle Pressure. EXAMPLE: At a nozzle pressure of 130 psi static thrust is 14.5 lbs. and S.F.C. = 6.4 lbs/lb/hr. This means that to maintain a thrust of 1.0 lb. for one hour, 6.4 lbs. of fuel will be used. At lower thrust the S.F.C. will be higher. However, at jet forward speed of about 300 ft./sec. the DYNAMIC S.F.C. will be about 2 lbs/lb/hr. for G8-2-13 on blade-tip.

The Graph (B) below shows the Net Available Horse Power vs jet speed, at jet Gross Thrust of 15 lbs. constant. The ΔD_0 designates Jet Hot Drag plus Scoop Profile Drag at various speeds in pounds.



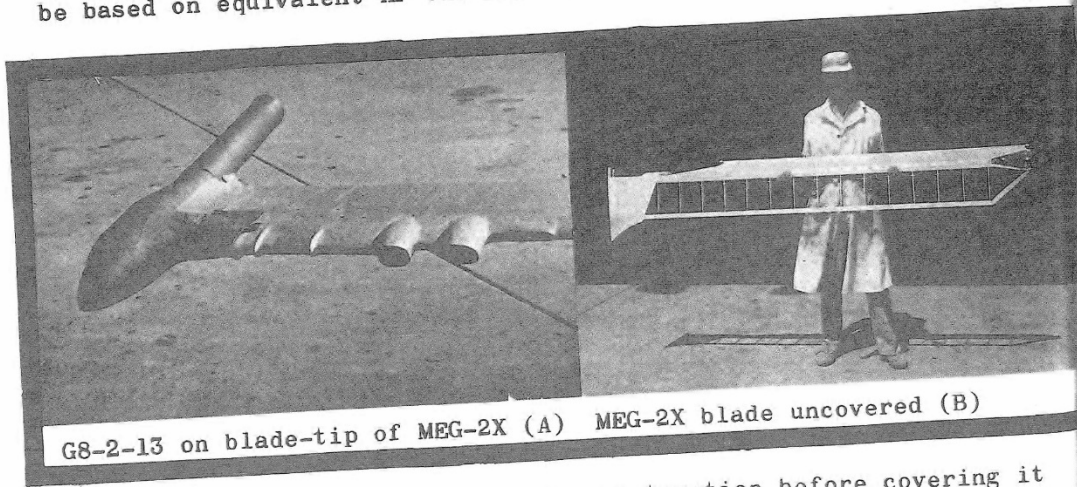
With the improved G8-2-15 Jet, throttle turned to full power, each jet will produce 18 lbs. of thrust. The total available HP then will be 22.7 hp. This demonstrates that MEG-2X has a 47.5% reserve power, as compared to piston engine driven helicopters that usually have only 20% reserve power in hovering.

Now with the latest G8-2-20 Jet producing in excess of 23 lbs. of thrust, the MEG-2X will have an excellent performance.

Gross HP vs RPM for MEG-2X with 23 lbs thrust/jet.

<u>ROTOR RPM</u>	<u>JET SPEED (ft/sec)</u>	<u>GROSS HP</u>
100	105	8.7
200	210	17.5
300	315	26.4
400	420	35.2
500	525	44.0

Static HP is given as equivalent HP and is used only as a comparison to rate a pure thrust jet engine in static performance. The equivalent HP of the G8-2-15 as discussed above is $18/4 = 4.5$ HP. With two jets we have a total of 9 HP, but tests prove that 14.9 HP is needed for MEG-2X to be air-borne. If the HP assumptions were to be based on equivalent HP the MEG-2X would never get off the ground.



G8-2-13 on blade-tip of MEG-2X (A) MEG-2X blade uncovered (B)

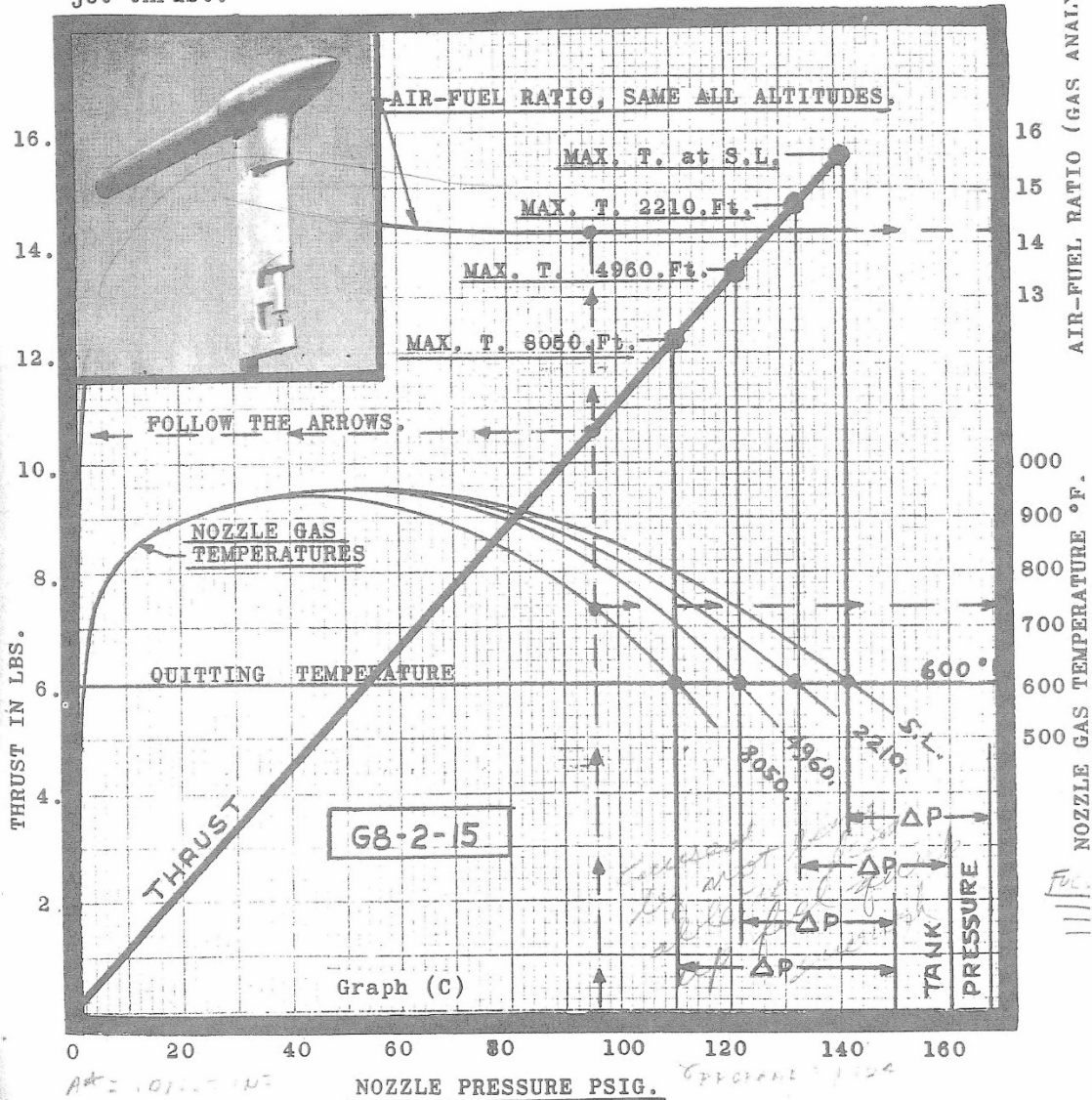
Photo (B) above shows the blade construction before covering it with fabric. Identical blades were used on MEG-1X, 2X and 3X. The blade consists of Spruce L.E. with steel straps on top and bottom to carry the jet centrifugal load directly to the root fitting. Balsa wood ribs are glued to the spar and Spruce T.E. The aluminum tip-fairing and fuel lines are visible in the L.E. The root fitting plates are made of 7075-T6 aluminum alloy. The complete blade with tip-fairing weighs 8 lbs.

Ref. DWG # 307-X Blade Assembly, DWG # 308-0 Tip-Fairing, DWG # 301-X Jet Installation on Blade.

ALTITUDE STATIC PERFORMANCE

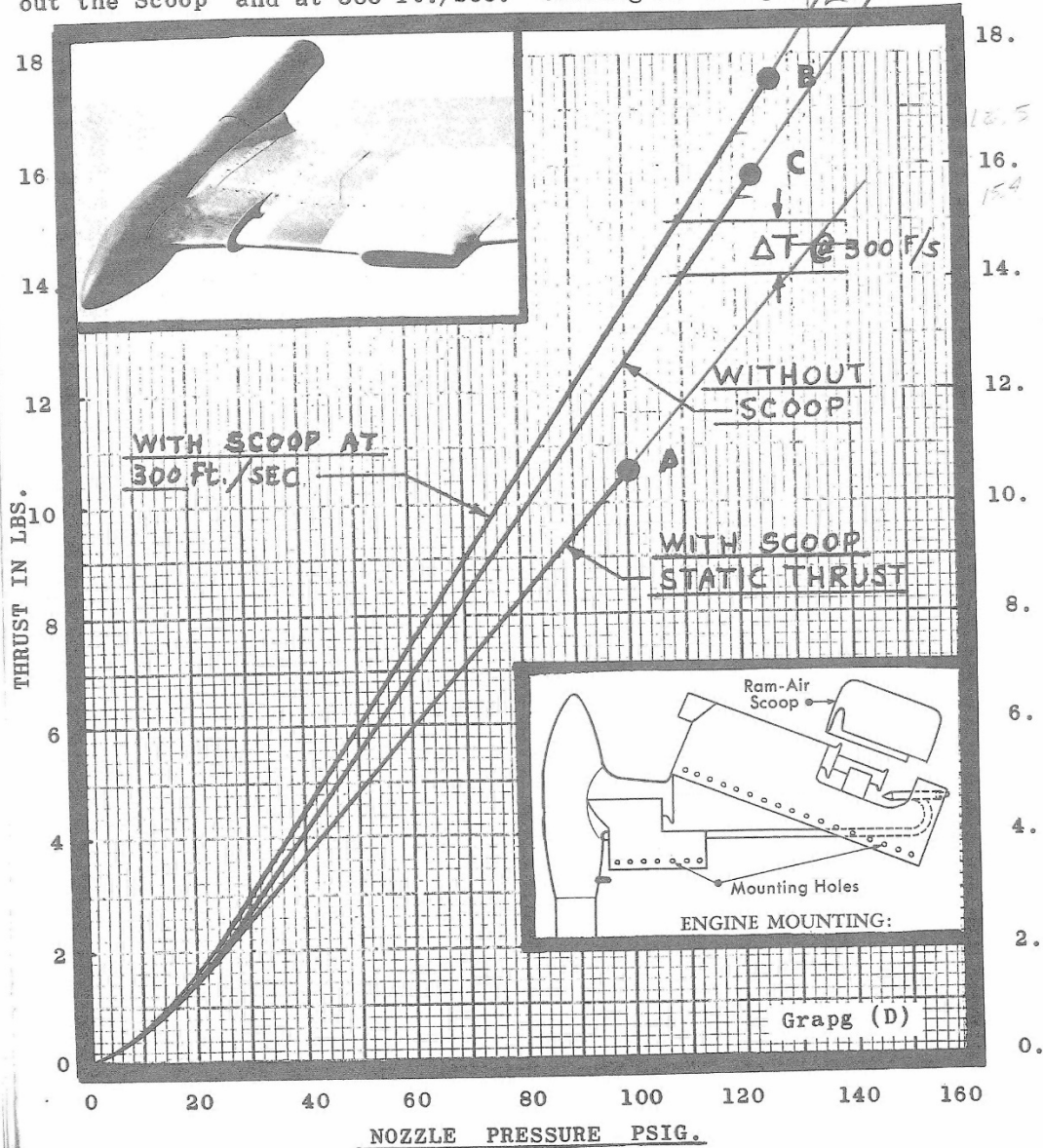
Performance at Sea Level and Different Altitude was obtained by taking the G8-2-15 Jet Engine on a test stand to the top of a mountain, stopping at following altitudes, on the way up and down. Sea Level (SL), 2210 ft., 4960 ft., 8050 ft. and running the engine through the entire range of nozzle pressure up to the max. jet thrust.

r-
P
o
d.



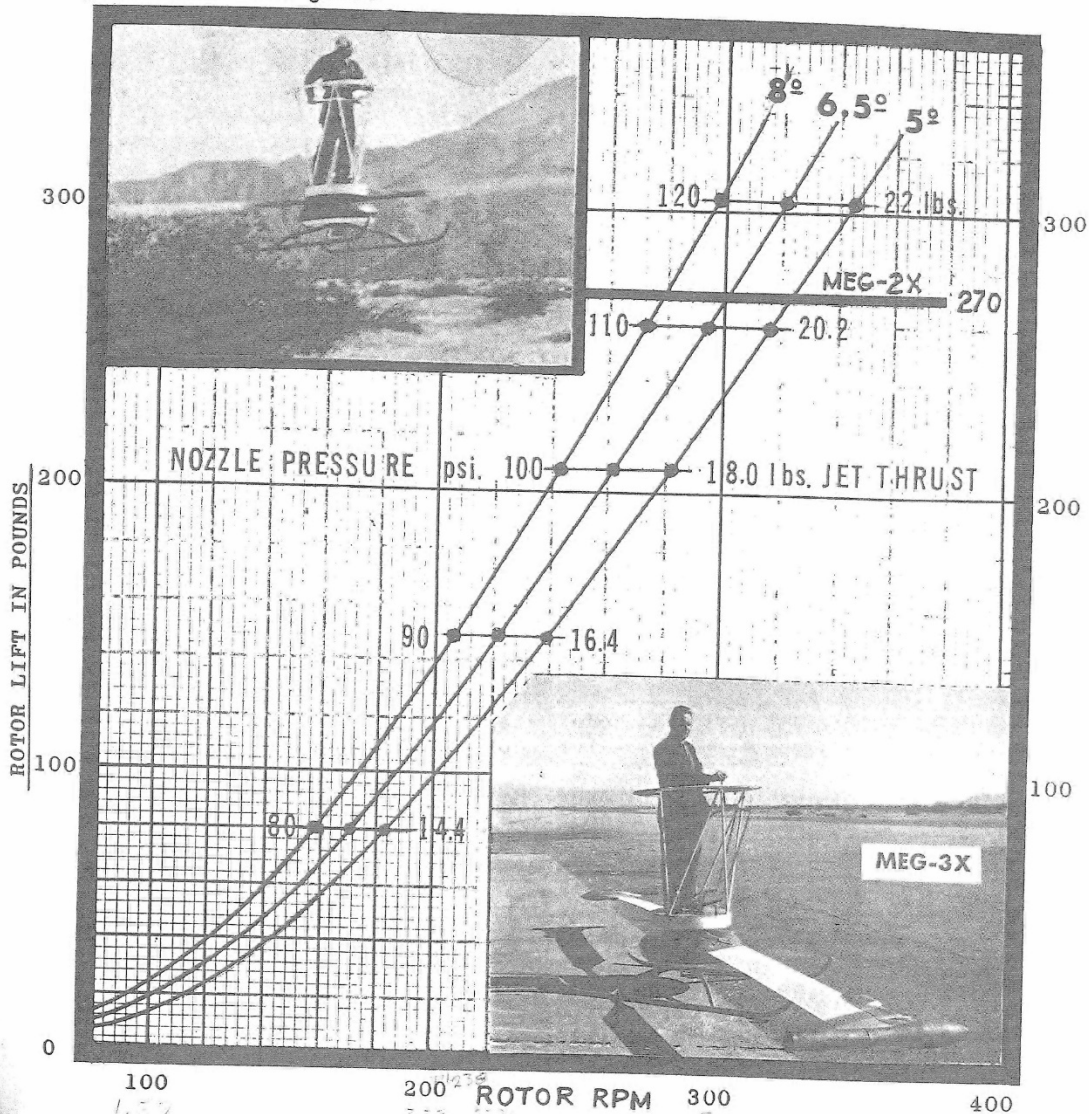
PERFORMANCE S.L.

This Graph Presents a Wind-Tunnel Data of the G8-2-15 Jet Engine as tested with and without the scoop, static and dynamic conditions. Curve (A) Static Performance with Scoop. Curve (B) Dynamic Performance with Scoop at 300 ft./sec. Curve (C) Static Performance without the Scoop and at 300 ft./sec. showing no change.



ACTUAL FLIGHT PERFORMANCE

This Graph Presents the Actual Hovering Flight Performance of the MEG-2X One-Man Portable Helicopter and MEG-3X Jet Flying Platform. Both aircraft powered by two G8-2-15 Jet Engines on blade-tip of 20 ft. diameter rotor. Graph shows rotor lift at blade pitch angle of 5°, 6.5°, 8° vs RPM and Nozzle Pressure in psig. Left hand side gives nozzle pressure, Right side gives total jet thrust in pounds for two jets.



212P

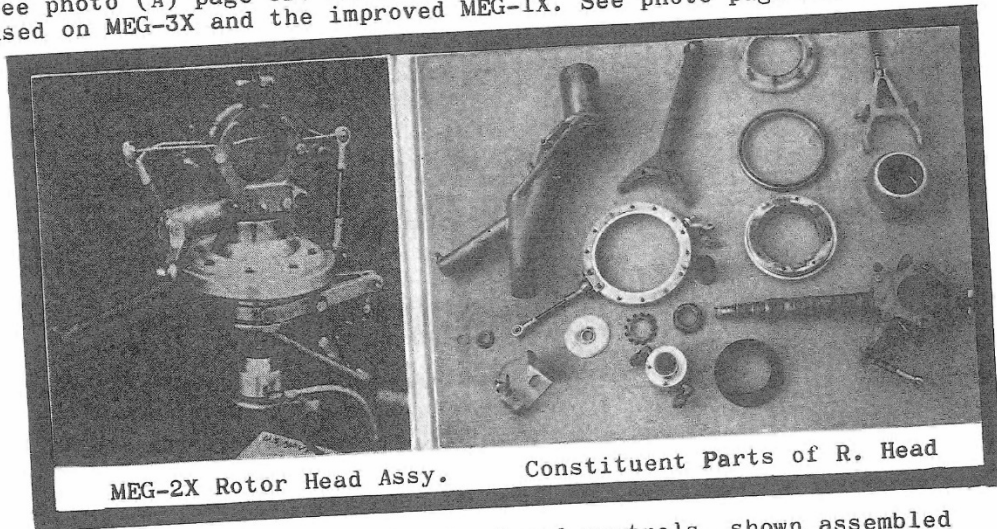
51

100
1.57
FPS

200²³⁶
312
FPS
- 35 -
300
56
FPS

Ram Air Scoop is very important to achieve good jet performance at higher forward speed. The reason is at normal static operation the jet engine produces its rated thrust, utilizing the propane vapor blast to induce air into the jet intake, at a rate of 15 to 1 by weight. This means that for one pound of propane it induces 15 pounds of air. In forward flight the ram-air is being pushed into the intake system on top of the air induced by the propane blast. Consequently the result is more thrust or lower S.F.C. for a given thrust. Higher the forward speed better the jet performance. However, without the scoop there will be no improvements.

The original scoop used on MEG-2X consisted of two small scoops see photo (A) page 32. Later a better scoop was designed which was used on MEG-3X and the improved MEG-1X. See photo page 28.



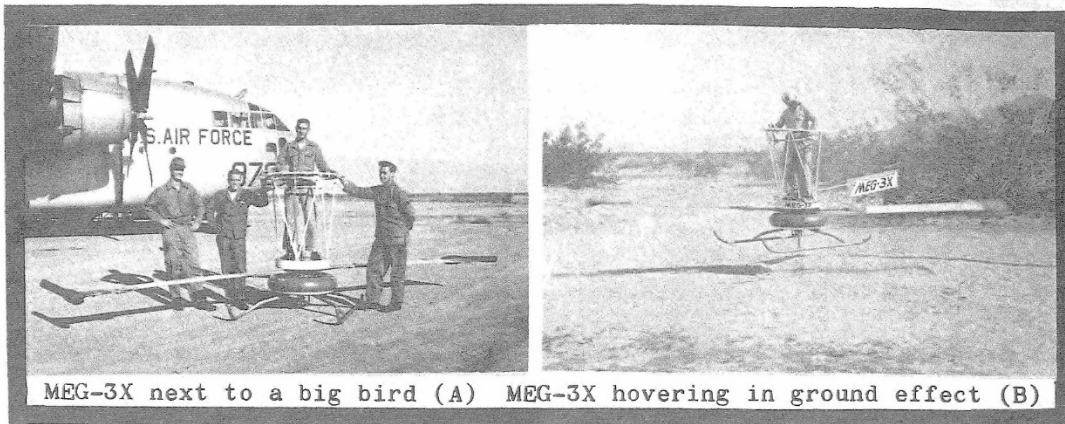
The above is MEG-2X rotor head and controls, shown assembled and disassembled. The control system functions exactly as a conventional helicopter control system.

The swoosh-plate controls the directional flight and the pitch control controls up and down motion. The outer swoosh plate is connected to the blade by means of two links and it is being turned by a scissors mechanism. The two swoosh plates are connected to each other by a "Kendon" torque tube bearing. The inner swoosh plate is stationary and it swivels on an aluminum ball.

The pitch control is achieved by raising and lowering the swoosh plate assy. by means of a mechanical lever, as seen on photo. This lever is attached to the lower end of the aluminum ball. The whole assembly slides up and down on a cylinder that houses the shaft bearings and is referred to as the beer-can.

The shaft is inserted from the top of the beer-can through the bearings and locked at the bottom. The lower end of the shaft fits into a rotary fuel transfer which rides on oilite bushings and teflon "O" rings. The very bottom of the shaft rides in a nylon commutator that connects ignition to both jets. This rotor head has no precision parts, all parts ride on nylon bushings, completely free of slop and impervious to sand and grit. (ref. DWG # 350-X).

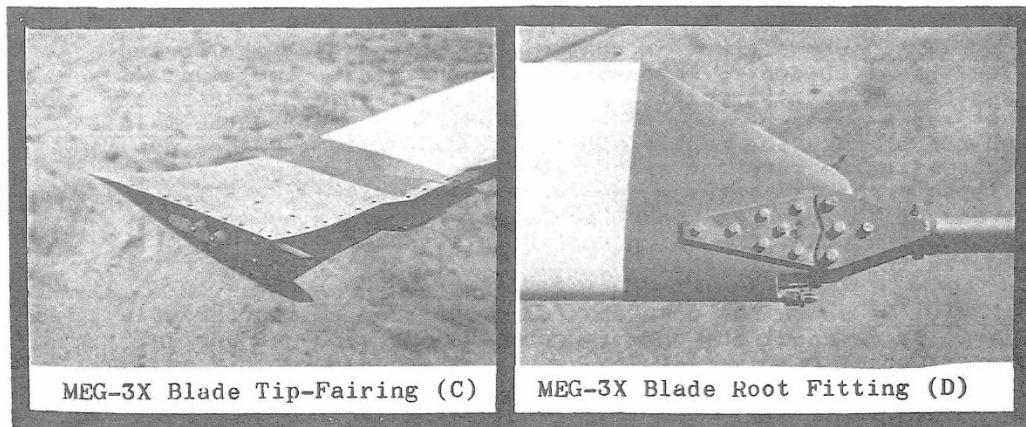
MEG-3X FLYING PLATFORM



MEG-3X next to a big bird (A) MEG-3X hovering in ground effect (B)

SPECIFICATIONS

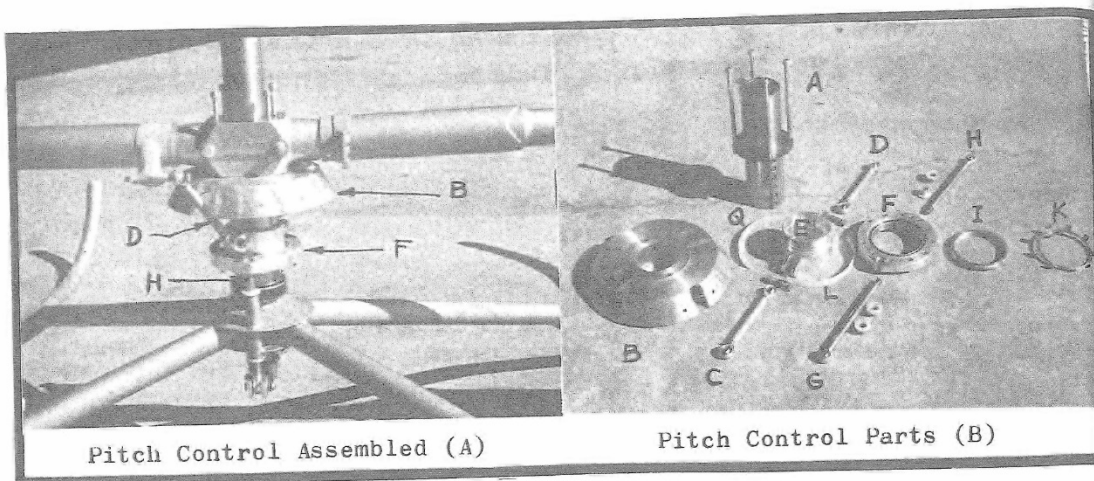
Rotor Diameter	20.0 ft.
Number of blades.....	2
Blade Chord.....	12.0 in.
Airfoil Section, Root NACA..	.0012
Airfoil Section, Tip NACA..	.0009
Power Plant, Pressure Jet...	G8-2-15
Max. Jet Thrust, (Dynamic)..	18-20 lbs.
weight Empty.....	143.0 lbs.
Fuel 20 Gallons Propane.....	80.0 lbs.
Gross Weight.....	408.0 lbs.
Flight RPM Hovering.....	360-415
No Azimuth Flight Control...	
Control by C.G. change.....	
Pitch Control Range.....	+1° to +18°
MEG-3X is positively stable.	
Test Pilot; E.M. Gluhareff	



MEG-3X Blade Tip-Fairing (C)

MEG-3X Blade Root Fitting (D)

Ref. DWG.# 308-0 Tip-Fairing, DWG.# 307-X, 347-X Root Fitting.



Pitch Control Assembled (A)

Pitch Control Parts (B)

PITCH CONTROL MECHANISM

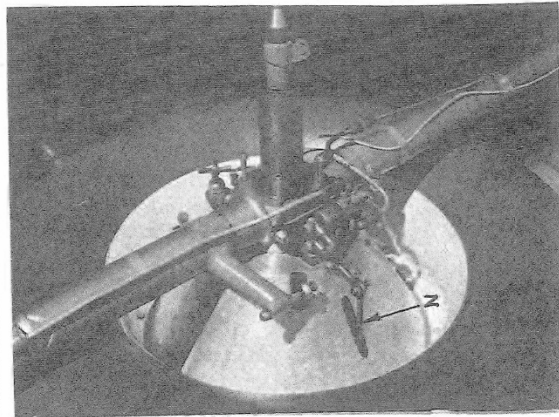
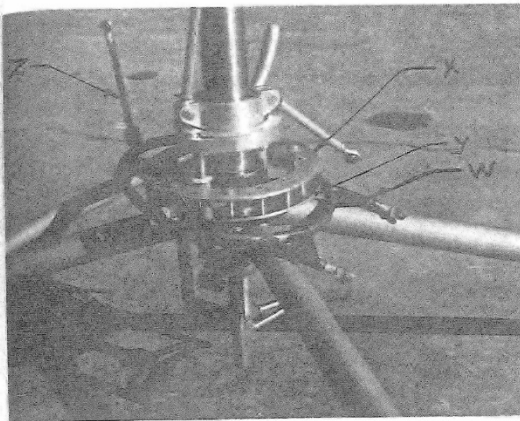
PHOTO (A) shows the assembly of pitch control mechanism of MEG-3X. It is located below the fuel tank. The fuel tank is a donut shaped, made of filament wound fiberglass, it is mounted on the aluminum cone (B) and rotates with the rotor. Push-rod (D) connects blade pitch horn to swoosh-plate (E) and (F). Swoosh-plate assembly slides up and down along shaft (A) photo (B). The outer swoosh-plate (F) is stationary and is actuated by two push-rods (H) and (G), which in turn are actuated by linkage connected to the main push-rod through the center of main stationary shaft.

PHOTO (B) shows component parts of pitch mechanism. The shaft (A) rotates about the main stationary shaft. The fuel tank mounting cone (B) fits on top section, the swoosh-plate assembly (E & F) slides up and down on lower portion of shaft (A) and is prevented from rotation by a key-way. The push-rods (H & G) slide up and down on nylon bushings.

THROTTLE CONTROL MECHANISM

PHOTO (C) shows throttle control mechanism which is located below the pitch-control mechanism. It consists of two aluminum discs bolted together with a spacer between. This disc assembly floats up & down actuated by 3 push-rods connected to the main push-rod through the center shaft. The disc assembly does not rotate with the rotor, a steel tubular ring holds two plastic rollers, which fit between the two aluminum discs (X & Y). One end of the ring is connected to the fuel tank by means of two (W), the other end is connected to a push-rod (Z) that actuates the throttle valve.

PHOTO (D) shows the push-rod (Z) connection to the throttle valves. It is required to have one valve for each jet engine. However, the two valves are linked together and properly adjusted to allow exactly the same amount of fuel to each jet. At the top of the main shaft two other shafts are visible. They are pitch control and throttle control actuators.

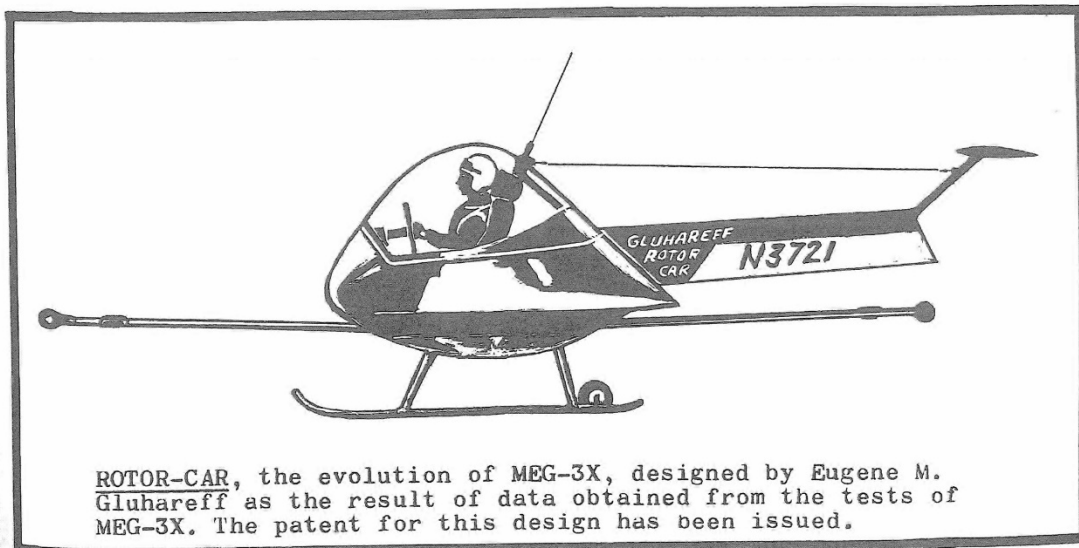


Throttle Control Mechanism (C) Throttle Valves Linkage (D)

COMMENTS

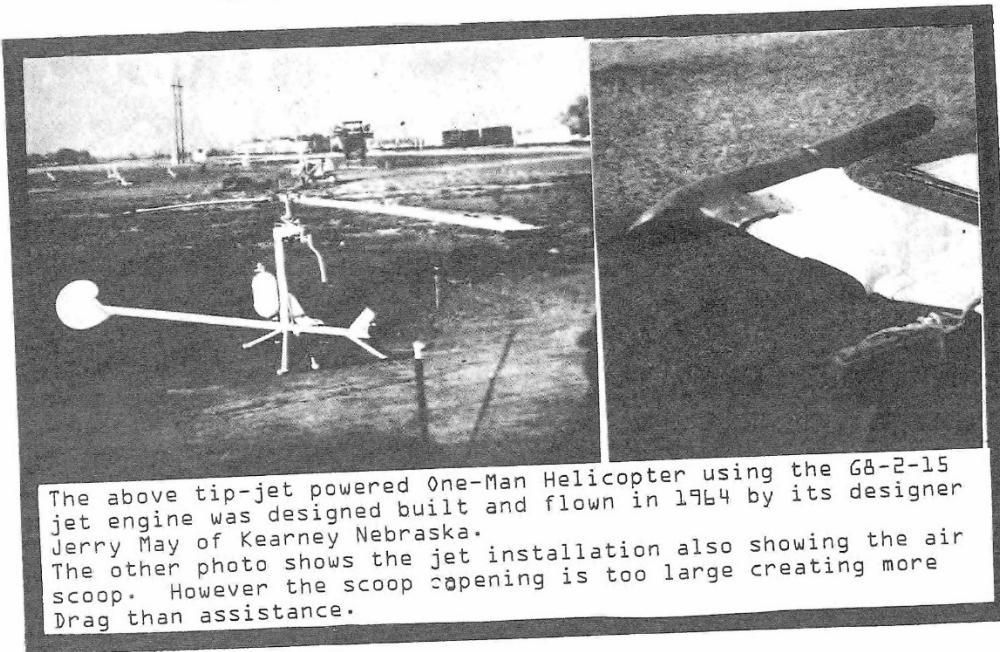
The test results of MEG-3X are extremely educational, (for Lift vs RPM, see graph (E) page 35). The striking feature is that the MEG-3X is a HOVERCRAFT, On take-off it rises to about 3 ft. altitude, blade disc to ground and floats there, following the contour of the terrain. At this position the sand and dust is blown up through the center of the rotor, a very undesirable place to be.

With the increase of the jet thrust the platform rises and hovers in ground-effect, with the additional increase of jet thrust the platform moves up and out of ground-effect. With stirrups bolted to the platform floor the control is easy by leaning one way or another. The aircraft is very stable and tends to hover. It is difficult to judge the altitude on landing, it appears lower than it actually is.



ROTOR-CAR, the evolution of MEG-3X, designed by Eugene M. Gluhareff as the result of data obtained from the tests of MEG-3X. The patent for this design has been issued.

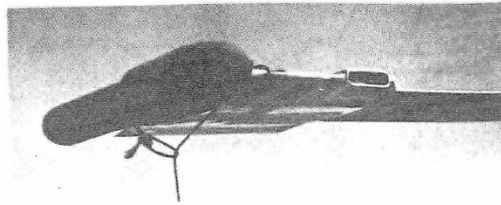
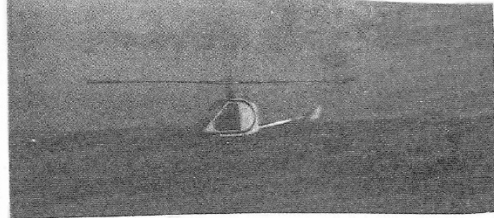
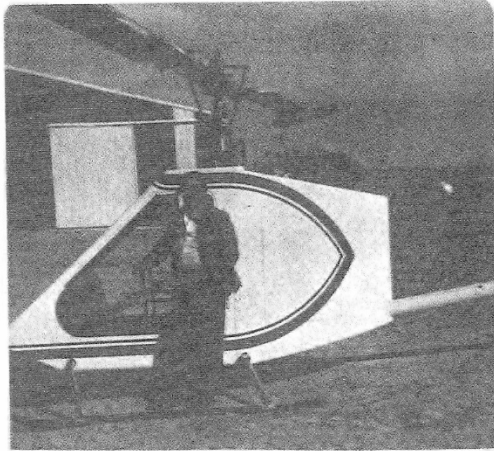
JET HELICOPTER



The above tip-jet powered One-Man Helicopter using the G8-2-15 jet engine was designed built and flown in 1964 by its designer Jerry May of Kearney Nebraska. The other photo shows the jet installation also showing the air scoop. However the scoop opening is too large creating more Drag than assistance.

SPECIFICATIONS

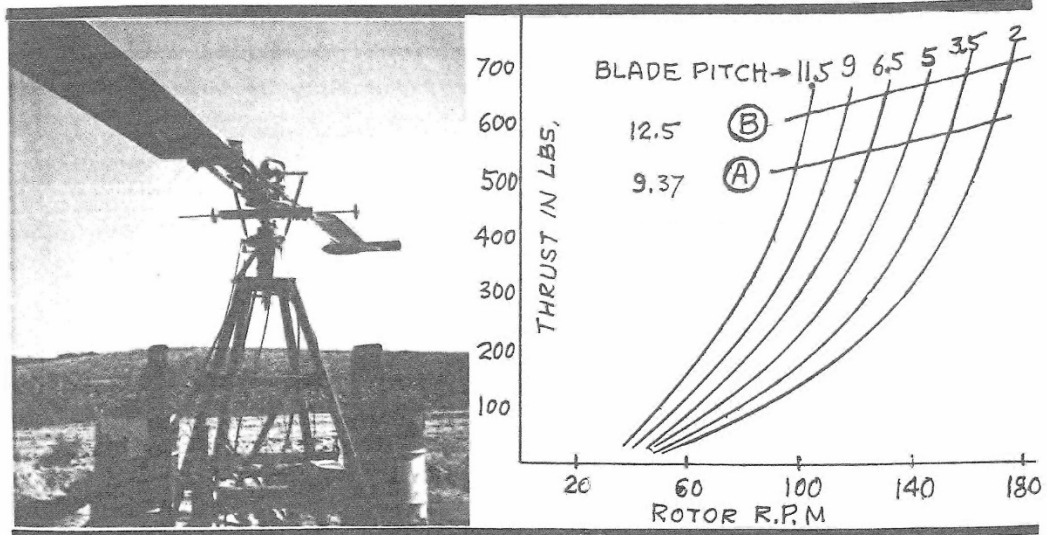
Rotor Diameter.....	26.5 ft.
Number of Blades.....	2
Blade Chord.....	12.0 in.
Airfoil Section.....	NACA... .0012
Power Plant, Pressure Jet...	G8-2-15
Max. Jet Thrust (static)....	15 lbs.
Weight Empty.....	147.0 lbs.
Fuel 7.2 Gallons Usable.....	30.5 lbs.
Useful Load (fuel included).	253.0 lbs.
Gross Weight.....	400.0 lbs.
Flight RPM Hovering.....	275-300
Flight Duration.....	N/A
Fuel Consumption Overall....	N/A
Fuel Tank Capacity.....	8.0 gals.
Fuel Tank Weight.....	19.0 lbs.
Weight Lifted per 1 lb. Thrust	13.3 lbs.
Construction.....	Aluminum Tubing
Blade Construction..	Wood & Steel Straps
Landing Gear.....	Skids-Aluminum Tube
First Flight.....	February 1964
Forward Speed Flown.	10 mph. approx.
Total Flight Time...	10 hours approx.



Mr. Gluhareff is shown standing next to another tip jet powered helicopter. The small photos show the helicopter and the tip jet. The experimental two bladed rotor was powered by two G8-2-40 jets. The helicopter did not get-off the ground. The reason is shown on the graph below that shows the lift. The helicopter Weight Empty was 850 lbs. and Gross Weight was 1200 lbs.

The 36 ft. DI. rotor and 14 in. chord resulted in max. lift of 600 lbs. with two jets that produced only 28 lbs. of thrust per jet, instead of 40 lbs. the reason is that someone attempted to mix Propane and Kerosens which did damage the jet Heat Exchanger coil. ref. line A. Line B shows a thrust 700 lbs. this was obtained with a 32 lb. thrust jet.

If one will divide the max. lift by total jet thrust of $700/64 = 10.9$ lbs. and line A $600/56 = 10.7$. The number indicates that for every pound of jet thrust the rotor lifts 10.9 and 10.7 lbs. This indicates poor streamlining. Good streamlining lifts 13.5 lbs. A 40 lbs. thrust per jet can do better.



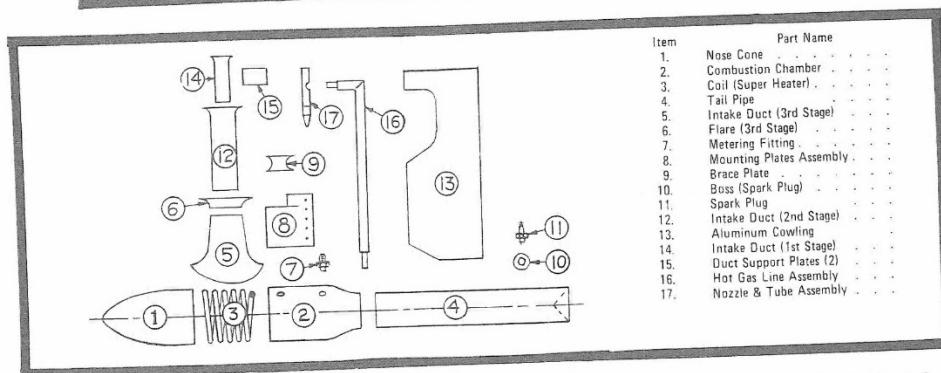


Above a photo of another jet helicopter built by Duan Klettke of K & V Aircraft Ltd. Kelowna, B.C. VIX-263 in 1981. It was powered by two G8-2-20 jets on blade tips.

Mr. Klettke visited EMG Engineering Co. in April 1982 Mr. Klettke owned a machine shop all his work was real good workmanship The rotor was his own design.

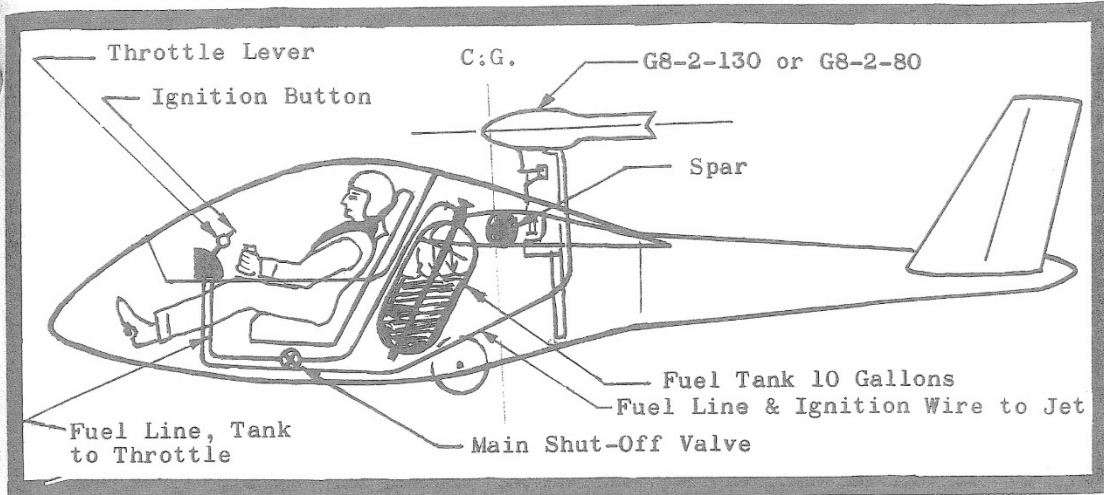
There are several companies that sell jet helicopters like Duan's such as BW-Rotor Co. of Towanda, Kansas, and Helicraft Inc. of Baltimore, Maryland that use G8-2-20 jet engines for power.

JET ENGINE PARTS LIST



The above drawing illustrates the basic component parts of the G8-2 Jet Engine. The part numbers in the circle identifies the part and it also corresponds to the dash-number in the Construction Plans for the same part, and all references.

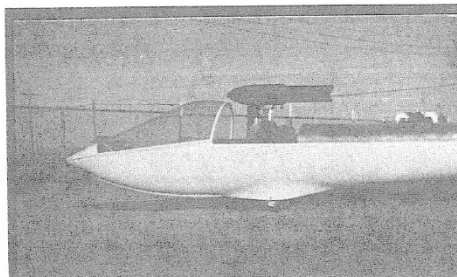
JET GLIDER POWER



TYPICAL G8-2 JET INSTALLATION

Shown above is a typical G8-2 Jet Power System with a fixed or retractable jet. The whole arrangement is extremely simple and involves only three items. The G8-2 Jet Engine, a fuel tank, ignition system and throttle valve. The distribution of these items must be not to dislocate the original C.G. of the glider.

The fuel tank must be located on C.G. or close to it, to avoid C.G. change with full or empty tank. The G8-2 Jet located on the other side of C.G. to balance the fuel tank and throttle. The 5/16 OD. aluminum fuel line must connect fuel tank and throttle, same OD. fuel line must connect the throttle and the G8-2 Jet. The ignition system as shown on page 27 can be located next to the throttle. The push-button can be located in the throttle knob. This ignition system weighs only 2 oz. The high voltage wire should be taped to the fuel line from throttle to G8-2 Jet and the fuel line also should be used as ground.



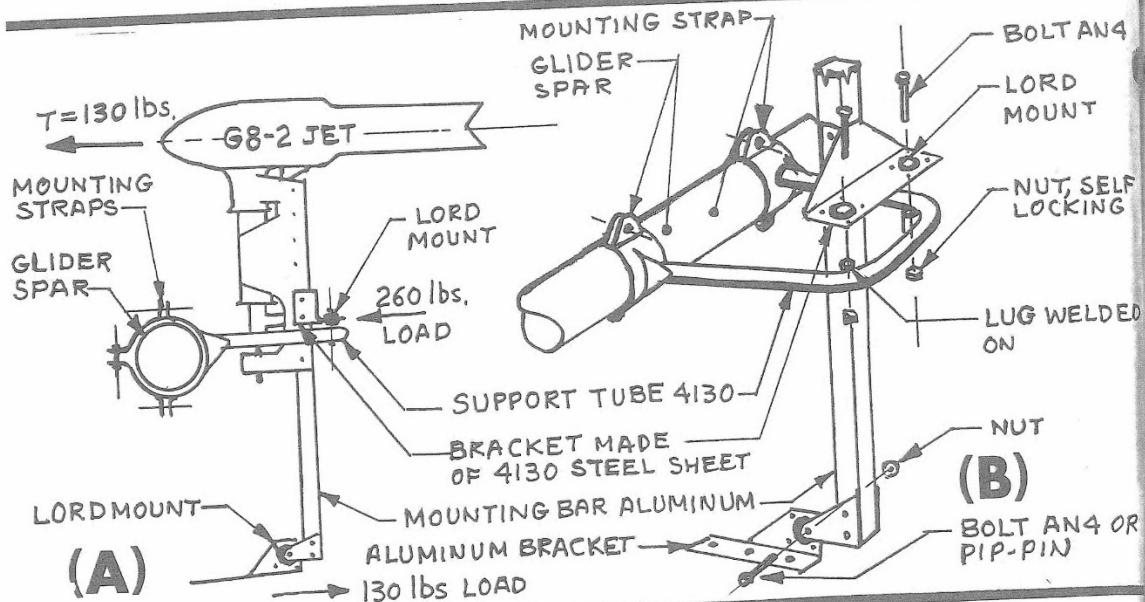
Typical Jet Installation

WEIGHT OF POWER SYSTEM

Engine, G8-2-130R.....	23. lbs
Fuel Tank Alum. 10 gals..	19. lbs
Ignition System.....	2. oz.
Throttle and Gauges.....	3. lbs
Fuel Lines and Wires.....	1. lb.
Total Fixed Equipment	<u>46. lbs</u>
Fuel Propane 10 gallons	<u>40. lbs</u>
Equipment & Fuel.....	<u>86. lbs</u>

The expected duration of a flight on full power using the G8-2-130R Jet and based on S.F.C. data from Space-Ranger of 0.77 lbs/lb/hr., on 10 gallons of Propane, will be 20 - 30 minutes. (see page 53)

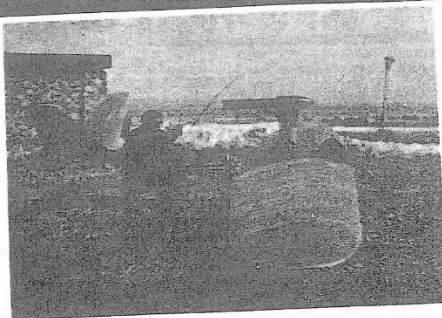
SAMPLE INSTALLATION



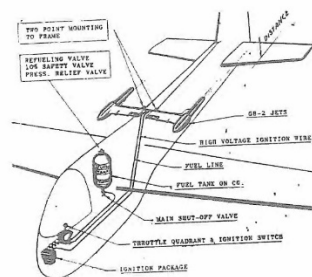
The above sketch shows details of a sample installation of the G8-2-130 on a glider that has a tubular spar. However, other types of glider installations can be made by following the basic concept of using the Lord mounts, as a means of attachment.

The Lord-Mounts are an absolute must, because without them the noise vibrations from the jet would feed into the glider structure and amplify itself. It also could affect the instruments.

A retractable jet arrangement can be designed by mounting the jet on a short mounting-bar and let the bar slide up & down, using the original mounting-bar as guide post. See sketch (A) above. The thrust required for one-man glider minimum is about 60 lbs. but with the G8-2-130 the performance will be excellent.



MIDGET U-2 sailplane build by our customer using G8-2-15 jet.



Two Jet Power Version using G8-2-40 or G8-2-80 jets.

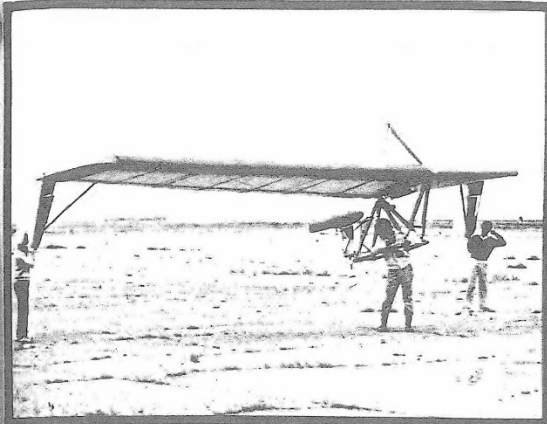
JET ICARUS V HANG GLIDER

AN4

T

SELF
ING

ELDE



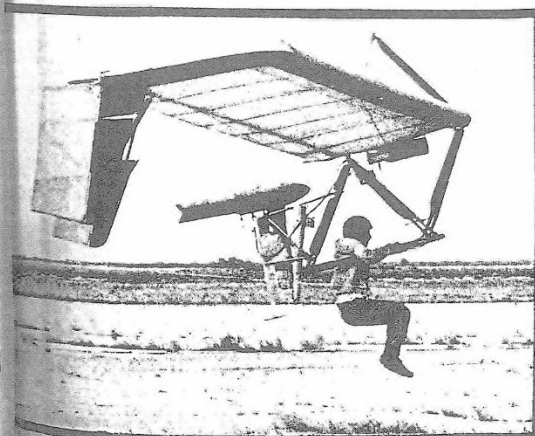
4 OR

THE FIRST FLIGHT OF JET POWERED HANG-GLIDER was in May 1981 piloted by Ted Ancona. The builder of the Icarus-V Hang-Glider and the installer of the GB-2-130 Pressure Jet.

The GB-2-130 Jet is capable of 130 lbs. of Static thrust but only 50-70 lbs. were used by Ted Ancona due to a small tank.

The sequence of take-off is depicted by the 3 photos. Photo {A} Ted cracked the throttle and pushed the Ignition button. Fuel ignites and the jet became alive emitting a slight roar. While the jet was idling and warming-up Ted prepared for take-off, made a last check and pushed the throttle forward with his right hand. The jet roared and with only three steps forward Ted was airborne. Photo {B} few seconds later Photo {C} Ted was climbing into the blue-yonder with impressive rate of climb and flew away.

ing



With a 2 gallons fuel tank. The usable fuel was 1-1.2 gallons allowing flight duration of 4 to 5 minutes.

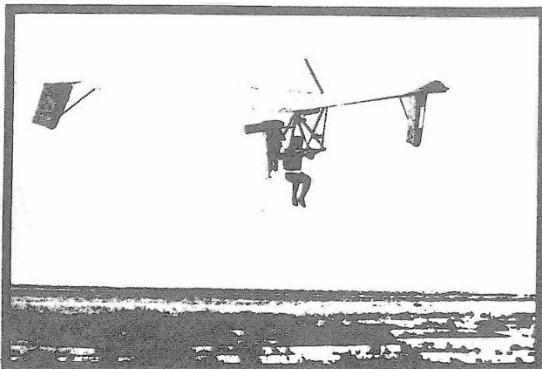
FOR LONGER AND BETTER FLIGHT it is advised to use a larger fuel tank for several reasons. One; DOT requirement is to allow 10% of tank volume as gas space for safety, because the liquid Propane has very high coefficient of expansion.

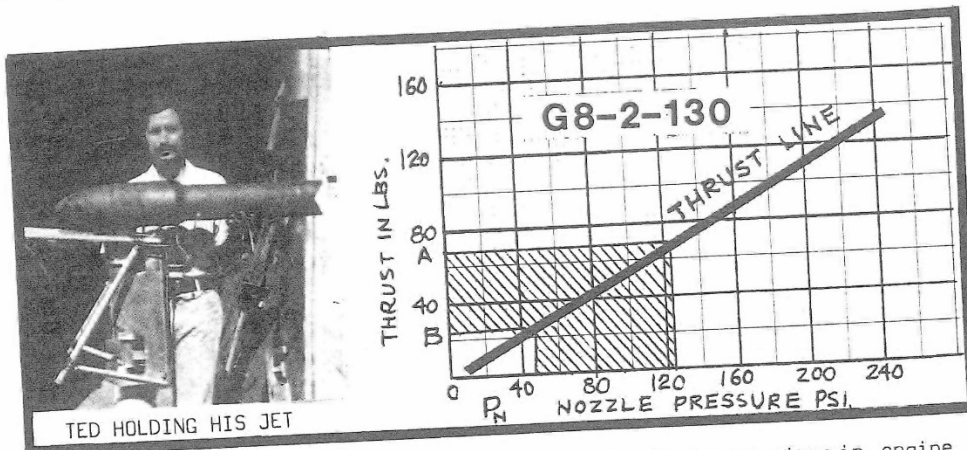
Second; When the tank is too small and fuel is withdrawn rapidly the tank pressure will drop rapidly. The evaporation of Propane will reduce the temperature and the pressure will drop. To raise the pressure the tank must be preheated or pressurized with Nitrogen to be able maintain high pressure to use all of the available fuel. With Teds tank pressure was very high at start about 250 psi, but dropped rapidly when it got past 1/2 gallon mark the pressure was too low. Thus the fuel was not used effectively because jet thrust is a function of tank pressure. With a larger fuel tank the pressure will be maintained.

DESCRIPTION OF JET SYSTEM:

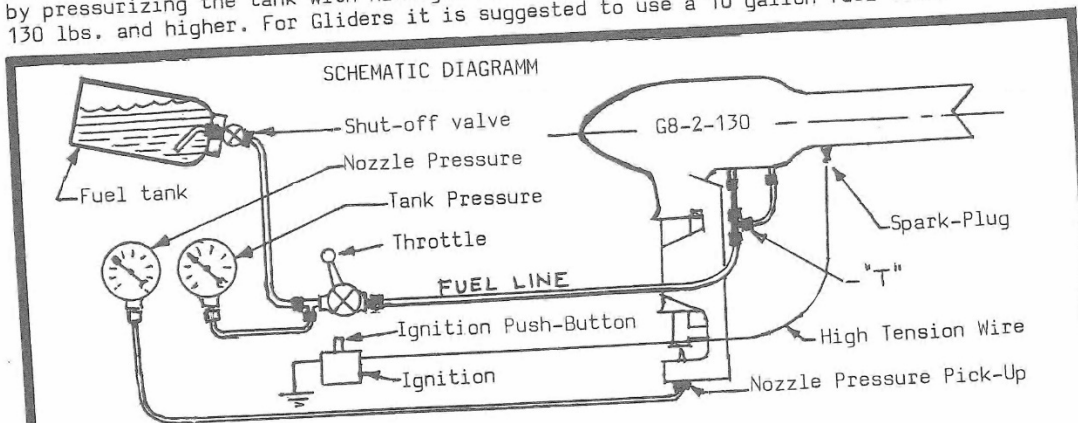
The Jet is mounted on "N" type structure to the Hang-Glider with Pip-Pins for quick and easy disconnect and disassembling. Location of jet thrust line is on center of Drag. The jet engine has no torque like the props thus making it safer on turns.

The fuel tank is located under the wing on C.G. of the aircraft. 1/4 in. Aluminum fuel lines connect the shut-off valve on tank and throttle located at Teds right hand for ease of control. From the throttle the fuel line runs up the strut as shown on photo 'B' then it connects to a flex hose which runs the rest of the way to the jet.





The graph above shows the performance of The G8-2-130 Jet Engine as given in engine spec. The shaded area describes the power range used by Ted Ancona. The thrust ranges from point (A) at take-off. As time goes on the tank pressure drops and finally it winds up at point (B) which terminates Teds Powered Flight. A larger fuel tank would remedy the situation. The tank pressure will not drop. With 250 psi. Teds original tank pressure he would be operating in the higher range. Consequently the use of a larger tank with higher pressure by painting the tank black, wrapping it in transparent Milar, or by pressurizing the tank with Nitrogen to 300 psi. will boost the operating range to 130 lbs. and higher. For Gliders it is suggested to use a 10 gallon fuel tank.

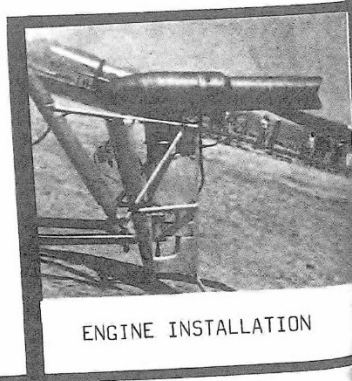


SPECIFICATIONS

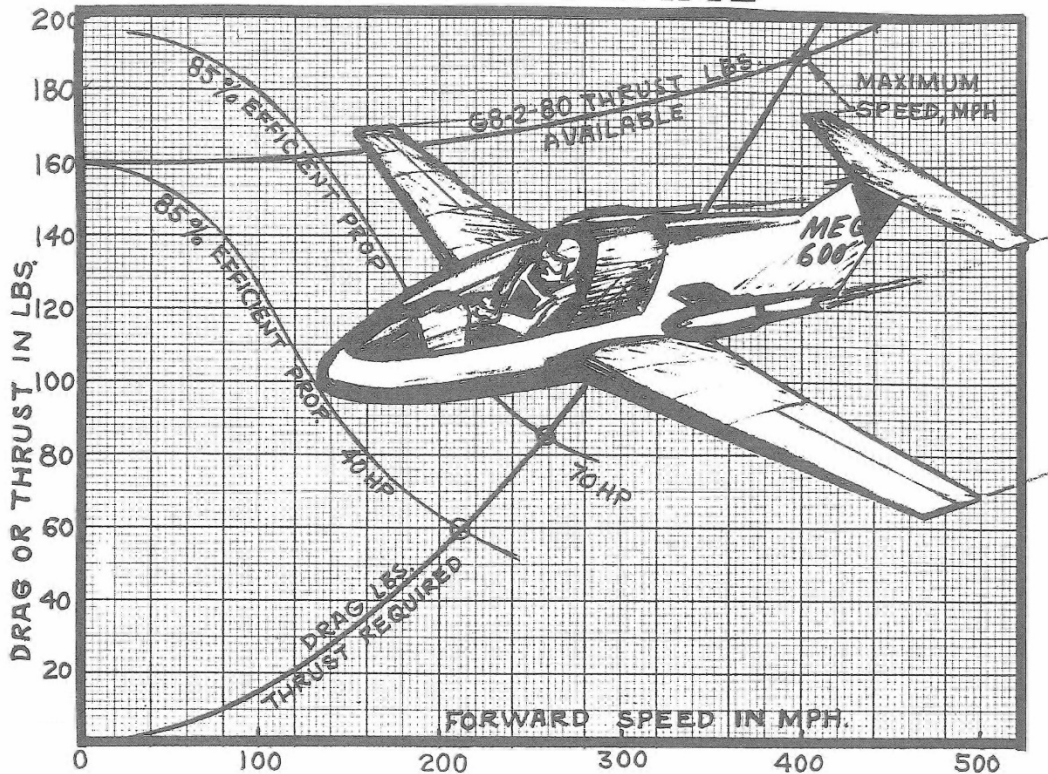
Icarus V Hang-Glider Empty Weight	75 lbs.
Wing Span	32 ft.
Wing Area	160 ft.sq.
Airfoil Thickness in percent of chord	18 %
L/D Glide Ratio	10
Engine Weight (G8-2-130).....	24.5lbs.
Fuel Tank Weight	7.5lbs.
Fuel Tank Capacity in Gallons	2. gals.
Weight of Fuel (Propane 4.23 lbs./gal.)...	6. lbs.
Pilot Weight (Ted Ancona).....	175. lbs.
Wt. of Throttle, Ignition, Lines & Brackets	4. lbs.

PERFORMANCE

Flight Duration in minutes	4 to 5 min.
Max. Forward Speed (Aprox.).....	30 MPH.
Rate of Climb (Aprox.).....	200-300 ft./min.
Take-off Distance with 10 MPH. wind	3 steps.



G8-2 JET PLANE



JET ENGINE FOR HOME-BUILT AIRCRAFT

Two jet models are available, The G8-2-80 and the G8-2-130. They can be used singly or in pairs. The arrangement is similar to the DC-9. The two jets can be mounted on one common mounting-bar and the bar attached to an aircraft via Lord-Mounts for smooth and quiet operation. One ram-air scoop can be used for both jets. (see sketch (B) page 48 and 49).

The curve above is for an aircraft of BD-5 class, Gross Weight of 600 lbs and powered by two G8-2-80 jets. For 800 - 1000 lbs Gross Weight (2) G8-2-130 jets are suggested.

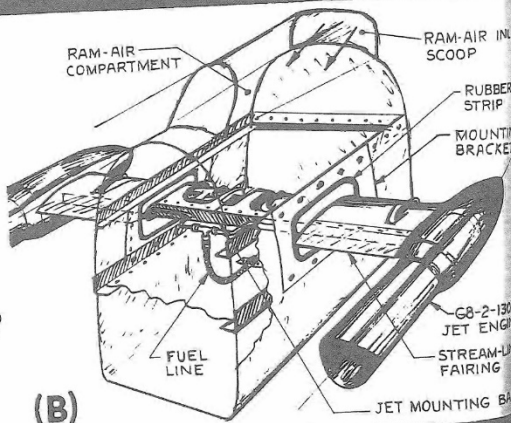
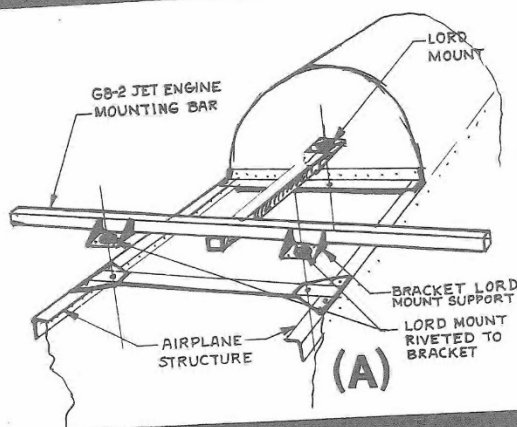
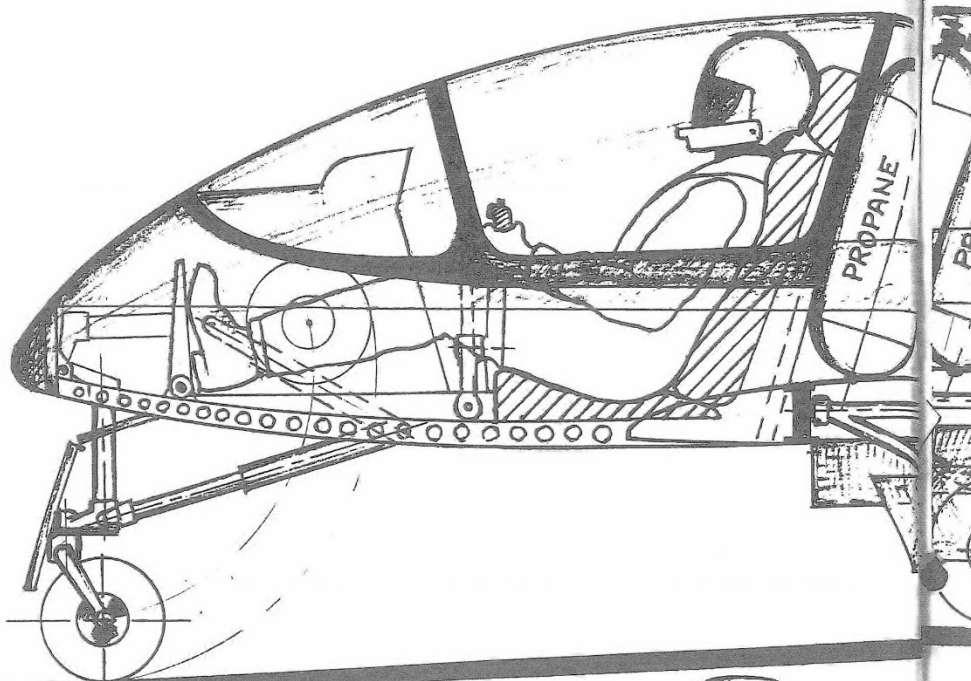
A SIMPLE BALL PARK ANALYSIS based on static S.F.C. = 0.77 lbs/lb/hr obtained from SPACE-RANGER data. (see page 49). How much fuel will be used in 2 hours, if flying at 400 mph using 600 lbs Gross Weight aircraft powered by (2) G8-2-80 Jets, producing 160 lbs of thrust. (see graph above)

$$\text{Fuel Used} = \frac{T \times \text{SFC} \times t}{3 \times W_f} = \frac{160 \times 0.77 \times 2}{3 \times 4.23} = 19.42 \text{ gallons}$$

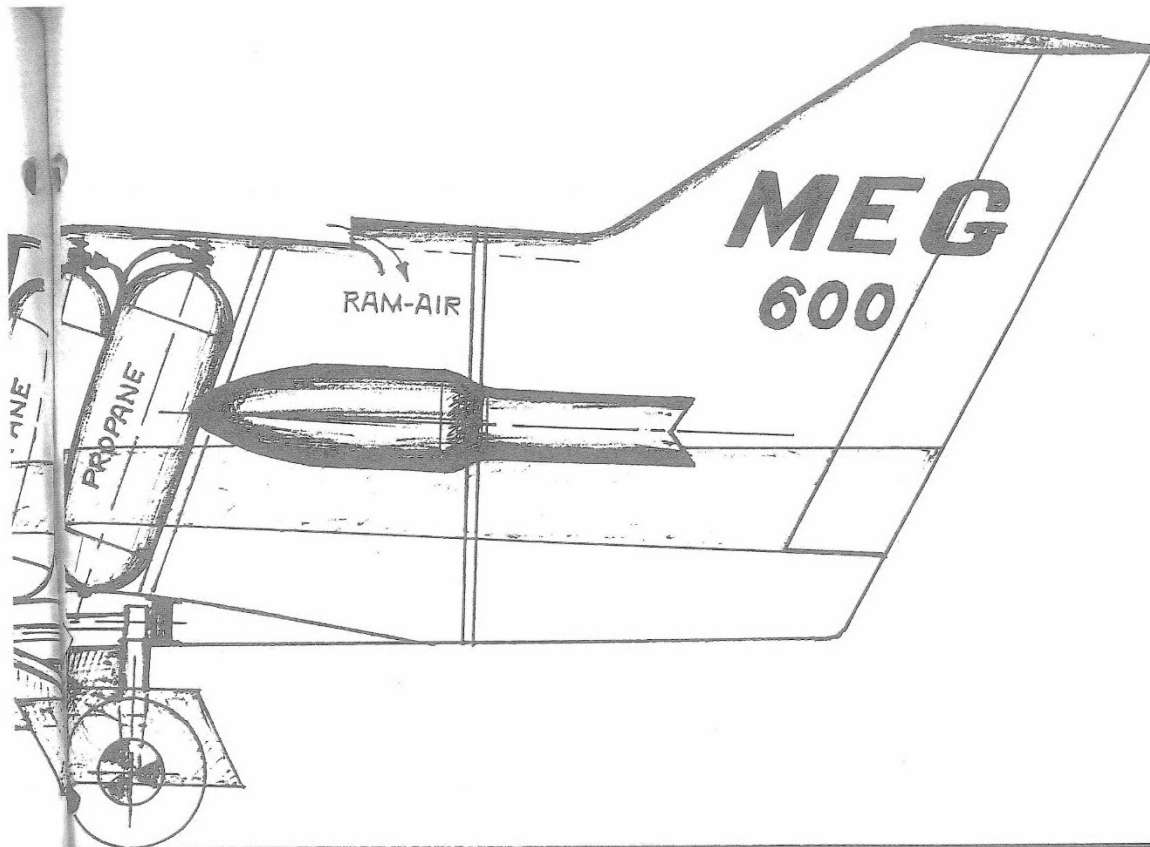
$$\text{Miles per gallon} = \frac{\text{MPH} \times t}{\text{gallons}} = \frac{400 \times 2}{33.4} = 41 \text{ mpg}$$

It would be advisable to carry on board 40 gallons of Propane and 60 gallons if using (2) G8-2-130 Jets. One must make allowance for higher S.F.C. on take-off. (for HP calculation see page 18)

MEG - 600



Sketch (A) illustrates a simple mounting of the G8-2 Jet. This is achieved by welding the lord-mount support brackets to the jet mounting-bar. A third support point is required to hold the jet firm. Therefore, a forward extension of the mounting-bar is welded on which holds the third Lord-Mount. The whole unit bolts to the aircraft structure at 3 points via Lord-Mounts.



Sketch (B) illustrates another way of installing the G8-2 Jet on an airplane. Perhaps it is a simpler way to achieve a leak-proof engine compartment. The Lord-Mounts are not used, but instead the jets are mounted via a soft rubber strip between two brackets, one bracket attaches to the aluminum cowling, the other bracket attaches to the airplane frame, (see sketch (B)) as they do for automobile windows.

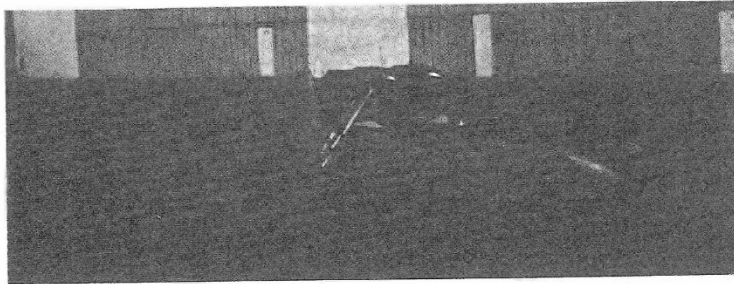
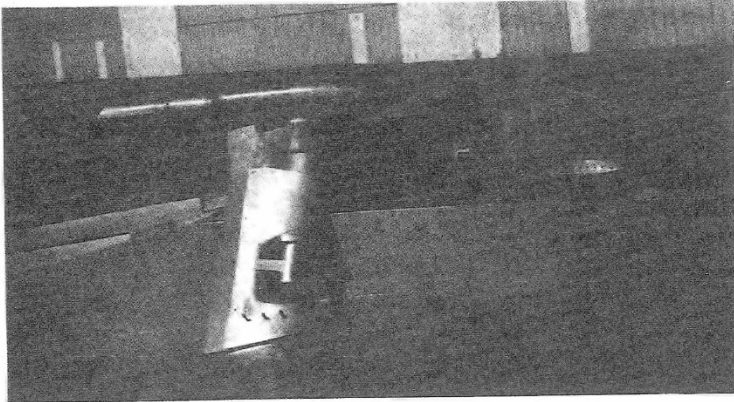
THE MEG-600 JET PLANE was designed by Eugene M. Gluhareff to promote the use and applications of the G8-2 Jet Engines. This also demonstrates the simplicity of installation of the G8-2 Jets.

The MEG-600 is powered by two G8-2-80 Jets. These jets can be replaced by the G8-2-130 Jets if better performance is desired. The MEG-600 has sweep back wings with camber air-foil. Its weight breakdown is as follows;

MEG-600 Weight Breakdown

Pilot + Parachute.....	200 lbs
Fuel 40 gallons (Propane)..	160 lbs
Useful Load.....	360 lbs
Weight Empty.....	308 lbs.
Gross Weight.....	668 lbs.
Gross Weight Average.....	595 lbs.

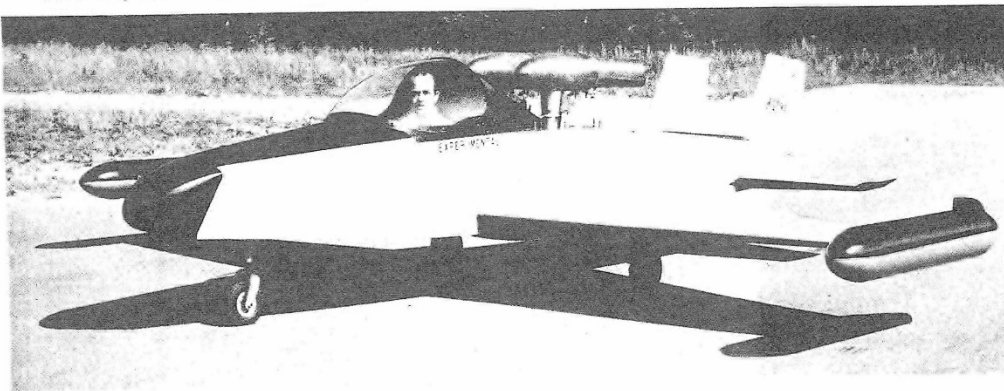
WHILLING PJ-1



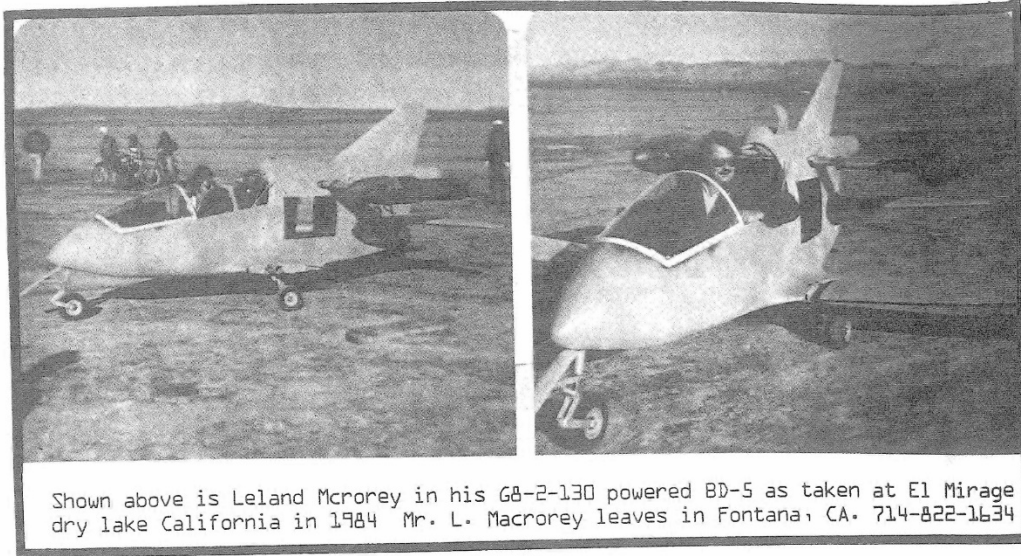
Another G8-2-130 Jet Powered Airplane designed and built by Doug Whilling of WHILLING AIRCRAFT CO. Pontiac Michigan.

The version presented above uses G8-2-130 Oval Intake. The engines are mounted on the outside. Doug realized that flexing wing will also move the engines up and down creating a stress problem. It was also found that the engines will interfere with the fuselage and raise the total Drag.

The version below shows same plane but with two G8-2-130R located inside the fuselage. This arrangement will improve the Ram-Air scoop and also will improve the SFC consequently extend the range.



JET BD-5

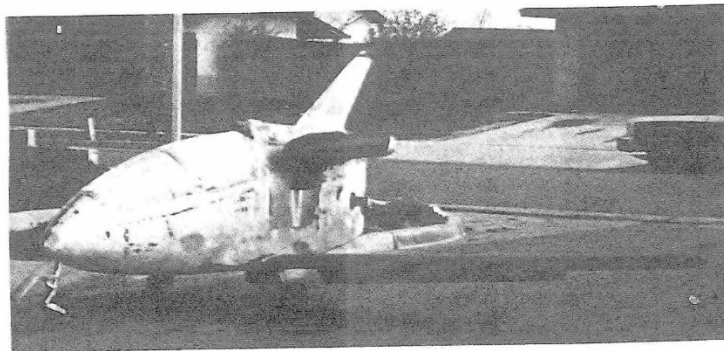


Leland is the first BD-5 owner to power his BD-5 with EMG's G8-2-130 with oval intakes. Installed on a steel bar through the fuselage and mounted on Lord Mounts to the fuselage to separate the jet noise from the metal Air-frame.

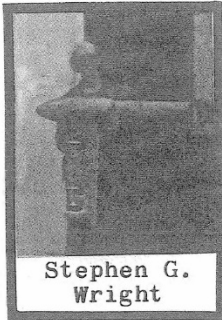
Due to the BD-5 being so small he run in to a problem. He managed to have on board only 13 gallons of Propane. There was room only for two fuel tanks a 5 gallon one and an 8 gallon tank. Actually he needs about 40 to 60 gallons for a decent range. The fuel must be located on c.g. of aircraft bur BD-5 has only few inches of c.g. travel allowable.

Testing the aircraft Leland run into a minor problem, since he had one throttle for both jets. One jet produced more thrust than the other at same throttle setting he couldnot keep the aircraft on a straight pat on take-off. Instead of installing a dual throttle he decided to relocate the engines.

The jets were 6 ft. between noses thus Leland realised that he could not fly on one jet due to a large lever arm which could not be overcome by the Ruther. The photo below shows the new installation. He thinks that he can fly on one jet if needed safely.

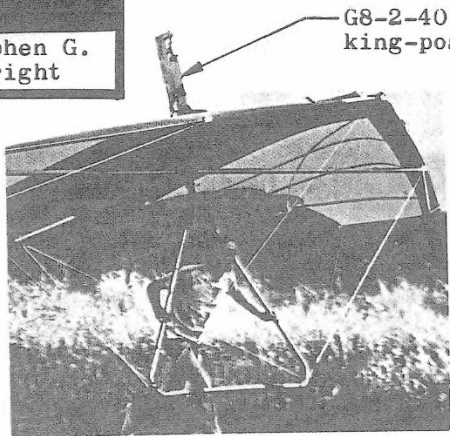


JET POWERED HANG-GLIDER

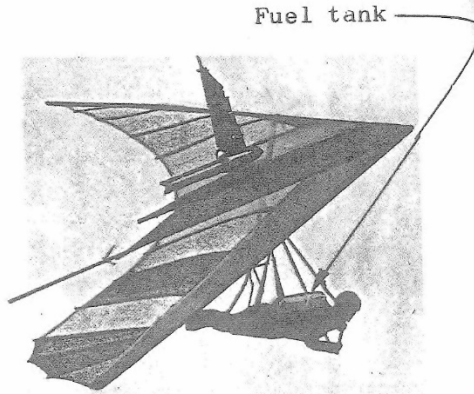


Stephen G. Wright

Who needs hills or cliffs, now you can take-off on flat land with G8-2-40 Jet power. Climb to 3500 ft. altitude, shut your jet and look for thermals. Olympus & Cirrus Hang-Gliders were outfitted with one G8-2-40 Jet and successfully test flown by Stephen G. Wright in 1977.



G8-2-40 on king-post



Fuel tank

DATA

Olympus & Cirrus Hang-Gliders;	
Pilot Weighs.....	165 lbs
Hang-Glider Weight	45 lbs
Jet Power System..	30 lbs
Gross Weight.....	240 lbs

Rate/Climb 250-1050 ft/min.
 Altitude Gain 2500-3500 ft
 Fuel Used (Propane) 2 gallons
 Power Plant one G8-2-40 Jet
 Hang-Glider L/D.... 7.5: 1
 Air Starts and Restarts.

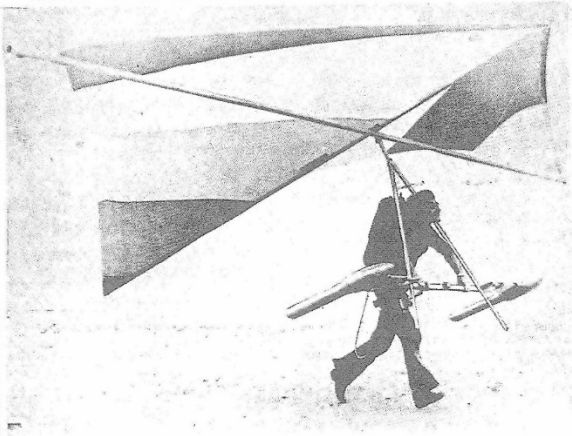
Mr. Stephen G. Wright, Pres.
 ULTRAJET SYSTEMS, INC.
 21615 - 80th Avenue, West
 Edmonds, Washington 98020

EXAMPLE

How much jet thrust is needed for level flight of your hang glider?

If you know your hang gliders L/D ratio, divide your Gross Weight by L/D ratio to obtain jet thrust required, level flight no thermals.

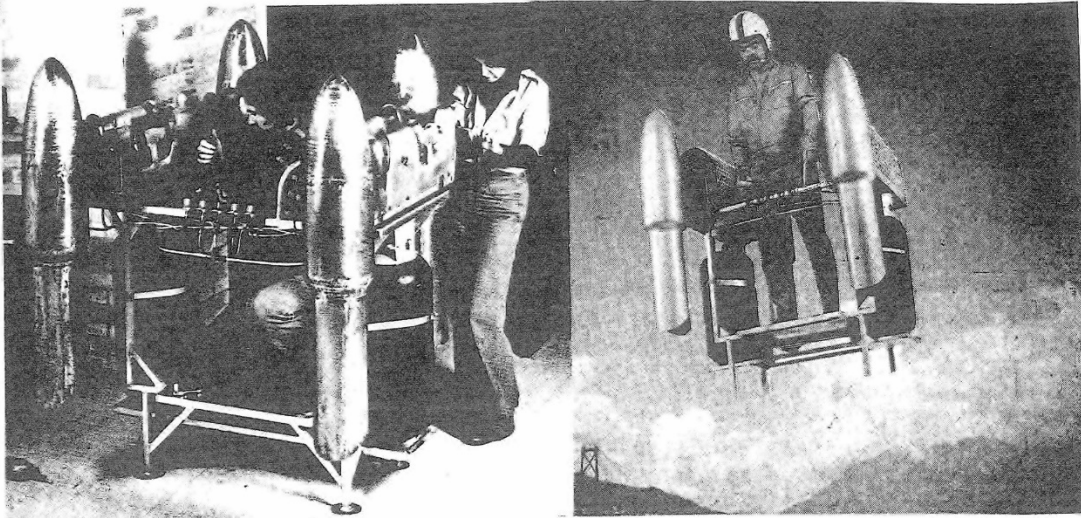
JET POWERED PORTO-WING



PORTO-WING HANG-GLIDER designed by Eddie Paul Whitney of El Segundo, California in 1974. It is powered by two G8-2-15 Jet Engines. A 3 gallon fuel tank on pilots back with flex hose and quick-disconnect connection to throttle.

Data not available.

SPACE RANGER



SPACE RANGER POWERED BY [4] G8-2-130 JETS

The SPACE RANGER is now available in a complete build-it-yourself construction package

- Vertical take-off and landing.
- Hovers like a helicopter
- Safe, easy to fly
- Runs on easily obtainable fuel
- Can fly to a height of 5,000 ft.
- Stable and easy to control using body-weight to manoeuvre
- Flies forwards, backwards and sideways
- Extremely low operating costs
- No moving parts, nothing to wear out
- Made of durable stainless steel and aluminum
- Total weight: 250 lbs.
- Can be easily assembled in your workshop or at your local welding shop
- Can be assembled and constructed in a matter of days

SPECIFICATIONS

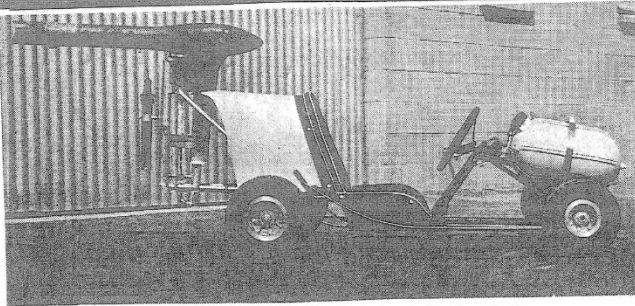
Weight Empty.....	250 lbs
Usefull Load.....	270 lbs
Gross Weight.....	520 lbs
Poewr Plant.....	(4) G8-2-130 Jets
Fuel 20 gallons (Propane).....	80 lbs
Duration of Flight.....	8-15 min
Maximum Forward Speed.....	40 mph
Range.....	10 mil
S.F.C. at 12 min. duration.....	0.77 lbs/lb/hr
First Flight (R. Timewell Pilot) Aug. 15, 1977	



Richard Ross Timewell
Inventor, builder and
pilot of SPACE-RANGER

Mr. Timewell President
of Space-Ranger Corp.
119 Terminal Building,
Boeing Field,
Seattle, Wa. 98108
Phone; (206)-762-5820

JET GO KARTS



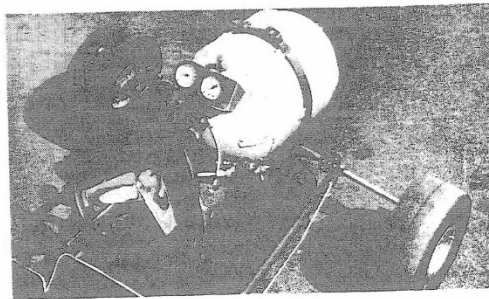
G8-2-15 Jet Powered Go-Kart # 1.

Gluhareff's Jet Powered Go-Kart No.1 built and tested in 1960.

Maximum Speed.. 45 mph
 Go-Kart Weight. 153 lbs
 Drivers Weight. 170 lbs
 Power Plant Jet G8-2-15
 Max. Jet Thrust 15 lbs
 Fuel Tank Cap. 4 gals

PHOTO shows fuel tank installation, gauges for nozzle and tank pressures, ignition button, main shut-off valve and foot pedal operated throttle.

For more information see the July 1961 Kart Magazine. Cover, article and many photos.



G8-2-40 Jet Powered Go-Kart driven by Andre E. Gluhareff

THE ZOOM-BOOM

EMG's Jet Go-Kart # 2 Powered by G8-2-40 Jet Engine, built and tested in 1972.

Maximum Speed..... 75 mph
 Go-Kart Weight..... 160 lbs
 Drivers Weight..... 165 lbs
 Power Plant, Jet.... G8-2-40
 Maximum Jet Thrust.. 43 lbs
 Fuel Tank Capacity.. 8 gals

For more information see the May 1973 issue of Science and Mechanics Magazine. Cover, article and many photos.

RACING JET GO-KART



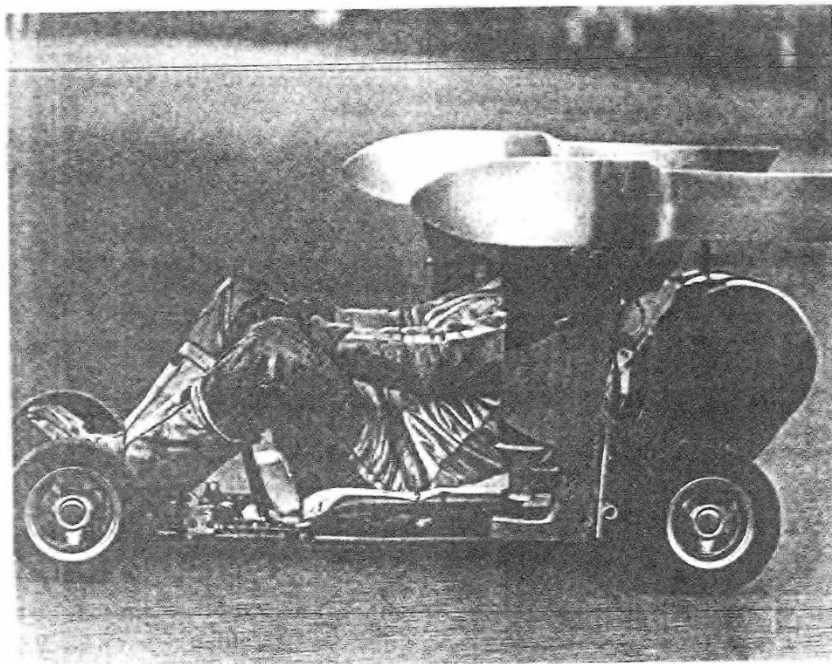
Greg King Preparing for a Race

DATA

Max. Speed in 1/4 mile 85 mph
Max. Speed is over.... 100 mph

Go-Kart Weight Empty.. 158 lbs
Drivers Weight..... 185 lbs
Fuel 8 gals. Propane.. 32 lbs
Gross Weight..... 375 lbs

Tank Pressurized to... 350 psi
Max. Thrust per jet... 55 lbs
Pressurized with Nitrogen



Jet Go-Kart shown above is powered by two G8-2-40 Jets built in 1977 by Greg B. King, a Stunt Driver of 5225 W. Gray Drive Wall, Mississippi 38680.

Greg King races between Jolopy Races as The Dare Devil Spectacular in his twin jet Go-Kart all over USA booked by his manager.

JET BICYCLES

Three inventors independently have powered their bicycles with The G8-2-15 Jet Engine over a period of several years.



In 1974 Barry C. Cooley of Fort Lauderdale, Florida claimed to be the first man to build a jet bike, using the G8-2-15 Jet Engine.

Max. speed was 50 mph.
Duration at max. thrust was 20 minutes.
Max. jet thrust 15 lbs.
Fuel tank cap. 3 gallons.

In 1975 Ray Kesler of 1712 E. Colorado Blvd., Los Angeles, California was the second man to install the G8-2-15 Jet on his 10 speed bike.

Maximum jet thrust was 18 lbs.
Fuel tank capacity 2 gallons.

Data not available



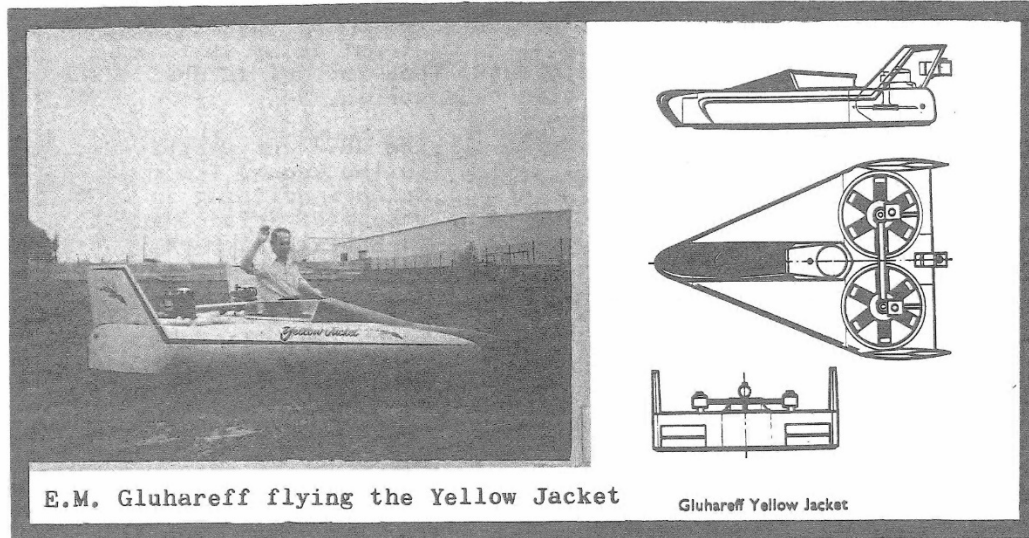
In 1977 Bob Lazar of 20650 Martha Street, Woodland Hills, California 91364 was the third man to power his bike with the G8-2-20 Jet Engine.

Max. speed reached was 57 mph. However, Bob claims he can reach 65 mph. after biffing up the bike structure.

Max. jet thrust was 23 lbs.
Fuel tank capacity 3 gallons.



JET PROPELLED HOVERCRAFT



E.M. Gluhareff flying the Yellow Jacket

Gluhareff Yellow Jacket

The Yellow Jacket shown above was designed and built by Eugene M. Gluhareff in 1960 with the help of his elder son, Eugene E. Gluhareff. It is 10 feet long and 80 inches wide. It is powered by two 10 hp Chrysler two cycle engines, which turn two counter-rotating rotors of 33.5 in. diameter. Each rotor has six blades and turns at 3600 RPM.

The Yellow Jacket weighs empty 155 lbs, its Gross Weight is 335 lbs. It hovers at 6-8 inches, skirt to ground. At forward speed of about 28 mph, and over it flies at 12 inches skirt to ground due to its lifting Delta-Wing. Max. speed attained on Yellow Jacket over land was about 60 mph.

For additional information see the March 1971 issue of Popular Mechanics Magazine. Cover, story and many photos. (Plans available \$15)

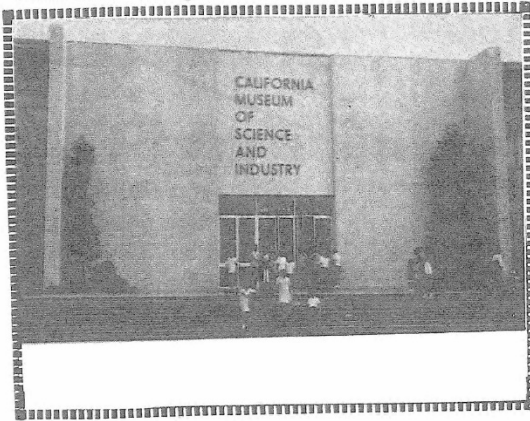
The Yellow Streak Jet Powered Hovercraft is similar to The Yellow Jacket but a bit larger. It also has the same motors and rotors. It is powered by two G8-2-20 Jets mounted on top of vertical fins to improve speed over water and to achieve precision control.

Jets and fins turn together and each jet is differentially controlled for instant response.



JET MUSEUM EXHIBITS

The jet ignites, a short period of warm-up, then it gradually increases to its maximum thrust and automatically shuts itself off. The whole process takes one minute. Then the jet is shut off for 10 minutes to give the public time to disperse.



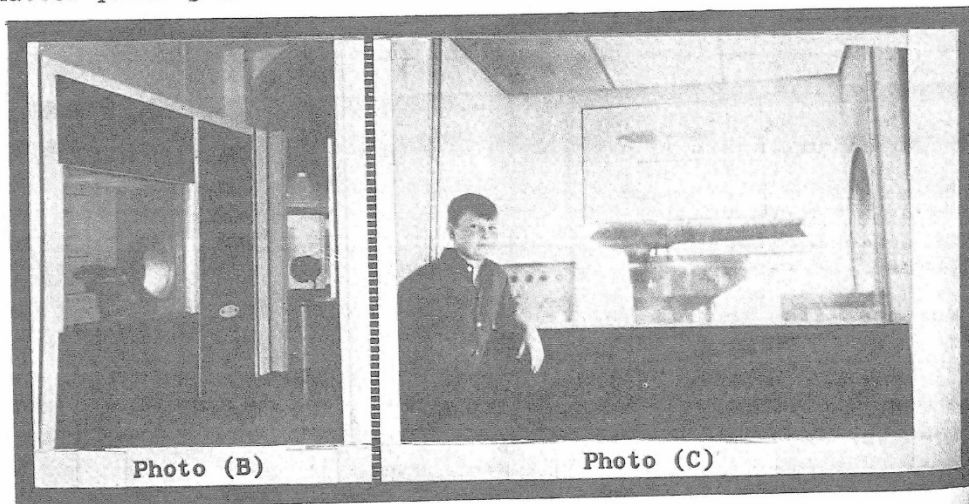
The G8-2 Jet Exhibit is located on the second floor of the Science Building in The Calif. Museum of Science and Industry, in Exposition Park, Los Angeles, California.

The Exhibit has been there since March 1961. It runs every 10 min. from 8 am to 5 pm, seven days a week.

From the time the visitor pushes the start button, the entire Jet Exhibit is operated automatically by an electronic control unit.

PHOTO (B) Shows the outside appearance of the exhibit and the enclosure, shows the starting button and red indicator light, which means the jet is ready for firing. The Exhibit Director is Mr. Norman Bilderbach.

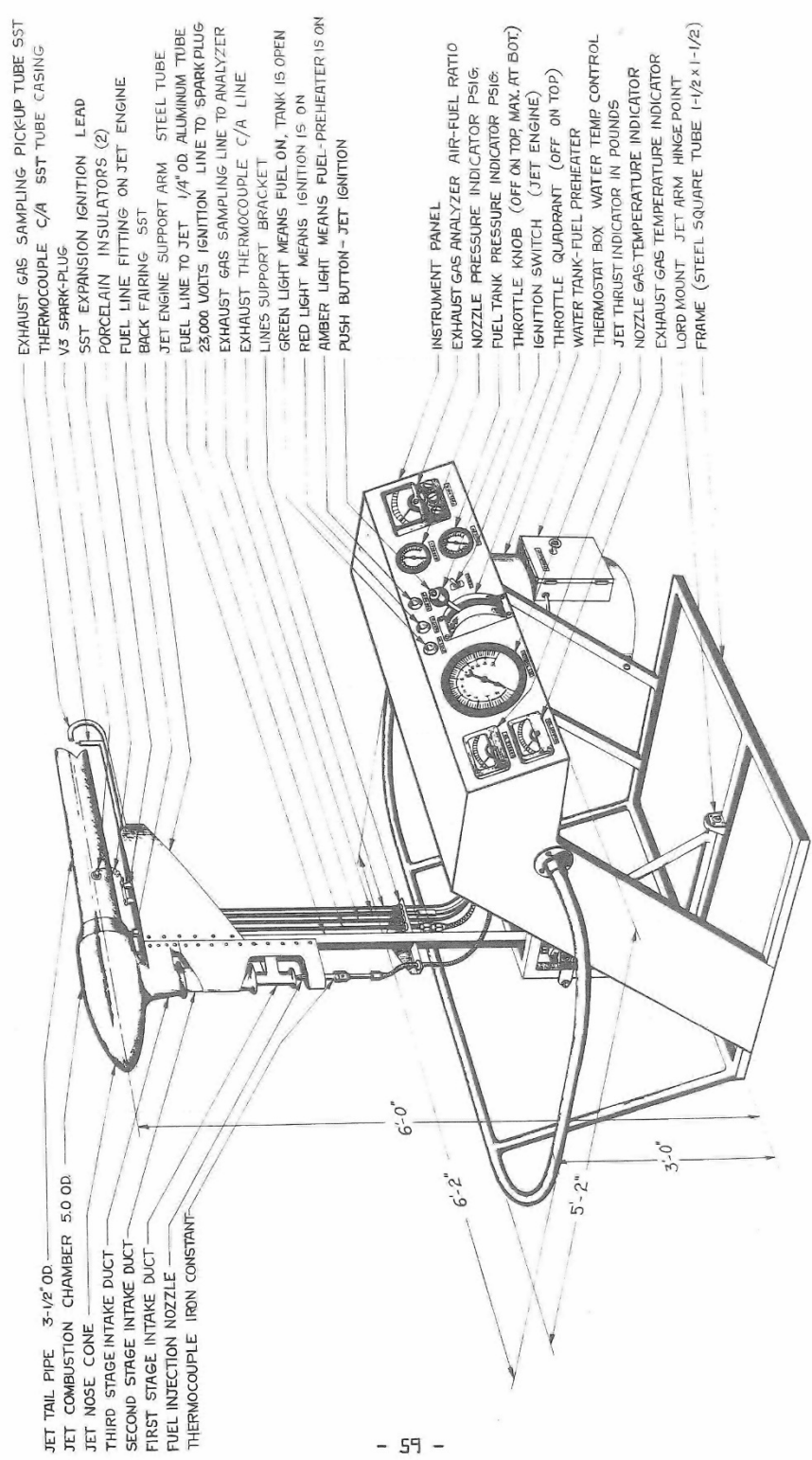
PHOTO (C) Shows The G8-2-15 Jet installed in the firing cell. The jet exhaust blast is aimed into a 20 in. diameter vent-hole visible in photo (B). The jet starts with the tail-pipe near the exhaust vent. As the jet thrust increases it moves 8 inches forward and returns to its original position at the end of the cycle. The engine glows red-hot and is separated from the spectators by a heat resistant and shatter-proof glass.



Another similar G8-2-15 Jet Exhibit exists in Canada at The Centennial Centre of Science and Technology, Don Mills, Ontario, Canada.

)
 d
 r,
 is,
 ice
 lin.
 a
 les
 let
 illy
 iclo-
 is
 ie
 :
 nt.
 o
 T

GTS-15 TEACHING TEST STAND



- JET TAIL PIPE 3-1/2" OD.
- JET COMBUSTION CHAMBER 5.0 OD.
- JET NOSE CONE
- THIRD STAGE INTAKE DUCT
- SECOND STAGE INTAKE DUCT
- FIRST STAGE INTAKE DUCT
- FUEL INJECTION NOZZLE
- THERMOCOUPLE IRON CONSTANT

- EXHAUST GAS SAMPLING PICK-UP TUBE SST
- THERMOCOUPLE C/A SST TUBE CASING
- V3 SPARK-PLUG
- SST EXPANSION IGNITION LEAD
- PORCELAIN INSULATORS (2)
- FUEL LINE FITTING ON JET ENGINE
- BACK FAIRING SST
- JET ENGINE SUPPORT ARM STEEL TUBE
- FUEL LINE TO JET 1/4" OD. ALUMINUM TUBE
- 23,000 VOLTS IGNITION LINE TO SPARK PLUG
- EXHAUST GAS SAMPLING LINE TO ANALYZER
- EXHAUST THERMOCOUPLE C/A LINE
- LINES SUPPORT BRACKET
- GREEN LIGHT MEANS FUEL ON, TANK IS OPEN
- RED LIGHT MEANS IGNITION IS ON
- AMBER LIGHT MEANS FUEL-PREHEATER IS ON
- PUSH BUTTON - JET IGNITION

- INSTRUMENT PANEL
- EXHAUST GAS ANALYZER AIR-FUEL RATIO
- NOZZLE PRESSURE INDICATOR PSIG.
- FUEL TANK PRESSURE INDICATOR PSIG.
- THROTTLE KNOB (OFF ON TOP, MAX. AT BOT.)
- IGNITION SWITCH (JET ENGINE)
- THROTTLE QUADRANT (OFF ON TOP)
- WATER TANK-FUEL PREHEATER
- THERMOSTAT BOX WATER TEMP. CONTROL
- JET THRUST INDICATOR IN POUNDS
- NOZZLE GAS TEMPERATURE INDICATOR
- EXHAUST GAS TEMPERATURE INDICATOR
- LORD MOUNT JET ARM HINGE POINT
- FRAME (STEEL SQUARE TUBE 1-1/2" x 1-1/2")

F. GTS-15 Example Calculation Workbook for Students

INTRODUCTION

THIS EXPERIMENT BOOK IS FOR THE INDIVIDUAL STUDENT'S OWN LAB. EXPERIMENTS RECORD. RECORD ALL DATA SPECIFIED AND STATED IN EACH EXPERIMENT.

WRITE THE VALUES INTO THE EQUATIONS IN SPACE PROVIDED, MARKED BY PARENTHESIS.

DO THE ARITHMETIC TO OBTAIN THE REQUIRED ANSWERS. ALL VALUES OF PRESSURE AND TEMPERATURE USED IN THE EQUATIONS ARE ABSOLUTE VALUES.

REFER TO THE THE GTS-15 TECHNICAL HANDBOOK FOR DETAILS. THE INSTRUCTOR SHOULD DIRECT THE SCOPE OF EXPERIMENT AND FILL IN PERTINENT VALUES.

EXPERIMENT No. A-

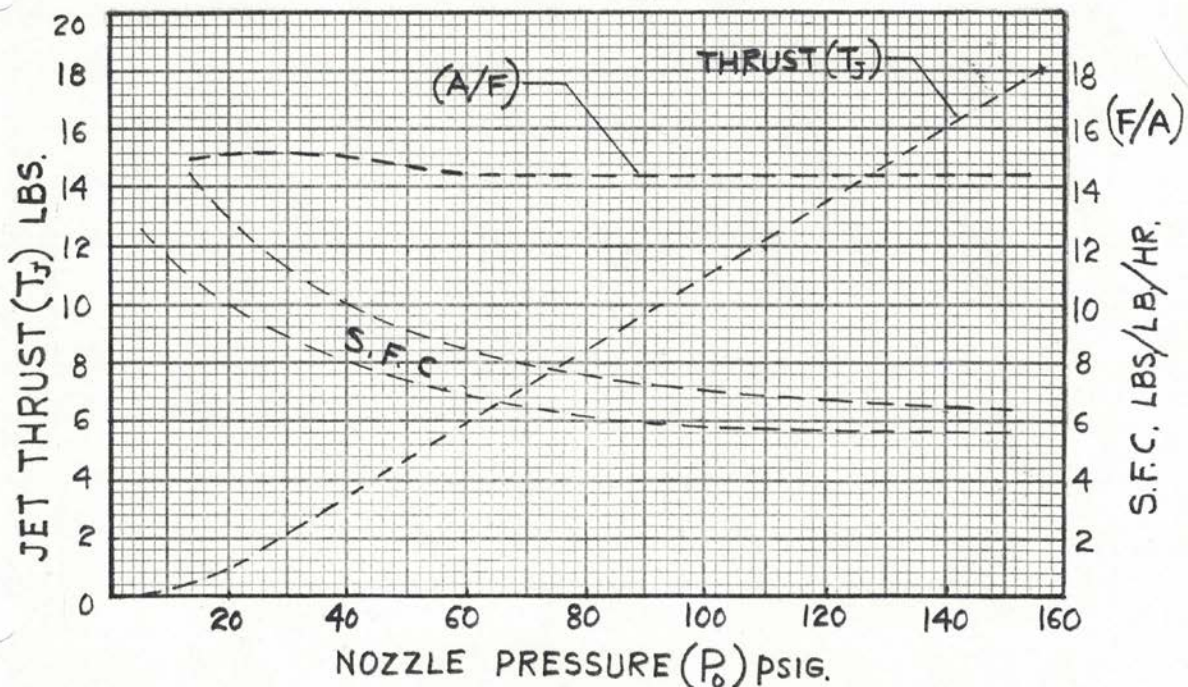
DETERMINATION OF SPECIFIC FUEL CONSUMPTION S.F.C.

CALCULATE S.F.C. BY DETERMINING THE AMOUNT OF FUEL USED IN GIVEN TIME. CONVERT DATA TO WEIGHT OF FUEL USED IN ONE HOUR, AND DIVIDE BY THE JET THRUST.

RECORD:		HR. MIN. SEC.
JET THRUST $(T_J) = (\quad)$ lbs.		TIME OF END $(t_1) = (\quad - \quad - \quad)$
NOZZLE PRES. $(P_0) = (\quad)$ psig.		TIME OF START $(t_0) = (\quad - \quad - \quad)$
NOZZLE GAS T. $(T_0) = (\quad)$ °F.		TIME OF RUN $(\Delta t) = (\quad)$ min.
AIR FUEL RATIO $(A/F) = (\quad)$		WEIGHT AT START $(wt_0) = (\quad)$ lbs.
TANK PRESSURE $(P_T) = (\quad)$ psig.		WEIGHT AT END $(wt_1) = (\quad)$ lbs.
		FUEL USED $(\Delta wt.) = (\quad)$ lbs.

$$S.F.C. = \frac{(\Delta wt.) \times 60}{T_J \times \Delta t} = \frac{(\quad) \times 60}{(\quad) \times (\quad)} = (\quad) \text{ lbs./lb./hr.}$$

THRUST VS. NOZZLE P. VS S.F.C.



EXPERIMENT No. B-

JET ENGINE PERFORMANCE

CALCULATE THE FOLLOWING VALUES:

1. WEIGHT OF FUEL FLOW.....(W_f) = () lbs./sec.
2. WEIGHT OF AIR FLOW.....(W_a) = () lbs./sec.
3. EXHAUST EXIT VELOCITY.....(V_e) = () ft./sec.
4. HORSE POWER AT _____ ft./sec..(HP_o) = () hp.
5. OVERALL THERMAL EFFICIENCY...(E_o) = () %
6. STATIC EQUIVALENT HORSE POWER(HP_i) = () hp.

RECORD:

- JET ENGINE THRUST.....(T_J) = () lbs.
 OBTAIN FROM GRAPH... (S.F.C.) = () lbs./lb./hr.
 AIR FUEL RATIO.....(A/F) = () ratio
 NOZZLE PRESSURE.....(P_o) = () psig.
 NOZZLE GAS TEMPERATURE(T_o) = () °F.
 TANK PRESSURE.....(P_T) = () psig.

$$1. W_f = \frac{T_J \times (S.F.C.)}{3600} = \frac{(\quad) (\quad)}{3600} = (\quad) \text{ lbs./sec.}$$

$$2. W_a = (A/F) \times W_f = (\quad) (\quad) = (\quad) \text{ lbs./sec.}$$

$$3. V_e = \frac{T_J g}{W_a + W_f} = \frac{(\quad) 32.2}{(\quad) + (\quad)} = (\quad) \text{ ft./sec.}$$

$$4. HP_o = \frac{T_J \times V_e}{550} = \frac{(\quad) (\quad)}{550} = (\quad) \text{ hp.}$$

$$5. E_o = \frac{HP_o \times 2545 \times 100}{W_f \times BTU \times 3600} = \frac{(\quad) 2545 \times 100}{(\quad) 21,690 \times 3600} = (\quad) \%$$

$$6. HP_i = T_J / 5 = (\quad) / 5 = (\quad) \text{ hp.}$$

EXPERIMENT No. C-

INJECTION NOZZLE ANALYSIS

CALCULATE THE FOLLOWING VALUES:

1. FUEL FLOW RATE (w_{fc}) = () lbs./sec.
2. NOZZLE EFFICIENCY... (η_n) = () %
3. NOZZLE EXIT VELOCITY (V_n) = () ft./sec.

RECORD:

USE ABSOLUTE VALUES

- JET ENGINE THRUST (T_J) = () lbs.
 NOZZLE PRESSURE (P_o) = () psig. ($14.7 + P_o$) = () psia.
 NOZZLE GAS TEMP. (T_o) = () ° F. ($460 + T_o$) = () °R.
 AIR FUEL RATIO (A/F) = () ratio
 ORIFICE DIAMETER (D_t) = () in. OR. AREA (A_t) = () in.²

$$1. \quad w_{fc} = A_t P_o \left(\frac{2}{k+1} \right)^{\frac{1}{k-1}} \left[\frac{2gk}{RT_o (k+1)} \right]^{\frac{1}{2}} =$$

$$w_{fc} = (\quad) (\quad) \left(\frac{2}{2.15} \right)^{6.66} \left[\frac{2 \times 32.2 \times 1.15}{35.1 (\quad) (2.15)} \right]^{\frac{1}{2}} = (\quad) \text{ lbs./sec.}$$

$$w_f = T_J (\text{S.F.C.}) / 3600 = \frac{(\quad) (\quad)}{3600} = (\quad) \text{ lbs./sec.}$$

$$2. \quad \eta_n = w_f \times 100 / w_{fc} = (\quad) 100 / (\quad) = (\quad) \%$$

$$T_h = T_o \left(\frac{P_i}{P_o} \right)^{\frac{k-1}{k}} = (\quad) \left[\frac{14.7}{(\quad)} \right]^{\frac{1}{7.67}} = (\quad) \text{ °R.}$$

$$\omega_o = P_o / RT_o = 144 (\quad) / 35.1 (\quad) = (\quad) \text{ lbs./ft.}^3$$

$$V_{nc} = \left[2gJ \omega_o C_p (T_o - T_h) \right]^{\frac{1}{2}} =$$

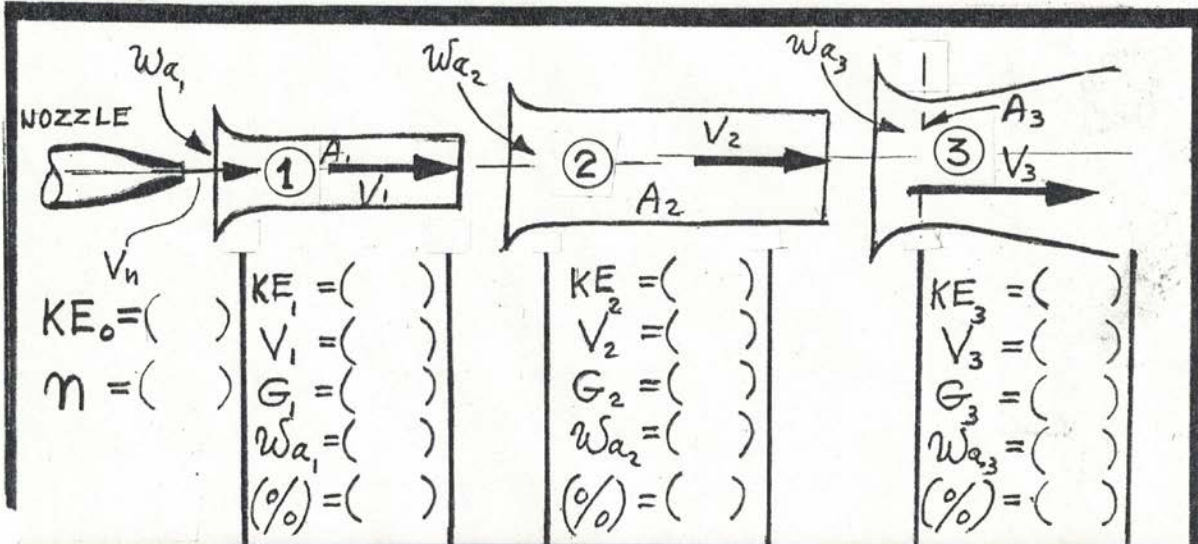
$$= \left\{ 2 \times 32.2 \times 778 (\quad) .39 \left[(\quad) - (\quad) \right] \right\}^{\frac{1}{2}} = (\quad) \text{ ft./sec.}$$

$$3. \quad V_n = \eta_n \times V_{nc} = (\quad) (\quad) = (\quad) \text{ ft./sec.}$$

EXPERIMENT No. D- AIR INTAKE SYSTEM ANALYSIS

(SHEET 1 OF 3)

CALCULATE THE FOLLOWING VALUES FOR ALL 3 STAGES, AND THE OVERALL INTAKE EFFICIENCY (η).



RECORD:

JET THRUST... (T_J) = () lbs.
 NOZZLE PRES.. (P_0) = () psig.
 NOZZLE GAS T. (T_0) = () °F.
 TANK PRESSURE (P_T) = () psig.
 AIR FUEL RATIO(A/F) = ()
 AMBIENT TEMP. (T_1) = () °F.

USE AREAS SPECIFIED ABOVE OR MEASURE YOUR OWN:

NOZZLE ORIFICE AREA (A_T) = () in.
 1ST STAGE SECTION.. (A_1) = () in.
 2ND STAGE SECTION.. (A_2) = () in.
 3RD STAGE SECTION.. (A_3) = () in.
 FROM GRAPH (S.F.C.) = () lbs/lb/hr.

REFER TO EXPERIMENT No. "C", CALCULATE NOZZLE EXIT VELOCITY (V_n), NOZZLE KINETIC ENERGY (KE_0). USE ABSOLUTE VALUES FOR PRES. & TEMP.

$$KE_0 = \frac{V_n^2 T_J (S.F.C.)}{2g \times 3600} = \frac{(\quad)(\quad)(\quad)}{2 \times 32.2 \times 3600} = (\quad) \text{ Ft. lbs.}$$

$$G_3 = \frac{T_J (S.F.C.)}{3600} (1 + (A/F)) = \frac{(\quad)(\quad)}{3600} [1 + (\quad)] = (\quad) \text{ lbs./SEC.}$$

$$\omega_1 = \omega_2 = \omega_3 = \frac{P_1}{RT_1} = \frac{14.7 \times 144}{53.3(\quad)} = (\quad) \text{ lbs./ft.}$$

$$V_3 = \frac{G_3 \times 144}{A_3 \times \omega_3} = \frac{(\quad)144}{(\quad)(\quad)} = (\quad) \text{ ft./sec.}$$

$$KE_3 = G_3 V_3^2 / 2g = \frac{(\quad)(\quad)}{2 \times 32.2} = (\quad) \text{ ft.lbs./sec.}$$

OVERALL INTAKE EFFICIENCY (η).

$$\eta = \sqrt[3]{\frac{(KE_3)}{(KE_0)}} = \sqrt[3]{\frac{(\quad)}{(\quad)}} = (\quad) \square$$

KINETIC ENERGY (KE).

$$KE_1 = \eta (KE_0) = (\quad)(\quad) = (\quad) \text{ ft.lbs./sec.}$$

$$KE_2 = \eta^2 (KE_0) = (\quad)(\quad) = (\quad) \text{ ft.lbs./sec.}$$

$$KE_3 = \eta^3 (KE_0) = (\quad)(\quad) = (\quad) \text{ ft.lbs./sec.}$$

FIRST STAGE:

$$V_1 = \sqrt[3]{\frac{2g(KE_1)}{A_1 \omega_1}} = \sqrt[3]{\frac{2 \times 32.2(\quad)144}{(\quad)(\quad)}} = (\quad) \text{ ft./sec.}$$

$$G_1 = V_1 A_1 \omega_1 = \frac{(\quad)(\quad)(\quad)}{144} = (\quad) \text{ lbs./sec.}$$

$$\omega_{a_1} = G_1 - \omega_f = (\quad) - (\quad) = (\quad) \text{ lbs./sec.}$$

SECOND STAGE

$$V_2 = \sqrt[3]{\frac{2g(KE_2)}{A_2 \omega_2}} = \sqrt[3]{\frac{2 \times 32.2 (\quad) 144}{(\quad) (\quad)}} = (\quad) \text{ ft./sec.}$$

$$G_2 = V_2 A_2 \omega_2 = \frac{(\quad) (\quad) (\quad)}{144} = (\quad) \text{ lbs./sec.}$$

$$\omega_{a_2} = G_2 - G_1 = (\quad) - (\quad) = (\quad) \text{ lbs./sec.}$$

THIRD STAGE

$$V_3 = \sqrt[3]{\frac{2g(KE_3)}{A_3 \omega_3}} = \sqrt[3]{\frac{2 \times 32.2 (\quad) 144}{(\quad) (\quad)}} = (\quad) \text{ ft./sec.}$$

$$G_3 = V_3 A_3 \omega_3 = \frac{(\quad) (\quad) (\quad)}{144} = (\quad) \text{ lbs./sec.}$$

$$\omega_{a_3} = G_3 - G_2 = (\quad) - (\quad) = (\quad) \text{ lbs./sec.}$$

TOTAL AIR INDUCED (ω_a).

$$\begin{aligned} \omega_a &= \omega_{a_1} + \omega_{a_2} + \omega_{a_3} \\ &= (\quad) + (\quad) + (\quad) = (\quad) \text{ lbs./sec.} \end{aligned}$$

PERCENTAGE OF INDUCED AIR PER STAGE.

$$\text{1ST STAGE (\%)} = \frac{100 \times \omega_{a_1}}{\omega_a} = \frac{100 (\quad)}{(\quad)} = (\quad) \%$$

$$\text{2ND STAGE (\%)} = \frac{100 \times \omega_{a_2}}{\omega_a} = \frac{100 (\quad)}{(\quad)} = (\quad) \%$$

$$\text{3RD STAGE (\%)} = \frac{100 \times \omega_{a_3}}{\omega_a} = \frac{100 (\quad)}{(\quad)} = (\quad) \%$$

EXPERIMENT No. E-

SYNCHRONIZATION OF INTAKE SYSTEM

CALCULATE THE RESONANT FREQUENCY (f_0) OF THE G8-2-15 JET ENGINE INTAKE SYSTEM, AND AVERAGE TEMPERATURE OF 3RD STAGE (T_2) AT GIVEN AMBIENT TEMPERATURE.

RECORD:

AMBIENT TEMPERATURE (T_1) = () °F., ($T_1 + 460$) = () °R.
2ND STAGE DUCT LENGTH (l) = () IN., ($l/12$) = () FT.
3RD STAGE DUCT LENGTH (L) = () IN., ($L/12$) = () FT.

CALCULATE FREQUENCY (f).

$$f_0 = \sqrt{\frac{kgRT_1}{2l}} = \sqrt{\frac{1.4 \times 32.2 \times 53.3 ()}{2 ()}} = () \text{ cps.}$$

CALCULATE 3RD STAGE AV. TEMPERATURE (T_2).

$$T_2 = \frac{(4Lf)^2}{kgR} = \frac{[4 () ()]^2}{1.4 \times 32.2 \times 53.3} = () \text{ °R.}$$

CONVERT TEMPERATURE (T_2) FROM (°R) TO DEGREES FAHRENHEIT (°F).

$$T = T_2 - 460 = () - 460 = () \text{ °F.}$$

G. An Investigation of Rotor Tip Jet Propulsion

**A Theoretical and Experimental Investigation
of an Efficient Rotor Tip-Jet Propulsion System**

by

Ron Barrett

Professor Saeed Farokhi Advising

**University of Kansas
Aerospace Engineering Department
Lawrence, Kansas
15 April 1988**

Abstract

Measurements were made on two types of rotor tip-jets fired statically and at velocities in excess of 450 ft/s at the Mal Harned Propulsion Laboratory of the University of Kansas through the student founded K.U. Center for Rotorcraft Propulsion. Data was taken in the form of stagnation temperatures, stagnation and static pressures, thrust, and fuel flow rates so as to determine the operating characteristics of both engines. The data taken was used to compute TSFC, mass air flow rates, thermal and propulsive efficiencies, and other parameters necessary to model the engine cycle. The first tip-jet that was tested operated as a ramjet, and accordingly showed poor subsonic performance with a TSFC of 34 lbm/lbfhr, producing only 4.3 lbf thrust at 450 ft/s. The second tip-jet operated as a self-inducing pressure jet and a continuous combustion wave engine and showed significantly better performance with a static TSFC of 4.8 lbm/lbfhr. At 300 ft/s its TSFC dropped to 1.67 lbm/lbfhr producing in excess of 23 lbf thrust. Using the cycle analysis data gathered from both sets of experiments, the engine cycles were modeled and the performance was predicted at various flight speeds for the pressure jet. The performance of the engine on the tip of a rotor was also modeled and showed the tip-jet propulsion system to be fairly efficient in comparison to turboshaft engines that power many of today's helicopters.

Table of Contents

	page no.
Abstract	i
List of Symbols	iii
1 Introduction	1-2
2 Theoretical and Actual B-1 Ramjet Operation	3-8
2.1 B-1 Ramjet Dimensions and Configuration	3-5
2.2 Ramjet Testing	5-7
2.3 Analysis of Test Data and Performance Predictions	7-8
3 Theoretical and Actual G8-2 Wave Engine Operation	9-22
3.1 G8-2 Wave Engine Dimensions and Configuration	9-10
3.2 G8-2-20 Wave Engine Operation	11-12
3.3 Analysis of Engine Components and their Characteristics	13-16
3.4 G8-2 Performance Prediction Using Experimental Data	16-22
4 Rough Comparison of G8-2 Performance on a Tip-Jet Propelled Helicopter versus a Turboshaft Helicopter	23-24
4.1 G8-2 Installation and Propulsion Configuration	23
4.2 Engine Performance Comparison	23-24
5 Conclusions and Recommendations	25
References	
Appendix A Spread Sheet Sample Manipulation	
 List of Figures	
Figure 1 Ramjet Assembly	4
Figure 2 B-1 Mounted in Thrust Stand	5
Figure 3 Ramjet Stations	6
Figure 4 Combustor Exit Temperature Estimation by Optical Examination of Flow Protrusion	7
Figure 5 TSFC and T/m_a for the B-1	8
Figure 6 G8-2-20 Assembly	10
Figure 7 G8-2 Mounted in Thrust Stand	11
Figure 8 G8-2-20 Stations	12
Figure 9 Measurement of Combustor Stagnation Temperature	12
Figure 10 G8-2 Flow Types and Regions	13
Figure 11 G8-2 Inlet Operational Characteristics	14
Figure 12 Formation of a Turbulent Boundary Layer	16
Figure 13 Calculated and Actual Nozzle Exit Area	18
Figure 14 G8-2-20 T-S Diagram for Maximum Static Thrust	21
Figure 15 G8-2-20 P-V Diagram at Maximum Static Thrust	21
Figure 16 TSFC and Velocity for G8-2-20	22
Figure 17 Gross Thrust and Velocity for the G8-2-20	22
Figure 18 G8-2-20 Installation on 20 ft Diameter Rotor	23

List of Symbols

Symbol	Definition	Units
A	Area	ft ²
C _p	Specific Heat at Constant Pressure	BTU/lbm°R
d	(d), Boundary layer thickness	ft
d	Diameter	ft
f	Fuel-air ratio	-
g	(g) Ratio of specific heats	-
h _b	(h _b) Burner efficiency	-
M	Mach number	-
m	Fuel flow rate	lbm/s
m	(m) Absolute viscosity	lbfs/ft ²
n	(n) Kinematic viscosity	ft ² /s
P	Pressure	lbf/ft ²
P	(P) Pi (3.1415...)	-
Q _r	Heat of combustion	BTU/lbm
R	Gas constant	BTU/lbm°R
S	Entropy	BTU/lbm°R
T	Temperature (subscripted)	°R
T	Thrust (not subscripted)	lbf
U	Velocity	ft/s
V	Specific Volume	ft ³ /lbm
x	Characteristic Length	ft

Subscripts

a,1,2,3,4,5	Station location (without "o" denotes static value)	-
f	Fuel	-
o	Stagnation	-
tot	Total mass flow	lbm/s

1. Introduction

In considering the many apparent advantages of jet driven rotors, the question arises as to why more jet rotors have not been developed. Jet-rotor propulsion is a very old field of aerospace with its roots dating back to 1915. The first attempt at jet rotor propulsion was tried by two French experimenters, Papin and Rouilly (ref. 1). With the exception of two modern day research groups, jet driven rotors have completely fallen by the wayside as turboshaft and piston engines flourish. Some of the advantages of jet-rotor propulsion are as obvious as the elimination of the heavy and inefficient transmissions and antitorque rotors. Other benefits include extremely low acquisition and maintenance costs and good useful load capability. The larger of the two present-day research groups are headed by the French through Helicop-Jet Co. of Paris. The Helicop-Jet group concentrates on cold jet drive rotors which offer many operational benefits over turboshaft and piston driven rotors. However, the friction losses associated with blowing air through the rotor blades is considerable, and the early (1976) models could only lift the pilot. The other group associated with jet driven rotors is American. And much in the style of Goddard, this group is headed by an individual researcher that perseveres with limited resources in an obscure corner of research. Eugene M. Gluhareff leads the development of hot cycle tip-jets. Gluhareff's engine, the G8-2 is the major subject of this investigation as it offers a great deal of promise, and its performance and operational characteristics surpass the characteristics of the tip-jet engines that have come before. Before the development of the G8-2 series engines, many companies experimented with various kinds of tip-jets. The leader in the experimentation and development field of tip-jet propulsion was Hiller. One of the most famous tip-jet driven prototype helicopters was the Hiller H-32. This helicopter was powered by two ramjet engines that had operating TSFC's of no less than 11 lbm/lbfhr, flew thousands of test flights and performed well in comparison to other tip-jet helicopters of the day (ref. 2). Needless to say, the H-32 did not perform nearly as well as piston and turboshaft driven helicopters of the same era. The ramjets of the H-32 operated with a very good efficiency as far as subsonic ramjets go (ref. 3). But the ramjets had operational problems that contributed to its demise. The 8RJ2B ramjets that powered the the H-32

were noisy, could produce no static thrust and had to be started by a small piston engine. Also, rapid descent problems were caused during autorotation. The problems of the 8RJ2B were not uncommon among tip-jet driven rotorcraft, and the cancellation of many tip-jet programs were caused by the inability of researchers to overcome these problems. These operational difficulties are still of much concern to the tip-jet propulsion field, but with the development of the G8-2 series engines these have diminished to the point that they are no longer of a prohibitive nature. The G8-2 engines operate at TSFC's ranging from one half to one tenth of that experienced by previous subsonic athodyd engines. The engine is more streamline in shape which reduces the problems during autorotation. And the engine produces static thrust, which allows the engine to start the rotor without the aid of another power source. The noise is of a lower level than several types of tip jets like pulse jets because it operates with continuous combustion. Overall, the G8-2 series engines are ideally suited to many types of aircraft including helicopters, homebuilts (the market that Gluhareff has chosen to target), tilt-rotors, subsonic jet fixed wing aircraft, and possibly even prop-driven fixed wing aircraft.

With excellent operational characteristics and extremely wide ranging fields of applicability, one asks why these engines have not been significantly noticed and subsequently developed. As it appears to this author, a great deal of anti-tipjet sentiment prevails in the technical community, and rightly so, in light of previous tipjet problems. Accordingly, few technologists have looked into resurrecting tipjet propulsion and it has been since the early 1960's since papers have been regularly published on tipjet propulsion. This paper is the only published, scientific investigation on the G8-2 tipjet known to this author. And its own inventor has yet to publish an in-depth explanation on how his engine works. This paper should contribute to the field of aerospace propulsion in three ways: 1.) presenting a comparison between the G8-2 and a typical subsonically operating athodyd engine so that their characteristics can be compared, 2.) presenting an analysis method for the prediction of the performance of the G8-2 with varying flight speed, 3.) presenting a rough comparison between the installed performance of G8-2 engine on a helicopter versus the installed performance of a typical turboshaft engine so that the merits of the G8-2 can be more clearly seen.

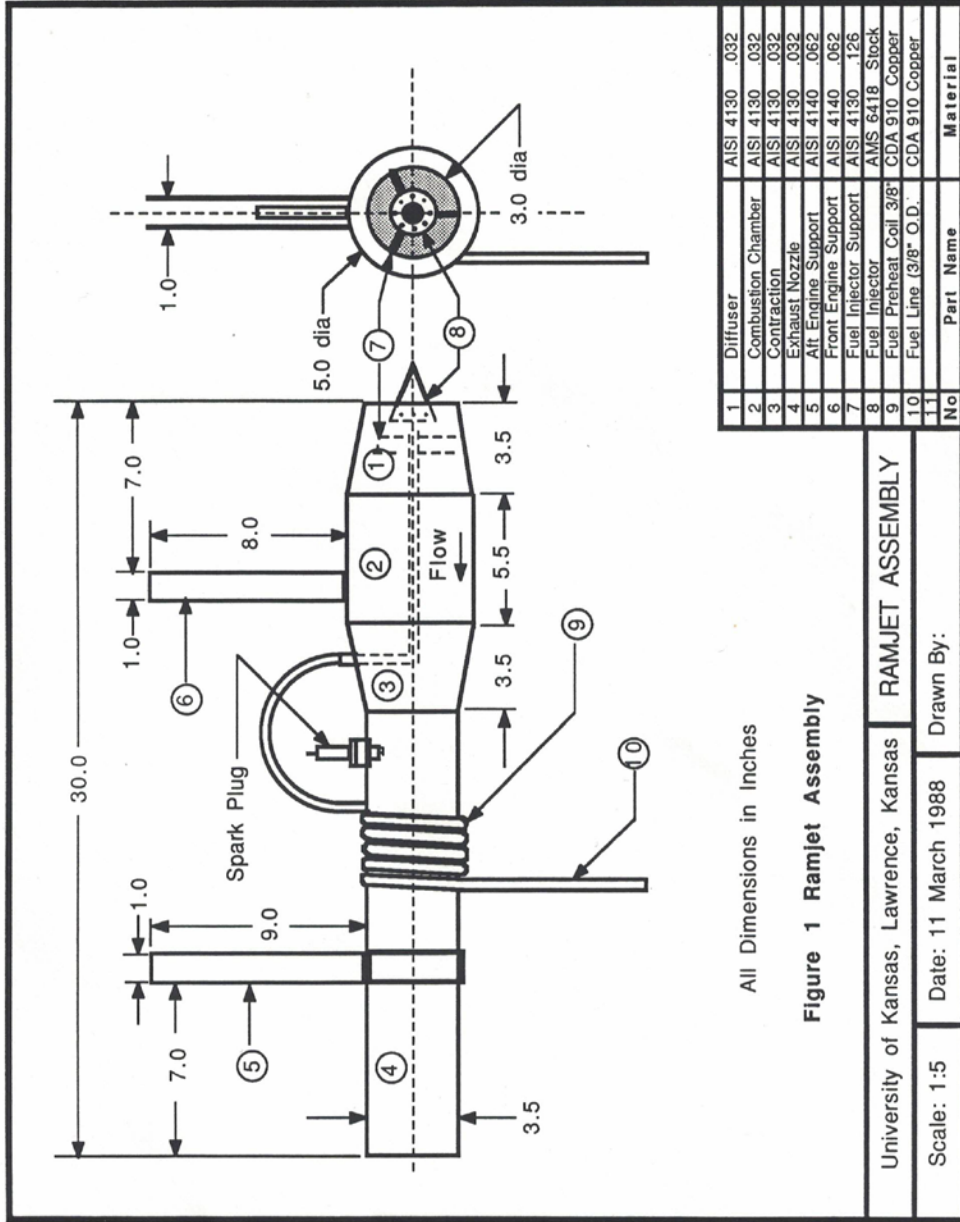
2. Theoretical and Actual B-1 Ramjet Operation

The purpose of this section is to show the reader what kind of operating conditions must be present and what kind of performance can be expected from a typical athodyd engine operating subsonically. This section will deliver representative subsonic athodyd characteristics so that the wave engine (also a type of athodyd) of chapter 3 can be compared and assessed accordingly.

2.1 B-1 Ramjet Dimensions and Configuration

2.1.1 B-1 Ramjet Configuration Selection

The B-1 ramjet used in this investigation was modeled after two engines: the first jet engine to receive CAA certification, the Hiller 8RJ2B tip ramjet, and the BW Rotor Co.'s tip ramjet. The Hiller design was the result of millions of research dollars and tens of thousands of man-hours (ref. 1). The Hiller design used a central spike and fuel injector mounted in the front of the engine. The Hiller engine had the problem of being unable to burn all of the fuel within its length. And, accordingly, the unspent fuel ignited outside of the engine itself (fig. 26, ref. 2). This was due to two reasons, the first of which was the use of liquid, unvaporized fuels; the second was the lack of a long enough exit nozzle. Accordingly, for the B-1 ramjet the exit nozzle was extended so as to capture more of the burning energy. The second design modification was the use of pressurized propane as a fuel instead of avgas. As far as the differences between the BW Rotor Co's engine and the B-1 ramjet are concerned, the major difference is the addition of a fuel preheat coil as seen in figure 1, in which the propane is vaporized. This facilitates even mixing and more complete combustion of the fuel. The B-1 ramjet has also been sized to propel a 20 ft diameter rotor so that the B-1 and the wave engine of chapter 3 can be compared on a more even basis.



All Dimensions in Inches

Figure 1 Ramjet Assembly

University of Kansas, Lawrence, Kansas

RAMJET ASSEMBLY

Scale: 1:5

Date: 11 March 1988

Drawn By:

2.1.2 B-1 Ramjet Dimensions and Components

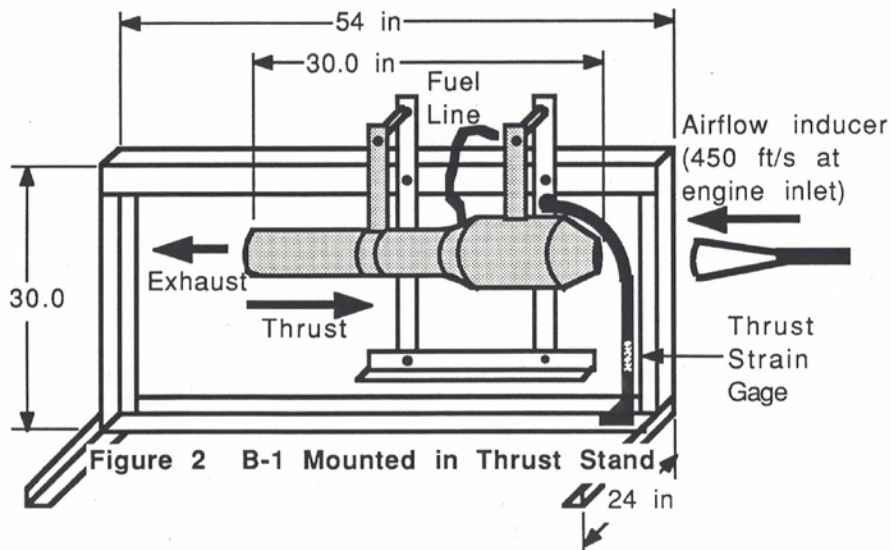
Relatively few components make up the B-1 ramjet as can be seen in Figure 1. And the component layout is simple enough to be self explanatory.

2.2 B-1 Ramjet Testing

The testing of the B-1 ramjet was conducted in the Mal Harned Propulsion Laboratory at the University of Kansas. The testing was partially sponsored by the author's student organization, the K.U. Center for Rotorcraft Propulsion.

2.2.1 Test Apparatus

In addition to the test rig shown in Figure 2, the test apparatus for the B-1 engine included an airflow inducer which forced air through the engine at speeds up to 450ft/s. This airflow inducer was powered by a 45 hp compressor which fed high pressure, higher temperature air through a hose to a diffuser where it was slowed and then fed into the engine. Thrust was measured by a strain gage system on a lever arm, as shown in figure 2. And the fuel flow rate was measured by a scale/timer system connected to the 30 lb propane tank. Airflow was measured by sampling the inlet static pressure, total pressure and total temperature prior to firing, but with the engine and test apparatus in a firing configuration.



2.2.2 Test Procedure

Since the B-1 ramjet or any other type of true ramjet cannot operate statically, the B-1 was started with a slight airflow being induced through it. This airflow was of the order of 10 to 20 ft/s and was held for 30 seconds after ignition so as to warm up the fuel preheat coil. After the coil was warmed, the fuel flow rate and airspeed were increased simultaneously, allowing the fuel-air mixture to remain at approximately 16:1. When the airspeed reached its maximum of 450ft/s, the fuel flow was reduced to .0406 lbm/s, a flow rate just above the flame-out rate. The fuel flow rate, thrust, sound levels and combustion chamber wall temperature were then recorded.

2.2.3 Test Results

The results of testing the B-1 showed consistent performance and operating characteristics.

2.2.3.1 Definition of Test Stations

For calculation and experimental reference purposes, the stations of the ramjet are defined as follows:

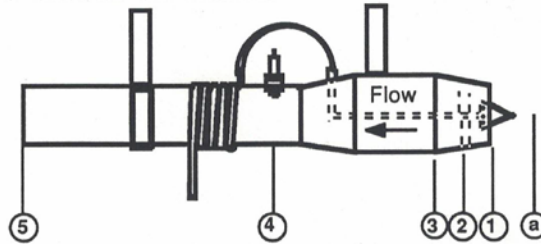


Figure 3 Ramjet Stations

2.2.3.2 Definition of Test Methods and Calculations

The way in which each of the measured quantities and some of the calculated values were calculated is described as follows:

- 1.) Inlet Static Temperature, T_a : taken by measuring the inlet static pressure, stagnation temperature and stagnation pressure at 16 radially distributed stations over the engine inlet and averaging the values: $T_{Oa} = 627^\circ R$, $P_{Oa} = 2316 \text{ lbf/ft}^2$, $P_a = 2104 \text{ lbf/ft}^2$. Using isentropic point relationships, T_a was computed by the following:

$$T_a = T_{Oa} \left(\frac{P_a}{P_{Oa}} \right)^{\frac{\gamma-1}{\gamma}} = 610^\circ R \quad (\text{eq. 2-1})$$

2.) Fuel Flow Rate, m_f : measured by establishing a constant fuel flow rate and measuring the weight of the propane tank at known time intervals: $m_f = .0406 \text{ lbm/s}$

3.) Airspeed, U : calculated by using the following:

$$U = \sqrt{2C_p(T_{ca} - T_a)} = 452 \text{ ft/s} \quad (\text{eq. 2-2})$$

4.) Mass Airflow Rate, m_a : calculated by using continuity and equation of state: $m_a = P_a U A_a / RT_a = 1.96 \text{ lbm/s}$ (eq. 2-3)

5.) Thrust: measured by the strain gage system shown in fig.2:
 $T = 4.3 \text{ lbf}$

6.) Combustor Exit Temperature, T_{o4} : measured at the hottest section aft of the combustion chamber, which was at the spark plug as can be seen in figure 4. Optical examination of the spark plug tip which protruded into the flow allowed for temperature estimation: $T_{o4} = 2120^\circ\text{R}$.

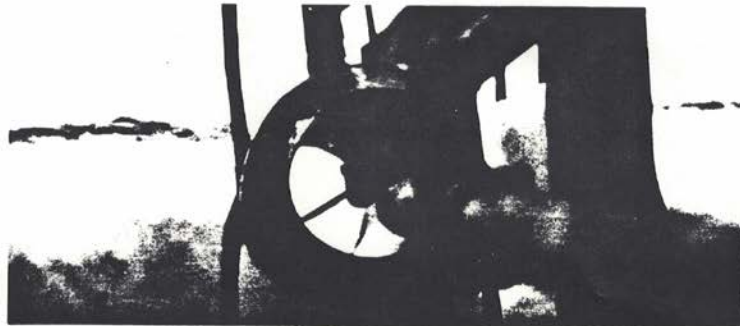


Figure 4 Combustor Exit Temperature Estimation by Optical Examination of Flow Protrusion

2.3 Analysis of Test Data and Performance Predictions

2.3.1 Determination of Engine Characteristics

To estimate the performance of the B-1 at different flight speeds, several characteristics must be determined, as follows:

i.) Estimate C_p and g at sta. 4-5: from fig. 7-29, ref.3, at $f = .02$, 2000°R , $g = 1.31$, $C_p = .29 \text{ btu/lbm}^\circ\text{R}$

ii.) Calculate U_5 : Using eq. 6-6 of ref. 3 with $P_5 = P_a$

$$U_5 = \frac{\sqrt{m_a + U}}{(1 + f)} = 510 \text{ ft/s} \quad (\text{eq. 2-4})$$

iii.) Calculate M_5 : assuming $T_{05} = T_{04}$, M_5 is calculated as follows:

$$M_5 = \left(\frac{g_5 R T_{04}}{U_5^2} + \frac{1 - g_5}{2} \right)^{\frac{1}{2}} = .235 \quad (\text{eq. 2-5})$$

iv.) Calculate P_{05}/P_{0a} : using isentropic point relationships and $P_5 = P_a$:

$$\frac{P_{05}}{P_{0a}} = \frac{\left(1 + \frac{g_5 - 1}{2} M_5^2 \right)^{\frac{g_5}{g_5 - 1}}}{\left(1 + \frac{g_a - 1}{2} M_a^2 \right)^{\frac{g_a}{g_a - 1}}} = .94 \quad (\text{eq. 2-6})$$

v.) Calculate h_b : rearranging eq. 6-26 of ref. 3 yields: ($Q_R = 21646$ Btu/lbm $^\circ$ R)

$$h_b = \frac{C_{P4}}{Q_R} \left(\frac{T_{04} - T_{0a}}{f} + T_{04} \right) = .97 \quad (\text{eq. 2-7})$$

2.3.2 Prediction of B-1 Performance at Various Flight Speeds

Using the stagnation pressure ratio found by eq. 2-6 and the burner efficiency calculated by equation 2-7, at sea-level on a standard day, the B-1 performance is predicted with the help of equations 2-1 to 2-7 and equations 6-6 and 6-28 of ref. 3. The result is shown below for comparison with the G8-2-20 performance of chapter 3.

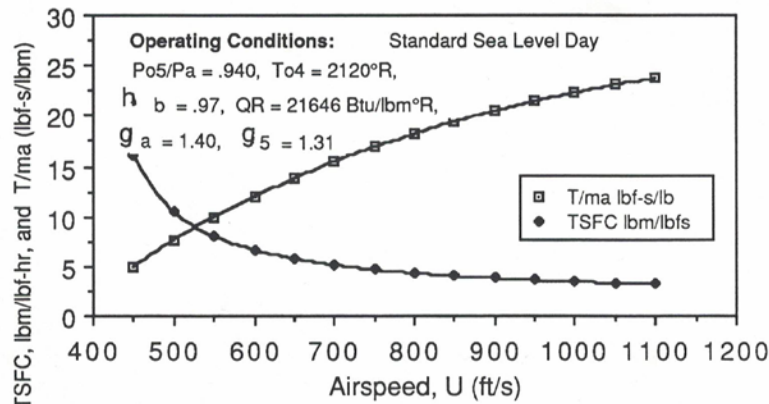


Figure 5 TSFC and T/ma for the B-1

3. Theoretical and Actual G8-2 Wave Engine Operation

The purpose of this chapter is to show the reader the operational characteristics, physical dimensions, analysis method and predicted performance of the G8-2 wave engine. The forementioned characteristics of the G8-2 engine should be compared with the same characteristics of the B-1 ramjet of chapter 2. Accordingly, the reader should see the superior qualities of the G8-2 over other subsonic athodyds like the B-1.

3.1 G8-2 Wave Engine Dimensions and Configuration

3.1.1 Configuration Development

The development of the G8-2 was performed by Mr. Eugene M. Gluhareff. His quest to produce a lightweight, efficient rotor tip-jet culminated in the invention of the G8-2 series engines. One of those engines is the object of this investigation, the G8-2-20. Development of the G8-2 engines started in 1955 for an Air Force competition involving man-portable helicopters. The G8-2 designs have improved since then at a slow, but steady rate. Much credit should be given to Mr. Gluhareff for persevering in a forgotten field of aerospace (tip-jet propulsion), and the G8-2 engines should signal the rebirth of this area of propulsion. However, several obstacles to this renaissance have accompanied Mr. Gluhareff's efforts. Most noteworthy is the inventor's (and any other published author's) inability to analytically model the engine that he himself invented. Granted, this is a formidable task, but not impossible as this chapter will show.

3.1.2 G8-2 Dimensions

The dimensions of the G8-2 series engines are not constant as they vary with static thrust rating. The G8-2 engines that are now available from Mr. Gluhareff's company are rated from 5 lbf to 700 lbf of static thrust and range from less than 2 ft in length to over 6 ft. The G8-2-20 is the second smallest engine produced, with dimensions that can be seen in figure 6.

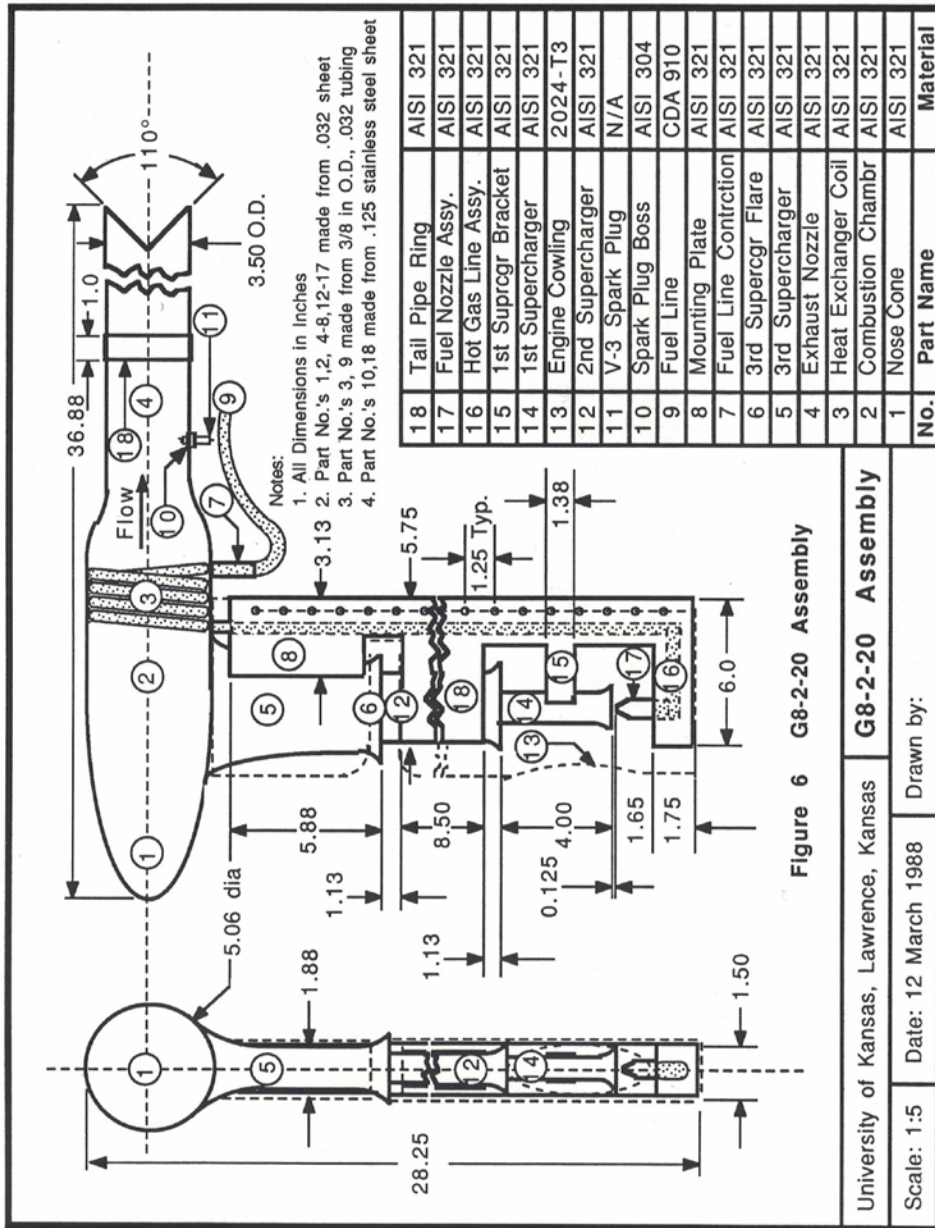


Figure 6 G8-2-20 Assembly

University of Kansas, Lawrence, Kansas **G8-2-20 Assembly**

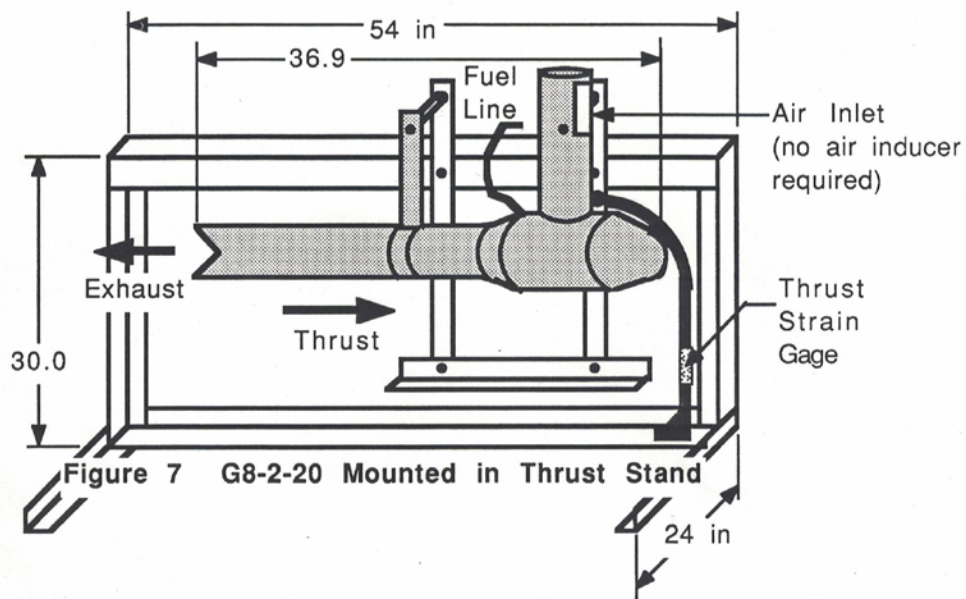
Scale: 1:5 Date: 12 March 1988 Drawn by:

3.2 G8-2-20 Wave Engine Testing

The testing of the G8-2-20 was conducted in a manner very much like the testing of the B-1 Ramjet as discussed in section 2.2.

3.2.1 Test Apparatus

The rig that was used for testing the G8-2-20 was the same device that was used for testing the B-1. The major difference is that the G8-2-20 was only tested statically so as to verify the data taken by Mr. Gluhareff. The test rig set-up is shown in figure 7 as follows:



3.2.2 Test Procedure

After an initial firing for stress relieving of the metal, the G8-2-20 was fired statically under two conditions. The first condition was to introduce the maximum amount of fuel into the engine that it would accept. The second condition was to introduce the minimum amount of fuel that the engine could operate on for efficient thrust. Fuel flow rates, thrust, and temperatures were measured in the same manner that they were measured for the B-1 engine as described in section 2.2.

3.2.3 Test Results

The results of testing the G8-2-20 showed excellent correlation to the data gathered by Mr. Gluhareff which speaks well for both sets of data.

3.2.3.1 Definition of Test Stations

For calculation and experimental reference purposes, the stations of the G8-2 wave engine are defined as follows:

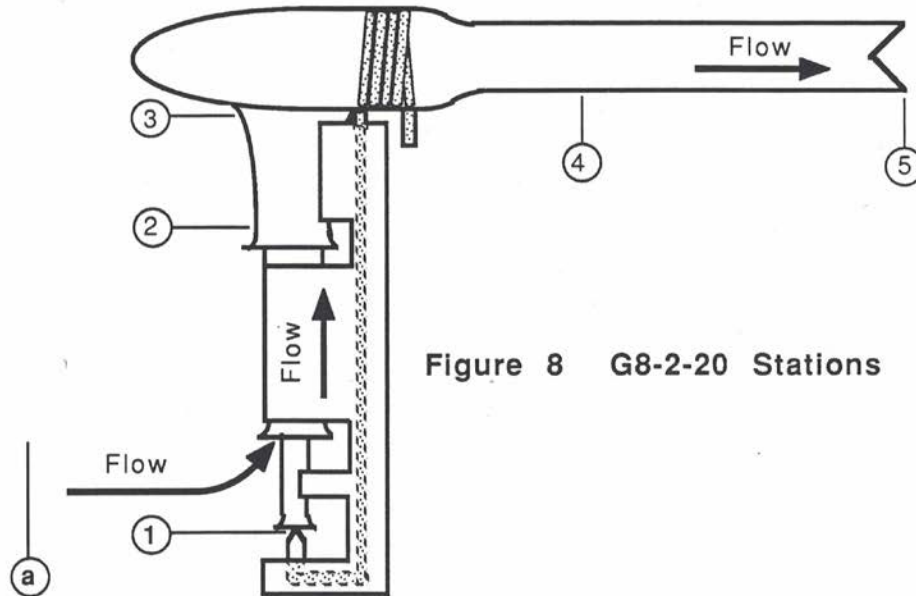


Figure 8 G8-2-20 Stations

3.2.3.2 Definition of Test Methods Raw Data Calculations

The methods that were used to calculate and measure the flows, forces and temperatures in the G8-2-20 were the same as described in section 2.2.3.2 of this report. Figure 9 shows the optical To4 measurement:

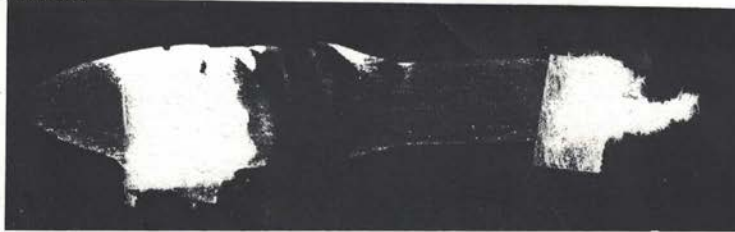
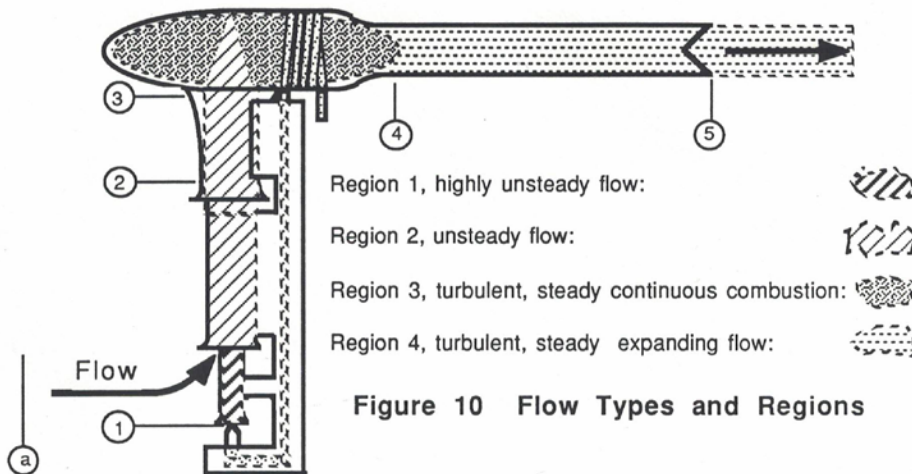


Figure 9 Measurement of Combustor Stagnation Temperature

3.3 Analysis of Engine Components and their Characteristics

3.3.1 Flow Types, and Analysis Tools Available

The G8-2 series engines are not pure wave engines, ramjets or pressure jets, but they are a mix of the forementioned. The G8-2 is mostly a wave engine in that the inlet develops a harmonic tuning and therefore allows the engine to do what few athodyds can do statically: produce thrust. The G8-2 is a ramjet aft of the inlet in that it operates with continuous combustion and expands the flow without extracting some kind of shaft work as in a turbojet. And, as Mr. Gluhareff calls the G8-2, it is a pressure jet, in that some of the energy to run the engine is supplied from a pressurized outside source that induces airflow through the engine via the energy of the pressurized (and heated) gas flow. This author chooses to call it a wave engine, but may refer to it by the other terms when appropriate. Because of its flow complexity, extensive observations were made on the flow by way of optical examination, pressure taps and probes and vibration meters. The result is the following representation of the flow in the engine:



As one can see, the tools for analysis involving steady, one dimensional flow are not applicable to regions 1 and 2, as the flow is unsteady. As a result, only regions 3 and 4 will be analyzed using those methods. Only conservation of energy will be employed in the analysis of regions 1 and 2.

3.3.2 The G8-2 Inlet Operational Characteristics and Analysis

The most complex portion of the G8-2 series engines is the inlet, that is, complex to analyze, but not complicated in structure. The inlet is composed of three staged inlet ducts, this author and Mr. Gluhareff refer to them as superchargers as seen in figure 6. At the end of the first supercharger is the fuel nozzle. This nozzle introduces a sonic stream of gaseous propane. This stream is heated in the fuel preheat coil and exits at velocities in excess of 1000 ft/s. This high speed propane jet causes a region of high turbulence and resonance in the first supercharger duct which acts effectively as a high pressure pulse generator that drives the other two superchargers. The sound waves that are developed in the first supercharger travel into the second and third superchargers and cause a rise in stagnation temperature and pressure. The jump in stagnation temperature can be calculated by using conservation of energy and T_{03} can be calculated. However, since both the ambient air and the propane stream participate in strengthening the sonic waves and therefore do work on the flow, the rise in stagnation pressure is unpredictable using one dimensional analysis and therefore will not be calculated. But the sonic waves developed in the inlet are of great importance as their presence alone insures the efficient operation of the engine. Figure 11 shows the location of the sonic waves and how they interact with the superchargers' walls, the combustor, and the fuel injector.

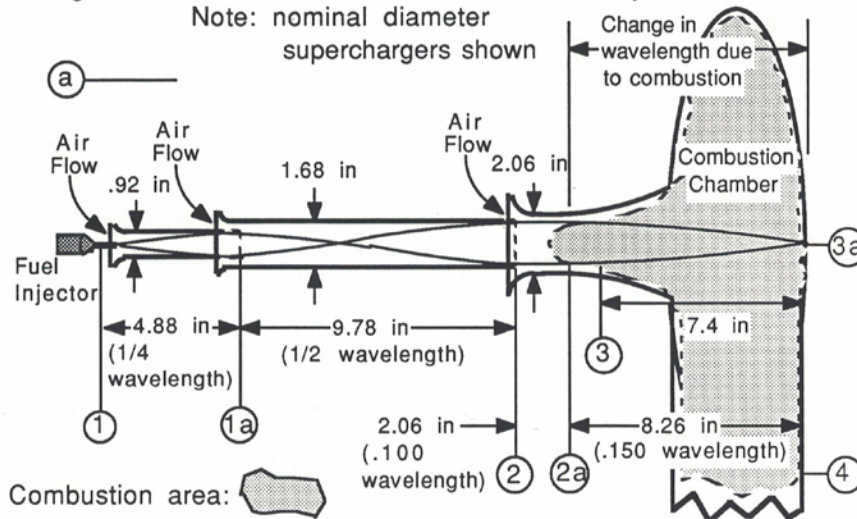


Figure 11 G8-2 Inlet Operational Characteristics

The waves generated in the G8-2 inlet are very much like those used in large two stroke piston engine exhausts and some kinds of four stroke piston engine exhausts to reduce backpressure. The piston engine's tuned exhaust can reduce the backpressure as much as 60%. Accordingly, the experimentalist can think of the G8-2's inlet as a tuned exhaust in reverse.

The waves that were set-up in the inlet operate at a frequency between 620 and 660 Hz. These experimentally established results are most helpful in that the wavelengths can now be determined. The inlet average frequency was 640 Hz and on a standard day, the wavelength would be 20.95 in. The sonic waves of this length match up exactly with stations 1 to 2. The key to the operation of the inlet, however, is not only the precise lengths of the intake ducts, but their position with respect to the far wall of the combustion chamber, off of which the sound waves reflect. This combustion chamber wall reflection acts as an automatic wavelength compensation device, with an explanation as follows:

- i.) The length of the sound waves are shortened because the ambient air temperature in which the engine is operating has been reduced.
 - a.) As a result, the sonic waves between stations 1 and 2a move back, and become weakened as they can no longer converge at station 3a.
 - b.) The weaker sonic waves produce a lesser pressure jump between stations 1 and 2a which allows the flame front at station 2a to move forward.
 - c.) The new location of the flame front causes the wavelength between stations 2 and 3a to become longer up to the point where the sonic waves re-converge at station 3a and accordingly re-establish the strong sonic compression system.

A similar series of interactions take place when the inlet ambient air temperature is higher than that of the optimal design temperature. This problem may sound trivial to the average technologist, but it was primarily this problem (along with noise) that killed the development of wave engines, of both the continuous combustion type and the intermittent combustion type (ref. 4). Accordingly, Mr. Gluhareff is to thank for discovering this unique property that overcomes a fundamental vulnerability of wave engines. But, alas, Mr. Gluhareff knows not why his modification works, and to this author's knowledge, this is the first published paper that exposes the workings of the G8-2 engine inlet principles in any detail.

3.3.3 G8-2 Combustor Operational Characteristics and Analysis

The combustor of the G8-2 must be one of the most simply designed in existence. As one can see in figure 11, it is composed of a 90° turn with a fuel preheat coil located at the exit. The combustor does not need a flameholder that protrudes into the flow because of one of the unique properties of propane. Above 1100°R, propane adheres to the walls and any other boundary of the combustion chamber. Since the flow is turbulent, but steady flowing in nature, standard analysis techniques can be applied for one dimensional flow. Section 2.3 demonstrates these principles as do the following sections.

3.3.4 G8-2 Exit Nozzle Operational Characteristics and Analysis

The exit nozzle of the G8-2 engine operates with continuous, turbulent flow and, accordingly can be analyzed using the methods outlined in section 2.3 and following sections. One major characteristic of the exit nozzle of the G8-2 is the presence of a relatively large boundary layer at the exit, and associated with it, a large blockage area. This blockage area will be of the upmost importance in the performance estimations of the engine as will be seen in section 3.4.1.

3.4 G8-2 Performance Prediction Using Experimental Data

3.4.1 Prediction of the Nozzle Exit Area

The nozzle exit area is a critical aspect of any jet engine as it directly relates to the operation of the engine. This varying area is due to the formation of a turbulent boundary layer within the exit nozzle that grows as it progresses toward the exit. This boundary layer tends to reduce the amount of area through which the exhaust gases can flow freely. The formation of this type of boundary layer is shown in figure 12:

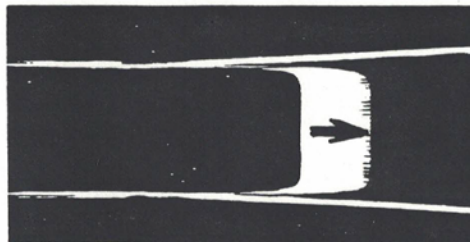


Figure 12 Formation of a Turbulent Boundary Layer
(Reproduced from reference 5)

3.4.1.1 Theoretical Estimation of A_5

The turbulent area shown in figure 12 can be estimated by the use of turbulent boundary layer estimation equations. One equation as such is equation 6.2.13 of ref. 5: $d_5 = .37(n_5/U_5)^{1/5}(x_5)^{4/5}$ (eq. 3-1)

From examination of the G8-2-20 exit nozzle, a suitable trip step is found where the nozzle is welded to the combustion chamber, and the sheet metal changes from .032 to .020 in thick. The distance from that step to station 5 will be taken to be $x_5 = 1.38$ ft. The kinematic viscosity, n_5 , of the exit gas is slightly more involved to determine. From ref. 6 the absolute viscosity of the exit gas, m_5 , is found to relate directly to the static temperature of the gas, as follows: $m_5(\text{lbs/ft}) = -2.864 \times 10^{-14}(T_5)^2 + 4.352 \times 10^{-10}(T_5) + 1.755 \times 10^{-7}$ (T in °R) (eq. 3-2)

Equation 3-2 is valid $\pm 2\%$ for temperatures between 720 and 3960°R. Using gas laws and continuity, A_5 can be related to U_5 , P_5 , and T_5 with $x_5 = 1.38$ ft, and an internal exit diameter of 3.436 in. as follows:

$$A_5 = P \left[1432 - 2.132 \left(\frac{T_5(-2.864 \times 10^{-14} T_5^2 + 4.352 \times 10^{-10} T_5 + 1.755 \times 10^{-7})}{P_5 U_5} \right)^{1/5} \right]^2$$

(eq. 3-3)

3.4.1.2 Experimental Determination of A_5

To predict the nozzle exit area, A_5 , many parameters must be known about the engine operationally. Several of these parameters were beyond the ability of this author to obtain experimentally because of prohibitive equipment costs. However, Mr. Gluhareff has compiled an excellent set of data on the G8-2 engine. The data that will be used for this section is found on p. 33 of ref.7. This data includes TSFC, T , f , P_f , and T_f . The procedure for calculating the nozzle exit area with a sample calculation is as follows:

- i.) Establish test conditions: $f = .0704$, $T = 14.5$ lbf, $U = 0$ ft/s,
 $m_f = .0258$ lbm/s, $m_a = .3660$ lbm/s, $m_{tot} = .3918$ lbm/s, $T_{of} = 1060$ °R,
 $T_{oa} = 520$ °R, $C_{pf} = .407$ btu/lbm°R, $C_{p5} = .290$ btu/lbm°R, $C_{pa} = .24$
 btu/lbm°R, $T_{o4} = 4060$ °R, $g_f = 1.124$, $g_5 = 1.31$, $g_a = 1.4$.
- ii.) Calculate T_{o3} : $T_{o3} = T_{oa} m_a / m_{tot} + (T_{of} m_f / m_{tot}) (C_{pf} / C_{pa}) = 604$ °R (eq. 3-4)

iii.) Calculate U_5 : $U_5 = \frac{\sqrt{m_a + U}}{(1 + f)} = 1190 \text{ ft/s}$ (eq. 2-4)

iv.) Calculate M_5 : $M_5 = \left(\frac{g_5 R T_{04}}{U_5^2} + \frac{1 - g_5}{2} \right)^{\frac{1}{2}} = .399$ (eq. 2-5)

v.) Calculate $\frac{P_{05}}{P_{0a}}$: $\frac{P_{05}}{P_{0a}} = \frac{\left(1 + \frac{g_5 - 1}{2} M_5^2 \right)^{\frac{g_5}{g_5 - 1}}}{\left(1 + \frac{g_a - 1}{2} M_a^2 \right)^{\frac{g_a}{g_a - 1}}} = 1.109$ (eq. 2-6)

vi.) Calculate T_5 : $T_5 = T_{04} - U^2 / (2C_{p5}) = 3962 \text{ }^\circ\text{R}$ (eq. 3-5)

vii.) Calculate A_5 : $A_5 = m_5 R T_5 / (P_5 U_5) = .0329 \text{ ft}^2$ (eq. 3-6)

The data that was supplied by Mr. Gluhareff ranged from 0 to 14.5 lb thrust. Nine A_5 's were calculated from this set of data and were compared to the boundary layer estimation of A_5 . In comparing the experimental and theoretical data, equation 3-3 was revised to more precisely fit the experimental data by the addition of several contiguity factors as follows:

$$A_5 = p \left[1432 - 2.132 \left(\frac{T_5 (-2.864 \times 10^{-14} T_5^2 + 4.352 \times 10^{10} T_5 + 1.755 \times 10^{-7})}{P_5 U_5} \right)^{\frac{1}{5}} \right]^2 +$$

$$2.47 \times 10^{-5} (U_5 - 1050) - .0045 \quad (\text{eq. 3-7})$$

The A_5 's calculated with the Gluhareff data, equation 3-3 and equation 3-7 can be seen on figure 13:

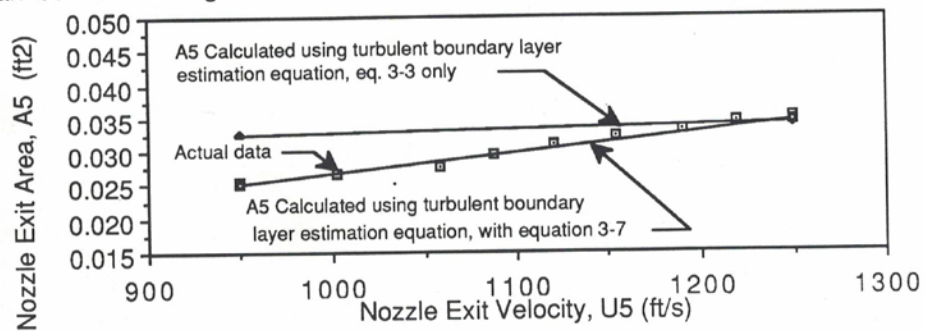


Figure 13 Calculated and Actual Nozzle Exit Area

3.4.2 Prediction of Stagnation Pressure Ratio, P_{05}/P_{0a} Trend with Increasing Engine Velocity, U and Burner Efficiency, h_b

3.4.2.1 Determination of Test Data

From the experiments conducted for this investigation, two sets of data were collected for static firing conditions:

i.) Condition 1, maximum thrust, maximum fuel flow rate:

$$\begin{array}{ll} \text{TSFC} = 4.8 \text{ lbm/lbf-hr} & T = 23.5 \text{ lbf} \\ P_5 = 2116 \text{ lbf/ft}^2 & T_{04} = 4060 \text{ }^\circ\text{R} \end{array}$$

ii.) Condition 2, minimum TSFC, minimum acceptable T_{04} :

$$\begin{array}{ll} \text{TSFC} = 1.30 \text{ lbm/lbf-hr} & T = 17.9 \text{ lbf} \\ P_5 = 2116 \text{ lbf/ft}^2 & T_{04} = 1200 \text{ }^\circ\text{R} \end{array}$$

Since a wind tunnel for firing engines was unavailable, and a rotor whirl test stand has yet to be completed, data was used from pp. 9, 33, 34 of ref. 7:

iii.) Condition 3, minimum T_{04} , maximum gross thrust = 23.6 lbf:

$$\begin{array}{ll} \text{TSFC} = 1.67 \text{ lbm/lbf-hr} & T = 23.5 \text{ lbf} \\ P_5 = 2116 \text{ lbf/ft}^2 & T_{04} = 1195 \text{ }^\circ\text{R} \end{array}$$

3.4.2.2 Manipulation of Test Data to Arrive at P_{05}/P_{0a} , and h_b

The equations to process the data of section 3.4.2.2 are quite cumbersome and therefore a spread sheet program was developed to cope with these. The operations performed in the spread sheet program are listed below and the letters below correspond to the sample spread sheet column letters of appendix A. The reader should notice that the data listed above is noted in appendix A by boldly lettered rows. The reader is asked to follow the calculations of appendix A by performing them as directed below.

A.) U_5 : chosen for iteration

B.) P_5 : $P_5 = P_a = 2116 \text{ lbf/ft}^2$ (left as a variable for performance at alt.)

C.) T_a : $T_a = 520 \text{ }^\circ\text{R}$, (left as a variable for performance at alt.)

D.) T_{04} : entered from section 3.4.2.1

E.) TSFC: entered from section 3.4.2.1

F.) U : Enter U from section 3.4.2.1

G.) g_5 : g_5 as a function of T_5 was calculated from fig. 7-29, ref. 3 with an error probability of $\pm 5\%$ from 520°R to 4000°R including effects of increasing f with T_5 :

$$g_5 = 8.859 \times 10^{-9} T_5^2 - 8.312 \times 10^{-5} T_5 + 1.441 \quad (\text{eq. 3.8})$$

H.) C_{p5} : C_{p5} as a function of T_5 was calculated using the above relationship and $C_{p5} = gR/(g-1)$ to arrive at:

$$C_{p5} = -5.112 \times 10^{-5} T_5^2 + .971 T_5 + 5516 \text{ (ft}^2/\text{s}^2\text{R)} \quad (\text{eq. 3.9})$$

I.) T_5 : eq. 3-5

J.) A_5 : eq. 3-7

K.) (intermediate calculation step)

L.) T : T was calculated using continuity and rearranging eq. 2-4:

$$T = \frac{(U - U_5) \left(\frac{P_5 U_5 A_5}{T_5 R} \right)}{\frac{\text{TSFC } U}{3600} - 32.174} \quad (\text{eq. 3.10})$$

M.) M_a : $M_a = U/(gRT_a)^{1/2}$

N.) m_f : $m_f = \text{TSFC } T$

O.) m_a : $m_a = \text{eq. 2-4}$

P.) m_{tot} : $m_{\text{tot}} = m_a + m_f$

Q.) M_5 : eq. 2-5

R.) P_{05}/P_{0a} actual: eq. 2-6

S.) P_{05}/P_{0a} estimated by taking trend of known data on P_{05}/P_{0a} and developing a linear relationship between P_{05}/P_{0a} and U :

$$P_{05}/P_{0a} = 1.152 + (1.297 \times 10^{-4})U \quad (\text{eq. 3-11})$$

T.) T_{03} : eq. 3-4

U.) h_p : eq. 2-7

V.) $f = m_f/m_a$

By an iterative process, using the three sets of data of section 3.4.2.1, the burner efficiency was found to be .957 and a relationship between P_{05}/P_{0a} and U was established as shown above in section S.

3.4.3 Cycle Analysis at Maximum Static Thrust

Choosing one experimental point as the object of interest, the P-v and T-S diagrams were composed using the pressure, temperature, velocity and related data. The diagrams depict a Brayton type cycle, and the entropy rises were calculated with 3-12 and 3-13 providing the curves between the known data points at a, 3, 4, and 5:

$$\Delta S = C_p \ln(T_1/T_0) - R \ln(P_1/P_0)$$

(eq. 3-12)

$$\Delta S = C_p \ln(T_1/T_0) - R \ln(V_1/V_0)$$

(eq. 3-13)

The result of this estimation is as follows:

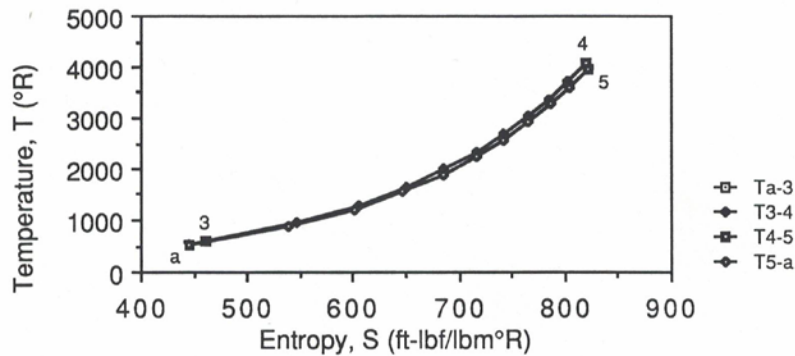


Figure 14 G8-2-20 T-S Diagram for Maximum Static Thrust

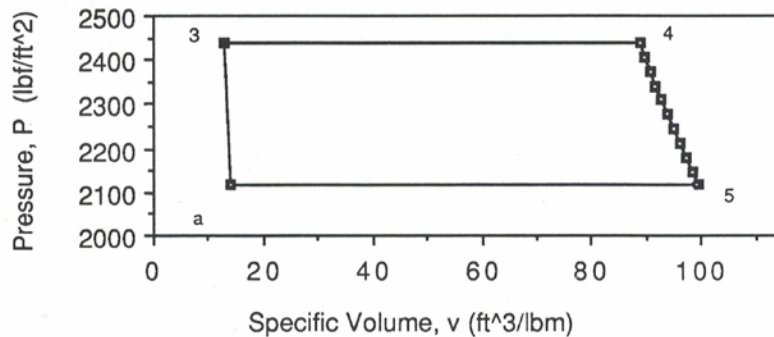


Figure 15 G8-2-20 P-v Diagram at Maximum Static Thrust

3.4.4 Performance Estimation

The performance of the G8-2-20 can now be predicted. Two types of engine performance were investigated. The first was the engine performance at the minimum operating combustion chamber temperature of $T_{04} = 1200$ °R. The second operating condition was the 23.5 lbf thrust line. Both conditions were set and solutions for the unknown variables were solved for using the iterative procedure developed in section 3.4.2.2, and the burner efficiency of $\eta_b = .957$, and the P_{05}/P_{0a} trend of $P_{05}/P_{0a} = 1.152 + (1.297 \times 10^{-4})U$ which were developed in section 3.4.2.2. The following are had:

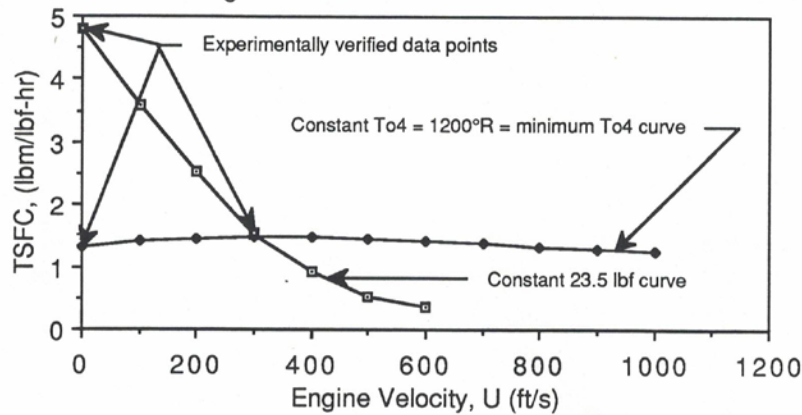


Figure 16 TSFC and Velocity for G8-2-20

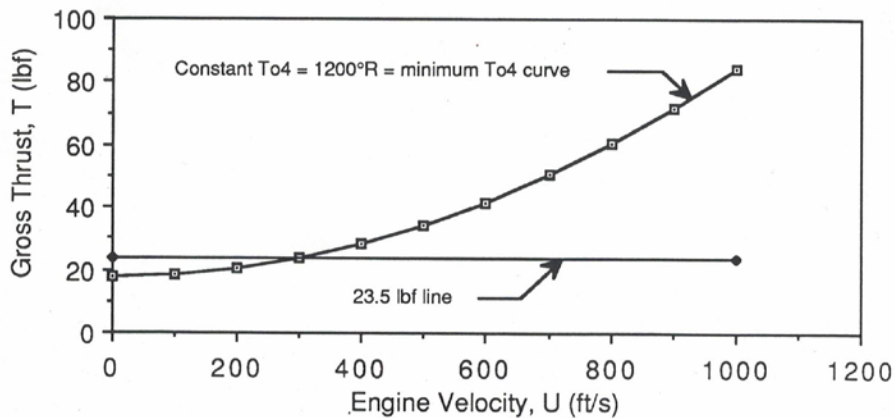


Figure 17 Gross Thrust and Velocity for the G8-2-20

4. Rough Comparison of G8-2 Performance on a Tip-Jet Propelled Helicopter Vs. a Turboshaft Propelled Helicopter

The purpose of this chapter is to estimate roughly, and compare the performance of the G8-2 engines and standard turboshaft engines as they relate to the powering of a helicopter.

4.1 G8-2 Installation and Propulsion Configuration

The installation of the G8-2 engines is fairly straight forward and standard with respect to tip-jet driven helicopters. The installation of the engine is as follows:

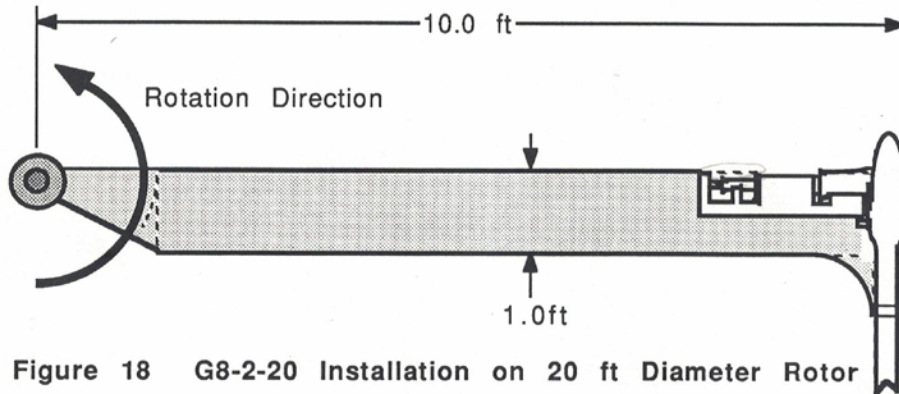


Figure 18 G8-2-20 Installation on 20 ft Diameter Rotor

4.2 Engine Performance Comparison

Since helicopter rotors generally operate between 550 and 700 ft/s rotor tip speed, the operating speed of the tip-jet will be considered at 700 ft/s. From figure 17 and appendix A, one can see that the gross thrust is 50.4 lbf. Accordingly, the fuel flow rate is .0193 lbm/s. This results in an equivalent BSFC of 1.083 lbm/Hp-hr. The characteristics of both propulsion systems should be compared on an even basis, since the tip-jet requires no tail rotor, transmission, or, relatively heavy, turbine.

i.) Tail rotor power loss:

An estimate of the power lost by the tail rotor in a hover is 10% according to p. 87, ref. 8. Tip jet loss would be 0%.

ii.) Transmission efficiency:

An estimate of the transmission efficiency is between 82-87% according to pp. 5-6 of ref. 9. Tip-jet engines equivalent efficiency is 100%.

iii.) Engine Weight as a Percent of Airframe Weight:

Using the McDonnell Douglas 500 as a baseline, the weight of the turbine is approximately 8% of the gross T-O weight. Tip-jet engines average about .1%.

iv.) Transmission Weight as a Percent of Airframe Weight:

Using the estimation that the transmission is as heavy as the engine of a turboshaft powered helicopter, the transmission would occupy approximately 8% of the empty weight. The tip-jet helicopter transmission weight is 0%.

Taking the product of the relative power inefficiencies and power losses, the turboshaft system is seen to be $((1-.10)(.87)(1-.08)(1-.08) =)$ 66% as efficient as the tip-jet system, not including the engine efficiencies.

If one is to introduce the engine efficiency of the G8-2, the "relative" BSFC is seen to be: $(.66)(1.083 \text{ lbm/Hp-hr}) = .715 \text{ lbm/Hp-hr}$. This is within the range of specific fuel consumptions for turboshafts, although it is on the inefficient side.

1441
3550

5. Conclusions and Recommendations

5.1 Conclusions

- i.) It can be concluded that the G8-2-20 engine is far superior to subsonic athodyds like the ramjet, in terms of TSFC and flight conditions that must be present to produce thrust.
- ii.) The G8-2-20 has a static TSFC of 4.8 lbm/lbf-hr at its maximum static thrust of 23.5 lbf.
- iii.) The G8-2-20 has a dynamic TSFC of 1.67 lbm/lbf-hr at 300 ft/s and a thrust of 23.5 lbf.
- iv.) The modelling of the G8-2-20 by using exit area boundary layer estimations is seen to be adequate up to at least 300 ft/s.
- v.) The predicted efficiency of the G8-2-20 when installed on the tip of a helicopter rotor compares favorably to the installed efficiency of helicopter turboshaft engines and their associated systems.

5.2 Recommendations

This author recommends that industry and/or the government fund the further research of G8-2 rotor tip-jet systems. The research to be performed should be a detailed verification/modification of the performance prediction methods outlined in this investigation. And experimentation with the engines so as to improve their efficiencies must follow so as to expand the engines' applications.

References

- 1) Velkoff, Henry R., et al., "An Evaluation of the Jet Rotor Helicopter," Wright Air Development Center, Washington, D.C., April 17-18, 1958.
- 2) Sargent, E. R., R. M. Lockwood, and M. F. Gates, "Environmental Effects on Rotor Tipjet Propulsion," Dallas, Texas, October, 1956.
- 3) Hill, Phillip G, and Carl R. Peterson, "Thermodynamics of Jet Engines," *Mechanics and Thermodynamics of Propulsion*, Addison-Wesley, Reading, Massachusetts, 1970.
- 4) Nichols, J. B., "A Second Look at the Helicopter Propulsion Problem," Hiller Helicopters, Palo Alto, California, November 4-5, 1954.
- 5) Streeter, Victor, and E. Benjamin Wylie, "External Flows," *Fluid Mechanics*, McGraw Hill, New York, 1985 pp. 251-255.
- 6) Weast, Robert C., et al., "Thermodynamic and Transport Properties of Air," *64 th Edition CRC Handbook of Chemistry and Physics*, CRC Publishing, Boca Raton, Florida, 1983, pp. F-12, F-37.
- 7) Gluhareff, Eugene M., *G8-2 Technical Handbook*, Published by the author, Hesperia, California, 1985.
- 8) Prouty, R. W., "Helicopter Engineering," *Helicopter Aerodynamics*, PJS Publications, Peoria, Ill., 1985.
- 9) Shapiro, Jacob, "Transmissions and Installation," *Principles of Helicopter Engineering*, McGraw-Hill Publications, New York, 1955, pp 101-102.

Appendix A

Spread Sheet Sample Manipulation

	A	B	C	D	E	F	G	H	I	J	K
1	US	P5	Ta	To4	TSFC	U	Gama5	Cp5	TS	AS	TCI
2	757	2116	520	1200	1.3	0	1.36	6522	1156	.0294	0.762
3	1396	2116	520	4060	4.80	0	1.25	8560	3946	.0386	0.541
4	800	2116	520	1200	1.40	100	1.36	6522	1151	.0307	0.846
5	1250	2116	520	2900	3.57	100	1.28	7834	2800	.0371	0.658
6	865	2116	520	1200	1.46	200	1.36	6522	1143	.0326	0.98
7	1105	2116	520	1980	2.53	200	1.32	7161	1895	.0360	0.833
8	948	2116	520	1200	1.49	300	1.36	6522	1131	.0351	1.168
9	945	2116	520	1195	1.50	300	1.36	6518	1126	.0351	1.167
10	1043	2116	520	1200	1.49	400	1.36	6522	1117	.0379	1.406
11	883	2116	520	860	0.93	400	1.38	6224	797.4	.0355	1.558
12	1147	2116	520	1200	1.46	500	1.36	6522	1099	.0410	1.696
13	872	2116	520	690	0.54	500	1.40	6071	627.4	.0365	2.013
14	1255	2116	520	1200	1.42	600	1.36	6522	1079	.0441	2.035
15	909	2116	520	632	0.35	600	1.40	6018	563.4	.0381	2.441
16	1365	2116	520	1200	1.38	700	1.36	6522	1057	.0473	2.421
17	1475	2116	520	1200	1.33	800	1.36	6522	1033	.0504	2.854
18	1585	2116	520	1200	1.28	900	1.36	6522	1007	.0535	3.341
19	1692	2116	520	1200	1.24	1000	1.36	6522	980.5	.0566	3.872

	L	M	N	O	P	Q	R	S	T	U	V
1	T	Ma	mf	ma	mtot	M5	Po5/Pot	Po5/Pa	To3	Etab	f
2	17.9	.0000	.0065	.7560	.7625	.4609	1.152	1.152	531	.955	.0086
3	23.5	.0000	.0313	.5098	.5411	.4797	1.152	1.152	594	.957	.0614
4	18.4	.0895	.0072	.8386	.8458	.4881	1.165	1.165	532	.957	.0085
5	23.6	.0895	.0234	.6343	.6577	.5044	1.167	1.165	566	.958	.0368
6	20.3	.1790	.0082	.9722	.9804	.5297	1.178	1.178	534	.961	.0085
7	23.5	.1790	.0165	.8165	.8330	.5342	1.175	1.178	549	.961	.0202
8	23.6	.2684	.0098	1.1583	1.1681	.5835	1.191	1.191	538	.959	.0084
9	23.5	.2684	.0098	1.1574	1.1672	.5828	1.190	1.191	538	.949	.0084
10	28.2	.3579	.0117	1.3942	1.4059	.6462	1.204	1.204	544	.957	.0084
11	23.4	.3579	.0061	1.5515	1.5575	.6420	1.204	1.204	538	.957	.0039
12	34.3	.4474	.0139	1.6826	1.6965	.7163	1.217	1.217	551	.959	.0083
13	23.3	.4474	.0035	2.0094	2.0129	.7116	1.220	1.217	543	.954	.0017
14	41.7	.5369	.0164	2.0181	2.0346	.7909	1.230	1.230	560	.960	.0081
15	23.5	.5369	.0023	2.4388	2.4411	.7816	1.230	1.230	551	.967	.0009
16	50.4	.6263	.0193	2.4016	2.4209	.8693	1.243	1.243	571	.956	.0080
17	60.4	.7158	.0223	2.8322	2.8545	.9502	1.256	1.256	583	.957	.0079
18	71.8	.8053	.0255	3.3155	3.3411	1.0342	1.269	1.269	597	.958	.0077
19	84.1	.8948	.0290	3.8429	3.8719	1.1192	1.282	1.282	612	.953	.0075

IX. References

- [1] Farokhi, S., 2009, Aircraft Propulsion, John Wiley & Sons.
- [2] Flack, R., 2005, Fundamentals of Jet Propulsion with Applications, Cambridge University Press.
- [3] Mattingly, J., 2006, Elements of Propulsion: Gas Turbines and Rockets, AIAA.
- [4] Merlin, P., 2001, Mach 3+: NASA/USAF YF-12 Flight Research 1969-1979, NASA.
- [5] Diedrich, G., 1948, "Project Squid: The Aero-Resonator Power Plant of the V-1 Flying Bomb," Princeton University.
- [6] Geng, T., Kiker, A., Ordon, R., Kuznetsov, A., Zeng, T., and Roberts, W., 2007, "Combined Numerical and Experimental Investigation of a Hobby-Scale Pulsejet," AIAA Journal of Propulsion and Power, 23(1).
- [7] Laird, D. E., 1997, "Tiger Jet Plans by Tiger Engineering Co.."
- [8] Crowe, R., 1976, "Pulsating Combustion Device Miniaturization," Master's Thesis, Naval Postgraduate School.
- [9] Gohardani, A., 2013, "A synergistic glance at the prospects of distributed propulsion technology and the electric aircraft concept for future unmanned air vehicles and commercial/military aviation," Progress in Aerospace Sciences, 57.
- [10] Ogorolec, B., 2005, "Valveless Pulsejet Engines 1.5: A Historical Review of Valveless Pulsejet Designs," <http://www.pulse-jets.com/valveless/>.
- [11] Heuer, G., Lockwood, R., and Corporation, H. A., 1960, "Summary Report: Investigation of a Resonant Combustor Concept," ONR, ed.
- [12] Cloyd, J., and Company, H. A., 1964, "Summary Report on Investigation of Miniature Valveless Pulsejets," U. A. T. R. Command, ed.
- [13] Lockwood, R., Bennett, E., and Graber, D., 1969, "Pulse Jet Engine," United States.
- [14] Astrand, J., 2014, "Performance Prediction of a Valved and Valveless Pulse-jet Engine Running on Alternative Fuel," Master's Thesis, Lulea University of Technology, Lulea, Sweden.
- [15] Gluhareff, E. M., 1985, "G8-2 Technical Handbook."
- [16] Barrett, R., and Gluhareff, I., 2008, "Gluhareff Pressure Jet Engine: Past, Present, and Future," 46th AIAA Aerospace Sciences Meeting and Exhibit, American Institute of Aeronautics and Astronautics, Reno, NV.
- [17] Leishman, J. G., 2006, Principles of Helicopter Aerodynamics, Cambridge University Press.

- [18] Gluhareff, I., "Gluhareff Family Documents."
- [19] Gluhareff, E. M., 1963, "Valveless Jet Engine with Inertia Tube," United States.
- [20] Makofski, R., and Shivers, J., 1956, "Exploratory Investigation of a Helicopter Pressure-Jet System on the Langley Helicopter Test Tower," Langley Aeronautical Laboratory.
- [21] Krebs, R. P., and Miller, W. S., 1955, "Analysis of a Pressure-Jet Power Plant for a Helicopter," Lewis Flight Propulsion Laboratory.
- [22] Thoms, W., 1975, "A Jet Engine You Can Build In Your Own Shop," *Mechanix Illustrated*, pp. 28-29.
- [23] Stram, M., 2001, "Valveless Pulse-Jet Engine with Forward Facing Intake Duct," United States.
- [24] Laforest, L., and Collins, D., 2011, "Pulse Combustor Including Acoustic Elements," United States.
- [25] Anderson, J. D., 1995, *Computational Fluid Dynamics*, McGraw Hill.
- [26] Cebeci, T., Shao, J., Kafyeke, F., and Laurendeau, E., 2005, *Computational Fluid Dynamics for Engineers*, Springer.
- [27] Tu, J., Yeoh, G.-H., and Liu, C., 2013, *Computational Fluid Dynamics: A Practical Approach*, Elsevier.
- [28] Science, C., 2014, "CONVERGE 2.2.0 Theory Manual," Convergent Science.
- [29] Bramlette, R., Langness, C., Mangus, M., and Depcik, C., 2014, "Employing Adaptive Mesh Refinement for Simulating the Exhaust Gas Recirculation Mixing Process," International Mechanical Engineering Congress & Exposition (IMECE), ASME, Montreal, CA.
- [30] Geng, T., 2007, "Numerical Simulations of Pulsejet Engines," Doctor of Philosophy Dissertation, North Carolina State University, Raleigh, NC.
- [31] Geng, T., Schoen, M. A., Kuznetsov, A., and Roberts, W., 2007, "Combined Numerical and Experimental Investigation of a 15-cm Valveless Pulsejet," *Flow Turbulence Combust*, 78, pp. 17-33.
- [32] Geng, T., Zheng, F., Kiker, A., Kuznetsov, A., and Roberts, W., 2007, "Experimental and Numerical Investigation of an 8-cm Valveless Pulsejet," *Experimental Thermal and Fluid Sciences*, 31, pp. 641-647.
- [33] Zheng, F., 2009, "Computational Investigation of High Speed Pulsejets," Doctor of Philosophy Dissertation, North Carolina State University, Raleigh, NC.
- [34] Depcik, C., 2012, "ME-636 Internal Combustion Engines," *ME-636 Internal Combustion Engines*, C. Depcik, ed., School of Engineering, University of Kansas.

- [35] Werle, S., and Wilk, R., 2010, "Ignition of Methane and Propane in High-Temperature Oxidizers with Various Oxygen Concentrations," *Fuel*, 89, pp. 1833-1839.
- [36] Law, C. K., 1989, "Dynamics of stretched flames," *Symposium (International) on Combustion*, 22(1), pp. 1381-1402.
- [37] Dagaut, P., Cathonnet, M., Rouan, J. P., Foulatier, R., Quilgars, A., Boettner, J. C., Gaillard, F., and James, H., 1986, "A jet-stirred reactor for kinetic studies of homogeneous gas-phase reactions at pressures up to ten atmospheres (≈ 1 MPa)," *Journal of Physics E: Scientific Instruments*, 19(3), p. 207.
- [38] El Bakali, A., Dagaut, P., Pillier, L., Desgroux, P., Pauwels, J. F., Rida, A., and Meunier, P., 2004, "Experimental and modeling study of the oxidation of natural gas in a premixed flame, shock tube, and jet-stirred reactor," *Combustion and Flame*, 137(1-2), pp. 109-128.
- [39] Wakelyn, N., Jachimowski, C., and Wilson, C., 1978, "Experimental and Analytical Study of Nitric Oxide Formation During Combustion of Propane in a Jet-Stirred Combustor," NASA Langley Research Center.
- [40] Norman, F., Van den Schoor, F., and Verplaetsen, F., 2006, "Auto-ignition and upper explosion limit of rich propane-air mixtures at elevated pressures," *Journal of Hazardous Materials*, 137(2), pp. 666-671.
- [41] Razus, D., Brinzea, V., Mitu, M., Movileanu, C., and Oancea, D., 2012, "Burning Velocity of Propane-Air Mixtures from Pressure-Time Records during Explosions in a Closed Spherical Vessel," *Energy & Fuels*, 26(2), pp. 901-909.
- [42] Razus, D., Brinzea, V., Mitu, M., Movileanu, C., and Oancea, D., 2011, "Temperature and pressure influence on maximum rates of pressure rise during explosions of propane-air mixtures in a spherical vessel," *Journal of Hazardous Materials*, 190(1-3), pp. 891-896.
- [43] Razus, D., Brinzea, V., Mitu, M., and Oancea, D., 2010, "Temperature and pressure influence on explosion pressures of closed vessel propane-air deflagrations," *Journal of Hazardous Materials*, 174(1-3), pp. 548-555.
- [44] Razus, D., Oancea, D., Brinzea, V., Mitu, M., and Movileanu, C., 2010, "Experimental and computed burning velocities of propane-air mixtures," *Energy Conversion and Management*, 51(12), pp. 2979-2984.
- [45] Razus, D., Brinzea, V., Mitu, M., and Oancea, D., 2009, "Explosion characteristics of LPG-air mixtures in closed vessels," *Journal of Hazardous Materials*, 165(1-3), pp. 1248-1252.
- [46] Razus, D., Movileanu, C., and Oancea, D., 2007, "The rate of pressure rise of gaseous propylene-air explosions in spherical and cylindrical enclosures," *Journal of Hazardous Materials*, 139(1), pp. 1-8.

- [47] Razus, D., Oancea, D., and Movileanu, C., 2006, "Burning velocity evaluation from pressure evolution during the early stage of closed-vessel explosions," *Journal of Loss Prevention in the Process Industries*, 19(4), pp. 334-342.
- [48] Eckhoff, R. K., Ngo, M., and Olsen, W., 2010, "On the minimum ignition energy (MIE) for propane/air," *Journal of Hazardous Materials*, 175(1-3), pp. 293-297.
- [49] Lewis, B. B., and von Elbe, G., 1987, *Combustion, Flames and Explosions of Gases*, Academic Press, Orlando, FL.
- [50] Steinberg, M., and Kaskan, W. E., 1955, "The ignition of combustible mixtures by shock waves," *Symposium (International) on Combustion*, 5(1), pp. 664-672.
- [51] Hawthorn, R. D., and Nixon, A. C., 1966, "Shock tube ignition delay studies of endothermic fuels," *AIAA Journal*, 4(3), pp. 513-520.
- [52] Sulzmann, K. G. P., 1964, "High temperature, shock tube CO₂-transmission measurements at 4·25 μ ," *Journal of Quantitative Spectroscopy and Radiative Transfer*, 4(3), pp. 375-413.
- [53] Myers, B. F., and Bartle, E. R., 1969, "Reaction and ignition delay times in the oxidation of propane," *AIAA Journal*, 7(10), pp. 1862-1869.
- [54] Brokaw, R., "Thermal ignition, with particular reference to high temperatures," *Proc. Selected Combustion Problems, Proc. 2nd Agard Colloq.*, Butterworths London, pp. 115-138.
- [55] Burcat, A., Lifshitz, A., Scheller, K., and Skinner, G. B., 1971, "Shock-tube investigation of ignition in propane-oxygen-argon mixtures," *Symposium (International) on Combustion*, 13(1), pp. 745-755.
- [56] Burcat, A., Scheller, K., and Lifshitz, A., 1971, "Shock-tube investigation of comparative ignition delay times for C₁-C₅ alkanes," *Combustion and Flame*, 16(1), pp. 29-33.
- [57] Lifshitz, A., Scheller, K., Burcat, A., and Skinner, G. B., 1971, "Shock-tube investigation of ignition in methane-oxygen-argon mixtures," *Combustion and Flame*, 16(3), pp. 311-321.
- [58] Glass, G. P., Kistiakowsky, G. B., Michael, J. V., and Niki, H., 1965, "The oxidation reactions of acetylene and methane," *Symposium (International) on Combustion*, 10(1), pp. 513-522.
- [59] Crossley, R. W., Dorko, E. A., Scheller, K., and Burcat, A., 1972, "The effect of higher alkanes on the ignition of methane-oxygen-argon mixtures in shock waves," *Combustion and Flame*, 19(3), pp. 373-378.
- [60] Eubank, C. S., Rabinowitz, M. J., Gardiner Jr, W. C., and Zellner, R. E., 1981, "Shock-initiated ignition of natural gas—Air mixtures," *Symposium (International) on Combustion*, 18(1), pp. 1767-1774.

- [61] Krishnan, K. S., Ravikumar, R., and Bhaskaran, K. A., 1983, "Experimental and analytical studies on the ignition of methane-acetylene mixtures," *Combustion and Flame*, 49(1-3), pp. 41-50.
- [62] Cheng, R. K., and Oppenheim, A. K., 1984, "Autoignition in methane-hydrogen mixtures," *Combustion and Flame*, 58(2), pp. 125-139.
- [63] Frenklach, M., and Bornside, D. E., 1984, "Shock-initiated ignition in methane-propane mixtures," *Combustion and Flame*, 56(1), pp. 1-27.
- [64] Spadaccini, L. J., and Colket Iii, M. B., 1994, "Ignition delay characteristics of methane fuels," *Progress in Energy and Combustion Science*, 20(5), pp. 431-460.
- [65] Frenklach, M., Wang, H., and Rabinowitz, M. J., 1992, "Optimization and analysis of large chemical kinetic mechanisms using the solution mapping method—combustion of methane," *Progress in Energy and Combustion Science*, 18(1), pp. 47-73.
- [66] Qin, Z., 1998, "Reaction mechanism of propane oxidation," Ph.D Dissertation, University of Texas at Austin.
- [67] Brown, C. J., and Thomas, G. O., 1999, "Experimental studies of shock-induced ignition and transition to detonation in ethylene and propane mixtures," *Combustion and Flame*, 117(4), pp. 861-870.
- [68] Jachimowski, C. J., 1984, "Chemical kinetic reaction mechanism for the combustion of propane," *Combustion and flame*, 55(2), pp. 213-224.
- [69] Cadman, P., Thomas, G. O., and Butler, P., 2000, "The auto-ignition of propane at intermediate temperatures and high pressures," *Physical Chemistry Chemical Physics*, 2(23), pp. 5411-5419.
- [70] Sung, C. J., Li, B., Wang, H., and Law, C. K., 1998, "Structure and sooting limits in counterflow methane/air and propane/air diffusion flames from 1 to 5 atmospheres," *Symposium (International) on Combustion*, 27(1), pp. 1523-1529.
- [71] Westbrook, C. K., and Dryer, F. L., 1984, "Chemical kinetic modeling of hydrocarbon combustion," *Progress in Energy and Combustion Science*, 10(1), pp. 1-57.
- [72] Dagaut, P., Cathonnet, M., Boetiner, J. C., and Gaillard, F., 1987, "Kinetic Modeling of Propane Oxidation," *Combustion Science and Technology*, 56(1-3), pp. 23-63.
- [73] Glassman, I., Yetter, R. A., and Glumac, N. G., 2014, *Combustion*, Academic press.
- [74] Konnov, A. A., 2000, "Detailed reaction mechanism for small hydrocarbons combustion," <http://homepages.vub.ac.be/~akonnov/science/mechanism/main.html>.

- [75] Smith, G. P., Golden, D. M., Frenklach, M., Moriarty, N. W., Eiteneer, B., Goldenberg, M., Bowman, C. T., Hanson, R. K., Song, S., Gardiner, W. C., Lissianski, V. V., and Qin, Z., 2000, "GRI-Mech 3.0," http://www.me.berkeley.edu/gri_mech/.
- [76] Kim, K., and Shin, K. S., 2000, "Shock Tube and Modeling Study of the Ignition of Propane," *Bulletin of the Korean Chemical Society*, 22(3), pp. 303-307.
- [77] Qin, Z., Yang, H., and Gardiner Jr, W. C., 2001, "Measurement and modeling of shock-tube ignition delay for propene," *Combustion and Flame*, 124(1-2), pp. 246-254.
- [78] Burcat, A., and Radhakrishnan, K., 1985, "High temperature oxidation of propene," *Combustion and flame*, 60(2), pp. 157-169.
- [79] Tan, Y., Dagaut, P., Cathonnet, M., Claude Boettner, J., Sylvain Bachman, J., and Carlier, P., 1994, "Natural gas and blends oxidation and ignition: Experiments and modeling," *Symposium (International) on Combustion*, 25(1), pp. 1563-1569.
- [80] Tan, Y., Dagaut, P., Cathonnet, M., and Boettner, J. C., 1994, "Oxidation and Ignition of Methane-Propane and Methane-Ethane-Propane Mixtures: Experiments and Modeling," *Combustion Science and Technology*, 103(1-6), pp. 133-151.
- [81] Lamoureux, N., and Paillard, C. E., 2003, "Natural gas ignition delay times behind reflected shock waves: Application to modelling and safety," *Shock Waves*, 13(1), pp. 57-68.
- [82] Konnov, A. A., 2000, "Archived: Detailed reaction mechanism for small hydrocarbons combustion," <https://web.archive.org/web/20110706132600/http://homepages.vub.ac.be/~akonnov/science/mechanism/main.html>.
- [83] Curran, H. J., Gaffuri, P., Pitz, W. J., and Westbrook, C. K., 1998, "A Comprehensive Modeling Study of n-Heptane Oxidation," *Combustion and Flame*, 114(1-2), pp. 149-177.
- [84] Herzler, J., Jerig, L., and Roth, P., 2004, "Shock-Tube Study of the Ignition of Propane at Intermediate Temperatures and High Pressures," *Combustion Science and Technology*, 176(10), pp. 1627-1637.
- [85] Penyazkov, O. G., Ragothar, K. A., Dean, A. J., and Varatharajan, B., 2005, "Autoignition of propane-air mixtures behind reflected shock waves," *Proceedings of the Combustion Institute*, 30(2), pp. 1941-1947.
- [86] Huang, J., and Bushe, W. K., 2006, "Experimental and kinetic study of autoignition in methane/ethane/air and methane/propane/air mixtures under engine-relevant conditions," *Combustion and Flame*, 144(1-2), pp. 74-88.
- [87] Heyne, S., Roubaud, A., Ribaucour, M., Vanhove, G., Minetti, R., and Favrat, D., 2008, "Development of a natural gas reaction mechanism for engine simulations based on rapid compression machine experiments using a multi-objective optimisation strategy," *Fuel*, 87(13-14), pp. 3046-3054.

- [88] de Vries, J., and Petersen, E. L., 2007, "Autoignition of methane-based fuel blends under gas turbine conditions," *Proceedings of the Combustion Institute*, 31(2), pp. 3163-3171.
- [89] Healy, D., Curran, H. J., Simmie, J. M., Kalitan, D. M., Zinner, C. M., Barrett, A. B., Petersen, E. L., and Bourque, G., 2008, "Methane/ethane/propane mixture oxidation at high pressures and at high, intermediate and low temperatures," *Combustion and Flame*, 155(3), pp. 441-448.
- [90] Healy, D., Curran, H. J., Dooley, S., Simmie, J. M., Kalitan, D. M., Petersen, E. L., and Bourque, G., 2008, "Methane/propane mixture oxidation at high pressures and at high, intermediate and low temperatures," *Combustion and Flame*, 155(3), pp. 451-461.
- [91] Rubtsov, N. M., Seplyarskii, B. S., Troshin, K. Y., Tsvetkov, G. I., and Chernysh, V. I., 2011, "High-speed colour cinematography of the spontaneous ignition of propane-air and n-pentane-air mixtures," *Mendeleviev Communications*, 21(1), pp. 31-33.
- [92] Huzayyin, A. S., Moneib, H. A., Shehatta, M. S., and Attia, A. M. A., 2008, "Laminar burning velocity and explosion index of LPG-air and propane-air mixtures," *Fuel*, 87(1), pp. 39-57.
- [93] Wu, C. K., and Law, C. K., 1984, "On the determination of laminar flame speeds from stretched flames," *Symposium (International) on Combustion*, 20(1), pp. 1941-1949.
- [94] Liu, G., Ye, Z., and Sohrab, S., 1986, "On radiative cooling and temperature profiles of counterflow premixed flames," *Combustion and flame*, 64(2), pp. 193-201.
- [95] Tsuji, H., and Yamaoka, I., 1982, "Structure and extinction of near-limit flames in a stagnation flow," *Symposium (International) on Combustion*, 19(1), pp. 1533-1540.
- [96] Ishizuka, S., and Law, C. K., 1982, "An experimental study on extinction and stability of stretched premixed flames," *Symposium (International) on Combustion*, 19(1), pp. 327-335.
- [97] Sato, J. i., 1982, "Effects of lewis number on extinction behavior of premixed flames in a stagnation flow," *Symposium (International) on Combustion*, 19(1), pp. 1541-1548.
- [98] Sohrab, S. H., Ye, Z. Y., and Law, C. K., 1985, "An experimental investigation on flame interaction and the existence of negative flame speeds," *Symposium (International) on Combustion*, 20(1), pp. 1957-1965.
- [99] Mizomoto, M., Asaka, Y., Ikai, S., and Law, C. K., 1985, "Effects of preferential diffusion on the burning intensity of curved flames," *Symposium (International) on Combustion*, 20(1), pp. 1933-1939.
- [100] Axelbaum, R. L., Law, C. K., and Flower, W. L., 1989, "Preferential diffusion and concentration modification in sooting counterflow diffusion flames," *Symposium (International) on Combustion*, 22(1), pp. 379-386.
- [101] Vandsburger, U., Kennedy, I., and Glassman, I., 1984, "Sooting Counterflow Diffusion Flames with Varying Oxygen Index," *Combustion Science and Technology*, 39(1-6), pp. 263-285.

- [102] Zhu, D. L., Egolfopoulos, F. N., and Law, C. K., 1989, "Experimental and numerical determination of laminar flame speeds of methane/(Ar, N₂, CO₂)-air mixtures as function of stoichiometry, pressure, and flame temperature," Symposium (International) on Combustion, 22(1), pp. 1537-1545.
- [103] Koert, D. N., and Cernansky, N. P., 1992, "A flow reactor for the study of homogeneous gas-phase oxidation of hydrocarbons at pressures up to 20 atm (2 MPa)," Measurement Science and Technology, 3(6), p. 607.
- [104] Koert, D. N., Miller, D. L., and Cernansky, N. P., 1992, "Results of reactivity mapping studies through the negative temperature coefficient region for propane at pressures from 5 to 15 atm," Energy & Fuels, 6(4), pp. 485-493.
- [105] Koert, D. N., Miller, D. L., and Cernansky, N. P., 1994, "Experimental studies of propane oxidation through the negative temperature coefficient region at 10 and 15 atmospheres," Combustion and Flame, 96(1-2), pp. 34-49.
- [106] Egolfopoulos, F. N., and Law, C. K., 1991, "An experimental and computational study of the burning rates of ultra-lean to moderately-rich H₂/O₂/N₂ laminar flames with pressure variations," Symposium (International) on Combustion, 23(1), pp. 333-340.
- [107] Vagelopoulos, C. M., Egolfopoulos, F. N., and Law, C. K., 1994, "Further considerations on the determination of laminar flame speeds with the counterflow twin-flame technique," Symposium (International) on Combustion, 25(1), pp. 1341-1347.
- [108] Vagelopoulos, C. M., and Egolfopoulos, F. N., 1998, "Direct experimental determination of laminar flame speeds," Symposium (International) on Combustion, 27(1), pp. 513-519.
- [109] Egolfopoulos, F. N., Zhang, H., and Zhang, Z., 1997, "Wall effects on the propagation and extinction of steady, strained, laminar premixed flames," Combustion and Flame, 109(1-2), pp. 237-252.
- [110] Davis, S. G., and Law, C. K., 1998, "Determination of and Fuel Structure Effects on Laminar Flame Speeds of C₁ to C₈ Hydrocarbons," Combustion Science and Technology, 140(1-6), pp. 427-449.
- [111] Holton, M. M., 2008, "Autoignition Delay Time Measurements for Natural Gas Fuel Components and their Mixtures," Master of Science MS Thesis, University of Maryland, College Park, MD.
- [112] Gokulakrishnan, P., Gaines, G., Currano, J., Klassen, M. S., and Roby, R. J., 2006, "Experimental and Kinetic Modeling of Kerosene-Type Fuels at Gas Turbine Operating Conditions," Journal of Engineering for Gas Turbines and Power, 129(3), pp. 655-663.
- [113] Gokulakrishnan, P., Gaines, G., Klassen, M. S., and Roby, R., 2007, "Autoignition of Aviation Fuels: Experimental and Modeling Study," 43rd AIAA/ASME/SAE/ASEE Joint Propulsion Conference & Exhibit, American Institute of Aeronautics and Astronautics.

- [114] Koert, D. N., 1991, "Effects of pressure on hydrocarbon oxidation chemistry," Ph.D Dissertation, Drexel University.
- [115] Lefebvre, A. H., Freeman, W., and Cowell, L., 1986, Spontaneous ignition delay characteristics of hydrocarbon fuel-air mixtures, Purdue University, School of Mechanical Engineering.
- [116] Holton, M. M., Gokulakrishnan, P., Klassen, M. S., Roby, R. J., and Jackson, G. S., 2010, "Autoignition Delay Time Measurements of Methane, Ethane, and Propane Pure Fuels and Methane-Based Fuel Blends," *Journal of Engineering for Gas Turbines and Power*, 132(9), pp. 091502-091502.
- [117] Horning, D. C., and Engineering, S. U. D. o. M., 2001, A Study of the High-temperature Autoignition and Thermal Decomposition of Hydrocarbons, Stanford University.
- [118] Gallagher, S. M., Curran, H. J., Metcalfe, W. K., Healy, D., Simmie, J. M., and Bourque, G., 2008, "A rapid compression machine study of the oxidation of propane in the negative temperature coefficient regime," *Combustion and Flame*, 153(1–2), pp. 316-333.
- [119] Gokulakrishnan, P., Fuller, C. C., Klassen, M. S., Joklik, R. G., Kochar, Y. N., Vaden, S. N., Lieuwen, T. C., and Seitzman, J. M., 2014, "Experiments and modeling of propane combustion with vitiation," *Combustion and Flame*(0).
- [120] Gray, B. F., and Felton, P. G., 1974, "Low-temperature oxidation in a stirred-flow reactor—I. Propane," *Combustion and Flame*, 23(3), pp. 295-304.
- [121] Barnard, J. A., and Harwood, B. A., 1974, "Physical factors in the study of the spontaneous ignition of hydrocarbons in static systems," *Combustion and Flame*, 22(1), pp. 35-42.
- [122] Ashmore, P. G., Tyler, B. J., and Wesley, T. A. B., 1967, "Experimental investigations of conductive and convective heat transfer in relation to thermal ignitions," *Symposium (International) on Combustion*, 11(1), pp. 1133-1140.
- [123] Fine, D. H., Gray, P., and Mackinven, R., 1969, "Some Consequences of the Rapid Admission of Gas to an Evacuated Vessel," *Nature*, 223(5204), pp. 393-394.
- [124] Cathonnet, M., Boettner, J. C., and James, H., 1981, "Experimental study and numerical modeling of high temperature oxidation of propane and n-butane," *Symposium (International) on Combustion*, 18(1), pp. 903-913.
- [125] Dagaut, P., Cathonnet, M., and Boettner, J. C., 1988, "Experimental study and kinetic modeling of propene oxidation in a jet stirred flow reactor," *The Journal of Physical Chemistry*, 92(3), pp. 661-671.
- [126] Gardiner Jr, W. C., 1984, *Combustion Chemistry*, Springer-Verlag, New York, NY.
- [127] Nenniger, J. E., 1983, "Polycyclic aromatic hydrocarbon production in a jet stirred combustor," Massachusetts Institute of Technology.

- [128] Nenniger, J. E., Kridiotis, A., Chomiak, J., Longwell, J. P., and Sarofim, A. F., 1985, "Characterization of a toroidal well stirred reactor," *Symposium (International) on Combustion*, 20(1), pp. 473-479.
- [129] Egolfopoulos, F. N., Cho, P., and Law, C. K., 1989, "Laminar flame speeds of methane-air mixtures under reduced and elevated pressures," *Combustion and Flame*, 76(3-4), pp. 375-391.
- [130] Peters, N., and Rogg, B., 1993, *Reduced Kinetic Mechanisms for Applications in Combustion Systems*, Springer-Verlag Heidelberg.
- [131] Dagaut, P., Cathonnet, M., and Boettner, J.-C., 1992, "Kinetic modeling of propane oxidation and pyrolysis," *International Journal of Chemical Kinetics*, 24(9), pp. 813-837.
- [132] Dagaut, P., Cathonnet, M., and Boettner, J.-C., 1992, "A Kinetic Modeling Study of Propene Oxidation in JSR and Flame," *Combustion Science and Technology*, 83(4-6), pp. 167-185.
- [133] Dagaut, P., Cathonnet, M., and Boettner, J.-c., 1991, "Kinetics of ethane oxidation," *International Journal of Chemical Kinetics*, 23(5), pp. 437-455.
- [134] Dagaut, P., Boettner, J.-C., and Cathonnet, M., 1991, "Methane Oxidation: Experimental and Kinetic Modeling Study," *Combustion Science and Technology*, 77(1-3), pp. 127-148.
- [135] Dagaut, P., Boettner, J.-C., and Cathonnet, M., 1990, "Ethylene pyrolysis and oxidation: A kinetic modeling study," *International Journal of Chemical Kinetics*, 22(6), pp. 641-664.
- [136] Zamansky, V. M., and Borisov, A. A., 1992, "Promotion of high-temperature self-ignition," *Progress in Energy and Combustion Science*, 18(4), pp. 297-325.
- [137] Zamansky, V., and Borisov, A., 1989, "Mechanism and Promotion of Self-Ignition of Alternative Fuels," *Itogi nauki i tehniki. Seria: Kinetika. Kataliz*, 19.
- [138] Dagaut, P., Luche, J., and Cathonnet, M., 2001, "Reduction of NO by propane in a JSR at 1 atm: experimental and kinetic modeling," *Fuel*, 80(7), pp. 979-986.
- [139] Dagaut, P., Lecomte, F., Chevaller, S., and Cathonnet, M., 1998, "Experimental and Detailed Kinetic Modeling of Nitric Oxide Reduction by a Natural Gas Blend in Simulated Reburning Conditions," *Combustion Science and Technology*, 139(1), pp. 329-363.
- [140] Dagaut, P., and Hadj Ali, K., 2003, "Kinetics of oxidation of a LPG blend mixture in a JSR: experimental and modeling study," *Fuel*, 82(5), pp. 475-480.
- [141] Westbrook, C. K., and Dryer, F. L., 1981, "Simplified Reaction Mechanisms for the Oxidation of Hydrocarbon Fuels in Flames," *Combustion Science and Technology*, 27(1-2), pp. 31-43.
- [142] Norton, D. G., and Vlachos, D. G., 2004, "A CFD study of propane/air microflame stability," *Combustion and Flame*, 138(1-2), pp. 97-107.

- [143] Federici, J. A., and Vlachos, D. G., 2008, "A computational fluid dynamics study of propane/air microflame stability in a heat recirculation reactor," *Combustion and Flame*, 153(1–2), pp. 258-269.
- [144] Anetor, L., Osakue, E., and Odetunde, C., 2012, "Reduced Mechanism Approach of Modeling Premixed Propane-Air Mixture using Ansys Fluent," 16(1).
- [145] Leung, K. M., and Lindstedt, R. P., 1995, "Detailed Kinetic Modeling of C₁ - C₃ Alkane Diffusion Flames," *Combustion and Flame*, 102, pp. 129-160.
- [146] Koert, D. N., Pitz, W. J., Bozzelli, J. W., and Cernansky, N. P., "Chemical Kinetic Modeling of High-Pressure Propane Oxidation and Comparison to Experimental Results," Proc. Twenty-Sixth Symposium (International) in Combustion, The Combustion Institute, pp. 633-640.
- [147] Marinov, N. M., Castaldi, M. J., Melius, C. F., and Tsang, W., 1997, "Aromatic and polycyclic aromatic hydrocarbon formation in a premixed propane flame," *Combustion science and technology*, 128(1-6), pp. 295-342.
- [148] Davis, S. G., Law, C. K., and Wang, H., 1999, "Propene pyrolysis and oxidation kinetics in a flow reactor and laminar flames," *Combustion and Flame*, 119(4), pp. 375-399.
- [149] Haworth, D. C., Blint, R. J., Cuenot, B., and Poinot, T. J., 2000, "Numerical simulation of turbulent propane-air combustion with nonhomogeneous reactants," *Combustion and Flame*, 121(3), pp. 395-417.
- [150] Qin, Z., Lissianski, V. V., Yang, H., Gardiner, W. C., Davis, S. G., and Wang, H., 2000, "Combustion chemistry of propane: A case study of detailed reaction mechanism optimization," *Proceedings of the Combustion Institute*, 28(2), pp. 1663-1669.
- [151] Curran, H. J., Jayaweera, T. M., Pitz, W. J., and Westbrook, C. K., 2004, "A Detailed Modeling Study of Propane Oxidation," Western States Section of the Combustion Institute Davis, CA.
- [152] UCSD, Referenced 2014, "Chemical-Kinetic Mechanisms for Combustion Applications," <http://web.eng.ucsd.edu/mae/groups/combustion/mechanism.html>.
- [153] Petrova, M. V., and Williams, F. A., 2006, "A small detailed chemical-kinetic mechanism for hydrocarbon combustion," *Combustion and Flame*, 144(3), pp. 526-544.
- [154] Koutmos, P., Giannakis, G., and Marazioti, P., 2007, "A Global Oxidation Scheme for Propane-Air Combustion Suitable for Use Into Complex Reacting Flow Computations," *Engineering Transactions*; Vol 55, No 4 (2007).
- [155] Petersen, E. L., Kalitan, D. M., Simmons, S., Bourque, G., Curran, H. J., and Simmie, J. M., 2007, "Methane/propane oxidation at high pressures: Experimental and detailed chemical kinetic modeling," *Proceedings of the Combustion Institute*, 31(1), pp. 447-454.

- [156] Wang, H., You, X., Joshi, A. V., Davis, S. G., Laskin, A., Egolfopoulos, F. N., and Law, C. K., 2007, "USC Mech Version II: High-Temperature Combustion Reaction Model of H₂/CO/C₁-C₄ Compounds," http://ignis.usc.edu/USC_Mech_II.htm.
- [157] Bourque, G., Healy, D., Curran, H., Zinner, C., Kalitan, D., de Vries, J., Aul, C., and Petersen, E., 2009, "Ignition and Flame Speed Kinetics of Two Natural Gas Blends With High Levels of Heavier Hydrocarbons," *Journal of Engineering for Gas Turbines and Power*, 132(2).
- [158] Le Cong, T., and Dagaut, P., 2009, "Experimental and Detailed Modeling Study of the Effect of Water Vapor on the Kinetics of Combustion of Hydrogen and Natural Gas, Impact on NO_x," *Energy & Fuels*, 23(2), pp. 725-734.
- [159] Healy, D., Kalitan, D. M., Aul, C. J., Petersen, E. L., Bourque, G., and Curran, H. J., 2010, "Oxidation of C₁-C₅ Alkane Quinternary Natural Gas Mixtures at High Pressures," *Energy & Fuels*, 24(3), pp. 1521-1528.
- [160] Agafonov, G. L., Smirnov, V. N., and Vlasov, P. A., 2011, "Shock Tube and Modeling Study of Soot Formation During the Pyrolysis and Oxidation of a Number of Aliphatic and Aromatic Hydrocarbons," *Proceedings of the Combustion Institute*, 33, pp. 625-632.
- [161] Titova, N. S., Kuleshov, P. S., and Starik, A. M., 2011, "Kinetic Mechanism of Propane Ignition and Combustion in Air," *Combustion, Explosion, and Shock Waves*, 47(3), pp. 249-264.
- [162] Andreis, G. S. L., Gomes, R. S., and De Bertoli, A. L., 2012, "A Reduced Kinetic Mechanism for Propane Flames," *Thermal Engineering*, 11(1-2), pp. 37-43.
- [163] Metcalfe, W. K., Burke, S. M., Ahmed, S. S., and Curran, H. J., 2013, "A Hierarchical and Comparative Kinetic Modeling Study of C₁ - C₂ Hydrocarbon and Oxygenated Fuels," *International Journal of Chemical Kinetics*, 45(10), pp. 638-675.
- [164] McLain, A. G., and Jachimowski, C. J., 1977, "Chemical Kinetic Modeling of Propane Oxidation Behind Shock Waves," N. A. S. Administration, ed., NASA Langley Research Center, Washington, D. C., p. 33.
- [165] Dagaut, P., Cathonnet, M., and Boettner, J. C., 1988, "Experimental Study and Kinetic Modeling of Propene Oxidation in a Jet Stirred Flow," *Journal of Physical Chemistry*, 92, pp. 661-671.
- [166] Smyth, K. C., Tjossem, P. J. H., Hamins, A., and Miller, J. H., 1990, "Concentration measurements of OH· and equilibrium analysis in a laminar methane-air diffusion flame," *Combustion and Flame*, 79(3-4), pp. 366-380.
- [167] Smyth, K. C., Miller, J. H., Dorfman, R. C., Mallard, W. G., and Santoro, R. J., 1985, "Soot Inception in a Methane/Air Diffusion Flame as Characterized by Detailed Species Profiles," *Combustion and Flame*, 62, pp. 157-181.

- [168] Miller, H., and Taylor, P. M., 1987, "Methyl Radical Concentrations and Production Rates in a Faminar Methane/Air Diffusion Flame," *Combustion Science and Technology*, 52(1-3), pp. 139-149.
- [169] Smyth, K. C., and Tjossem, P. J. H., 1991, "Relative H-atom and O-atom concentration measurements in a laminar, methane/air diffusion flame," *Symposium (International) on Combustion*, 23(1), pp. 1829-1837.
- [170] Norton, T. S., and Smyth, K. C., 1991, "Laser-Induced Fluorescence of $\text{CH} \cdot$ in a Laminar CH_4/Air Diffusion Flame: Implications for Diagnostic Measurements and Analysis of Chemical Rates," *Combustion Science and Technology*, 76(1-3), pp. 1-20.
- [171] Tsuji, H., and Yamaoka, I., 1971, "Structure analysis of counterflow diffusion flames in the forward stagnation region of a porous cylinder," *Symposium (International) on Combustion*, 13(1), pp. 723-731.
- [172] Tsuji, H., and Yamaoka, I., 1969, "The structure of counterflow diffusion flames in the forward stagnation region of a porous cylinder," *Symposium (International) on Combustion*, 12(1), pp. 997-1005.
- [173] Glarborg, P., Miller, J. A., and Kee, R. J., 1986, "Kinetic modeling and sensitivity analysis of nitrogen oxide formation in well-stirred reactors," *Combustion and Flame*, 65(2), pp. 177-202.
- [174] Kee, R. J., Miller, J. A., Evans, G. H., and Dixon-Lewis, G., 1989, "A computational model of the structure and extinction of strained, opposed flow, premixed methane-air flames," *Symposium (International) on Combustion*, 22(1), pp. 1479-1494.
- [175] Sloane, T. M., 1989, "Ignition and Flame Propagation Modeling With an Improved Methane Oxidation Mechanism," *Combustion Science and Technology*, 63(4-6), pp. 287-313.
- [176] Egolfopoulos, F. N., Zhu, D. L., and Law, C. K., 1991, "Experimental and numerical determination of laminar flame speeds: Mixtures of C_2 -hydrocarbons with oxygen and nitrogen," *Symposium (International) on Combustion*, 23(1), pp. 471-478.
- [177] Hoffman, J. S., Lee, W., Litzinger, T. A., Santavicca, D. A., and Pitz, W. J., 1991, "Oxidation of Propane at Elevated Pressures: Experiments and Modelling," *Combustion Science and Technology*, 77(1-3), pp. 95-125.
- [178] Hori, M., Matsunaga, N., Marinov, N., William, P., and Charles, W., 1998, "An experimental and kinetic calculation of the promotion effect of hydrocarbons on the $\text{NO}-\text{NO}_2$ conversion in a flow reactor," *Symposium (International) on Combustion*, 27(1), pp. 389-396.
- [179] Vermeer, D. J., Meyer, J. W., and Oppenheim, A. K., 1972, "Auto-ignition of hydrocarbons behind reflected shock waves," *Combustion and Flame*, 18(3), pp. 327-336.
- [180] Coats, C. M., and Williams, A., 1979, "Investigation of the ignition and combustion of n-heptane-oxygen mixtures," *Symposium (International) on Combustion*, 17(1), pp. 611-621.

- [181] Burcat, A., Farmer, R. F., and Matula, R. A., 1981, Symposium (International) on Shock Tubes and Waves, 13, pp. 826-833.
- [182] Ciezki, H. K., and Adomeit, G., 1993, "Shock-tube investigation of self-ignition of n-heptane-air mixtures under engine relevant conditions," *Combustion and Flame*, 93(4), pp. 421-433.
- [183] Ciezki, H. K., and Adomeit, G., 1987, Symposium (International) on Shock Tubes and Waves, 16, pp. 481-486.
- [184] Chakir, A., Bellimam, M., Boettner, J. C., and Cathonnet, M., 1992, "Kinetic study of n-heptane oxidation," *International Journal of Chemical Kinetics*, 24(4), pp. 385-410.
- [185] Dagaut, P., Reuillon, M., and Cathonnet, M., 1995, "Experimental study of the oxidation of n-heptane in a jet stirred reactor from low to high temperature and pressures up to 40 atm," *Combustion and Flame*, 101(1-2), pp. 132-140.
- [186] Dagaut, P., Reuillon, M., and Cathonnet, M., 1993, "High Pressure Oxidation of Liquid Fuels From Low to High Temperature. 1. n-Heptane and iso-Octane," *Combustion Science and Technology*, 95(1-6), pp. 233-260.
- [187] Vermeersch, M., Held, T., Stein, Y., and Dryer, F., 1991, "Autoignition Chemistry Studies of n-Butane in a Variable Pressure Flow Reactor," SAE Technical Paper(912316).
- [188] Callahan, C. V., Held, T. J., Dryer, F. L., Minetti, R., Ribaucour, M., Sochet, L. R., Faravelli, T., Gaffuri, P., and Rani, E., 1996, "Experimental data and kinetic modeling of primary reference fuel mixtures," *Symposium (International) on Combustion*, 26(1), pp. 739-746.
- [189] Blin-Simiand, N., Rigny, R., Viossat, V., Circan, S., and Sahetchian, K., 1993, "Autoignition of Hydrocarbon/Air Mixtures in a CFR Engine: Experimental and Modeling Study," *Combustion Science and Technology*, 88(5-6), pp. 329-348.
- [190] Sahetchian, K. A., Rigny, R., and Circan, S., 1991, "Identification of the hydroperoxide formed by isomerization reactions during the oxidation of n-heptane in a reactor and CFR engine," *Combustion and Flame*, 85(3-4), pp. 511-514.
- [191] Sahetchian, K. A., Blin, N., Rigny, R., Seydi, A., and Murat, M., 1990, "The oxidation of n-butane and n-heptane in a CFR engine. Isomerization reactions and delay of autoignition," *Combustion and Flame*, 79(3-4), pp. 242-249.
- [192] Sahetchian, K. A., Heiss, A., Rigny, R., and Ben-aim, R. I., 1982, "Determination of the gas-phase decomposition rate constants of heptyl-1 and heptyl-2 hydroperoxides C₇H₁₅OOH," *International Journal of Chemical Kinetics*, 14(12), pp. 1325-1337.
- [193] Leppard, W., 1992, "The Autoignition Chemistries of Primary Reference Fuels, Olefin/Paraffin Binary Mixtures, and Non-Linear Octane Blending," SAE Technical Paper(922325).

- [194] Cavaliere, A., Ciajolo, A., D'Anna, A., Mercogliano, R., and Ragucci, R., 1993, "Autoignition of n-heptane and n-tetradecane in engine-like conditions," *Combustion and Flame*, 93(3), pp. 279-286.
- [195] Li, H., Prabhu, S., Miller, D., and Cernansky, N., 1994, "Autoignition Chemistry Studies on Primary Reference Fuels in a Motored Engine," SAE Technical Paper(942062).
- [196] Cox, A., Griffiths, J. F., Mohamed, C., Curran, H. J., Pitz, W. J., and Westbrook, C. K., 1996, "Extents of alkane combustion during rapid compression leading to single-and two-stage ignition," *Symposium (International) on Combustion*, 26(2), pp. 2685-2692.
- [197] Griffiths, J. F., Hughes, K. J., Schreiber, M., and Poppe, C., 1994, "A unified approach to the reduced kinetic modeling of alkane combustion," *Combustion and Flame*, 99(3-4), pp. 533-540.
- [198] Griffiths, J. F., Halford-Maw, P. A., and Rose, D. J., 1993, "Fundamental features of hydrocarbon autoignition in a rapid compression machine," *Combustion and Flame*, 95(3), pp. 291-306.
- [199] Minetti, R., Carlier, M., Ribaucour, M., Therssen, E., and Sochet, L. R., 1995, "A rapid compression machine investigation of oxidation and auto-ignition of n-Heptane: Measurements and modeling," *Combustion and Flame*, 102(3), pp. 298-309.
- [200] Sun, C. J., Sung, C. J., Wang, H., and Law, C. K., 1996, "On the structure of nonsooting counterflow ethylene and acetylene diffusion flames," *Combustion and Flame*, 107(4), pp. 321-335.
- [201] Wang, H., and Frenklach, M., 1997, "A detailed kinetic modeling study of aromatics formation in laminar premixed acetylene and ethylene flames," *Combustion and Flame*, 110(1-2), pp. 173-221.
- [202] Tsang, W., and Herron, J. T., 1991, "Chemical Kinetic Data Base for Propellant Combustion I. Reactions Involving NO, NO₂, HNO, HNO₂, HCN and N₂O," *Journal of Physical and Chemical Reference Data*, 20(4), pp. 609-663.
- [203] Tsang, W., 1990, "Chemical Kinetic Data Base for Combustion Chemistry Part 4. Isobutane," *Journal of Physical and Chemical Reference Data*, 19(1), pp. 1-68.
- [204] Tsang, W., 1988, "Chemical Kinetic Data Base for Combustion Chemistry. Part 3: Propane," *Journal of Physical and Chemical Reference Data*, 17(2), pp. 887-951.
- [205] Wang, H., Hahn, T. O., Sung, C. J., and Law, C. K., 1996, "Detailed oxidation kinetics and flame inhibition effects of chloromethane," *Combustion and Flame*, 105(3), pp. 291-307.
- [206] Sun, C. J., Sung, C. J., He, L., and Law, C. K., 1999, "Dynamics of weakly stretched flames: quantitative description and extraction of global flame parameters," *Combustion and Flame*, 118(1-2), pp. 108-128.

- [207] Kwon, S., Tseng, L. K., and Faeth, G. M., 1992, "Laminar burning velocities and transition to unstable flames in H₂/O₂/N₂ and C₃H₈/O₂/N₂ mixtures," *Combustion and Flame*, 90(3–4), pp. 230-246.
- [208] Davis, S. G., Law, C. K., and Wang, H., 1998, "An experimental and kinetic modeling study of propyne oxidation," *Symposium (International) on Combustion*, 27(1), pp. 305-312.
- [209] Curran, H., Simmie, J. M., Dagaut, P., Voisin, D., and Cathonnet, M., 1996, "The ignition and oxidation of allene and propyne: Experiments and kinetic modeling," *Symposium (International) on Combustion*, 26(1), pp. 613-620.
- [210] Kennel, C., Göttgens, J., and Peters, N., 1991, "The basic structure of lean propane flames," *Symposium (International) on Combustion*, 23(1), pp. 479-485.
- [211] Leung, K. M., Lindstedt, R. P., and Jones, W. P., 1991, "A simplified reaction mechanism for soot formation in nonpremixed flames," *Combustion and Flame*, 87(3–4), pp. 289-305.
- [212] Lindstedt, P., 1994, "Simplified Soot Nucleation and Surface Growth Steps for Non-Premixed Flames," *Soot Formation in Combustion*, H. Bockhorn, ed., Springer Berlin Heidelberg, pp. 417-441.
- [213] Petersen, E. L., Hall, J. M., Smith, S. D., de Vries, J., Amadio, A. R., and Crofton, M. W., 2007, "Ignition of Lean Methane-Based Fuel Blends at Gas Turbine Pressures," *Journal of Engineering for Gas Turbines and Power*, 129(4), pp. 937-944.
- [214] Ó Conaire, M., Curran, H. J., Simmie, J. M., Pitz, W. J., and Westbrook, C. K., 2004, "A comprehensive modeling study of hydrogen oxidation," *International Journal of Chemical Kinetics*, 36(11), pp. 603-622.
- [215] Curran, H. J., Fischer, S. L., and Dryer, F. L., 2000, "The reaction kinetics of dimethyl ether. II: Low-temperature oxidation in flow reactors," *International Journal of Chemical Kinetics*, 32(12), pp. 741-759.
- [216] Curran, H. J., Gaffuri, P., Pitz, W. J., and Westbrook, C. K., 2002, "A comprehensive modeling study of iso-octane oxidation," *Combustion and Flame*, 129(3), pp. 253-280.
- [217] Davis, S. G., Joshi, A. V., Wang, H., and Egolfopoulos, F., 2005, "An optimized kinetic model of H₂/CO combustion," *Proceedings of the Combustion Institute*, 30(1), pp. 1283-1292.
- [218] Laskin, A., Wang, H., and Law, C. K., 2000, "Detailed kinetic modeling of 1,3-butadiene oxidation at high temperatures," *International Journal of Chemical Kinetics*, 32(10), pp. 589-614.
- [219] Dagaut, P., 2002, "On the kinetics of hydrocarbons oxidation from natural gas to kerosene and diesel fuel," *Physical Chemistry Chemical Physics*, 4(11), pp. 2079-2094.
- [220] Higgin, R. M. R., and Williams, A., 1969, "A shock-tube investigation of the ignition of lean methane and n-butane mixtures with oxygen," *Symposium (International) on Combustion*, 12(1), pp. 579-590.

- [221] Zellner, R. E., Niemitz, K. J., Warnatz, J., and Gardiner, W. C., 1983, "Hydrocarbon induced acceleration of methane-air ignition," *Flames, lasers, and reactive systems*(A 84-28387 12-25). New York, American Institute of Aeronautics and Astronautics, Inc., 1983, 80, pp. 252-272.
- [222] Goy, C., Moran, A., and Thomas, G., "Autoignition characteristics of gaseous fuels at representative gas turbine conditions," *Proc. ASME Turbo Expo 2001: Power for Land, Sea, and Air*, American Society of Mechanical Engineers, pp. V002T002A018-V002T002A018.
- [223] Kim, H., Lim, Y., Min, K., and Lee, D., 2002, "Investigation of autoignition of propane and n-butane blends using a rapid compression machine," *KSME International Journal*, 16(8), pp. 1127-1134.
- [224] Gersen, S., Anikin, N. B., Mokhov, A. V., and Levinsky, H. B., 2008, "Ignition properties of methane/hydrogen mixtures in a rapid compression machine," *International Journal of Hydrogen Energy*, 33(7), pp. 1957-1964.
- [225] Herzler, J., and Naumann, C., 2009, "Shock-tube study of the ignition of methane/ethane/hydrogen mixtures with hydrogen contents from 0% to 100% at different pressures," *Proceedings of the Combustion Institute*, 32(1), pp. 213-220.
- [226] Naydenova, I., Nullmeier, M., Warnatz, J., and Vlasov, P. A., 2004, "Detailed Kinetic Modeling of Soot Formation During Shock-Tube Pyrolysis of C₆H₆: Direct Comparison With The Results of Time-Resolved Laser-Induced Incandescence (LII) and CW-Laser Extinction Measurements," *Combustion Science and Technology*, 176(10), pp. 1667-1703.
- [227] Richter, H., Granata, S., Green, W. H., and Howard, J. B., 2005, "Detailed modeling of PAH and soot formation in a laminar premixed benzene/oxygen/argon low-pressure flame," *Proceedings of the Combustion Institute*, 30(1), pp. 1397-1405.
- [228] Skjøth-Rasmussen, M. S., Glarborg, P., Østberg, M., Johannessen, J. T., Livbjerg, H., Jensen, A. D., and Christensen, T. S., 2004, "Formation of polycyclic aromatic hydrocarbons and soot in fuel-rich oxidation of methane in a laminar flow reactor," *Combustion and Flame*, 136(1-2), pp. 91-128.
- [229] Frenklach, M., and Warnatz, J., 1987, "Detailed Modeling of PAH Profiles in a Sooting Low-Pressure Acetylene Flame," *Combustion Science and Technology*, 51(4-6), pp. 265-283.
- [230] Frenklach, M., Gardiner, W. C., Stein, S. E., Clary, D. W., and Yuan, T., 1986, "Mechanism of Soot Formation in Acetylene-Oxygen Mixtures," *Combustion Science and Technology*, 50(1-3), pp. 79-115.
- [231] Correa, C., Niemann, H., Schramm, B., and Warnatz, J., 2000, "Reaction mechanism reduction for higher hydrocarbons by the ILDM method," *Proceedings of the Combustion Institute*, 28(2), pp. 1607-1614.
- [232] Lifshitz, A., and Frenklach, M., 1975, "Mechanism of the high temperature decomposition of propane," *The Journal of Physical Chemistry*, 79(7), pp. 686-692.

- [233] Borisov, A., Knorre, V., Pchel'nikov, A., Skachkov, G., and Troshin, K. Y., 2000, "Ignition of propane-air mixtures in a wide range of temperatures," *Khim. Fiz.*, 19, pp. 68-73.
- [234] Horning, D. C., Davidson, D. F., and Hanson, R. K., 2002, "Study of the High-Temperature Autoignition of n-Alkane/O/Ar Mixtures," *Journal of Propulsion and Power*, 18(2), pp. 363-371.
- [235] Kosarev, I. N., Aleksandrov, N. L., Kindysheva, S. V., Starikovskaia, S. M., and Starikovskii, A. Y., 2009, "Kinetics of ignition of saturated hydrocarbons by nonequilibrium plasma: C₂H₆- to C₅H₁₂-containing mixtures," *Combustion and Flame*, 156(1), pp. 221-233.
- [236] Dautov, N., and Starik, A., 1997, "On the problem of choosing a kinetic scheme for the homogeneous reaction of methane with air," *Kinetics and Catalysis*, 38(2), pp. 185-208.
- [237] Starik, A. M., Kuleshov, P. S., and Titova, N. S., 2009, "Comprehensive analysis of combustion initiation in methane-air mixture by resonance laser radiation," *Journal of Physics D: Applied Physics*, 42(17), p. 175503.
- [238] Starik, A. M., Titova, N. S., and Yanovskii, L. S., 1999, "Kinetics of the oxidation of the products from the thermal destruction of C₃H₈ and n-C₄H₁₀ in the mixtures with air," *Kinetics and Catalysis*, 40(1), pp. 7-22.
- [239] Starik, A. M., Lukhovitskii, B. I., and Titova, N. S., 2007, "Mechanism of the initiation of combustion in CH₄(C₂H₂)/Air/O₃ mixtures by laser excitation of the O₃ molecules," *Kinetics and Catalysis*, 48(3), pp. 348-366.
- [240] Starik, A. M., Titova, N. S., Sharipov, A. S., and Kozlov, V. E., 2010, "Syngas Oxidation Mechanism," *Combustion, Explosion, and Shock Waves*, 46(5), pp. 491-506.
- [241] Kojima, S., 1994, "Detailed modeling of n-butane autoignition chemistry," *Combustion and Flame*, 99(1), pp. 87-136.
- [242] Mehl, M., Curran, H., Pitz, W., Dooley, S., and Westbrook, C., 2009, "Chemical Kinetic Modeling of Component Mixtures Relevant to Gasoline," *European Combustion Meeting*.
- [243] Galway, N., 2013, "Combustion Chemistry Center: Saudi Aramco Mechanism Release," http://www.nuigalway.ie/c3/Mechanism_release/frontmatter.html.
- [244] Faravelli, T., Frassoldati, A., and Ranzi, E., 2003, "Kinetic modeling of the interactions between NO and hydrocarbons in the oxidation of hydrocarbons at low temperatures," *Combustion and Flame*, 132(1-2), pp. 188-207.
- [245] ElKady, A. M., Evulet, A., Brand, A., Ursin, T. P., and Lynghjem, A., 2009, "Application of Exhaust Gas Recirculation in a DLN F-Class Combustion System for Postcombustion Carbon Capture," *Journal of Engineering for Gas Turbines and Power*, 131(3), pp. 034505-034505.
- [246] Guethe, F., Stankovic, D., Genin, F., Syed, K., and Winkler, D., 2011, "Flue Gas Recirculation of the Alstom Sequential Gas Turbine Combustor Tested at High Pressure," *ASME*

2011 Turbo Expo: Turbine Technical Conference and Exposition, American Society of Mechanical Engineers, Vancouver, British Columbia, Canada, p. 10.

[247] Mokhov, A. V., and Levinsky, H. B., 2000, "A LIF and cars investigation of upstream heat loss and flue-gas recirculation as NO_x control strategies for laminar, premixed natural-gas/air flames," *Proceedings of the Combustion Institute*, 28(2), pp. 2467-2474.

[248] Al-Qurashi, K., Lueking, A. D., and Boehman, A. L., 2011, "The deconvolution of the thermal, dilution, and chemical effects of exhaust gas recirculation (EGR) on the reactivity of engine and flame soot," *Combustion and Flame*, 158(9), pp. 1696-1704.

[249] Cavaliere, A., and de Joannon, M., 2004, "Mild Combustion," *Progress in Energy and Combustion Science*, 30(4), pp. 329-366.

[250] Amato, A., Seitzman, J. M., and Lieuwen, T. C., 2013, *Emissions from Oxyfueled or High-Exhaust Gas Recirculation Turbines*
Gas Turbine Emissions, Cambridge University Press.

[251] Fleck, B. A., Sobiesiak, A., and Becker, H. A., 2000, "Experimental and Numerical Investigation of the Novel Low NO_x CGRI Burner," *Combustion Science and Technology*, 161(1), pp. 89-112.

[252] Kalb, J. R., and Sattelmayer, T., 2004, "Lean Blowout Limit and NO_x Production of a Premixed Sub-ppm NO_x Burner With Periodic Recirculation of Combustion Products," *Journal of Engineering for Gas Turbines and Power*, 128(2), pp. 247-254.

[253] Benezech, L. J.-M., 2008, "Premixed hydrocarbon stagnation flames : experiments and simulations to validate combustion chemical-kinetic models," *Aeronautics*, California Institute of Technology, Pasadena, CA.

[254] Janicka, J., and Sadiki, A., 2005, "Large eddy simulation of turbulent combustion systems," *Proceedings of the Combustion Institute*, 30(1), pp. 537-547.

[255] Zhou, L. X., Hu, L. Y., and Wang, F., 2008, "Large-eddy simulation of turbulent combustion using different combustion models," *Fuel*, 87(13–14), pp. 3123-3131.

[256] Boudier, G., Gicquel, L. Y. M., and Poinso, T. J., 2008, "Effects of mesh resolution on large eddy simulation of reacting flows in complex geometry combustors," *Combustion and Flame*, 155(1–2), pp. 196-214.

[257] Wang, P., and Bai, X. S., 2005, "Large eddy simulation of turbulent premixed flames using level-set G-equation," *Proceedings of the Combustion Institute*, 30(1), pp. 583-591.

[258] Richards, K. J., Senecal, P. K., and Pomraning, E., 2012, "CONVERGE (Version 1.4.1)," CEI Software.

- [259] Roux, A., Reichstadt, S., Bertier, N., Gicquel, L., Vuillot, F., and Poinso, T., 2009, "Comparison of numerical methods and combustion models for LES of a ramjet," *Comptes Rendus Mécanique*, 337(6–7), pp. 352-361.
- [260] Gicquel, L. Y. M., and Roux, A., 2011, "LES to Ease Understanding of Complex Unsteady Combustion Features of Ramjet Burners," *Flow Turbulence Combust*, 87(2-3), pp. 449-472.
- [261] Ye, L., Pan, Y., Jiang, J., and Zhang, W., 2014, "A numerical study of the auto-ignition temperatures of CH₄–Air, C₃H₈–Air, CH₄–C₃H₈–Air and CH₄–CO₂–Air mixtures," *Journal of Loss Prevention in the Process Industries*, 29, pp. 85-91.
- [262] Werle, S., 2008, "Investigation of the ignition of gas in the oxidizer at a high temperature," *Politechnika Slaska Instytut Techniki Cieplnej*.
- [263] Depcik, C., Mangus, M., and Ragone, C., 2014, "Ozone-Assisted Combustion—Part I: Literature Review and Kinetic Study Using Detailed n-Heptane Kinetic Mechanism," *Journal of Engineering for Gas Turbines and Power*, 136(9).
- [264] Heywood, J. B., 1988, *Internal Combustion Engine Fundamentals*, McGraw-Hill.
- [265] Agarwal, D., Singh, S. K., and Agarwal, A. K., 2011, "Effect of Exhaust Gas Recirculation (EGR) on performance, emissions, deposits and durability of a constant speed compression ignition engine," *Applied Energy*, 88(8), pp. 2900-2907.
- [266] Abd-Alla, G. H., 2002, "Using exhaust gas recirculation in internal combustion engines: a review," *Energy Conversion and Management*, 43(8), pp. 1027-1042.
- [267] Angrill, O., Geitlinger, H., Streibel, T., Suntz, R., and Bockhorn, H., "Influence of exhaust gas recirculation on soot formation in diffusion flames," *Proc. Proceedings of the Combustion Institute*, pp. 2643-2649.
- [268] Selim, M. Y. E., 2003, "Effect of exhaust gas recirculation on some combustion characteristics of dual fuel engine," *Energy Conversion and Management*, 44(5), pp. 707-721.
- [269] Jangi, M., Lucchini, T., D'Errico, G., and Bai, X.-S., "Effects of EGR on the structure and emissions of diesel combustion," *Proc. Proceedings of the Combustion Institute*, pp. 3091-3098.
- [270] Nandi, S., and Mulemane, A., 2009, "Evaluating the EGR Distribution Effectiveness of Intake Manifolds by CFD Technique," *SAE International*.
- [271] Galloni, E., Fontana, G., and Palmaccio, R., 2012, "Numerical analyses of EGR techniques in a turbocharged spark-ignition engine," *Applied Thermal Engineering*, 39(0), pp. 95-104.
- [272] Siewert, R. M., Krieger, R. B., Huebler, M. S., Baruah, P. C., Khalighi, B., and Wesslau, M., 2001, "Modifying an Intake Manifold to Improve Cylinder-to-Cylinder EGR Distribution in a DI Diesel Engine Using Combined CFD and Engine Experiments," *SAE International Fall Fuels & Lubricants Meeting & Exhibition*, SAE, San Antonio, TX.

- [273] Partridge, W. P., Lewis, S. A., Ruth, M. J., Muntean, G. G., Smith, R. C., and Stang, J. H., 2002, "Resolving EGR Distribution and Mixing," SAE Powertrain & Fluid Systems Conference & Exhibit, SAE International.
- [274] Morimoto, S. S., Kawabata, Y., Sakurai, T., and Amano, T., 2001, "Operating Characteristics of a Natural Gas-Fired Homogeneous Charge Compression Ignition Engine (Performance Improvement Using EGR)," SAE 2001 World Congress, SAE International.
- [275] Jang, J., Lee, Y., Cho, C., Woo, Y., and Bae, C., 2013, "Improvement of DME HCCI engine combustion by direct injection and EGR," *Fuel*, 113(0), pp. 617-624.
- [276] Sjöberg, M., and Dec, J. E., "Effects of EGR and its constituents on HCCI autoignition of ethanol," *Proc. Proceedings of the Combustion Institute*, pp. 3031-3038.
- [277] Fang, Q., Fang, J., Zhuang, J., and Huang, Z., 2012, "Influences of pilot injection and exhaust gas recirculation (EGR) on combustion and emissions in a HCCI-DI combustion engine," *Applied Thermal Engineering*, 48(0), pp. 97-104.
- [278] Tominaga, R., Morimoto, S. S., Kawabata, Y., Matsuo, S., and Amano, T., 2004, "Effects of Heterogeneous EGR on the Natural Gas Fueled HCCI Engine Using Experiments, CFD and Detailed Kinetics," SAE 2004 World Congress & Exhibition, SAE International.
- [279] Jiménez-Espadafor, F. J., Garcia, M. T., Herrero, J. A. C., and Villanueva, J. A. B., 2009, "Effect of Turbulence and External Exhaust Gas Recirculation on HCCI Combustion Mode and Exhaust Emissions," *Energy & Fuels*, 23(9), pp. 4295-4303.
- [280] Fuster, D., Bagué, A., Boeck, T., Le Moyne, L., Leboissetier, A., Popinet, S., Ray, P., Scardovelli, R., and Zaleski, S., 2009, "Simulation of primary atomization with an octree adaptive mesh refinement and VOF method," *International Journal of Multiphase Flow*, 35(6), pp. 550-565.
- [281] Langness, C., Mangus, M., and Depcik, C., 2014, "Construction, Instrumentation, and Implementation of a Low Cost, Single-Cylinder Compression Ignition Engine Test Cell," SAE 2014 World Congress & Exhibition, Society of Automotive Engineers, Detroit, MI, USA, p. 14.
- [282] Ragone, C., 2012, "Emission Reduction and Assisted Combustion Strategies for Compression Ignition Engines with Subsequent Testing on a Single-Cylinder Engine," Master of Science, University of Kansas, Lawrence, KS.
- [283] Software, C., 2014, "CONVERGE CFD Software," <http://www.ceisoftware.in/cei-data-files/Converge.htm>
- [284] Benelli, G., De Michele, G., Cossalter, V., Da Lio, M., and Rossi, G., 1992, "Twenty-Fourth Symposium on Combustion Simulation of large non-linear thermo-acoustic vibrations in a pulsating combustor," *Symposium (International) on Combustion*, 24(1), pp. 1307-1313.
- [285] Zhonghua, W., 2007, "Thesis Summary: Mathematical Modeling of Pulse Combustion and its Applications to Innovative Thermal Drying Techniques," *Drying Technology*, 25(5), pp. 941-942.

- [286] Qian, Y. F., Xu, Y. Y., and Xu, T. H., 2013, "Combustion Characteristics of a Helmholtz-Type Valveless Self-Excited Pulse Combustor," *Applied Mechanics and Materials*, pp. 1719-1722.
- [287] Ponizy, B., and Wojcicki, S., 1985, "On modeling of pulse combustors," *Symposium (International) on Combustion*, 20(1), pp. 2019-2024.
- [288] Keller, J. O., Barr, P. K., Bramlette, T. T., Evens, L. J., and Marchant, R. N., 1989, "Pulse Combustion: Demonstration of the Characteristic Mixing Time in a Commercial Burner," *Combustion Science and Technology*, 66(1-3), pp. 127-137.
- [289] Wan, Q., Roberts, W. L., and Kuznetsov, A. V., 2005, "Computational analysis of the feasibility of a micro-pulsejet," *International Communications in Heat and Mass Transfer*, 32(1-2), pp. 19-26.
- [290] Geng, T., Zheng, F., Kuznetsov, A., Roberts, W., and Paxson, D., 2010, "Comparison Between Numerically Simulated and Experimentally Measured Flowfield Quantities Behind a Pulsejet," *Flow Turbulence Combust*, 84, pp. 653-667.
- [291] Isac, J. K. R., Mohanraj, L., Sai, E. S., and Kannan, V. K., 2014, "Numerical simulation of a hydrocarbon fuelled valveless pulsejet," *Propulsion and Power Research*, 3(2), pp. 90-95.
- [292] Möller, S.-I., and Lindholm, A., 1999, "Theoretical and Experimental Investigation of the Operating Characteristics of a Helmholtz Type Pulse Combustor due to Changes in the Inlet Geometry," *Combustion Science and Technology*, 149(1-6), pp. 389-406.
- [293] Meng, X., de Jong, W., and Kudra, T., 2016, "A state-of-the-art review of pulse combustion: Principles, modeling, applications and R&D issues," *Renewable and Sustainable Energy Reviews*, 55, pp. 73-114.
- [294] Wang, Y., Dong, Q., and Wang, P., 2015, "Numerical Investigation on Fluid Flow in a 90-Degree Curved Pipe with Large Curvature Ratio," *Mathematical Problems in Engineering*, 2015, p. 12.
- [295] Dutta, P., Saha, S. K., Nandi, N., and Pal, N., 2016, "Numerical study on flow separation in 90° pipe bend under high Reynolds number by k-ε modelling," *Engineering Science and Technology, an International Journal*.
- [296] COMSOL, 2016, "COMSOL Multiphysics 5.2 - Flow Through a Pipe Elbow," https://www.comsol.com/model/download/268231/models.cfd.pipe_elbow.pdf.
- [297] Kim, J., Yadav, M., and Kim, S., 2014, "Characteristics of Secondary Flow Induced by 90-Degree Elbow in Turbulent Pipe Flow," *Engineering Applications of Computational Fluid Mechanics*, 8(2), pp. 229-239.
- [298] Kalpakli, A., 2012, "Experimental study of turbulent flows through pipe bends," *Royal Institute of Technology, Stockholm, Sweden*.

- [299] Jayakumar, J. S., Mahajani, S. M., Mandal, J. C., Iyer, K. N., and Vijayan, P. K., 2010, "CFD analysis of single-phase flows inside helically coiled tubes," *Computers & Chemical Engineering*, 34(4), pp. 430-446.
- [300] Homicz, G. F., 2004, *Computational fluid dynamic simulations of pipe elbow flow*, United States. Department of Energy.
- [301] Ilori, O. M., Mao, X., and Jaworski, A. J., 2015, "CFD study of oscillatory flow through 90° bends of thermoacoustic devices," *Proceedings of ICR2015*.
- [302] Wee, S. T., Hann, D. B., Abakr, Y. A., and Riley, P., 2012, "PIV wave propagation investigation of non-linear losses through 90 degree bends in a thermoacoustic engine's feedback loop," *AIP Conference Proceedings*, 1440(1), pp. 1092-1098.
- [303] Dean, W. R., 1928, "LXXII. The stream-line motion of fluid in a curved pipe (Second paper)," *The London, Edinburgh, and Dublin Philosophical Magazine and Journal of Science*, 5(30), pp. 673-695.
- [304] Dean, W. R., 1927, "XVI. Note on the motion of fluid in a curved pipe," *The London, Edinburgh, and Dublin Philosophical Magazine and Journal of Science*, 4(20), pp. 208-223.
- [305] Sudo, K., Sumida, M., and Hibara, H., 1998, "Experimental investigation on turbulent flow in a circular-sectioned 90-degree bend," *Experiments in Fluids*, 25(1), pp. 42-49.
- [306] DATAQ, 2014, "DI-149 8-Channel USB Data Acquisition Starter Kit User's Manual," DATAQ Instruments, Inc., Akron, OH, p. 30.
- [307] Freescale Semiconductor, I., 2010, "MPX5050 Data Sheet - Integrated Silicon Pressure Sensor On-Chip Signal Conditioned, Temperature Compensated and Calibrated," p. 18.
- [308] Freescale Semiconductor, I., 2015, "MPXV7002 Data Sheet - MPXV7002 Integrated Silicon Pressure Sensor On-Chip Signal Conditioned, Temperature Compensated and Calibrated," p. 12.
- [309] Scientific, S., "800024 Instruction Manual - 4-Channel Datalogging Thermometer," p. 7.
- [310] Harries, D., and Heer, B., 1993, *Basic Blacksmithing: An Introduction to Toolmaking with Locally Available Materials*, Intermediate Technology.
- [311] Richardson, M. T., 1888, *Practical Blacksmithing*, M.T. Richardson Company.
- [312] Bailey, A. R., 1960, *A Textbook of Metallurgy*, Macmillan.
- [313] Verhoeven, J. D., 2007, *Steel Metallurgy for the Non-Metallurgist*, ASM International.
- [314] Totten, G. E., 2006, *Steel Heat Treatment: Metallurgy and Technologies*, Taylor & Francis.
- [315] Bergman, T. L., Incropera, F. P., DeWitt, D. P., and Lavine, A. S., 2011, *Fundamentals of Heat and Mass Transfer*, Wiley.

[316] Jomaas, G., 2008, "Propagation and stability of expanding spherical flames," 3324293 Ph.D., Princeton University, Ann Arbor.

[317] Ishizuka, S., Miyasaka, K., and Law, C. K., 1982, "Effects of heat loss, preferential diffusion, and flame stretch on flame-front instability and extinction of propane/air mixtures," *Combustion and Flame*, 45(0), pp. 293-308.

[318] Gluhareff, E. M., 1990, "Private Communication on Design and Manufacturing of the G8 Family of Pressure Jet Engines," R. Barrett, ed. Hesperia, CA.

[319] Martens, S., 2003, "Shelf truncated chevron exhaust nozzle for reduction of exhaust noise and infrared (IR) signature," Google Patents.

[320] Alec, D. Y., Geoffrey, M. L., Westley, R., End, W., and Lane, W., 1964, "Jet noise suppression means," Google Patents.

[321] Barter, J. W., Brausch, J. F., Hoff, G. E., and Janardan, B. A., 1999, "Chevron exhaust nozzle," Google Patents.